Transient behavior and role of barriers in the North Chile - South Peru seismic gap

Jorge Jara

Communauté
UNIVERSITÉ Grenoble Alpes

THÈSE

Pour obtenir le grade de

DOCTEUR DE LA

COMMUNAUTE UNIVERSITÉ GRENOBLE ALPES

Spécialité : **Terre Solide (CETSOL)**

Arrêté ministériel : 25 mai 2016

Présentée par

Jorge JARA

Thèse dirigée par **Anne SOCQUET, Enseignant-Chercheur, UGA**

préparée au sein du **Laboratoire Institut des Sciences de la Terre** dans **l'École Doctorale Terre, Univers, Environnement**

Comportement transitoire et role des barrières dans la lacune sismique Nord Chili – Sud Pérou

Transient behavior and role of barriers in the North Chile – South Peru seismic gap

Thèse soutenue publiquement le **1 Mars 2018**,
devant le jury composé de :

Monsieur Raúl Madariaga
Professeur Emérite, École Normale Supérieure de Paris, Rapporteur
Monsieur Jean-Mathieu Nocquet
Directeur de Recherche, IRD – Géoazur, Université de Nice – Sophia Antipolis, Rapporteur, Président du Jury
Monsieur Antonio Avallone
Chargé de Recherche, INGV – Istituto Nazionale di Geofisica e Vulcanologia, Examinateur
Monsieur Stéphane Mazzoti
Professeur des Universités, Géosciences Montpelier, Université Montpellier 2, Examinateur
Madame Marianne Métois
Maîtresse de Conferences, LGLTPE, Université de Lyon, Examinatrice
Madame Anne Socquet
Physicienne des Observatoires, CNAP – ISTerre – UGA, Directrice de Thése

To my uncle Koke
and my dear Nona

Abstract

The aim of this Ph.D. thesis is to have a better comprehension of the interactions between coupling, slow slip events (SSEs) and the seismic ruptures in subduction zones. This work focuses on the North Chile - South Peru subduction zone that has been recognized as a mature seismic gap. Thus, the region has been the target of an important international effort in geophysical instrumentation (GPS and seismological stations), since the mid-2000s. The region has been affected by several well-registered earthquakes, that makes it good case to study the earthquake preparation phase and the relationship between coupling, SSE and seismic rupture.

The 65 stations available in the region have been processed in double differences using the GAMIT-GLOBK software in the period 2000 - 2014. The GPS displacement time series have been analyzed and the associated displacements to the different stages of the seismic cycle as well as seasonal signals have been modeled.

The analysis of the tendencies in the GPS time-series evidences a change in the velocity field before and after the Tarapaca slab-pull earthquake occurrence (M_w 7.8) in June 2005, in the range of latitude affected by Iquique earthquake (M_w 8.1) in 2014. This velocity change is associated with a change in the shallow (z $<$ 40 km) and deep (z $>$ 80 km) seismicity rates. The analysis of the declustered catalog shows that the velocity change observed affects the background seismicity as well, that often seen as a proxy for the tectonic loading. Finally, we find interactions between shallow and deep seismicity, that may play an important role in the interface earthquakes preparation phase. At a shorter time scale, the time series show another change in velocity 8 months before Iquique earthquake. Models indicate that the velocity change corresponds to an SSE M_w 6.5, mainly aseismic, corresponding to the long preparation phase of the earthquake.

The short-term GPS velocity variations have also been analyzed on residual signal. It allows identifying, thanks to a matched-filter, 41 small SSEs during the interseismic period. These events are localized mostly in the deeper part of the seismogenic zone, in areas where the coupling is low (38% of SSEs where $\phi < 0.25$) or with intermediate values (27% of SSEs where $0.25 < \phi < 0.75$). It suggests that the slip in these regions is produced in burst way. Some of those events are correlated with peaks of seismic activity, especially at intermediate depths.

Finally, the kinematic rupture process of Iquique earthquake process and its biggest aftershock are studied, employing a combination of high-rate GPS and strong motion data. The static displacements are inverted to characterize the slip. This static solution is used as *apriori* information

for a sequence of kinematic inversions in the frequency domain. The results show that both events have a bimodal slip distribution, segmented along dip. The lateral extension of the mainshock is centered on a forearc offshore basin associated with a gravity anomaly, and may be controlled by tectonic structures of the upper crust. The aftershock is located in an area with strong Coulomb Stress Changes induced by the mainshock, suggesting that it was triggered by the mainshock.

Thanks to the combination of geodetic and seismological data, this thesis provides a detailed vision of the processes involved during the Iquique earthquake and the previous decades. The research prospects raised by this work are numerous, particularly on the possibilities of refined observations of the phenomena associated with the seismic cycle and the preparation of large subduction earthquakes.

Résumé

Ce travail de thèse vise à mieux comprendre les interactions entre couplage, glissement lent et rupture sismique en contexte de subduction. L'objet d'étude retenu est la subduction Nord Chili – Sud Pérou, qui a été reconnue comme une lacune sismique mature et qui, en conséquence, a fait l'objet d'un important effort international d'instrumentation géophysique (stations GPS et sismologiques) depuis le milieu des années 2000. Cette zone a récemment été affectée par plusieurs tremblements de terre qui ont été bien enregistrés, ce qui en fait une cible bien adaptée pour étudier les mécanismes de préparation des grands séismes de subduction, et le lien entre couplage, glissements lents et rupture sismique.

Les 65 stations GPS installées dans la zone ont été traitées en doubles différences avec le logiciel GAMIT-GLOBK sur la période 2000-2014. Les séries temporelles de position obtenues ont été analysées et les déplacements associés aux différentes phases du cycle sismique et aux mouvements saisonniers ont été modélisés.

L'analyse des tendances dans les séries temporelles GPS ont permis de mettre en évidence un changement de vitesse intersismique avant et après le séisme en slab-pull de Tarapacà (M_w 7.8) de juin 2005, dans la région qui a été rompue la le séisme d'interface d'Iquique (M_w 8.1) en 2014. Ce changement de vitesse décennal est associé à un changement de taux de sismicité superficielle (z $<$ 40 km) et profonde (z $>$ 80 km). Le déclustering du catalogue de sismicité indique que ce changement de taux, affecte également la sismicité de fond, caractéristique du taux de chargement. Enfin, nous avons pu mettre en évidence que des interactions existent entre sismicité profonde et superficielle, et pourraient jouer un rôle important dans la préparation des grands séismes d'interface. A plus courte échelle de temps, les séries temporelles ont montré un autre changement de vitesse 8 mois avant le séisme d'Iquique. La modélisation indique que ce changement correspond à un glissement lent de M_w 6.5, essentiellement asismique, correspondant à la phase de nucléation long-terme de ce tremblement de terre.

Nous avons également analysé les variations court terme dans les signaux non-modélisés des séries temporelles GPS, qui ont permis d'identifier, grâce à une méthode de 'Template Matching' 41 petits événements de glissement lent pendant la période de chargement intersismique. Ces événements sont basés pour leur grande majorité en dessous de la zone sismogénique dans des zones de couplage très faible (38% de SSEs où $\phi < 0.25$), ou de couplage intermédiaire (27% de SSEs où $0.25 < \phi < 0.75$), indiquant que le glissement se fait par relâchements successifs. Souvent ces événements transitoires sont corrélés à des pics d'activité sismique, notamment profonde.

Enfin, la cinématique de la source du séisme d'Iquique (2014/04/01, M_w 8.1) et de sa plus grosse réplique (2014/04/03, M_w 7.7) a été étudiée en combinant données GPS à haute fréquence et données accélérométriques. Les déplacements statiques ont été inversés pour caractériser la répartition du moment géométrique. Cette source statique a ensuite été utilisée comme prior pour une séquence d'inversions cinématiques en fréquence. Les résultats ont montré que ces deux séismes présentent une distribution de glissement bimodale, segmentée selon la profondeur. L'extension latérale du choc principal correspond à celle d'un bassin submergé d'avant arc associé à une anomalie de gravité, et pourrait être contrôlée par les structures tectoniques de la croûte supérieure. La réplique principale est située dans une zone de fort changement de contrainte de coulomb induit par le choc principal, ce qui suggère qu'elle a été déclenchée par celui ci.

Grâce à une combinaison originale de données géodésiques et sismologiques, ce travail de thèse offre donc une vue détaillée des processus en jeu au cours du séisme d'Iquique et des décades qui l'ont précédé. Les perspectives de recherches soulevées par ce travail sont nombreuses au Chili et au-delà, notamment sur les possibilités d'observations raffinées des phénomènes associés au cycle sismique et à la préparation des grands tremblements de terre de subduction.

Resumen

El objetivo de esta tesis de doctorado es tener una mejor comprensión de las interacciones entre el acoplamiento, los deslizamiento lentos (SSEs) y las rupturas sísmicas, en un contexto de zonas de subducción. Este trabajo se centra en la subducción del Norte de Chile y sur del Perú, que por un largo tiempo ha sido reconocida como una laguna sísmica madura y que, en consecuencia, ha sido objeto de un gran esfuerzo internacional de instrumentación geofísica (estaciones de GPS y sismológicas) desde mediados de la década de los 2000. Esta región ha sido afectada por varios terremotos que han sido bien registrado, lo que la transforma en un buen lugar para el estudio de los mecanismos de preparación de grandes terremotos y la relación entre el acoplamiento, SSEs y rupturas sísmicas.

Las 65 estaciones de GPS disponibles en la región son procesadas en dobles diferencias con el programa GAMIT-GLOBK en el periodo 2000 - 2014. Las series temporales de posición que se obtienen han sido analizadas y los desplazamientos asociados a las diferentes fases del ciclo sísmico y señales estacionales han sido modeladas.

El análisis de las tendencias en las series de GPS ha permitido mostrar la evidencia de un cambio de velocidad intersísmica antes y después del sismo *slab-pull* de Tarapacá (M_w 7.8) en junio 2005, en la misma región que ha sido afectada por el sismo de interfaz de Iquique (M_w 8.1) en 2014. Este cambio en la velocidad decadal está asociado a un cambio en la tasa de sismicidad superficial (z $<$ 40 km) y profunda (z $>$ 80 km). El *declustering* del catalogo de sismicidad indica que este cambio en la tasa, afecta de igual manera a la sismicidad de fondo, que es una característica de la tasa de carga de la placa. Finalmente, hemos mostrado que existen interacciones entre la sismicidad profunda y superficial, que podrían desempeñar un papel importante en la fase de preparación de grandes terremotos de interfaz. En una escala de tiempo más corta, las series temporales mostraron otro cambio de velocidad 8 meses antes del terremoto de Iquique. El modelo de estos datos, indica que el cambio corresponde a un deslizamiento lento de M_w 6.5, esencialmente asísmico, que corresponde a la fase de preparación a largo plazo de este terremoto.

Se han analizado también las variaciones de corto plazo en las señales no modeladas de las series temporales de GPS. Esto ha permitido identificar, gracias a la aplicación de un *matched-filter*, 41 pequeños eventos de deslizamiento lento durante el periodo de carga intersísmica. Estos eventos se encuentran localizados en su mayoría en la parte profunda de la zona sismogénica, en áreas donde el acoplamiento es muy bajo (38% de SSEs donde $\phi < 0.25$) o con valores intermedios (27% de SSEs donde $0.25 < \phi < 0.75$), lo que indica que el deslizamiento de produce por relajamientos sucesivos.

Algunos de estos eventos transitorios se encuentran correlacionados con *peaks* de actividad sísmica, especialmente de sismicidad de profundidad intermedia.

Finalmente, se estudia la cinemática de la ruptura del sismo de Iquique (2014/04/01, M_w 8.1) y su mayor réplica (2014/04/03, M_w 7.7) utilizando una combinación de datos GPS de alta frecuencia y de aceleración. Los desplazamientos estáticos son invertidos para caracterizar la repartición de *slip*. Esta solución estática es utilizada como un modelo *apriori* para una secuencia de inversiones cinemáticas en el dominio de la frecuencia. Los resultados muestran que los dos sismos presentan una distribución de *slip* bimodal, segmentada en profundidad. La extensión lateral del sismo principal se encuentra centrada en una cuenca de antearco asociada a una anomalía de gravedad y que podría ser controlada por las estructuras tectónicas de la corteza superior. La réplica está situada en una zona de fuerte cambio de esfuerzos de Coulomb inducido por el evento principal, lo que sugiere que fue gatillada por este.

Gracias a la combinación de datos geodésicos y sismológicos, este trabajo de tesis ofrece una visión detallada de los procesos involucrados durante el terremoto de Iquique y en las décadas que lo precedieron. Las perspectivas de investigación planteadas por este trabajo son numerosas, particularmente en las posibilidades de observaciones refinadas de fenomenos asociados tanto con el ciclo sísmico, como la preparación de grandes terremotos de subducción.

Acknowledgments

The end of this thesis brings great personal and emotional satisfaction at the end of a four-year cycle, which formally kicks off my career as a researcher. Many people have been participants in this process and I have only to offer them a little gratitude through these lines.

I would like to begin these acknowledgments, by thanking Jean-Mathieu and Raul for agreeing to review my manuscript, fruit of all the work done during the course of this thesis. I would also want to thank Marianne, Stephane and Antonio, for agreeing to be part of the jury as examiners. It is a real pleasure share and discuss this work with you.

I would like to express my deepest gratitude to Anne, for having accompanied me and advised me in these four years of thesis. I thank you in particular for your enthusiasm and for always pushing me to go beyond what has already been done, in order to make new discoveries. I can not fail to mention your patience when explaining and thanking you for all the passionate and philosophical scientific discussions we had (and I hope we continue to have). I hope someday to have your "visual ability" to detect things that I have always overlooked. I think it is important to mention that man does not only live in science: in today's competitive scientific world it is difficult to find people with your human qualities. One thing that I have learned with you and hope to apply in the future, is that it is not necessary to stop being an excellent person to be a good researcher, both qualities are compatible.

There are several people who during the course of this work, marked my way of looking and doing science, to which I owe a thank you for it. Thank you Michel Bouchon for your always enthusiastic way of looking at things, talking to you have always been a pleasure due to the motivation you transmit. A quality learned from you and that I hope not to lose in the future, is leaving behind the preconceived ideas to go sailing towards new discoveries, along with the importance of looking carefully at the data: the information is there, is in one the power to exploit it. Thanks David, you arrived at a crucial moment of the thesis to collaborate with my work, and it was an excellent interaction. Thank you for teaching me that skepticism is not a bad quality, but the key to walk towards robust and convincing results. Thank you Jean for providing key ideas to finish part of my thesis work, iit has always been a pleasure to have scientific discussions with you and thanks for helping me lose the fear of the fascinating inversion world. A big thank you to Fabrice. Although you were not physically present in the laboratory, you were always attentive to the work I was doing and open to collaborating with your technical skills, as well as with words of encouragement. Thanks a lot Andrea, my teacher in GPS data processing, without your help half of this thesis would not have been possible. It has always been a pleasure to talk with you, moments in which you contributed

with the precise comments to arrive at good port in the processing. Thanks Nathalie also for the help provided in the processing of GPS data and for the time to talk about life in general. Thank you to Mark for receiving me in the internships that I did at Seismolab, showing me that in science you always have to be practical.

I thank ISTerre Laboratory for these four years, and especially the Seismic Cycle team, from which I take the best memories of the shared moment. I can not forget my office colleagues during this period: Simón, Baptiste and Laura. For tolerating my bad French and for making my stay pleasant at the office, sharing with me the good and bad moments of the PhD. I have to make a special mention to you Yacine, since from the first moment you were a great support and company when I arrived in France. Thank you for all the moments we share together, from meals and beers, to political discussions and life talks. I can not fail to mention the people of the laboratory in general, but I would like to make special mention of two people who accompanied me in different steps of this PhD. Thank you John, for the beers, the video games, for going to the stadium to see such a bad football team, for the shared work and good for the parties buddy! In summary, thank you for everything. Also, I can not forget to thank Hugo, it has been a pleasure to meet you and be able to work with you. I take a couple of lessons with me about this time shared with you: there are always much more important things to worry about in life and that humor is essential to survive, especially in science. To the different friends that I made during this period in the laboratory: Maureen, Blandine, Ariana, Olivier, James, Mathilde, Ismael, among others. Honorable mention to Jesus, the pleasure of being able to speak Chilean almost every day so far from Chile, is something that only those of us who have lived abroad appreciate. Thanks for the discussions, the coffees, for being in the good times and the bad and for helping me in the beginning of the doctorate with the tedious and bureaucratic French administration.

Thank you Jean-Noel for all the help provided in the computational part and in the processes on the servers, your advice was of great help during all my work. Thank you Sandrine for always being a warm person and for helping to the maximum that the French administration did not cause me to collapse.

I would like to thank from the distance to the guilty that I like to look at the world from this science trench. Thanks Daniel and Eduardo for starting this road 7 years ago. I must also thank my now colleagues, but also friends for a long time: Javier, Pancho and Andrei. Your willingness to cooperate with this work and to receive me in the DGF during my visits, made my working time in Santiago a more than a pleasant stay.

I have to thank those who are not physically with me, but who accompanied me to the distance in my heart. To my parents, to whom I owe to be living this experience in France. Thank you for always respecting and supporting the decisions I have made in life. To my brothers: Daniel, Andrea and Emilia, because in their smiles I have always found the joy to continue walking in this life. To my aunt Isa for her constant concern and for her company in the visits and trips we made in Europe, together with Aunt Meche. My uncle Fernando, who motivated me since my childhood curiosity and

love for computers. Special mention to a person that I owe a lot in this life and unfortunately last year left us: Nona, you could not see me become a doctor as it was your dream, but you are always present in this journey. It is with all certainty that you are enjoying eternal freedom. To my aunts and cousins who have always made my stays in Chile a pleasant and entertaining family moment. To my soul friends, whom I miss and always in one way or another make me feel connected with them: Marcelo, Lucía, Jaime, Priscilla, Luzma, Carito, Paula, Karin, Pancho, Carlos and Cristian. I can not finish these lines without thanking you Claudia: for the company, the love and support during this PhD. For putting up with the bad temper during this last period and for being workaholic, but also for teaching me that there are a million more important things in life than work: traveling, the beach and many others... with all my heart, thank you!

This work was possible thanks to the financing given by the Government of Chile through its program "Becas Chile – Doctorado en el Extranjero". Also, I would like to thank all the institutions that provide the data employed during this thesis: International Associated Laboratory Montessus de Ballore (LIA-MB), Integrated Plate Boundary Observatory Chile (IPOC), Central Andean Tectonic Observatory Geodetic Array (CAnTO, Caltech), Instituto Geofísico del Perú (IGP), Departament of Geophysics (DGF) at University of Chile and Centro Sismológico Nacional (CSN, Universidad de Chile).

Contents

List of Figures

List of Tables

Chapter 1

General Introduction

Subduction zones are the most tectonically active regions worldwide, being responsible of the largest historical earthquakes of seismological history. *Lay* [2015] points out that, in the period between 1900 until 2014, almost all of the great earthquakes ($M_w \geq 8.0$) take place in subduction zones, affecting millions of lives around the world. Only during the 50's and 60's, 13 large earthquakes had occurred in subduction zones, including the biggest instrumentally ever recorded events: Kamchatka 1952 (Russia, M_w 9.2), Valdivia 1960 (Chile, M_w 9.5) and Alaska 1964 (USA, M_w 9.2). Since then, and for approximately 40 years of relative calm characterized by low earthquake activity, it is in the first decade of the 21st century that a significant seismic reactivation of the Earth was observed, again with a sequence of large events generated in now sadly famous subduction zones: Sumatra 2004 (Indonesia, M_w 9.2) [e.g., *Ishii et al.*, 2005; *Vigny et al.*, 2005; *Ammon et al.*, 2005; *Kanamori*, 2006; *Chlieh et al.*, 2007; *Lorito et al.*, 2010], Maule 2010 (Chile, M_w 8.8) [e.g., *Moreno et al.*, 2010; *Delouis et al.*, 2010; *Lorito et al.*, 2011; *Vigny et al.*, 2011; *Ruiz et al.*, 2012; *Lin et al.*, 2013] and Tohoku-Oki 2011 (Japan, M_w 9.1) [e.g., *Simons et al.*, 2011; *Suzuki et al.*, 2011; *Yao et al.*, 2011; *Ozawa et al.*, 2011; *Asano and Iwata*, 2012]. On the single Central Andes subduction zone, 4 earthquakes occurred in the last 28 years: Arequipa 2001 (Peru, M_w 8.1) [e.g., *Ruegg et al.*, 2001; *Melbourne and Webb*, 2002; *Tavera et al.*, 2002; *Perfettini et al.*, 2005; *Pritchard et al.*, 2007], Pisco 2007 (Peru, M_w 8.0) [e.g., *Tavera and Bernal*, 2008; *Biggs et al.*, 2009; *Perfettini et al.*, 2010; *Sladen et al.*, 2010], Iquique 2014 (Chile, M_w 8.1) [e.g., *Ruiz et al.*, 2014; *Schurr et al.*, 2014; *Hayes et al.*, 2014; *Yagi et al.*, 2014; *Duputel et al.*, 2015] and Illapel 2015 (Chile, M_w 8.3) [e.g., *Ruiz et al.*, 2016; *Melgar et al.*, 2016; *Tilmann et al.*, 2016; *Klein et al.*, 2017]. However, it results interesting noting that although the rate of major earthquakes has increased over the past 20 years, they have not managed to liberate even half of the seismic moment released in the decades of the 50's and the 60's [*Ammon et al.*, 2010].

Following these observations, the understanding of the physical behavior of subduction zones is critical for seismic hazard. The better comprehension of this physical phenomenon eventually allows to the local authorities and the engineering community to propose adequate strategies to mitigate its effects. For this reason, the scientific community has focused great efforts on studying these critical zones, by installing extensive permanent networks in different subduction zones around the world. And it is thanks to this great effort, that seismology and space geodesy have developed in a very fast way during the last two decades, generating extensive databases, with better standardization

processes and open to the public.

From the different networks installed around the world, in particular, the GPS networks provide a measure of the spatial and temporal evolution of the deformation of the crust. This deformation mapping allowed to derived the interseismic locking level in subduction zones in between large earthquake [e.g., *Chlieh et al.*, 2011; *Loveless and Meade*, 2011; *McCaffrey*, 2014; *Nocquet et al.*, 2014; *Métois et al.*, 2016; *Nocquet et al.*, 2016; *Villegas-Lanza et al.*, 2016a]. These interseismic locking maps, also known as coupling maps, suggest that the interface of a subduction zone is not loading homogeneously (by displaying several patches on the same area with different coupling levels) and suggest a segmentation of the seismogenic zone. The highly locked areas have shown to be well correlated with recent seismic ruptures and previously calculated coupling maps [e.g., *Moreno et al.*, 2010; *Loveless and Meade*, 2011; *Nocquet et al.*, 2016; *Métois et al.*, 2016; *Klein et al.*, 2017], and are often interpreted as asperities with a larger likelihood of breaking in the future. On the other hand, the areas with low locking values are often interpreted as zones acting as a barrier to the propagation of seismic ruptures, affected by slow creep, that seem to occur on a transient manner and with a limited release of seismic energy [*Avouac*, 2015].

The coupling factor is a kinematic view of the state of locking of the subduction. Therefore, coupling maps are not able to image all the complexity of the subduction interface, and that their relationship with the mechanics of the interface remains an open question [e.g., *Moreno et al.*, 2010; *Kaneko et al.*, 2010; *Hetland and Simons*, 2010; *Kanda et al.*, 2013; *Métois et al.*, 2016]. Despite of these limitations, these maps have shown to be helpful to locate the locked or creeping sections, but do not provide the details of the interface processes.

Several authors have observed that the interseismic period is not just a quiescent period waiting for a new earthquake to hit, but a period with smaller events, sometimes difficult to detect, such as aseismic transients or slow slip events [e.g., *Linde et al.*, 1996; *Dragert et al.*, 2001; *Lowry et al.*, 2001; *Frank*, 2016; *Melnick et al.*, 2017]. Both, aseismic transients and slow slip events can range a wide spatio-temporal spectrum [*Obara and Kato*, 2016], with amplitudes that can sometimes go below the observations noise level [*Frank*, 2016; *Rousset et al.*, 2017] making them very difficult to detect with standard techniques. To try overcoming this problem, seismologists have studied the seismic noise signals through cross-correlation techniques, resulting in seismic tomography images [e.g., *Shapiro et al.*, 2005], detection of tectonic tremors [e.g., *Obara*, 2002; *Dragert et al.*, 2004] or low frequency earthquake [e.g., *Shelly et al.*, 2006; *Ide et al.*, 2007a] based on noise records. In some regions around the world (e.g. Cascadia, Mexico, Japan) when tectonic tremors and low-frequency earthquakes are detected, concurrent aseismic transients and/or slow slip events have also been reported using geodetic data. This therefore suggests that creep most probably occurs in burst way, and that small transient slip signals are likely hidden in the GPS data. This raises methodological challenges to analyze GPS noise and extract transient signals [*Frank*, 2016; *Rousset et al.*, 2017], following the seismologists' approach of the seismic noise analysis. A better characterization of the variability of these transients is indeed necessary to better understand the mechanisms that control them.

The interactions between seismic and aseismic slip still remain an open question, and critically the understanding of the preparation phase of earthquakes. Laboratory experiments show that earthquakes feature a nucleation phase [e.g., *Dieterich*, 1992; *Ohnaka*, 2003] that has been associated with aseismic deformation [*McLaskey and Lockner*, 2014; *Scuderi et al.*, 2016]. This resulted in physical models capable to explain the seismic rupture initiation [*Ellsworth et al.*, 1995; *Dodge et al.*, 1996]. For instance, one model assumes that the accelerated moment release observed before large earthquakes [*Bowman and King*, 2001] is triggered by a slow slip event on the fault interface [*Dodge et al.*, 1996; *Bouchon et al.*, 2013; *Ruiz et al.*, 2014]. The alternative model proposes that a slow cascade of failures may eventually trigger the mainshock [*Dodge et al.*, 1996]. However, all these models of the earthquake precursory phase have been studied mostly using seismological data [*Kanamori and Cipar*, 1974; *Cifuentes and Silver*, 1989; *Ellsworth et al.*, 1995; *Dodge et al.*, 1996; *Bouchon et al.*, 2011, 2013], while the geodetic data are less employed, due to the lack of resolution. The link between the foreshock activity and transient phenomena has never been directly established for periods exceeding a few weeks, although it has been suggested that is last for a longer period of time [*Obara and Kato*, 2016]. Similarly to small transient detection issues, pushing the limits of detection of precursory signals in geodetic time series is probably a key issue to better document and understand the preparation of a great earthquake and relate it to the foreshock activity.

A related question is what is the driving mechanism of these precursory slow slips before a megathrust. Geodetic and seismological observations show that intermediate depth seismicity has a big impact on the processes occurring on the seismogenic interface and the deformation of the upper plate [*Durand et al.*, 2014; *Bouchon et al.*, 2016; *Delbridge et al.*, 2017; *Lay et al.*, 2017]. Notably *Bouchon et al.* [2016] suggest that the slab seems to deform and plunge prior to great interface earthquakes. This suggests that the slab has an important role in the preparation phase of earthquakes, implying that the impact of slab-pull earthquakes on the seismogenic interface and shallow seismicity should be further investigated.

On the rupture process itself, static and kinematic models are commonly used to study the seismic rupture [e.g., *Hartzell and Heaton*, 1983; *Cotton and Campillo*, 1995; *Vigny et al.*, 2011; *Simons et al.*, 2011; *Duputel et al.*, 2015]. The information provided by the kinematics models can be interpreted on the basis of the asperity and barrier models [*Das and Aki*, 1977; *Aki*, 1979; *Kanamori*, 1986; *King*, 1986], providing useful insights on the segmentation of the seismogenic zone that can be compared with structural complexities mapped independently [*Aki*, 1979; *King*, 1986; *Song and Simons*, 2003; *Wells et al.*, 2003; *Audin et al.*, 2008; *Perfettini et al.*, 2010; *Carena*, 2011; *Contreras-Reyes and Carrizo*, 2011; *Kopp*, 2013]. A good understanding of the seismogenic zone segmentation is of critical importance since it is a first-order element for seismic hazard studies [*Carena*, 2011; *Pagani et al.*, 2014; *Drouet et al.*, 2016]. A detailed mapping of the seismogenic segmentation is a prerequisite for a better understanding of the physical conditions that contribute to enhance or end the seismic ruptures (slip deficit, state of stress, friction or structural complexities), and to evaluate the complementarity and potential interactions with the pre-existing slip/locking pattern.

This PhD research work is particularly motivated by a better characterization of the behavior of the creeping zones on the subduction interface, and of their relationships with the seismic rupture. An objective is to gain in time-space resolution of the seismic/aseismic deformation: the slow slip that is likely occurring in the low coupling zones on one side (notably assess if it is released in a steady state manner or through a series of bursts), and the seismic ruptures on the other side. To do this, we use geodetic and seismological data in a complementary ways to characterize the occurrence of slow slip and seismic rupture on the subduction interface. First, we look at the transient and spatially consistent movements hidden in the GPS time-series in order to detect slow slips on the subduction interface. Second, we use models describing the seismicity recurrence that separate the seismicity into "triggered" events versus "background" events that do not result from the triggering by a previous earthquake [e.g., *Ogata*, 1988; *Marsan et al.*, 2017]. This background seismicity is usually considered to be a good proxy of the tectonic loading in a specific area, so that any important deviation from the average trend can be associated with slow slip events and fluid or magmatic migrations [*Marsan et al.*, 2013; *Reverso et al.*, 2015, 2016; *Marsan et al.*, 2017]. This makes it possible to detect aseismic slip using geodetic or seismological data independently. Eventually the relationship between both dataset is analyzed, in order to assess whether both datasets are able to detect similar processes and to evaluate their complementary and potential interactions. Third, we characterize the source of great subduction earthquakes, by inverting kinematically high-rate GPS and strong motion data in the frequency domain.

South Peru - North Chile has been selected as the study case because it is an exceptional natural laboratory to explore the different questions we want to address, and because good quality and amount of seismological and geodetic data are publicly available for research purposes. This region has been considered as a seismic gap for a long time [*Kelleher*, 1972; *Nishenko*, 1985; *Comte and Pardo*, 1991], with strong evidence that the area is segmented from geodetic coupling maps [*Li et al.*, 2015; *Métois et al.*, 2016]. Moreover, the occurrence of the slab-pull Tarapaca earthquake (M_w 7.8) in 2005 in the same latitude range as the interplate Iquique earthquake (M_w 8.1, 2014) that happened 9 years later allows to study the relationship between deep and shallow processes. Also, the Iquique (M_w 8.1, 2014) earthquake was preceded by an important foreshock activity [*Ruiz et al.*, 2014; *Schurr et al.*, 2014; *Bedford et al.*, 2015; *Cesca et al.*, 2016; *Kato et al.*, 2016] that have been well monitored by cGPS and seismological stations. It therefore represents an excellent opportunity to study the precursory phase, as well as the rupture process and its relationship with the foreshocks sequence, the segmentation of the seismogenic zone and the coupling maps available in the region.

The different questions discussed along this section are further discussed in this manuscript, beginning with a review of the subduction and seismic cycle state of the art in Chapter 2 and about the Central Andes geodynamic settings in Chapter 3. The methodologies employed to process GPS data and data quality assessment are explained in Chapter 4. Chapter 5 addresses the long-term shallow and deep seismicity interactions, together with the potential relationship with aseismic deformation in the form of a paper published in GRL, together with its supplementary material. Chapter 6 covers the detection of transient deformations in South Peru - North Chile area, by analyzing and characterizing its spatiotemporal behavior. Chapter 7 details the preparation phase of Iquique (M_w 8.1,

2014) earthquake through a published paper in GRL and supplementary material. Chapter 8, to be submitted to EPSL, describes the rupture process for Iquique (M_w 8.1, 2014) earthquake and its largest aftershock, discussing the segmentation revealed by the event. Finally, general conclusions together with the potential future work and perspectives are discussed in Chapter 9.

Chapter 2

Subduction Zones and Seismic Cycle: State of the Art

2.1 Phenomenological Description of the Seismic Cycle

After the big earthquake in San Francisco (California, USA) in 1906, *Reid* [1910] proposed a model to explain how this event occurred. The deeper part of the San Andreas fault would have accumulated a slip of several meters as an effect of the continuous movement of the North American plate and Pacific plates. This phenomenon generated an elastic deformation at the surface. When the shear stress produced reached a maximum threshold, the fault broke seismically. This theory has been called Elastic Rebound, and constitutes the most basic view of the Seismic Cycle. This concept describes how the tectonic forces are accumulated and relaxed over time.

When *Reid* [1910] proposed the Elastic Rebound Theory, the seismic cycle was seen as a simple as two steps phenomenon: the interseismic and coseismic phases (Figure 2.1a). With the development of the space geodesy during the 90's and 2000's, different phenomena were discovered such as postseismic deformation [e.g., *Heki et al.*, 1997; *Peltzer et al.*, 1998; *Klotz et al.*, 2001; *Jonsson et al.*, 2003; *Hsu et al.*, 2006; *Wang et al.*, 2007], slow slip events (SSEs) [e.g., *Dragert et al.*, 2001; *Lowry et al.*, 2001; *Rogers and Dragert*, 2003; *Dragert et al.*, 2004] and small transients of deformation (Figure 2.1b and c) [e.g., *Mavrommatis et al.*, 2014; *Frank*, 2016; *Rousset et al.*, 2017], complexifying the vision of the earthquake cycle.

2.1.1 Interseismic Phase

The interseismic phase is the longest phase of the seismic cycle. It can last decades to centuries and up to millennia, depending on the characteristics of the region considered, taking ∼90% of cycle's time [*Ruegg*, 1994; *McCaffrey*, 2007]. During the interseismic period, the fault zone is usually locked (not slipping) up to a certain degree, generating a slip deficit at the plate boundaries. This generates a tectonic loading stress accumulation on the seismogenic contact and produces deformation at the surface that can be, at the first order, modeled through a slipping dislocation in an elastic medium. In subduction zones, the deformation is characterized by a horizontal movement going away from the trench and with velocities varying from mm/yr to cm/yr (Figure 2.2a). The vertical deformation

component is characterized by a subsidence between the coast and the trench and by uplift onshore (Figure 2.2a). The location of the maximum subsidence corresponds at the first order to the upper limit of the locked region on the subduction interface, while the hinge line corresponds at the first order to the lower limit of the locked portion on the interface.

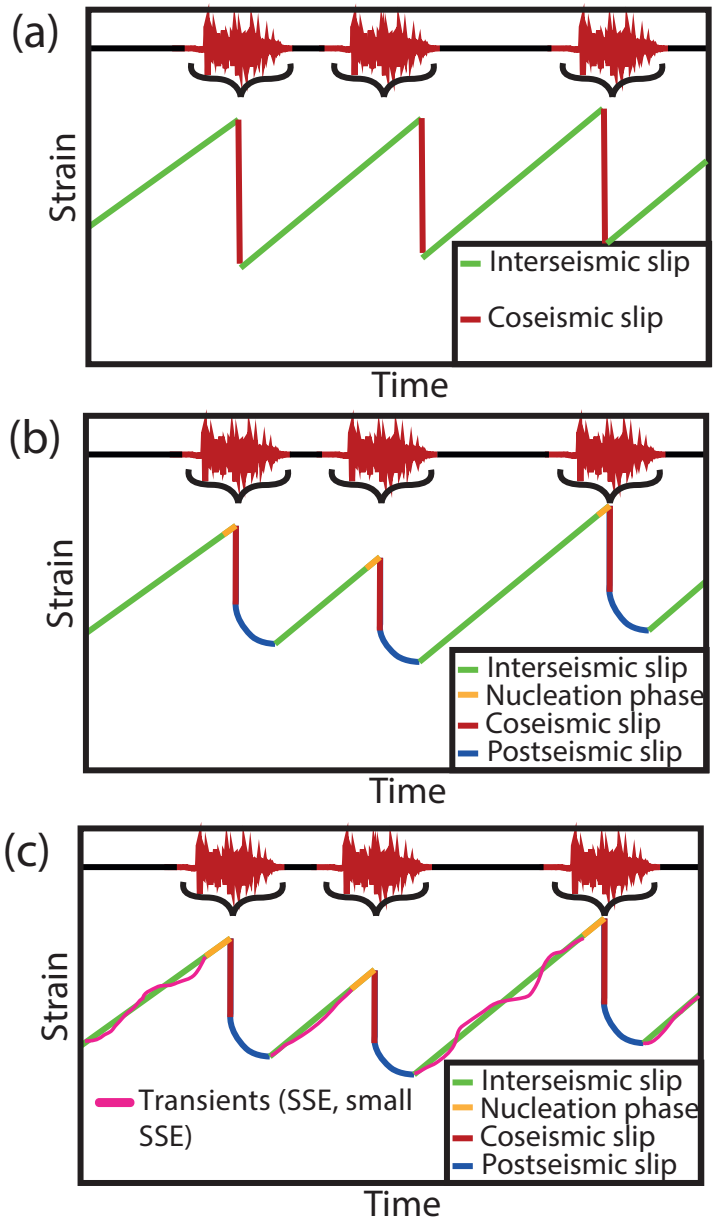

Figure 2.1: Schematic evolution of the seismic cycle. (a) Simplest seismic cycle proposed by *Reid* [1910] in San Andreas fault after the occurrence of 1906 earthquake. (b) Image of the seismic cycle during the 90's and early 2000, when with the development of the GPS, postseismic phase and SSE were detected. (c) A current picture of the seismic cycle, where the interseismic and preseismic (nucleation) phase seems to be more complex due to detection of aseismic slip. The coseismic stage is represented by a step on the plots and its associated seismogram for each event. Figure modified from *Gardonio* [2017].

2.1.2 Coseismic Phase

The coseismic phase corresponds to the occurrence of a large earthquake. The seismic rupture is associated with a stress drop that release part (or all) the elastic stress accumulated during the interseismic. It lasts from seconds to minutes. The horizontal deformation pattern is inverted with respect to the one observed during the interseismic phase, following a movement towards to the trench (Figure 2.2b). The vertical pattern is also opposed: uplift in the offshore forearc and subsidence in the onshore forearc (Figure 2.2b). For great earthquakes, the displacement recorded at the surface ranges from cm to m.

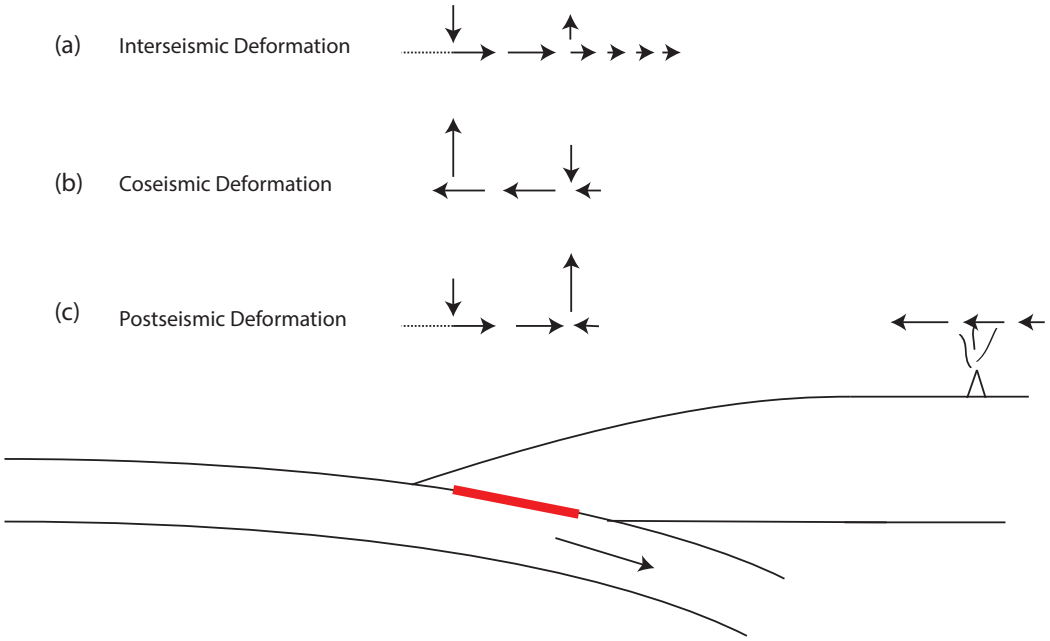

Figure 2.2: Scheme of deformation sense (horizontal and vertical patterns) in subduction zones for each step of the seismic cycle (interseismic, coseismic and postseismic phases, modified from *Wang* [2007]).

2.1.3 Postseismic Phase

The postseismic period is the transition between the coseismic and interseismic phases. It is all the period after the earthquake occurrences up to the interseismic loading is reached again, with a duration ranging from days to decades. Three different mechanisms of stress relaxation have been described to explain this phenomenon:

- **Afterslip**: It occurs through a slow slip on the fault plane in the areas surrounding the seismic rupture, especially in those with a small amount of coseismic slip. It can liberate a seismic moment similar to the mainshock, having a duration of days to years [*Heki et al.*, 1997; *Bürgmann et al.*, 2001].
- **Viscoelastic Relaxation**: It is a long-term (year and decades) mechanism, where the upper mantle responds in a viscoelastic manner to the stresses produced by the coseismic rupture.

This phenomenon has, for example, been observed in the area struck by the Valdivia earthquake (M_w 9.5, 1960), and has been lasting more than 50 yr [*Klotz et al.*, 2001; *Khazaradze et al.*, 2002; *Wang*, 2007; *Klein et al.*, 2016].

- **Poroelastic Rebound**: This phenomenon is caused by pore fluid reequilibration flows, induced by the coseismic stress changes [*Peltzer et al.*, 1998; *Jonsson et al.*, 2003]. This phenomenon is usually seen at low depths, and has essentially been described for strike-slip or normal faults. If it happens in subduction zones, it should rather affect the shallow area close to the trench that is submerged.

The surface deformation depends on the phenomena controlling the process. In the afterslip case, the movement follows the same direction observed during the coseismic phase, but with a lower magnitude and slowly regarding the propagation, very concentrated in the rupture boundaries. In the case of viscoelastic relaxation, the stations far away from the trench exhibit a movement towards the trench, while the stations closer to the trench show after some months/years a movement similar to the interseismic phase[*Klotz et al.*, 2001; *Khazaradze et al.*, 2002; *Wang*, 2007; *Klein et al.*, 2016], that is likely associated with the relocking of the subduction interface [*Remy et al.*, 2016].

2.2 Recent Observations on Faults, Complexities During the Seismic Cycle

2.2.1 Aseismic Transients in the Earthquake Cycle

The development of continuously recording GPS networks during the 90's allowed the discovery of aseismic transients during the seismic cycle. Although the postseismic phase is considered as a transient phenomenon of deformation, we focus below on describing the transients occurring in the interseismic or preseismic periods.

Slow Slip Events (SSEs)

Also called silent earthquakes, they are slip events occurring during the interseismic period without classical seismic radiation but producing surface deformation ranging from mm to cm, and with a duration going from days to years [*Schwartz and Rokosky*, 2007; *Ide et al.*, 2007b; *Peng and Gomberg*, 2010; *Beroza and Ide*, 2011] (e.g., Figure 2.3a). These phenomena have been detected in many subduction zones around the world such as Nankai [*Hirose et al.*, 1999; *Ozawa et al.*, 2001; *Miyazaki et al.*, 2003], New Zeland [*Douglas et al.*, 2005; *Wallace and Beavan*, 2006; *McCaffrey et al.*, 2008; *Wallace and Beavan*, 2010], Cascadia [*Dragert et al.*, 2001; *Rogers and Dragert*, 2003], Mexico [*Lowry et al.*, 2001; *Larson et al.*, 2004; *Vergnolle et al.*, 2010; *Radiguet et al.*, 2011, 2012] or Ecuador-Peru [*Vallee et al.*, 2013; *Villegas-Lanza et al.*, 2016b; *Vaca et al.*, 2017]. Those SSEs are often associated with the occurrence of non-tectonic tremors [*Obara*, 2002; *Dragert et al.*, 2004; *Ide et al.*, 2007a; *Schwartz and Rokosky*, 2007; *Bartlow et al.*, 2011] or low-frequency earthquakes

(LFEs) [*Shelly et al.*, 2006; *Ide et al.*, 2007b; *Beroza and Ide*, 2011; *Frank*, 2016], suggesting that SSEs are occurring on the deeper part of the seismogenic zone. Some shallower SSEs also has been reported, mainly associated with superficial tremors or during a seismic swarm occurrence [*Walter et al.*, 2011; *Vallee et al.*, 2013; *Villegas-Lanza et al.*, 2016b].

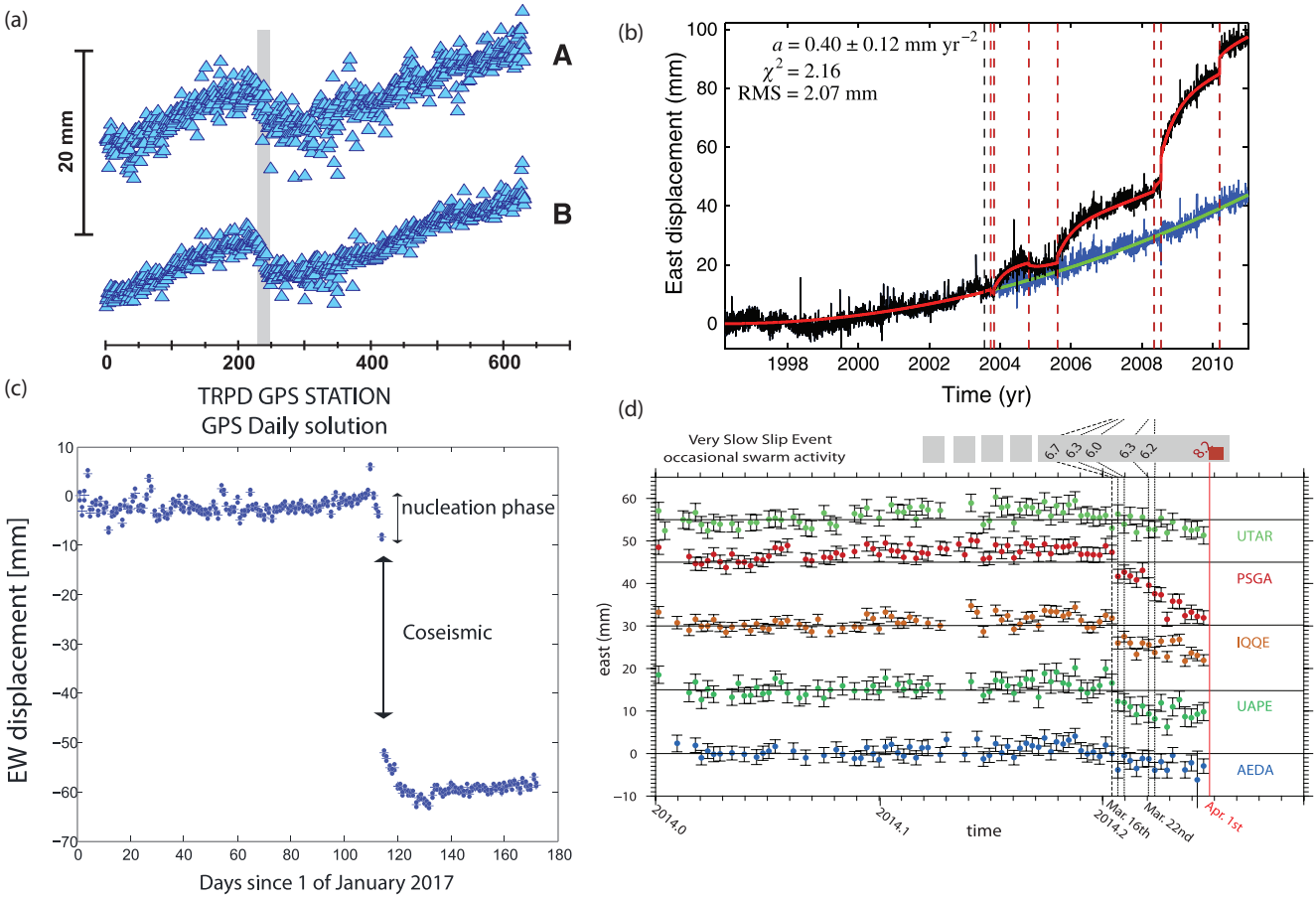

Figure 2.3: Examples of Transients Deformation observed with GPS. (a) An example of an SSE detected in the deeper part of Cascadia subduction zone reported by *Dragert et al.* [2001]. (b) Decadal-scale deformation transient observed at one GPS station prior to Tohoku-Oki earthquake M_w 9.0 [*Mavrommatis et al.*, 2014]. (c) Short-term transient deformation (∼10 days) prior to M_w 6.9 earthquake in Valparaiso, Chile (2017) [*Ruiz et al.*, 2017a]. (d) 2 weeks of transient deformation previous to Iquique earthquake M_w 8.1 reported by *Ruiz et al.* [2014].

Earthquake Preparation Phase

Several efforts have been realized to understand the preseismic phase, by observing different phenomena (aseismic slip or changes in the seismicity rate) or variations in physical properties (wave propagation, hydrological or electrical parameters), although the question of the mechanism leading the great earthquakes remains open. A preparation phase of earthquakes has been observed in laboratory experiments [*Dieterich*, 1979; *Tse and Rice*, 1986; *Dieterich*, 1992; *Ohnaka*, 2003], that has been related to aseismic deformation [*McLaskey and Lockner*, 2014; *Scuderi et al.*, 2016]. The observations about this phase have been mainly made using seismological data. The first evidence of this preseismic phase on a subduction zone was done using seismological data before the 1960

Valdivia earthquake (M_w 9.5) [*Kanamori and Cipar*, 1974; *Cifuentes and Silver*, 1989] and for a M_w 7.7 earthquake in the northern part of Japan [*Linde et al.*, 1988]. Some evidence on strike-slip faults have also been reported, like in Izmit 1999 earthquake (Turkey, M_w 7.6) [*Bouchon et al.*, 2011] or US [*Ellsworth et al.*, 1995]. Other preseismic signals observed with seismology include: acceleration in the background seismicity [*Marsan et al.*, 2013, 2017; *Schurr et al.*, 2014], seismicity migration [*Kato et al.*, 2012; *Kato and Nakagawa*, 2014; *Kato et al.*, 2016; *Cesca et al.*, 2016], changes in the seismicity rate [*Bouchon et al.*, 2013, 2016] and repeaters detection that are interpreted as aseismic slip occurrences *Igarashi et al.* [2003]; *Uchida et al.* [2003]; *Kato et al.* [2012, 2016]; *Meng et al.* [2015]; *Yagi et al.* [2014]. Two models of seismic rupture initiation are alternatively invoked to explain these observations [*Dodge et al.*, 1996]. First, a model assuming that the accelerated moment release observed before the large earthquakes *Bowman and King* [2001] is triggered by a slow slip event on the fault interface [*Dodge et al.*, 1996; *Bouchon et al.*, 2013; *Ruiz et al.*, 2014]. Alternatively, a slow cascade of failures may trigger the mainshock [*Dodge et al.*, 1996].

Geodetic observations are more rare. *Pritchard and Simons* [2006] have reported the occurrence of a pulse of aseismic deformation using InSAR data that may be responsible for triggering a M_w 7.1 earthquake on the north Chile subduction zone. In Guerrero (Mexico), *Radiguet et al.* [2016] have shown that the Papanoa earthquake (M_w 7.3, 2014) has been triggered by a slow slip event. The Iquique earthquake was preceded during ∼20 days by a strong transient signal [*Schurr et al.*, 2014; *Ruiz et al.*, 2014; *Lay et al.*, 2014; *Bedford et al.*, 2015; *Cesca et al.*, 2016; *Kato et al.*, 2016]. But, a debate remains on the mechanisms leading to this foreshock activity, notably on the existence or not of aseismic slip preceding the earthquake. Finally, *Mavrommatis et al.* [2014] or by *Yokota and Koketsu* [2015] have shown decadal-scale deformation transient before Tohoku-Oki earthquake, where a clear acceleration in the GPS signal over time is observed, leaving open the understanding the long-term mechanisms controlling the earthquake preparation phase.

Another interesting feature observed recently is related to the slab deformation a large scale before an earthquake. *Durand et al.* [2014] have shown in Greece that an increase of the intermediate-depth seismicity produces a large spread deformation, triggering activity in the shallower part of the subduction zone and in the upper plate itself. Also, *Bouchon et al.* [2016] show a precursory seismicity at shallow and intermediate depths, occurring synchronously before recent earthquakes (Maule M_w 8.8, Tohoku-Oki M_w 9.1, and Iquique M_w 8.1). The reduced magnitude of this precursory activity makes direct triggering unlikely but instead suggests a broader slab deformation or plunge leading to the megathrust rupture. These studies all focus on the pre-earthquake period (relatively short time), but the long-term mechanisms of shallow-intermediate depths seismicity interactions are still poorly understood.

Small Interseismic Transients of Deformation

As mentioned in the section about the interseismic stage, new observations have shown that this period of the earthquake cycle is not constant over time. Recently, *Frank* [2016] has shown in the inter-SSE period in Mexico, that some signal is hidden in the GPS noise, giving an idea about the

complex process of tectonic loading/release. Also in Mexico, [*Rousset et al.*, 2017] have developed and applied a cross-correlation technique on the GPS time series, detecting 28 small deformation transients masked in the noise for the period 2005 - 2014. These transients phenomena could be present in all type of faults, including strike-slip faults. Employing InSAR data, *Jolivet et al.* [2013] in Haiyuan fault (China) and *Rousset et al.* [2016] in the North Anatolian Fault (Turkey), have found aseismic deformation, where the creep occurs in burst way.

2.2.2 Interseismic Coupling

The GPS networks around the world have caught the deformation process occurring in the lithosphere since the 90's, shedding light on the different steps of the seismic cycle. A major drawback using those datasets is related to the inability to register a complete cycle, having an incomplete view of the interseismic phase. A kinematic approach has been commonly used to study the interseismic period to retrieve the interseismic locking (or coupling), that corresponds to the ratio of the slip deficit in the interseismic period to long-term slip. Following the description given by *Avouac* [2015], the interseismic coupling (χ_i) can be quantified as:

$$\chi_i \;=\; \chi_s \;+\; \chi_a \tag{2.1}$$

where χ_s is the interseismic coupling that corresponds to the ratio of cumulative seismic slip to long-term slip. On the other hand, χ_a is the aseismic slip ratio that corresponds to the ratio of cumulative aseismic transients (afterslip and SSEs). However, it is important to note that the "interseismic coupling" here is related to tectonic geodesy and not to the coupling terms used by seismologists to describe the seismic energy liberated in the interseismic phase [*Scholz and Campos*, 1995, 2012]. Interseismic coupling maps have been carried out in many places around the world, as: Japan [e.g., *Mazzotti et al.*, 2000; *Loveless and Meade*, 2011; *McCaffrey*, 2014; *Johnson et al.*, 2016], Chile [e.g., *Bevis et al.*, 2001; *Ruegg et al.*, 2009; *Chlieh et al.*, 2011; *Métois et al.*, 2012, 2013, 2016; *Li et al.*, 2015; *Melnick et al.*, 2017], Peru - Ecuador [e.g., *Chlieh et al.*, 2011; *Nocquet et al.*, 2014, 2016; *Villegas-Lanza et al.*, 2016a], Kamchatka [e.g., *Bürgmann et al.*, 2005], Cascadia [e.g., *Wang et al.*, 2003a; *Yoshioka et al.*, 2005] or Indonesia (Sumatra) [e.g., *Prawirodirdjo et al.*, 1997; *Simoes et al.*, 2004; *Vigny et al.*, 2005; *Chlieh et al.*, 2008] . These maps provide an insight into the state of the interseismic period, linking the surface deformation with processes occurring at depth. An interesting result from those maps is the variability of the locking degree along the strike, revealing that the seismogenic zone is highly segmented [*Moreno et al.*, 2010; *Chlieh et al.*, 2011; *Loveless and Meade*, 2011; *Rousset et al.*, 2015; *Métois et al.*, 2016; *Melnick et al.*, 2017]. Nevertheless, although there is a good first-order correlation between coupling maps and seismic ruptures [e.g., *Konca et al.*, 2008; *Perfettini et al.*, 2010; *Moreno et al.*, 2010; *Loveless and Meade*, 2011; *Métois et al.*, 2016; *Ruiz et al.*, 2016], the relationship between the kinematic coupling and the mechanical properties on the subduction interface remains as an open question [*Métois et al.*, 2016; *Avouac*, 2015]. The link between the kinematic approach and the mechanical modeling is discussed in further detail in the next section.

2.3 Frictional Framework

2.3.1 Friction Laws, Earthquakes and Stability Regimenes

Earthquakes occur by the generation and propagation of a fracture, followed by sudden slip along a pre-existing fault. It corresponds to an instability friction phenomenon, better known as stick-slip [*Brace and Byerlee*, 1966]. This behavior leads to understanding the earthquakes as processes mainly governed by frictional changes.

In the stick-slip mode, the slip starts when the ratio between the shear and normal stress achieves the static friction (μ_s), which leads to a drop in frictional resistance until achieving the dynamic friction (μ_d) (Figure 2.4a and b). The static friction depends on the surface slip history. If the surfaces are in static contact under a load for a time t, then μ_s increases slowly as $log(t)$ [*Dieterich*, 1972]. Because of the dynamic friction is under a static equilibrium regime (steady-state) depends on the slip velocity (V), that is usually related to the materials in contact. The critical distance to slip D_c, is the distance needed to change the contact properties as the slip velocity.

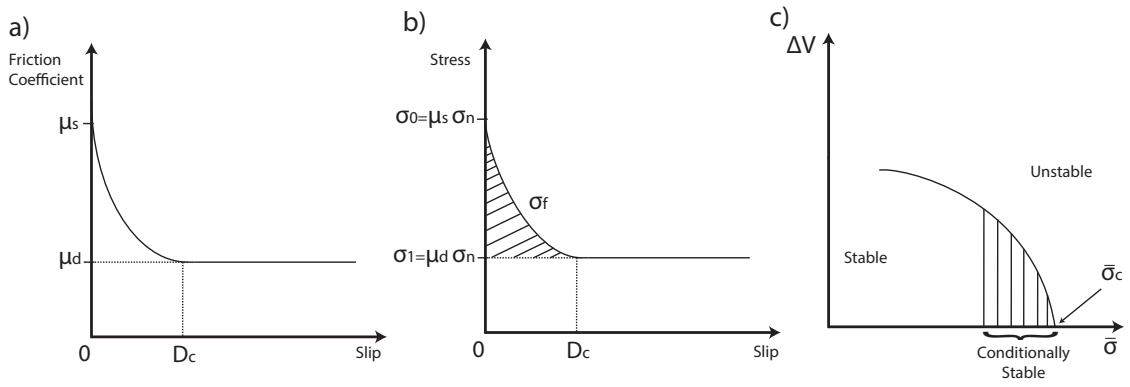

Figure 2.4: (a) Friction coefficient as a function of the slip, where the drop occurs at critical distance D_c. (b) Frictional Stress for the model described in (a) as a function of the slip. (c) Stability Regime, where $\bar{\sigma_c}$ denotes the critical normal stress to separate the stable and unstable states. (Figures modified from *Kanamori and Brodsky* [2004] and *Scholz* [1998]).

Based on laboratory experiments *Dieterich* [1979], *Ruina* [1983] and *Rice* [1983] determined one approach commonly used today and known as the Rate-and-State Friction Law, which is described by:

$$\tau \;=\; \left[\mu_0 \;+\; a\,\ln\left(\frac{V}{V_0}\right) \;+\; b\,\ln\left(\frac{V_0\theta}{D_c}\right)\right]\,\bar{\sigma} \tag{2.2}$$

Where:

- τ: Shear Stress.
- μ_0: State of the friction in $V \;=\; V_0$.

- V: Slip velocity.
- V_0: Reference Velocity.
- θ: State Variable. In the static case, it can be $\theta = t$. *Dieterich* [1979] proposed that it can be the mean age of the plates. θ can be obtained from:

$$\dot{\theta} \;=\; 1 \;-\Big(\frac{V\,\theta}{D_c}\Big) \tag{2.3}$$

- D_c: Slip critical distance.
- a and b: Properties defined from the material involved in the process.

The Equation 2.2 is also known as “slowness law" because, at the steady-state, the state variable (θ) is proportional to the slowness ($\theta_{ss} \;=\; \frac{D_c}{V}$) [*Scholz*, 1998]. The critical distance D_c is often interpreted as the sliding distance required to renew the contact population. Also, it is important to mention that even when μ_s and μ_d disappear from the equations, they are implicitly involved in the process through the state variable (θ) and in the slip velocity (V).

Analyzing the system stability based on the friction properties described above depends on two parameters: the slip critical distance D_c and the combined parameter $(a-b)$, defined as the velocity dependence of the steady-state friction, given by:

$$a - b = \frac{\partial \mu^{ss}}{\partial[\ln(V)]} \tag{2.4}$$

This equation generates two cases:

- If $(a - b) \geq 0$, the material presents a rate-strengthening behavior, which is intrinsically stable. Earthquakes cannot be nucleated in areas exhibiting this behavior and the ruptures will generate a negative stress drop stopping the rupture propagation.
- If $(a - b) < 0$, the material presents a rate-weakening behavior, which leads to a bifurcation of the regimes, expressed in the critical value of the effective normal stress ($\bar{\sigma_c}$):

$$\bar{\sigma_c} = \frac{D_c k}{-(a-b)} \tag{2.5}$$

When $\bar{\sigma} > \bar{\sigma_c}$, the slip is unstable under a quasi-static loading. It is only in this regime that the earthquakes can be nucleated. Conversely, if $\bar{\sigma} < \bar{\sigma_c}$, the system is conditionally stable, that means stable under quasistatic loading but may become unstable under sufficiently strong dynamic loading. The earthquakes may propagate into the conditionally stable field but cannot be nucleated [*Scholz*, 1998] (Figure 2.4c).

2.3.2 Seismic Cycle and Rate-and-State Friction Law

Today, it is widely accepted that friction on the faults is heterogeneous with interlacing rate-weakening and rate-strengthening patches [*Avouac*, 2015]. Classifying the fault according to the slip behavior leads to the following interpretation: seismic in areas where rate-weakening patches are tightly packed, and aseismic where they are sparse. The rate-weakening patches form asperities where stress builds up as the surrounding rate-strengthening areas creep. The manner how areas will interact and generate earthquake or not depends on the stress field configuration. As the stress builds up on the asperities during the interseismic period, they will be clustered forming just one asperity with a locking value close to 1 (maximum lock, Figure 2.5). The stresses responsible for the asperity clustering process are called "stress shadows" [*Bürgmann et al.*, 2005; *Hetland and Simons*, 2010; *Kanda et al.*, 2013; *Avouac*, 2015]. The areas surrounding this formed asperity are expected to host the earthquakes initiatiation (coseismic stage, Figure 2.5), and the way they will propagate depends on the state of stress on the fault plane. Besides, afterslip (early postseismic, Figure 2.5) would result from the aseismic slip of the rate-strengthening areas [*Hsu et al.*, 2006; *Perfettini et al.*, 2010]. One advantage of this model is that it allows generating SSEs [e.g., *Liu and Rice*, 2007] and tsunami earthquakes [e.g., *Bilek and Lay*, 2002], due to small heterogeneities on the contact.

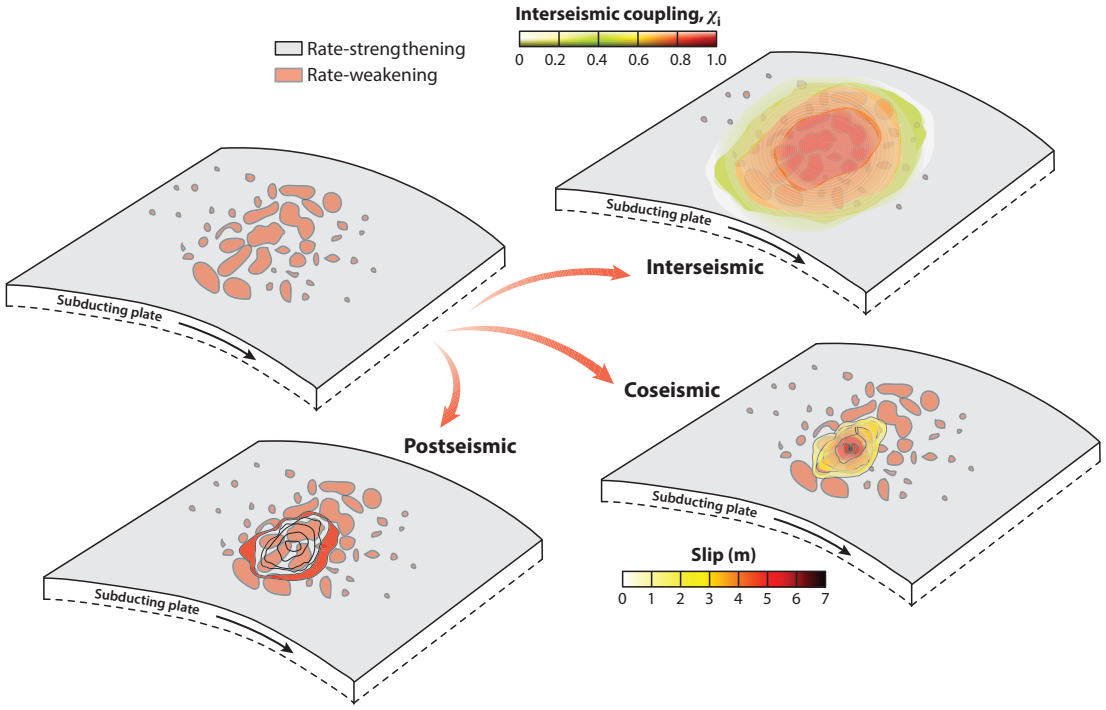

Figure 2.5: Rate-and-State behavior during the different steps of the seismic cycle (modified from *Avouac* [2015]).

2.4 Main Characteristics of Seismogenic Zones

2.4.1 Along Dip Segmentation

Scholz [1998] describes a general model of the subduction zones derived from the stability regimes mentioned above. Figure 2.6 shows that unstable regime mainly governs the seismogenic zone

[*Scholz*, 1998]. This unstable region is limited to the top and bottom by transition zones in conditionally stable regimes that flow into areas with a stable regime. Those areas mark a limit in the seismic behavior [*Scholz*, 1998].

The updip region is located offshore and close to the trench in convergent margins. It is characterized by an aseismic slip behavior, and in many cases by an absence of seismicity [*House and Jacob*, 1983; *Byrne et al.*, 1988; *Byrne and Fisher*, 1990; *Pacheco et al.*, 1993; *Moscoso et al.*, 2011; *Maksymowicz et al.*, 2017]. This area might be limited by the contact between the subduction interface and the accretionary wedge, where the transition between stable and unstable regime should occur. In this region, the transition from smectite to illite might occur at temperatures in the range 100°- 150°C [*Vrolijk*, 1990; *Hyndman and Wang*, 1993, 1995], and depths between 2 - 10 km [*Hyndman et al.*, 1997; *Oleskevich et al.*, 1999]. Where the temperature producing smectite dehydration is not reached, the contact of the subduction interface and the crystalline rocks is proposed as the updip limit. Also, *Moore and Saffer* [2001] have observed a good correlation between the updip limit and areas where the diagenesis process is seen, that corresponds to the sedimentary rock formation through the sediment compaction. The frictional behavior in this region is difficult to describe, because of the lack of data (stations are far away from the trench region), impacting the resolution of the kinematic models that try to explain the coupling on these areas [*Wang and Dixon*, 2004; *Lay and Schwartz*, 2004].

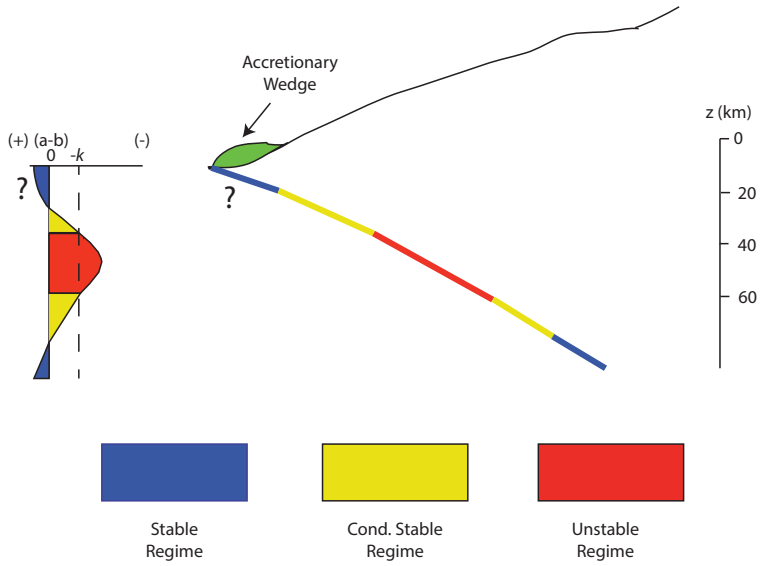

Figure 2.6: Scheme of the seismogenic zone at depth and in its vicinity, depending on the frictional regime characterized by (a-b). Question marks symbolize areas where the behavior is suspected, but it is not well understood yet. Figure modified from *Scholz* [1998].

Thermal models locate the downdip limit in the 350°C isotherm [*Savage and Plafker*, 1991; *Tichelaar and Ruff*, 1993; *Hyndman and Wang*, 1993; *Oleskevich et al.*, 1999]. This isotherm value corresponds to the ductility of quartz, obtained from laboratory experiments [*Tse and Rice*, 1986; *Blanpied et al.*, 1991, 1995], correlating as well with the maximum depth of subduction interface earthquakes around the world [*Brace and Byerlee*, 1970; *Molnar and Chen*, 1983; *Tse and Rice*, 1986;

Wong and Chapman, 1990; *Ito*, 1990; *Hyndman and Wang*, 1993]. An abrupt change of regime from an unstable to a stable can be considered unrealistic, thus a transition zone has been proposed between 350°- 450°C isotherms. This area relates to the ductile-fragile transition and some authors propose this region under a conditionally stable regime, due to the change from rate-weakening to rate-strengthening [*Scholz*, 1998; *Chlieh et al.*, 2004; *Avouac*, 2015]. The elements controlling the thermal behavior might be the thickness of subducted sediments, the age of the subducted slab, heat flows, convergence rates and slab dip [*Hyndman and Wang*, 1993; *Wang et al.*, 1995]. Some convergent margins exhibit a downdip limit where the 350°C isotherm is not reached. These observations have been made in areas where the oceanic plate subducts beneath a thin oceanic crust in island arcs and/or where the subducted slab is extremely old and/or where a thin sediment layer is present [*Tichelaar and Ruff*, 1991, 1993; *Hyndman et al.*, 1997; *Oleskevich et al.*, 1999]. In these cases, the Moho might mark the limit with a stable regime characterized by aseismic slip associated with the contact with serpentinized mantle [*Reinen et al.*, 1992; *Hyndman et al.*, 1997; *Peacock and Hyndman*, 1999; *Oleskevich et al.*, 1999]. Although these thermal values seem to be a robust indicator of the downdip limits, some exceptions have been seen. *McCaffrey et al.* [2008] have reported in Hikurangi (New Zeland) subduction zone, some evidence that downdip limit might be located at the 250°C isotherm, considerably lower than the one seen in other areas worldwide, most probably because of fluid interactions and/or mineralogical changes and/or unknown factors. Also, after Sumatra earthquake (M_w 9.1, 2004) the seismic rupture extended deeper than the known downdip limit [*Simoes et al.*, 2004], crossing the depth of continental Moho reported using wide-angle seismic data [*Dessa et al.*, 2009]. This behavior can be produced by the crust dehydration before the contact between the Moho and the subduction interface, or because the fluids do not infiltrate into the mantle, but drain on the subduction interface [*Seno*, 2005].

Using teleseismic data and analyzing the frequency content of great megathrust earthquakes through back-projection technique, *Lay et al.* [2012] have shown the dependency with the radiated energy at depth. This model has allowed relating the earthquake's size to the seismogenic zone segmentation, defining different domains on the subduction interface (Figure 2.7).

To the top of the seismogenic zone is defined the Domain A, near to the trench and where the tsunami earthquakes take place [*Kanamori and Kikuchi*, 1993; *Ammon et al.*, 2006; *Lay et al.*, 2011]. This area is characterized by an anelastic deformation and a stable sliding, at depths between 2 - 15 km (Figure 2.7a and b). The transition zone (deeper part) may be governed by conditionally stable regime surrounded by small asperities.

The Domain B is located between 15 - 35 km depths (Figure 2.7a and b). This region is where the megathrust earthquakes are nucleated, generating large slip and a high amount of low-frequency radiation. It may be governed mainly by unstable regime with some aseismic slip surrounding the asperities.

In the domain C, located between 35 - 60 km depths (Figure 2.7a and b), a large amount of high-frequency radiations are emitted. It is characterized by patches with a small amount of slip

(asperities much smaller than in region B) and governed by a regime mixed between stable, unstable and conditionally stable areas.

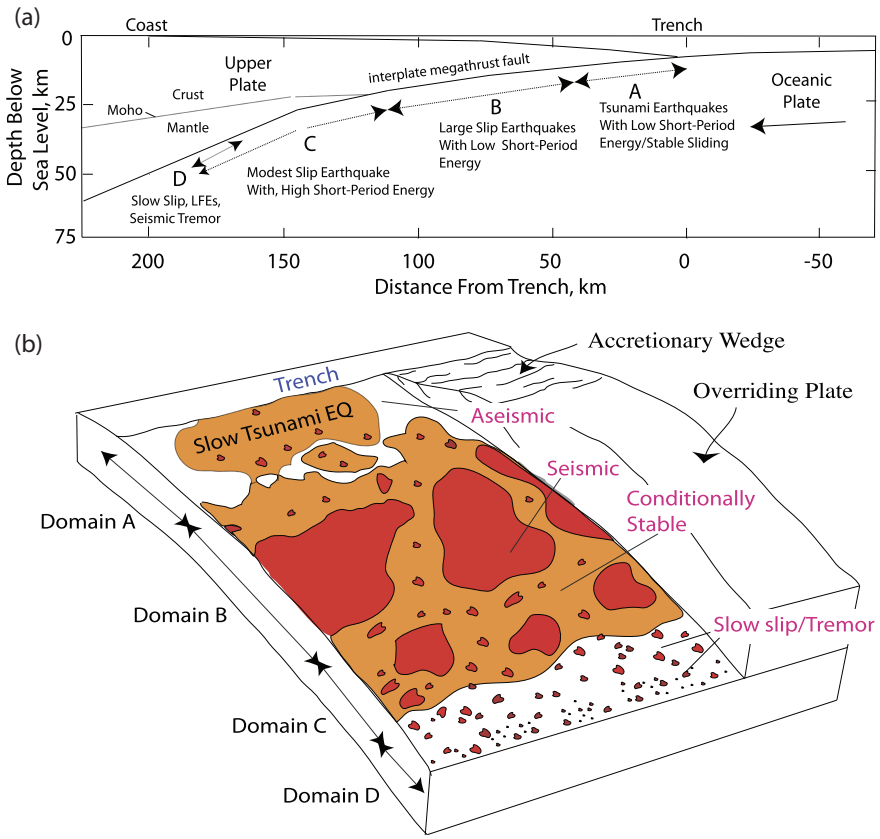

Figure 2.7: (a) Schematic cross-section of a subduction zone, indicating the four domains of megathrust rupture characteristics regarding frequency content and earthquake type generation. (b) Cut-away schematic characterization of the megathrust frictional environment, related to Domains A, B, C and D defined in (a). Figure from *Lay* [2015].

Finally, the Domain D is placed deeper than 60 km (Figure 2.7a and b). This region represents a transition at the deep edge of the seismogenic zone, only present in some regions, with diverse observations of SSEs, low-frequency earthquakes, and/or seismic tremor. This area is mainly governed by stable regime, with some small embedded areas of conditionally stable and stable regime.

2.4.2 Along Strike Segmentation

The observations and models have shown that the subduction zones are not only segmented along dip, but also along strike, being able to define two main features. The segments that break during an earthquake with high mean stress regimes are defined as asperities [*Scholz and Engelder*, 1976; *Lay and Kanamori*, 1981]. They are usually characterized by a high coseismic slip [e.g., *Béjar-Pizarro et al.*, 2010; *Peyrat et al.*, 2010; *Vigny et al.*, 2011; *Moreno et al.*, 2012; *Duputel et al.*, 2015; *Klein et al.*, 2017], while those areas where the seismic rupture is stopped are called barriers [e.g., *Das and Aki*, 1977] and they can be classified either as geometrical barriers or as inhomogeneous barrier [*Aki*, 1979].

Concerning the along strike segmentation in subduction zones, there are varied interpretations about the barriers and asperities. In some regions, the segmentation can be related with morphologic structures on the incoming plate such as seamounts [*Kelleher and McCann*, 1976, 1977; *Cummins et al.*, 2002; *Bilek et al.*, 2003; *Kodaira et al.*, 2002], oceanic ridges [*Kelleher and McCann*, 1976; *Perfettini et al.*, 2010] or fracture zones *Aki* [1979]; *Contreras-Reyes and Carrizo* [2011]. Seamounts have been proposed to increase the seismic coupling, influencing the size of the maximum slip or asperity of megathrust earthquakes [*Bilek et al.*, 2003]. This characteristic allows for those structures to act as barriers *Kodaira et al.* [2002] or as asperities [*Abercrombie et al.*, 2001; *Bilek et al.*, 2003], because the seamount frictional behavior depends on the seafloor heterogeneity, the properties of the subducting material, the temperature, the pressure and the step of the seismic cycle in the region [*Bilek et al.*, 2003]. Also, structures of the overriding plate seem to affect the segmentation of the seismogenic zone such as peninsulas [*Armijo and Thiele*, 1990; *Béjar-Pizarro et al.*, 2010; *Perfettini et al.*, 2010; *Carena*, 2011; *Schurr et al.*, 2012; *Villegas-Lanza et al.*, 2016a] and fault systems [*Collot et al.*, 2004; *Audin et al.*, 2008], as they correlate with structures at depth, that are uncoupled and act as a seismic barrier [*Ruegg et al.*, 1996; *Delouis et al.*, 1996; *Kodaira et al.*, 2006; *Delouis et al.*, 2009; *Melnick et al.*, 2009; *Béjar-Pizarro et al.*, 2010]. The geometrical barriers are not a feature observed just along strike, but they have also been proposed as along dip barrier that might stop the seismic rupture. Such is the case of abrupt changes in the dip of the subducting plate that might stopped the seismic rupture or diminished the amount of slip [*Aki*, 1979; *King*, 1986; *Armijo and Thiele*, 1990; *Cummins et al.*, 2002; *Ito et al.*, 2005; *Wesnousky*, 2006; *Contreras-Reyes et al.*, 2012].

Gravimetric and seismic data also help to better understand the along strike segmentation of the seismogenic zone, providing a complementary view. *Wells et al.* [2003] evidence a spatial correlation between forearc basins and the peak of slip of several great earthquakes, suggesting that the basin is an indicator of a long-term seismic moment release. *Song and Simons* [2003] have proposed another way to analyze the gravity data through the definition of the Trench Parallel Gravity Anomaly (TPGA), where areas negatives values correlate with the coseismic slip in subduction zones. For example, *Maksymowicz et al.* [2016] have shown in North Chile that strong changes in the density (obtained through gravimetric data modeling) seems to be along strike barrier indicators, with a debated temporal persistence.

Coupling maps offer another independent view of the segmentation along strike. They provide a wide vision about lock/unlocked areas on the seismogenic zone, observing a good correlation between recent seismic ruptures and high lock patches [e.g., *Ruiz et al.*, 2014; *Métois et al.*, 2016; *Nocquet et al.*, 2016; *Villegas-Lanza et al.*, 2016a]. Besides, poorly coupled areas seem to be well correlated with regions where the seismic rupture are stopped, many times related to morphological structures (peninsulas, ridges, fractures zone or fault systems) [e.g., *Béjar-Pizarro et al.*, 2010; *Perfettini et al.*, 2010; *Béjar-Pizarro et al.*, 2013; *Nocquet et al.*, 2016; *Métois et al.*, 2016; *Ruiz et al.*, 2016].

Chapter 3

The Subduction Zone of Central Andes

3.1 Plate Kinematics between Nazca (NA) and South American (SOAM) Plates

3.1.1 Convergence between NA and SOAM

The Andes are a long mountain belt of ∼8000 km long (Figure 3.1) that results from the convergence between Nazca (NA) and South American (SOAM) plates. Geological dating and global tectonic models have been used to rebuild the history of the convergence rate and azimuth. Global plate tectonic models use the paleomagnetic anomalies registered in the oceanic seafloor, directions of transform faults and/or hot-spot track to reconstruct past motions of tectonic plates, averaged over a few million years [*Gordon and Jurdy*, 1986; *Pardo-Casas and Molnar*, 1987; *Gripp and Gordon*, 2002]. Some of those models are: [*Minster et al.*, 1974], NUVEL-1 [*DeMets et al.*, 1990], NUVEL-1A [*DeMets et al.*, 1994; *Bird*, 2003] or HS3-NUVEL-1A [*Gripp and Gordon*, 2002]. In the Andean region (10°- 20°S), using this kind of models the convergence rate and the azimuth reported are 75 - 80 mm/yr and N72°E - N75°E [e.g., *DeMets et al.*, 1994; *Gripp and Gordon*, 2002; *Bird*, 2003].

During the 90's, the spatial geodesy provided constraints on current tectonic motion around the world [*Larson et al.*, 1997; *Norabuena et al.*, 1998; *Altamimi et al.*, 2002, 2011, 2016; *Bird and Kreemer*, 2015]. Using present-day kinematic models, the angle of convergence between NA and SOAM plates has been estimated to N76°E - N77°E [*Angermann et al.*, 1999; *Klotz et al.*, 2001; *Vigny et al.*, 2009], with convergence velocities ranging between 60 - 80 mm/yr depending on the model and the analyzed region [*Norabuena et al.*, 1998; *Angermann et al.*, 1999; *Klotz et al.*, 2001; *Bevis et al.*, 2001; *Kendrick et al.*, 2001, 2003, 2006; *Vigny et al.*, 2009; *Villegas-Lanza et al.*, 2016a].

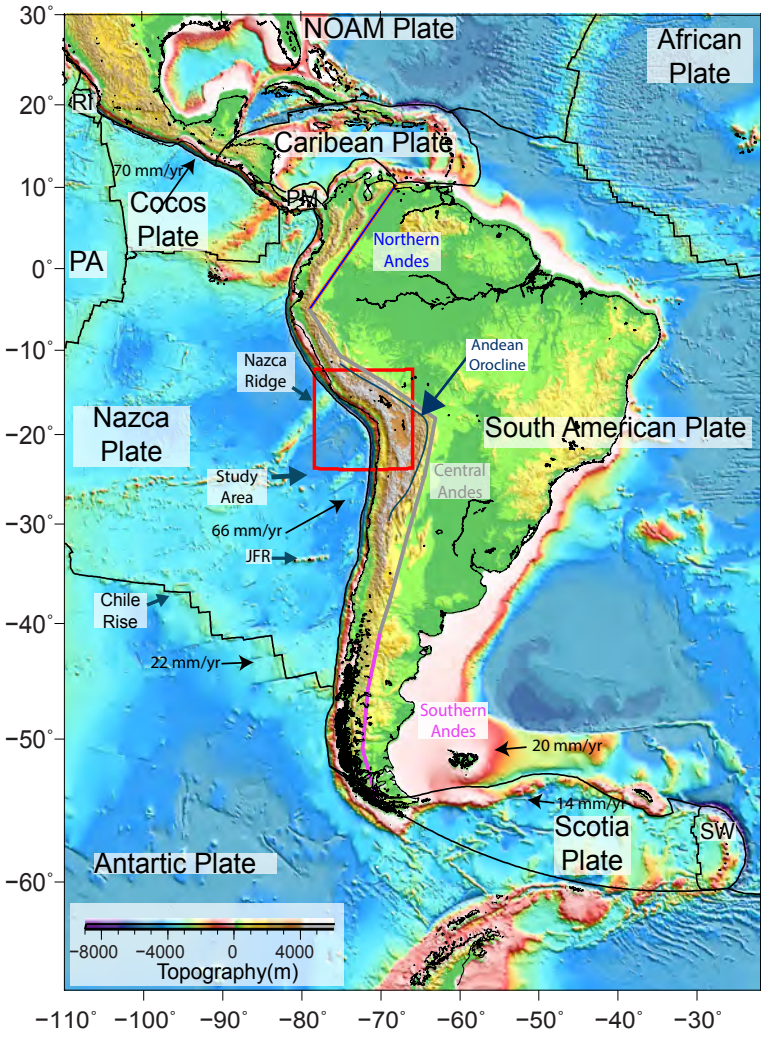

Figure 3.1: Location and Tectonic context of the study area (red square). The plates boundaries are from *Bird* [2003]. Pacific plate (PA), Rivera Plate (RI), Panama Plate (PM), Sandwich Plate (SW) and Juan-Fernandez Ridge (JFR). Velocities are from *Angermann et al.* [1999]; *Trenkamp et al.* [2002]; *Bird* [2003].

3.1.2 Main Blocks and Movements in the Central Andes

The increase in the deformation field resolution worldwide, associated with the rise in the number of GPS stations, allows detecting others processes, such as internal deformation of the continents and slip partitioning. Forearc-sliver translation accommodating the margin-parallel component of oblique convergence is a common process at subduction zones that has first been described to explain the existence of Great Sumatran strike-slip fault in parallel to the Sumatra subduction zone [*Fitch*, 1972]. Those models are now validated by the strain-rates provided by the GPS, showing that much of the along strike shear is accommodated by permanent deformation of the upper plate along fault zones [*McCaffrey*, 1992; *Prawirodirdjo et al.*, 1997; *McCaffrey and Nabelek*, 1998; *Wang et al.*, 2007]. This kind of behavior has been reported along the Andean region, notably at the latitude of Ecuador, Peru, and South Chile. *Nocquet et al.* [2014] have characterized the North Andean Sliver in Ecuador (Figure 3.2) that moves as a rigid block at 7.5 - 9.5 mm/yr towards the northeast . In Peru, the Inca sliver is wedged between the NA and SOAM plates [*Nocquet et al.*, 2014; *Villegas-*

Lanza et al., 2016a]. The western part of the Inca sliver presents a rigid block motion ranging from north (border with Ecuador, ∼5°S) to south (Arica bend, ∼20°S) with values of 4.4 - 5.3 mm/yr (Figure 3.2). Slip partitioning between the western Peruvian sliver and the eastern Peruvian - Subandean range exists, with velocities between 1.2 - 2.5 mm/yr [*Villegas-Lanza et al.*, 2016a] (Figure 3.2).

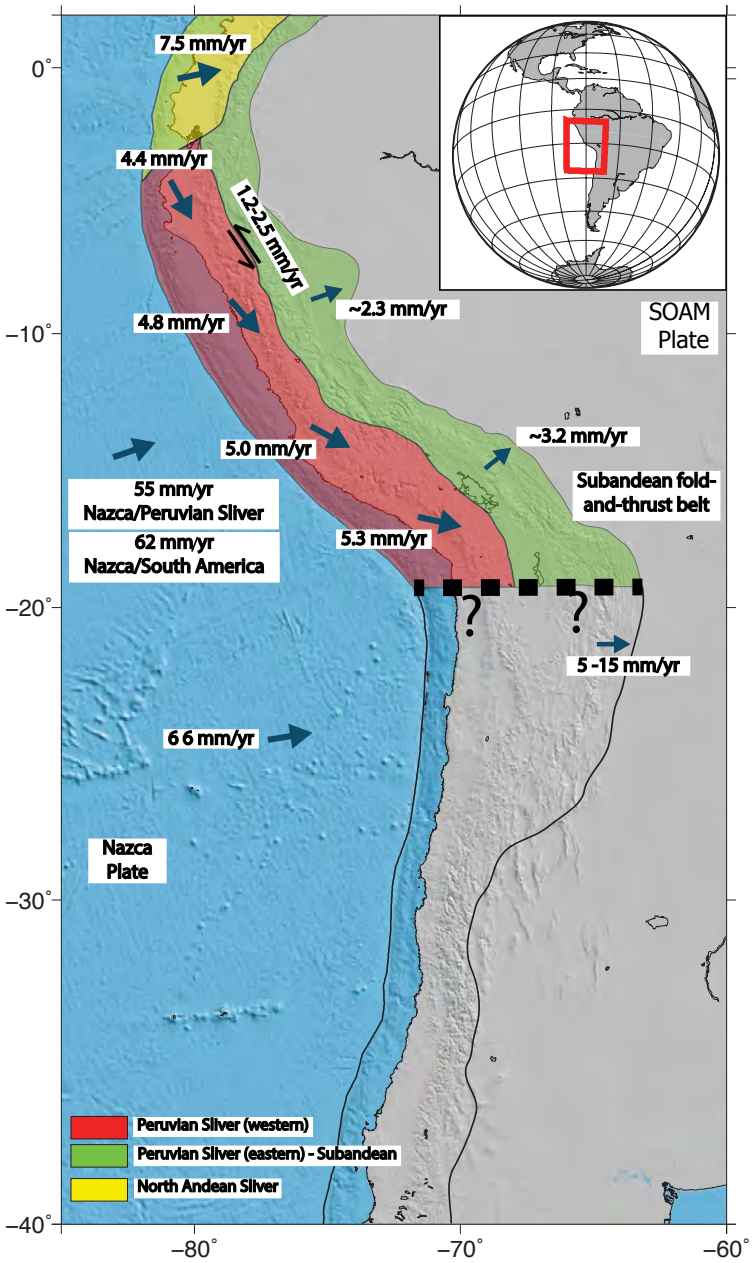

Figure 3.2: Scheme of the main continental slivers contributing to the deformation partitioning in the North and Central Andes. The arrows indicate the convergence velocities. Question marks symbolize the open question about where the slivers end in Chile. Figure modified from *Villegas-Lanza et al.* [2016a] and *Métois et al.* [2016].

In the southern part of Chile (∼40°S), the Liquiñe-Ofqui fault moves in strike-slip 6.5 mm/yr to accommodate the lateral sliver motion and the obliquity of the convergence [*Wang et al.*, 2007]. In Chile, between 18°S and 37°S, there is no clear evidence of sliver block motion that would accommodate the obliquity of the convergence. However, a tectonic sliver, located between the subduction and

the Subandean ranges has an individual movement that differs from stable South America [*Chlieh et al.*, 2011; *Métois et al.*, 2013, 2016] (Figure 3.2). *Kley* [1996] has shown using geological data the existence of shortening at the east flank of the Andes, especially at the latitude of the Central Andes, revealed by a fold-and-thrust belt. At the end of the 90's, GPS started to measure shortening in the area, confirming the geological evidence with rates ranging from 5 to 15 mm/yr, in the Bolivian Subandean ranges [e.g *Norabuena et al.*, 1998; *Bevis et al.*, 2001; *Chlieh et al.*, 2011; *Brooks et al.*, 2011] (Figure 3.2). To the north, *Nocquet et al.* [2014] and *Villegas-Lanza et al.* [2016a] have measured 2.3 - 3.2 mm/yr of shortening across the Ecuadorian and Peruvian Subandean ranges. These results describe a complex deformation process in the Central Andes region, where internal deformation combining shortening and strike slip are superimposed to the deformation associated with the seismic cycle on the subduction zone [*Chlieh et al.*, 2011; *Métois et al.*, 2013; *Nocquet et al.*, 2014; *Villegas-Lanza et al.*, 2016a; *Métois et al.*, 2016].

3.1.3 Main Tectonic Features

Structures of the Overriding Plate

The Andes were built as a response to the subduction of NA plate beneath the SOAM plate, where a crustal thickening is observed, associated with a lithosphere thinning below the Altiplano Plateau proposed by some authors [*Isacks*, 1988; *Allmendinger et al.*, 1997; *Garzione et al.*, 2006]. *Armijo et al.* [2010, 2015] divided the area in two major structures: the marginal block and the Andes (Figure 3.3b), that can be subdivided as explained below.

The Marginal Block and the Coastal Structures The marginal block is composed by the Continental Margin, the Central Depression and the Precordillera.

The Continental Margin (CM Figure 3.3) is extending from the trench until the coast (almost completely under water) including the Continental Slope Scarp [*James*, 1971; *Huene and Scholl*, 1991; *Patzwahl et al.*, 1999; *Contreras-Reyes et al.*, 2012]. Two kinds of basal erosion has been reported: seamounts subduction [*Ranero and Von Huene*, 2000] and the existence of horst-grabens, which are a contribution to the uplift and extension of the continent [*von Huene and Pecher*, 1999].

A Coastal Scarp marks the limit between the Continental Margin and the Coastal Cordillera (Figure 3.3b). Two main theories have been proposed to explain the creation and existence of this feature. The first one suggests that this coastal scarp is a characteristic generated by marine erosion [*Mortimer*, 2010]. The second one suggests that it is a big normal fault, related to the subduction, with ∼1000 km length [*Armijo and Thiele*, 1990]. This last hypothesis is also supported by the change in the dip angle of the slab shown using seismic data by *Contreras-Reyes et al.* [2012]. The Coastal Scarp would be the surface expression of a crustal fault caused by anomalous stresses on the overriding plate, generated by a strong gradient on the coupling around the kink area [*Armijo*

and Thiele, 1990; *Contreras-Reyes et al.*, 2012].

One of the characteristics that can be observed along the coast is the presence of peninsulas, such as the Mejillones Peninsula in Chile (∼23°S), or the Ilo peninsula in Peru. The Mejillones peninsula represents an anomaly in the Coastal Scarp with a length of ∼50 km and a width of ∼30 km and is characterized by a series of smaller normal faults parallel to the coast [*Armijo and Thiele*, 1990; *Delouis et al.*, 1997; *Allmendinger and González*, 2010]. One hypothesis about its formation is that this structure is an uplifted block [*Armijo and Thiele*, 1990; *Victor et al.*, 2011], at estimated rates of ∼0.25 mm/yr in the last 500 Kyr [*Ortlieb et al.*, 1996]. In southern Peru, the Ilo Peninsula is a 100 km long feature associated with an extensional regime characterized by faults in the EW direction [*Audin et al.*, 2008; *Ortlieb et al.*, 1996]. Both peninsulas are important tectonic structures that act as permanent barriers for subduction earthquakes [*Audin et al.*, 2008; *Béjar-Pizarro et al.*, 2013; *Métois et al.*, 2016].

Finally, the Coastal Cordillera (CC in Figure 3.3b) is a structure that begins at the Coastal Scarp and ends in the Central Depression. Its altitude is less than 2000 m, disappearing southern Ilo Peninsula in Peru and reappearing at ∼20°S. This region marks the transition between the Continental Margin and the Andes [*Isacks*, 1988; *Armijo and Thiele*, 1990; *Scheuber and Reutter*, 1992; *Charrier et al.*, 2005; *Armijo et al.*, 2015].

The Andes The Andes can be divided into four big entities: the Western Cordillera, the Altiplano Plateau, the Eastern Cordillera and the Subandean ranges (Figure 3.3a and b).

The Western Cordillera (Figure 3.3) has mean heights of 3800 - 4500 m and it is the place where the volcanic arc is located, bounded to the west by the Precordillera and to the east by the Altiplano Plateau. The Altiplano Plateau is a depression area between the Western and Eastern Cordillera, where the mean heights are 4000 m (Figure 3.3), ranking it as the second highest plateau around the world after the Tibet [*Allmendinger et al.*, 1997]. This area is cut by several reverse faults of high angle [*Allmendinger et al.*, 1983] and is composed of sedimentary and volcanic rocks. One characteristic of this region is that it has its own drainage system within the depression.

The Eastern Cordillera (Figure 3.3) is an area where the height is going over 6500 m, which is formed by a flexure belt where is possible find reverse fault of high complexity. In this region, a cortical shortening is observed due to the subduction with a complex pattern of deformation depending on the latitude [*Chlieh et al.*, 2011; *Métois et al.*, 2013; *Nocquet et al.*, 2014; *Villegas-Lanza et al.*, 2016a; *Métois et al.*, 2016].

Finally, to the east, the Subandean ranges is composed by an active fold and thrust belts (Figure 3.3). Here is accommodated most of the crustal shortening in the Central Andes [*Kley and Monaldi*, 1998]. Geological shortening velocities vary between 5 - 25 mm/yr [*Baby et al.*, 1997; *Kley and Monaldi*, 1998], while the geodetic shortening vary between 3 - 15 mm/yr [*Norabuena et al.*, 1998;

Klotz et al., 1999; *Bevis et al.*, 2001; *Khazaradze and Klotz*, 2003; *Chlieh et al.*, 2004, 2011; *Brooks et al.*, 2011; *Métois et al.*, 2016].

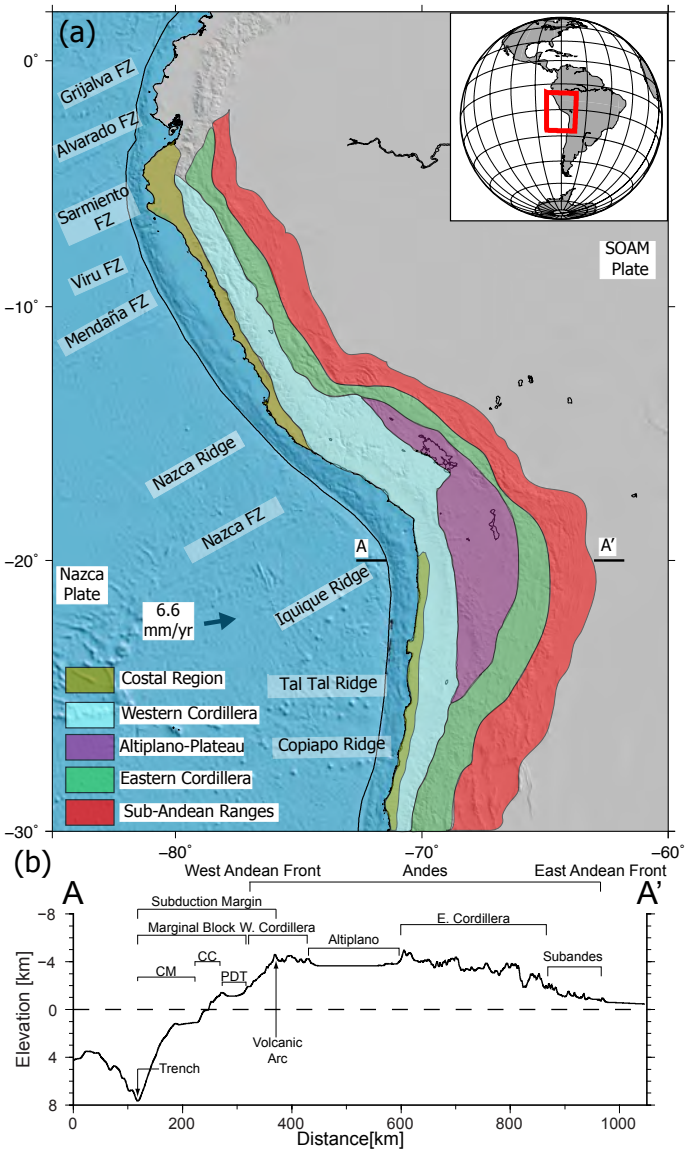

Figure 3.3: (a) Topography and first order geology of the Central Andes. A-A' denotes the location of the profiles observed below. FZ denotes Fracture Zone. (b) A profile that shows the morphotectonics division proposed by *Armijo et al.* [2010]. MC is the continental margin, CC is the coastal cordillera, PDT is the Central Depression and the Precordillera. Figure modified from *Armijo et al.* [2010, 2015]; *Villegas-Lanza et al.* [2016a].

Structural Features on the NA Oceanic Plate

The Nazca oceanic plate is cut by tectonic features (ridges and fractures zones) that have been proposed to affect the lateral segmentation of the subduction zone [*Aki*, 1979; *Hoffmann-Rothe et al.*, 2006; *Béjar-Pizarro et al.*, 2010; *Contreras-Reyes and Carrizo*, 2011; *Carena*, 2011]. The ridges are oceanic hotspot tracks that can be detected employing bathymetric data. For example, the Nazca Ridge (Figure 3.3a) was formed at the Easter Island hotspot on the Pacific-Farallon/Nazca spreading center [*Pilger*, 1984]. Other ridges are in the zone such as Iquique, Copiapo, and Tal - Tal ridges

(Figures 3.3a).

The oceanic Nazca plate is further segmented by several oceanic fracture zones (Figure 3.3a) formed at the Pacific-Nazca and Antarctic-Nazca spreading centers (Tebbens et al., 1997), such as Nazca, Mendaña, Viru, Sarmiento, Alvarado and Grijalva Fractures Zones. Also, these features seem to be related with the subduction segmentation, limiting seismic ruptures and/or patches of high coseismic slip [*Contreras-Reyes and Carrizo*, 2011].

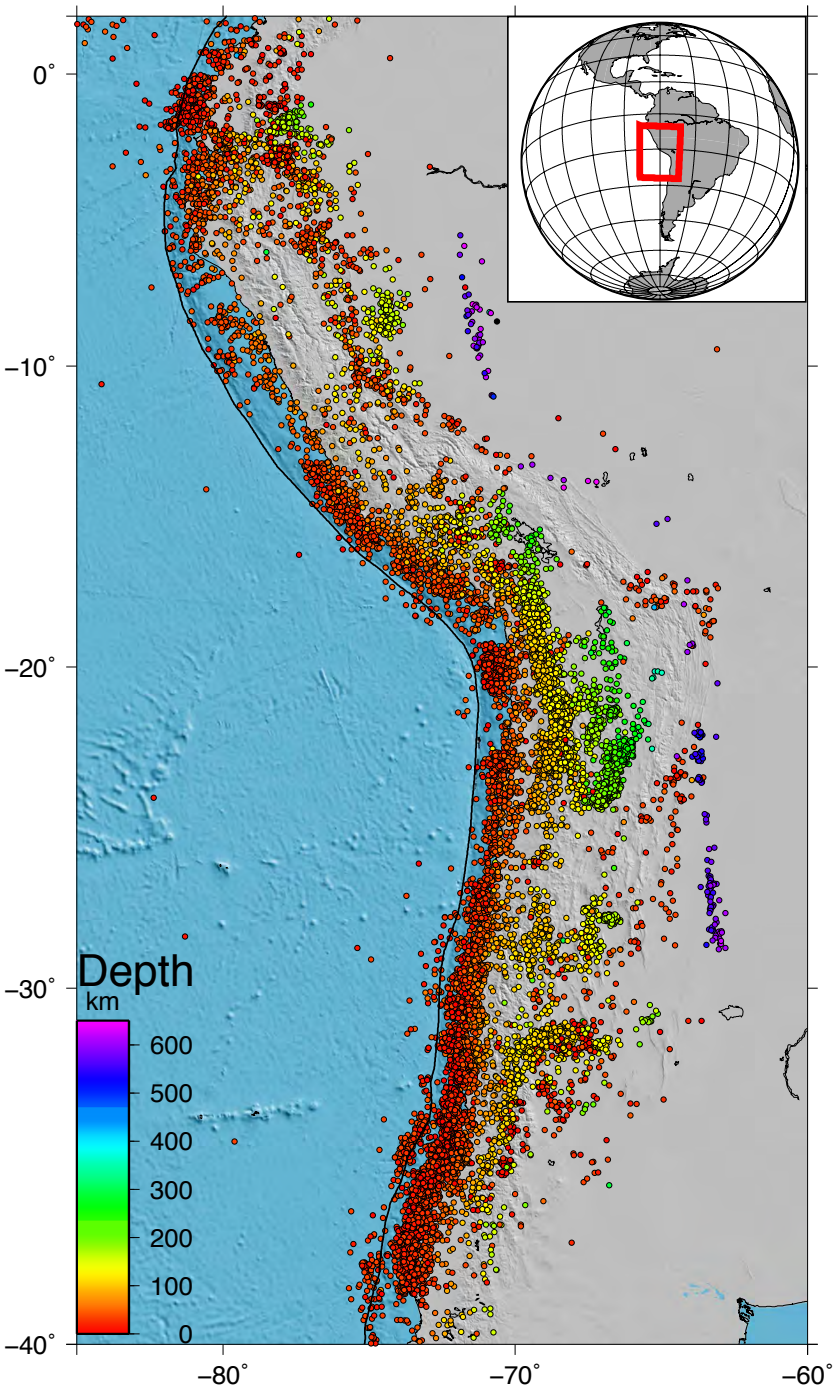

Figure 3.4: Distribution of seismicity along the Central Andes in the period 1990 - 2014 and color-coded by depths. The seismicity is taken from *International Seismological Centre* [2017] with magnitudes ranging from M 4.0 - 8.0.

3.2 Seismological Features

3.2.1 Seismicity Distribution

The Figure 3.4 shows the seismicity distribution in the Central Andes, exhibiting an heterogeneous pattern both along strike and dip. Along the entire Continental Margin seismicity occurs on the subduction interface and its vicinity, ranging depth between 0 - 50 km (red dots in Figure 3.4). Most of the seismicity is associated with the occurrence of events during the period 1990 - 2014 such as Arequipa, Nazca, Pisco, Iquique, Tocopilla, or Antofagasta earthquakes.

A specific feature observed in the central part of the Andes (15°- 25°S) is related to the high activity of intermediate-depth seismicity (orange-yellow dots Figure 3.4), characterized by depths between 80 - 150 km. Three hypotheses have been proposed to explain the occurrence of such seismicity: transformational faulting, ductile shear instability and dehydration embrittlement [*Hacker et al.*, 2003]. *Astiz and Kanamori* [1986] proposed that tensional (slab-pull) events may occur before large thrust events in the coupled plate interface, while compressional (slab-push) events occur after the main thrust event. This last idea is intriguing because almost all the focal mechanisms reported for this period, in the ISC catalog [*International Seismological Centre*, 2017], are slab pull [*Bouchon et al.*, 2016; *Jara et al.*, 2017]. Also, this region presents a high activity of deep seismicity (green dots Figure 3.4), ranging depths of 150 - 300 km, with mechanisms poorly understood and complicated seismic ruptures patterns [*Frohlich*, 2006].

In the Subandean ranges, the shallow seismic activity is observed at depths of 0 - 15 km (red dots on the east of the region, Figure 3.4), mostly associated with the shortening processes mentioned above and with the capacity of generating great earthquakes [*Brooks et al.*, 2011]. Some very deep activity is seen close to ∼10°S and ∼25°S (purple dots in Figure 3.4). Those deep events are associated with the change in the style of the subduction. In those two regions, the subduction is in flat slab manner [*Gutscher et al.*, 2000; *Gutscher*, 2001; *Pardo et al.*, 2002].

3.2.2 Great Historical and Instrumental Earthquakes

Based on the historical seismicity and the morphological features of the subducting NA plate, it is possible to divide the study area into four major segments (Figure 3.5) [*Silgado Ferro*, 1978; *Kausel*, 1986; *Dorbath et al.*, 1990; *Comte and Pardo*, 1991; *Nishenko*, 1991; *Madariaga*, 1998; *Tavera and Buforn*, 1998; *Bilek*, 2010; *Carena*, 2011]:

- The northern Peru segment between of 3°- 10°S, limited by the Guayaquil Gulf to the north and by the Mendaña fracture zone to the south.
- The central Peru segment, bounded by the Mendaña fracture zone (10°S) to the north and the Nazca Ridge (∼15°S) to the south.
- The southern Peru segment, extending from the Nazca Ridge to the Arica bend (∼18°S).

- The northern Chile segment between the Arica bend down to the Mejillones Peninsula in the south (∼23°S)

The northern Peru segment is characterized by the absence of great earthquakes ($M_w \geq 8.5$) and the sparse occurrence of moderate- to large-earthquakes ($M_w \geq 7.5$) that can trigger local tsunamis. The largest earthquakes reported in this region are the 1619 earthquake (M_w 7.7), 1953 (M_w 7.8), 1959 (M_w 7.5), 1960 (M_w 7.6) and 1996 (M_w 7.5) (Figure 3.5).

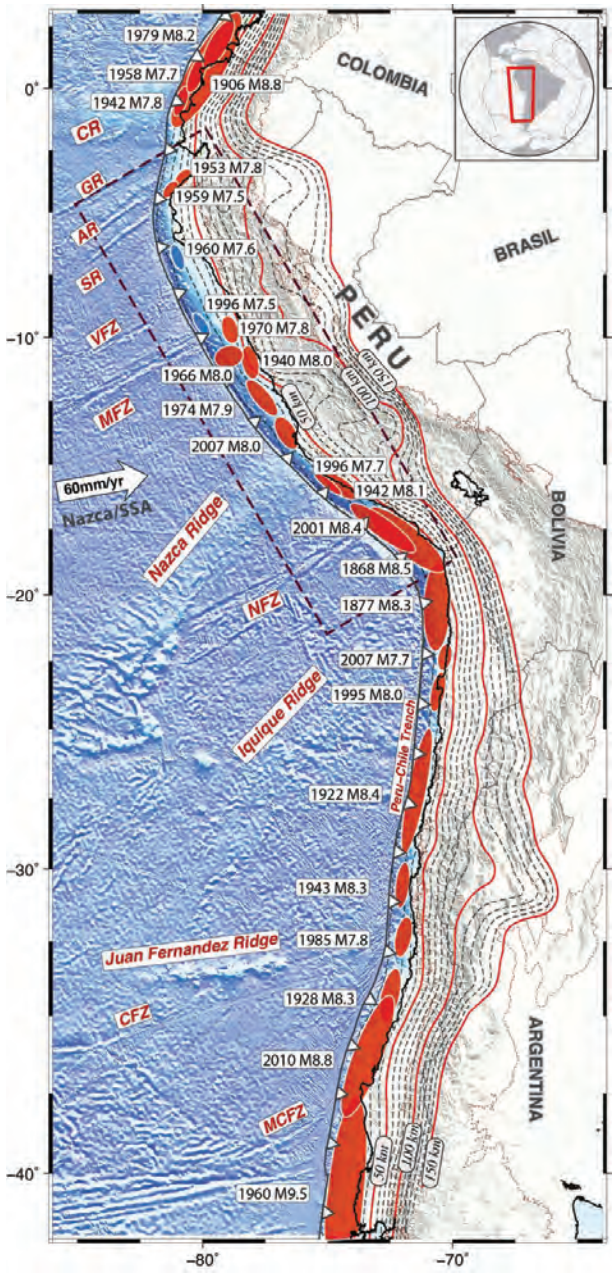

Figure 3.5: South American tectonic setting from *Villegas-Lanza et al.* [2016a]. The red ellipses indicate the approximate rupture areas of large subduction earthquake (M ≥ 7.5) between 1868 and 2015 [*Silgado Ferro*, 1978; *Beck and Ruff*, 1989; *Dorbath et al.*, 1990; *Beck*, 1998]. Main bathymetric features are indicated with the names in white boxes.

The central Peru segment presents great- and large-earthquakes occurrences. The region was struck by two great historical earthquakes in 1687 (M_w 8.4) and by the Lima earthquake in 1746

(M_w 8.6), both very destructive events and with large tsunamis reported. Also, large earthquakes (historical and recent) occurred in this region, such as 1586 earthquake (M_w 8.1), 1664 (M_w 7.5), 1678 (M_w 8.0), 1725 (M_w 7.5), 1806 (M_w 7.5), 1828 (M_w 7.5), Lima-Callao earthquake in 1940 (M_w 8.0), Lima-Callao earthquake in 1966 (M_w 8.0), Lima earthquake in 1974 (M_w 7.9) and Pisco earthquake in 2007 (M_w 8.0) (Figure 3.5).

The south Peru region has been hit by several great earthquakes that generated huge destructive tsunamis, such as 1604 earthquake (M_w 8.7), 1784 (M_w 8.4), 1868 (M_w 8.8) and the Arequipa earthquake (M_w 8.4). Also, large historical and recent earthquakes have been reported in the region, as the 1512 earthquake (M_w 7.7), 1582 (M_w 7.5), 1687 (M_w 8.0), 1715 (M_w 7.5), 1821 (M_w 7.8), 1833 (M_w 7.7), 1913 (M_w 7.8), the Nazca 1942 and 1996 earthquakes (M_w 8.2 and M_w 7.7) (Figure 3.5).

The north Chile segment have presented great historical earthquakes, such as the events in 1604 (M_L 8.7) and in 1877 (M_L 8.8), both generating destructive tsunamis. The large-historical and -recent earthquakes reported in the region include: the 1543 earthquake ($M_s \leq 7.7$), 1615 (M_s 7.9), 1768 (M_s 7.7), 1933 (M_s 7.5), the Tocopilla earthquake in 2007 (M_w 7.7) and Iquique earthquake in 2014 (M_w 8.1). Although it did not occur in this region itself, it is important to mention the occurrence of the Antofagasta earthquake in 1995 (M_w 8.1), in the southern part of the segment, because of its relationship with the Mejillones Peninsula, which acted as a barrier for the seismic rupture [*Ruegg et al.*, 1996; *Delouis et al.*, 1996; *Klotz et al.*, 1999; *Carlo et al.*, 1999; *Pritchard et al.*, 2002] (Figure 3.5).

As it was mentioned in the previous section (Figure 3.4), the region shows a high-rate of intermediate-depth seismicity. Less often than subduction events, this region exhibits some recorded large earthquakes, which recurrence time is unknown. The Lamas earthquake in 2005 (M_w 7.5) hit at 115 km depth the northern Peruvian segment. In 2005, Tarapaca earthquake (M_w 7.8) struck the central part of the northern Chile area at 100 km depth [*Peyrat et al.*, 2006; *Delouis and Legrand*, 2007; *Peyrat and Favreau*, 2010], while in 1950, the southern part of the Chilean region was affected by the Calama slab-pull event M_w 8.0 [*Kausel and Campos*, 1992].

Deep earthquakes occur less often and their mechanism of generation are poorly understood [*Frohlich*, 2006]. Large deep earthquakes have been reported in the Central Andes, more precisely in the south Peru segment. One of the biggest recent events recorded occurred in Bolivia at ∼600 km depth in 1994 with a magnitude M_w 8.3 [*Kikuchi and Kanamori*, 1994; *Silver et al.*, 1995; *Ihmlé*, 1998]. *Ruiz et al.* [2017b] have studied the deep doublet earthquakes occurred in 2015 with focus depth of ∼600 km with magnitudes of M_w 7.5 and M_w 7.6. These events in the region seem to occur along the Wadati-Benioff zone, which delineates the cold core of subducting oceanic lithosphere [*Frohlich*, 2006] or because of a kink in the subducted lithosphere [*Ihmlé*, 1998].

3.2.3 Seismic Gaps, Interseismic Coupling and Lateral Segmentation

A seismic gap, defined as a region of simple plate boundaries that have not ruptured in great earthquakes since many decades, is a likely site for future events [*Kelleher et al.*, 1973; *McCann et al.*, 1979; *Nishenko and McCann*, 1981; *Nishenko*, 1991]. To considere a plate boundary segment as being a seismic gap, it must have a history of prior great earthquakes ant not have ruptured in a event for a long period of time [*McCann et al.*, 1979; *Nishenko*, 1991]. Based on the historical and recent earthquakes information, three areas can be considered as seismic gaps in the Central Andes: the central and southern Peruvian segments and the north Chile region (described in the previous section).

The central Peru segment has not been hit by a great earthquake since 1746, although several large events have been reported. Interseismic coupling maps available in the region indicate that the area is locked, indicating that the segment is quite mature and hosts a great earthquake in the next decade. The magnitudes expected are between 8.6 - 9.2 M_w , comprising an area of ∼300 km from the Mandaña fracture zone up to the Nazca ridge zone [*Chlieh et al.*, 2011; *Villegas-Lanza et al.*, 2016a].

The south Peru zone was considered as a mature seismic gap [*Dorbath et al.*, 1990; *Nishenko*, 1991; *Comte and Pardo*, 1991] until the occurrence of Arequipa earthquake in 2001 (M_w 8.4) that broke the central part of this region. *Villegas-Lanza et al.* [2016a] performed a detailed analysis of the geodetic data, obtaining a high and heterogeneous coupling in the region. They show that coupling is localized within two regions of 100 - 150 km at latitudes of 16°S and 18°S. The northern area is located south of the Nazca ridge and seems to have a relationship with the ruptures of large earthquakes in 1913, 1942 and 1996, while the southern region previously broke during the large earthquake in 1833 and with the great event in 1868. In both cases, the potential earthquake expected may have a magnitude ∼M_w 8.0. The area appears segmented by the region hit by Arequipa earthquake in 2001. A shallow and highly coupled region, associated with the area of high 2001 coseismic slip patch, is much smaller than the full 2001 rupture surface. The highly coupled area is surrounded by unlocked areas, which supports the idea of ongoing postseismic processes in this region [*Villegas-Lanza et al.*, 2016a].

Finally, the north Chile segment was considered a mature seismic gap for a long time, due to the lack of great earthquakes since 1877 [*Dorbath et al.*, 1990; *Nishenko*, 1991; *Comte and Pardo*, 1991]. *Métois et al.* [2016] provide an updated coupling map in the region, observing two main regions of high locking degree (Camarones and Loa segments), separated by the Iquique low coupling region separating them. The Tocopilla earthquake in 2007 (M_w 7.7) broke the southern part of the gap (Loa segment), in the area of the Mejillones Peninsula and specifically the deeper part of the seismogenic zone [*Béjar-Pizarro et al.*, 2010; *Peyrat et al.*, 2010]. Then, in 2014, Iquique earthquake struck the central part of the gap breaking a small portion of the Camarones segment [*Ruiz et al.*, 2014; *Hayes et al.*, 2014; *Schurr et al.*, 2014; *Yagi et al.*, 2014; *Duputel et al.*, 2015]. These earthquakes did not release the energy accumulated since the 1877 historical earthquake, leaving open the possibility to generate earthquakes of $M_w \geq 8.0$, on the Loa or Camarones segment [*Béjar-Pizarro et al.*, 2010;

Chlieh et al., 2011; *Métois et al.*, 2013; *Hayes et al.*, 2014; *Ruiz et al.*, 2014]. Nevertheless, the possibility to have a great earthquake breaking both segments at the same time cannot be ignored [*Métois et al.*, 2013; *Schurr et al.*, 2014].

Chapter 4

Processing and Analysis of GPS Data

4.1 Global Positioning System, GPS

4.1.1 Operating Principles

The Global Positioning System is a satellite constellation operated by the United States Department of Defense to support military and civilian positioning, navigation and timing. At the beginning, it was created as military system during the 70's, and was open to all public during the 90's. The constellation consists of 32 satellites orbiting the Earth in 6 nodal planes every 12 hours, allowing between 5 to 12 satellites to be always visible at one point on the Earth surface. Each GPS satellite transmits a unique signal coded on two L-band frequencies: L1 at 1575.42 MHz and L2 at 1227.60 MHz (equivalent to 19 cm and 24 cm wavelengths). This signal consists of L-band carrier waves modulated with a Standard or S code (C/A, Coarse Acquisition code), with a Precise or P code and with a Navigation Message containing the coordinates of the satellites as a function of time. C/A code was originally created for civilian activities with a wavelength of ∼300 m and a precision of ∼100 m and at the beginning just on L1 band. The P code was created for military purposes using a wavelength of ∼30 m, a precision of ∼10 m, coded on L1 and L2 bands. Initially, the signal was encrypted, limiting the precision to civilians, but in 2000's the anti-spoofing signal was eliminated. Due to the cost of installation, at the beginning of the system, not to many GPS stations were installed, but the number of stations increased significantly during the 90's. Because of the storage capacity, original receivers would register data at 15 - 30 s, but this sampling rate can reach up to 1-20 Hz today.

Using this information, it is possible to calculate the position of the GPS antenna using either the pseudo-ranges or the phases. Pseudo-ranges or code measurements can be based on either P or C/A code and they are based mainly in the measurement of the distances contaminated by clock errors (Figure 4.1). When 4 satellites are visible at one point on the surface, the 3D-position and the receiver clock offset can be determined, with a precision depending on the configuration geometry of the visible satellites and the station. Positioning by carrier phase measurements are more precise than pseudo-ranges. It consists of the difference between the incoming satellite phase signal and the phase signal generated by the receiver.

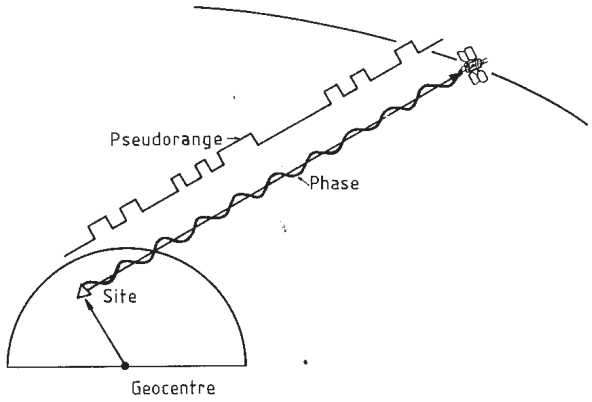

Figure 4.1: Pseudo-range and phase measurement. Figure from *King* [1986].

4.1.2 GPS as an instrument of high precision

GPS is commonly used today around the world to get real-time position, but if the user wants to obtain high precision positioning, some work needs to be done. The distance satellite-station (l_i^j, where i represent a station and j represent the satellite) is affected by delays (following equations described by *Bock and Melgar* [2016]):

$$l_i^j = r_i^j(t, t-\tau_i^j(t)) + c\,[dt_i(t) + dt^j(t-\tau_i^j(t))] + M_i^j ZTD_i^j - I_i^j + \lambda\,(N_i^j + B_i - B_j) + m_i^j + \epsilon_i^j \quad (4.1)$$

where r_i^j is the geometric distance between the station i and the satellite j, t is the time of the signal reception, τ_i^j is the time delay between the transmission and the reception, and c is the speed of the light. The second term on the right includes dt_i the receiver clock error and dt^j the satellite clock error. ZTD_i^j (Zenithal Total Delay) is the tropospheric propagation delay in the zenith direction, and M_i^j is a function that maps the ZTD to lower elevation angles. I_i^j is the total delay due to the ionosphere along the signal's path. N_i^j denotes the integer-cycle phase ambiguity, B_i and B^j denote the non-integer (fractional) parts of the receiver and satellite-specific clock biases, respectively, and λ is the wavelength at either $L1$ or $L2$ frequency. m_i^j denotes the signal associated with multipath effect and ϵ_i^j denotes the measurement error. The generation and effect of each term are discussed below.

Satellite orbits are available from different institutions (e.g., International GNSS Service, IGS) with a precision of ∼100 m (Figure 4.2). To increase the precision re-processed orbits, with uncertainty values of ∼2.5 cm, are needed. Those recalculated precise orbits are available after few weeks.

The signal is affected when it crosses through the ionosphere, a dispersive medium that affects the electric wavelength propagation, corrupting the distance measure and the inferred station position. Ionospheric delay depends on the content of charged particles (ions and electrons) and the frequency

of the considered wave (Figure 4.2). The particle content changes over time. Dual frequency GPS allows to determine the number of particle and then to quantify the ionospheric delay on either L1 or L2. GPS can be used to compute Total Electronic Content (TEC) maps of the ionosphere.

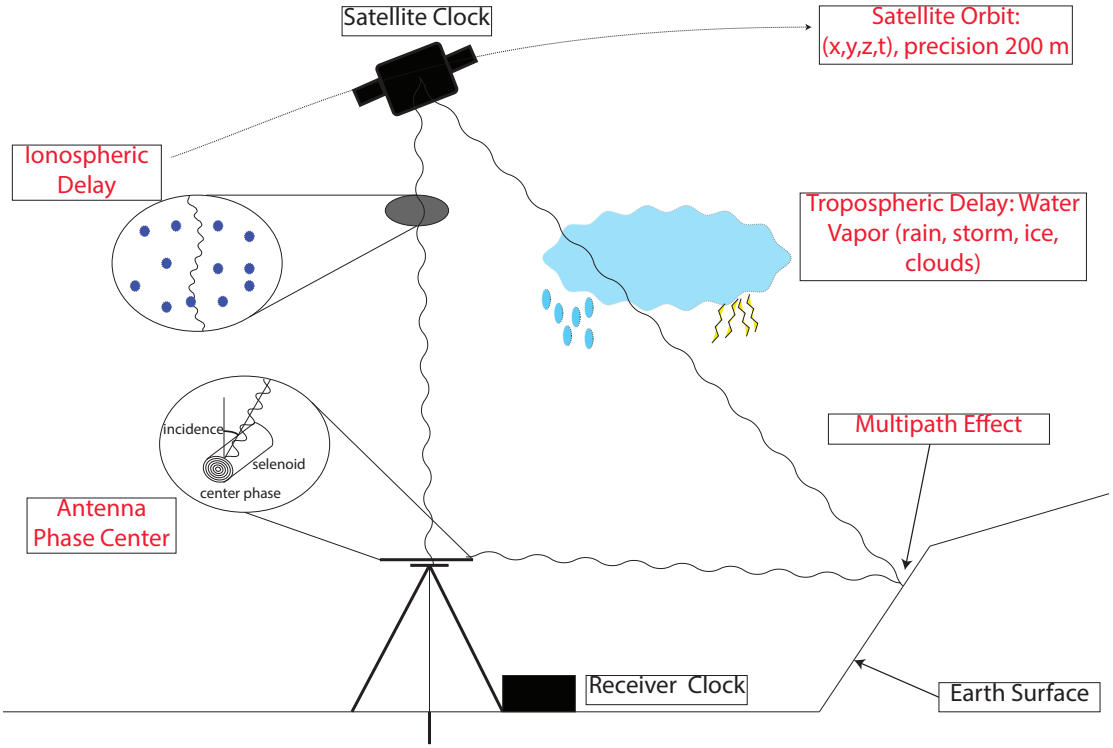

Figure 4.2: GPS Error Sources. The different GPS error sources affecting the calculation of GPS-satellite distance are shown in red (see main text for further explanation). Figure modified from *Metois* [2012].

After the pass of the signal through the troposphere, also have been observed some delays (ZTD) that produce positioning error of 1-50 cm. The ZTD can be modeled as the sum of a dry and wet part (Figure 4.2). The zenithal dry delay (ZDD) depends on the molecular content of the atmosphere in hydrostatic equilibrium, depending on the surface pressure, latitude and height. The standard deviation of current modeled estimates of this delay is $\sim$0.5 mm. The non-hydrostatic or zenith wet delay (ZWD) is associated with the amount of water vapor that is not in hydrostatic equilibrium. It is very difficult to model because the water vapor in the atmosphere is highly variable in space and time. The standard deviation of current modeled estimates of this delay is $\sim$2 cm [*Bevis et al.*, 1992, 1994].

Antennas are very diverse (radomes, shapes, etc) and not standard around the world. The antenna phase center is the wire in which the radio wave converted into an electric signal (Figure 4.2). It is a mathematical point, which exact position depends on the signal alignment with the wire (azimuth and elevation). There is not a direct access to the antenna phase center, so the user setup the antenna using the Antenna Reference Point (ARP), and the offset between it and phase center (1-2 cm) is needed to be corrected. The most common correction of this error is made using antenna phase center variations available from IGS.

Multipaths effects are produced because the GPS signal may be reflected by surfaces near the receiver (wall, car, tree, etc), so the antenna receives a superposition of direct and reflected signals (Figure 4.2). The multipath errors are up to 50 m using code measurements and up to 5 cm when phase measurements are used. The Multipath effect repeats daily, because of repeat time of GPS constellation, thus it can be used to filter it out. It is most critical at low elevation and for short sessions, for which it is difficult to design a filtering.

Considering the clock errors (Figure 4.2), GPS satellites move at about 1 km/s, so 1 ms time error results in 1 m range error. Using pseudo-range positioning, 1 ms is not a trouble. In the case of phase positioning, if 1 mm error is required, the needed time accuracy should therefore be 10^{-6} s. The satellites have stable atomic clocks. The instability is $\sim 10^{-14}$ s ($\Leftrightarrow \sim 10^{-9}$ s/day), taking into account that there is a synchronization between all the satellites, and the navigation message contains the clocks corrections. The receivers clocks are much more unstable (10^{-5} - 10^{-6}, $\Leftrightarrow \sim 10^{-1}$ - 10^{-2} s/day), and regularly synchronized with GPS time. Single differences are affected by satellites clock uncertainties or by the station clock uncertainties. To fix globally the those errors, double-differencing is used in this thesis because it is free from any clock uncertainty (Figure 4.3). In this case, the measurement of distances is performed between points or baselines, resulting in a relative positioning. This procedure eliminates any common error between the receivers, and also the atmospheric propagation errors are cancelled if receivers are close enough to each other. Therefore, short baselines provide greater precision than long ones.

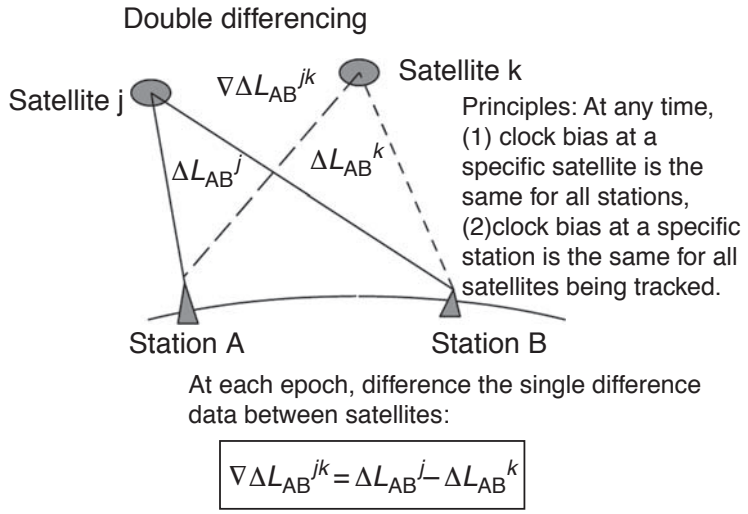

Figure 4.3: Diagram illustrating double differencing of GPS. Figure from *Blewitt* [2007].

Two methods are broadly used today in geophysics to estimate positions (with errors estimates of the order of mm). The precise point positioning (PPP) [*Zumberge et al.*, 1997] consists in calculating the position of single stations using precise orbits and clock data. Softwares based on this technique include BERNESE, by Astronomical Institute, University of Bern, Switzerland [*Rothacher et al.*, 1990], GIPSY-OASIS II software, by JPL, California Institute of Technology, USA [*Webb and Zumberge*, 1993], or GINS (CNES). The relative positioning by double-differenced data using precise

orbit data. The most common software based on this technique is GAMIT-GLOBK [*Herring et al.*, 2016] (BERNESE also provides this type of analysis), that has been used for the GPS processing made for this Ph.D.

4.2 GPS Data used in this Ph.D. project

In the 90's, geoscientists started to step up different campaign networks in the study area, such, as South America-Nazca Plate Project (SNAPP) [*Norabuena et al.*, 1998], Central Andes GPS Project (CAP) [*Kendrick et al.*, 2001], South American Geodynamic Activities (SAGA) [*Klotz et al.*, 1999] and Laboratoire International Associé "Montessus de Ballore" (LIA-MB) associated with French institutions. During the 2000's, LIA-MB [*Métois et al.*, 2013, 2016] and *Brooks et al.* [2011] densified the existent networks in North Chile and in Bolivia. During this same decade and due to the facilitate for the reduction of price and maintenance of GPS, permanent networks begun to be installed as: Integrated Plate Boundary Observatory Chile (Chilean, French and German cooperation), Central Andean Tectonic Observatory (CAnTO, Caltech), Instituto Geofísico Peruano (IGP), Institute des Sciences de la Terre (ISTerre) and Centro Sismológico Nacional (CSN, Chile). Those networks save data between 15 - 30 s at low frequency and between 1 - 20 Hz at high frequency, depending of the institution in charge.

Although during this present thesis, only the continuous GPS data were processed and used in the modeling and interpretation, some fieldwork was done as well. After the occurrence of Iquique earthquake in 2014, the South Peru and North Chile survey networks were remeasured under the leadership of the Department of Geophysics at the University of Chile. I was in charge of one team whose work consists of: preparing the material needed to install the GPS (tripods, batteries, receivers, cables, antennas, tools and accessories). Also the receiver needed to be set up in terms of time to save the data. Sessions of 30 s and 1 Hz were performed. The team was in charged to perform measurements in Arica, Camarones, Pisagua, Iquique and Patache profiles in sessions of 3 days (Figure 4.4). Then, in 2015, a great effort between Peruvian, Chilean and French teams was performed to make measurements in the all South Peru - North Chile seismic gap. The work realized during this fieldwork was the same mentioned above, but in the profiles: Tocopilla, Patache, Iquique, Pisagua and Camarones (Figure 4.4). Those datasets collected in the campaign effort has been valorized for one master student in Chile (Department of Geophysics at University of Chile) and by the laboratory ISTerre in order to calculate the interseismic velocity field and coupling map associated, but they are not used during this work because they did not meet the objectives of the Ph.D.

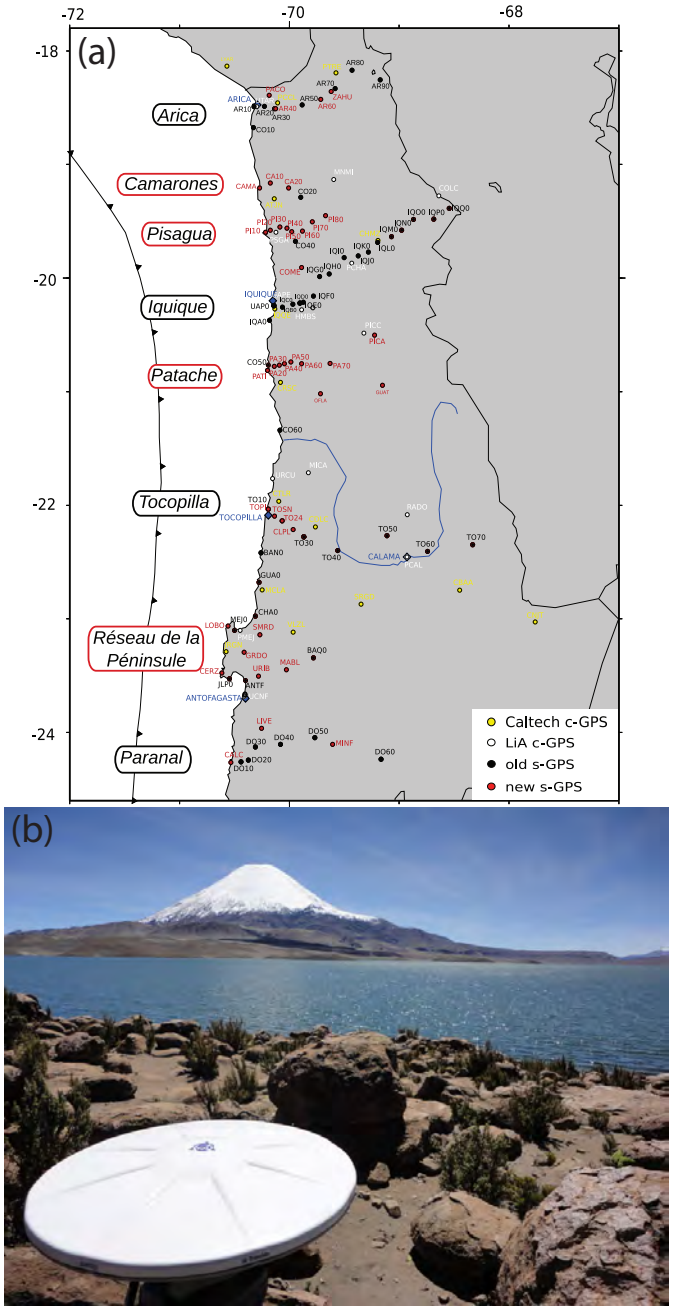

Figure 4.4: (a) Map of sGPS Network in North Chile. The name of the profile is located on the left. (b) Picture of sGPS AR90, located at side of Chungara Lake in the boundary between Chile and Bolivia at 4500 m. Figure (a) from *Metois* [2012] and (b) credits by Jorge Jara.

4.3 GPS Processing

4.3.1 Subnetworking

All the cGPS data available in the area were processed (65 stations from different institutions as was mentioned above Figure 4.4) using GAMIT 10.5 software. Because the maximum number of

stations allowed by the software is 99, the Andean network was divided in two [1]. The time span of the entire network is 2000 - 2014, but the data availability is not constant with time. Each subnetwork is composed of 50 stations, with 33 common stations to both subnetworks (Figure 4.5a). One subnetwork spans 2000 - 2014 and the second one spans 2007 – 2014. 49 IGS stations surrounding the subnetworks were selected, 22 located in South America continent and 2 in the Nazca Plate (the two only available stations over the long term on this plate).

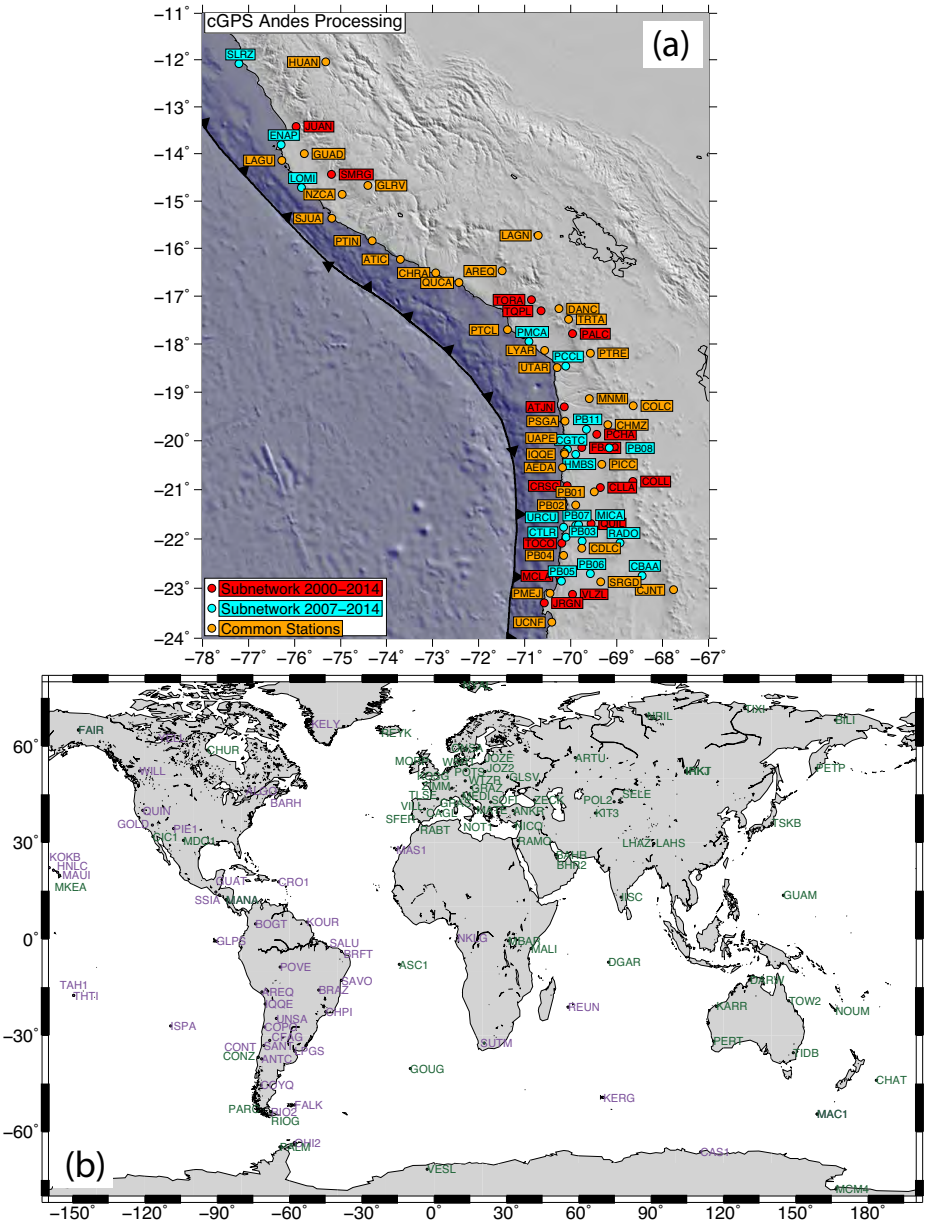

Figure 4.5: (a) Map of the 2 local GPS subnetworks processed (Andes 2000 - 2014 in red and Andes 2007 - 2014 in cyan). Orange denotes the stations included in both subnetworks in the processing. (b) Global GPS network processed. Green color indicates IGS stations included in the Global Processing, while purple indicate IGS stations overlapping with the Andean subtnetworks.

[1] At the beginning of this thesis, GAMIT 10.6 was not available. This program allows to separate the subnetworks in an automatic manner. This is one of the two reasons why we chose the subnetwork strategy. The second reason relates to the number of baselines calculated during the processing. If this number is higher, better results and more stable solution can be expected.

The fact that the stations in SOAM plate are not all available since 2000 creates a problem in the time series stabilization process (discussed in detail in the next section). To avoid this problem and a get more accuracy during the processing, an IGS global network was designed and processed. The IGS stations selected were the 49 (purple dots in Figure 4.5b) used in the processing of the subnetworks mentioned above, plus 50 (green dots in Figure 4.5b) stations covering Mexico, Europe and Iran, that are project which the Seismic Cycle team at ISTerre is involved.

4.3.2 Daily Processing

GAMIT/GLOBK software needs some *apriori* information to perform the data processing, such as data from the GPS, the antenna and receiver information, and *apriori* coordinates of the stations. The experiment parameter was set up as RELAX, implying that the orbital parameters are re-calculated during the processing. The ZTD is estimated every two hours and one couple of horizontal tropospheric gradients per 24h session, using the Vienna Mapping Function (VMF1) [*Boehm et al.*, 2006], to map the tropospheric delay in zenithal direction, with a priori ZDD evaluated from pressure and temperature values from the VMF1 grids. The precise orbits from the International GNSS Service for Geodynamics (IGS, www.igs.org), precise EOPs from the IERS bulletin B (www.iers.org), IGS tables to describe the phase centers of the antennas, FES2004 ocean-tidal loading corrections, as well as atmospheric loading corrections (tidal and non-tidal). The Choice of Observables was set up as LC_AUTCLN, which means that the observables are the ionosphere-free. It means that the program uses as observable directly the linear combination (LC) of the L1 and L2 phases. In this case the total number of full carrier wave cycles travelled by the GPS signal is unknown, this is widely known as integer-cycle phase and needs to be estimated. One way to extract the number of integer-cycle phase ambiguities is using the “wide-lane" ot “Malrbourne-Wübbena" combination with an effective wavelength of 86.2 cm [*Hatch*, 1991; *Melbourne*, 1985; *Wübbena*, 1985]. It allows to remove the ionospheric effects and most of the noise, facilitating the detection of the cycle slips.

4.3.3 Reference Frame

The terrestrial Earth-centered Earth-fixed reference frame system is a convention taken by the International Union of Geodesy and Geophysics. It is realized through the International Terrestrial Reference Frame (ITRF) defined by the positions (X,Y,Z, Figure 4.6) and velocities (V_x,V_y,V_z) of selected stations around the world.

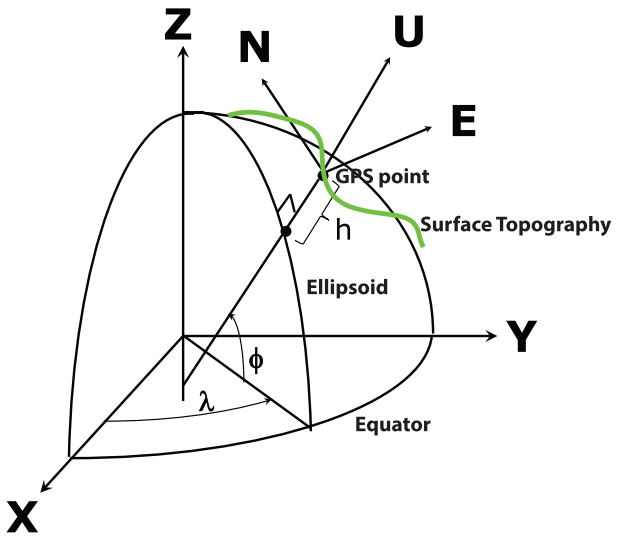

Figure 4.6: Geodetic coordinate system. GPS analysis is performed in the global Earth-centered fixed reference frame in (X,Y,Z) and then transformed into local reference frame (N,E,U). Figure from *Bock and Melgar* [2016].

In order to obtain GPS time series, a stabilization process was used. To accomplish this, the GAMIT daily solutions from the networks (2 local and 1 global) were combined using GLOBK software. The program PYACS [*Nocquet*, 2017] was employed to do this part of the work due to the robustness and facility, using ITRF08 [*Altamimi et al.*, 2011] and then using the fix pole of stable SOAM plate proposed by *Nocquet et al.* [2014] (see Table 4.1 for the statistics about the reference frame used in the study and Figure 4.5b for station locations).

4.4 Times Series Analysis

4.4.1 Trajectory Model of the Seismic Cycle

Each station (65 in total) is modeled following a Trajectory Model [*Bevis and Brown*, 2014], in order to obtain a first-order modeling of the main phases of the seismic cycle. The Trajectory Model is described by:

$$x(t) \;=\; x_R \;+\; v(t-t_R) \;+\sum_{j=1}^{n_j} b_j H(t-t_j) \;+\; \sum_{k=1}^{n_F}[s_k \sin(\omega_k t) \;+c_k \cos(\omega_k t] \;+\; \sum_{i=1}^{n_T} a_i \log(1 \;+\; \Delta t_i/T_i) \tag{4.2}$$

where x_R is the reference position and t_R its time. v symbolizes the velocity. H denotes the Heaviside function applied each time an antenna change is registered at the station or an earthquake affects the station signal. Here the strategy differentiates the earthquakes depending on their magnitude. If the earthquake magnitude is $6.0 \leq \mathrm{M} \leq 7.5$, a simple offset is inverted using a Heaviside function. To discriminate if the earthquake affects or not the station, we use the station – epicenter distance criterion proposed by the Nevada Geodetic Laboratory (www.geodesy.unr.edu) such as:

SITE	Lon(^{o})	Lat (^{o})	wrms E (mm)	wrms N (mm)	wrms U (mm)	vel E (mm/yr)	vel N (mm/yr)	vel U (mm/yr)
AJAC	8.7626	41.9275	1.5	1.6	4.4	0.0	-0.1	-0.3
ARTU	58.5605	56.4298	1.7	1.6	5.8	0.1	0.0	0.1
BARH	-68.2217	44.3950	1.9	1.7	4.7	-0.1	-0.1	-0.2
BRAZ	-47.8779	-15.9475	2.8	2.4	9.2	0.0	0.0	-0.0
BRFT	-38.4255	-3.8774	1.8	2.4	6.7	0.0	0.0	0.1
CAGL	8.9728	39.1359	2.0	1.5	5.0	0.0	-0.1	-0.0
CAS1	110.5197	-66.2834	2.6	2.5	5.3	0.1	0.1	-0.1
CHAT	-176.5658	-43.9558	2.2	2.1	5.2	-0.0	0.0	-0.1
CHPI	-44.9852	-22.6871	2.3	2.5	6.9	-0.1	0.1	0.3
CIC1	-116.6658	31.8707	2.0	1.9	4.7	0.0	-0.2	0.2
CRO1	-64.5843	17.7569	2.9	1.9	8.7	0.1	-0.1	0.5
DARW	131.1327	-12.8437	3.4	3.9	8.9	0.1	0.0	0.1
DGAR	72.3702	-7.697	3.2	3.0	8.5	-0.1	0.0	0.1
FAIR	-147.4992	64.9780	3.5	2.7	7.0	-0.1	-0.1	-0.2
FALK	-57.8741	-51.6937	2.0	2.2	4.3	0.0	0.1	-0.2
GLPS	-90.3037	-0.7430	1.8	1.8	4.2	-0.0	0.0	-0.3
GLSV	30.4967	50.3642	2.5	2.3	5.3	0.0	-0.1	0.0
GRAS	6.9206	43.7547	3.9	2.3	5.9	0.0	-0.1	-0.1
GRAZ	15.4935	47.0671	1.4	1.5	4.8	0.0	-0.0	0.1
GUAT	-90.5202	14.5904	3.8	2.3	8.8	-0.3	-0.1	-0.0
HNLC	-157.8645	21.3033	3.1	3.6	8.2	0.2	-0.1	0.2
HOFN	-15.1979	64.2673	3.3	1.7	5.5	0.1	-0.0	-0.2
IRKT	104.3162	52.2190	3.6	3.2	6.6	-0.2	-0.1	0.1
ISPA	-109.3444	-27.1250	2.7	2.3	7.7	-0.1	-0.3	-0.2
KIT3	66.8854	39.1348	3.6	3.1	9.6	-0.3	-0.0	0.3
KOKB	-159.6649	22.1263	2.9	2.5	7.2	0.1	-0.2	-0.1
KOUR	-52.8060	5.2522	4.8	2.9	10.1	0.1	-0.1	0.7
MAC1	158.9358	-54.4995	2.8	2.5	5.5	0.1	0.2	0.1
MAS1	-15.6333	27.7637	1.7	1.8	5.1	-0.1	-0.1	0.1
MATE	16.7045	40.6491	1.5	1.4	3.7	0.1	-0.1	0.1
MAUI	-156.2570	20.7067	2.1	2.9	5.5	0.2	-0.2	-0.0
MAW1	62.8707	-67.6048	2.0	2.3	4.2	0.0	-0.0	-0.3
NKLG	9.6721	0.3539	3.1	3.6	8.5	-0.0	0.1	0.0
NOT1	14.9898	36.8758	2.1	1.6	4.9	0.0	-0.1	0.0
NRIL	88.3598	69.3618	1.9	1.7	5.7	0.0	-0.1	0.2
ONSA	11.9255	57.3953	1.1	1.2	4.2	-0.0	-0.0	-0.1
PENC	19.2815	47.7896	1.2	1.4	4.3	0.1	-0.1	-0.1
PIE1	-108.1189	34.3015	4.0	2.2	5.2	-0.2	-0.1	0.1
QUIN	-120.9444	39.9746	2.4	2.8	8.1	-0.2	-0.1	0.2
RIOG	-67.7511	-53.7855	2.3	2.6	5.6	0.0	0.3	0.1
SALU	-44.2125	-2.5935	2.6	2.3	8.9	-0.6	0.1	0.7
SAVO	-38.4323	-12.9392	2.2	2.1	7.0	0.1	0.1	0.2
STJO	-52.6777	47.5952	2.2	2.1	5.2	-0.0	-0.0	-0.1
SUTH	20.8105	-32.3802	2.4	2.5	6.0	-0.1	0.1	-0.1
SUTM	20.8109	-32.3814	2.9	3.0	6.1	-0.2	0.4	0.0
THTI	-149.064	-17.5771	2.9	2.7	8.7	0.0	-0.0	0.0
TIDB	148.9800	-35.3992	3.0	2.4	6.3	0.1	0.1	0.2
WILL	-122.1678	52.2369	1.9	2.2	5.0	-0.1	-0.1	0.1
WSRT	6.6045	52.9146	1.1	1.1	4.1	-0.0	-0.0	0.2
WTZR	12.8789	49.1442	1.5	1.4	4.1	-0.1	-0.1	0.1
ZECK	41.5651	43.7884	3.2	2.6	6.6	-0.0	-0.1	0.2
ZIMM	7.4653	46.8771	2.2	1.8	4.2	0.0	-0.1	0.1

Table 4.1: GPS positions of the reference frame used during this study, with their respective statistics (wrms and velocity). Everything is referenced in ITRF08 [*Altamimi et al.*, 2011].

$$d(M) \;\leq\; 10^{M/2-0.8} \tag{4.3}$$

where M is the magnitude of the considered earthquake, and d(M) the distance epicenter – station . If the distance is lower than d the earthquake is modeled. The threshold in magnitude is fixed in this case as $M = 6.0$. The study area being very active, several jumps are seen associated with seismicity.

If the considered earthquake is of magnitude $M \geq 7.5$ a Heaviside function is applied H, but also a *log* function to account for the postseismic signal generated by the earthquake (Equation 4.2). T_i is the relaxation time for each earthquake. The area is affected by 5 big earthquakes that can be seen in the time series: Arequipa (M_w 8.4, 2001),Tarapaca (M_w 7.7), Pisco (M_w 7.7, 2007), Tocopilla (M_w 7.7, 2007) and Iquique (M_w 8.1, 2014). To remove the post-seismic signal, the Relaxation Time τ is estimated. We start by fitting the postseismic signal of the older earthquake (here, Arequipa earthquake in 2001), taking all the stations available and affected by the earthquake, and then include iteratively younger earthquakes going forward in time. For each large earthquake, the value of τ is explored from 1 to 1000 days. The best τ value is obtained minimizing the Model RMS (τ = 61 days for 2001 Arequipa earthquake, Figure 4.7, see Table 4.2 for τ values). The functions sin and cos are used to estimate annual and semi-annual seasonal signal. The stations positions and velocity field obtained during the processing are in the Table 4.3, in the SOAM fixed reference frame. All the parameters obtained during the processing can be found in the Appendix A. An example of the model for AREQ station can be seen in the Figure 4.8 (All the models for each station can be found in the Appendix A).

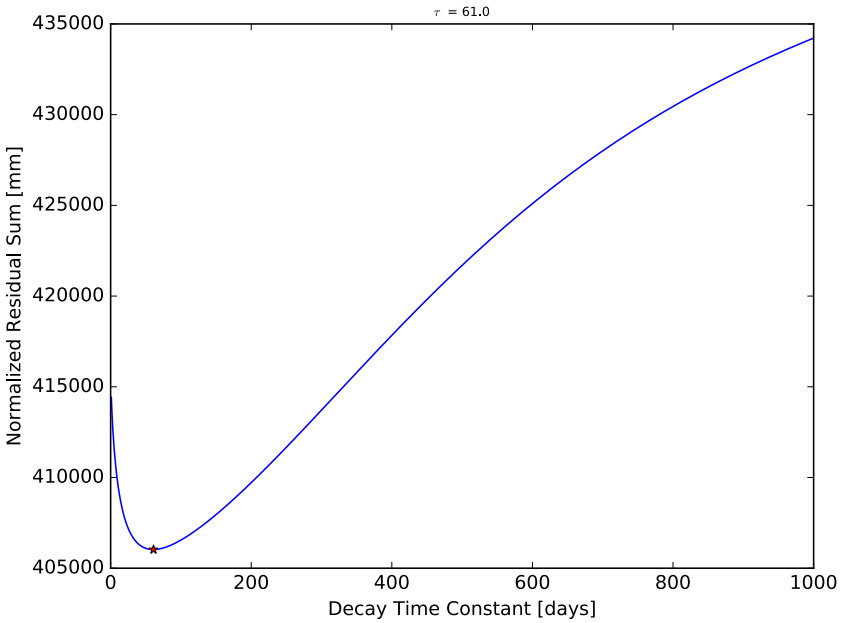

Figure 4.7: Normalized RMS from modeled time series as a function of the Relaxation Time (τ = 61 days).

Earthquake	τ (days)
Arequipa	61
Tarapaca	66
Pisco	26
Tocopilla	6
Iquique	84

Table 4.2: Relaxation Time modeled for each earthquake M $\geq$ 7.5, for Arequipa earthquake.

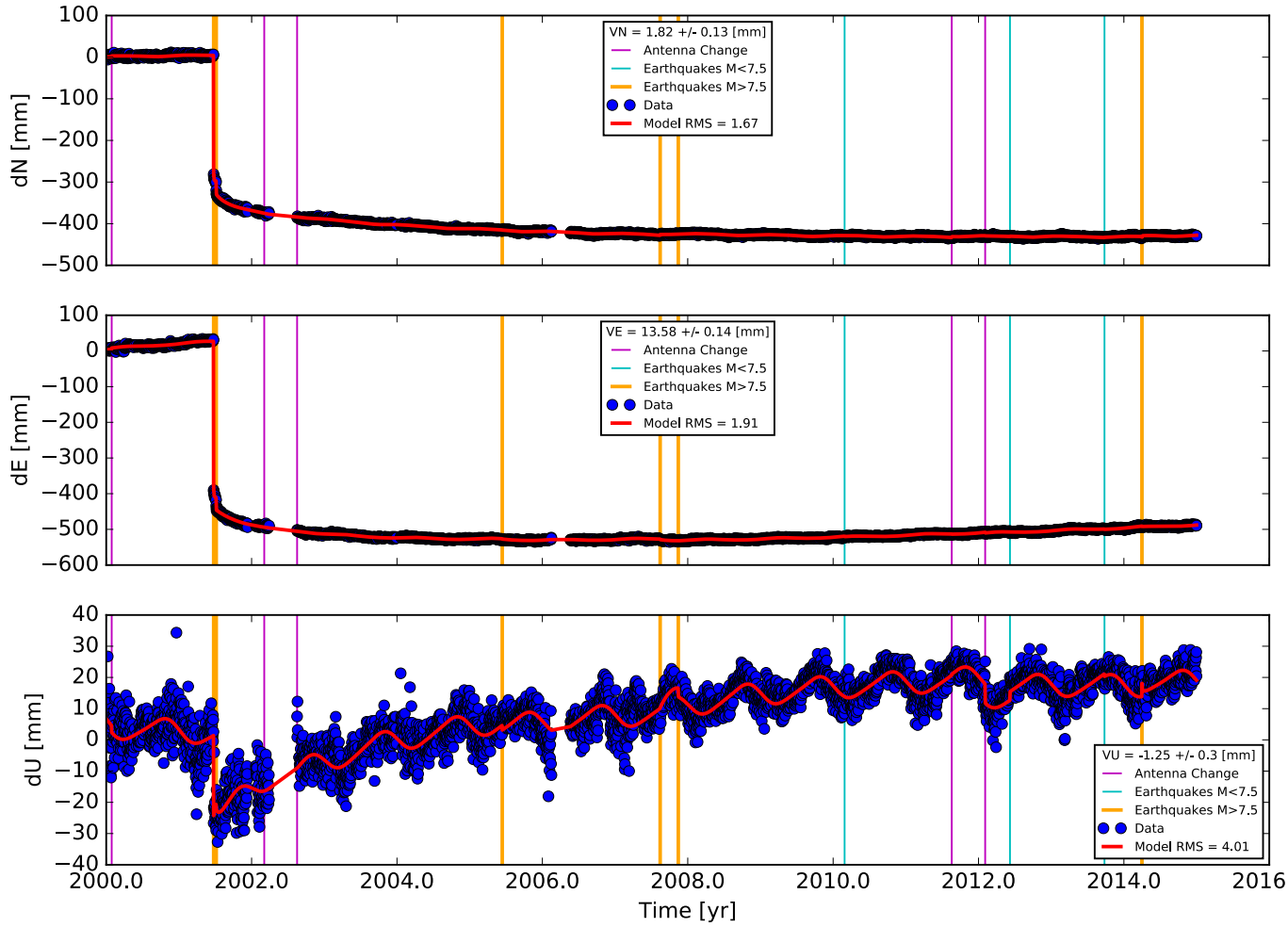

Figure 4.8: North, East and Vertical time series of AREQ stations. Blue dots represent the daily position time series of the station while the red shows the model obtained from Equation 4.2. The box shows the velocity obtained for each component with its respective error associated. Purple vertical lines indcate the antenna changes, yellow vertical lines are earthquake with $M \geq 7.5$ (for which post-seismic signal is modeled), while cyan vertical lines represent the earthquakes $6.0 \leq M < 7.5$. Model RMS is annotated on the information boxes.

Station	Lon(^{o})	Lat(^{o})	wrms N	wrms E	wrms V	North	East	Vertical
AEDA	-70.178	-20.546	1.7	1.36	4.45	7.37+/-0.09	25.14+/-0.12	-4.29+/-0.31
AREQ	-71.493	-16.466	1.91	1.67	4.01	1.82+/-0.13	13.58+/-0.14	-1.25+/-0.39
ATIC	-73.697	-16.231	1.59	1.39	3.51	2.19+/-0.08	24.38+/-0.09	1.36+/-0.19
ATJN	-70.137	-19.301	1.45	1.34	2.98	5.26+/-0.06	23.58+/-0.06	0.83+/-0.13
CBAA	-68.448	-22.746	1.41	1.31	2.73	5.01+/-0.04	18.87+/-0.04	-1.5+/-0.09
CDLC	-69.762	-22.19	1.47	1.32	3.04	7.23+/-0.04	29.45+/-0.05	4.69+/-0.1
CGTC	-70.069	-20.177	1.41	1.28	2.81	5.29+/-0.02	24.94+/-0.02	2.14+/-0.04
CHMZ	-69.194	-19.669	1.38	1.26	2.82	6.99+/-0.03	20.3+/-0.04	-0.5+/-0.07
CHRA	-72.929	-16.517	1.48	1.39	5	2.59+/-0.07	18.48+/-0.07	1.23+/-0.25
CJNT	-67.761	-23.028	1.44	1.32	3.07	3.82+/-0.05	16.32+/-0.06	-0.45+/-0.12
CLLA	-69.357	-20.955	1.38	1.27	2.86	4.87+/-0.04	24.71+/-0.04	0.21+/-0.08
COLC	-68.639	-19.276	1.68	1.5	4.53	5.54+/-0.07	19.82+/-0.08	0.61+/-0.22
COLL	-68.65	-20.831	1.55	1.4	3.04	1.19+/-0.11	24.18+/-0.12	3.59+/-0.23
CRSC	-70.08	-20.918	1.45	1.3	2.74	7.61+/-0.04	28.06+/-0.04	1.37+/-0.08
CTLR	-70.097	-21.964	1.43	1.39	3.51	8.49+/-0.07	29.13+/-0.07	5.87+/-0.17
DANC	-70.252	-17.265	1.43	1.33	3.05	4.35+/-0.06	9.77+/-0.06	-2.58+/-0.14
ENAP	-69.755	-20.135	1.89	1.48	4.21	1.79+/-0.12	25.01+/-0.16	-2.96+/-0.35
FBAQ	-74.404	-14.67	1.55	1.48	3.29	6.66+/-0.16	25.43+/-0.17	3.12+/-0.36
GLRV	-75.787	-13.999	1.45	1.36	3.01	4.08+/-0.05	11.12+/-0.05	-0.55+/-0.1
GUAD	-69.888	-20.278	1.68	1.38	4.23	0.84+/-0.07	16.95+/-0.08	1.2+/-0.2
HMBS	-75.321	-12.042	1.53	1.29	4.72	5.94+/-0.12	25.25+/-0.14	3.72+/-0.45
HUAN	-70.132	-20.274	1.6	1.35	3.77	1.34+/-0.09	9.62+/-0.11	0.85+/-0.25
IQQE	-70.575	-23.289	1.58	1.49	3.77	3.87+/-0.05	28.14+/-0.05	2.17+/-0.12
JRGN	-70.705	-15.723	1.61	1.47	3.29	11.25+/-0.04	34.28+/-0.04	-5.5+/-0.09
LAGN	-76.273	-14.145	1.28	1.31	3.53	29.5+/-3.62	39.55+/-3.53	14.05+/-9.73
LAGU	-75.851	-14.714	1.9	1.56	4.81	4.64+/-0.1	25.12+/-0.12	5.52+/-0.31
LOMI	-70.569	-18.134	1.92	2.73	3.64	-8.81+/-0.09	13.85+/-0.07	5.57+/-0.13
LYAR	-70.248	-22.746	1.41	1.3	3.34	2.71+/-0.07	18.09+/-0.08	1.91+/-0.18
MCLA	-69.827	-21.715	1.5	1.3	2.84	8.72+/-0.03	29.28+/-0.04	-0.04+/-0.07
MICA	-69.596	-19.131	1.34	1.29	2.64	5.63+/-0.04	27.58+/-0.04	5.35+/-0.08
MNMI	-74.964	-14.857	1.5	1.36	3.19	7.24+/-0.15	19.11+/-0.16	-4.22+/-0.34
NZCA	-69.957	-17.781	1.73	1.29	3.98	4.55+/-0.05	13.94+/-0.07	1.33+/-0.17
PALC	-69.488	-21.044	1.48	1.35	3.39	4.81+/-0.06	11.42+/-0.07	-1.04+/-0.15
PB01	-69.893	-21.315	1.42	1.36	3.48	6.18+/-0.06	26.09+/-0.06	-0.07+/-0.15
PB02	-69.752	-22.049	1.49	1.35	3.23	7.79+/-0.03	29.08+/-0.04	2.49+/-0.08
PB03	-70.15	-22.335	1.65	1.43	3.44	6.96+/-0.04	28.67+/-0.04	4.18+/-0.09
PB04	-70.203	-22.853	1.6	1.34	3.24	8.93+/-0.03	28.93+/-0.03	0.69+/-0.07
PB05	-69.572	-22.706	1.76	1.43	3.56	8.97+/-0.03	28.55+/-0.04	1.14+/-0.07
PB06	-69.886	-21.727	1.51	1.3	3.35	5.19+/-0.02	25.6+/-0.02	-0.64+/-0.05
PB07	-69.161	-20.143	1.56	1.36	3.56	7.3+/-0.03	29.61+/-0.03	4.96+/-0.07
PB08	-69.656	-19.761	1.55	1.43	3.33	6.23+/-0.02	21.56+/-0.02	1.26+/-0.05
PB11	-70.107	-18.458	1.66	1.12	2.87	12.94+/-0.37	34.36+/-0.55	-17.01+/-0.95
PCCL	-69.432	-19.87	1.45	1.29	3.23	4.4+/-0.06	16.71+/-0.07	-0.1+/-0.15
PCHA	-69.335	-20.49	1.58	1.55	3.99	6.55+/-0.07	21.92+/-0.01	1.35+/-0.17
PICC	-70.909	-17.949	1.81	1.64	3.6	7.86+/-0.18	23.94+/-0.2	-1.33+/-0.39
PMCA	-70.448	-23.101	1.43	1.32	3.52	1.49+/-0.04	18.49+/-0.04	1.77+/-0.09
PMEJ	-70.123	-19.597	1.7	1.37	4.05	9.89+/-0.05	32.55+/-0.06	-4.17+/-0.15
PSGA	-71.37	-17.701	1.55	1.3	3.68	6.41+/-0.06	24.71+/-0.07	3.17+/-0.17
PTCL	-74.311	-15.838	1.83	1.64	6.34	1.52+/-0.07	21.98+/-0.08	8.76+/-0.26
PTIN	-69.574	-18.194	1.5	1.41	3.63	3.6+/-0.06	23.97+/-0.06	1.91+/-0.15
PTRE	-72.429	-16.714	1.43	1.32	3.03	7.99+/-0.05	11.86+/-0.06	-3.4+/-0.12
QUCA	-69.558	-21.692	1.51	1.49	4.32	-2.99+/-0.13	14.61+/-0.13	12.07+/-0.38
QUIL	-68.927	-22.083	1.52	1.33	3.34	6.26+/-0.08	31.01+/-0.09	7.02+/-0.2
RADO	-75.188	-15.363	1.51	1.31	3.19	4.82+/-0.05	22.05+/-0.06	-1.32+/-0.12
SJUA	-77.211	-12.081	1.68	1.36	3.52	-1.65+/-0.05	26.71+/-0.06	-7.01+/-0.13
SLRZ	-69.348	-22.871	1.76	1.44	3.9	3.62+/-0.05	22.27+/-0.06	3.49+/-0.13
SRGD	-70.193	-22.089	1.46	1.3	3.44	5.22+/-0.04	24.95+/-0.04	0.18+/-0.1
TORA	-70.852	-17.076	1.63	1.4	4.17	0.63+/-0.03	7.41+/-0.03	3.11+/-0.08
TQPL	-70.643	-17.304	1.44	1.32	3.19	2.67+/-0.04	10.87+/-0.05	-0.48+/-0.1
TRTA	-70.041	-17.482	1.5	1.62	3.49	5.39+/-0.08	9.57+/-0.07	-1.1+/-0.17
UAPE	-70.141	-20.243	2.01	1.76	4.95	5.54+/-0.08	25.36+/-0.1	-0.28+/-0.23
UCNF	-70.409	-23.679	1.51	1.28	3.41	9.66+/-0.07	32.65+/-0.08	1.19+/-0.17
URCU	-70.153	-21.764	1.45	1.23	2.71	4.84+/-0.26	34.05+/-0.31	10.04+/-0.58
UTAR	-70.297	-18.491	1.8	1.57	4.27	3.67+/-0.08	17.95+/-0.09	2.89+/-0.22
VLZL	-69.965	-23.117	1.48	1.31	2.91	7.14+/-0.05	28.81+/-0.05	4.69+/-0.11

Table 4.3: Stations Locations, Statistics and Velocities for stations in the area of the seismic gap. Velocities are referred to SOAM fixed reference frame proposed by *Nocquet et al.* [2014]. Wrms are in mm. Velocities and errors are in mm/yr.

4.4.2 Common mode filtering

Large networks (involving large baselines between stations) are affected by common mode, associated with a spatially correlated positioning error [*Wdowinski et al.*, 1997; *Williams et al.*, 2004]. One way to reduce this effect is applying a spatial filtering that consists in stacking all the stations day by day and calculating the mean per day. Two different approaches have been applied depending on the problem addressed.

In the case of the long precursory phase of Iquique earthquake (Chapter 7), the times series are considered since 2010, applying on them the Equation 4.2 (Trajectory Model). The remaining noise has been reduced by removing the common mode, obtained by selecting stations located within a distance range of 50 - 500 km from the source region (SJUA, ATIC, CHRA, PTCL, LYAR, UTAR, PCCL, PB02, PB04, MCLA, PB05, PMEJ, JRGN, UCNF, NZCA, AREQ, TORA, TQPL, DANC, TRTA, PALC, PTRE, MNMI, COLC, CHMZ, PB11, PCHA, PB08, PB01, PB07, CDLC, RADO, PB06, CBAA, VLZL AND CJNT, Figure 4.5 a) and by averaging their detrended signals. Then, in order to mitigate the residual loading signal, from each time series the mean annual residual seasonal movement computed between 2010 and 2013 is removed. This procedure reduced significantly the scatter on the times series. In order to study the long-term transient in the times series, the data after March 15th, 2014 are excluded (when the strong preseismic signal occurred), and then the average velocity variations computed, by fitting a linear regression in a six-month sliding window of the obtained detrended and de-noised time series. The Figures 4.9 and 4.10, show the effects of removing the common mode and residual seasonal signals on the times series, using 1-year sliding window to calculate the mean velocity, while Figures 4.11 and 4.12 show this using a six-month sliding window. From these analyses, it is possible to appreciate that the preseismic signal is present in the times series but more clear and clean in those ones which common mode and seasonal effect have been removed.

For the interseismic transient deformation study (Chapter 6), we calculated the common mode on the entire network, because of the wide area analyzed (∼1300 km along strike). The impact of the common mode removal can be seen in Figures 4.13 and 4.14 for the coastal stations of the network and in Figures 4.15 and 4.16 for the inland ones. In these cases, the preseismic signal is still present in the time series but now is more difficult to observe. This effect is produced by removing the foreshocks sequence through the modeling of the times series (Trajectory Model, Equation 4.2). The effect is smaller and therefore less strong in the time series.

4.4.3 Noise analysis

To describe the noise of the GPS times series, a power law model $P(f) = P_0/f^n$ is used, where f denotes the frequency and n is the spectrum index [*Mandelbrot and Pignoni*, 1983; *Agnew*, 1992]. *Williams et al.* [2004] has shown that the best form to model the GPS noise, it is summing the white noise ($n = 0$) and the colored noise ($1 < n < 2$). For each residual time series obtained, the spectrum is computed calculating the spectral index (Table 4.4), which is a combination of the white and colored noise. The Figures 4.17, 4.18, 4.19, 4.20, 4.21, 4.22, 4.23, 4.24, 4.25 and 4.26 show

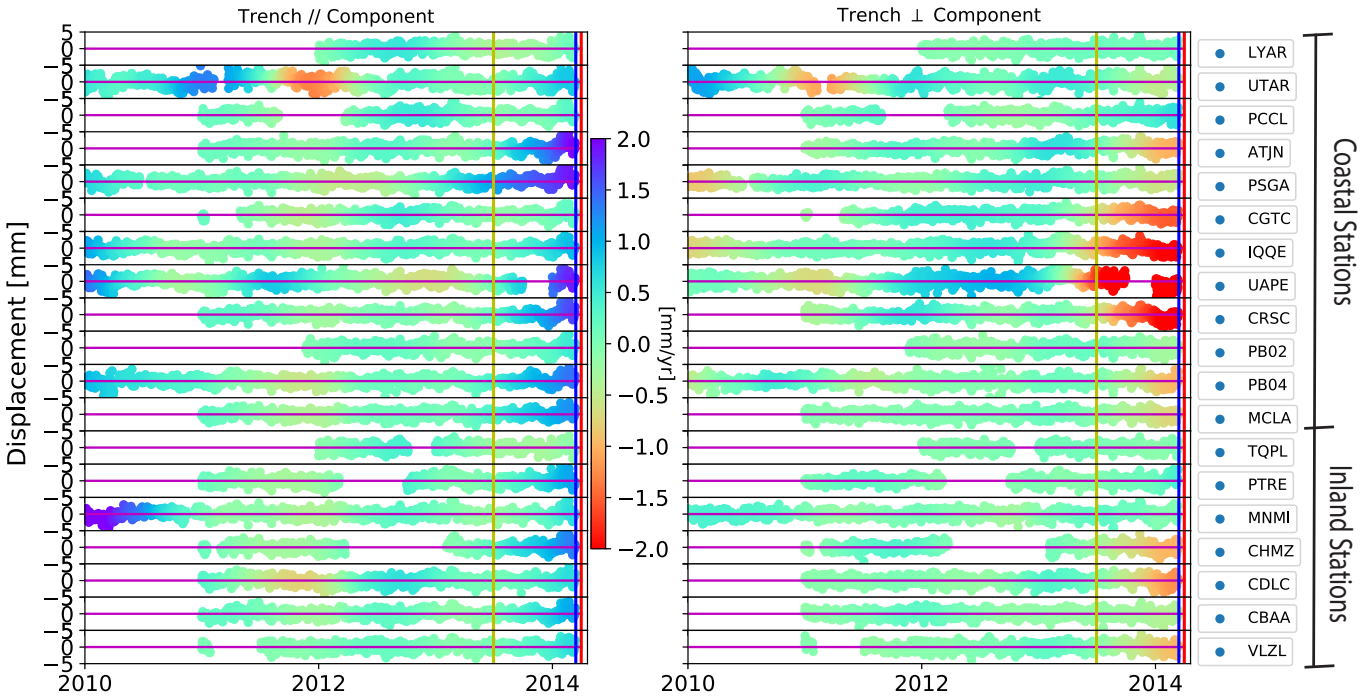

Figure 4.9: Detrended displacement time series for a selection of stations along the coast and inland, without removing the common mode. Colors, indicate the trench parallel (left side) and trench perpendicular (right side) velocities obtained by computing the average velocity over one year sliding windows. Vertical yellow line denotes the date of the swarm occurrence in July 2013. The vertical blue line indicates March 15th, when the Iquique seismic crisis started, while the red one shows the date of the mainshock (2014/04/01).

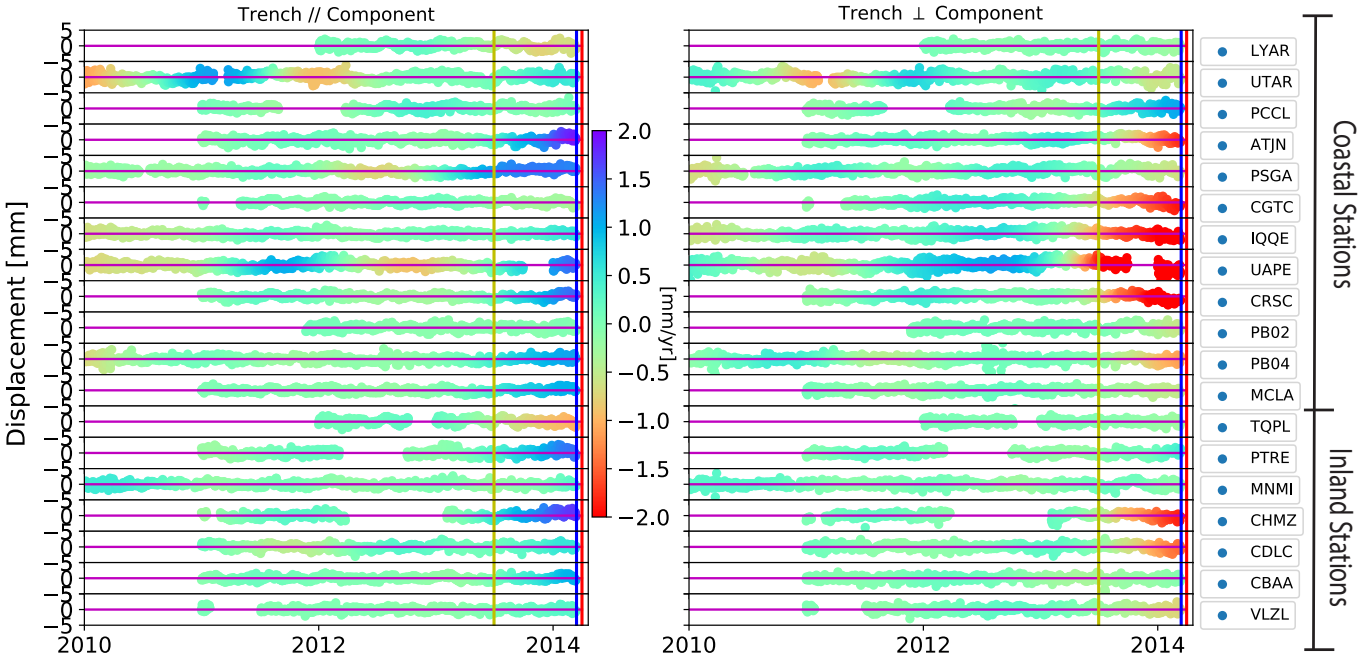

Figure 4.10: Same caption as in Figure 4.9, but removing the common mode and seasonal effects.

examples of the Noise Analysis performed during this work at the stations: ATJN, CJNT, COLC, DANC, IQQE, JRGN, LYAR, PB03, PICC and SJUA (Figure 4.5). The spectral values obtained during this procedure can be used to construct synthetic time series, later used in the Chapter 6 to perform synthetic tests.

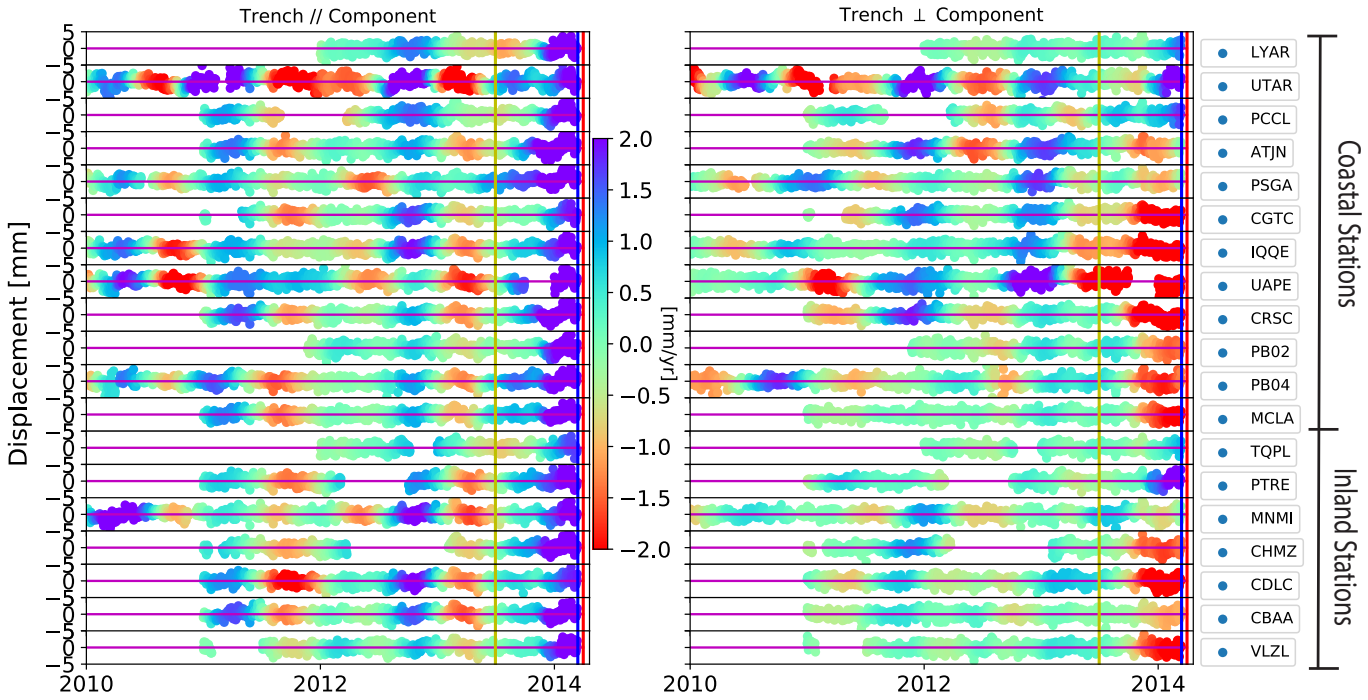

Figure 4.11: Detrended displacement time series for a selection of stations along the coast and inland, without removing the common mode. Colors, indicate the trench parallel (left side) and trench perpendicular (right side) velocities obtained by computing the average velocity over six-month sliding windows. Vertical yellow line denotes the date of the swarm occurrence in July 2013. The vertical blue line indicates March 15th, when the Iquique seismic crisis started, while the red one shows the date of the mainshock (2014/04/01).

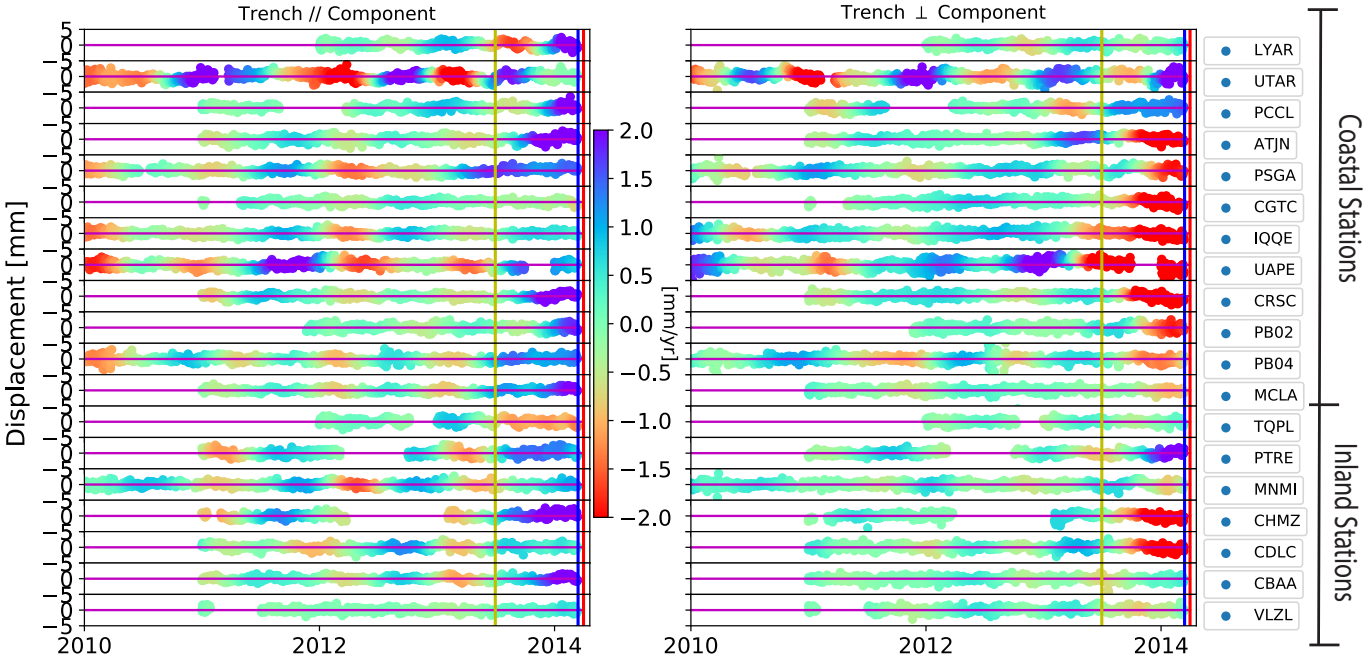

Figure 4.12: Same caption as in Figure 4.11, but removing the common mode and seasonal effects.

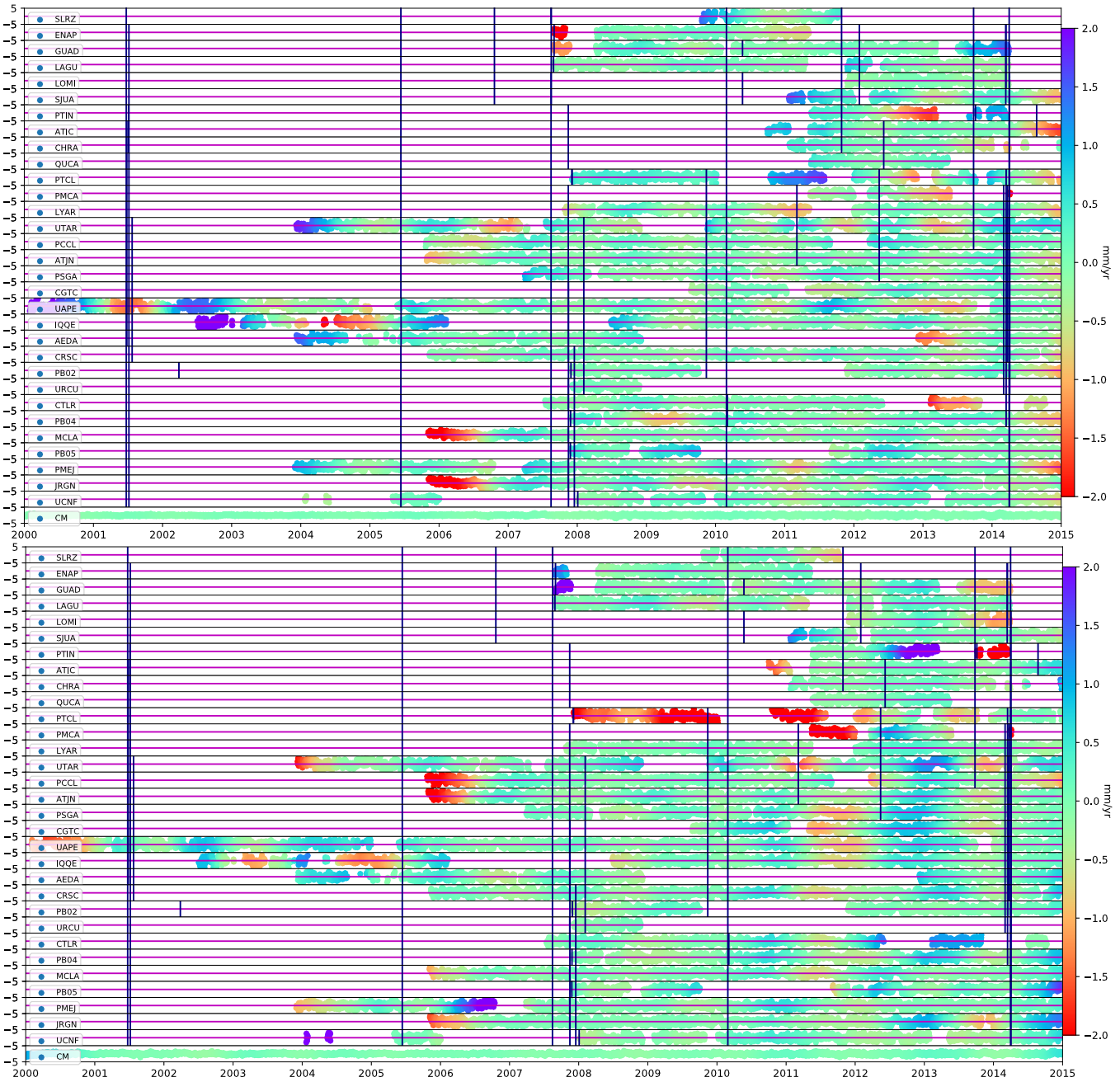

Figure 4.13: Detrended displacement time series for all the coastal stations ordered by latitude (Figure 4.5), without removing the common mode. Colors indicate the trench parallel (on top) and trench perpendicular (on bottom) velocities obtained by computing the average velocity over one year sliding window. Vertical lines the date of earthquakes of magnitude ≥ 6.0.

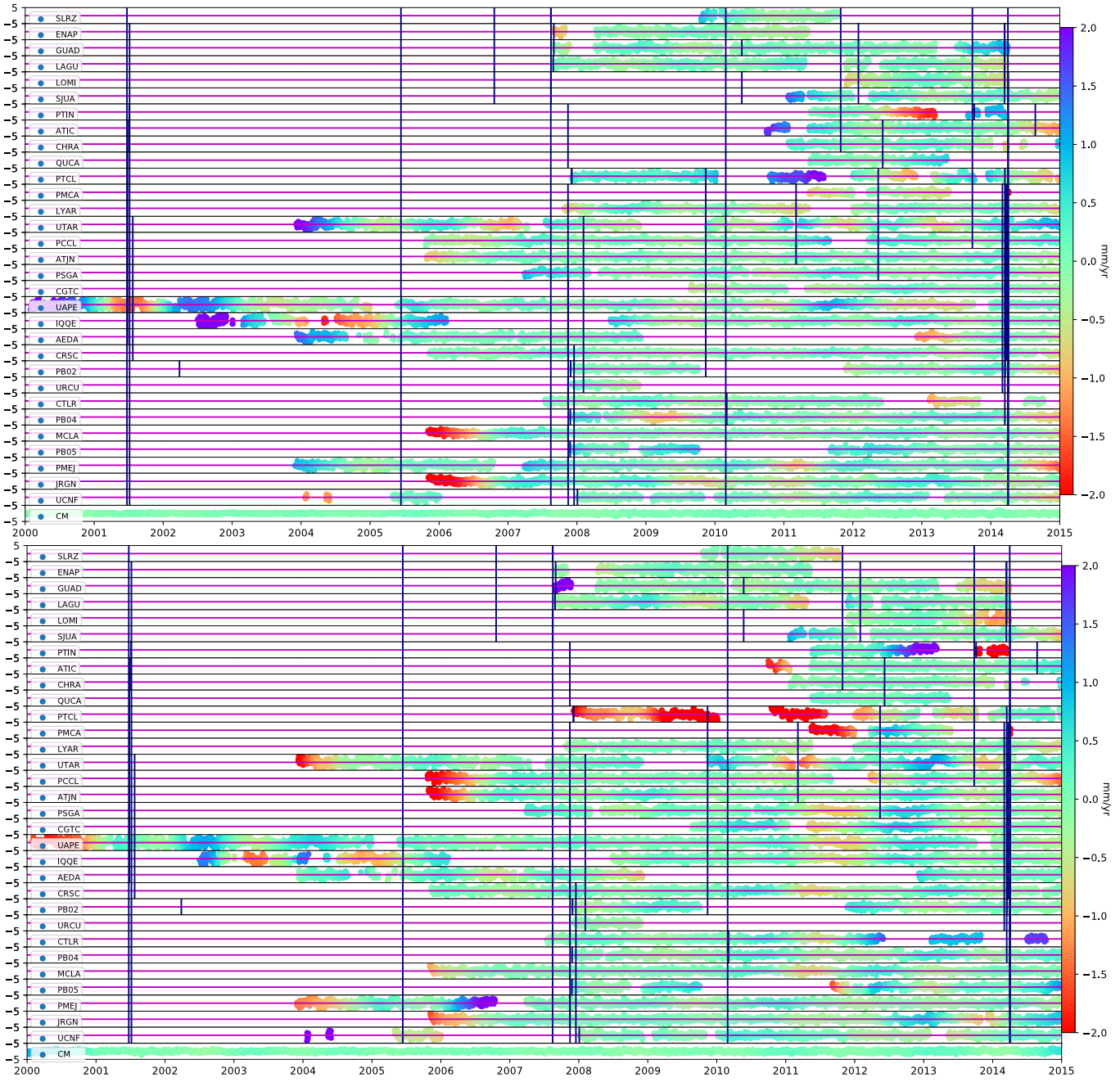

Figure 4.14: Same caption as in Figure 4.13, but removing the common mode.

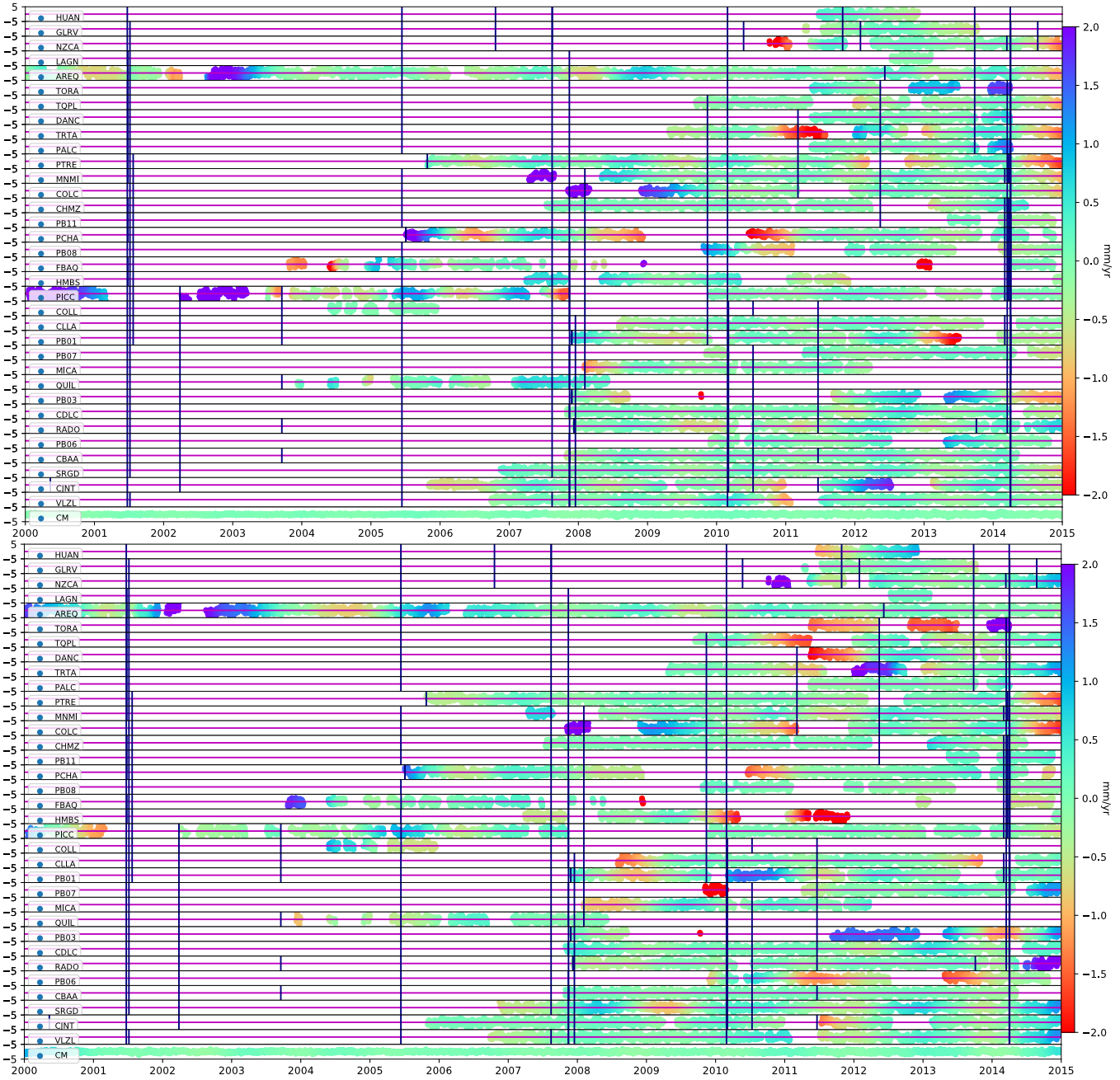

Figure 4.15: Detrended displacement time series for all the inland stations ordered by latitude (Figure 4.5), without removing the common mode. Colors indicate the trench parallel (on top) and trench perpendicular (on bottom) velocities obtained by computing the average velocity over one year sliding window. Vertical lines denote the date of earthquakes of magnitude ≥ 6.0.

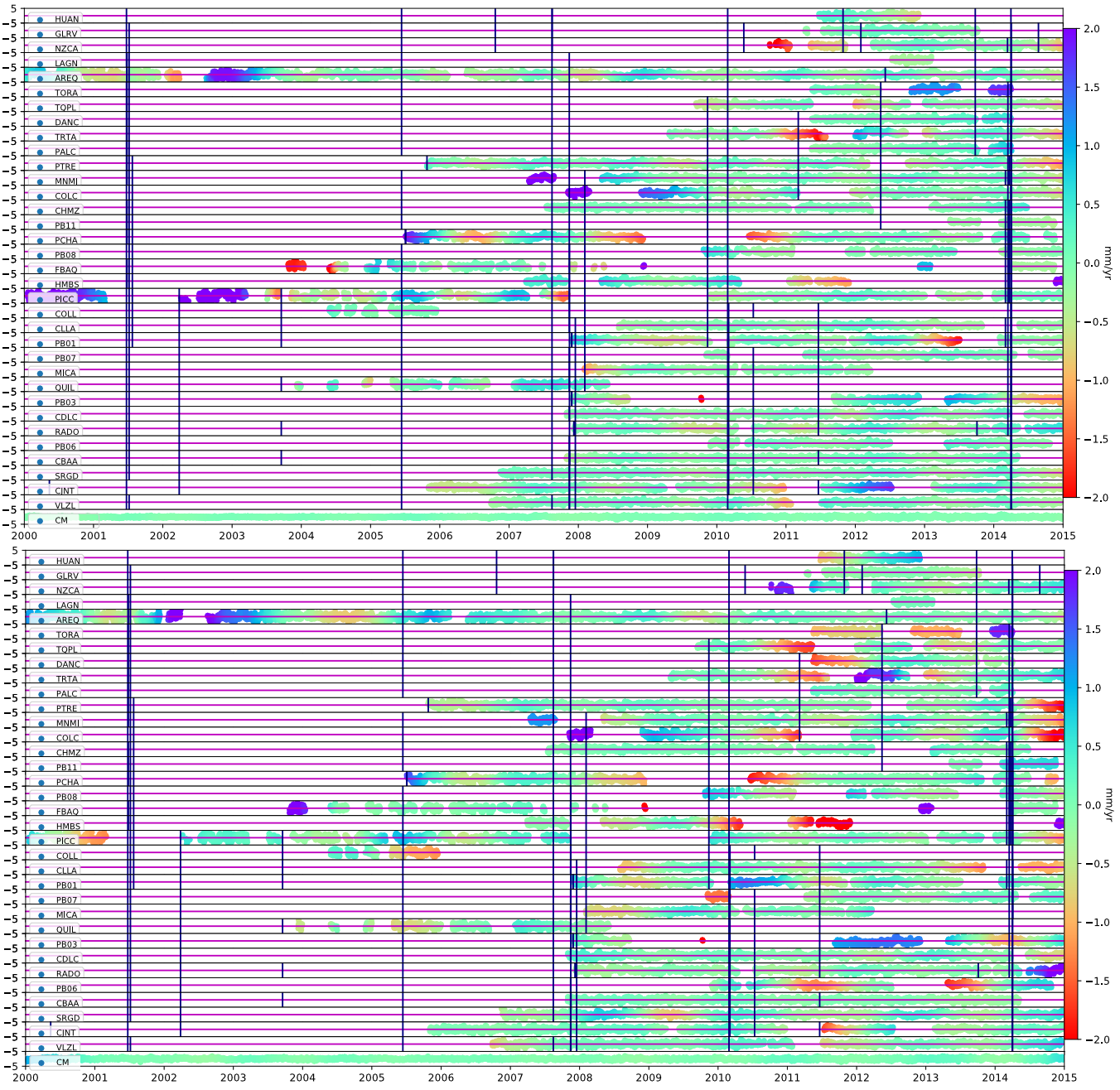

Figure 4.16: Same caption as in Figure 4.15, but removing the common mode.

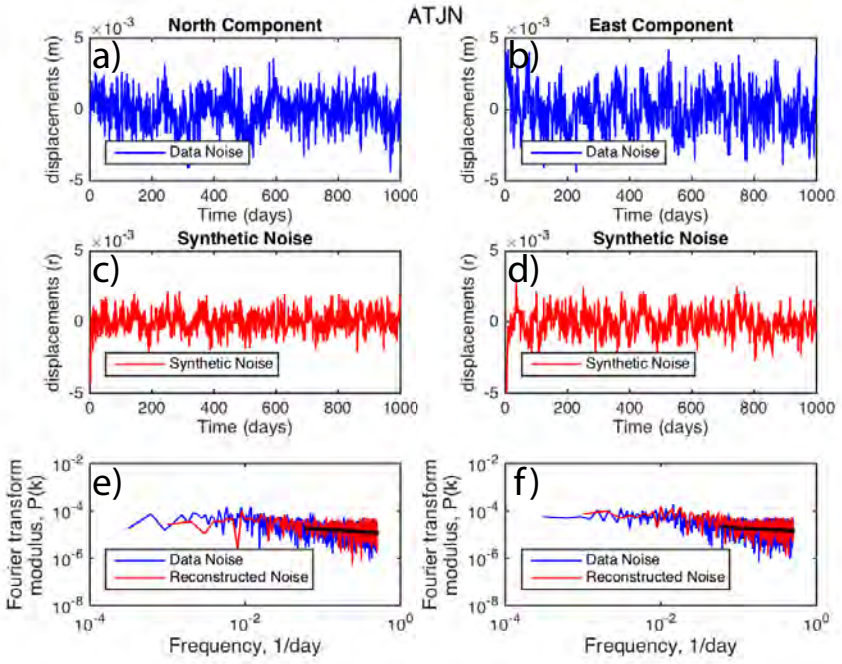

Figure 4.17: GPS noise analysis on North and East components at ATJN station. a) and b) show the North and East residual time series over 1000 days in blue. c) and d) North and East synthetic noise calculated as the sum of white and colored noises in red. e) and f) North and East Fourier transform $P(f)$ of the residual ATJN times series (blue) and the computed synthetic noise (red). The black line shows the slope used to model the colored noise.

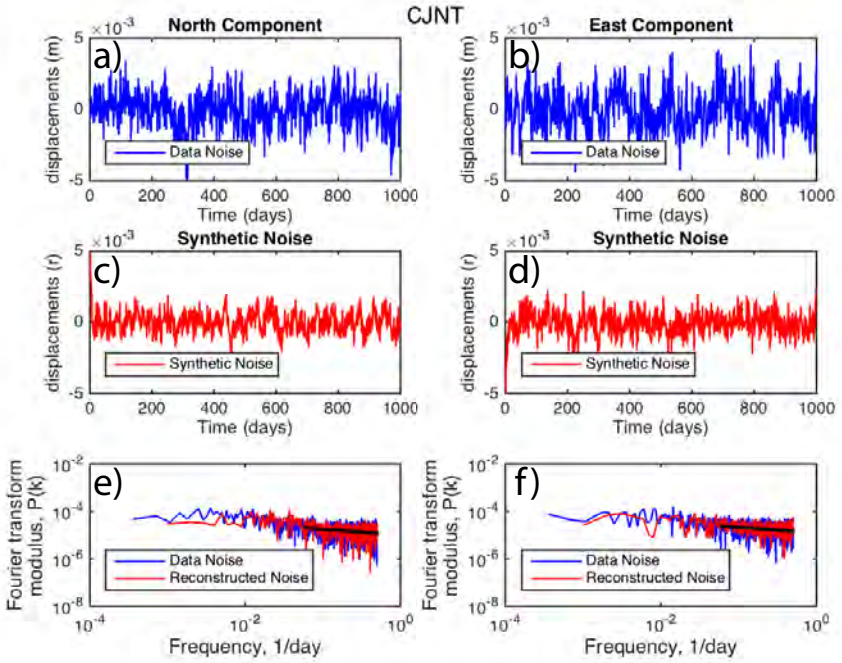

Figure 4.18: GPS noise analysis on North and East components at CJNT station. a) and b) show the North and East residual time series over 1000 days in blue. c) and d) North and East synthetic noise calculated as the sum of white and colored noises in red. e) and f) North and East Fourier transform $P(f)$ of the residual CJNT times series (blue) and the computed synthetic noise (red). The black line shows the slope used to model the colored noise.

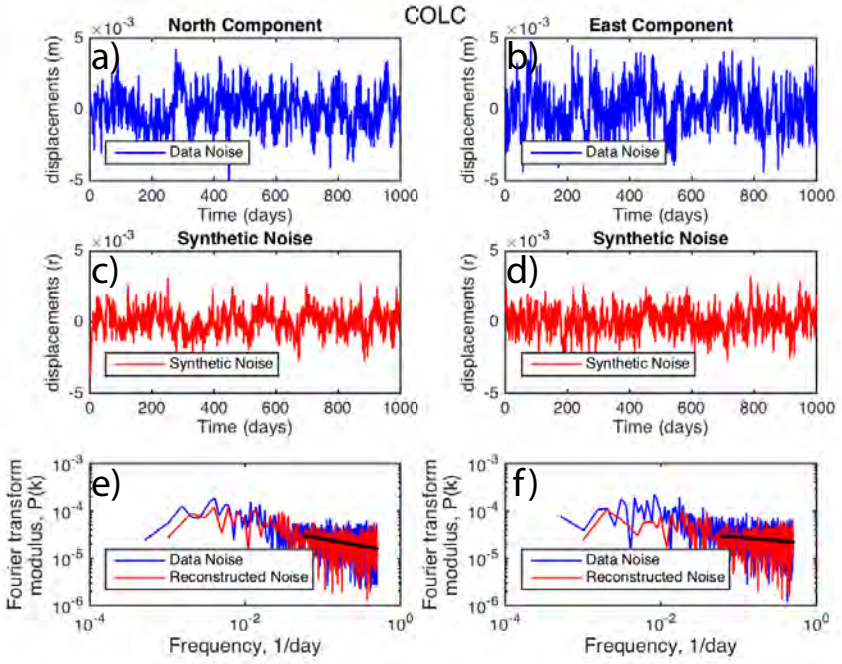

Figure 4.19: GPS noise analysis on North and East components at COLC station. a) and b) show the North and East residual time series over 1000 days in blue. c) and d) North and East synthetic noise calculated as the sum of white and colored noises in red. e) and f) North and East Fourier transform $P(f)$ of the residual COLC times series (blue) and the computed synthetic noise (red). The black line shows the slope used to model the colored noise.

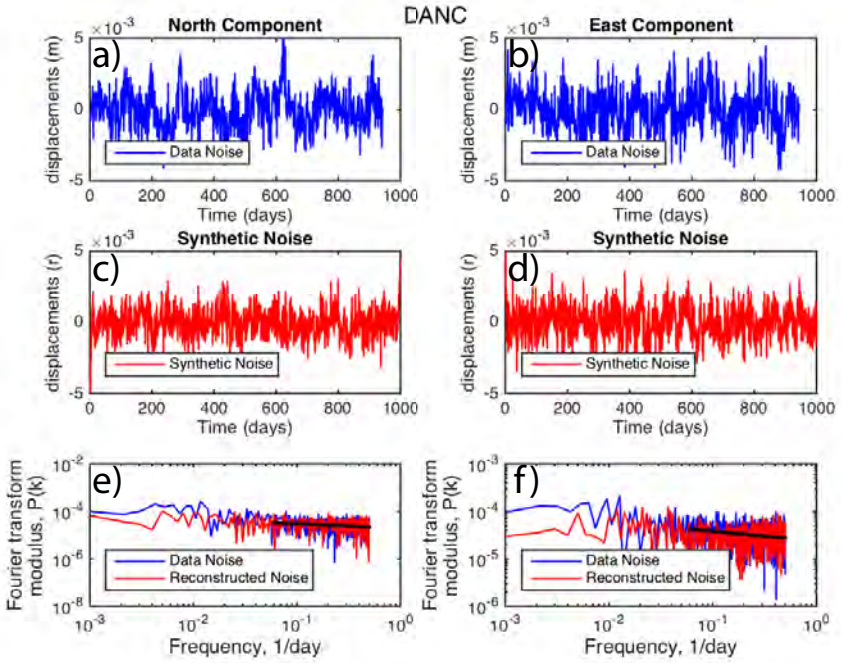

Figure 4.20: GPS noise analysis on North and East components at DANC station. a) and b) show the North and East residual time series over 1000 days in blue. c) and d) North and East synthetic noise calculated as the sum of white and colored noises in red. e) and f) North and East Fourier transform $P(f)$ of the residual DANC times series (blue) and the computed synthetic noise (red). The black line shows the slope used to model the colored noise.

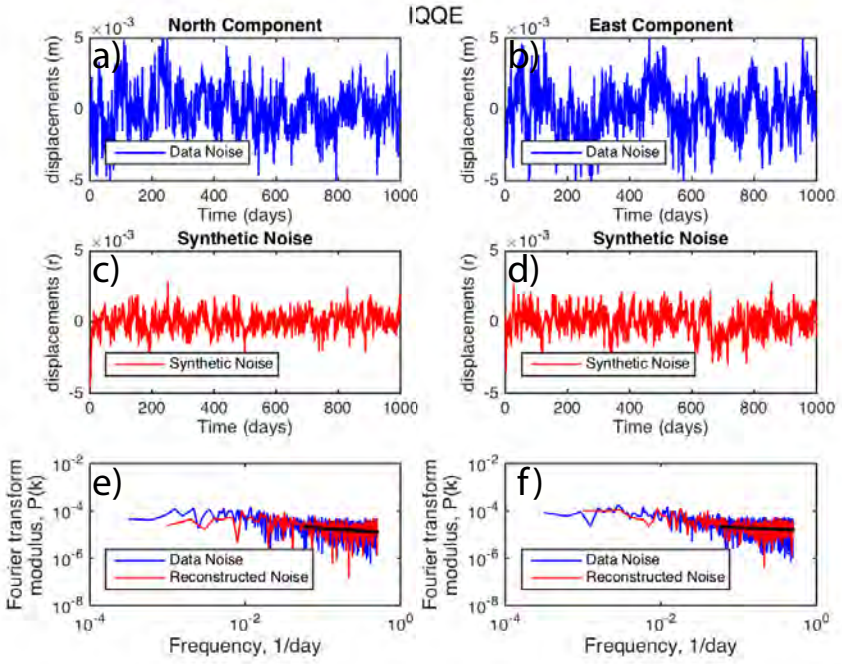

Figure 4.21: GPS noise analysis on North and East components at IQQE station. a) and b) show the North and East residual time series over 1000 days in blue. c) and d) North and East synthetic noise calculated as the sum of white and colored noises in red. e) and f) North and East Fourier transform $P(f)$ of the residual IQQE times series (blue) and the computed synthetic noise (red). The black line shows the slope used to model the colored noise.

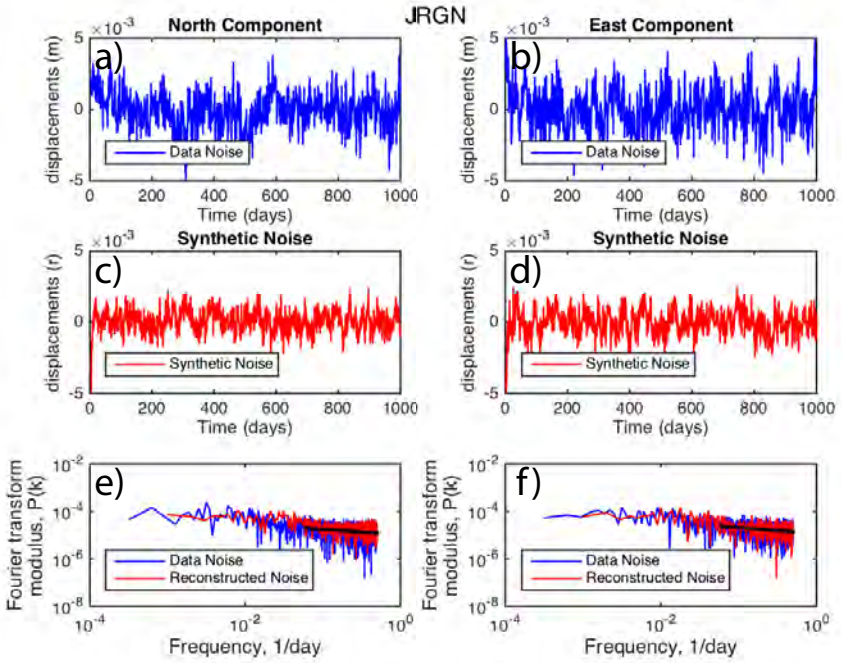

Figure 4.22: GPS noise analysis on North and East components at JRGN station. a) and b) show the North and East residual time series over 1000 days in blue. c) and d) North and East synthetic noise calculated as the sum of white and colored noises in red. e) and f) North and East Fourier transform $P(f)$ of the residual JRGN times series (blue) and the computed synthetic noise (red). The black line shows the slope used to model the colored noise.

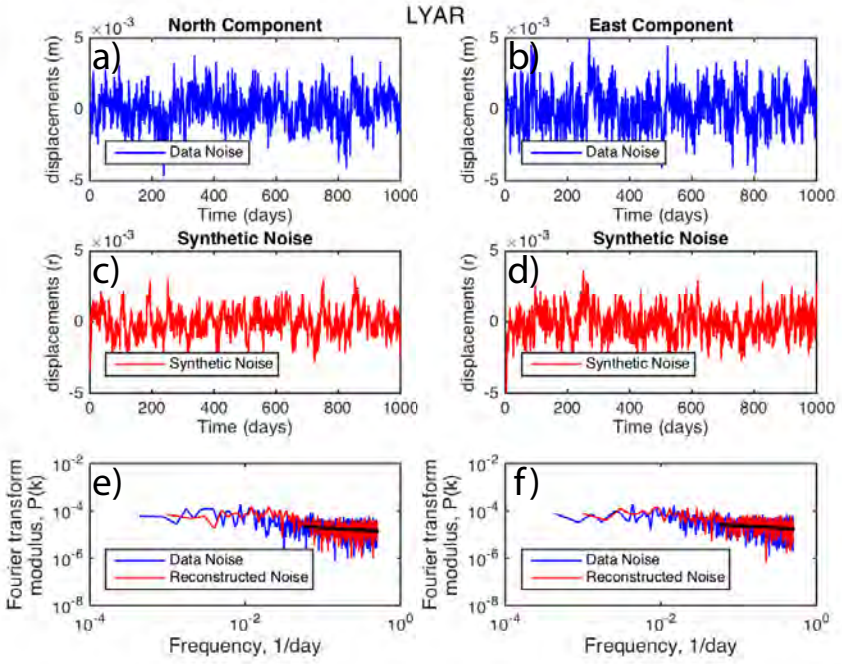

Figure 4.23: GPS noise analysis on North and East components at LYAR station. a) and b) show the North and East residual time series over 1000 days in blue. c) and d) North and East synthetic noise calculated as the sum of white and colored noises in red. e) and f) North and East Fourier transform $P(f)$ of the residual LYAR times series (blue) and the computed synthetic noise (red). The black line shows the slope used to model the colored noise.

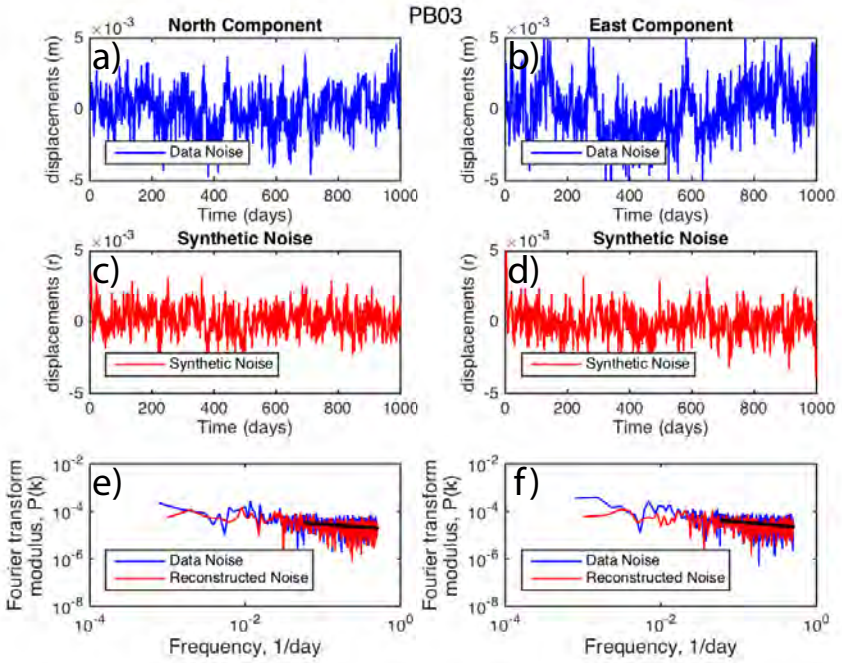

Figure 4.24: GPS noise analysis on North and East components at PB03 station. a) and b) show the North and East residual time series over 1000 days in blue. c) and d) North and East synthetic noise calculated as the sum of white and colored noises in red. e) and f) North and East Fourier transform $P(f)$ of the residual PB03 times series (blue) and the computed synthetic noise (red). The black line shows the slope used to model the colored noise.

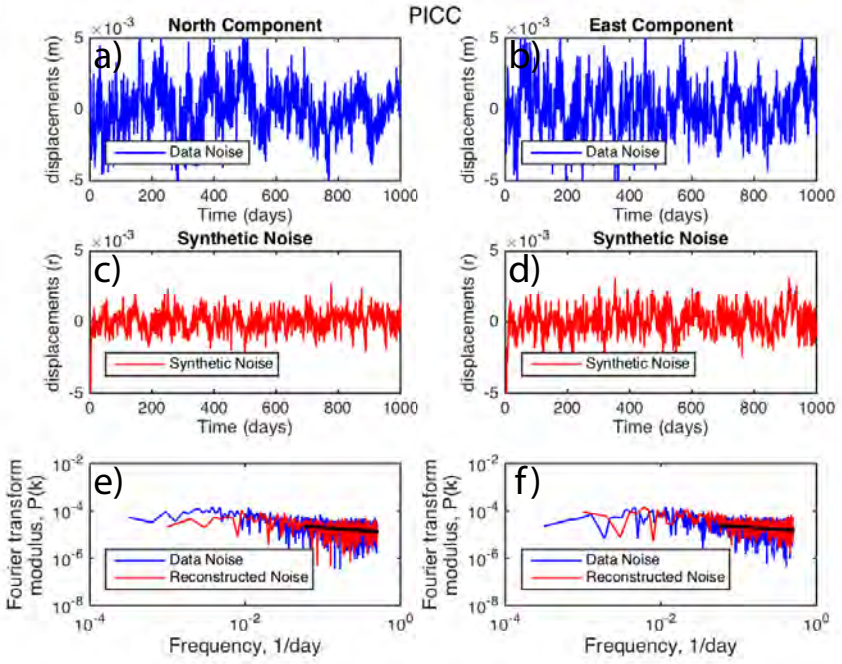

Figure 4.25: GPS noise analysis on North and East components at PICC station. a) and b) show the North and East residual time series over 1000 days in blue. c) and d) North and East synthetic noise calculated as the sum of white and colored noises in red. e) and f) North and East Fourier transform $P(f)$ of the residual PICC times series (blue) and the computed synthetic noise (red). The black line shows the slope used to model the colored noise.

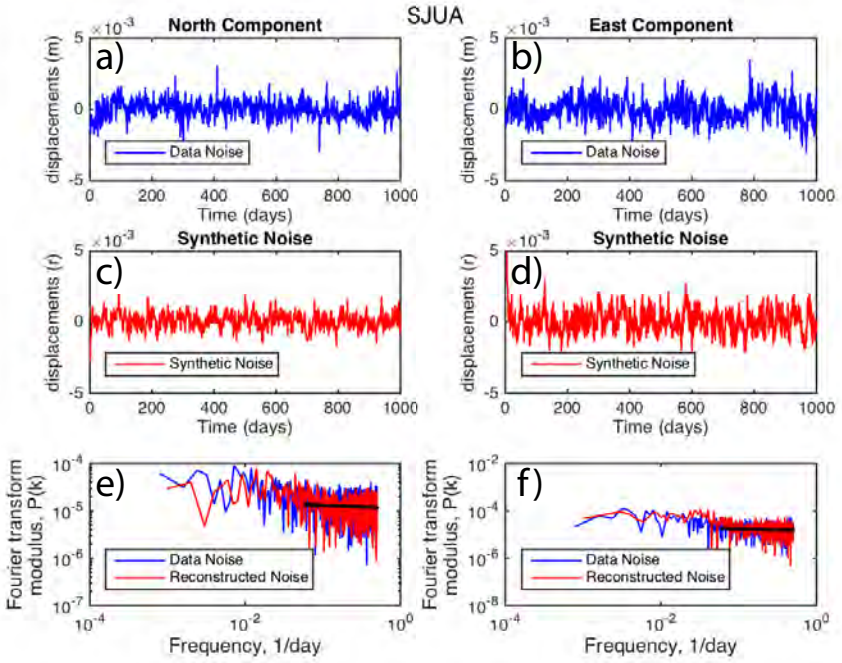

Figure 4.26: GPS noise analysis on North and East components at SJUA station. a) and b) show the North and East residual time series over 1000 days in blue. c) and d) North and East synthetic noise calculated as the sum of white and colored noises in red. e) and f) North and East Fourier transform $P(f)$ of the residual SJUA times series (blue) and the computed synthetic noise (red). The black line shows the slope used to model the colored noise.

SITE	North	East
AEDA	1.95E-01	1.51E-01
AREQ	2.09E-01	1.65E-01
ATIC	2.39E-01	2.06E-01
ATJN	2.13E-01	1.76E-01
CBAA	2.29E-01	1.99E-01
CDLC	1.68E-01	1.37E-01
CGTC	2.30E-01	2.30E-01
CHMZ	2.75E-01	2.49E-01
CHRA	1.66E-01	1.49E-01
CJNT	2.43E-01	2.30E-01
CLLA	1.66E-01	1.75E-01
COLC	2.91E-01	1.38E-01
COLL	1.36E-01	2.39E-02
CRSC	1.69E-01	2.17E-01
CTLR	2.46E-01	1.89E-01
DANC	1.92E-01	2.09E-01
ENAP	2.11E-01	1.66E-01
FBAQ	2.00E-01	2.82E-01
GLRV	2.54E-01	1.73E-01
GUAD	1.56E-01	1.38E-01
HMBS	1.68E-01	1.75E-01
HUAN	2.52E-01	3.66E-01
IQQE	2.27E-01	1.24E-01
JRGN	2.36E-01	2.38E-01
LAGN	1.18E-01	1.96E-01
LAGU	2.17E-01	1.26E-01
LOMI	5.00E-01	3.85E-01
LYAR	1.91E-01	1.91E-01
MCLA	2.05E-01	1.27E-01
MICA	1.82E-01	2.01E-01
MNMI	1.96E-01	1.72E-01
NZCA	1.87E-01	1.87E-01
PALC	2.02E-01	2.03E-01
PB01	2.36E-01	2.86E-01
PB02	2.32E-01	1.73E-01
PB03	2.48E-01	2.82E-01
PB04	1.77E-01	1.87E-01
PB05	2.86E-01	2.55E-01
PB06	2.33E-01	2.00E-01
PB07	2.10E-01	1.89E-01
PB08	2.97E-01	1.68E-01
PB11	1.94E-01	3.24E-01
PCCL	2.01E-01	1.60E-01
PCHA	2.02E-01	2.78E-01
PICC	2.37E-01	2.23E-01
PMCA	1.91E-01	6.23E-02
PMEJ	2.42E-01	1.99E-01
PSGA	1.84E-01	7.20E-02
PTCL	2.83E-01	1.54E-01
PTIN	2.97E-01	2.69E-01
PTRE	1.44E-01	1.08E-01
QUCA	2.45E-01	1.57E-01
QUIL	9.14E-02	3.80E-02
RADO	2.22E-01	2.85E-01
SJUA	6.82E-02	9.40E-02
SLRZ	2.04E-01	9.86E-02
SRGD	1.94E-01	1.69E-01
TORA	4.16E-02	1.58E-01
TQPL	1.88E-01	1.17E-01
TRTA	8.68E-02	2.42E-01
UAPE	1.49E-01	7.63E-02
UCNF	1.53E-01	1.29E-01
URCU	1.43E-01	-2.06E-01
UTAR	1.57E-01	5.54E-02
VLZL	1.85E-01	8.03E-02

Table 4.4: North and East spectral index for each GPS station used in the study.

4.5 Kinematic processing

High frequency GPS records (1 - 5 Hz) have been used and processed in kinematic way using TRACK software. One reference site is chosen, far from the earthquake epicenter, and the relative position between each station in the network and this reference site is calculated one hour and after the earthquake occurrence. It allows to calculate the static offset produced by the earthquake, not including postseismic offsets or early afterslip, that in general contaminate the signal using daily GPS positioning [e.g., *Ding et al.*, 2015]. This technique allows to get seismograms that can be used in kinematic inversions after some filtering processing (e.g., sidereal filtering and common mode).

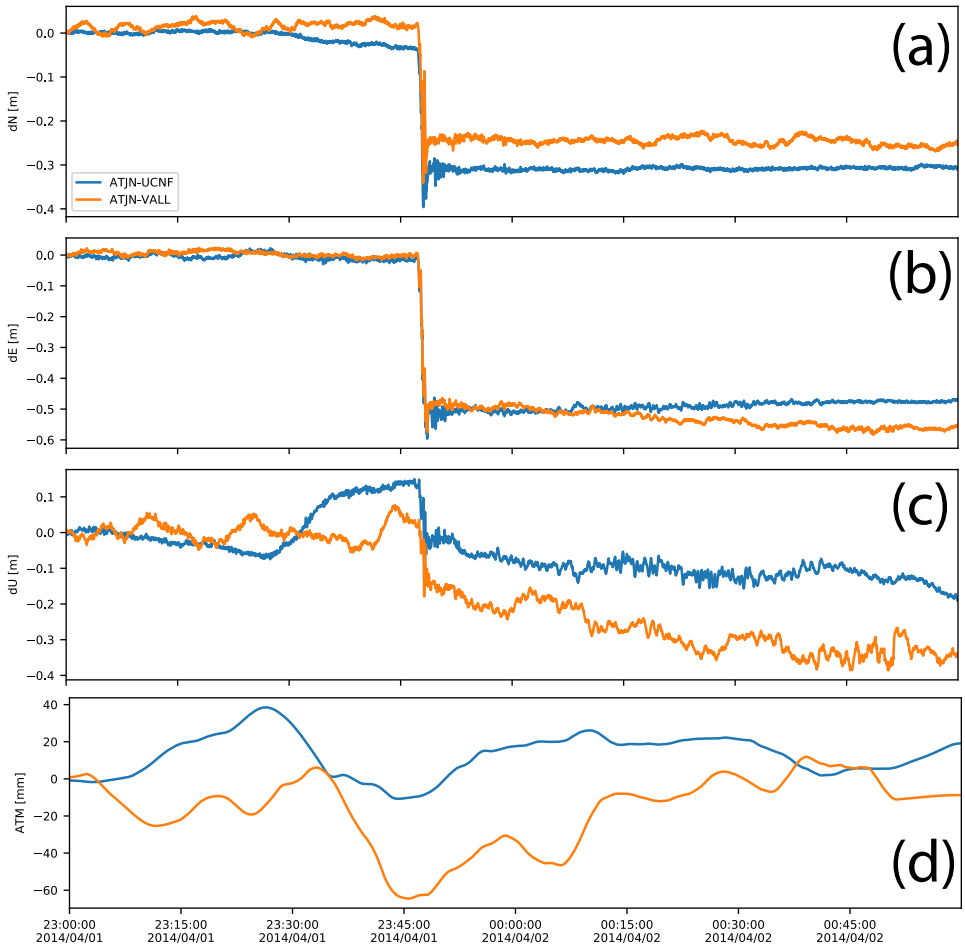

Figure 4.27: North (a), East (b) and Vertical (c) components of ATJN station together with the ATM values, using UCNF (blue) and VALL (orange) as reference site.

The HRGPS data from 25 stations for the Iquique earthquake mainshock and 20 for its biggest aftershock were employed during this Ph.D. (Figure 8.B.1). To do so, two reference sites are tested during the procedure, VALL station that is located ∼1000 km south of the epicenter of Iquique earthquake, while UCNF station sited ∼500 km from the epicenter. The tropospheric delays are re-estimated starting from two-hour estimates given by the static daily solution obtained with GAMIT software (Section 4.3). It allows having precise local atmospheric parameters, improving the TRACK model that uses a global atmosphere model [*Rivera*, 2015; *Klein et al.*, 2017]. The station UCNF

is chosen as the reference site because the scatter on the signal is lower than VALL (Figure 4.27). Although at the first order the shape of the signal is similar, some scatter is produced by the long distance between VALL station and the network, where the atmospheric parameters might change considerably, compared with the distance UCNF station - network.

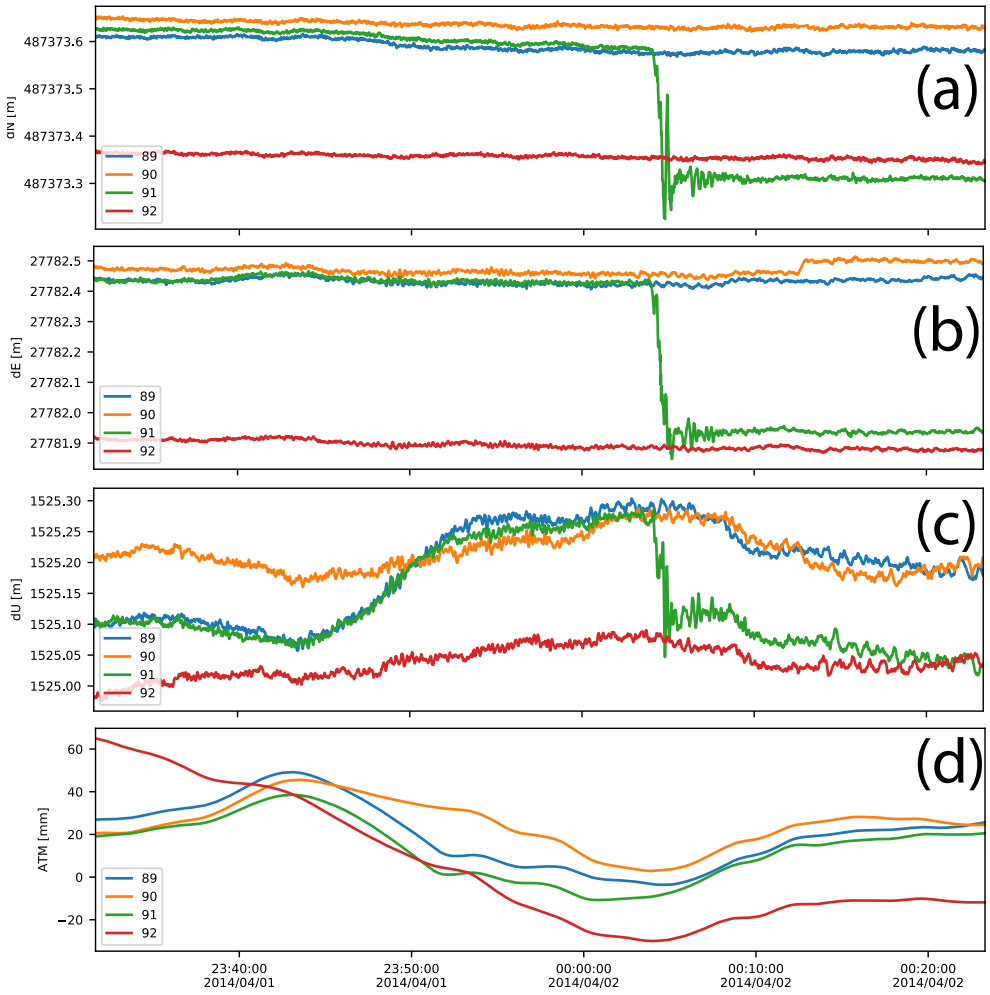

Figure 4.28: Signal repeatability observed at the three components and atmosphere paratement at ATJN Station: (a) north, (b) east, (c) vertical and (d) atmosphere. Each color denotes the day analyzed.

After the processing, the signal repeatability observed in each station (e.g., Figure 4.28) is removed by applying a sidereal filtering. This filter removes the errors coming from the orbits or multipath effect [*Larson et al.*, 2003; *Zhong et al.*, 2010]. The filter is estimated using 2 days before or one day after the mainshock (depending on the data availability). The sidereal delay is taken into account at the moment to calculate the kinematic processing for the previous and after days of each earthquake. This value is considered as 246 s [*Larson et al.*, 2007]. For each component (East, North and Vertical), the signal obtained at the time of the earthquakes in the days preceding or following it is stacked, and then removed from the coseismic signal (e.g., Figure 4.29).

After removing the sidereal filtering from the original signal, a spatial filtering or common mode has been calculated. It allows to remove any effect produced by the earthquake, notably the effect

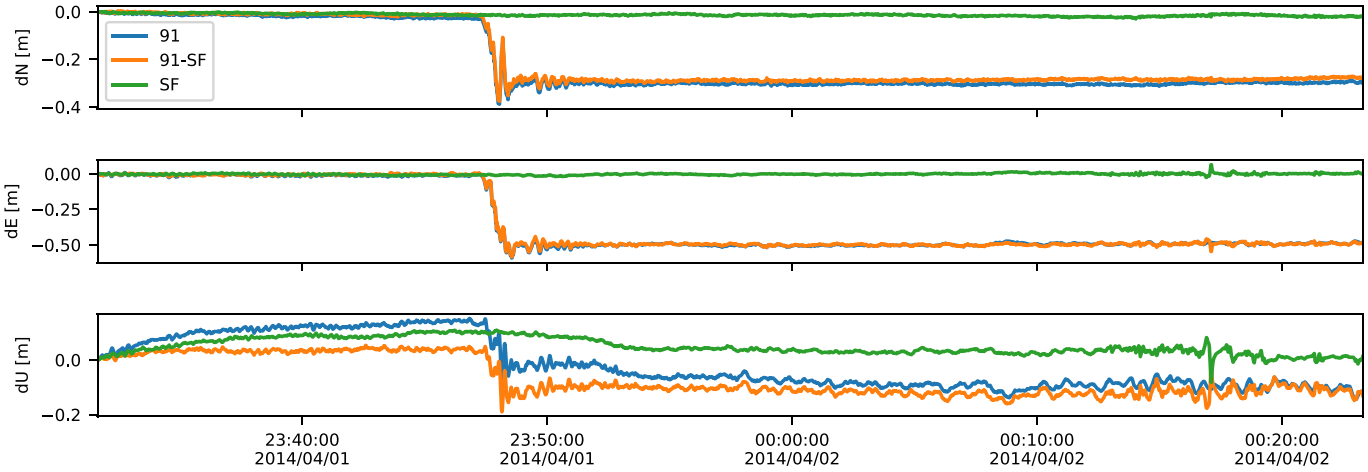

Figure 4.29: North, East and Vertical sidereal filtering (green), original GPS signal for ATJN station (blue) and corrected GPS signal by the sidereal filtering (orange)

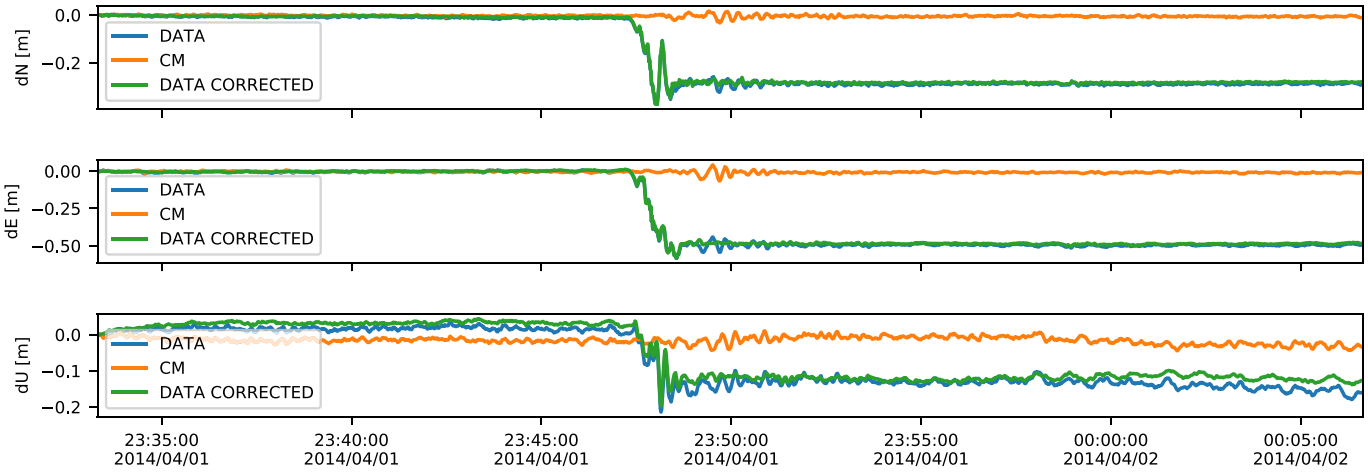

Figure 4.30: Common mode signal (orange), GPS signal corrected from Figure S2 (ATJN station, blue) and GPS corrected by Common Mode (green).

of the arrival of surface waves, at the reference site [*Wdowinski et al.*, 1997]. The closest stations to the reference site UCNF (PB06, PB05, PB04, PB07, PB02 and PB03, that are located within a distance range of 100 km of the reference station) are stacked, and removed this signal from the entire network (e.g., Figure 4.30), thus removing the effect of the surface waves passing through the reference site.

Chapter 5

Long-Term Interactions Between Intermediate Depth and Shallow Seismicity in North Chile Subduction Zone

Paper published: Jara, J., Socquet, A., Marsan, D. & Bouchon, M. (2017). Geophysical Research Letters, pp. 2983–2922, doi:10.1002/2017GL075029, 2017GL075029.[1]

5.1 Abstract

We document interactions between intermediate depth and interplate seismicity in the North Chile subduction zone, over a 25 year period (1990–2015). We show that the 2005 Mw 7.8 Tarapaca slab-pull earthquake was followed by 9 years of enhanced deep and shallow seismicity, together with the decrease of eastward average GPS velocities and associated interplate coupling, eventually leading to the 2014 M_w 8.1 Iquique megathrust earthquake. In contrast, megathrust ruptures (e.g., M_w 8.0 Antofagasta in 1995, or M_w 8.1 Iquique in 2014) initiate several years of silent background seismicity in the studied area, both at shallow and intermediate depths. The plunge of a rigid slab into a viscous asthenospheric mantle could explain the observed synchronization between deep and shallow seismicity and their long-term interactions.

5.2 Introduction

Mechanisms leading to large megathrust earthquakes are still not well understood and described. Recent studies showed that a triggering link exists between intermediate depth seismicity and the occurrence of megathrust earthquakes. For example, *Lay et al.* [2017] showed, from a detailed analysis of source parameters using teleseismic body wave modeling, that the 2016 M_w 7.9 Solomon Islands

[1]Supporting Information of this work can be found at the end of this Chapter.

earthquake was a compound event initiating as a compressional intraslab rupture that coseismically triggered a plate boundary thrust. More intriguing, *Bouchon et al.* [2016] have observed that precursory seismicity, down to magnitude M = 1, at shallow and intermediate depths,occurred synchronously before recent megathrust earthquakes(e.g., M_w 8.8 Maule, Chile, 2010, M_w 9.1 Tohoku-Oki, Japan, 2011, and M_w 8.2 Iquique, Chile, 2014). The reduced magnitude of this precursory seismicity makes direct triggering unlikely, but rather suggests a wider slab deformation or plunge leading to the megathrust rupture. These studies all focus on a preearthquake period that is relatively short in time. Although addressing a time span for deep-shallow seismicity interactions longer than direct coseismic triggering, the latter study remains focused on the 2–3 months preceding the megathrust rupture. However, it has been shown that megathrust earthquakes can be preceded by a long (several months to years) preparation phase [*Bouchon et al.*, 2013; *Mavrommatis et al.*, 2014; *Yokota and Koketsu*, 2015; *Socquet et al.*, 2017], but interaction between such long precursors and deep processes has not been evidenced so far. *Durand et al.* [2014] have described seismicity interplay lasting up to 4 years distributed over a wide area in Greece. The authors proposed that an intermediate-depth earthquake started a broad deformation of the slab which led to a large interface earthquake and stretched the overriding plate over far distances. However, until now, no study exists that analyzes the interactions at the decadal scale between deep and shallow subduction earthquakes and their relationship with the megathrust earthquake cycle.

As North Chile subduction undergoes an important seismic activity at intermediate depths (Figure 5.1) and at the same time is a well-known seismic gap [*Béjar-Pizarro et al.*, 2013; *Comte and Pardo*, 1991; *Métois et al.*, 2016] with different earthquakes occurring in neighboring parts of the thrust, it represents an excellent case to study this inherent influence and interaction between deep and shallow seismicity. On 13 June 2005, the M_w 7.8 Tarapaca slab-pull earthquake occurred at 100 km depth [*Delouis and Legrand*, 2007; *Peyrat et al.*, 2006; *Peyrat and Favreau*, 2010]. Nine years later, on 1 April 2014, the M_w 8.1 Iquique megathrust earthquake broke the subduction interface in the same latitude range [*Duputel et al.*, 2015; *Hayes et al.*, 2014; *Lay et al.*, 2014; *Ruiz et al.*, 2014; *Schurr et al.*, 2014; *Yagi et al.*, 2014], following an important foreshock seismic activity [*Kato et al.*, 2016; *Meng et al.*, 2015; *Ruiz et al.*, 2014; *Schurr et al.*, 2014] associated with a slow slip on the subduction interface that initiated up to 8 months before the mainshock [*Socquet et al.*, 2017]. Here we use both geodetic and seismological data available in the area to characterize the evolution of deformation and seismicity several years before the occurrence of the megathrust and explore the relation between deep and shallow processes, by focusing on the area affected by Tarapaca slab-pull (M_w 7.8, 2005) and Iquique megathrust (M_w 8.1, 2014) earthquakes.

5.3 Data, Methods, and Results

5.3.1 GPS Data, Processing, and Average Velocities

GPS data from different networks in South Peru and North Chile (IPOC, LIA "Montessus de Ballore", CAnTO, ISTerre, IGP, and CSN) were processed in double difference using GAMIT 10.5 software [*Herring et al.*, 2016]. The results were mapped into the ITRF 2008 (Altamimi et al., 2011)

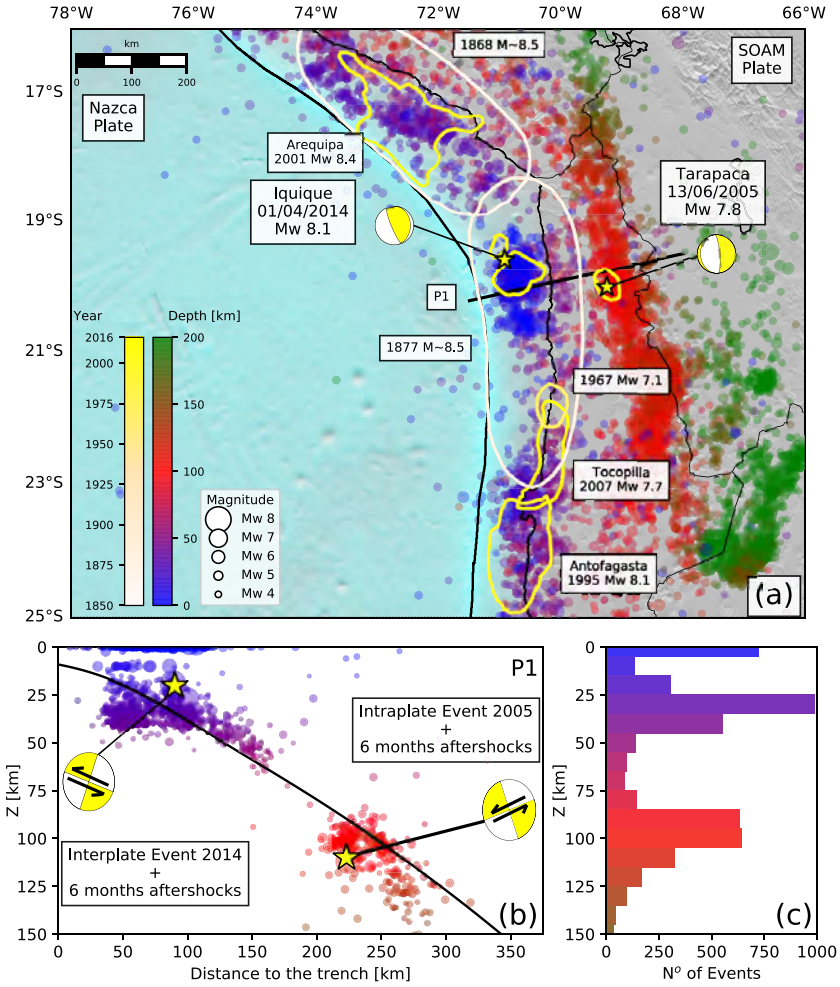

Figure 5.1: Seismotectonic context of North Chile-South Peru subduction zone. Historical and instrumental rupture areas are color coded as a function of their date of occurrence. Dates and magnitudes of all earthquakes M > 7.0 in the area are indicated in squared boxes. Yellow stars and focal mechanisms indicate the epicenters of M_w 7.8 Tarapaca slab-pull earthquake in 2005 [*Delouis and Legrand*, 2007] and M_w 8.1 Iquique megathrust earthquake in 2014 [*Duputel et al.*, 2015]. The 1990–2016 seismicity (M $\geq$ 4.0) from the International Seismological Centre (ISC) (2017) is color coded by depth and scaled by magnitude. The black line indicates the location of the profile represented in Figure 1b. (b) Trench-perpendicular profile showing the slab interface from Slab 1.0 [*Hayes et al.*, 2012]. Earthquake hypocenters and hemispheric projection of the focal mechanisms are shown in yellow. Also 6 months of aftershocks for each earthquake are plotted, color coded by depth and scaled by magnitude. Tarapaca earthquake fault plane is indicated with a black line above its hypocenter star. (c) Seismicity histogram at depth between 19°S and 21°S, taking into account 10 km to separate each segment.

(see supporting information for details [*Boehm et al.*, 2006]).

To calculate the average interseismic velocities, the date of the Tarapaca earthquake is taken as the origin date(13 June 2005). The period preceding the earthquake covers from 1 day after the Arequipa earthquake (M_w 8.4, 23 June 2001 [*Perfettini et al.*, 2005]) until the day before the Tarapaca earthquake. The period following the Tarapaca earthquake starts 1 day after it and ends at the beginning of August 2013, in order to avoid the 8 month precursory phase preceding Iquique earthquake [*Socquet et al.*, 2017]. A simple model taking into account the position x_R at a given reference time t_R, the velocity v, and one displacement step for each large earthquake H (Heaviside function), at a given time t_j, is inverted to calculate the velocities, following the Trajectory Model principle [*Bevis and Brown*, 2014] (Equation 5.1). This model does not consider afterslip or

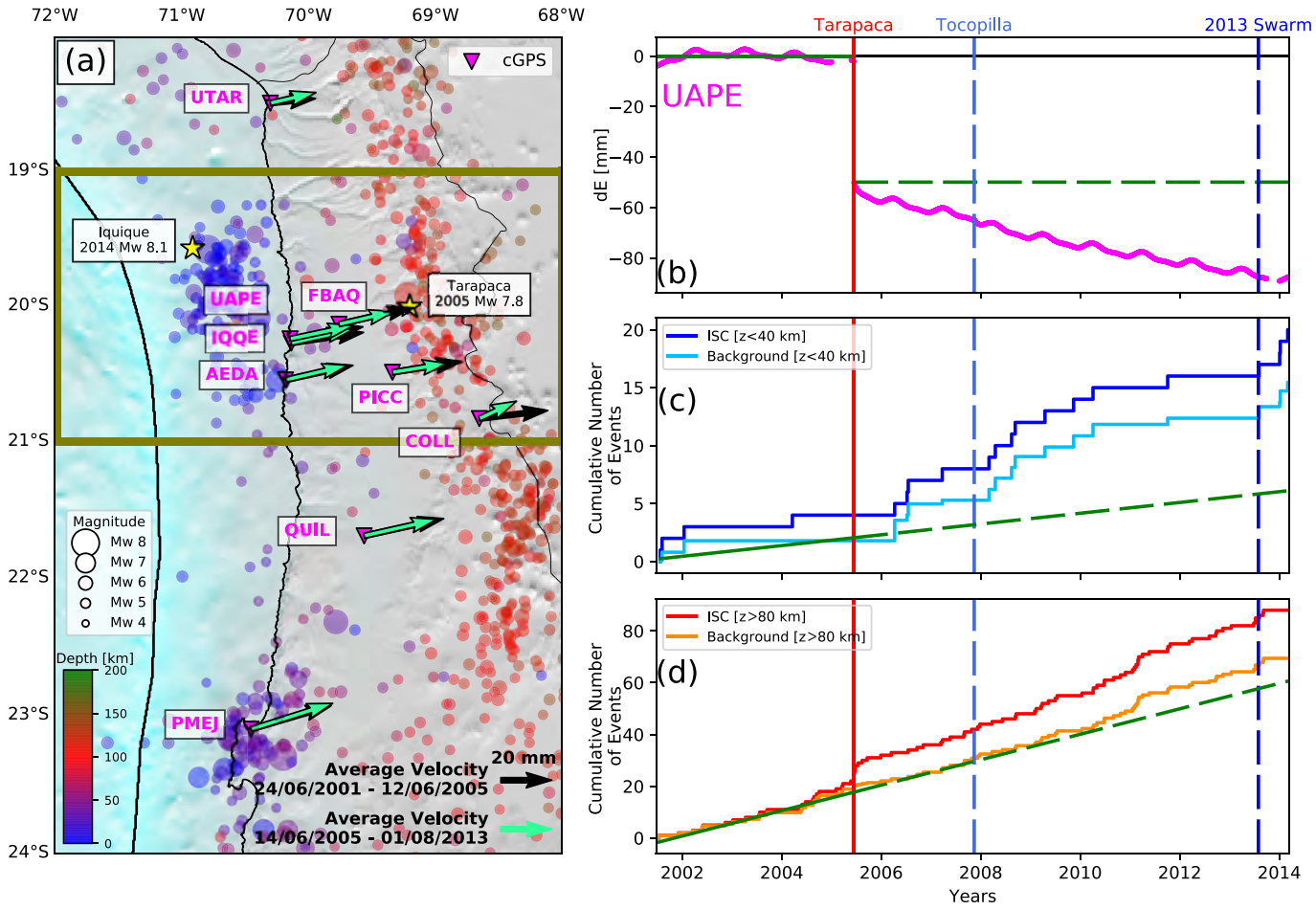

Figure 5.2: Map of average GPS velocities before (black arrows) and after (green arrows) Tarapaca earthquake 2005. The first period covers 1 day after Arequipa earthquake (2001 M_w 8.4) until 1 day before Tarapaca earthquake. The second period covers 1 day after Tarapaca earthquake up to the swarm activity seen in August 2013, preceding Iquique earthquake. Pink inverted triangles symbolize the location of GPS stations with their respective names at side. The 1990–2016 ISC seismicity is color coded by depth and scaled by magnitude (M $\geq$ 4.7, completeness magnitude). The box shows the target zone where the seismicity is studied. Yellow stars indicate the epicenter of Tarapaca and Iquique earthquakes. (b) East component displacement time series of UAPE station, detrended using 2001.44–2005.45 period as reference. Green dashed line shows the coseismically offset projection of the first period trend. Vertical lines point out an earthquake or swarm occurrence: continuous lines represent events that occurred in the study area and dashed events outside it. (c, d) The time evolution of shallow (z $\leq$ 40 km) and deep (z $\geq$ 80 km) seismicity, respectively. Blue (red) and light blue (orange) are the cumulative number of events for ISC catalog and background seismicity, respectively (M $\geq$ 4.7). Green lines show the seismicity trend in the period one (as in Figure 5.2b and dashed lines show the trend projected to the second period.

viscoelastic relaxation, due to the fact that there are no clear postseismic signal visible on the GPS time series because of the earthquake depth (100 km) (Figure 5.2b).

$$x(t) = x_R + v(t - t_R) + \sum_{j=1}^{n_j} b_j H(t - t_j) \tag{5.1}$$

These velocities are calculated for nine stations that have enough data before and after Tarapaca earthquake (Figure 5.2a, see supporting information for further details on position time series, velocities and errors). The eastward velocity of UAPE cGPS coastal station decelerates by 4 mm/yr

after the occurrence of Tarapaca earthquake (Figure 5.2b). A similar change in velocity affects most of the cGPS stations within the study area. Coastal stations in this region (IQQE and AEDA) decelerate by 2 to 4 mm/yr, while inland stations (FBAQ, PICC, and COLL) decelerate by ∼6 mm/yr (Figure 5.2a and see supporting information for further details on the velocity values). In comparison, stations located away from the study area (e.g., UTAR and PMEJ) do not exhibit such a change in the average velocity (Figure 5.2). We hypothesize that this change in velocity is due to a partial decoupling of the slip interface at depth; we thus aim at searching for futher evidences of this in the seismicity.

5.3.2 Catalog and Background Seismicity

The ISC event catalog [*International Seismological Centre*, 2014] from 1990 to 2017 is used to analyze raw and background seismicity. The area analyzed covers the latitude range between 11∘S–25∘S, and the longitude range 80∘W–66∘W (Figure 5.1a). We make use of a method developed by *Ogata and Katsura* [1993] and *Daniel et al.* [2008] to compute the catalog completeness magnitude. Because IPOC seismic network was installed in 2007 in Northern Chile, two different periods are considered: from 1990 to 2006 and from 2007 to 2017. Our approach assumes that both periods are characterized by the same b value, thus allowing for a better resolved magnitude of completeness (one for each period). The calculated completeness magnitudes are $M_c = 4.5$ for the first period and $M_c = 4.0$ for the second period (in the whole South Peru-North Chile area considered on which the declustering has been done). We have fixed $M_c = 4.5$ for the whole period 1990 – 2017 (see supporting information for further details).

An epidemic-type aftershock sequence (ETAS) model is performed to decluster the catalog and estimate the background seismicity [*Marsan et al.*, 2013, 2017]. The number of earthquakes (λ) per unit of area (x and y) and unit of time (t) is modeled as the sum of two contributions:

$$\lambda(x, y, t) = \mu(x, y, t) + \nu(x, y, t) \tag{5.2}$$

where $\nu(x, y, t)$ accounts for triggered earthquakes by a previous one (i.e., aftershocks) and μ is the background seismicity rate (i.e., not triggered by a previous event). The parameters x and y represent the location and t the time of occurrence of each event.

The aftershock rate $\nu(x, y, t)$ is obtained using

$$\nu(x, y, t) = \sum_{i|t_i<t} \nu_i(x, y, t) \tag{5.3}$$

where t_i is the occurrence time of the ith earthquake; $\nu_i(x, y, t)$ is computed as

$$\nu_i(x,y,t) = \frac{\kappa(m_i)}{(t+c-t_i)^p} \cdot \frac{(\gamma-1)L(m_i)^{\gamma-1}}{2\pi\big((x-x_i)^2+(y-y^2)+L(m_i)^2\big)^{(\gamma-1)/2}} \tag{5.4}$$

That is, the product of the Omori-Utsu law with a power spatial density, with c, γ, and p constants. $L(m) = L0 \times 10^{0.5(m-4.7)}$ is the characteristic length in kilometer [*Elst and Shaw*, 2015; *Utsu and Seki*, 1955]; and $\kappa(m)$ is the productivity law, with α constant [*Ogata*, 1988].

Parameters α, p, c, L_0, and γ are here imposed a priori to realistic values: $\alpha = 2$, $p = 1$, $c = 10^{-3}$ days, $\gamma = 2$, and $L_0 = 1.78$ km. While these parameters can be optimized given the data, in presence or not of a time- and space-varying background rate [*Reverso et al.*, 2015], it is easier and generally sufficient to impose fixed values (see *Marsan et al.* [2017], for a discussion on this in the context of the northeast Japanese subduction zone). A parameter exploration is performed in the supporting information to evaluate how the results of our analysis depend on this choice. In contrast, parameters κ and $\mu(x,y,t)$ are inverted. The background rate $\mu(x,y,t)$ is calculated as

$$\mu(x,y,t) = \sum_i \frac{\mu(x_i,y_i,t_i)}{\lambda(x_i,y_i,t_i)} e^{-\sqrt{(x-x_i)^2+(y-y_i)^2}/\ell} e^{-|t-t_i|/\tau} \times \frac{1}{2\pi\ell^2 a_i} \tag{5.5}$$

Where ℓ and τ are two smoothing parameters for space and time. a_i is defined as $a_i = 2\tau - \tau(e^{-\frac{t_s-t_i}{\tau}} - e^{-\frac{t_e-t_i}{\tau}})$. t_s and t_e represent the starting and ending time of the catalog. Parameter κ is computed as

$$\kappa = \frac{\sum_i 1 - \frac{\mu(x_i,y_i,t_i)}{\lambda(x_i,y_i,t_i)}}{\sum_i e^{\alpha m_i}(\ln(t_e+c-t_i) - \ln c)} \tag{5.6}$$

We have used a smoothing length ℓ of 100 km and smoothing duration τ of 100 days to preserve the potential accelerations in the catalog [*Marsan et al.*, 2017].

We perform the declustering for the whole area (Figure 5.1a) and eventually focus on the region affected by the two mainshocks (box in Figure 5.2a). This smaller area is characterized by a slightly larger M_c of 4.7 compared to the whole area on which the declustering has been performed (see supporting information S1 for further details). Thus, the seismicity with magnitude over 4.7 is selected from the regional declustered catalog to perform the analysis on the specific zone.

We separated shallow (z $\leq$ 40 km) and deep (z $\geq$ 80 km) background seismicity (Figures 5.2c and 5.2d). This depth selection has been made to better separate deep and shallow events by avoiding the seismicity between 40 and 80 km at depth, that is, a depth range with very little seismicity (Figure 5.1c). It is obvious from Figure 5.2d that the declustering mostly removes the aftershocks following the Tarapaca earthquake. Despite this, a clear increase both in deep and shallow background seismicity can be seen after the 2005 Tarapaca earthquake (shallow seismicity

in 2006 and deep seismicity in 2011). In order to characterize its temporal variability, seismicity rates are calculated for reference periods ranging from 1 day to 2 years. Figures 5.3a and 5.3b offer a view of deep and shallow seismicity rates computed for different time windows, ranging from 1 day to 2 years, over 25 year time span. It shows that the 9 year period of increased deep and shallow seismicity following 2005 Tarapaca slab-pull earthquake, is followed by a period of quiescence after the occurrence of the 2014 earthquake. Similarly, the 1995 Antofagasta earthquake marks the limit between an important seismic activity before, and no background seismicity after. It also allows one to observe that the seismicity release does not occur steadily in the long-term, but rather through a series of pulses.

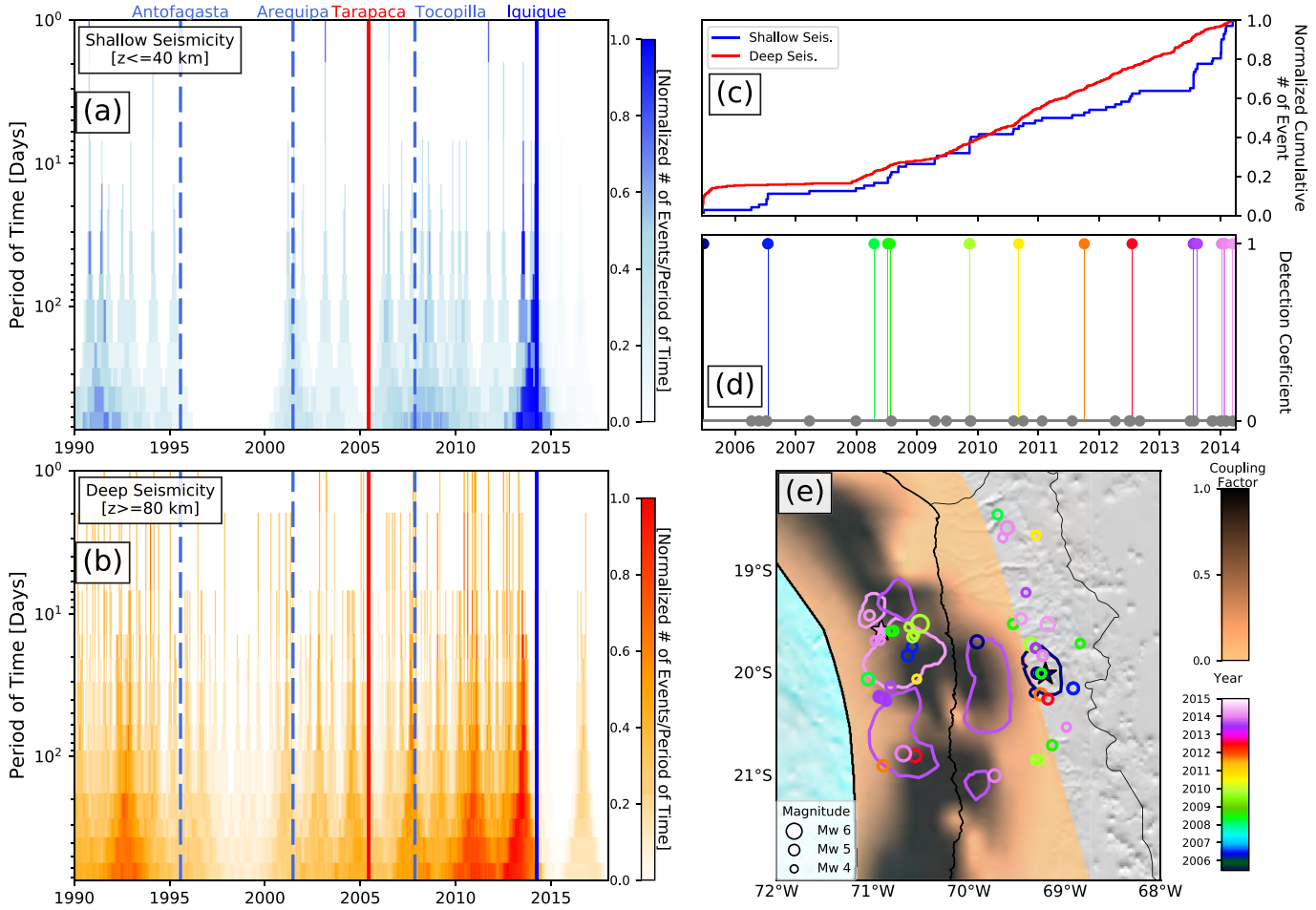

Figure 5.3: The time evolution of normalized background seismicity rate calculated for different periods of reference (from 1 day rate to 2 years rate), for shallow ($z \leq 40$ km) and deep ($z \geq 80$ km) seismicity. Continuous (dashed) lines indicate the time of occurrence of earthquakes into (outside) the study area. Blue (red) are shallow interplate (intermediate depth intraplate) earthquakes. Interactions between shallow and deep seismicity: (c) Normalized cumulative number of events for shallow (blue) and deep (in red) in the study area ($M_c = 4.0$). (d) Synchronization coefficients defined to identify interactions between deep-shallow seismicity. They are color coded by time for 1.0 value (positive interaction) and grey for 0 value (no interaction). (e) Map view of shallow-deep seismicity interaction identified between 14 June 2005 and 1 January 2014, color coded by time. Coupling map is from *Métois et al.* [2016]. Tarapaca and Iquique ruptures [*Delouis and Legrand*, 2007; *Duputel et al.*, 2015] and 8 month of preseismic slip [*Socquet et al.*, 2017] are plotted and color coded by time.

5.4 Discussion

5.4.1 A Change in Deformation and Seismicity After Tarapaca Slab-Pull Earthquake

After the 2005 Tarapaca earthquake, a significant change in the surface deformation can be observed (Figure 5.2a). The reduction in eastward velocity could be related to post-seismic deformation following the slab-pull event (e.g., poroelastic rebound [e.g., *Jonsson et al.*, 2003; *Peltzer et al.*, 1998], afterslip [e.g., *Hsu et al.*, 2006], or mantle's viscoelastic relaxation [e.g., *Khazaradze et al.*, 2002; *Klein et al.*, 2016]). Given the fact that the earthquake occurred at 100 km depth, it is likely that poroelastic rebound, which usually takes place at shallow depths within structural complexities of the fault [*Jonsson et al.*, 2003; *Peltzer et al.*, 1998]), does not exist or is hardly detectable in the surface deformation field (if any occurs). Part of this velocity reduction of the stations is located far from the coast (more than 6 mm/yr after the earthquake). Given the fact that the change in velocity affects a large area, a viscoelastic relaxation has been invoked [*Bie et al.*, 2017], although it is not possible to observe the associated long-term typical exponential-like transient in the GPS time series, that is usually associated with this type of mechanism. Whatever the mechanism, such long-term changes in the surface displacement rates suggest that Tarapaca intraplate earthquake had an important impact on the surface deformation field and therefore on the amount and pattern of the interseismic compression in the upper plate and at the plate boundary. This broad change in surface deformation generates a velocity reduction of $\sim$4 mm/yr at coastal stations and likely modifies the stress regime close to the plate boundary, enhancing unclamping as well as a change in the coupling on the subduction interface. Until recently, no slow slip events had been reported in the area. *Ruiz et al.* [2014] and *Schurr et al.* [2014] have shown a strong transient deformation, for which the aseismic nature is debated, during the weeks preceding the occurrence of Iquique earthquake, and *Socquet et al.* [2017] showed that an 8 month aseismic slow slip preceded the earthquake. These slow slip events have also been observed by the analysis of repetitive earthquakes. *Kato et al.* [2016], *Meng et al.* [2015] and *Yagi et al.* [2014] have pointed out the occurrence of aseismic deformation over the same period as *Ruiz et al.* [2014]. Taking a longer period of time, *Kato et al.* [2016] have detected an aseismic slip starting in 2008 with a continuous rate of 0.67 mm/yr until the 2013 seismic swarm. Because the average velocity field is calculated up to the 2013 swarm (avoiding the precursory phase of Iquique earthquake, [*Socquet et al.*, 2017]), the observed reduction of coastal velocities is compatible with *Kato et al.* [2016] and we interpret this behavior as a reduction of coupling on the subduction interface.

Associated with the decrease in eastward GPS velocities, an increase in seismicity rate is observable both at deep and shallow depths during the interearthquake period, either in the whole ISC catalog or in the background seismicity (Figures 5.2 and 5.3). The background seismicity is usually considered to be a proxy of the tectonic loading in a specific area, so that any important deviation from the average trend can be associated with slow slip events and fluid or magmatic migrations [*Marsan et al.*, 2017]. This therefore suggests an increase in the tectonic loading, which is compatible with the observed decrease in GPS eastward velocity interpreted as an interplate decoupling (and therefore an increased creep on the subduction interface). Interestingly, this increase in background

seismicity rates concerns both shallow and deep earthquakes, suggesting that a link exists between shallow and deep seismic responses.

5.4.2 Long-Term Interactions Between Shallow and Intraslab Seismicity

Figures 5.3a and 5.3b offer a view of the background seismicity rates over a 25 year time span, for deep and shallow seismicity. Before Antofagasta megathrust earthquake (M_w 8.0, 1995 [*Delouis et al.*, 1997]), both deep and shallow background activities are significant. After this earthquake, the study area entered in a silent period until the occurrence of the Arequipa earthquake in mid-2001 in South Peru (M_w 8.4 [*Perfettini et al.*, 2005]). The Arequipa earthquake initiates the reactivation of a subtle background seismic activity that accelerates at depth in the months preceding Tarapaca slab-pull earthquake. The Tarapaca intraslab earthquake triggers an increase in both deep and shallow seismicity rates. At the end of 2007, in the southern part of the gap, the Tocopilla earthquake (M_w 7.7 [*Béjar-Pizarro et al.*, 2010; *Peyrat and Favreau*, 2010]) triggers a burst of shallow seismicity. Then, 4 years before Iquique megathrust earthquake, the deep seismicity rate increases, followed in August 2013 by the increase of the shallow background seismicity rate, 8 months before the mainshock. In April 2014, Iquique megathrust earthquake ruptures a large part of the plate interface and concludes a period of enhanced deep and shallow background seismic activity that initiated 9 years before with the occurrence of Tarapaca slab-pull earthquake. Since the occurrence of the Iquique megathrust in April 2014 (up to now), the background seismic activity is almost zero, at least at $M_c = 4.7$.

Global tectonic models propose different forces leading the Earth's convection. One primary force responsible for this process is that generated by the slab subducting beneath the lithosphere. These models have shown that a relationship exists between the "slab-pull" force and the processes occurring in the seismogenic zone [e.g., *Bilek et al.*, 2005; *Conrad et al.*, 2004; *Conrad and Lithgow-Bertelloni*, 2002; *Spence*, 1987]. From a local seismotectonic point of view, models describe interactions between interplate and intraplate events. These models depend on how far in the seismic cycle the thrust is. Prior to a thrust event, the stress regime at intermediate depth exhibits tensional behavior generating preferentially slab-pull earthquakes. Conversely, after a thrust earthquake, the stress regime changes to the opposite, generating compressional slab-push events [e.g., *Astiz and Kanamori*, 1986; *Astiz et al.*, 1988; *Dmowska et al.*, 1988; *Lay et al.*, 1989; *Lemoine et al.*, 2001; *Malgrange and Madariaga*, 1983]. The observed period of enhanced deep and shallow seismicity after an intraslab event and silent periods following megathrust earthquakes might be explained by such mechanical models. Usually, previous works focus the attention in earthquake occurrence. Slab-push earthquakes in subduction zones have been documented after shallower activity [e.g., *Fuenzalida et al.*, 2013; *Lemoine et al.*, 2001, 2002; *Peyrat and Favreau*, 2010; *Ruiz et al.*, 2011]. However, the quiescent periods have been less reported. Here we suggest that the observed arrest of slab-pull seismicity ($M_c = 4.7$) could be explained by a similar mechanism. The observed increase in the seismicity (at deep and shallow depths) after the slab-pull rupture, would be controlled by a mechanism of afterslip and decoupling on the subduction interface, while the silent period following megathrust ruptures, by clamping of the faults cutting the slab through an increase of compressive

stress along the slab. In the shallow part, a possible mechanism could be the lack of interplate earthquakes in the area that previously ruptured coseismically because of the large amount of stress released during the earthquake, as it has been observed after Tohoku-Oki earthquake [*Asano et al.*, 2011].

5.4.3 Synchronization of Deep and Shallow Seismicity

Another interesting feature revealed by Figures 5.3a and 5.3b is the fact that the background seismic activity is not continuous in time, but rather occurs by bursts, both for shallow and deep events. These swarms are usually associated with aseismic episodes [*Reverso et al.*, 2015, 2016]. The shallow bursts are associated with swarms detected in 2006, 2008, and 2013 (see supporting information for details), which may indicate the occurrences of SSEs, plus a few isolated background earthquakes between 2005 and 2014 that occur as a response to tectonic loading (Figure 5.3). The fact that both deep and shallow bursts occur within a short time span suggests some type of interaction between deep and shallow seismic activities. In order to further explore these potential interactions, we have tried to characterize the correlation of shallow seismicity with deep seismicity. Using the cumulative number of earthquakes for shallow ($z \leq 40$ km) and deep ($z \geq 80$ km) seismicity (Figure 5.3c), we look for each shallow earthquake if a deep earthquake occurred in the 2 days preceding it (see supporting information for details in terms of time window selection, completeness magnitude, and probability of synchronizations by chance). If so, a value 1 is assigned, otherwise this value is 0 (Figure 5.3d). In this part of the work, all the seismicity over magnitude 4.0 is considered. Doing so, 16 interactions have been detected (Figure 5.3d), which is 133% of the number of interactions expected to occur by pure chance (see Supporting Information for further details on the statistical significance of the observed synchronizations). The results shown by *Bouchon et al.* [2016] (four synchronizations) are replicated from January to 1 April 2014. Before that 12 additional deep and shallow seismicity synchronizations are detected. The identified interactions correspond either to swarms (e.g., 2006, 2008, and 2013) or background earthquakes (e.g., 2009 and 2011). Three areas in the shallow part of the megathrust are systematically activated, surrounding the area that ruptured during the 2014 Iquique earthquake. We have in total 16 synchronization episodes where we can observe 24 shallow earthquakes. About 84% occurred in areas with a coupling factor between 0.3 and 0.8 [*Métois et al.*, 2016], i.e., areas not fully coupled (Figure 5.3, see supporting information for details in coupling model).

The 16 episodes of deep-shallow seismicity synchronization (Figures 5.3d and 5.3e) may represent, as proposed by *Bouchon et al.* [2016], a slab deformation and plunge preceding the shallow burst activity. These interactions help to identify where the aseismic deformation is occurring. Interestingly, the shallow seismicity triggered by these interactions is located in areas that are at the transition between high and low interseismic coupling (Figure 5.3e). Moreover, these triggered seismic events are all located at the border of the areas that have been shown to aseismically slip during the 8 months preceding the 2014 Iquique megathrust, or within the area that slipped coseismically (purple and pink contours, respectively, in Figure 5.3e [*Socquet et al.*, 2017]). This precursory activity marks the area that started to slip in the 9 years preceding the Iquique interface earthquake,

as a response to Tarapaca slab-pull earthquake.

The observed synchronization of seismic activity at intermediate depth and on the shallow subduction interface questions our understanding of the interaction mechanisms between deep and shallow processes. The fact that Iquique earthquake megathrust occurred 9 years after the Tarapaca slab-pull earthquake, rather pleads for a slow deformation process taking place within the slab, possibly with a transient acceleration phases, marked by these synchronized pulses of deep and shallow seismicity, rather than a simple static triggering (e.g., Coulomb stress increase) that is difficult to invoke at such spatial and temporal distances. Our observations suggest that there exists a strong link between interplate and intraslab seismicity. The presence of a rigid slab decoupled from the surrounding asthenospheric mantle would favor the stress migration and aseismic deformation propagation from the slab to the subduction interface. Such decoupling would be allowed by a low-viscosity channel, permitting transient deep rapid sliding of the slab, as it has been proposed down to 70 km depth by *Klein et al.* [2016] to explain the postseismic GPS time series following Maule earthquake Mw 8.8 in Chile.

5.5 Conclusions

This study presents clear evidence that strong interactions exist between the occurrence of intermediate depth and shallow seismicity in subduction zones. The occurrence of the Tarapaca slab-pull earthquake initiated a 9 year period of deep-shallow seismicity interactions in a burst form, associated with a decrease of the interplate interseismic coupling, eventually leading to the 2014 Mw 8.1 Iquique megathrust earthquake. Moreover, megathrust ruptures (Antofagasta 1995 and Iquique 2014) initiate long periods (several years) of silent background seismicity, both on the plate interface, probably due to decoupling associated with postseismic afterslip [*Chlieh et al.*, 2007; *Pritchard and Simons*, 2006], and at intermediate depth, probably by clamping of the faults cutting the slab through an increase of compressive stress [e.g., *Astiz et al.*, 1988; *Astiz and Kanamori*, 1986; *Dmowska et al.*, 1988; *Lay et al.*, 1989]. After a few years of silence, the background seismicity resumes both at intermediate and shallow depths, and initiates a new cycle of deep shallow interactions.

If the seismogenic zone is already highly loaded, the occurrence of a large intermediate-depth intraslab earthquake could trigger or clock-advance a megathrust event by enhancing the occurrence of foreshocks and preslip on the subduction interface as a response to stress migration. Conversely, if the interplate contact is not ready to nucleate a megathrust earthquake, our results suggest that the slab deformation and plunge accommodated by the occurrence of a large intraslab event generate an increased activity of deep and shallow seismicity that are most often synchronized. It changes the stress conditions in the slab, up to the shallower depths. As a result, a decrease of interseismic coupling (i.e., acceleration of slow slip on the plate interface) may change the average GPS velocities and increase the background seismicity rate, both processes taking place as a series of bursts. Such a long-term interaction between slab-pull and shallow earthquakes helps understand the mechanisms leading to a megathrust earthquake. If this were true, the occurrence of intermediate-

depth earthquakes could therefore significantly increase the probability of a possible future rupture in megathrust.

5.6 Acknowledgments

The authors thank the International Plate Boundary Observatory Chile (IPOC, www.ipoc-network.org), Laboratoire International Associé “Montessus de Ballore" (www.lia−mb.net), Central Andean Tectonic Observatory Geodetic Array (CAnTO, http://www.tectonics.caltech.edu), and Instituto Geofísico del Perú (www.igp.gob.pe) for making the raw GPS data available. Also, authors thank the Centro Sismológico Nacional de Chile (CSN, www.csn.uchile.cl) that provide the Chilean seismicity catalog analyzed during this study. Jorge Jara acknowledges a PhD scholarship granted by Chilean National Science Cooperation (CONICYT) through “Becas Chile" Program. The authors thank J.M. Nocquet for making PYACS software available, as well as Bogdan Enescu and an anonymous reviewer for their constructive comments on the manuscript.

Appendix

5.A GPS Processing and Modelling

5.A.1 GPS daily processing

186 continuous GPS (cGPS) were processed from different networks in the Andean region (Figure 5.D.1 a) and around the world (Figure 5.D.1 b). 67 cGPS located in South Peru - North Chile have been installed and maintained in the frame of the following projects: Integrated Plate boundary Observatory Chile (IPOC, www.ipoc-network.org), LIA-MB (www.lia-mb .net), CAnTO (www.tectonics.caltech.edu/), IGP (www.igp.gob.pe), ISTerre, CSN (www. sismologia.cl). The rest (119 cGPS) are part of the Intertational GNSS Service (IGS, http://www.igs.org/) global network. The stations included in the processing have been separated into 3 subnetworks (2 local and 1 global) with 33 stations overlapping stations. The separation has been performed as a function of stations measurement time span. Both local subnetworks contain 50 stations with 33 overlapping stations in common plus 49 IGS stations. Stations included in this first local subnetwork have been measuring from 2000 to 2014, while the second subnetwork covers 2007 - 2014. The global network includes 99 IGS stations around the world, 22 of which are located in South America. Data are processed in double difference using GAMIT 10.5 software [*Herring et al.*, 2016], choosing ionosphere-free combination and fixing the ambiguities to integer values. Precise orbits from the IGS, precise EOPs from the IERS bulletin B, IGS tables to describe the phase centers of the antennas, FES2004 ocean-tidal loading corrections, as well as atmospheric loading corrections (tidal and non-tidal) have been used. The estimation of one tropospheric zenith delay parameter every two hours and one couple of horizontal tropospheric gradients per 24h session is carried out using the Vienna Mapping Function (VMF1) [*Boehm et al.*, 2006]. It allows mapping the tropospheric delay in zenithal direction, with a priori ZHD evaluated from pressure and temperature values from the VMF1 grids. Daily solutions and position time series are combined using PYACS software [*Nocquet J.M.*, 2015, *personal communication*] in a regional stabilisation approach. The results are mapped into ITRF 2008 reference frame [*Altamimi et al.*, 2011].

5.B Catalogs and Background Seismicity

5.B.1 ISC Resolution

The ISC catalog is analyzed in the region 11°S - 25°S and 80°W - 66°W between 1990 to 2017 to perform the declustering. We follow a probabilistic approach [*Ogata and Katsura*, 1993; *Daniel et al.*, 2008] to fit the frequency-magnitude curve, even below the maximum curvature which roughly marks the completeness magnitude. This allows to homogenize the completeness magnitude for long periods of time. Two periods of time are required because of the number of stations increases in 2007 in northern Chile. The selected periods are 1990 - 2007 and 2007 - 2017. For each period i, we fit the number (N_i) of earthquakes per magnitude bin as:

$$N_i(m) = A_i \times 10^{-bm} \times q_i(m) \tag{5.7}$$

Where $q_i(m)$ is the probability that an earthquake of magnitude m, occurring in the period i, is effectively listed in the ISC catalog. We follow *Ogata and Katsura* [1993] and model q as:

$$q_i(m) = \frac{1}{2} + \frac{1}{2} erf\left(\frac{m - \mu_i}{\sqrt{2}\sigma}\right) \tag{5.8}$$

Here erf is the error function. Note that only the pre-factor A_i (which is only a normalization parameter) and, more important, μ_i depend on i. We optimize $[A_1, A_2, \mu_1, \mu_2, b, \sigma]$ given the data, and compute the completeness magnitude M_c as:

$$Mc_i = \mu_i + 2\sigma \tag{5.9}$$

i.e., a 97.7% probability threshold. M_c for the first period is 4.5 and for the second M_c is 4.0 with a b value of 0.99 (Figure 5.D.2 a). We eventually fix M_c=4.5 for the whole period 1990 - 2017. A similar analysis is done for the area where the mainschoks ocurred (Figure 4.2 a in Main Text, 19°- 21°S and 72°W - 68°W), giving $M_{c1} = 4.7$ and $M_{c2} = 4.0$ for the two periods. We thus take $M_c = 4.7$ for the whole period, for this subregion (Figure 5.D.2 b).

5.B.2 Background Seismicity Resolution

Realistic declustering parameters (Equation 4.4 in Main Text) have been used [e.g., *Marsan et al.*, 2013, 2017; *Reverso et al.*, 2015, 2016]. Three of those parameters (p, α and γ) are explored in order to see how much they affect the processing. p value has been varied from 1 to 1.3 with a step of 0.05, while γ and α have been changed from 1 to 2 with a step of 0.2. Using those values, 252 combinations of parameters, each generating 1 declustered catalog, have been tested (Figure 5.D.3). We observe in Figure 5.D.4 that aftershocks are succesfully removed from the declustering process after each mainshock, in the study area between 1990 - 2017, whatever the choice of parameter

combination. This behaviour is easier to note when the seismicity is divided in shallow (z $\leq$ 40 km) and deep (z $\geq$ 80 km) seismicity (Figure 5.D.4 b and c).

5.C Synchronization Detection Process

In order to explore potential synchronizations between deep (z $\geq$ 80 km) and shallow (z $\leq$ 40 km) earthquakes in the study area, we have analyzed the ISC catalog between 2006/06/14 and 2014/04/01. M_c=4.0 is used because we are mostly interested in the second period defined to perform the M_c analysis (Figure 5.D.2 b). For each shallow earthquake, we look for the occurrence of a deep event before it. We explore different bin time windows from 1 hour to 90 days. Selecting a time window of 2 days allows to reproduce the results obtained by *Bouchon et al.* [2016]: 16 synchronizations (Table 5.D.3) were found from 2005/06/14 to April 1st 2014. The choice of M_c = 4.0 is not a problem because the two interactions detected prior to 2007 involve earthquakes with magnitudes greater or equal to 4.7 (M_c for the first period analyzed, Figure 5.D.2 b). Also, we have explored the period from 1990/01/01 until 2005/06/13 to check if we could find synchronizations. No synchronizations were found for a 2-day time window using either M_c = 4.0 or M_c = 4.7, the first interaction appearing using 1-week time window (see Table 5.D.2).

In order to evaluate if the detected synchronizations might have occurred by chance, we have determined the probability to have the number of bins activated with at least one earthquake (shallow and deep) over certain period of time, i.e.:

$$\mathbb{P}(\geq N) = \sum_{k=N}^{\infty} \frac{\exp(-\frac{ns \times nd}{T})(\frac{ns \times nd}{T})^k}{k\,!} \tag{5.10}$$

Where ns and nd are the numbers of bins activated for shallow and deep activity, while T represents the number of bins in the period analyzed and N is the number of synchronizations detected. The results can be seen in Tables 5.D.2 and 5.D.3. The evolution of the probabilities by chance as a function of the bin time window considered (third column in Tables 5.D.2 and 5.D.3), as well as the number of detected (first column, N) versus expected (second column, $\frac{ns \times nd}{T}$) synchronizations, show that after Tarapaca earthquake the detected synchronizations do not occur by chance (Table 5.D.3). Therefore, the interactions found during the 2005-2014 period are likely related to an aseismic process than simply by chance. Instead, before Tarapaca, almost no synchronizations could be detected over a short time window (Table 5.D.2). This suggests that Tarapaca slab-pull earthquake marks an important change in deep-shallow interactions.

Also, we have investigated where is located the shallow seismicity activated during the synchronizations. By comparing these locations with the interseismic coupling distribution by *Métois et al.* [2016], we found that 84% of those earthquakes are located in areas of transition between low to high interseismic coupling (0.3 - 0.8, Figure 5.D.5).

5.D Appendix Figures and Tables

Table 5.D.1: GPS Position and Velocities for North (N), East (E) and Vertical (V) components before (B) and after (A) Tarapaca Earthquake 2005 with their errors (e). Velocity values are in mm/yr and with respect to ITRF 2008 reference frame.

GPS Station	Longitude	Latitude	N B	e N B	E B	e E B	V B	e V B	N A	e N A	E A	e E A	V A	e V A
UTAR	-70.297	-18.490	1.82	0.10	17.82	0.14	4.15	0.31	4.16	0.04	17.94	0.04	2.74	0.09
IQQE	-70.131	-20.273	4.16	0.05	28.49	0.05	2.05	0.14	5.37	0.01	24.25	0.01	1.11	0.03
UAPE	-70.141	-20.243	4.73	0.06	28.71	0.07	2.31	0.20	5.24	0.03	24.97	0.04	0.87	0.08
AEDA	-70.177	-20.546	5.74	0.14	26.61	0.18	3.29	0.53	5.75	0.07	24.51	0.06	-2.32	0.16
COLL	-68.649	-20.831	3.20	0.17	26.97	0.14	8.94	0.32	6.87	0.24	14.62	0.22	6.68	0.43
PICC	-69.334	-20.489	4.21	0.11	27.33	0.12	4.18	0.29	3.52	0.07	21.88	0.08	1.74	0.15
FBAQ	-69.755	-20.134	6.76	0.23	29.24	0.15	-0.35	0.33	5.01	0.06	21.78	0.07	3.75	0.11
QUIL	-69.557	-21.692	6.77	0.06	31.33	0.08	7.45	0.29	6.45	0.07	28.52	0.08	-1.10	0.11
PMEJ	-70.448	-23.100	9.28	0.09	31.58	0.11	-1.92	0.27	10.17	0.06	32.12	0.07	-5.32	0.15

Table 5.D.2: Number of synchronizations (N) over time, expected number of events ($\frac{ns \times nd}{T}$) and synchronization probabilities by chance (Equation 5.10) in % for the period 1990 - 2005/06/13. Bin duration are in hours (h) or days (d).

	$M_c = 4.0$			$M_c = 4.7$		
Bin Period	N	Expected N	Probability (%)	N	Expected N	Probability (%)
1h	0	0.1	100	0	0.01	100
3h	0	0.2	100	0	0.02	100
6h	0	0.4	100	0	0.04	100
12h	0	0.9	100	0	0.07	100
1d	0	1.7	100	0	0.1	100
2d	0	3.3	100	0	0.3	100
3d	2	4.7	94.85	0	0.4	100
4d	4	6.1	85.31	0	0.6	100
5d	6	7.8	78.37	0	0.7	100
6d	7	8.3	72.19	0	0.8	100
7d	8	9.4	72.33	1	0.9	60.47
8d	9	10.4	71.27	1	1.1	64.83
9d	10	11.2	67.73	1	1.1	68.04
10d	12	13.6	70.25	1	1.3	71.29
15d	21	16.5	16.42	3	1.9	28.65
20d	25	19.8	14.41	3	2.3	41.45
25d	29	22.8	11.64	4	2.8	30.33
30d	31	23.3	7.38	4	3.3	42.72
60d	37	25.9	2.33	8	4.3	8.65
90d	39	25.5	0.75	10	5.8	6.74

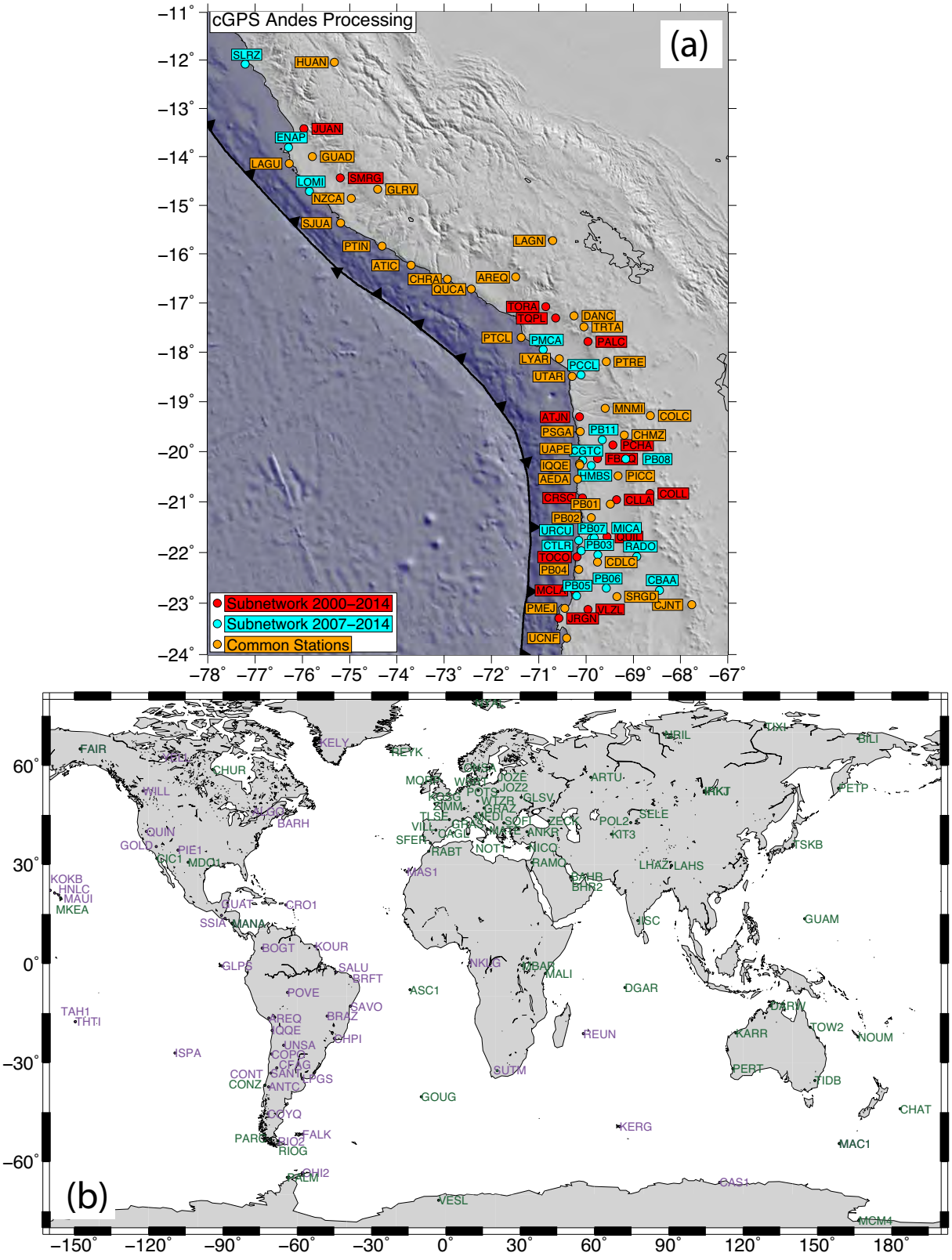

Figure 5.D.1: (a) Map of the 2 local GPS subnetworks processed (Andes 2000 - 2014 in red and Andes 2007 - 2014 in cyan). Orange denotes the stations included in both subnetworks in the processing. (b) Global GPS network processed. Green color indicates IGS stations included in the Global Processing, while purple indicate IGS stations overlapping with the Andean subtnetworks.

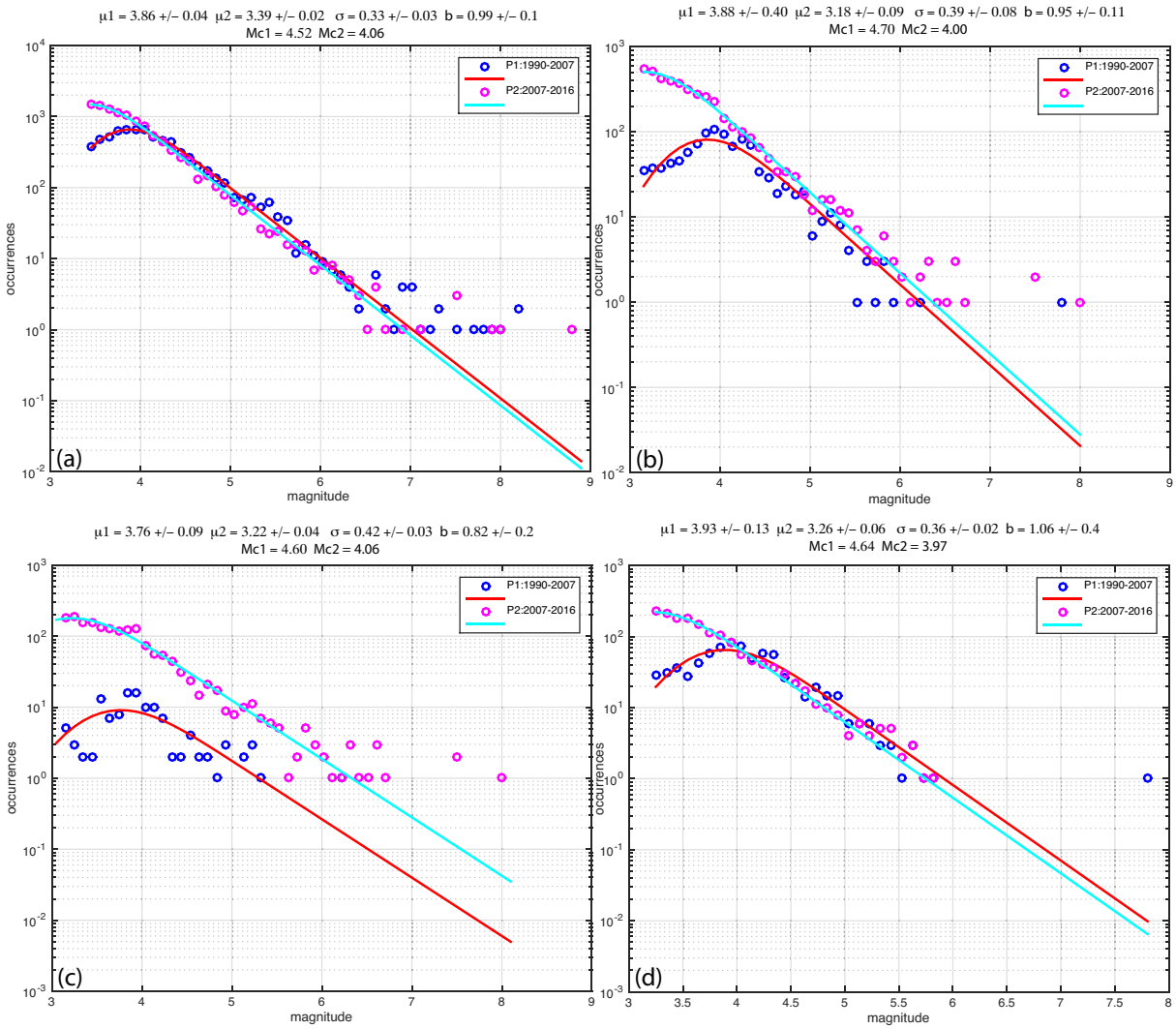

Figure 5.D.2: (a) Model of Equation 5.8 calculated for the whole area (11°S- 25°S and 80°W - 66°W) . The calculation is performed for 2 periods (P1: 1990 - 2007 in blue and P2: 2007 - 2016 in magenta), with a common b value. Completeness magnitudes (M_{c1} and M_{c2}) are 4.5 and 4.0 , estimated for both periods. (b) Same caption than (a) but for the seismicity in the study area (19°S - 21°S and 72°W - 68°W), for which we find $M_{c1} = 4.7$ and $M_{c2} = 4.0$. (c) Same caption than (b) but for shallow seismicity (z $\leq$ 40 km), where $M_{c1} = 4.6$ and $M_{c2} = 4.1$. (d) Same caption than (b) but for deep seismicity (z $\geq$ 80 km), where $M_{c1} = 4.6$ and $M_{c2} = 4.0$.

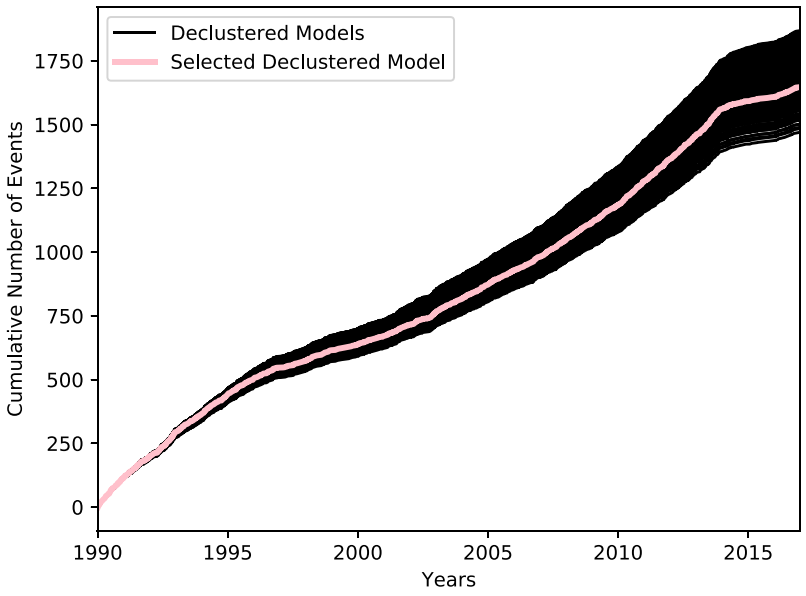

Figure 5.D.3: Temporal evolution of the 252 declustered models. In black, the 251 models obtained by varying the declustering parameters. The pink curve is the declustered model used for our analysis.

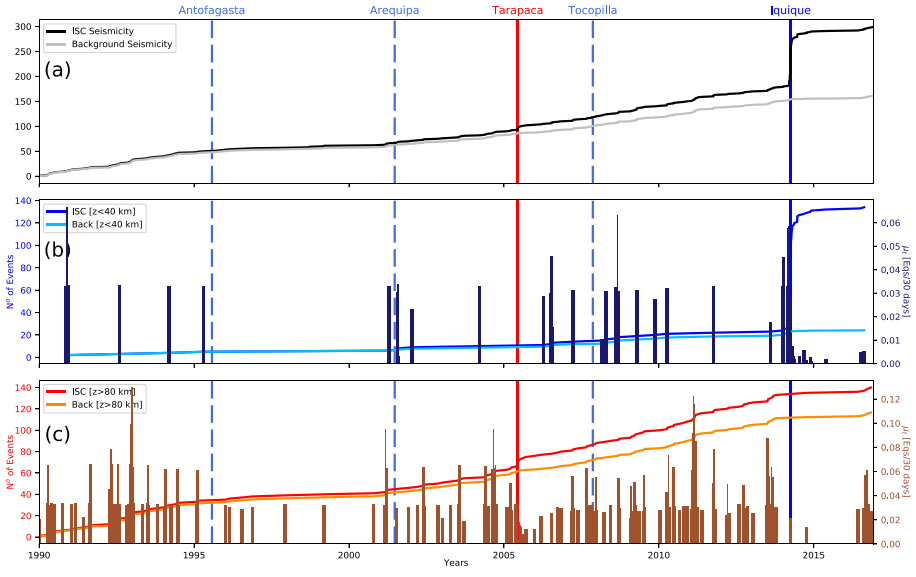

Figure 5.D.4: Temporal evolution of the seismicity in the study area. (a) ISC complete (black) and background (grey) cumulative seismicity for both depth ranges. The vertical lines depict earthquakes (plain in the study area, dashed out of the study area): megathrust earthquakes are in blue and intraslab earthquake in red. (b) Shallow ($z \leq 40$ km) and (c) deep cumulative seismicity ($z \geq 80$ km) for the ISC catalog (blue and red) and background seismicity (light blue and orange). The background rate (μ_t) calculated over 30 days is plotted in bar shape.

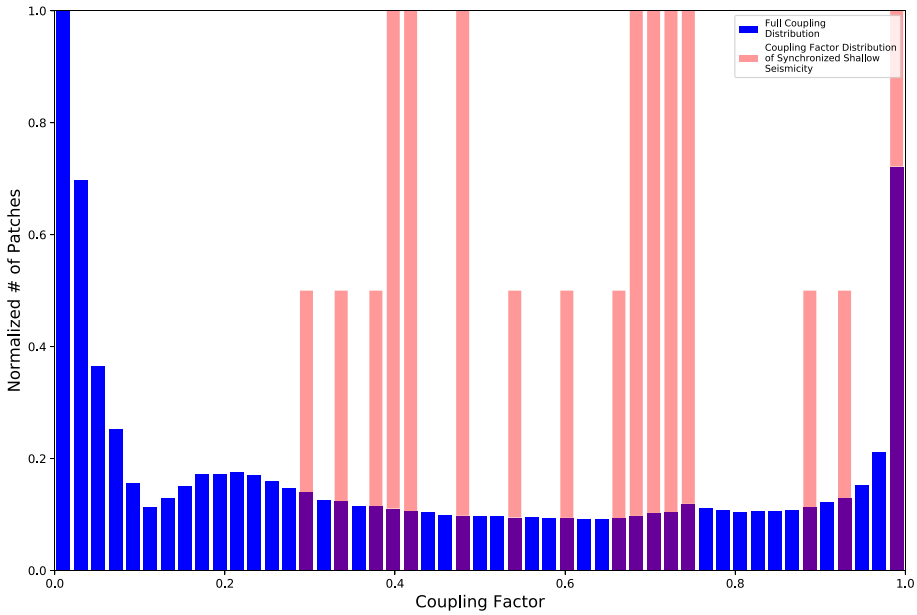

Figure 5.D.5: Normalized Histogram of Coupling distribution in the study area in blue using data published by *Métois et al.* [2016]. In red, normalized histogram of coupling factor for events occurring in synchronization in the shallow area. 84% of them are in zones of transition in terms of coupling factor (0.3 - 0.8).

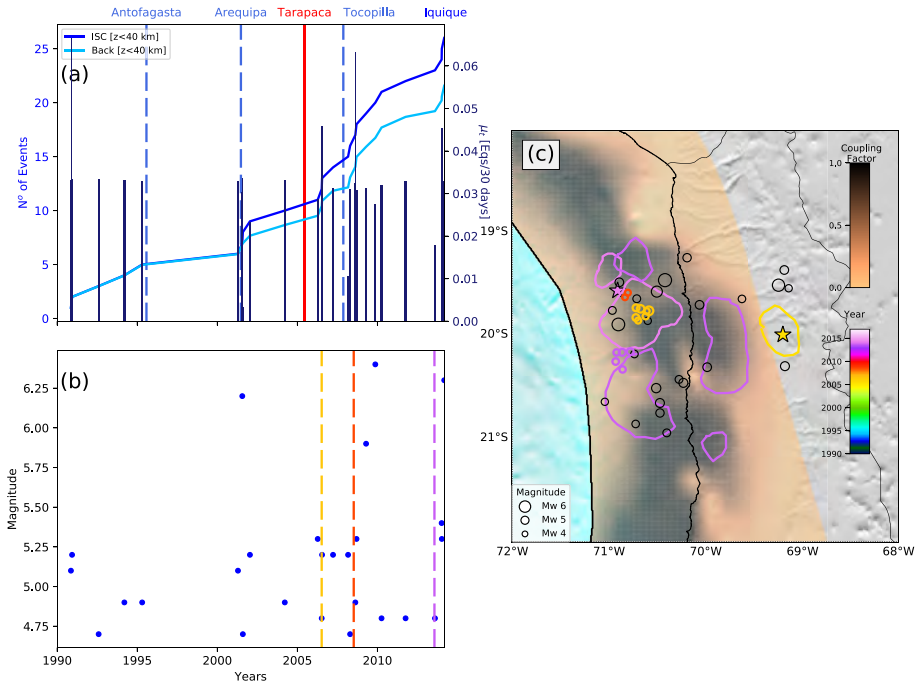

Figure 5.D.6: (a) time evolution of raw (blue) and background (light blue) seismicity in the study area. Dark blue bars are the background rate over 30 days. Continuous (dashed) vertical lines show the occurrences of earthquakes into (outside) the study area. (b) Magnitude as function of time in the study area. Vertical dashed lines denote the swarm time occurrence, color coded by time. (c) Map view of the seismicity analyzed to detect the swarm time. All the seismicity occurring during a pick in the background rate shown in (a). Swarms are color coded and scaled by time and magnitude. The rest of the seismicity (no swarms) are plotted in black. Coupling map by *Métois et al.* [2016].

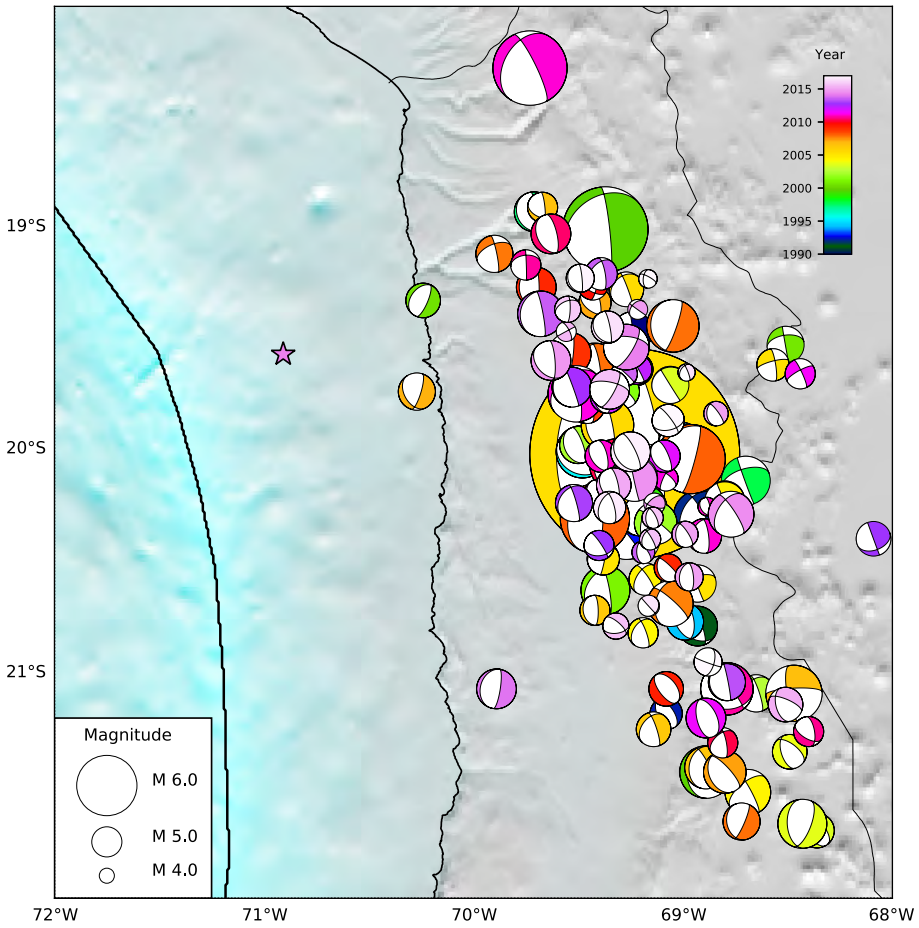

Figure 5.D.7: Focal mechanisms of deep seismicity (z $\geq$ 80 km) in the study area, scaled by magnitude and color coded by time. Focal mechanism data are from *International Seismological Centre* [2014], using GCMT (http://www.globalcmt.org) and NEIC (www.earthquake.usgs.gov/earthquakes/search). 124 events have a focal mechanism available and 91% of them are slab-pull. The star symbolizes the epicenter of Iquique earthquake in 2014.

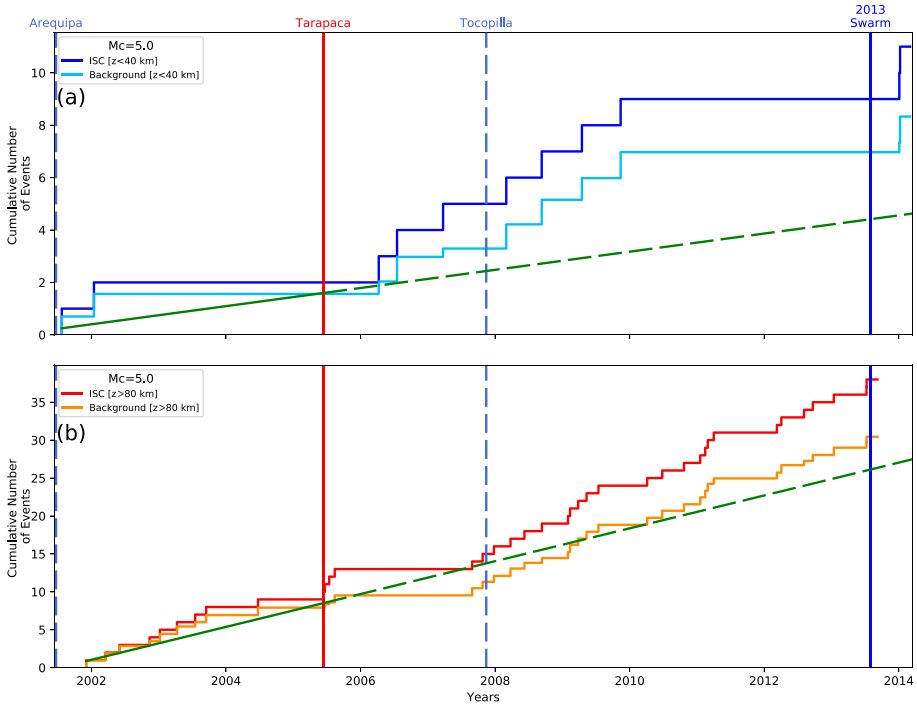

Figure 5.D.8: Time evolution for shallow and deep seismicity for completeness magnitude of 5.0. Blue (red) and light blue (orange) are the cumulative number of event for ISC catalog and background seismicity respectively (M $\geq$ 5.0). Vertical lines point out an earthquake or swarm occurrence: continuous lines represent events that occurred in the study area and dashed events outside it. Green lines show the seismicity trend in the period 2001/06/24 - 2005/-6/13 and dashed lines show the trend projected to the second period (2005/06/14 - 2014/03/16).

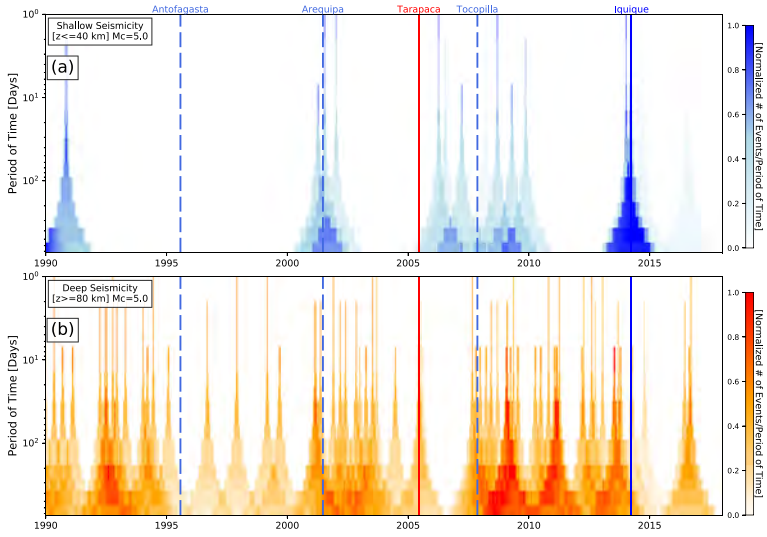

Figure 5.D.9: (a) and (b) show the time evolution of normalized background seismicity rate calculated for different periods of reference (from 1 day rate, up to 2 years rate) with M_c=5.0, for shallow (z $\leq$40 km) and deep (z $\geq$ 80 km) seismicity. Continuous (dashed) lines indicate the time of occurrence of earthquakes into (outside) the study area. Blue (red) are shallow interplate (intermediate depth intraplate) earthquakes.

Table 5.D.3: Number of synchronizations (N) over time, expected number of events ($\frac{ns \times nd}{T}$) and synchronization probabilities by chance (Equation 5.10) in % for the period 2005/06/14 to 2014/04/01. Bin duration are in hours (h) or days (d).

	$M_c = 4.0$			$M_c = 4.7$		
Bin Period	N	Expected N	Probability (%)	N	Expected N	Probability (%)
1h	1	0.4	33.86	0	0.1	100
3h	2	1.1	31.60	0	0.2	100
6h	2	2.1	62.30	0	0.3	100
12h	6	3.8	18.25	1	0.6	47.48
1d	11	6.8	8.44	3	1.2	12.84
2d	16	12.0	15.62	7	2.4	1.12
3d	17	15.3	36.86	7	3.3	5.22
4d	21	20.0	41.07	8	4.3	6.75
5d	26	20.4	13.07	9	4.7	5.20
6d	30	23.2	9.74	10	6.0	8.30
7d	33	25.2	7.79	10	6.5	11.88
8d	34	27.2	11.47	10	7.2	18.85
9d	39	26.4	1.28	12	7.5	7.69
10d	43	27.7	0.42	12	8.0	11.12
15d	46	31.1	0.70	13	10.5	26.10
20d	47	30.0	0.24	13	11.5	36.69
25d	49	31.6	0.25	17	13.8	22.49
30d	50	31.1	0.11	19	14.3	13.92
60d	52	24.1	5.74×10^{-5}	25	14.7	0.95
90d	53	21.2	4.59×10^{-6}	27	14.8	0.27

Chapter 6

Interseismic transient deformations in South Peru - North Chile seismic gap

6.1 Introduction

During several years, the interseismic period has been studied using geodetic data (e.g., GPS or InSAR) in different places worldwide [e.g., *Prawirodirdjo et al.*, 1997; *Mazzotti et al.*, 2000; *Bevis et al.*, 2001; *Yoshioka et al.*, 2005; *Bürgmann et al.*, 2005; *Chlieh et al.*, 2011; *Loveless and Meade*, 2011; *Béjar-Pizarro et al.*, 2013; *Rousset et al.*, 2015; *Jolivet et al.*, 2015; *Métois et al.*, 2016; *Villegas-Lanza et al.*, 2016a]. The coupling maps are an approach widely used today to investigate from a kinematic point of view, the state of locking on faults [e.g., *Chlieh et al.*, 2011; *Loveless and Meade*, 2011; *Béjar-Pizarro et al.*, 2013; *Métois et al.*, 2016], exhibiting a complex and heterogeneous pattern. Following those models, it is possible to distinguish two main areas on faults with different behaviors. First, the areas that are locked during the interseismic period, that seems to be well correlated with earthquake rupture regions [e.g., *Moreno et al.*, 2010; *Ruiz et al.*, 2016; *Métois et al.*, 2016; *Villegas-Lanza et al.*, 2016a], thus those areas are associated with a stress accumulation that will be liberated in a future earthquake. The second areas are those not fully locked, slipping in an aseismic manner and can be associated with steady creep or by spontaneous events. Although some models have described the interactions between the seismic and aseismic slip [*Kaneko et al.*, 2010; *Hetland et al.*, 2010; *Hetland and Simons*, 2010; *Kanda et al.*, 2013; *Avouac*, 2015], the mechanisms controlling the interseismic creeping are poorly understood, especially in subduction zones.

With the fast development of new techniques and the rise of the geodetic data resolution, data acquired during the interseismic period seems to exhibit small transient events. During the 90's and 2000s, slow slip events (SSEs) were reported in several areas around the world, such as in Cascadia [*Dragert et al.*, 2001; *Rogers and Dragert*, 2003], Mexico [*Lowry et al.*, 2001; *Larson et al.*, 2004; *Marquez-Azua and DeMets*, 2009], New Zealand [*Douglas et al.*, 2005; *Wallace and Beavan*, 2006] or Japan [*Heki et al.*, 1997; *Hirose et al.*, 1999; *Ozawa et al.*, 2001; *Miyazaki et al.*, 2003]. Apart from looking at these large SSEs, more and more evidences lead to looking carefully at the data because hidden slow slip events seem to be masked in the noise [*Frank*, 2016; *Gardonio*, 2017; *Rousset et al.*, 2017]. *Frank* [2016] has shown in Mexico and Cascadia that the interseismic period is

not quiescent, using the timing of cataloged low-frequency earthquakes (LFEs) and tremors, and comparing with GPS data, revealing the intermittency of the tectonic release due to transient deformation. Also in Mexico and applying a geodetic matched-filter, *Rousset et al.* [2017] point out the occurrence of SSEs that are masked in the noise and correlated with the occurrence of LFEs. The interseismic transient deformations are not only observed in subduction zones. It is possible to find some cases in strike-slip faults, where they have been associated with bursts of creep, as in China [*Jolivet et al.*, 2013] and Turkey [*Rousset et al.*, 2016]. However, interseismic transient deformations have not been reported in areas with no LFEs or tremor activity detected so far in subduction zones.

Given the presence of detailed geodetic monitoring of the South Peru - North Chile subduction zone, this is an excellent area to investigate the interseismic transient deformations. Aseismic deformation has been reported prior to Iquique earthquake (M_w 8.1, 2014/04/01) associated with a long precursory phase of 8-month [*Kato et al.*, 2016; *Socquet et al.*, 2017]. Also, this earthquake has been preceded by an intense two weeks of foreshocks, where a strong transient signal occurred [*Schurr et al.*, 2014; *Ruiz et al.*, 2014; *Lay et al.*, 2014; *Yagi et al.*, 2014; *Bedford et al.*, 2015; *Cesca et al.*, 2016; *Kato et al.*, 2016; *Socquet et al.*, 2017]. Nevertheless, a debate remains on the mechanism leading to this activity, notably on the existence or not of aseismic slip. Concerning the seismological data, *Kato et al.* [2016] has shown the occurrence of repeating earthquakes in the interseismic period in North Chile (2008-2013 July), relating them to the occurrence of aseismic slip. However, the occurrence of interseismic transient deformations has not been reported in the region, employing geodetic data. During this Chapter, the methodology proposed by *Rousset et al.* [2017] is followed, that consists in applying a matched-filter on the GPS residual time series, in order to explore the possibility of occurrence or not of aseismic deformation in the region.

6.2 Geodetic Matched-Filter

In order to detect and characterize potential transients of deformation (small slow slip events, sSSEs) hidden in the noise of geodetic time series, we use a 2-step process:

1. Detection in time and location of potential transients through correlation of a deformation rate template with the derivative of the GPS time series.

2. Characterization of the M_w and duration of the detected sSSEs using the position time series.

For each sSSEs detected, the network detection capacity is evaluated using synthetic time series. For sSSEs of different M_w occurring on the activated patch, the deviation from the true location, date of occurrence, duration and magnitude are computed to define a threshold. A detected sSSEs is validated if its M_w exceeds the M_w detection threshold.

6.2.1 Templates of Surface Displacement Time Series

The methodology proposed by *Rousset et al.* [2017] is based on a geodetic matched-filter, correlating synthetic templates with the real GPS time series. The generation of synthetic templates requires the calculation of static Green's functions that link the static surface displacement at each GPS station with a slip on a given area of the subduction interface. The Green's functions are calculated assuming that SSEs can be modeled as a slipping dislocation in an elastic half-space *Okada* [1985] using the program DISLOC. The fault geometry is constrained by the trace of the trench at the surface. A uniform dip of 15°and a variable rake are assumed, so that the slip direction is parallel to the plate convergence N77°E [*Angermann et al.*, 1999]. The fault is discretized into an array of 48 × 14 elements, measuring approximately 15 × 15 km, although their size varies locally since the fault follows the trench geometry (Figure 6.A.1).

The so-obtained static Green's functions are then convolved with a temporal slip evolution for a slip of unit amplitude, given by:

$$s(t_1) = \frac{1}{2}\left[1 - cos\Big(\frac{\pi t_1}{T}\Big)\right] \ , \ t1 \ = \ [0 : \Delta t : T] \tag{6.1}$$

And its derivative is given by:

$$\dot{s}(t_1) \ = \ \frac{\pi}{2T}\sin\Big(\frac{\pi t_1}{T}\Big) \tag{6.2}$$

where t_1 is the time vector of the template and T its total duration (Figure 6.1). The temporal sampling of t_1 (Δt), is a daily sampling for the GPS time series. The Figure 6.1 shows that $s(t)$ is a symmetrical function, with half of its duration corresponding to slip acceleration, followed by a deceleration during the second half duration, which is a reasonable evolution for the short-term SSEs searched in this study.

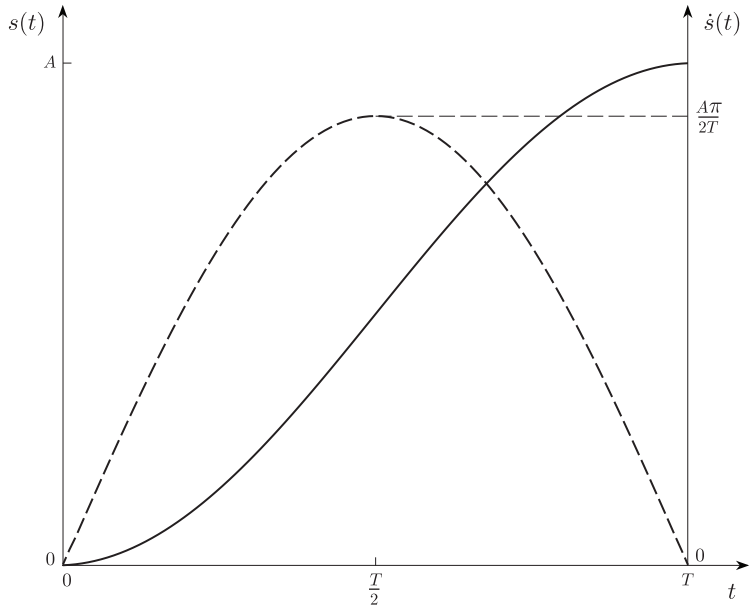

Figure 6.1: Temporal evolution of the template (solid line) and its derivative (dashed line). A is the maximum amplitude of the slip.

The template displacement time series at each GPS station ($\mathbf{w}^i$) are thus given by:

$$\mathbf{w}^i(t_1) \;=\; \mathbf{w}_s^i s(t_1) \tag{6.3}$$

where $\mathbf{w}_s^i$ represent the Green's Function for each component i (North and East) and s stands for the finite static displacement.

6.2.2 Correlation of Template and GPS Time Series

The correlation function $\mathbf{C}^i(t)$ between the template time series $\mathbf{w}_s^i(t_1)$ and the GPS time series $\mathbf{d}^i(t)$ recorded for the i North and East components at each station is computed, where t is the discrete time vector of the whole time series.

Time windows of $\mathbf{d}^i(t)$ with the same norm as $\mathbf{w}^i(t_1)$ are defined on $t2 = (t - t_1/2, ..., t + t_1/2)$ with the same temporal sampling as t_1 (Δt), so that $||t_1|| = ||t_2|| = N$, N being the number of days of the template. The inner product between $\mathbf{w}^i(t_1)$ and $\mathbf{d}^i(t_2)$ is defined by:

$$\Big\langle \mathbf{w}^i(t_1), \mathbf{d}^i(t_2) \Big\rangle_{N,\Delta t} \;=\; \sum_{j=0}^{N-1} \mathbf{w}^i(t_1 + j\Delta t)\; \mathbf{d}^i(t_2) + j\Delta t) \tag{6.4}$$

The correlation of non-monotonic functions is preferable, in order to optimize the correlation operation. The discriminatory nature of the stationary point of the surface velocity (time derivative of the surface displacement) at the middle of a SSE improves the timing precision (signal is clearer)

[*Rousset et al.*, 2017]. Thus, the temporal derivatives of $\mathbf{w}^i(t_1)$ and $\mathbf{d}^i(t_2)$ are used, where the fully normalized correlation function is defined as:

$$\mathbf{C}^i(t) \;=\; \frac{\left\langle \dot{\mathbf{w}}^i(t_1)\ ,\ \dot{\mathbf{d}}^i(t_2) \right\rangle_{N,\Delta t}}{\sqrt{\left\langle \dot{\mathbf{w}}^i(t_1), \dot{\mathbf{w}}^i(t_1) \right\rangle_{N,\Delta t} \left\langle \dot{\mathbf{d}}^i(t_2), \dot{\mathbf{d}}^i(t_2) \right\rangle_{N,\Delta t}}} \tag{6.5}$$

and the weighted Correlation $\mathbf{C_w}$ is:

$$\mathbf{C}^i_{\mathbf{w}}(t) \;=\; \frac{|\mathbf{w}^i_s|}{\max(|\mathbf{w}^i_s|)}\ \mathbf{C}^i(t) \tag{6.6}$$

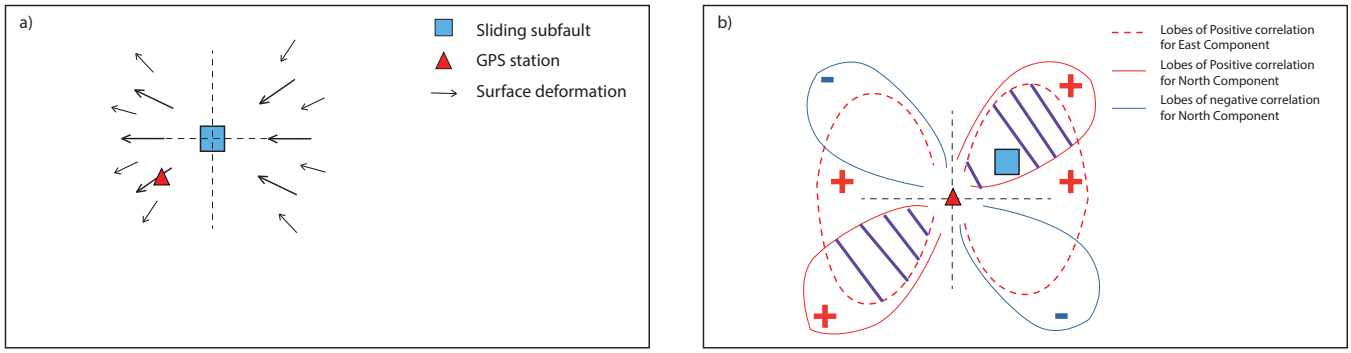

Figure 6.2: Scheme showing the surface displacement due to a patch slipping on the subduction interface. The patch is symbolized in blue and the GPS stations with a red triangle. b) Localization of areas on the fault plane where the correlation between the modeled signal and the real data is positive (red) or negative (blue). The scratched areas (purple lines) correspond to zones with maximum correlation values.

The stations used for the correlation procedure are selected employing $\mathbf{w}^i_s > \alpha \times \max(\mathbf{w}^i_s)$, α being an empirical coefficient that in this case is set to 0.1. This selection allows discarding stations that recorded nonexistent or too small amplitude transient signals. The detection of the small transients is made on a function computed as the sum (stack) of the weighted correlation functions (Equation 6.6) over all the selected stations and both horizontal components. The weightening expressed in the Equation 6.6 has the advantage to give the right sign to each data, which is not the case of the raw stack [*Rousset et al.*, 2017], and to give more weight to stations that are affected by a large signal (i.e., large signal / noise ratio), and less weight to stations that are affected by a small signal (i.e., on which the signal / noise ratio is small). As shown in the Figure 6.2, the preferential direction of deformation associated with a SSE on the North Chile subduction zone points toward the East, meaning that the potential SSE will be recorded mainly on the East component. This weighting procedure cleans the signal and facilitates the emergence of the transient deformation from the noise.

6.2.3 Synthetic Time Series

Before doing any detection on real data, the network capability to detect sSSEs is tested, applying the correlation procedure explained above on synthetic time series. The synthetics are constructed as the sum of realistic GPS noise and transient events generated by a given slip on the subduction interface. As explained in details in Chapter 4 (see the examples in this Chapter for further detail), the GPS noise is a combination of colored and white noise [*Williams et al.*, 2004]. Using a power law that combines these noises, 1000 synthetic GPS noise time series are generated.

The Figure 6.3 shows an example of a correlation analysis for a synthetic transient event of M_w 6.1 located in the southern part of the study area (Figure 6.3a). At the stations supposed to record the highest displacement associated to this event, such as PB07, the expected displacement is $\sim$2.5 mm (Figure 6.3 b and c). The sum of all non-weighted or weighted correlation functions shows peaks emerging at times of the transients events (Figure 6.3). Also, lower high amplitude peaks are observed at times corresponding to pure noise, only on the non-weighted correlation, showing that the use of the weighted correlations functions is a better manner to discriminate between noise and transient events. Thus, the detections of transients correspond to the maximum peaks of the weighted correlation function.

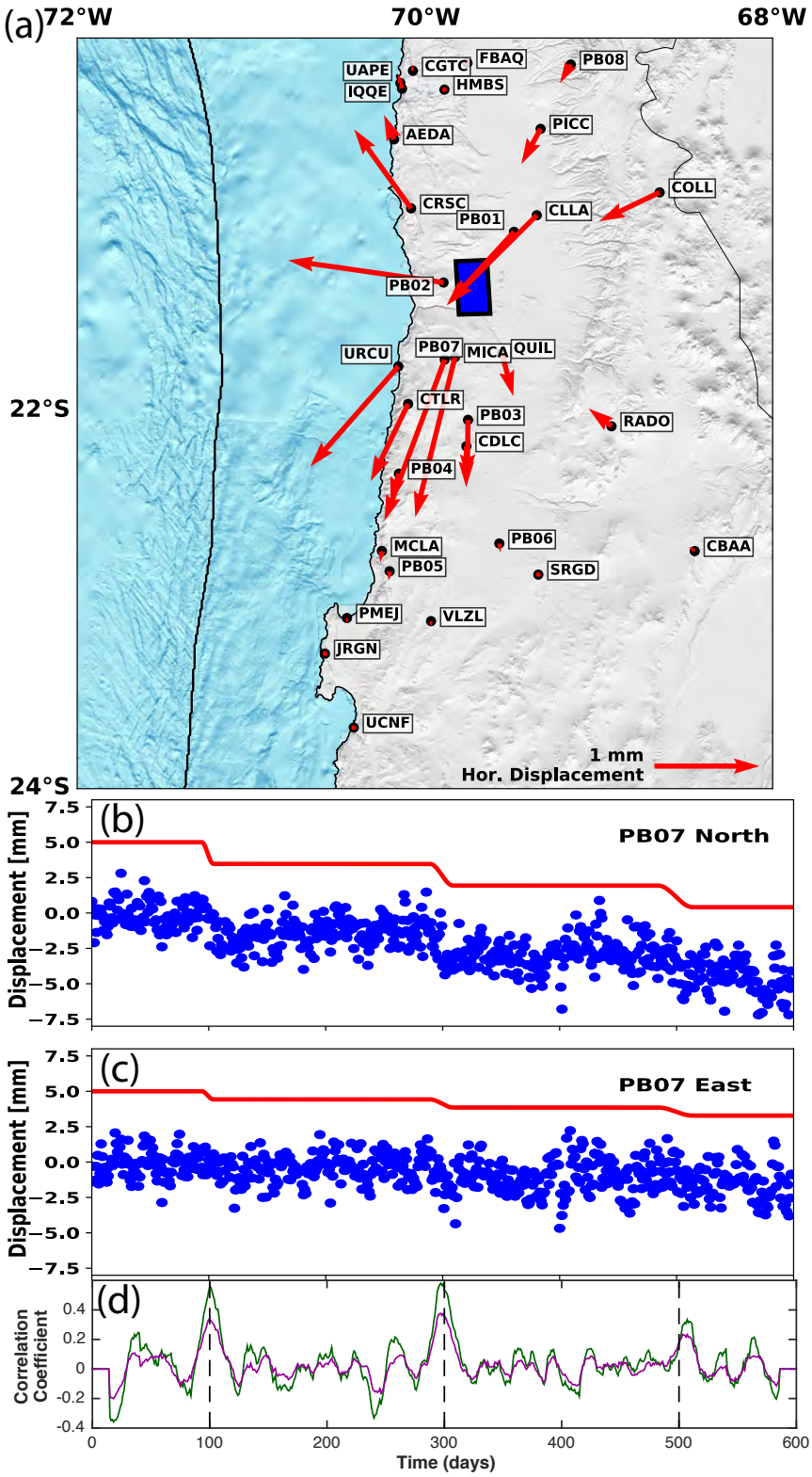

Figure 6.3: (a) Blue surface corresponds to one patch on the subduction interface sliding with a slip of 0.1 m, equivalent to M_w 6.1. The red arrows denote the static surface displacement due to the slip on the patch. The stations MICA, PB02 and PB07 have the maximum amplitude of surface displacement of ∼2.5 mm. (b) Synthetic time series at station PB07, for North component. The red curve shows 3 transient events (a 10-day transient centered on time 100 days, a 20-day transient event centered on time 300 days and a 30-day transient centered on time 500 days). The blue dots correspond to the synthetic displacement time series, built from the noise analysis plus the synthetic transient events. (c) Same as (b) for the East component. (d) The green and purple curves show stacks of the correlation functions on all the stations and both horizontal components. The green curve is a simple stack of all correlation functions for all selected stations, while the purple curve is a stack weighted by the amplitude of the synthetic displacement for a given pair station – component. The vertical dashed black lines denote the occurrence of a transient (at 100, 300 and 500 days).

6.2.4 Location, Duration and Magnitude Estimation

Based on the work of *Rousset et al.* [2017], for a given detection in time, the location of the slip is the patch on the subduction interface that maximizes the weighted correlation.

Because the correlation function is computed using velocity time series (Equation 6.5 and 6.6), the amplitude information is lost, that corresponds to the event magnitude. Consequently, the GPS displacement time series are examined directly. The stack of the times series is employed because transient signals on individual times series are likely small compared to the noise (Figure 6.4). The same weighting as the one applied to the correlation function (Equation 6.6) is used for the GPS weighted stack to give more weight to stations that recorded highest amplitude signal. On the stations located to the north or south of a sliding patch, the North components have opposite signs (Figure 6.2). If a simple stacking is performed, these opposite signs would remove the signal, so the weighting stack has the advantage to give to each weight the correct sign and clearer signal to noise ratio than the raw stack (Figure 6.4).

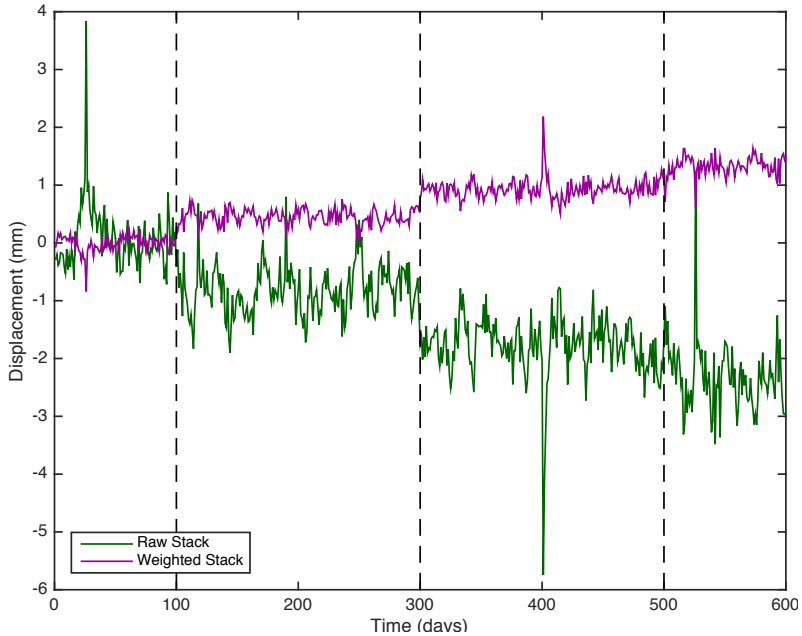

Figure 6.4: Green curve denotes the raw stack of all GPS time series, for North and East components, while the purple curve is the stack weighted by the amplitudes and polarities of the surface displacements of the template (Figure 6.2). Dashed black lines indicate the time of the synthetic transient slip events shown in Figure 6.3.

The duration and magnitude of each event are estimated by modeling the weighted stack of the GPS displacements. On a time window centered on the detection time, the model includes a transient signal modeled by $s(t)$ and linear terms before and after the transient. Then, the best model is estimated in a least-square sense, with more weight at the center of the window. The residuals are weighted by a triangular-shaped function that has an amplitude of one at its center and zero at its edges. Several models are tested varying the transient duration, taking the preferred duration as the model that minimizes the residuals.

Once the duration is estimated, the displacement amplitude in the weighted stack during the transient event is measured. The magnitude is estimated by comparing the measured displacement amplitude to the amplitudes obtained with templates of varying source slip area and slip amplitude. The magnitude is taken that minimizes the residuals.

6.2.5 Methodology Applied on Real Data

The geodetic matched filter described above is applied on a real case in the South Peru - North Chile subduction zone. The residual GPS times series obtained by the methodology explained in Chapter 4 are employed during this Chapter. To use these data on the matched-filter, the temporal derivative of the resulting time series is computed.

A threshold of four simultaneously active stations (i.e. stations with data) is taken, allowing for a possible detection. The template used lasts 30 days, allowing for searches of events of similar or shorter durations [*Rousset et al.*, 2017]. The correlation peaks that have amplitude higher than 20% of the maximum correlation in time are selected as positive detections. A slip event on a given patch produces positive detections of lower amplitude on surrounding patches, thus the dates for which more than 20 patches have a positive detection are kept. Once a detection is made for one day over 20 patches, the sSSEs location is defined on the patch where the maximum correlation is localized and then, an exploration is performed to analyze the chance of secondary events: all the patches at distances shorter than 0.5° from the maximum peak of correlation (primary event) are masked, then all the patches that have at least 70% of the maximum correlation are analyzed to search for a potential secondary event, repeating this procedure in an iterative way. This procedure allows for detections of spatially individualized secondary events.

The detections with several dates closely spaced in time are clustered. This clustering is because of multiple detections for a given event, corresponding to different locations of the templates for this event. The clustering is made estimating the duration of each detected event on the stacked displacement time series. If the estimated durations of two close events intersect, they are considered as a single one. The final detection times correspond to the mean of all detections in a cluster of events. The location of a detected transient event corresponds to the patch that has the maximum correlation at the detection time and then the magnitude and final duration are estimated.

A resolution analysis is performed to explore the reliability of each detection made during the procedure. To do that, the synthetic time series are used. The same steps applied during the detection process on real data are made on 1000 GPS noise times series. Then, synthetic time series are made combining sSSEs and GPS realistic noise. The patch where the detection is located is tested, using transients with durations of 10, 20 and 30 days, and magnitudes ranging between 5.5 - 7.0 M_w . The slip to define the magnitude changes according to each patch size. Then, the matched-filter is applied to the synthetic time series, estimating first the time of the detection, then the location (in the case of the location estimates, 100 synthetics are used by station instead of 1000 to save computing time), and finally estimating the duration and magnitude. A detailed comparison

is performed between the true and the estimated parameters, providing an idea of the offset between estimated parameters and the true ones. This procedure provides resolution thresholds for each transient duration (10, 20 and 30 days) considering the deviation from the true location, time of detection, duration and magnitude of the event as a function of the M_w . For a given patch and network configuration, the M_w threshold is defined as the maximum of the M_w corresponding to a given deviation from the true value for each tested parameter (location, time of detection, duration and magnitude) (Figure 6.5). The event detected is considered valid if it passes the corresponding patch threshold.

6.3 Results

Applying this methodology, 102 events are detected between August 2005 and July 2014 (Table 6.1). Although the network has stations since the beginning of 2000, it is not until mid-2005 that four stations are active close to Iquique area (∼20°S). The Figure 6.5 shows examples of these resolution tests. First, in Figure 6.5 (I) the resolution is shown for the patch where the event 9 is located (M_w 5.98). In this example, the deviation from the true locations controls the threshold magnitude, because it is not possible to estimate events lower than M_w 6.2 for synthetics with durations of 10 and 20 days, and M_w 6.3 for synthetics with duration of 30 days. As the event has a magnitude 5.98 and a duration of 3 days, in this case, it does not pass the threshold resolution (Table 6.1). Figure 6.5 (II) shows the resolution test made on the patch of events 39, 60, 73, 79 and 92. Also, the location plays an important factor, defining the threshold as M_w 6.4 for a synthetic duration of 10, 20 and 30 days. The magnitude of these events is $\sim M_w$ 6.4 with a duration $\sim$ of 20 days, thus they pass the threshold resolution.

Doing these resolution analyses, the number of detection reduces considerably down to 41 validated events. The Figure 6.9 shows the correlation values of the patches where the detections are performed. Also, the duration and magnitude of each final event are shown. The magnitudes range between 6.1 - 6.9, while the durations range between 3 - 93 days. This procedure has been done for all the patches, defining resolution maps shown in Figure 6.6 (10 days), Figure 6.7 (20 days) and Figure 6.8 (30 days).

Four examples of detections are shown in the Figure 6.11 (events id 37 and 80) and in the Figure 6.12 (events id 39 and 82). The weighted stack of GPS in these figures shows a characteristic shape of SSEs, while if we look at individual time series the occurrence of an event is not straightforward. The red lines on those plots are the static displacements at each station once the detection and modeling of the event have been done. These displacements have very small amplitudes, being close to or even below the GPS noise level, but in most of the cases being consistent with the data.

Id	Longitude	Latitude	Date	Duration	Mw	Resolution 10d	Resolution 20d	Resolution 30d	DTP
1	-69.69	-19.36	2005.61	47	6.83	6.7	6.7	6.8	y
2	-69.65	-23.29	2005.89	19	6.58	6.4	6.4	6.8	y
3	-69.41	-19.67	2006.05	19	6.88	6.5	6.5	6.5	y

4	-69.24	-19.63	2006.58	19	6.73	6.6	6.6	6.7	y
5	-70.35	-19.14	2007.83	29	6.68	6.7	6.7	6.8	n
6	-70.32	-22.73	2007.99	19	6.23	6.1	6.1	6.2	y
7	-69.44	-20.42	2007.99	17	6.5	6.5	6.5	6.6	y
8	-68.99	-21.93	2008.08	2	6.33	-	-	-	n
9	-70.09	-22.19	2008.08	3	5.98	6.2	6.2	6.3	n
10	-69.67	-20.10	2008.12	1	5.33	6.3	6.4	6.4	n
11	-71.00	-19.42	2008.12	14	6.35	6.7	6.7	6.7	n
12	-69.38	-22.52	2008.32	27	6.63	6	6	6	y
13	-69.93	-19.80	2008.41	12	5.73	6.1	6.1	6.7	n
14	-69.17	-21.93	2008.41	1	5	-	-	-	n
15	-69.85	-20.13	2008.72	47	6.1	6.2	6.2	6.3	y
16	-69.55	-18.78	2008.72	49	6.53	6.7	6.7	6.7	n
17	-69.38	-22.52	2008.78	17	6.4	6	6	6	y
18	-69.22	-20.73	2008.90	23	6.53	6.5	6.5	6.6	y
19	-70.32	-22.73	2008.90	25	6.43	6.1	6.1	6.2	y
20	-69.36	-19.25	2008.90	17	6.6	6.6	6.6	6.7	y
21	-69.32	-20.04	2008.98	61	6.28	6.5	6.6	6.6	n
22	-70.29	-22.46	2008.98	13	5.58	6.2	6.2	6.3	n
23	-69.38	-22.52	2009.29	15	6.6	6	6	6	y
24	-68.99	-21.93	2009.57	5	6.75	-	-	-	n
25	-70.62	-21.63	2009.57	15	6.15	6.7	6.7	6.7	n
26	-69.32	-20.04	2009.70	6	6.33	6.5	6.6	6.6	n
27	-70.29	-22.46	2009.70	23	5.95	6.2	6.2	6.3	n
28	-71.18	-19.11	2009.70	7	6.18	6.4	6.4	6.5	n
29	-69.50	-20.07	2009.81	1	5	6.4	6.4	6.4	n
30	-70.62	-17.31	2009.81	35	6.63	6.8	6.8	6.8	n
31	-69.72	-21.63	2009.81	3	6.15	6.3	6.3	6.3	n
32	-70.71	-22.94	2009.81	1	5	6.4	6.4	6.3	n
33	-72.37	-17.75	2009.81	3	6.45	-	-	-	n
34	-69.38	-22.52	2009.86	3	6.38	6	6	6	y
35	-70.10	-19.84	2010.06	33	6.25	6.2	6.1	6.3	y
36	-69.72	-21.63	2010.12	93	6.3	6.3	6.3	6.3	y
37	-69.38	-22.52	2010.48	17	6.48	6	6	6	y
38	-69.17	-21.93	2010.54	3	5.75	-	-	-	n
39	-69.50	-20.07	2010.66	23	6.35	6.4	6.4	6.4	y
40	-69.90	-21.35	2010.66	29	6.28	6.3	6.3	6.3	y
41	-69.67	-20.10	2010.80	25	6.23	6.3	6.3	6.4	n
42	-69.83	-18.30	2010.80	6	6.2	-	-	-	n
43	-71.60	-18.55	2010.94	10	6.8	6.5	6.6	6.6	y
44	-69.90	-21.35	2011.02	41	6.48	6.3	6.3	6.3	y
45	-70.44	-21.36	2011.18	1	5	6.6	6.6	6.6	n
46	-69.17	-21.93	2011.18	21	6.63	-	-	-	n
47	-69.90	-21.63	2011.25	15	6.18	6.3	6.3	6.3	n
48	-69.26	-20.40	2011.43	23	6.7	6.5	6.6	6.6	y
49	-69.72	-21.34	2011.43	21	6.45	6.3	6.3	6.3	y
50	-70.79	-20.00	2011.43	21	6.23	6.3	6.3	6.3	n
51	-70.32	-22.73	2011.53	43	5.98	6.1	6.1	6.2	n
52	-71.02	-17.64	2011.53	27	5.85	6.6	6.6	6.6	n
53	-69.85	-20.13	2011.53	43	5.8	6.2	6.2	6.3	n
54	-69.85	-20.13	2011.63	25	6.03	6.2	6.2	6.3	n
55	-70.26	-21.63	2011.63	1	5	6.5	6.5	6.6	n
56	-69.05	-22.85	2011.69	27	6.8	-	-	-	n
57	-72.07	-16.01	2011.71	3	6.13	7	7	7	n
58	-69.58	-20.76	2011.76	59	6.6	6.5	6.5	6.9	n
59	-70.87	-19.73	2011.76	93	6.58	6.4	6.4	6.4	y
60	-69.50	-20.07	2011.97	19	6.43	6.4	6.4	6.4	y

61	-69.05	-22.85	2012.16	37	6.75	-	-	-	n
62	-69.83	-18.30	2012.16	12	6.53	-	-	-	n
63	-69.72	-21.34	2012.23	1	5	6.3	6.3	6.3	n
64	-69.26	-20.40	2012.38	37	6.75	6.5	6.6	6.6	y
65	-69.38	-22.52	2012.38	27	6.43	6	6	6	y
66	-71.03	-19.02	2012.38	31	6.55	6.3	6.4	6.4	y
67	-72.83	-15.47	2012.39	11	7.45	-	-	-	n
68	-69.15	-20.00	2012.61	13	6.53	6.6	6.6	-	y
69	-69.00	-21.32	2012.65	27	6.85	-	-	-	n
70	-69.38	-22.52	2012.67	5	6.43	6	6	6	y
71	-71.39	-18.82	2012.73	5	6.75	6.4	6.4	6.8	y
72	-70.27	-22.18	2012.92	19	6.15	6.4	6.4	6.4	n
73	-69.50	-20.07	2012.93	21	6.35	6.4	6.4	6.4	y
74	-71.05	-18.13	2012.93	39	6.3	6.6	6.6	6.6	n
75	-70.64	-17.82	2013.18	11	6.15	6.6	6.6	6.7	n
76	-69.67	-20.10	2013.19	1	5.4	6.3	6.3	6.4	n
77	-70.08	-21.35	2013.19	31	6.45	6.2	6.2	6.3	y
78	-69.38	-22.52	2013.32	49	6.23	6	6	6	y
79	-69.50	-20.07	2013.32	65	6.48	6.4	6.4	6.4	y
80	-70.11	-17.91	2013.35	23	6.35	-	-	-	n
81	-70.27	-19.88	2013.53	4	6.3	6.5	6.5	6.5	n
82	-70.91	-18.03	2013.53	11	6.23	6.7	6.7	6.7	n
83	-72.01	-17.38	2013.53	7	6.43	6.8	6.8	6.8	n
84	-75.81	-14.52	2013.55	49	6.18	6.6	6.6	6.6	n
85	-69.22	-20.73	2013.60	23	6.78	6.5	6.5	6.6	y
86	-69.08	-23.09	2013.60	29	6.58	6.7	6.7	6.7	n
87	-70.79	-20.00	2013.60	25	6.28	6.3	6.3	6.3	y
88	-70.71	-22.94	2013.60	5	5.13	6.4	6.4	6.3	n
89	-71.18	-19.11	2013.71	1	5	6.4	6.4	6.5	n
90	-71.39	-18.82	2013.73	47	6.6	6.4	6.4	6.8	y
91	-69.83	-18.30	2013.73	7	6.15	-	-	-	n
92	-69.50	-20.07	2013.90	11	6.4	6.4	6.4	6.4	y
93	-70.29	-22.46	2013.90	1	5	6.2	6.2	6.3	n
94	-70.29	-22.46	2013.90	25	6.15	6.2	6.2	6.3	y
95	-69.61	-20.44	2014.18	34	6.25	6.4	6.4	6.4	n
96	-69.73	-22.20	2014.20	6	6.3	6.3	6.3	6.3	y
97	-71.42	-17.96	2014.40	29	6.48	6.7	6.7	6.7	n
98	-72.48	-15.71	2014.40	25	7.15	-	-	-	n
99	-69.46	-23.30	2014.40	25	6.58	6.8	6.8	6.8	n
100	-70.35	-22.97	2014.43	5	5.33	5.9	5.9	6	n
101	-69.38	-22.52	2014.43	1	5	6	6	6	n
102	-70.32	-20.53	2014.52	13	5.78	6.2	6.1	6.2	n

Table 6.1: Transient events detected with their id, localization (longitude and latitude), date of occurrence, duration and magnitude estimated. The column DTP (Detection Threshold Pass) indicates if the event passed (y) or not (n) the threshold Magnitude, based on the resolution analysis using synthetics. The columns Resolution 10-20-30 days show the threshold resolution for each SSE based on the duration of the synthetics tested.

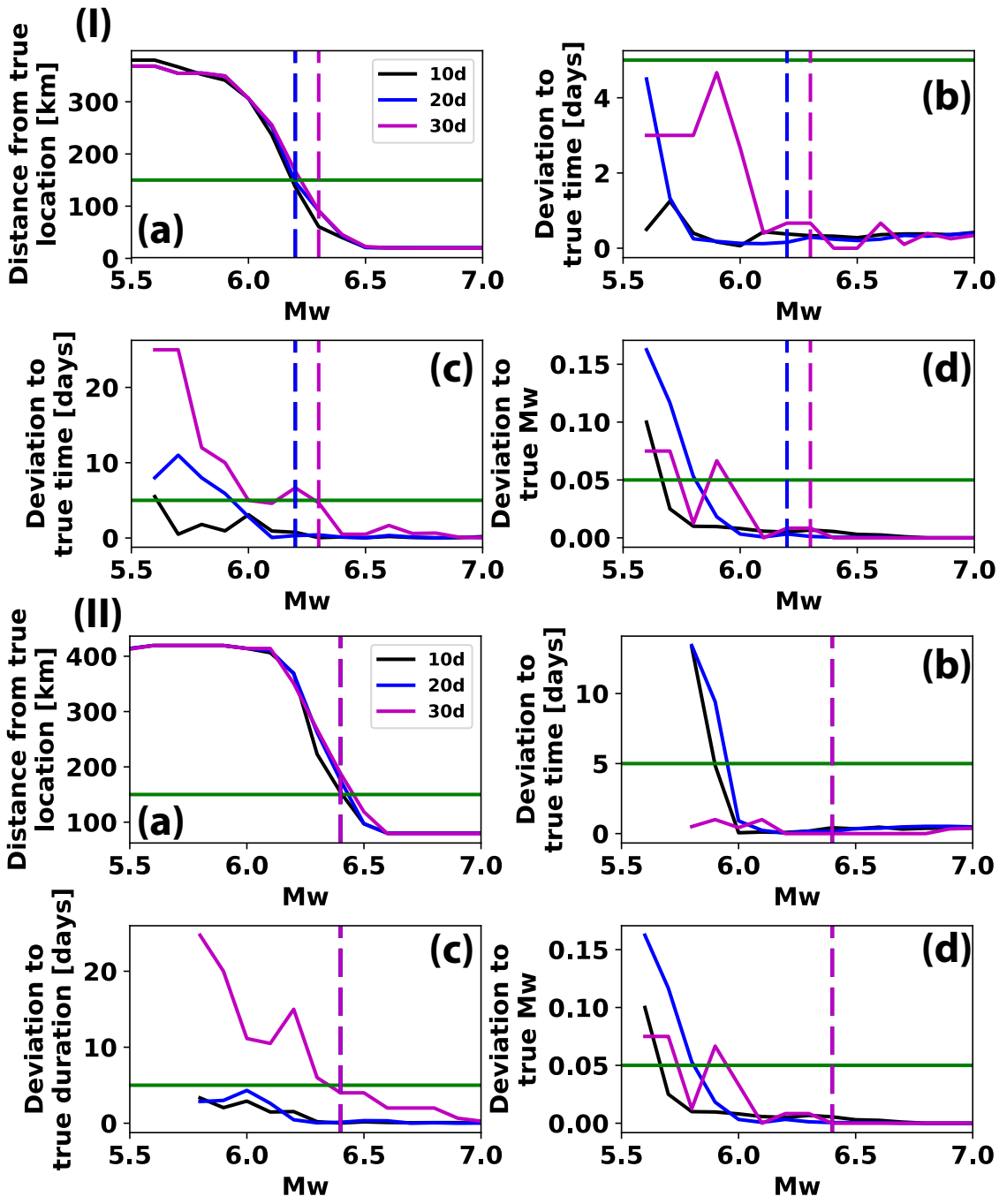

Figure 6.5: (I) Resolution test for the patch of the event 9. (a) Deviation from the true location in km as function of the M_w tested. Black (blue, pink) curve is for a synthetic duration of 10 days (20,30 days). Dashed vertical lines denote the magnitude threshold color-coded by the synthetic duration. (b) Deviation from the true detection time, (c) deviation from the true duration and (d) deviation from the true M_w . Horizontal green lines shows the limit used to define the threshold: 150 km in (a), 5 days in (b) and (c), and 0.05 in (d) (II) Same caption as in (I), but for the patch of events 39, 60, 73, 79 and 92 (Same patch and same network active)

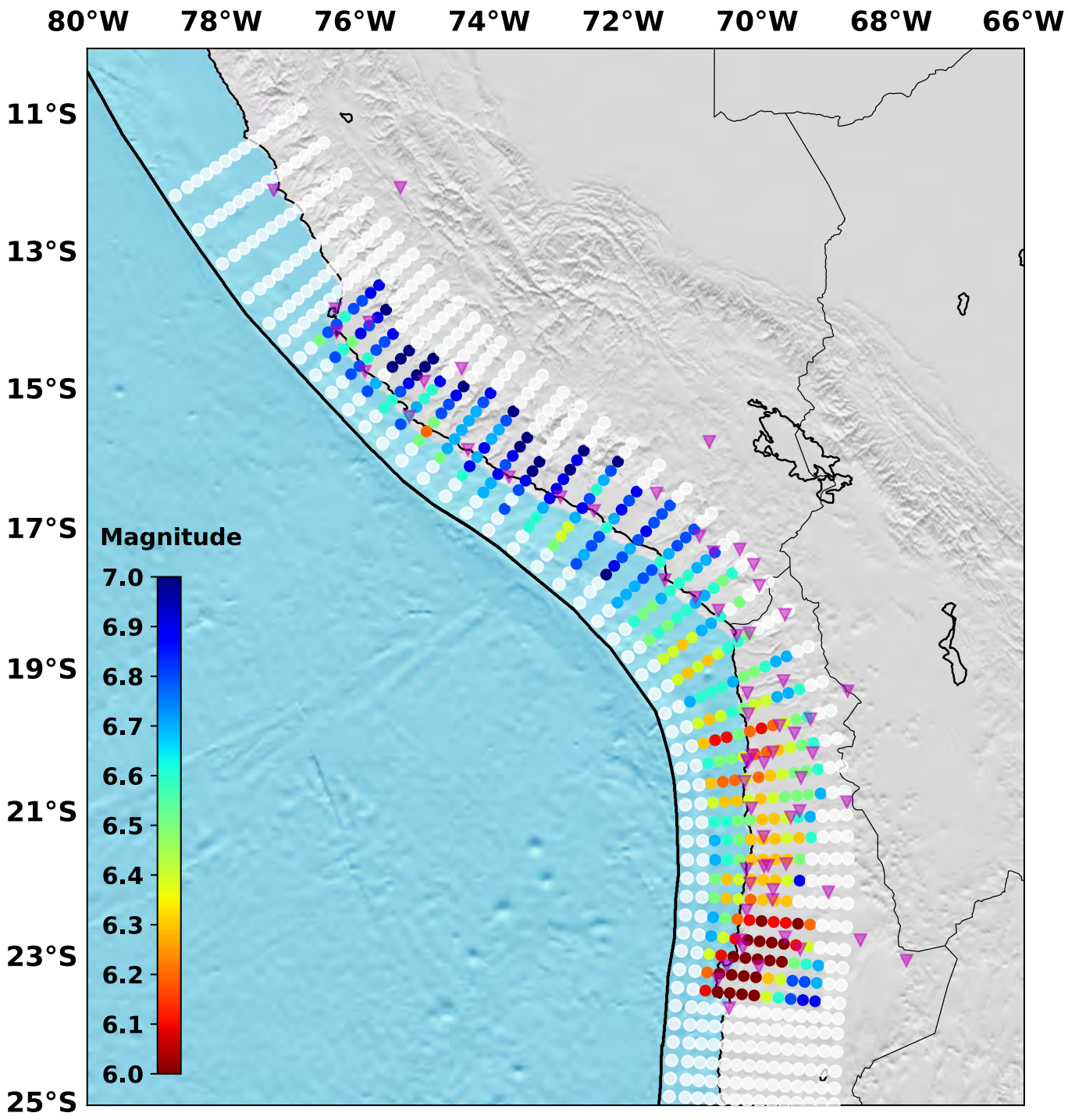

Figure 6.6: The map shows the minimum magnitude detectable for each fault patch, based on the method explain in the main text, for events with a duration of 10 days. Inverted blue triangles denote the location of one GPS station.

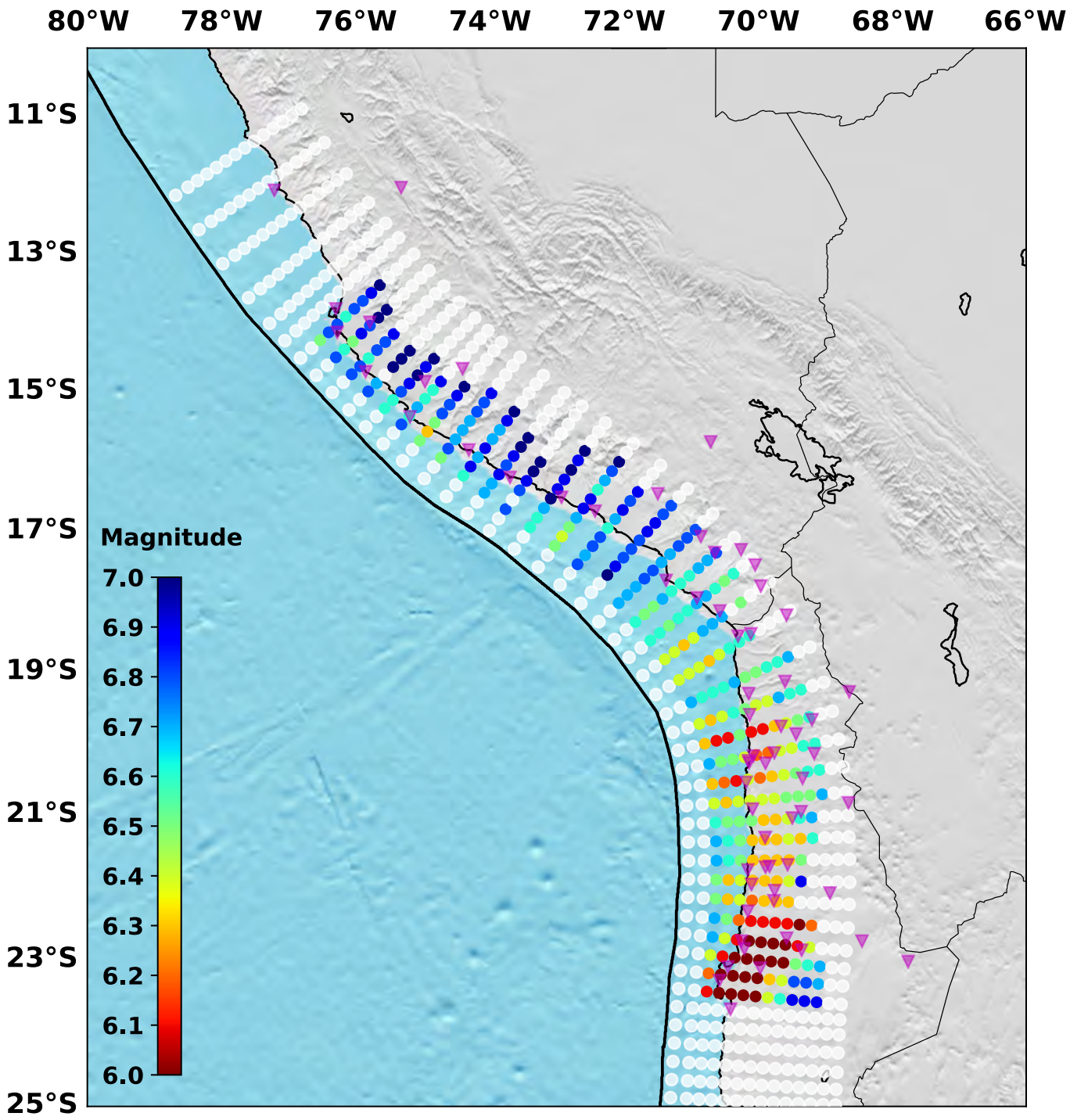

Figure 6.7: The map shows the minimum magnitude detectable for each fault patch, based on the method explain in the main text, for events with a duration of 20 days. Inverted blue triangles denote the location of one GPS station.

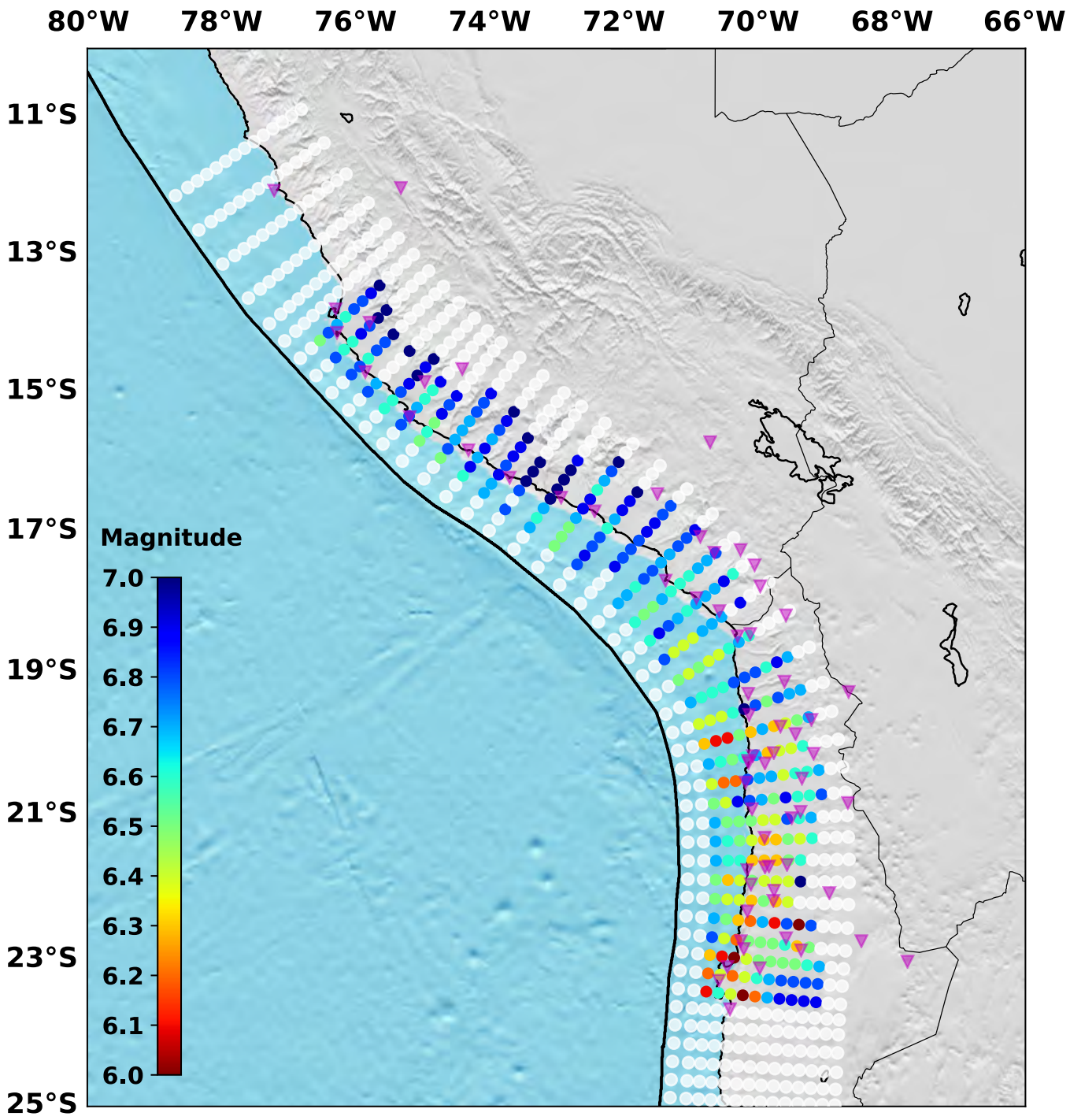

Figure 6.8: The map shows the minimum magnitude detectable for each fault patch, based on the method explain in the main text, for events with a duration of 30 days. Inverted blue triangles denote the location of one GPS station.

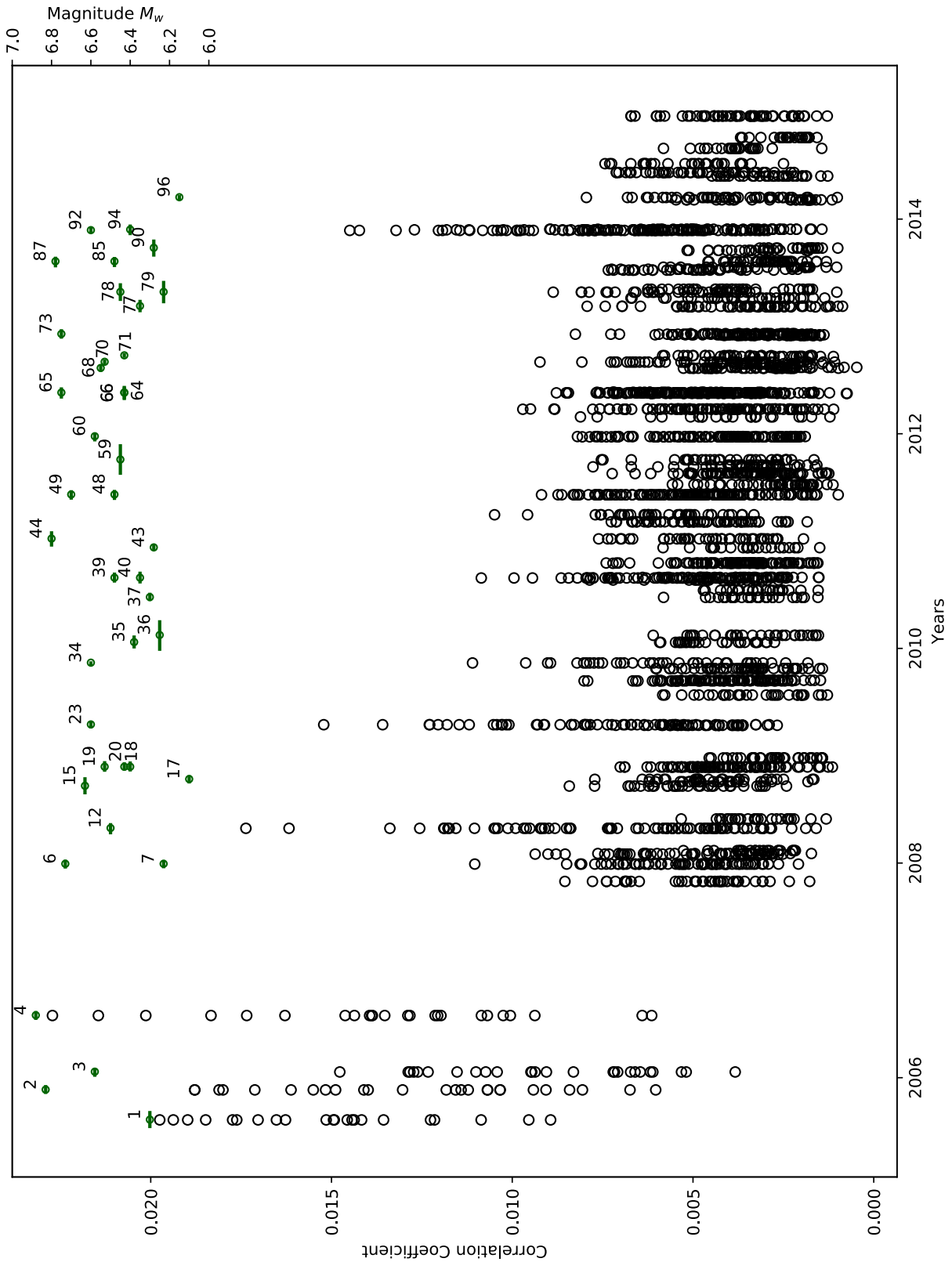

Figure 6.9: Black circles denote the cleaned detections on all patches. Detections made on less than 20 patches have been removed. The final detections are shown by green circles together with their estimated duration, magnitude and respective ids.

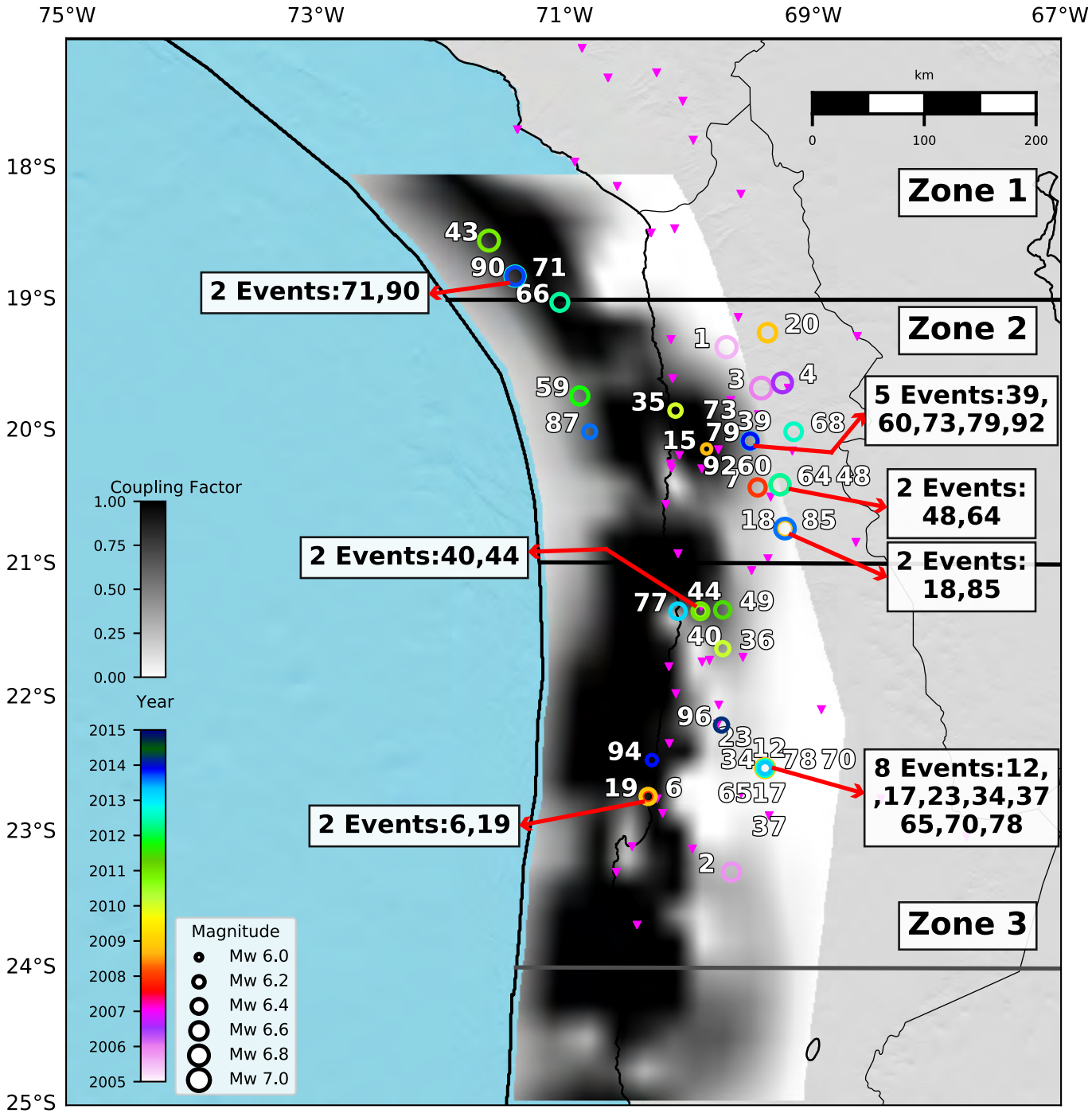

Figure 6.10: The map shows the locations of the transient detections color-coded by date of occurrence and scaled by magnitude. For those patches presenting more than one event, an arrow shows the number of detections and the id of the event. Coupling maps from *Métois et al.* [2016]. Inverted pink triangles indicate the location of the GPS stations employed in this work.

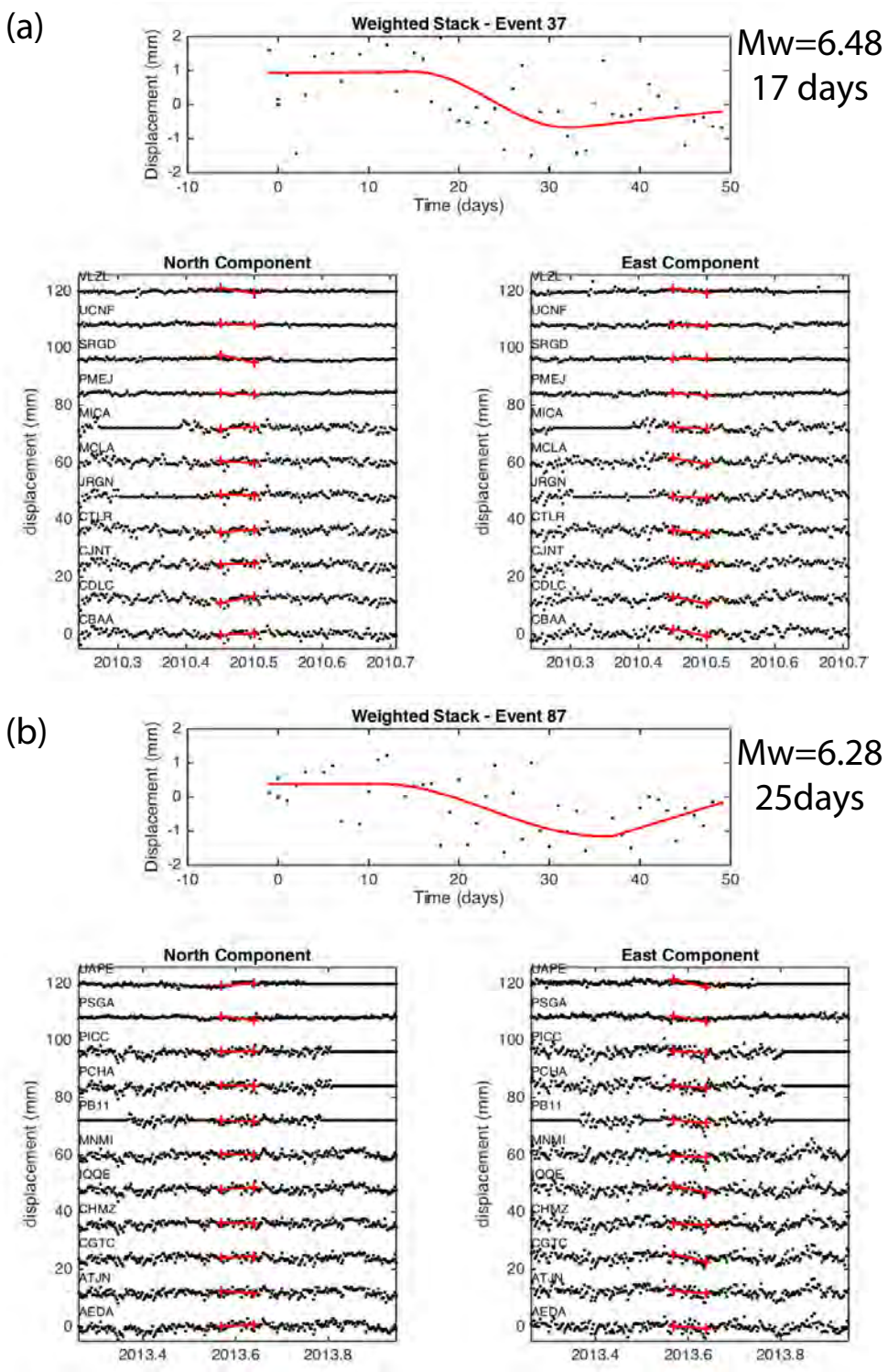

Figure 6.11: (a) On top, the stack of the GPS horizontal components time series centered on the detection time for the event 37 The black dots are the data and the red curve is the model from which the duration and magnitudes are estimated. On the bottom, the GPS time series are shown for the North and East components. The red line denotes the static amplitude of displacement at each station based on the location and magnitude estimated (indicate on top right). (b) same caption as in (a) but for the event 80.

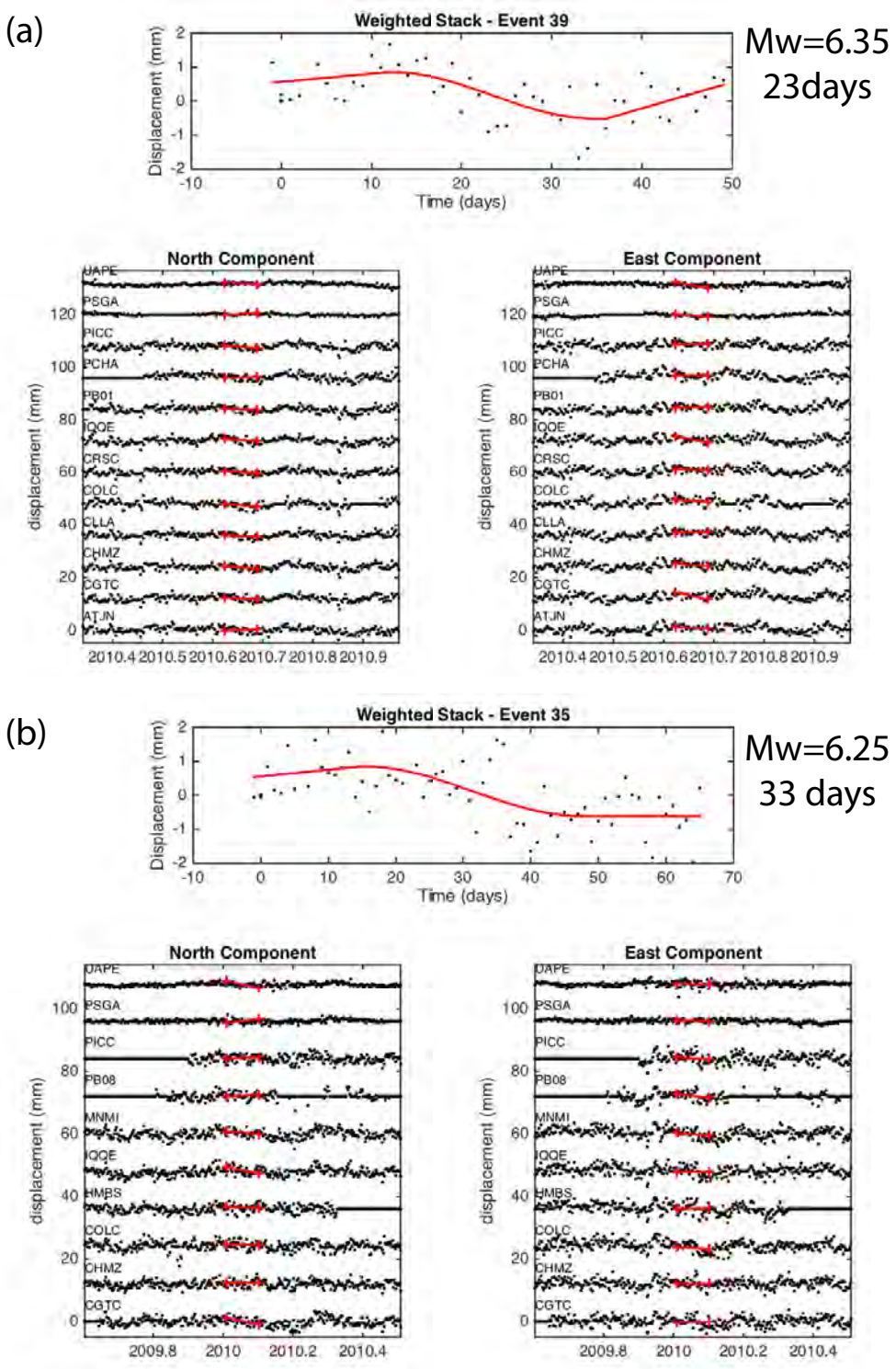

Figure 6.12: (a) On top, the stack of the GPS horizontal components time series centered on the detection time for the event 39. The black dots are the data and the red curve is the model from which the duration and magnitudes are estimated. On the bottom, the GPS time series are shown for the North and East components. The red line denotes the static amplitude of displacement at each station based on the location and magnitude estimated (indicate on top right). (b) same caption as in (a) but for the event 82.

6.4 Discussion

6.4.1 Interseismic Coupling and sSSEs Detected

The Figure 6.10 is a map view of the events color scaled by date of occurrence, comparing with the coupling map available in the region from *Métois et al.* [2016]. This map shows that almost all the events are located in the deeper part of the seismogenic zone. Three patches are activated twice during the analysis, one patch is activated seven times, and another one 5 times. Comparing the full coupling distribution from *Métois et al.* [2016] with the sSSEs detected coupling distribution we found that:

- 4 events are located outside of areas where the coupling is available (9.76%)
- 15 events are in areas where the coupling factor is low ($0 < \phi < 0.25$, 36.59%)
- 13 events are in areas where the coupling factor has intermediate values ($0.25 < \phi < 0.75$, 31.70%)
- 9 events are in areas where the coupling factor is high ($0.75 < \phi < 1.0$, 21.95%)

The fact that most small SSEs occur in areas characterized by a small coupling seems to indicate that slip does not occur continuously on the subduction interface, but rather as a series of bursts. Such burst behavior is for instance supported by two patches breaking repeatedly 5 times (event with ids 39, 60, 73, 79 and 92) and 8 times (events with ids 12, 17, 23, 34, 37, 65, 70 and 78) (Figure 6.10). The fact that some events activate the same patch repeatedly might be seen as an effect of increased loading in these zones.

The small SSEs located between 50 - 60 km depths correspond to areas with a low coupling factor, and may correspond to events in a transition zone, where the seismogenic zone ends and the slab begins to creep. This transition zone has been defined using geodetic data between 35 - 50 km [*Chlieh et al.*, 2004, 2011; *Métois et al.*, 2016], although using seismological data, thrust earthquakes have been reported down to depths of 60 km [*Comte and Suárez*, 1995; *Comte et al.*, 2016]. It suggests a complex interaction between seismic and aseismic slip at depths ranging between 35 - 60 km. Events that occur at depths greater than 60 km are usually associated very low coupling values ($\phi < 0.25$) may reflect the slow deformation of the slab, that is not steady state.

The events 1, 3 and 4 are close to the area affected by Tarapaca slab-pull earthquake which occurred at 100 km depth [*Peyrat et al.*, 2006; *Peyrat and Favreau*, 2010], and occur in the year that followed the earthquake. Some events also occur at depth at the latitude of Tocopilla earthquake [*Béjar-Pizarro et al.*, 2010; *Peyrat et al.*, 2010] (Figure 6.10). GPS time-series show a variation of velocity during several years after Tocopilla that is probably associated with postseismic viscoelastic relaxation in the mantle wedge that may drag the slab. These small SSEs following a great earthquake may be triggered by it, and reflect unmodeled complexities of the post-seismic relaxation process.

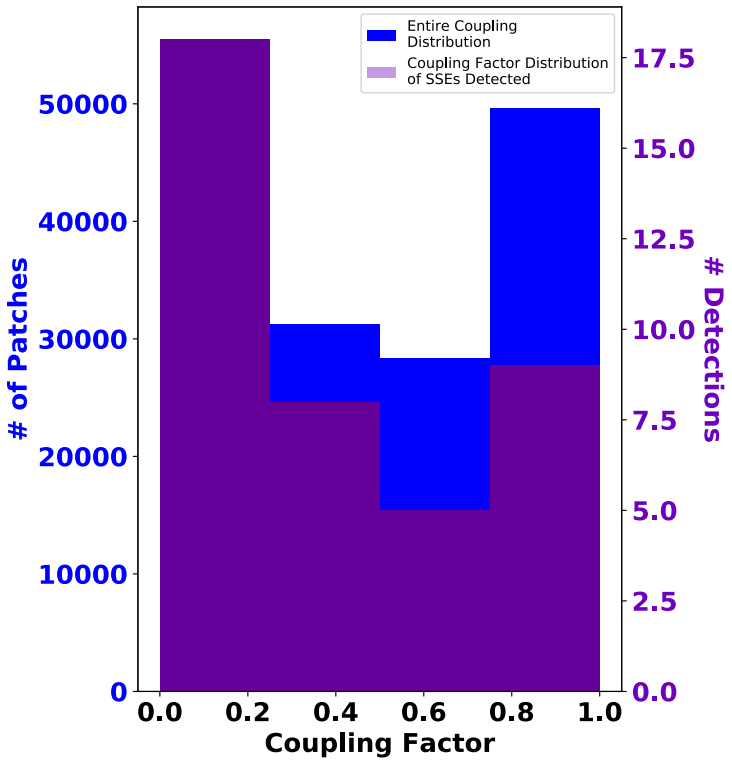

Figure 6.13: Histogram of the full coupling distribution in the region (blue) compared with the coupling distribution of sSSEs detected (red). Histogram bins are each 0.25.

6.4.2 Background Seismicity and sSSEs Detected

In order to assess potential interactions between slow slip and seismic ruptures, it appears important to compare the obtained small SSEs to the seismicity and background seismicity rate computed using the Methodology explained in the Chapter 5 ([*Jara et al.*, 2017]). Indeed, the background seismicity is usually seen as a good proxy for the tectonic loading, so any important deviation from its mean rate can be associated with aseismic deformation or fluid migration [*Reverso et al.*, 2016; *Marsan et al.*, 2017]. We have separated the seismicity in shallow (z $\leq$ 40 km) and deep (z $\geq$ 80 km) seismicity in three zones: Zone 1 that corresponds to the South of Peru and Arica bend (17°-19°S), Zone 2 associated with the Camarones segment that was affected by Tarapacà earthquake in 2005 and Iquique earthquake in 2014 (19°- 21°S) and finally Zone 3 that includes the Loa segment, the Mejillones peninsula and the Tocopilla seismic rupture in 2007 (21°- 24°S). The completeness magnitude calculated is M_c 4.7.

The background seismicity in Zone 1 is limited (Figure 6.14). There is no synchronization of shallow-deep seismicity, 1 sSSE (id 43) is associated with the occurrence of the shallow seismic activity, while 1 event (ids 71) is associated with deep seismicity. 1 event is not associated neither with shallow nor deep seismicity. In this area, the poor coupling resolution, the low seismicity rate, and the small amount event detected (due to the sparse GPS stations distribution) makes it difficult to

interpret and conclude.

In Zone 2 (Figure 6.15), the background seismicity is more intense than in Zone 1. 5 sSSEs are associated with both shallow and deep seismicity bursts (ids 4, 15, 59, 85 and 87). The event 4 is likely associated with the postseismic of Tarapaca slab pull earthquake. Events 85 and 87 are associated with the swarm that occurred in 2013, when Iquique earthquake presumably started to prepare [*Kato et al.*, 2016; *Socquet et al.*, 2017]. *Bouchon et al.* [2016] have shown interactions between shallow and deep seismicity, linking them by aseismic deformation due to the slab plunge. *Durand et al.* [2014] has observed a large-scale spread slab deformation with the capability to trigger shallow seismicity activity. Events 85 and 87 support this idea that slab processes may affect the interface seismic or aseismic slip . 8 sSSEs are related to the occurrence of deep background seismicity only (ids 1, 3, 7, 35, 39, 48, 68 and 73). These events occur mostly between 50 - 60 km, in the transition zone where the subduction interface starts to creep. 7 events are not associated with neither shallow nor deep seismicity. One option that can explain why they are not associated with seismicity is due to the high completeness magnitude employed in the analysis, suggesting that seismicity lower than M_c 4.7 can be involved in the process. This needs to be further explored in order to understand the mechanisms to explain them. Another interesting feature in the region, is that the aseismic deformation seems to increase close to the date of Iquique earthquake. It may be produced by the influence of Tarapaca slab-pull earthquake that may trigger aseismic deformation, facilitating the preparation phase of the megathrust event through aseismic deformation, either in the seismogenic interface and at slab depths.

The Zone 3 (Figure 6.16) presents 4 interactions between shallow slow slip and deep seismicity (ids 36, 37, 49 and 96), in areas where the coupling is in transition values. 10 events are connected with the occurrence of deep seismicity (ids 2, 6, 12, 23, 34, 40, 65, 77, 78 and 94), suggesting that the slab processes have an important impact on the aseismic deformation like in the Zone 2. 3 events do not have a relationship with shallow or deep seismicity, and like the results in Zone 2, they need to be further explored to explain the mechanisms of generation. Conversely to the increase of the aseismic deformation observed in the Zone 2, this Zone shows a more constant activity during all the period analyzed after the occurrence of Tocopilla earthquake, that had a long postseismic phase due to the viscoelastic relaxation of the mantle [*Weiss et al.*, 2016]. It suggests that Tocopilla earthquake has excited the aseismic deformation related to deep processes, doing it more constant over time because of the long postseismic phase.

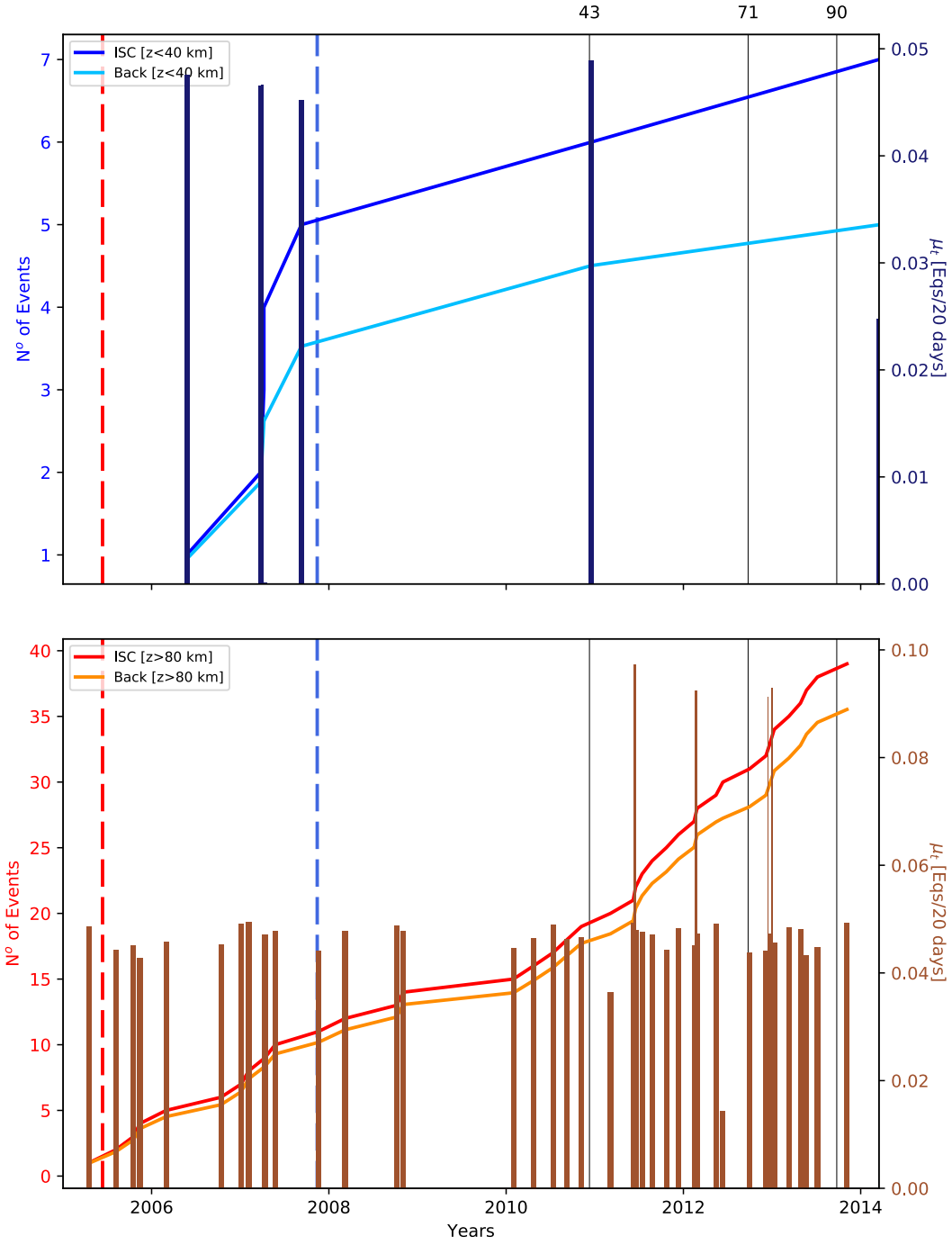

Figure 6.14: (a) shallow (z < 40 km) and (b) deep (z > 80 km) cumulative seismicity for the ISC catalog (blue and red) and background seismicity (light blue and orange) for Zone 1 (Figure 6.10). The background rate (μ_t) over 20 days is plotted in bar shape. Vertical black lines denote the occurrence of a sSSE and their ids are written on top.

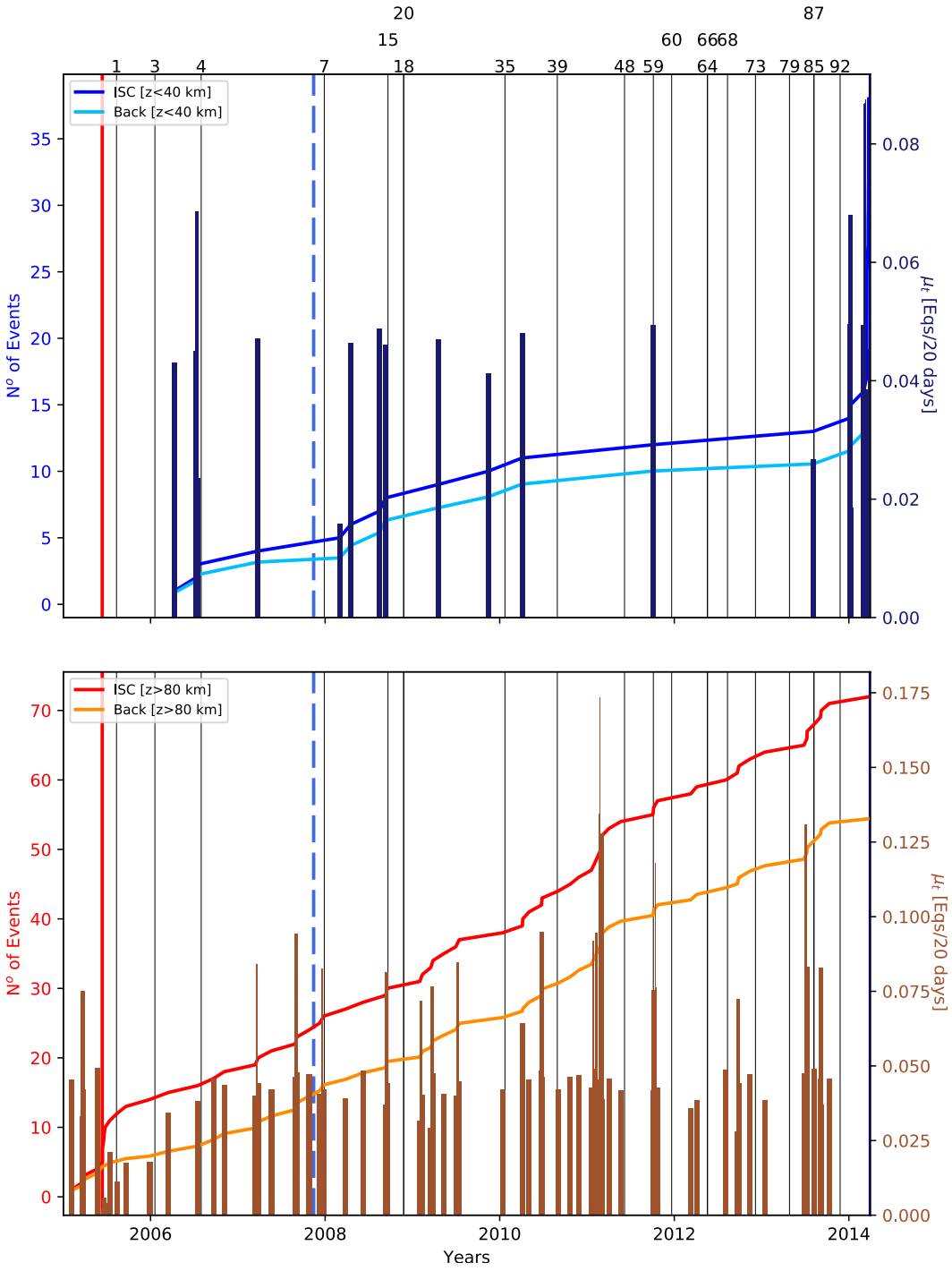

Figure 6.15: Same caption as in Figure 6.14, but for Zone 2 (Figure 6.10).

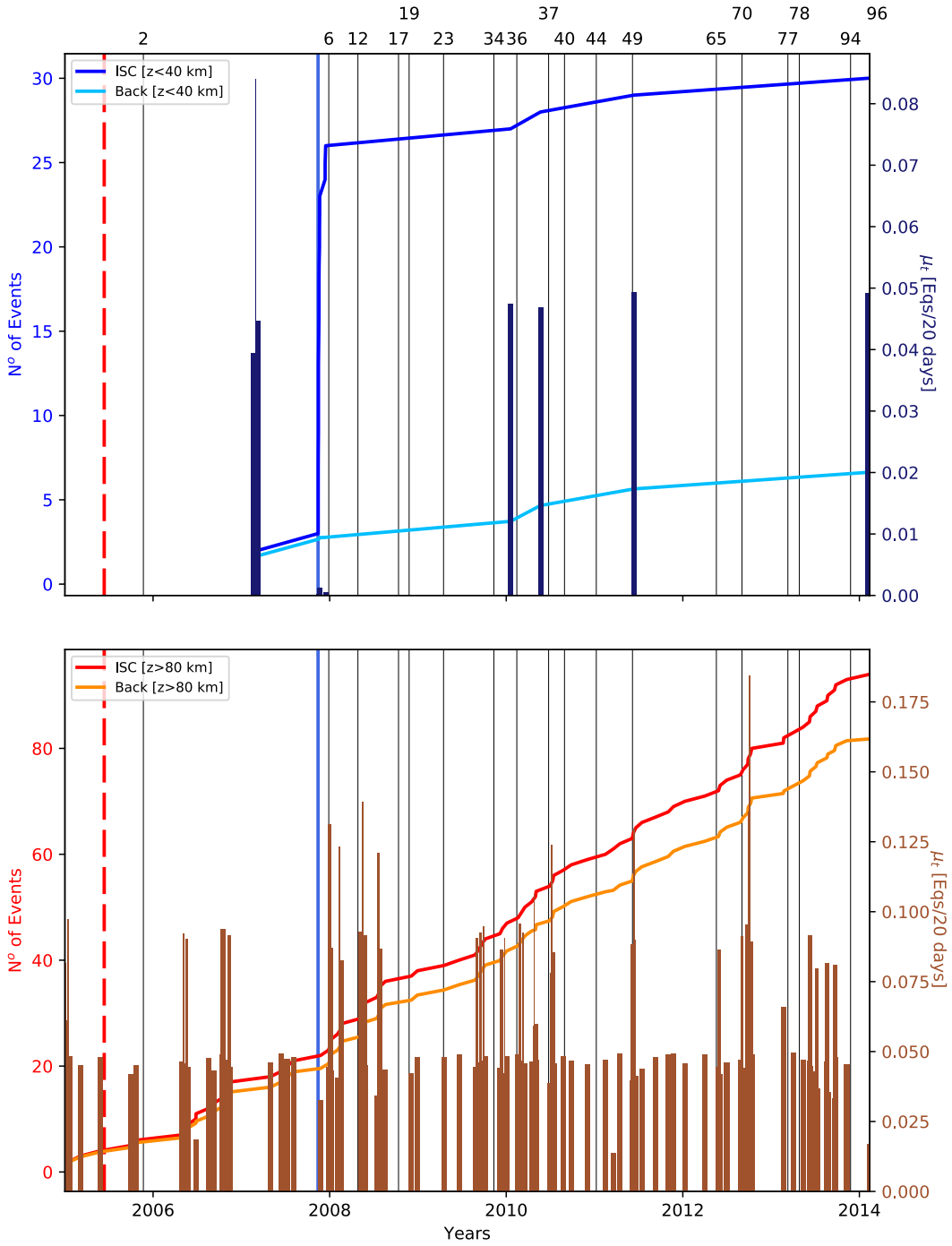

Figure 6.16: Same caption as in Figure 6.14, but for Zone 3 (Figure 6.10).

6.5 Conclusions

The conclusions of this Chapter are based on the preliminary results discussed above, but they need to be further explored and analyzed. 41 sSSEs are detected in the South Peru - North Chile subduction zone. These events are characterized by magnitudes ranging between 6.1 - 6.9 and durations of 3 - 93 days. All these events are mostly located in the deeper part of the seismogenic zone. The comparison of our results and the interseismic coupling shows that ∼68% of those events

are located in areas where the coupling factor is low or with intermediate values ($0.25 < \phi < 0.75$). The relationship between the background seismicity and the detected events reveals some interactions between shallow seismicity, sSSEs at the transition zone and deep seismicity, suggesting that the slab deformation may influence pulses of seismic and aseismic processes occurring on the subduction interface, at shallow depths or in the transition zone. The temporal evolution of the events detected shows that in the region affected by Tocopilla earthquake, the sSSEs are quite intense during the full period analyzed. This fact may be an indicator of a long post-seismic after Tocopilla earthquake, where the mantle wedge viscous relaxation may drag the slab and explain both the activity intensity and the repetitive transients detected in the area as well. Close to Iquique earthquake area, the increased sSSEs activity towards the date of the earthquake may be associated to the long preparation phase of the megathrust earthquake.

Appendix

6.A Appendix Figures and Tables

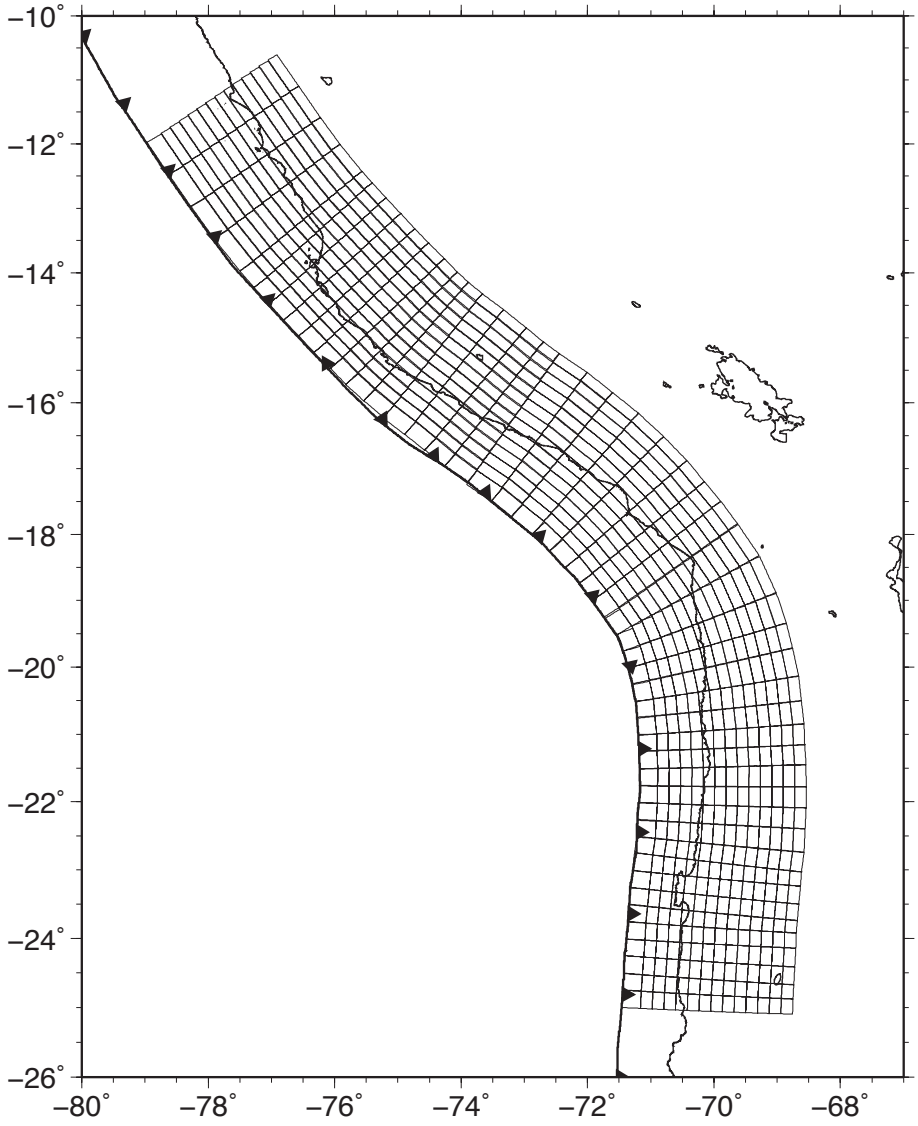

Figure 6.A.1: Geometry Design used in the SSEs detection.

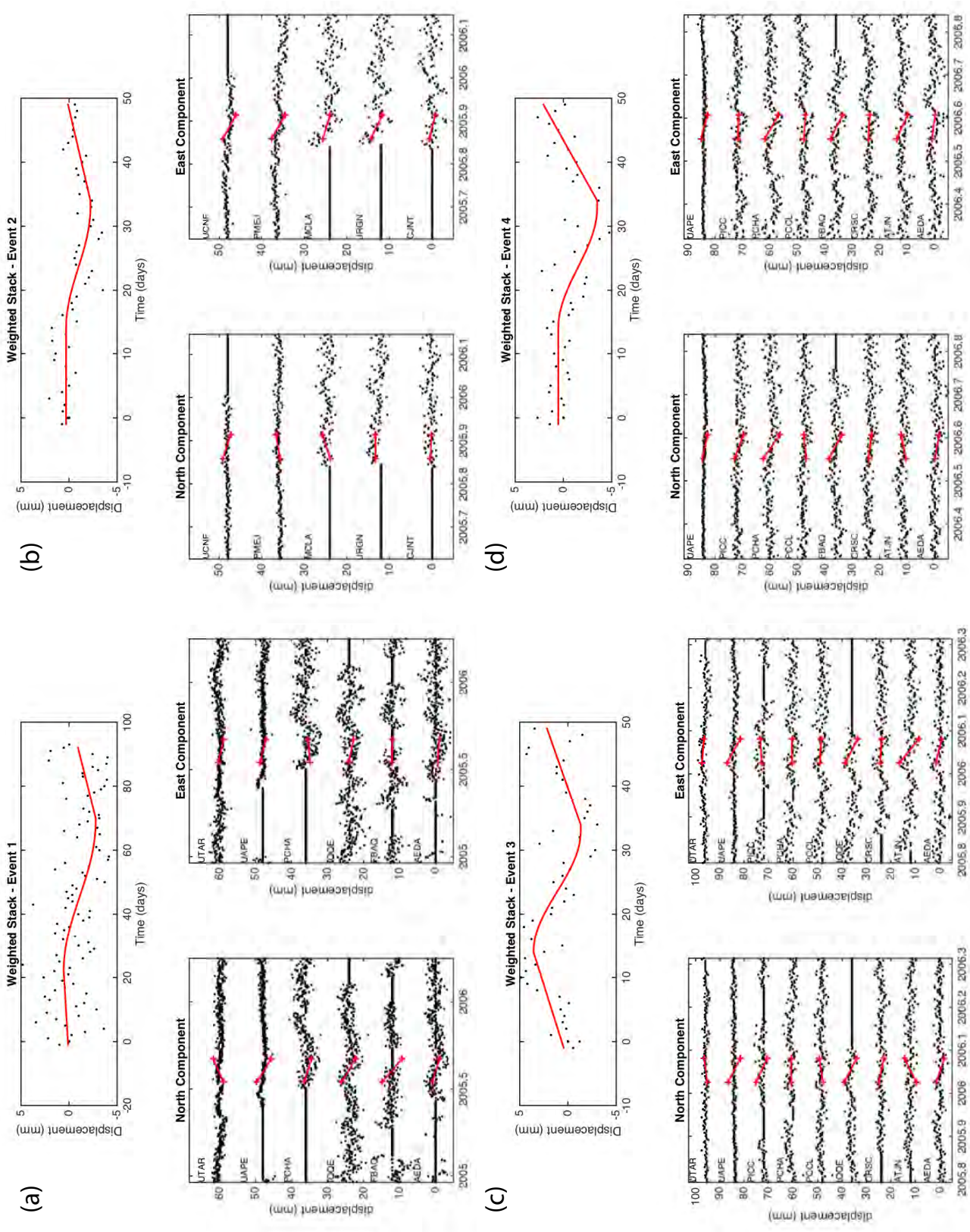

Figure 6.A.2: Same caption as in Figure 6.11 but for events 1, 2, 3 and 4.

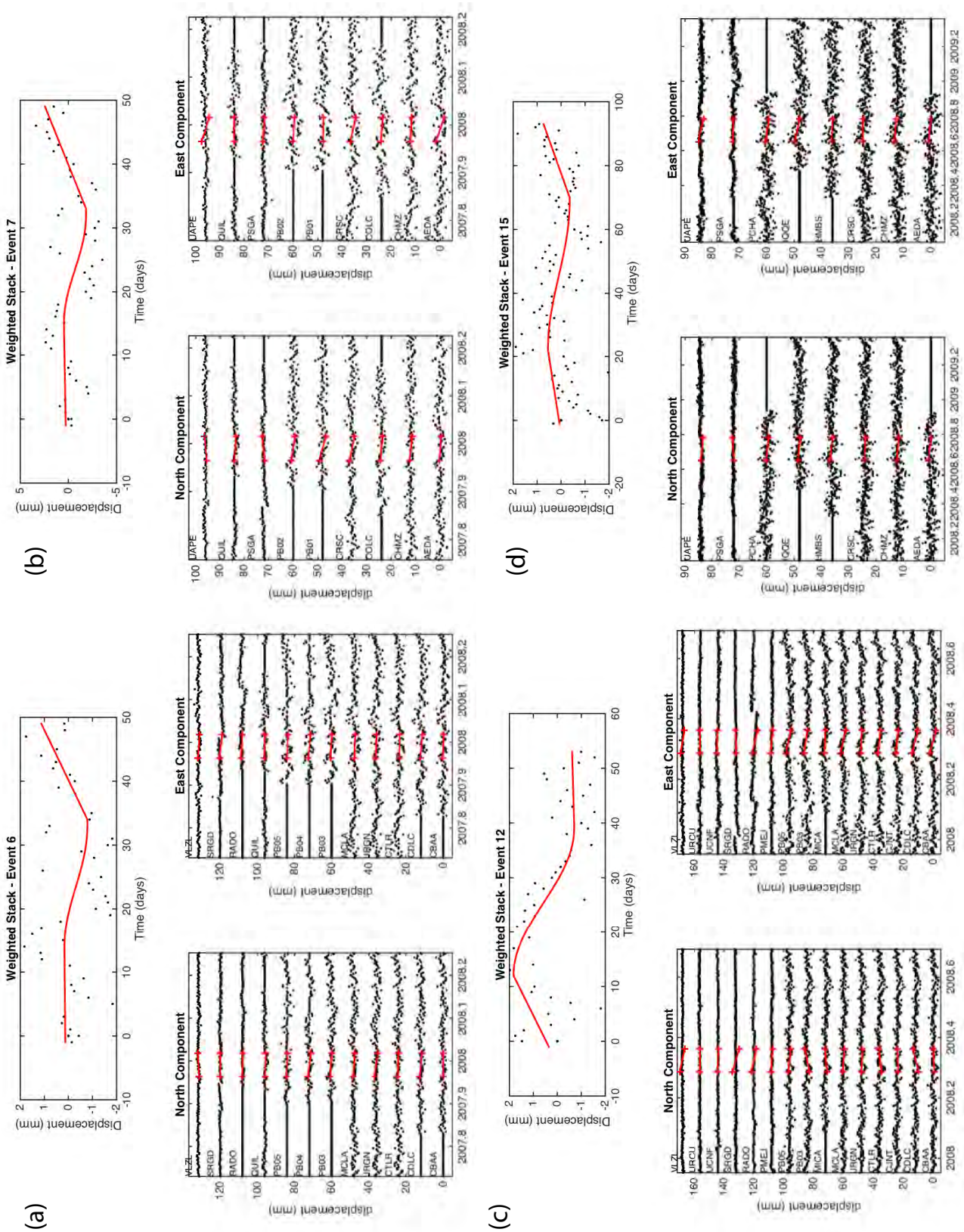

Figure 6.A.3: Same caption as in Figure 6.11 but for events 6, 7, 12 and 15.

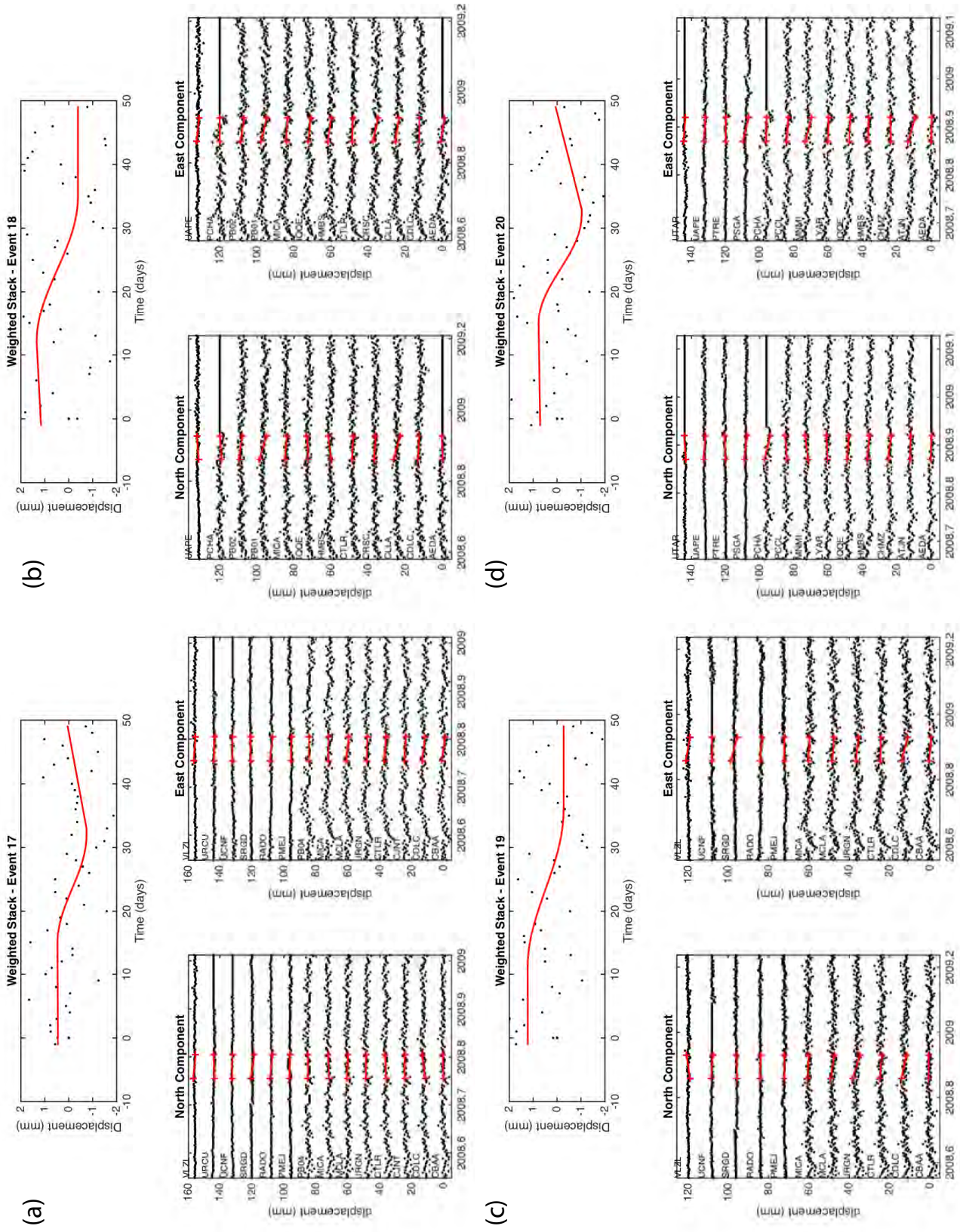

Figure 6.A.4: Same caption as in Figure 6.11 but for events 17, 18, 19 and 20.

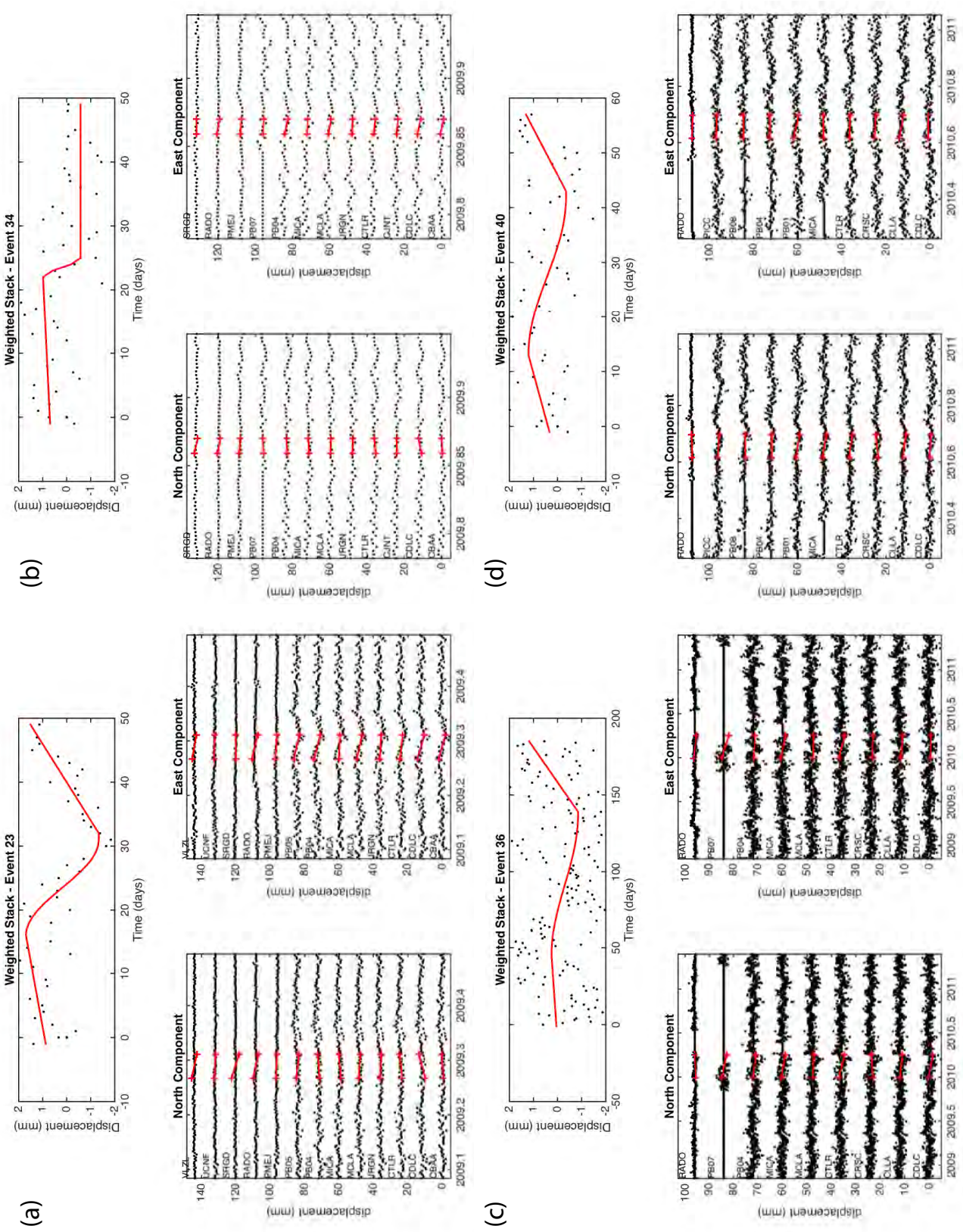

Figure 6.A.5: Same caption as in Figure 6.11 but for events 23, 34, 36 and 40.

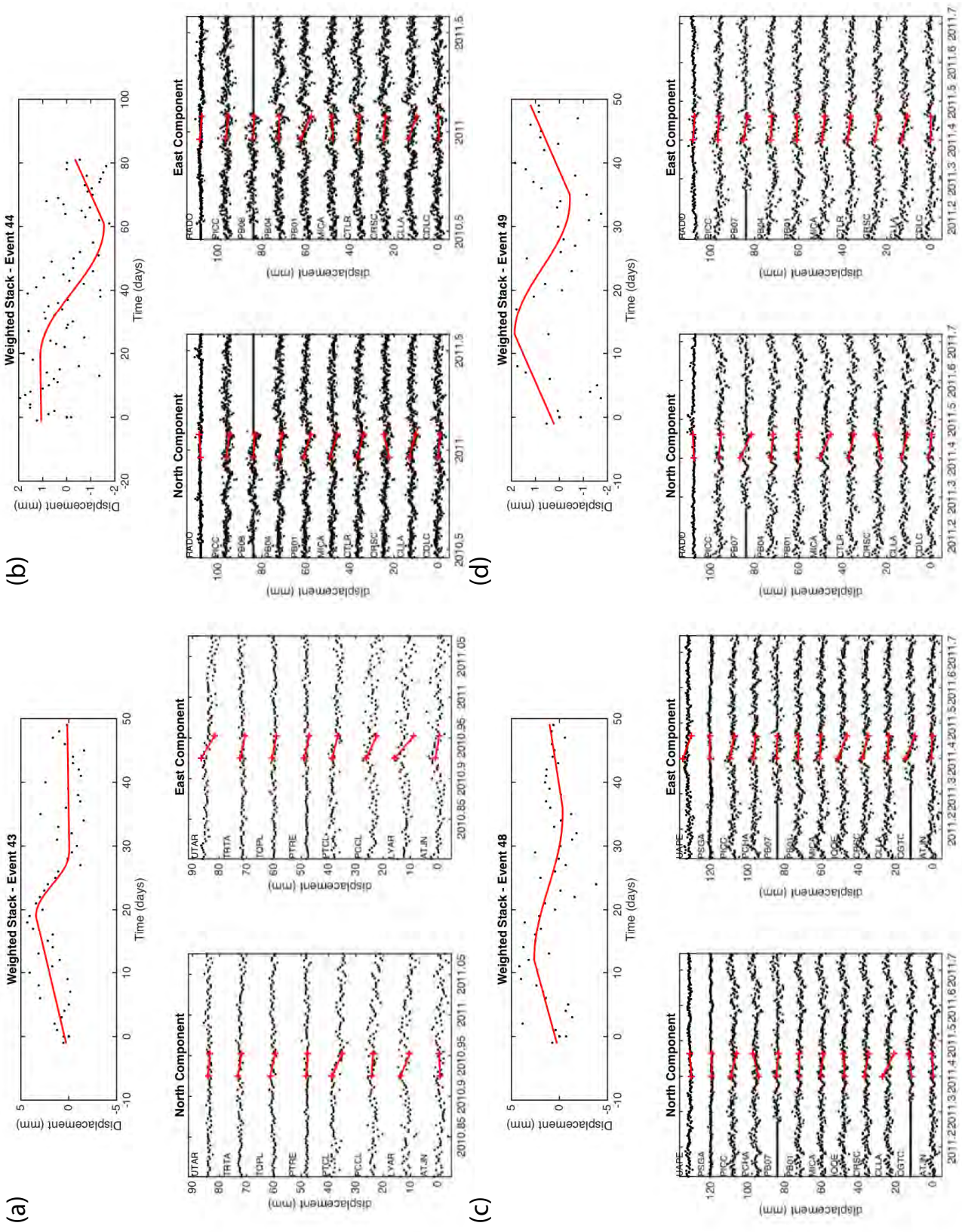

Figure 6.A.6: Same caption as in Figure 6.11 but for events 43, 44, 48 and 49.

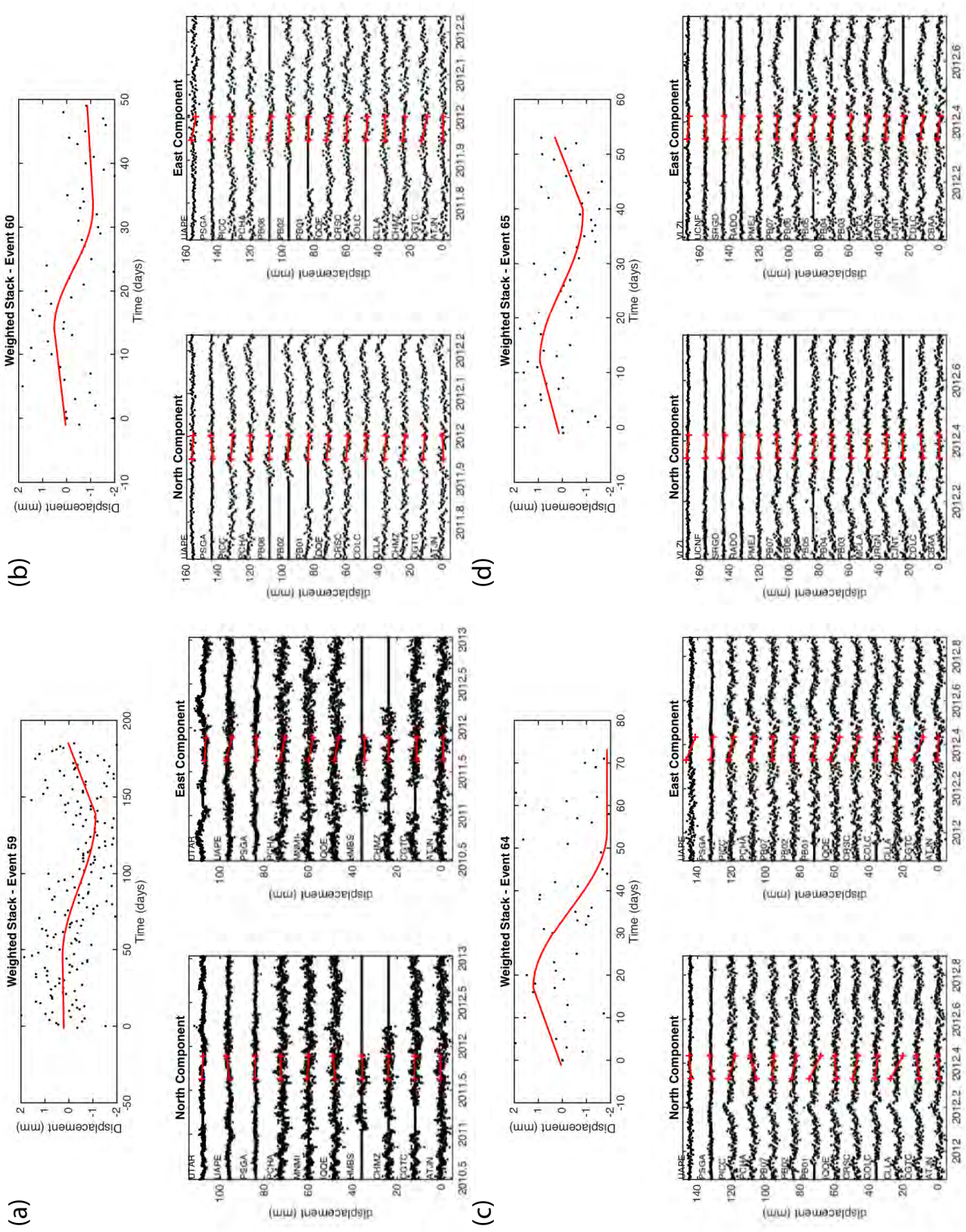

Figure 6.A.7: Same caption as in Figure 6.11 but for events 59, 60, 64 and 65.

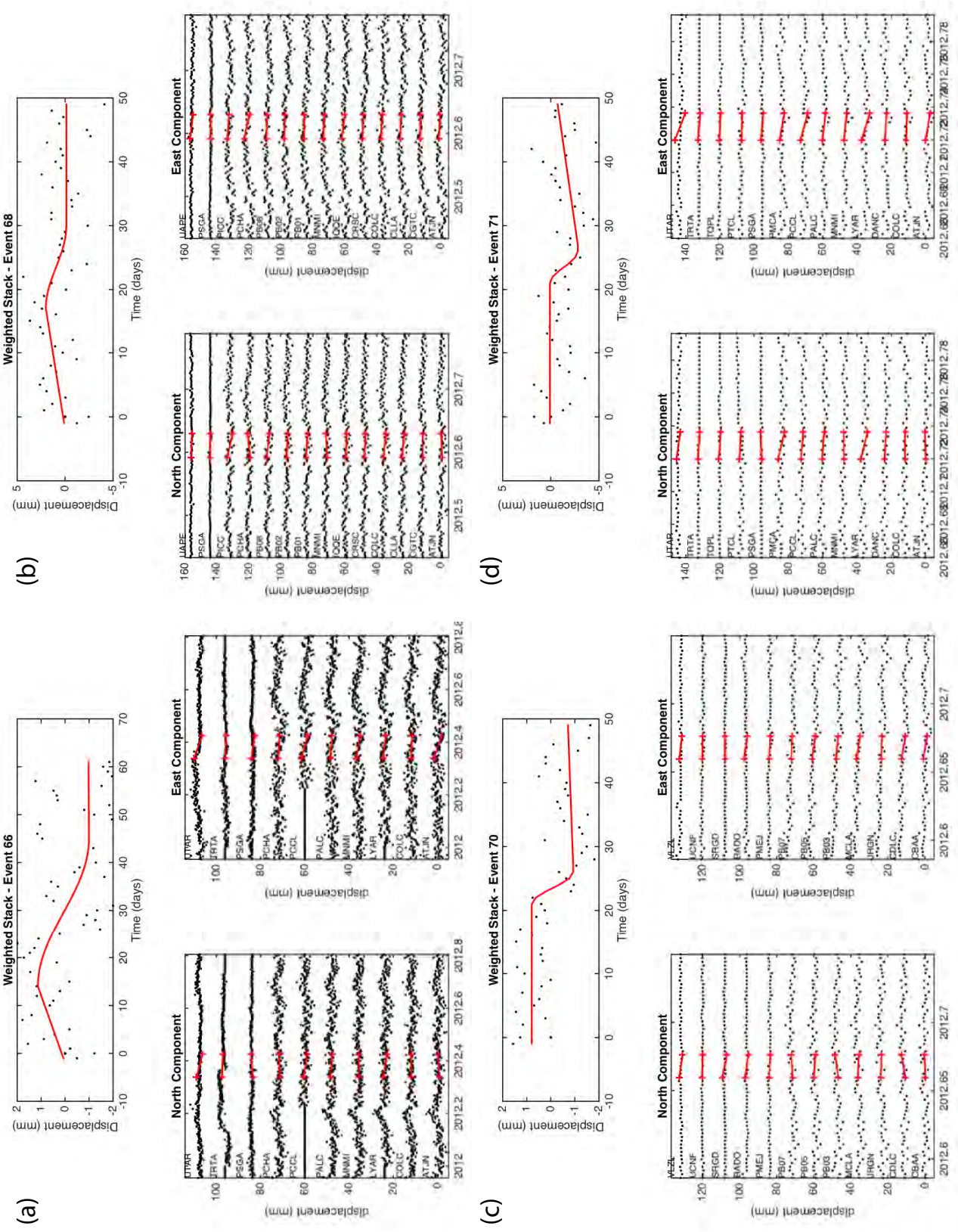

Figure 6.A.8: Same caption as in Figure 6.11 but for events 66, 68, 70 and 71.

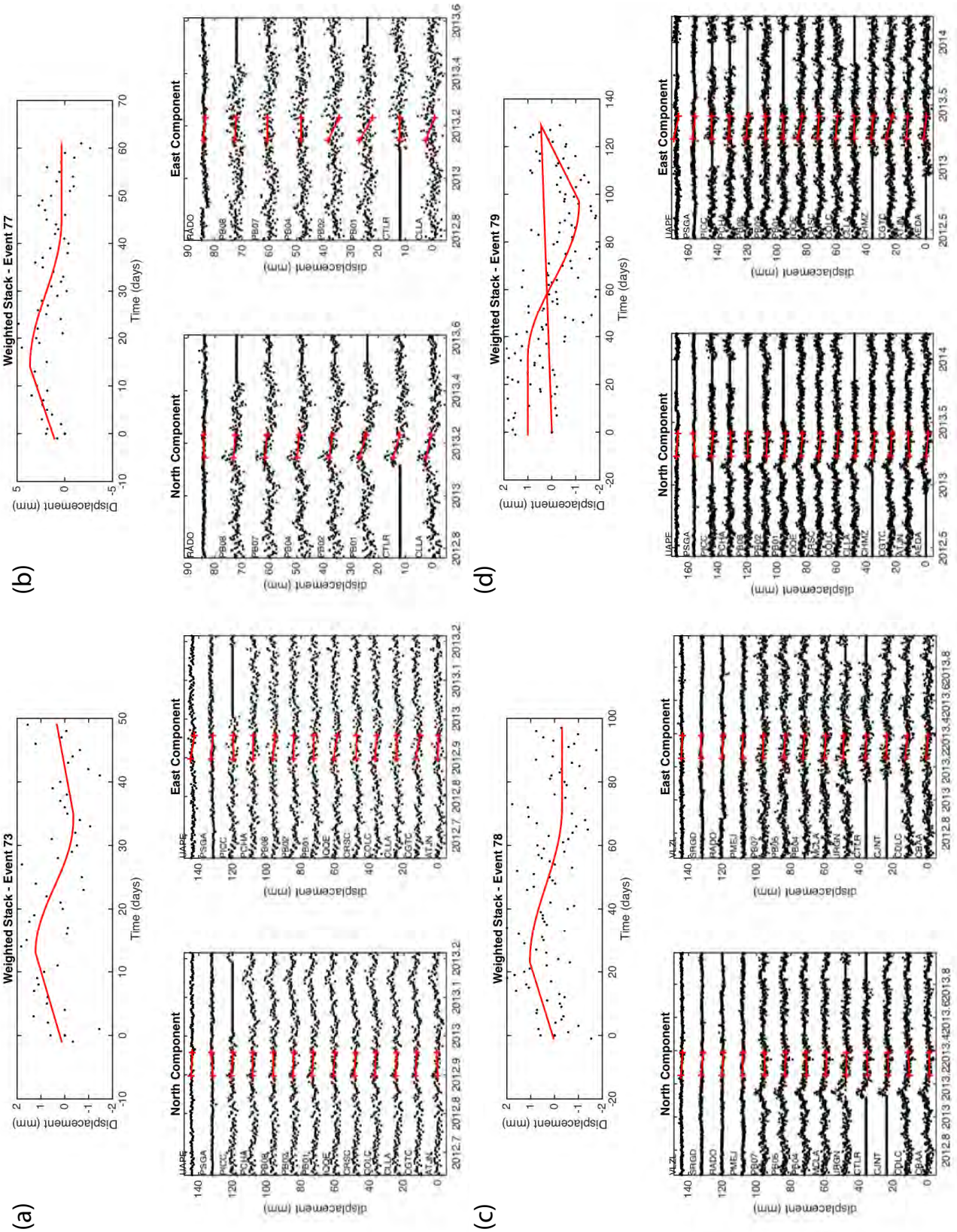

Figure 6.A.9: Same caption as in Figure 6.11 but for events 73, 77, 78 and 79.

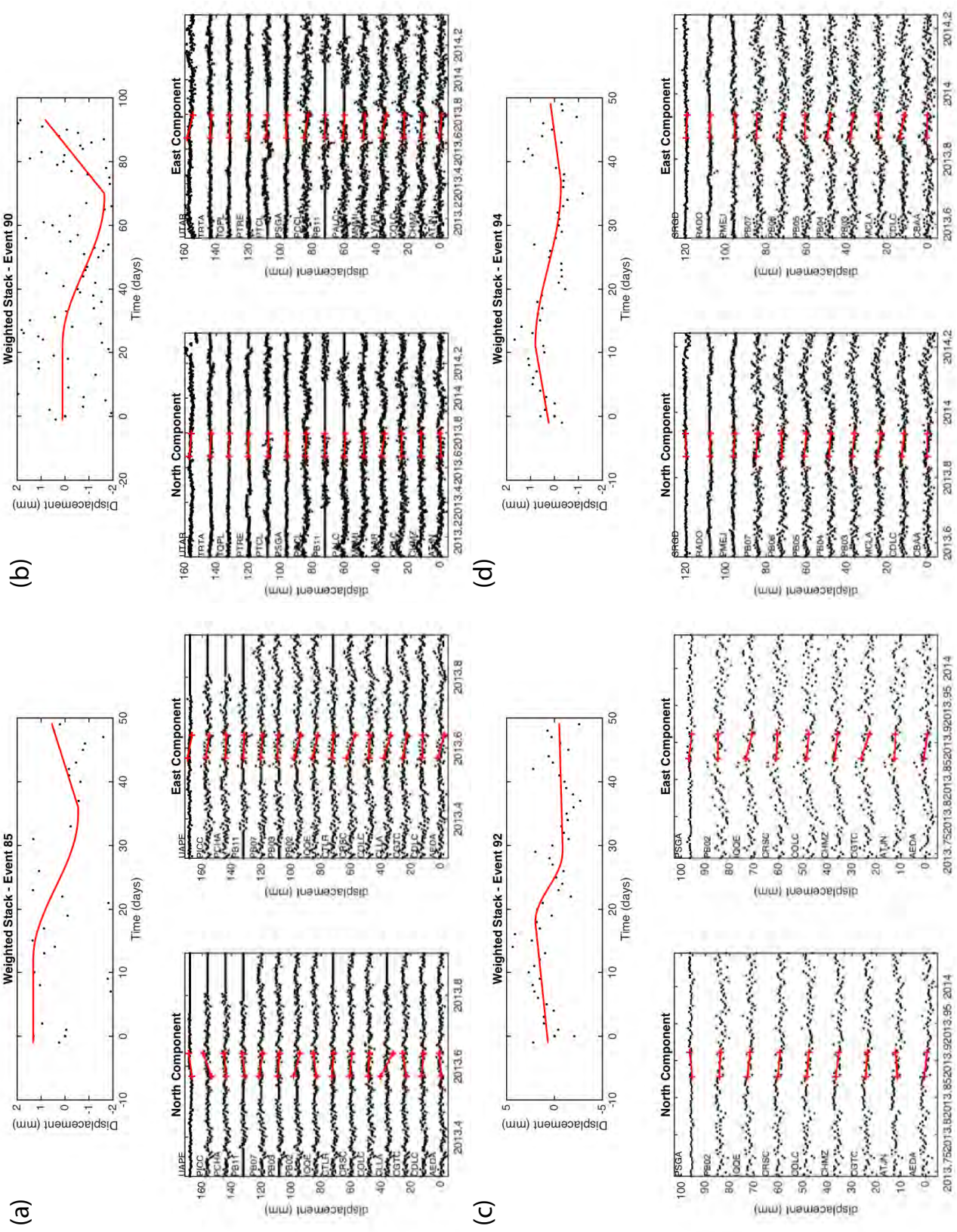

Figure 6.A.10: Same caption as in Figure 6.11 but for events 85, 90, 92 and 94.

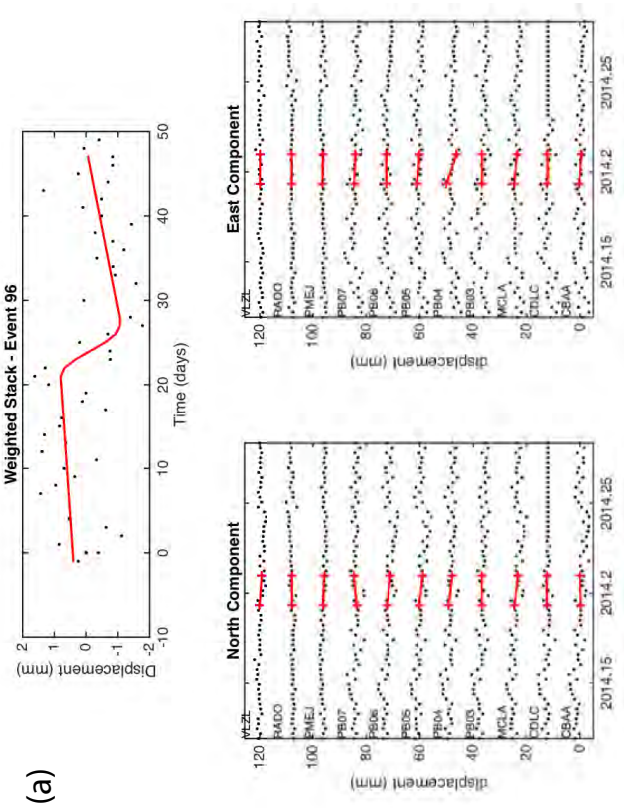

Figure 6.A.11: Same caption as in Figure 6.11 but for event 96.

Chapter 7

An 8 month slow slip event triggers progressive nucleation of the 2014 Chile megathrust

Paper published: Socquet, A., Pina-Valdes, J., Jara, J., Cotton, F., Walpersdorf, A., Cotte, N., Specht, S., Ortega-Culaciatti, F., Carrizo, D. & Norabuena, E. (2017). Geophysical Research Letters, 44(9), 4046–4053, doi:10.1002/2017GL073023. [1]

My contribution in this chapter consisted in: perform the GPS processing and reference frame analysis, calculation of mean velocity for GPS and static displacement for the differents periods analyzed and the participation in the discussion of this paper.

7.1 Abstract

The mechanisms leading to large earthquakes are poorly understood and documented. Here, we characterize the long-term precursory phase of the April 1st 2014 M_w 8.1 North Chile megathrust. We show that a group of coastal GPS stations accelerated westward eight months before the mainshock, corresponding to a M_w 6.5 slow slip event on the subduction interface, 80% of which was aseismic. Concurrent interface foreshocks underwent a diminution of their radiation at high frequency, as shown by the temporal evolution of Fourier spectra and residuals with respect to ground motions predicted by recent subduction models. Such ground-motions change suggests that, in response to the slow sliding of the subduction interface, seismic ruptures are progressively becoming smoother and/or slower. The gradual propagation of seismic ruptures beyond seismic asperities into surrounding metastable areas could explain these observations, and might be the precursory mechanism eventually leading to the mainshock.

[1] Supporting Information of this work can be found in the Appendix at the end of this Chapter.

7.2 Introduction

Some earthquakes have been preceded by an intense foreshock activity [*Bouchon et al.*, 2013; *Schurr et al.*, 2014; *Ruiz et al.*, 2014; *Lay et al.*, 2014; *Bedford et al.*, 2015; *Cesca et al.*, 2016; *Kato et al.*, 2016; *Meng et al.*, 2015; *Hasegawa and Yoshida*, 2015; *Kato et al.*, 2012; *Ozawa et al.*, 2012; *Sato et al.*, 2013; *Bouchon et al.*, 2011] raising the possibility that earthquake forecasting may be achieved through a better understanding of precursory mechanisms. Two concurrent models have been proposed to explain the initiation of seismic rupture [*Dodge et al.*, 1996]. A first model assumes that the accelerated moment release observed before large earthquakes [*Bowman and King*, 2001] is triggered by a slow slip event on the fault interface [*Bouchon et al.*, 2013; *Ruiz et al.*, 2014; *Dodge et al.*, 1996]. Alternatively a slow cascade of failures eventually may trigger the mainshock [*Dodge et al.*, 1996].

The precursory phase of earthquakes is most usually studied using seismological data, which is readily available in some regions. Because of limited in-situ monitoring combined with lower detection thresholds, geodetic data is less commonly used to study earthquake precursors. Therefore, the link between foreshock activity and associated deformation transients has never been directly established for periods exceeding a few weeks, although it has been observed and suggested ([*Obara and Kato*, 2016] and references therein).

The M_w 8.1 2014 Iquique earthquake occurred within the North Chile seismic gap, which had not experienced a megathrust rupture since 1877 [*Béjar-Pizarro et al.*, 2013; *Métois et al.*, 2016]. The earthquake ruptured a ∼150 km long portion of the subduction zone [*Schurr et al.*, 2014; *Ruiz et al.*, 2014], in an area that was partially locked before the earthquake [*Béjar-Pizarro et al.*, 2013; *Métois et al.*, 2016]. The earthquake was preceded by a series of earthquake swarms beginning in July 2013 [*Schurr et al.*, 2014; *Ruiz et al.*, 2014].

Given the presence of detailed seismic and geodetic monitoring of the Chilean subduction zone, this earthquake is an excellent case to monitor the precursory seismic activity and associated deformation. Previous studies focused mostly on the twenty days immediately preceding the earthquake when a strong transient signal occurred [*Schurr et al.*, 2014; *Ruiz et al.*, 2014; *Lay et al.*, 2014; *Bedford et al.*, 2015; *Cesca et al.*, 2016]. Nevertheless a debate remains on the mechanisms leading to this foreshock activity, notably on the existence or not of aseismic slip preceding the earthquake. Apart from the study of the foreshock sequence [*Schurr et al.*, 2014; *Ruiz et al.*, 2014; *Lay et al.*, 2014; *Bedford et al.*, 2015; *Cesca et al.*, 2016; *Kato et al.*, 2016; *Meng et al.*, 2015], very little is known about any potential long-term precursors, in particular in terms of deformation.

Here we use geodetic and seismological observations to document the precursory deformation and foreshock frequency content for the two years preceding the Iquique earthquake.

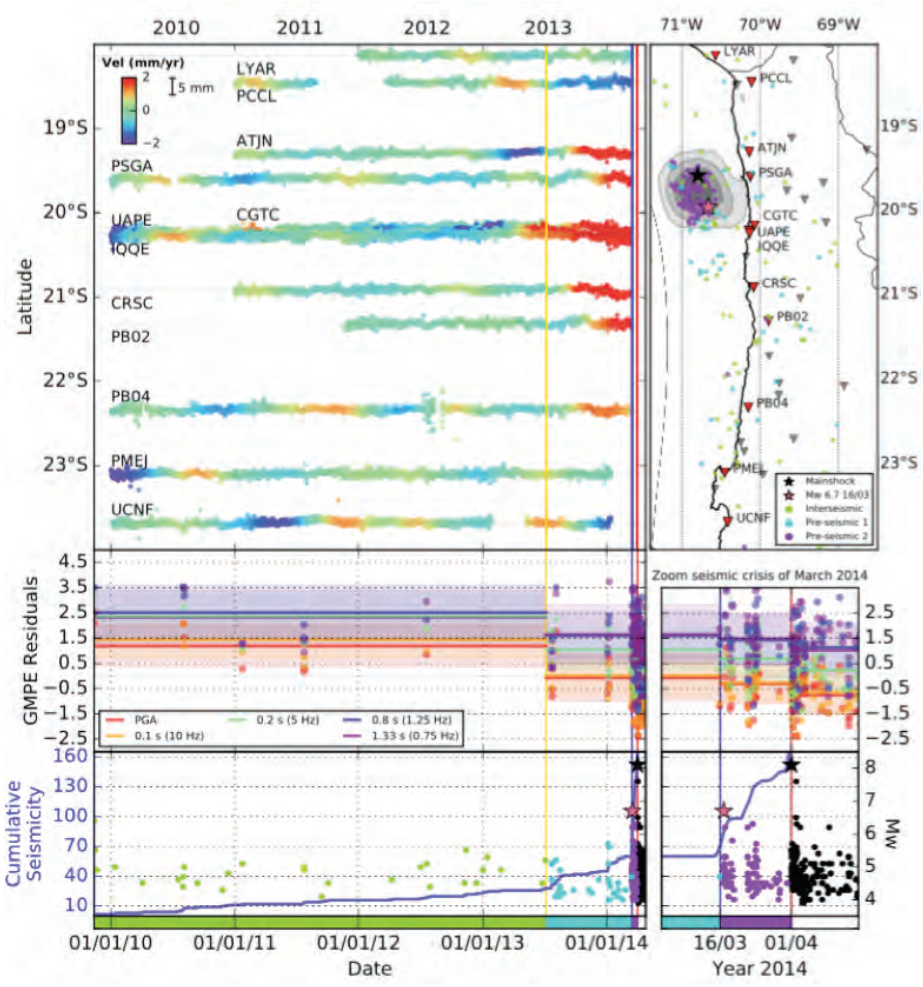

Figure 7.1: Pre-seismic ground deformation and foreshock frequency content over a four–year period, before the April 1st 2014 megathrust in North Chile. Top right: Map of seismicity: foreshock activity color-coded by periods, epicenters of Mw8.1 mainshock and M_w 6.7 foreshock are indicated by black and pink stars, M_w 8.1 slip distribution with 1-meter contours. Triangles indicate the location of GPS stations, the red ones being stations whose time series are shown to the left. Top left: Trench perpendicular, detrended time series of coastal cGPS, sorted by latitude. Colors show the variation of average GPS velocities computed in 6-month sliding windows. Center left: Frequency content evolution of interface foreshocks. Lines show average values of normalized residuals with respect to GMPE model [*Abrahamson et al.*, 2016] at high (reddish) and low (bluish) frequencies computed for each time-period. Standard deviation of the model is shown by shaded colors, while dots show single earthquakes residuals. Bottom left: Foreshock activity over time (dots). Blue curve shows the cumulative number of earthquakes. Red, blue and yellow vertical lines separate the 3 pre-seismic periods, and depict respectively the M_w 8.1 mainshock on 2014/04/01, the M_w 6.7 foreshock of 2014/03/16 that is followed by an increase of seismicity rate two weeks before the mainshock, and the July 2013 swarm.

7.3 Data and Methods

GPS data from several networks monitoring the North Chile subduction (IPOC, LIA Montessus de Ballore, ISTerre, Caltech Andean Observatory, IGS) have been processed in double differences, including tropospheric delays and gradients [*Boehm et al.*, 2006], and mapped into the ITRF 2008 [*Altamimi et al.*, 2011] (see supporting information for further details). The trend, as well as seasonal signals and common modes were removed from the time series. In order to study the long term transient in our time series, we excluded data after March 15th, 2014 (when a strong preseismic

signal occurred), and then computed the average velocity variations, by fitting a linear regression in a six-month sliding window of the detrended and de-noised time-series (Figure 7.1). In a second step, we compute the displacement during two preseismic periods (preseismic 1: July 2013- March 13th 2014, preseismic 2: March 14th 2014-March 31st 2014), by taking as a reference the mean interseismic loading trend before July 2013 (Figures 7.B.2 and 7.B.3).

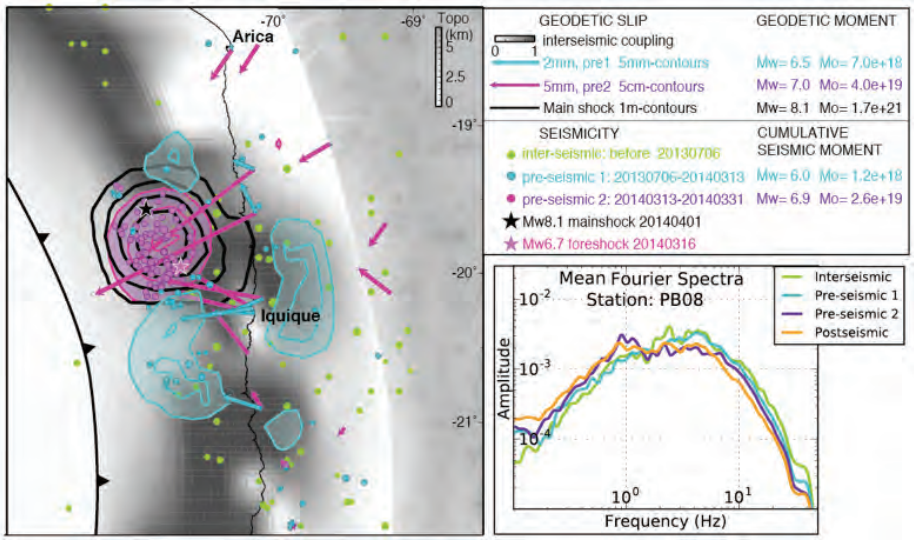

Figure 7.2: Left: Long- and short-term slip events (in blue and purple respectively), preceding the M_w 8.1 mainshock, superimposed on the interseismic coupling distribution [*Métois et al.*, 2016] in gray, and the co-seismic slip 1 m contours in black. Foreshock seismic activity for the same periods is also shown (in blue, purple and green, $M_w > 4$). Epicenters of the main shock and the M_w 6.7 foreshock are shown as black and pink stars. Right Inset: Mean Fourier spectra computed for interface earthquakes ($5.1 < M_w < 5.2$) grouped into 4 different time periods: interseismic in green, pre-seismic 1 in cyan, pre-seismic 2 in purple, and post-seismic in orange. Station PB08 being located at an even distance of the earthquakes studied, the computed variations in Fourier spectra shapes should be unaffected by variations in attenuation, but instead characterize earthquake's source.

The surface deformation fields were then inverted to retrieve the distribution of slip on the subduction interface (Figure 7.2), by discretizing it as a series of dislocations buried in a layered elastic half space [*Wang et al.*, 2003b]. A Laplacian smoothing has been applied; the best compromise between model roughness and data – model misfit has been chosen [*Jónsson et al.*, 2002]. The power of our data to constrain the slip on the interface [*Loveless and Meade*, 2011] is high from 15 km depth to more than 70 km depth in general (Figures 7.B.4-7.B.6). Although the details of slip distributions can vary from one inversion to the other, the estimated geodetic moment of pre-seismic slow slip events vary within less than 10% (Figure 7.B.7).

To complement the geodetic analysis, we analyzed the frequency content of interface seismicity. The interface seismicity catalog (Figure 7.B.9) was compiled using the GEOFON moment tensor catalog and the Global CMT catalog. We use a data driven algorithm to automatically determine focal mechanism clusters with similar Style-of-Faulting (strike, rake, and dip, Figure 7.B.10).

The horizontal response and Fourier spectra of interface earthquakes were computed from the

acceleration records of stations belonging to the IPOC network (Figure 7.B.9). The raw acceleration records were demeaned, tapered and a zero pad has been applied at the beginning and the end before being used to compute the spectra [*Boore et al.*, 2012; *Chiou et al.*, 2008]. The response spectra, were also computed for each horizontal component of the records following the *Nigam and Jennings* [1969] method with a damping of 5%. Finally, both Fourier and response horizontal spectra were computed as the geometrical mean of the two horizontal response spectra at each station. Fourier source spectra depend on source, propagations and site effects. Also, there is then a need to deconvolve the records from propagation and site properties to analyze earthquake source-properties. In order to compare the shape of Fourier spectra during the different time span studied, we selected three IPOC stations located at equal distance from the earthquakes swarm to get rid of the attenuation effects, and performed our analysis on earthquakes within a 0.1 magnitude range (Figure 7.B.11 and 7.2 right inset).

Second, we compared the measured ground accelerations, at different frequencies, with the response spectra predicted by the recent Ground Motion Prediction Equation (GMPE's) developed for subduction interface earthquakes by *Abrahamson et al.* [2016]. *Abrahamson et al.* [2016] model is recognized as one of the leading models to predict ground-motions in subduction areas and has been recently selected for the Global Earthquake Model [*Stewart et al.*, 2015]. The analysis of the obtained residuals confirmed that this model is well suited for our data set (see supplementary information for details). Between-event residuals were computed, for each frequency (0.75 Hz, 1 Hz, 1.25 Hz, 5 Hz, 10 Hz and PGA) and each earthquake, as the difference between the median of the observations of the given earthquake and the median of the model *Abrahamson and Youngs* [1992]. The Ground Motion Prediction Equations is acting here as a backbone model which takes into account first order magnitude and propagation effects. The analysis of relative time and spatial variations of between-event residuals allow us to compare the source-effects of earthquakes with various magnitude and locations [*Strasser et al.*, 2010; *Al Atik et al.*, 2010; *Youngs et al.*, 1995]. It has been shown that response between-event residuals are fully correlated with "classical" Fourier stress-drops [*Bindi et al.*, 2007], so there is no information lost using Response spectra and GMPE's compared to a more classical Stress-drop analysis. The between events residuals were then organized as a function of time, space and magnitude, in order to represent their variations and temporal evolution during the different periods before or after the mainshock (Figure 7.3, Figure 7.B.15).

7.4 Results

7.4.1 Precursory slow slip and associated seismicity

We detected a westward acceleration of some permanent GPS stations with respect to the average interseismic velocity (Figure 7.1). This acceleration begins ∼8 months before the mainshock, and affects mostly coastal stations located within an area 100 km south of the M_w 8.1 source, which was also affected by foreshock seismicity during the same period (Figure 7.1, blue dots). For comparison, during the preceding interseismic period, the seismicity is evenly distributed within the deeper part of the seismogenic zone (green dots on Figures 7.1 and 7.2). Inversion of these 8-month preseismic

displacements (from July 2013 to mid-March 2014) suggests that a slow slip event occurred on the subduction interface (Figure 7.2, blue contours), surrounding the mainshock slip patch. South of the mainshock, the slow slip occurs in a zone of low coupling during the interseismic period [*Métois et al.*, 2016], while it rather affects areas characterized by intermediate locking downdip and north of the mainshock. The geodetic precursor is collocated with long-term foreshock activity (Figure 7.2, blue dots). The comparison between geodesy and seismology shows that this long-term pre-seismic signal is at least 80% aseismic in nature; the cumulative seismic moment release (1.2 $\times$ 10^{18} Nm) representing 17 to 19% of the slip derived from GPS observations (6.4 to 7.0 $\times$ 10^{18} Nm).

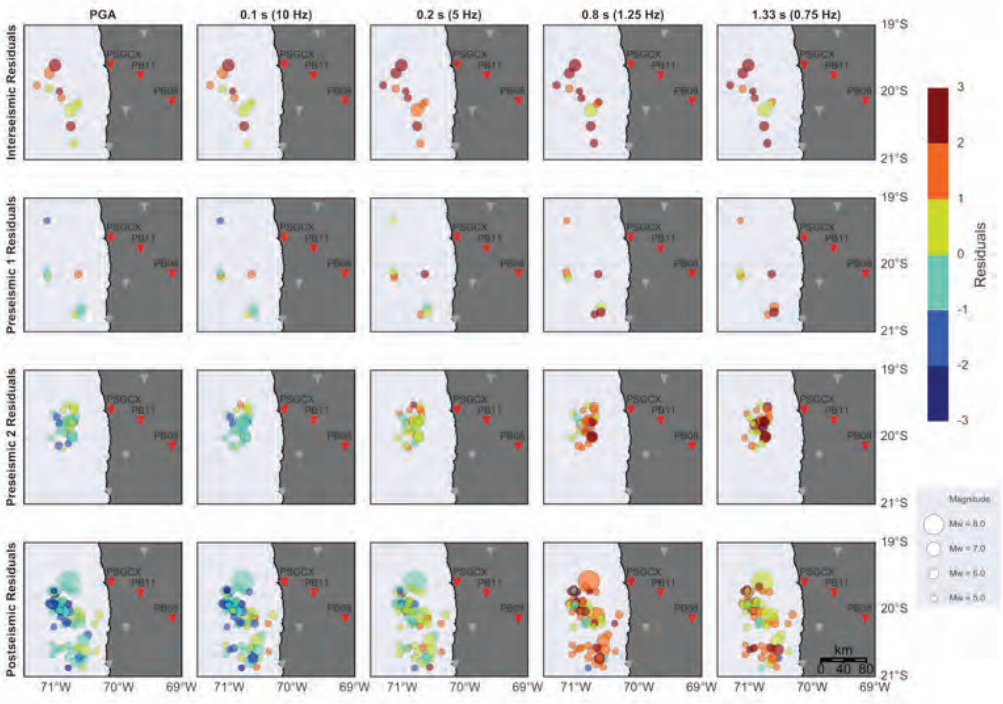

Figure 7.3: Time-space evolution of between-event residuals at the different frequency values shown in figure 1 (mid-panel). Residuals are normalized by the standard deviation of the GMPE model. Therefore average temporal changes can be considered significant from one standard deviation.

On March 16th, 2014, a M_w 6.7 intraplate earthquake [*Cesca et al.*, 2016] occurred two weeks before the mainshock, north of the creeping area (pink star, Figure 7.2). This foreshock is the largest of the whole sequence. It is followed by an abrupt increase of the seismicity rate and associated b-value [*Schurr et al.*, 2014], some of them in the upper plate, and most of them on the subduction interface [*Cesca et al.*, 2016], affecting the area that later ruptured during the M_w 8.1 megathrust. During this fifteen-day preseismic period, GPS stations were affected by a large deformation transient [*Ruiz et al.*, 2014] (Figure 7.2). This preseismic slip measured by geodesy resembles the one released seismically: the location and shape of geodetic slip mimics the spatial distribution of epicenters (Figure 7.2, purple contours and dots) [*Schurr et al.*, 2014], while the seismic moment is 65-67% of the geodetic moment (the remaining 33-35% is aseismic).

7.4.2 Evolution of interface earthquakes ground-motions

To complement these findings, we analyzed the frequency content of interface seismicity. Mean Fourier spectra at stations equidistant to the seismic crisis events show a consistent temporal decrease in high frequencies from interseismic to pre-seismic, and eventually post-seismic periods (Figures 7.2 and B11).

The comparison of the measured accelerations for interface earthquakes with respect to the ground-motion model [*Abrahamson et al.*, 2016] provides an independent assessment of ground-motion temporal variations. The time, space and magnitude dependencies of between event residuals have been analyzed in order to search for a potential evolution of the source characteristic (Figures 7.3 and B15). Measured residuals do not depend on earthquakes magnitude (as expected given the fact that the ground-motion predictive equation acts as a backbone model correcting for magnitude and propagation effects). However, at frequencies of 5Hz and above, a clear clustering of between-event residuals as a function of their time of occurrence is observed (Figure 7.B.15), indicating a diminution of high-frequency energy release from interseismic period to pre-seismic period and later. Also, the temporal evolution of residuals differs from one frequency band to the other: at frequencies below 1.25 Hz residuals remain more or less constant with time, while at higher frequencies (5 Hz and above) residuals decrease between interseismic period to pre-seismic and post-seismic periods (Figures 7.1, 7.2 and 7.3). During the second preseismic period (i.e. during the 15 days between the largest foreshock and the mainshock) and the post-seismic period, interface earthquakes show no significant change of their energy radiation.

These two independent assessments of interface earthquake ground-motions indicate a reduction of the high frequency radiation, which is coincident with the preseismic acceleration in GPS velocities eight months before the mainshock.

7.5 Discussion

Our results indicate that a geodetic precursor occurred simultaneously with an identified increase in the seismicity rate (Figure 7.1, bottom panel), and a decrease in the b-value [*Schurr et al.*, 2014]. Such observations can be modeled as an aseismic slow slip on the subduction interface collocated with long-term foreshock activity (Figure 7.2, blue dots). This is consistent with the slow sliding of conditionally stable area on the subduction interface, spread out by sparse, small seismic asperities [*Hetland and Simons*, 2010], the seismic activity arising from the response of seismic asperities to the aseismic forcing.

Seismic radiation spectra of interface events have been proposed, on average, to be representative of the different frictional regimes of a subduction interface [*Scholz*, 1998; *Lay et al.*, 2012]; regions of unstable sliding can have large slip but generate modest amounts of short-period radiation upon failure, while smaller patchy regions of unstable sliding produce coherent short-period radiation when

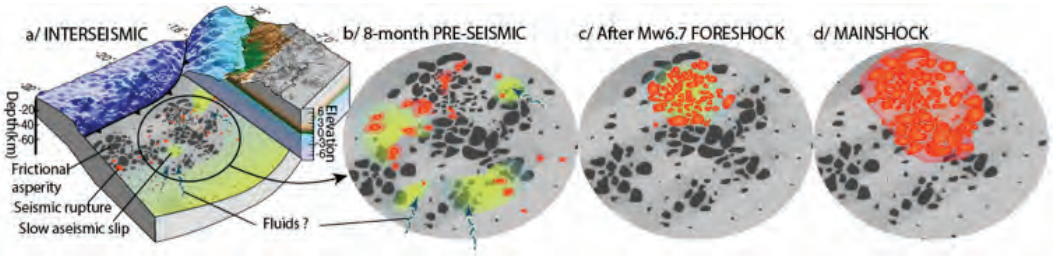

Figure 7.4: Schematic interpretation of the precursory phase of M_w 8.1 Earthquake. a) During the interseismic phase, the subduction interface slowly creeps (yellow) at depth and in low coupling areas, where frictional asperities are sparse. The rupture of small frictional asperities resisting this slow slip generates the background seismicity (red). b) Eight months before the mainshock, slow slip accelerates in the seismogenic zone (maybe facilitated by fluids migration), around the area ruptured by the mainshock. Seismic ruptures start to propagate into the conditionally stable area surrounding the frictional asperities (light red). c) After the largest foreshock on March 16th (M_w 6.7), slow slip goes on, but is superimposed onto a rough seismic signal generated by the post-seismic cascade. d) On April 1st 2014, M_w 8.1 earthquake ruptures a large portion of the subduction interface, breaking both frictional asperities (red) and surrounding conditionally stable areas (light red).

loaded to failure by creep of conditionally stable surrounding regions [*Lay et al.*, 2012; *Meng et al.*, 2015].

The reduction in high-frequency radiated energy often indicates a reduction in earthquake stress-drop (i.e. a decrease of corner frequency). This phenomenon might be explained either by (a) smoother ruptures [*Radiguet et al.*, 2009], (b) lower rupture velocities, or (c) increasing high-frequency attenuation. Given the foreshocks sequence does not migrate through time, a change in attenuation characteristics over such a short period of time seems unlikely. Rapid fluid migration within the fault zone may change the attenuation locally, within the few hundred meters of the damaged fault zone (high pore fluid pressures are accompanied by very low Qs/Qp ratios — 0.1 to 0.4 for saturated basalt that are primarily due to increased shear attenuation [*Tompkins and Christensen*, 2001]. However, once integrated over the whole path followed by seismic waves through continental crust (a few hundred meters with increased attenuation, versus tens of kilometers with no change), this local change in attenuation accounts for a minor part of the overall attenuation and only at large frequencies (higher than 15-20 Hz). It will be considered as part of the source, distance independent, high-frequency (kappa) attenuation. Therefore, the observed change of frequency content at 5-10 Hz rather seems related to a modification of the earthquake source parameters, such as a wider rupture area or slower rupture velocity. This is also compatible with the observed reduction in b-value during the precursory time period, implying an increasing proportion of large to small earthquakes. Such a decrease in b-value has been proposed as a precursor to major macro-failure [*Smith*, 1981]. Our observations suggest that a slow aseismic forcing that started eight months before the mainshock triggered an increased number of seismic events together with a modification of the earthquake frequency content, interpreted as a widening of rupture surfaces [*Lay et al.*, 2012]. This suggests a progressive expansion of failures into the conditionally stable areas surrounding small seismic asperities, in a mechanism that will eventually lead to the main rupture nucleation (Figure 7.4b).

Two weeks before the mainshock, the largest foreshock of the sequence triggered an increased

deformation, seismicity, and b-value. This seismicity, which is much more focused both spatially and temporally, might have been triggered by the M_w 6.7 foreshock that induced a significant increase of the Coulomb stress in the area. The seismicity and associated slow slip observed within the fifteen-days before the mainshock may therefore result from a regular aftershock sequence and associated afterslip following the M_w 6.7 event, overprinting the preexisting slow aseismic slip (Figure 7.4c).

On April 1st, 2014, the M_w 8.1 megathrust nucleates immediately north of the seismicity surge, in an area of increased stress resulting from adjacent preseismic slip. The maximum slip (Figure 7.2, black contours) occurs close to the area that started to slip before the mainshock (pink), slightly downdip associated foreshock activity (pink dots), including repeating earthquakes [*Meng et al.*, 2015]. However, the rupture extends deeper to areas that were fully locked during the interseismic period [*Métois et al.*, 2016]. To the south, the rupture stops abruptly when it reaches the metastable areas affected by the long-term aseismic precursor (blue).

7.6 Conclusions

These observations confirm that a long-term aseismic slip of the subduction interface led to the nucleation of the M_w 8.1 Iquique megathrust earthquake. During the interseismic period, the seismicity was evenly distributed within the deeper part of the seismogenic zone (green dots on Figures 7.1 and 7.2), and ruptured small frictional asperities in response to deep interplate aseismic sliding (Figure 7.4). Eight months before the mainshock, this slow sliding of plate interface started to accelerate within the seismogenic zone. South of the mainshock this precursory creep occurs in an area characterized by little interseismic coupling, while downdip and north of the mainshock, the slow slip affects more coupled areas (Figure 7.2) [*Métois et al.*, 2016], and may be seen as the slow rupture of locked patches surrounding the mainshock. Small seismic asperities scattered in this area ruptured repeatedly [*Meng et al.*, 2015; *Lay et al.*, 2012]. The change in the earthquake frequency content during the foreshock sequence (a reduction of the stress drop) suggests that seismic failures widen progressively, decelerate, and start to extend into the slowly sliding, conditionally stable areas surrounding frictional asperities. This process can be seen as the start of the precursory phase that will eventually lead to the megathrust rupture.

The simultaneous occurrence of slip acceleration, increased seismic activity and the slow decrease of the high frequency radiations of foreshocks may provide a way to detect the preparation of great earthquakes. Identifying aseismic slip combined with changes in associated earthquake spectra may therefore significantly help to mitigate seismic hazard at plate boundaries.

7.7 Acknowledgments

We are very grateful to Departamento de Geofísica de la Universidad de Chile (DGF) (www.dgf.uchile.cl), Centro Sismológico Nacional de Chile (CSN) (www.sismologia.cl), International Plate Boundary

Observatory Chile (IPOC) (http://geofon.gfz-potsdam.de/waveform), LIA “Montessus de Ballore" International Laboratory (www.lia-mb.net), Central Andean Tectonic Observatory Geodetic Array (CAnTO) (www.tectonics.caltech.edu), and Instituto Geofísico del Perú for making raw GPS and strong motion data available. This work has been supported by PNTS-2014-08, LabeX OSUG@2020, SMINGUE, IRD AO-Sud, and INSU-Aléas grants. J.P.V. and J.J. acknowledge support provided by CONICYT through “Becas Chile" PhD fellowships. F.O. acknowledges support from Proyecto Fondecyt 11140904 (CONICYT). The authors warmly thank J.M. Nocquet for making PYACS software available. Thank you to J. Hollingsworth for editing the English writing. This work benefited from fruitful discussion with PY. Bard, C. Beauval, D. Bindi, M. Bouchon, R. Bürgmann, M. Métois, G. Montalva, D. Marsan, and J. Ruiz among others.

Appendix

7.A Methods

7.A.1 cGPS data analysis

We used data from several cGPS networks spanning the whole central Andes subduction (IPOC, LIA Montessus de Ballore, ISTerre, and Caltech Andean Observatory), together with IGS stations. These cGPS data were analyzed in double differences, in two distinct regional subnetworks, plus a global network (Figure 7.B.1). The fifty stations available during the period 2000 - 2014 were used to design the first regional subnetwork. The second regional subnetwork includes 50 stations running from 2007 to 2014, 33 stations overlapping with the first subnetwork in order to ensure consistency between the subnetworks. The global network includes 99 IGS sites worldwide, 22 of them in South America, with 49 stations overlapping with the two regional subnetworks. 24-hour sessions were reduced to daily estimates of station positions using the GAMIT 10.5 software, choosing the ionosphere-free combination, and fixing the ambiguities to integer values. We use precise orbits from the International GNSS Service for Geodynamics, precise EOPs from the IERS bulletin B, IGS tables to describe the phase centers of the antennas, FES2004 ocean-tidal loading corrections, as well as atmospheric loading corrections (tidal and non-tidal). We estimated one tropospheric zenith delay parameter every two hours and one couple of horizontal tropospheric gradients per 24 h session, using the Vienna Mapping Function (VMF1) [*Boehm et al.*, 2006], to map the trophospheric delay in zenithal diraction, with a priori ZHD evaluated from pressure and temperature values from the VMF1 grids. Daily solutions and position time series are combined using PYACS software [*Nocquet J.M.*, 2015, *personal communication*] in a regional stabilisation approach. The results are mapped into ITRF 2008 reference frame [*Altamimi et al.*, 2011].

7.A.2 Time series analysis and identification of transient movements

Annual and semi-annual signals were removed from the obtained daily time series, as well as the long-term constant deformation associated with interseismic loading, by fitting a linear regression together with a pair of sinusoids terms. The remaining noise has been reduced by removing the common-mode, obtained by selecting stations located within a distance range of 50-500km from the source region (SJUA, ATIC, CHRA, PTCL, LYAR, UTAR, PCCL, PB02, PB04, MLCA, PB05, PMEJ, JRGN, UCNF, NZCA, AREQ, TORA, TQPL, DANC, TRTA, PALC, PTRE, MNMI, COLC, CHMZ, PB11, PCHA, PB08, PB01, PB07, PB03, CDLC, RADO, PB06, CBAA, VLZL, CJNT) and

by averaging their detrended signals. Then, in order to mitigate the residual loading signal present in our signal, we removed from each time series the mean annual residual seasonal movement computed between 2010 and 2013. This procedure reduced significantly the scatter in our time series. In order to study the long term transient in our time series, we excluded data after March 15th, 2014 (when a strong preseismic signal occurred), and then computed the average velocity variations, by fitting a linear regression in a six-month sliding window of the obtained detrended and de-noised time-series. The results indicate a velocity change in July 2013 (appr. eight months before the mainshock) at coastal stations located at 20.3°S close to the city of Iquique. This velocity change propagated bilaterally and reached stations located within a distance of appr. 100 km parallel to the strike of the subduction (parallel to the coastline). In a second step, we compute the average velocities by fitting a linear regression to the detrended cGPS time series on three different time periods before July 2013 (interseismic), July 2013- 13th March 2014 (preseismic 1), 14th March 2014-March 31st 2014 (preseismic 2) (Figures 7.B.2 and 7.B.3). Uncertainties on linear regressions correspond to standard deviation of one for each linear regression. Displacements for both pre-seismic periods have been obtained by multiplying each station velocity by the time span. For the preseismic period 1, we selected only stations showing a continuous time series since 2012, to avoid artifacts associated with jumps or data holes in the time series. For both preseismic periods, we discarded noisy time series generating the largest uncertainties in the displacement computation.

7.A.3 Slip distribution inversion and resolution

The surface deformation fields associated with the coseismic and preseismic phases were modeled using a dislocation buried in a layered elastic half space [*Wang et al.*, 2003b], taking Crust1.0 as a velocity model. The fault geometry was constrained by the trace of the trench at the surface. We assumed a uniform dip of 15° and a variable rake, so that the slip direction is parallel to the plate convergence (76°), and is taken constant at all patches.

The fault was discretized into an array of 24 × 11 elements, measuring approximately 15 × 15 km, although their size varies locally since the fault follows the trench geometry (Figures 7.B.4, 7.B.5 and 7.B.6). To solve for the slip distribution along the 264 fault patches, we used a least squares minimization with a non-negativity constraint on the slip. Slip was forced to zero at the edges of the fault. To limit oscillations of the solution, we applied smoothing by minimizing the second-order derivative of the fault slip. We determined the optimal solution roughness [*Jónsson et al.*, 2002] that was used in our final models searching for a compromise between the roughness and misfit of the solution. We estimate the sensitivity of our data set to unit displacements on each node of the grid by summing the horizontal deformation on the whole network after *Loveless and Meade* [2011]. The power of our data to constrain the coupling on the interface is high from 15 km depth to more than 70 km depth in general.

The coseismic offsets extracted from cGPS time series were used to invert for the coseismic slip (Figure 7.B.4). The roughness of the preferred co-seismic distribution is 0.04 cm/km for a RMS (L2-norm misfit) of 1.20 cm. The seismic moment is 1.7×10^{21} Nm, and corresponds to a Magnitude

8.1. The inverted slip distribution for pre-seismic period 2 (Figure 7.B.5) corresponds to a moment 3.9 $M_0 = \times 10^{19}$ Nm ($M_w = 7.0$) and a fit to the data with RMS = 1.3mm. The inverted slip distribution for pre-seismic period 1 (Figure 7.B.6) corresponds to a moment $M_0 = 7 \times 10^{18}$ ($M_w = 6.5$) and a fit to the data with RMS= 0.5 mm (Figure 7.B.7). Because we were able to estimate accurately the long term transient displacement on a subset of stations only, mostly located along the coast, the slip distribution for pre-seismic period 1 less well constrained than the co-seismic and pre-seismic period 2. However, the patches that are found to be slipping by our inversions are located in zones that are well constrained by our data (Figure 7.B.6). Depending on the smoothing applied to the model, the estimate of the geodetic moment of pre-seismic slow slip events (for periods 1 and 2) vary within less than 10% (Figure 7.B.7), and the main features of the slip distribution are quite stable whatever the smoothing applied (Figure 7.B.8).

7.B Appendix Figures

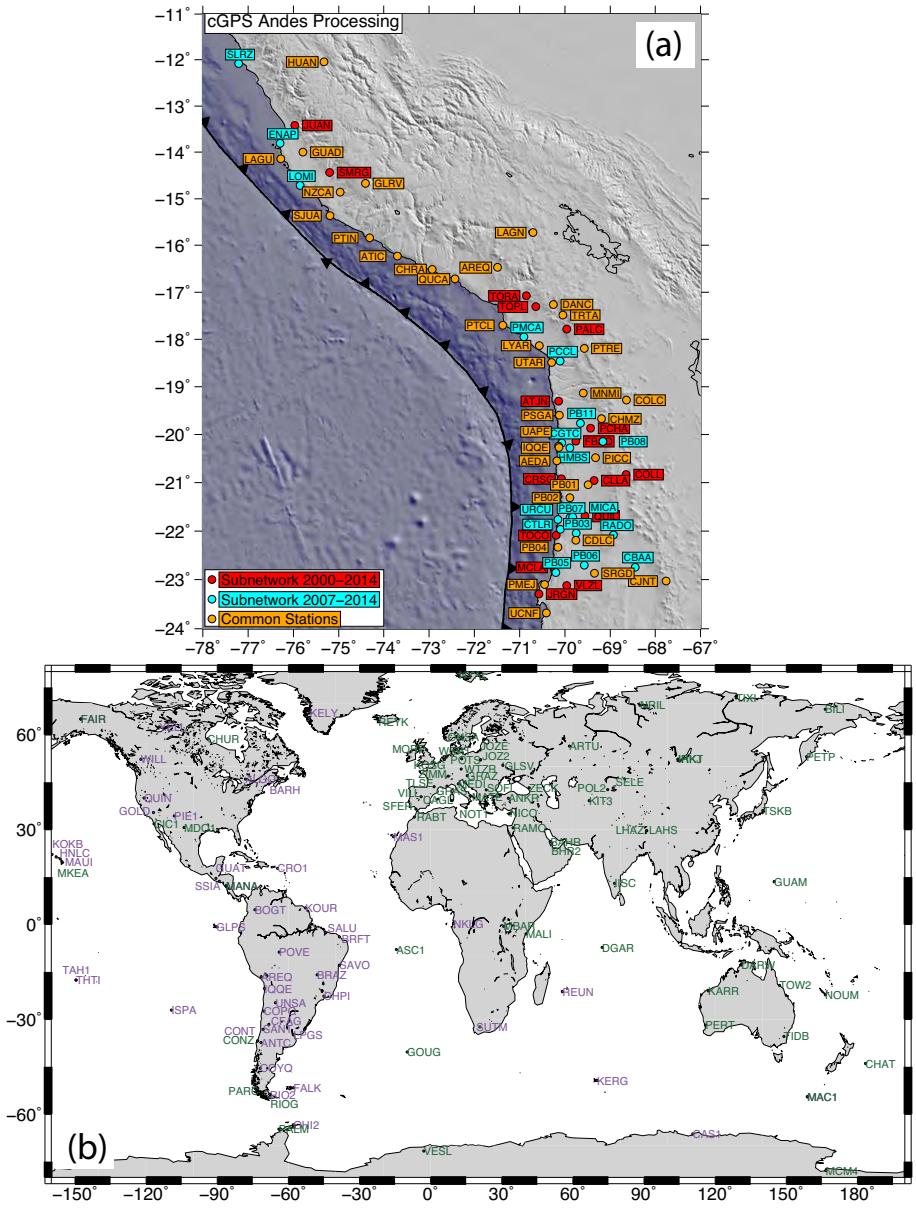

Figure 7.B.1: Map of the network used in this study, showing the three subnetworks (Andes 2000 – 2014, Andes 2007 – 2014 (a) , and the Global Network (b)), as well as the stations used for the reference frame computation. Green color in (b) indicates IGS stations included for global processing, while purple indicates IGS stations overlapping with the Andes subtnetworks.

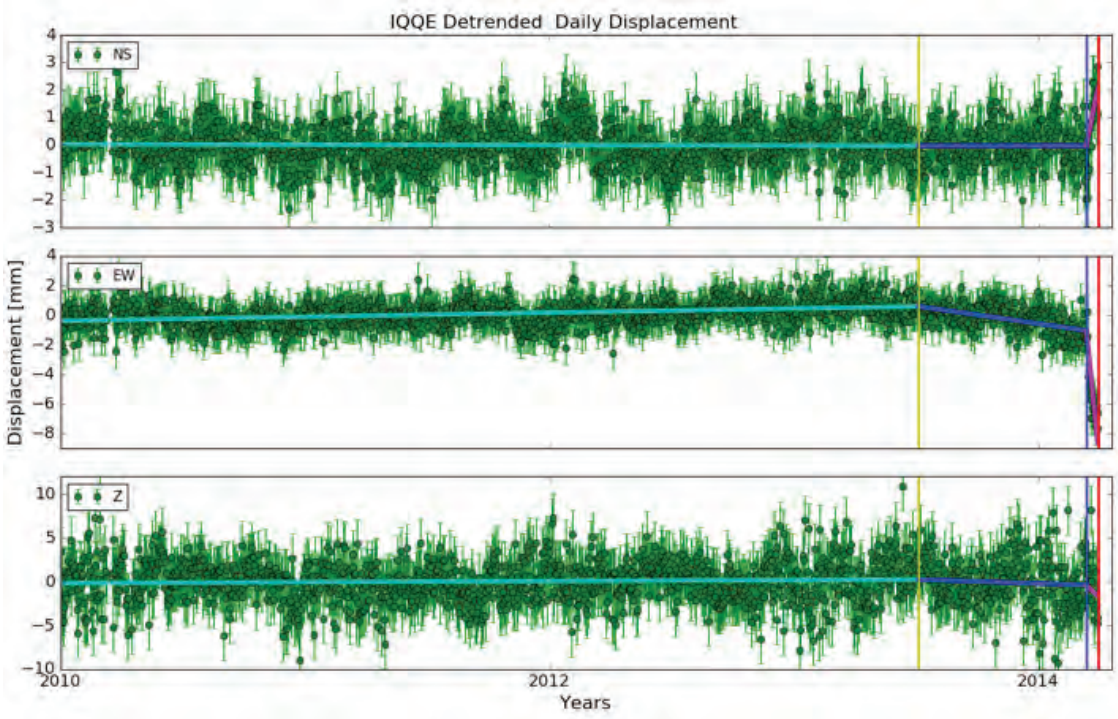

Figure 7.B.2: N, E, U detrended daily displacements for IQQE station since 2010. Vertical lines indicate the dates of the swarm of July 2013 (yellow), the M_w 6.7 foreshock on March 16th 2014 (blue) and the M_w 8.1 main shock on April 1st 2014 (red). Linear regressions for the three preseismic periods are shown.

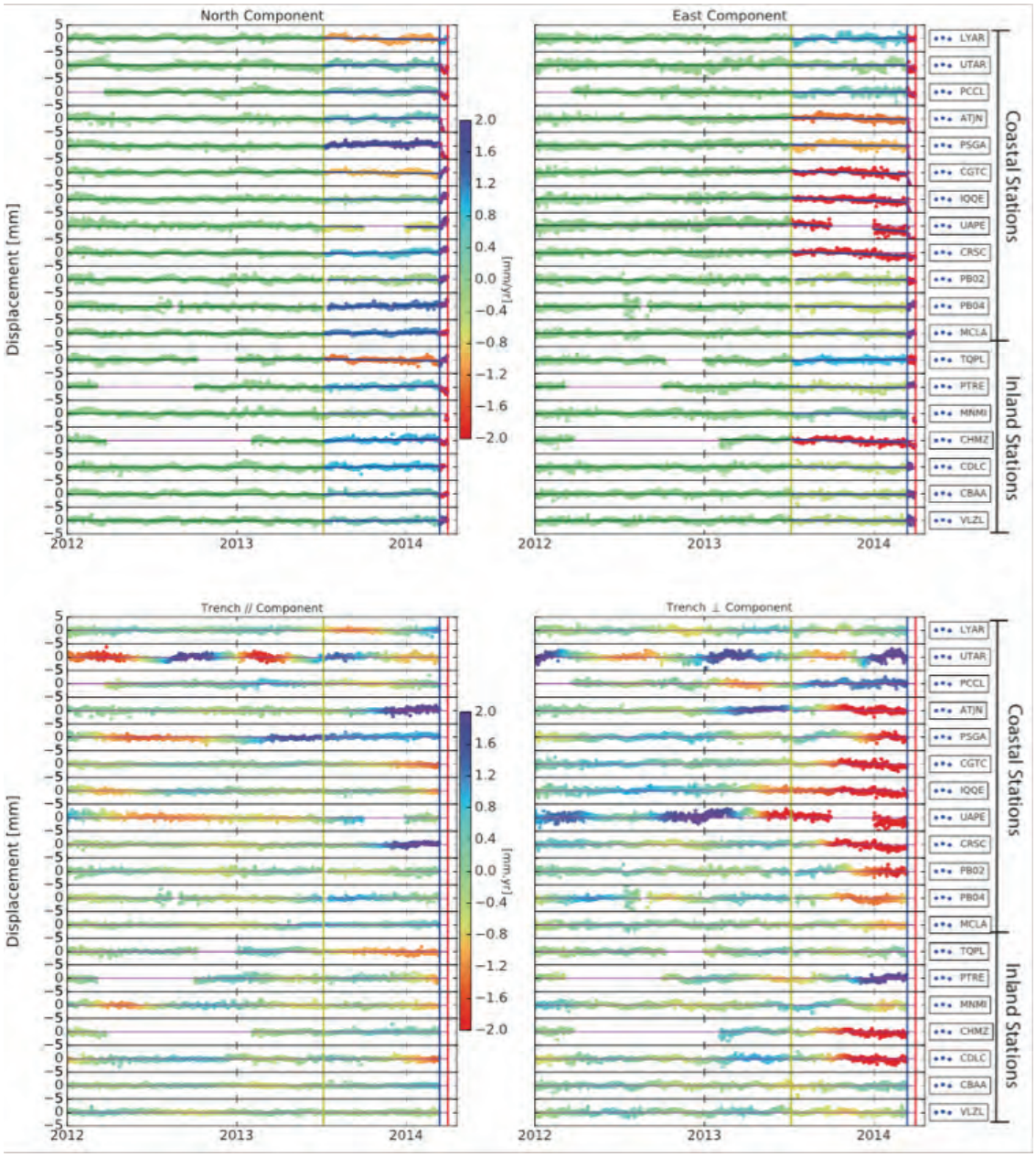

Figure 7.B.3: Detrended displacement time series for a selection of stations along the coast and inland. Bottom 2 panels: Colors, indicate the trench parallel (left panels) and trench perpendicular (right panels) velocities obtained by computing the average velocity over a six-month sliding window. Top 2 panels: Colors, indicate the N-S (left panels) and E-W (right panels) velocities obtained by fitting a linear regression on the displacement time series for the three preseismic periods.

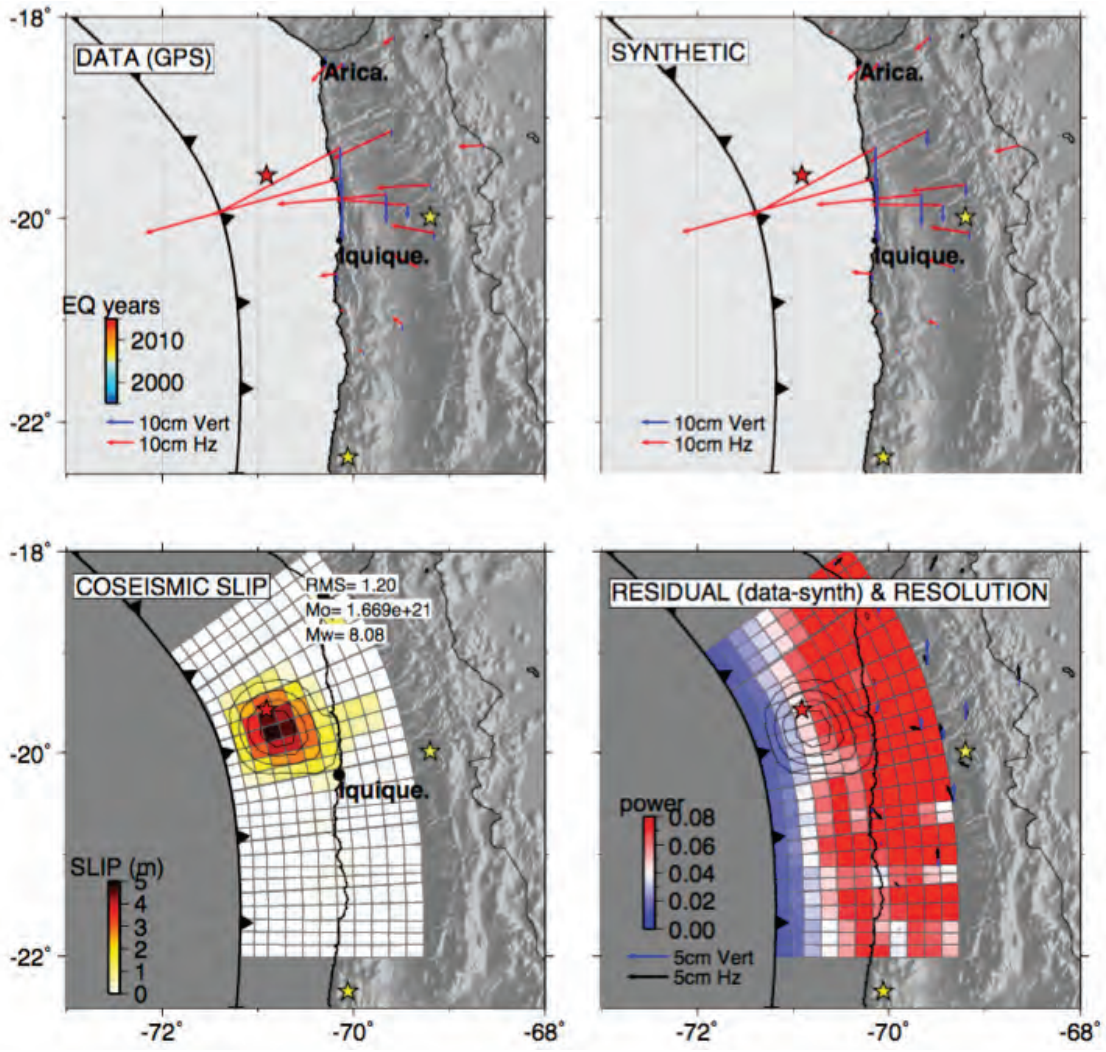

Figure 7.B.4: Co-seismic displacements (observed : top left, and modeled: top right), co-seismic slip distribution inverted from surface displacements (bottom left), residuals and power of GPS stations to constrain plate interface behavior (i.e., sum of the partial derivatives relating GPS displacement to unit slip [*Loveless and Meade*, 2011]) (bottom right). One-meter contours are drawn.

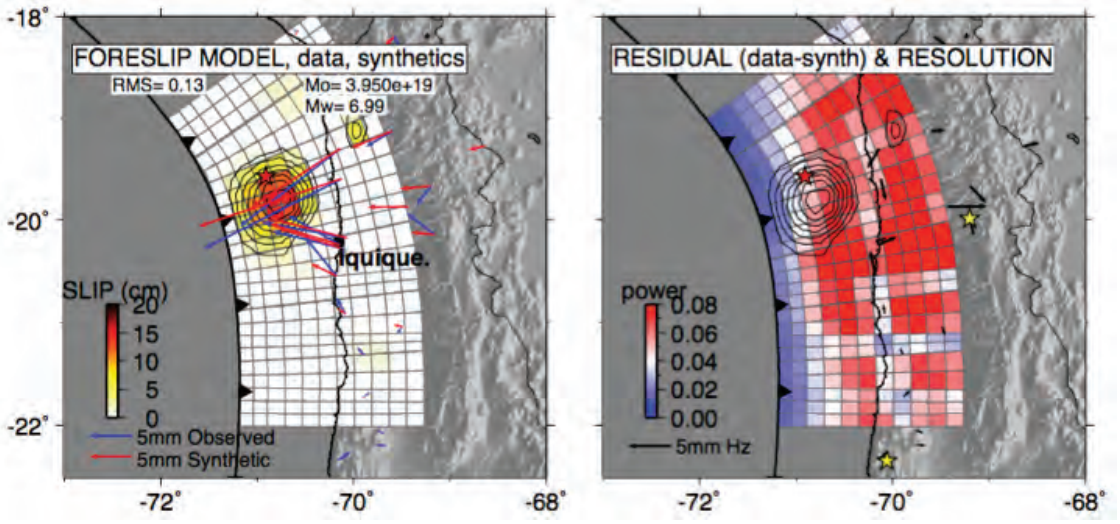

Figure 7.B.5: Left: Displacements (observed: blue, modeled: red) during preseismic period 2 (March 14th 2014 to March 31st 2014) and preseismic slip distribution for the two weeks preceding the main shock inverted from surface displacements, Right: residuals and resolution. Two-cm contours are drawn.

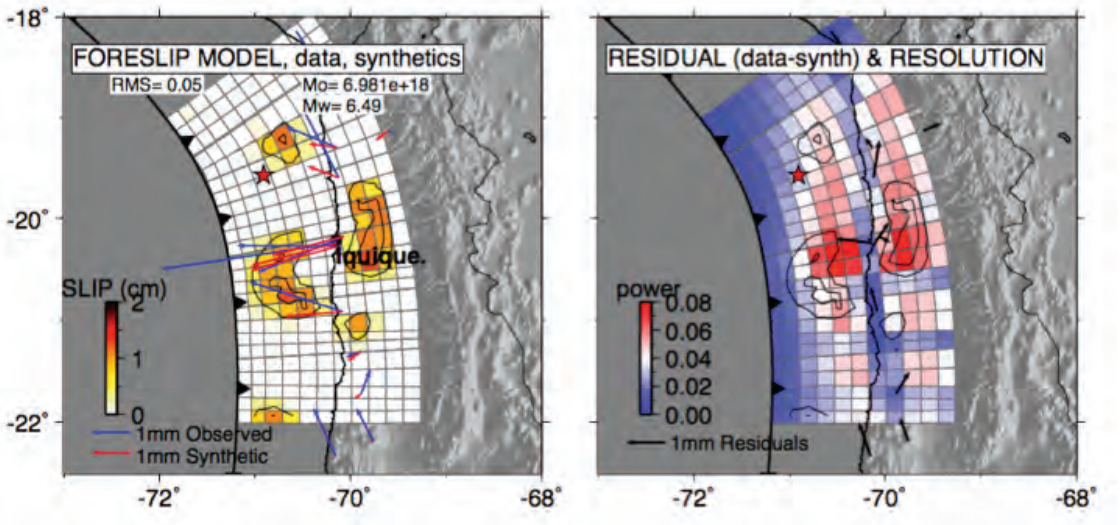

Figure 7.B.6: Left: Displacements (observed: blue, modeled: red) during preseismic period 1 (July 6th 2013 to March 13th 2014) and preseismic slip distribution for the two weeks preceding the main shock inverted from surface displacements, Right: residuals and resolution. Five-mm contours are drawn.

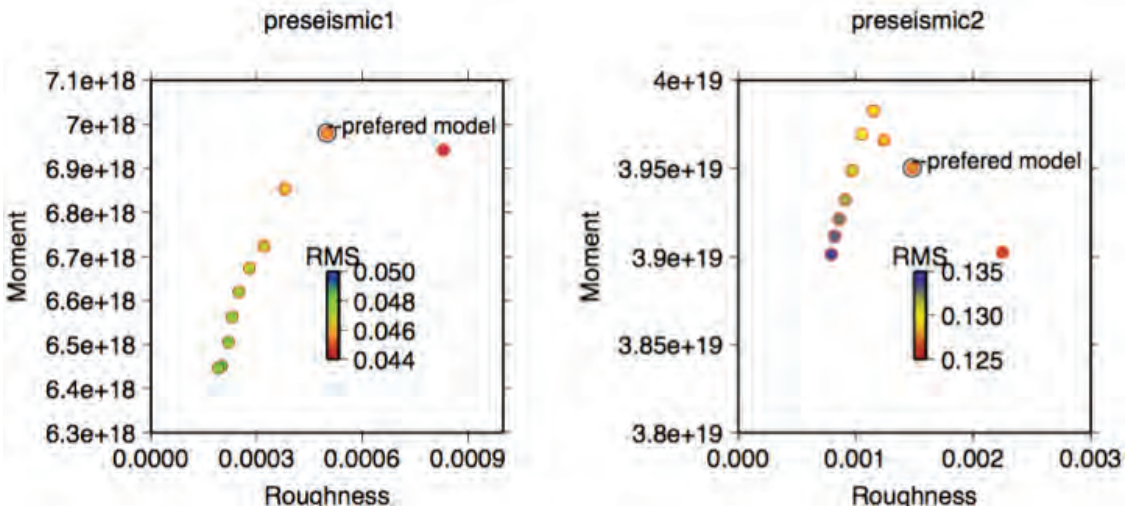

Figure 7.B.7: Geodetic moment as a function of the model roughness, for both preseismic models. Dots are color coded with the model – data misfit. The preferred model is chosen as a compromise between smoothness and RMS.

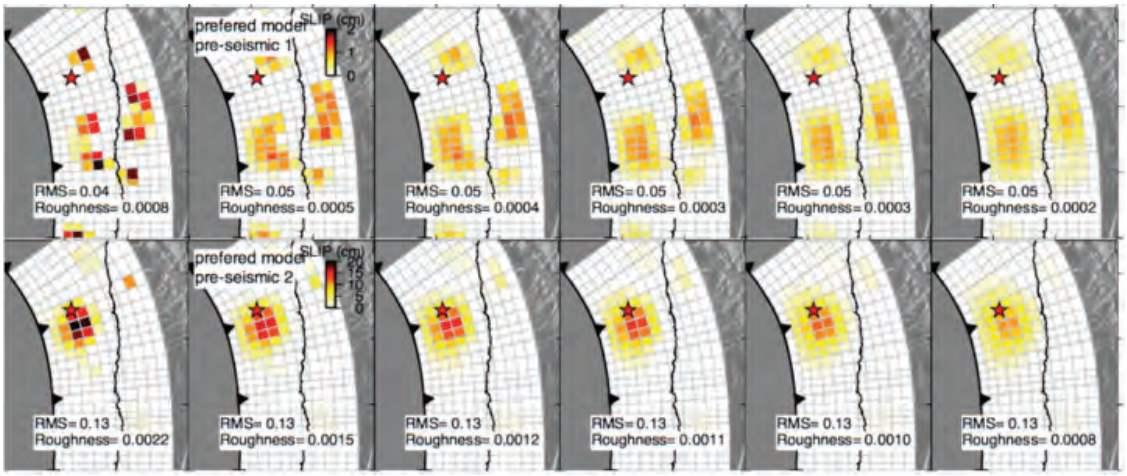

Figure 7.B.8: Pre-seismic slip distribution for different model roughnesses. Top: 8 months preseismic (july 2013 – mid-March 2014), Bottom: 15-day pre-seismic (Mid-March to End March 2014).

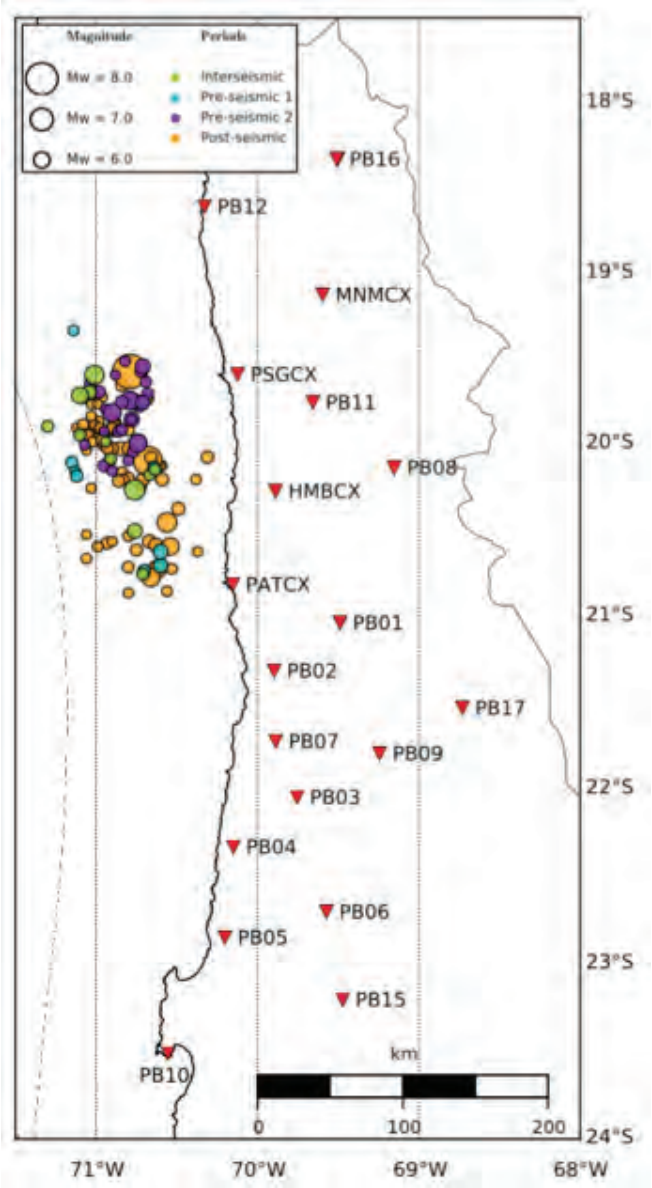

Figure 7.B.9: Map of the interface seismicity data set (dots colored as a function of the 4 periods defined in the paper), and network of IPOC accelerometric stations (red inverted triangles) used to perform earthquakes frequency content analysis. All these stations are installed on bedrock. Most of them are also colocated with GPS stations used in this paper.

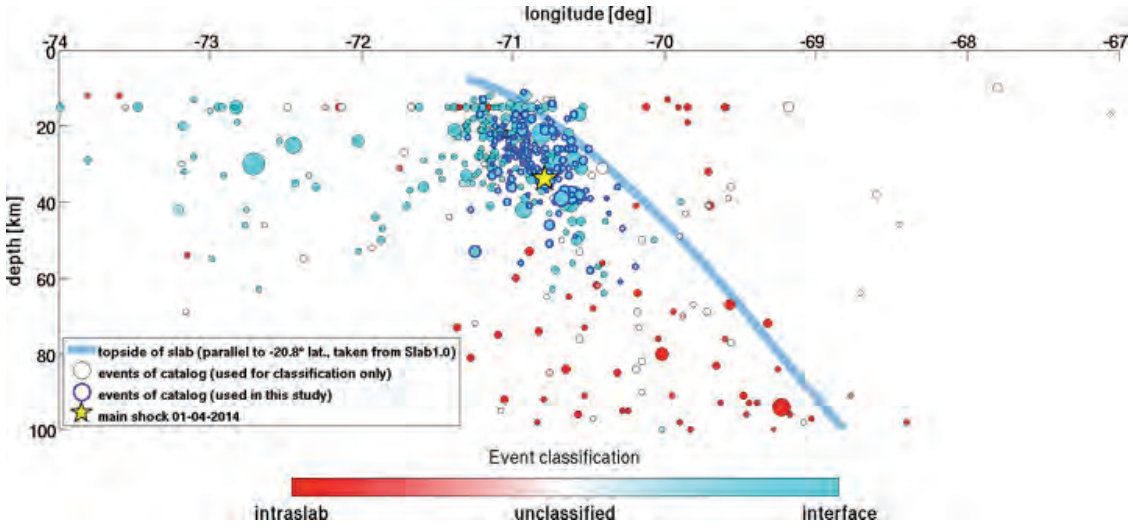

Figure 7.B.10: Cross section of IPOC catalogue of earthquakes in North Chile. Colored dots represents the classification of earthquakes (interface, unclassified or intraplate) as a function of their focal mechanism. The blue line represents the Slab1.0 subduction interface. The events used in this study (contoured in blue) have been selected as being interface events that occurred between January 2008 and June 2014.

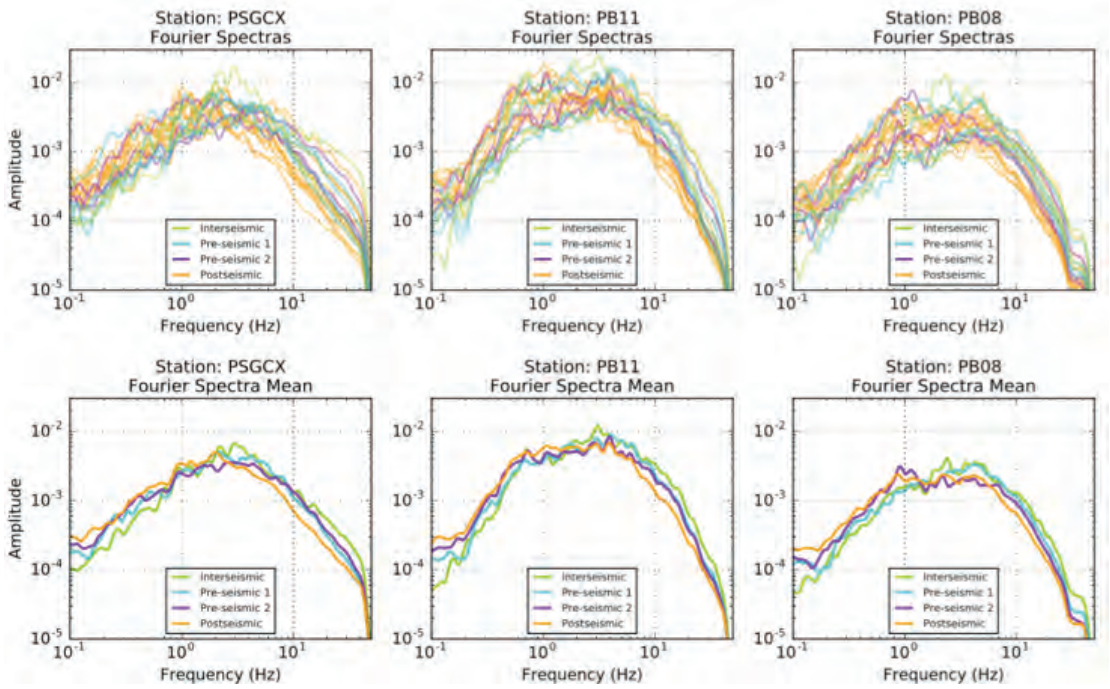

Figure 7.B.11: Acceleration Fourier Spectra computed at stations PSGX, PB11 and PB08 (see Figure 7.B.9 for location) for interface earthquake within 5.1-5.2 Magnitude range. Spectra are color-coded as function of the period when occured the earthquake (interseismic in green, pre-seismic 1 in cyan, pre-seismic 2 in purple, post-seismic in orange). Top line shows all individual spectra while bottom line shows the mean spectrum for each time period.

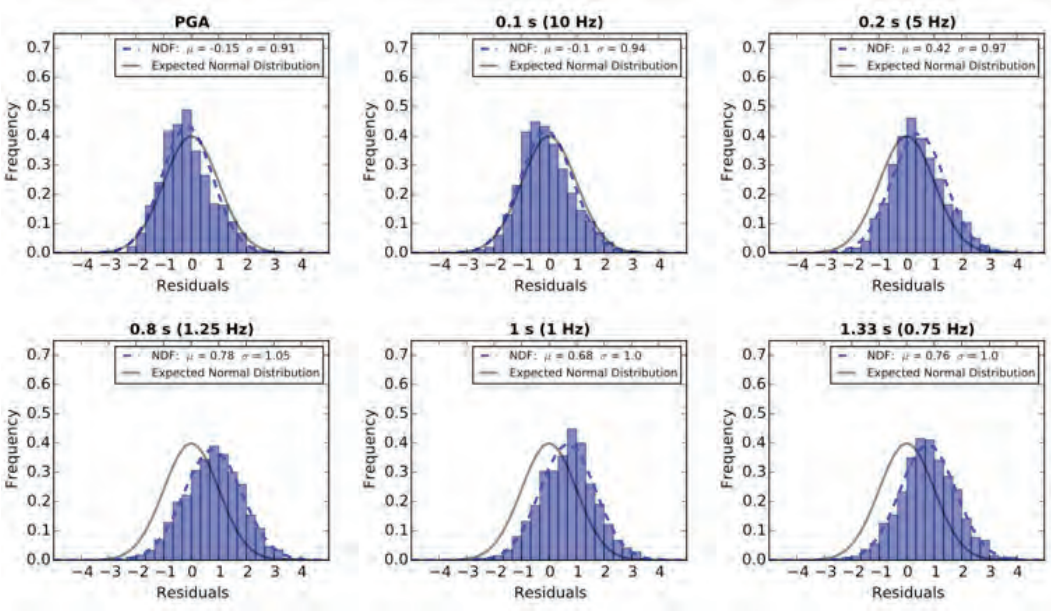

Figure 7.B.12: Histograms of ground motion absolute residuals normalized with respect to the total standard deviation of the GMPE model [*Abrahamson et al.*, 2016]. The Normal Density Function (NDF) of the residuals is shown by the dashed lines and the expected normal distribution is represented by the gray lines.

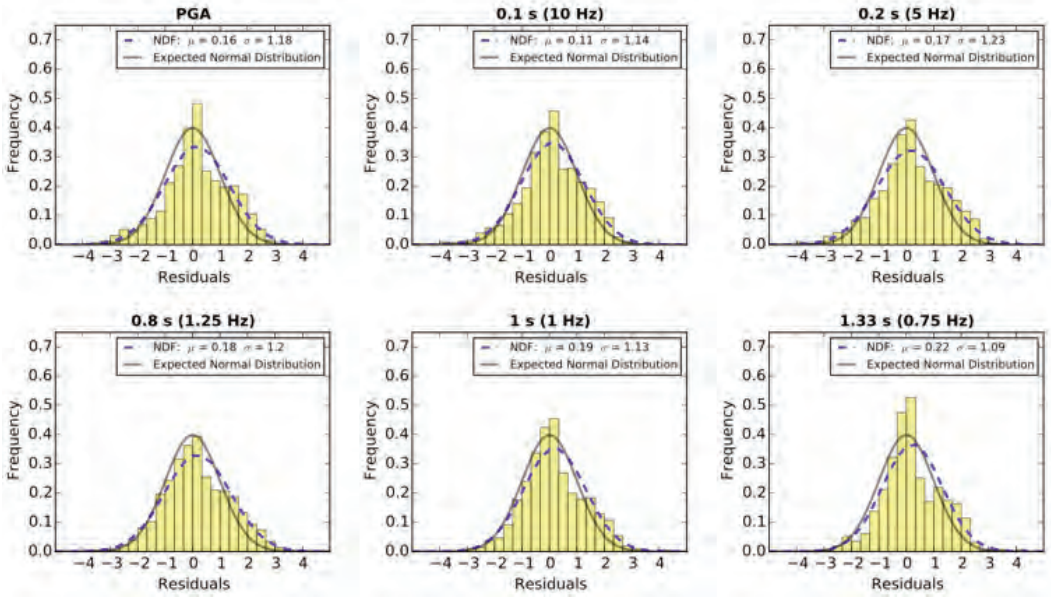

Figure 7.B.13: Histograms of the Within-Events residuals normalized with respect to the Within-Event standard deviation of the model. The Normal Density Function (NDF) of the residuals is shown by dashed lines and the expected normal distribution by gray lines.

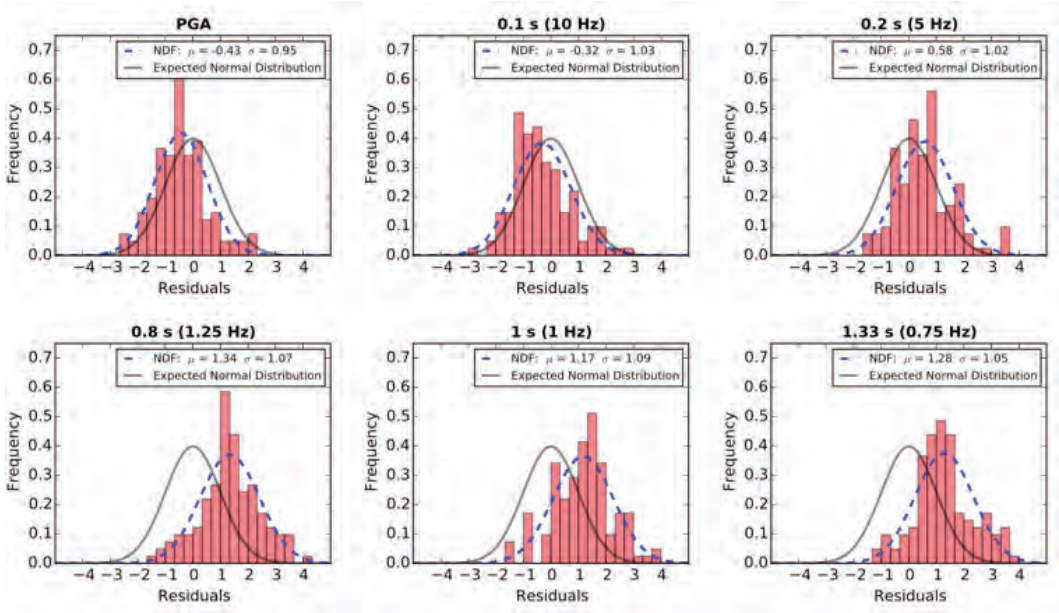

Figure 7.B.14: Histograms of the Between-Event residuals normalized with respect to the Between-Event standard deviation of the model. The Normal Density Function (NDF) of the residuals is shown by dashed lines and the expected normal distribution by gray lines.

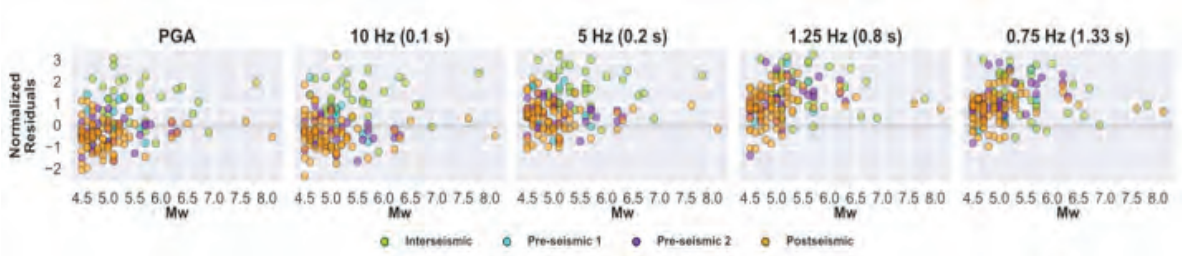

Figure 7.B.15: Between-event residuals as a function of event magnitude at the different frequency values shown in figure 1 (mid-panel). At frequencies above 5Hz, earthquakes occurring during the interseismic period exhibit significantly larger residuals than earthquakes belonging to preseismic and postseismic sequences. Instead, values of residuals are similar for all considered time periods at frequencies below 1.25Hz.

Chapter 8

Kinematic Study of Iquique 2014 M_w 8.1 earthquake: understanding the segmentation of the seismogenic zone

Paper to be submitted to EPSL: Jara, J., Sánchez-Reyes, H., Socquet, A., Cotton, J. Virieux, F., Maksymowicz, Díaz-Mojica, J., Walpersdorf, A., Ruiz, J., Cotte, N. & Norabuena E. (2018). [1]

8.1 Abstract

To understand the subduction segmentation in North Chile region, we present a complete study of the rupture processes of Iquique earthquake M_w 8.1 (2014/04/01) and its biggest aftershock M_w 7.7 (2014/04/03). High-rate Global Positioning System (GPS) recordings and strong motion data are used to reconstruct the evolution of the slip amplitude, rise time and rupture time of both earthquakes. A two-step inversion scheme is assumed, by first building prior models for both earthquakes from the inversion of the estimated static displacements and then, kinematic inversions in the frequency domain are carried out taken into account this prior information. The preferred model for the mainshock exhibits a seismic moment of 1.73×10^{21} Nm (M_w 8.1) and maximum slip of ∼9 m, while the aftershock model has a seismic moment of 3.88×10^{20} (M_w 7.7) and a maximum slip of ∼3 m. For both earthquakes, the final slip distributions show two asperities (one shallow and another deep) separated by an area with significant slip defficit, suggesting a segmentation along dip which might be related to the change of the dipping angle of the subducting slab, as inferred from gravimetric data. Along strike, the areas where the seismic ruptures stopped seem to be well correlated with geological features observed from geophysical information (high-resolution bathymetry, gravimetry and coupling maps), suggesting a complex along-strike and along-dip segmentation in the region. The results here presented support the idea that this seismic gap is not completely filled yet, considering the small portions that were broken by these two earthquakes.

[1] Supporting Information of this work can be found at the end of this Chapter.

8.2 Introduction

On 1 April 2014, a M_w 8.1 subduction earthquake struck the north of Chile offshore Iquique. This earthquake is of interest for two main reasons. First, the megathrust rupture was preceded by a long precursory phase characterized by a slow slip event that lasted several months [*Kato et al.*, 2016; *Socquet et al.*, 2017], and interactions between shallow and intermediate depth seismicity [*Bouchon et al.*, 2016; *Jara et al.*, 2017] that ended into an intense foreshock sequence, which origin remains debated in terms of slip behavior [*Ruiz et al.*, 2014; *Schurr et al.*, 2014; *Meng et al.*, 2015; *Kato et al.*, 2016]. This precursory phase has been the focus of a number of studies, and the present paper targets another interesting question raised by Iquique earthquake: the mainshock occurred in a mature seismic gap, where a moment deficit equivalent to $\sim M$ 8.6 has been accumulating since the 1877 historical earthquake [e.g., *Béjar-Pizarro et al.*, 2013; *Métois et al.*, 2016] (Figure 8.1). With a moment magnitude M_w 8.1, Iquique earthquake was therefore significantly smaller than what could be feared in this area, and the different slip models published show that the earthquake together with its larger aftershock of M_w 7.7 broke a spatially limited area (200 km along the subduction) [e.g., *Hayes et al.*, 2014; *Lay et al.*, 2014; *Ruiz et al.*, 2014; *Schurr et al.*, 2014; *Duputel et al.*, 2015; *Liu et al.*, 2015], leaving two regions with the potential capability to generate earthquakes of $M_w \geq$ 8.0 [*Hayes et al.*, 2014; *Schurr et al.*, 2014; *Ruiz et al.*, 2014; *Duputel et al.*, 2015]. But the reason why this earthquake together with its largest aftershock broke only this specific limited portion of the seismic gap remains elusive. What are the physical conditions (slip deficit, state of stress, friction or structural complexity) that contributed to enhance the ruptures, to end it? Do these earthquakes contribute to fill the slip deficit derived from interseismic geodetic coupling? Are the mechanisms that trigger the mainshock similar to the ones that initiate the aftershock? Is the ruptured area structurally peculiar? Here we explore the reasons of this apparent paradox by studying the rupture process of Iquique earthquake and its biggest aftershock (M_w 7.7, 2014/04/03), and then by comparing our results with complementary geophysical data that describe the interseismic coupling and the structural complexity in the area.

This earthquake has been well recorded by geodetic and strong motion networks (including co-located stations), providing a unique opportunity to explore the compatibility of both datasets and to show how high-rate GPS can help to better constrain the kinematic rupture processes. We perform a two-step inversion in the frequency domain proposed by *Hernandez et al.* [1999], that consists in carrying out a static inversion, used as *apriori* information in the kinematic models to explore the source of both earthquakes. Inverting in the frequency domain has then a great advantage since it can be evaluated how each frequency is explained (or not) by the inverted slip model. The method employed offers the opportunity to have a continuum (in the frequency domain) between the static and kinematic solution. However, frequency domain inversions have not been improving so much these last years and there then is a need to take into account the recent development and ideas of the slip inversion community (multigrid analysis [*Bunks et al.*, 1995], sensitivity analysis [*Duputel et al.*, 2015], better control of the smoothing process [*Wellington et al.*, 2017]), that are explored during this work.

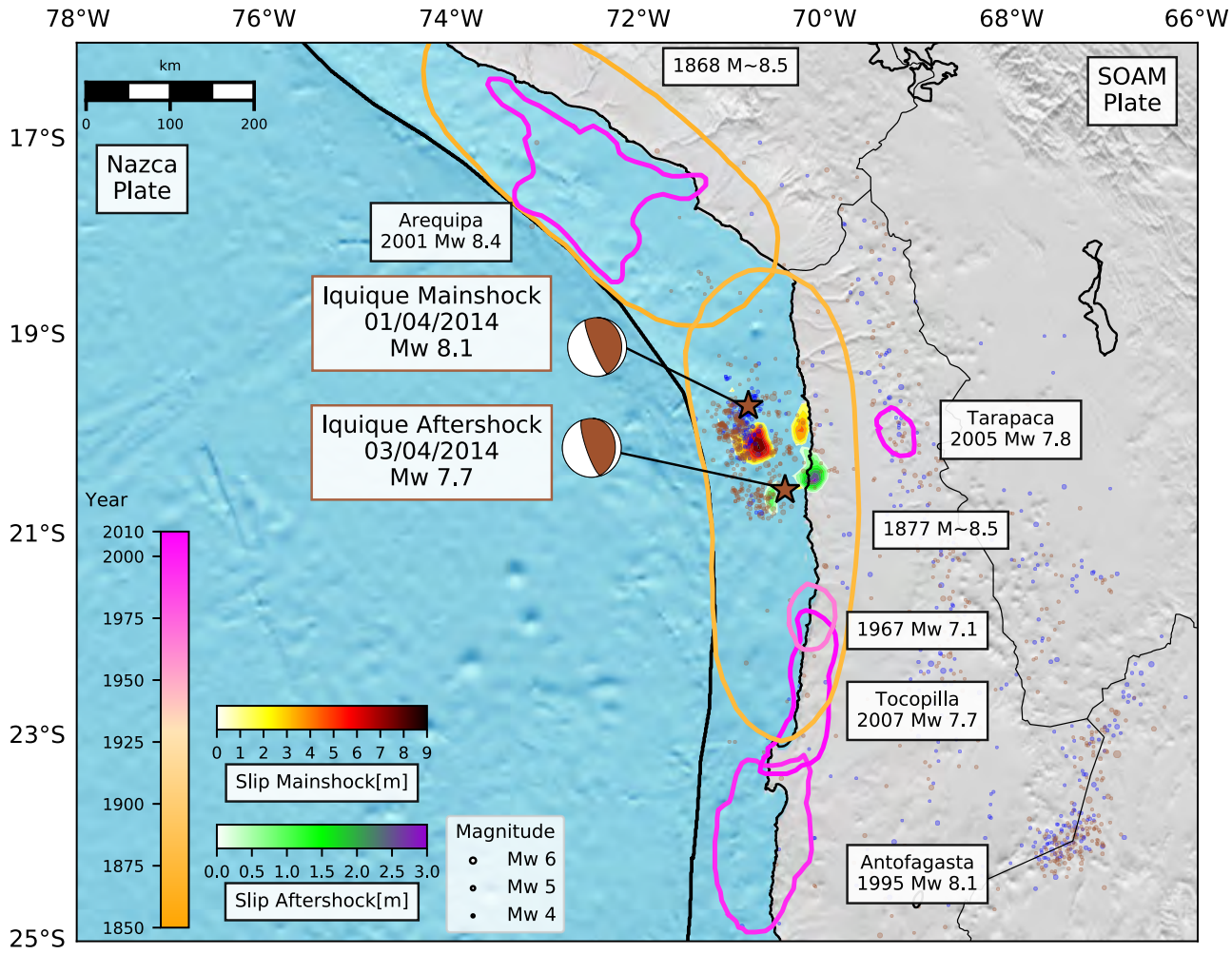

Figure 8.1: (a) Seismotectonic Context of North Chile - South Peru subduction zone. Historical and instrumental rupture areas are color coded as a function of their date of occurrence. Dates and magnitudes of all earthquakes M > 7.0 in the area are indicated in squared boxes. Mainshock (Mw 8.1 2014/04/01) and aftershock (Mw 7.7 2014/04/03) focal mechanisms from *Duputel et al.* [2015]. Stars symbolize the mainshock and aftershock epicenters from CSN catalog, as well as the seismicity since 2013/07/01 up to 2014/12/31 with magnitudes over 4.0, color coded by time (blue dots denote events before the mainshock and dark brown events after it.) and scaled by magnitude. Preferred slip models for the mainshock and aftershock are plotted with colors depending on the slip.

8.3 Data Analysis

8.3.1 High-rate Continuous GPS

High-rate GPS (HRGPS, 1 Hz) data from different networks located in South Peru - North Chile (IPOC, LIA "Montessus de Ballore", CAnTO, ISTerre, IGP and CSN, Figure 8.B.1) are processed using TRACK software [*Herring et al.*, 2016]. We use the LC combination and IGS precise orbits, employing the atmospheric delay estimated from daily GPS processing each 2 hours (see Supplementary Material for further details). TRACK computes a relative position with respect to a reference station supposed to be fixed. Here, we have chosen as a reference UCNF station (Figure 8.B.1), located ∼150 km from the epicenters. When the seismic waves reach the reference station,

its movement is reflected in the computed displacements of the whole network. This effect, together with orbital errors, is corrected by removing a common mode from the original signal and a sidereal filtering is applied to dismiss the multipath effects (Figures 8.B.2 and 8.B.3). The static co-seismic offsets are then estimated by fitting a step function in the HRGPS signal, 500 s before and after the earthquake (Figure 8.B.4 and Table 8.B.1).

8.3.2 Strong Motion versus HRGPS Seismograms

Strong motion stations located in North Chile from different networks are employed in this study (IPOC, LIA "Montessus de Ballore" and CSN, Figures 8.4 and 8.6 b). The signals are doubly integrated to obtain the ground displacement, and then filtered between 0.01 - 0.5 Hz. To validate our approach, we compare the signals from collocated HRGPS and strong motion stations. HRGPS are filtered in the same frequency band as strong motions. The superposition of both signals shows an excellent consistency in waveform between them (Figure 8.B.5). This procedure confirms the relevance of using HRGPS for the kinematic inversion, avoiding the loss of information due to the double integration procedure of the strong motion data.

8.4 Static and Kinematic Inversion Procedures

Let us first consider procedures for this two-step inversion where both the spatial discretization and the model covariance matrices play crucial roles for reducing the intrinsic ill-posedness of this inversion problem.

8.4.1 Static Inversion

GPS static displacements are inverted for the mainshock (M_w 8.1, 2014/04/01, Figure 8.2 b) and for the biggest aftershock (M_w 7.7, 2014/04/03, Figure 8.2 d) to get the final slip distribution associated with both earthquakes. A fault of 210 km x 175 km is discretized into 12 subfaults of 17.5 km along strike and 14 subfaults of 12.5 km along dip. The dip of the fault progressively increases with depth (the shallower segment dips at 5^o, followed by a segment at 9^o, 3 segments at 15^o, 4 at 20^o and finally the 5 deepest segments at 23^o). A constant strike is considered (346^o for the mainshock and 352^o for the aftershock). The rake angle is allowed to vary within the two perpendicular directions to the convergence angle of N77^oE [*Angermann et al.*, 1999]. In both cases, the fault plane is fixed to a geometry compatible with the one of Slab 1.0 [*Hayes et al.*, 2012] (Figures 8.B.6). The static Green's functions are calculated through the discrete wave number method [*Bouchon*, 1981] in an elastic stratified medium with AXITRA program [*Coutant*, 1989], employing the velocity model proposed by *Peyrat et al.* [2010] (Table 8.B.2). This procedure allows us to calculate the complete Green's functions, therefore the static displacement is simulated at zero frequency.

For each station, the three components of the displacement field, compactly designed as d, are inverted altogether in a least-squares sense [*Tarantola*, 2005], where the misfit function S is defined as:

$$S(m) = \frac{1}{2}[(Gm - d)^t C_d^{-1}(Gm - d) + (m - m_0)^t C_m^{-1}(m - m_0)] \tag{8.1}$$

The expected slip model m is defined by:

$$m = m_0 + C_m G^t (G C_m G^t + C_d)^{-1}(d - Gm) \tag{8.2}$$

where the prior model m_0 is defined as zero static slip for both events. The data covariance matrix C_d contains only diagonal terms with variances (σ_d^2) associated with estimated errors during the coseismic offsets calculation (Table 8.B.1). The model covariance matrix C_m is going to play an important role in building the slip, requiring a band-diagonal structure given by:

$$C_m(\mathbf{x}, \mathbf{x}') = \left(\frac{\lambda_0}{\lambda_{dip}\lambda_{strike}}\right) \sigma(\mathbf{x})\mathcal{F}(\mathbf{x}, \mathbf{x}'), \tag{8.3}$$

where the scaling factor λ_0 is usually taken as the size of an individual subfault [*Radiguet et al.*, 2011] (here 15 km for both events). This band-limited structure of the covariance matrix reduce its model-square complexity down to a more manageable model-like complexity. The model correlation between two different positions $\mathbf{x} = (dip, strike)$ and $\mathbf{x}' = (dip', strike')$ on the fault plane is expressed by the operator $\mathcal{F}$. Its expression with a laplacian decay

$$\mathcal{F}(\mathbf{x}, \mathbf{x}') = \exp\left(-\frac{|dip - dip'|}{\lambda_{dip}} - \frac{|strike - strike'|}{\lambda_{strike}}\right), \tag{8.4}$$

will provide more coupling than the often used Gaussian decay [*Wellington et al.*, 2017]: a key point for mitigating trade-off between parameter values for this static reconstruction. For static slip inversion, this relatively slow decay behavior has been found to behave better than the often used Gaussian decay [*Radiguet et al.*, 2011]. The correlation lengths λ_{dip} and λ_{strike} are considered as homogeneous in this work, although they can be tuned to vary with the fault position, especially when fault points are moving away from acquisition network. Correlation length λ_{dip} has been tested between 5 - 100 km, with a step each 5km. Following the L-curve criterion [*Hansen*, 1992], we have chosen the best compromise between the maximum slip and the normalized misfit (Figure 8.2 a and c): optimal values are 20 km (mainshock) and 30 km (aftershock).

The operator $\sigma(x)$ (with a model complexity) expresses the prior expected local variability or sensitivity of the static slip: small values will prevent the static slip reconstruction to move away

from the prior model value which is zero in our case. The operator $\sigma(x)$ compensates for poor geometry of the acquisition with respect to the active fault. The lack of sensitivity with depth can be also controlled by this operator. Moreover, we may increase the sensitivity of zones where we expect high values when fitting the data. The following operator

$$\sigma(x) = \sigma_{min} + (\sigma_{max} - \sigma_{min}) \exp\left(-\frac{|dip - dip_0|}{\lambda_{dip0}} - \frac{|strike - strike_0|}{\lambda_{strike0}}\right) \tag{8.5}$$

has been selected where the position $(dip_0, strike_0)$ is the zone with the most expected variation of the static slip for the mainshock. We have assumed a circular shape through the choice for quantities λ_{dip0} and $\lambda_{strike0}$ equal to 40 km and 40 km respectively, with values ranging from 0.01 to 2.5 m. For the aftershock, such single-shape operator has been considered in a first trial: the data gradient still drives us toward two zones of maximum slip. Therefore, we have considered in a second trial two joint prior shapes with σ values ranging from 0.01 to 1.0 m around these expected high-slip zones: the data gradient has built up a solution coherent with this second sensitivity design. In both cases λ_{dip0} and $\lambda_{strike0}$ are equal to 25 km and 52.5 km.

For the final solution, two different strategies could give us some ideas about the model resolution, although they theoretically assume a normal distribution around the solution which is rarely the case. On one side, the resolution matrix proposed by *Tarantola and Valette* [1982] given by:

$$R = C_m G^t (G C_m G^t + C_d)^{-1} G \tag{8.6}$$

gives us low resolution for all subfaults (Figures 8.B.7 for mainshock and 8.B.8 for the aftershock, a and b): for a perfectly resolved model, the matrix should be the identity. On the other side, the data sensitivity defined by *Duputel et al.* [2015] through:

$$Sen = diag(G^t C_d^{-1} G) \tag{8.7}$$

shows where the slip is well solved depending on the data error used during the inversion. This quantity provides another evaluation of the model resolution (Figures 8.B.7 for mainshock and 8.B.8 for the aftershock, c and d).

8.4.2 Kinematic Inversion

The kinematic reconstruction of the rupture process is an even more ill-posed problem: we have followed the two-step strategy proposed by *Hernandez et al.* [1999] for a reconstruction in the frequency domain building the solution by sweeping from low to high frequencies. At each frequency,

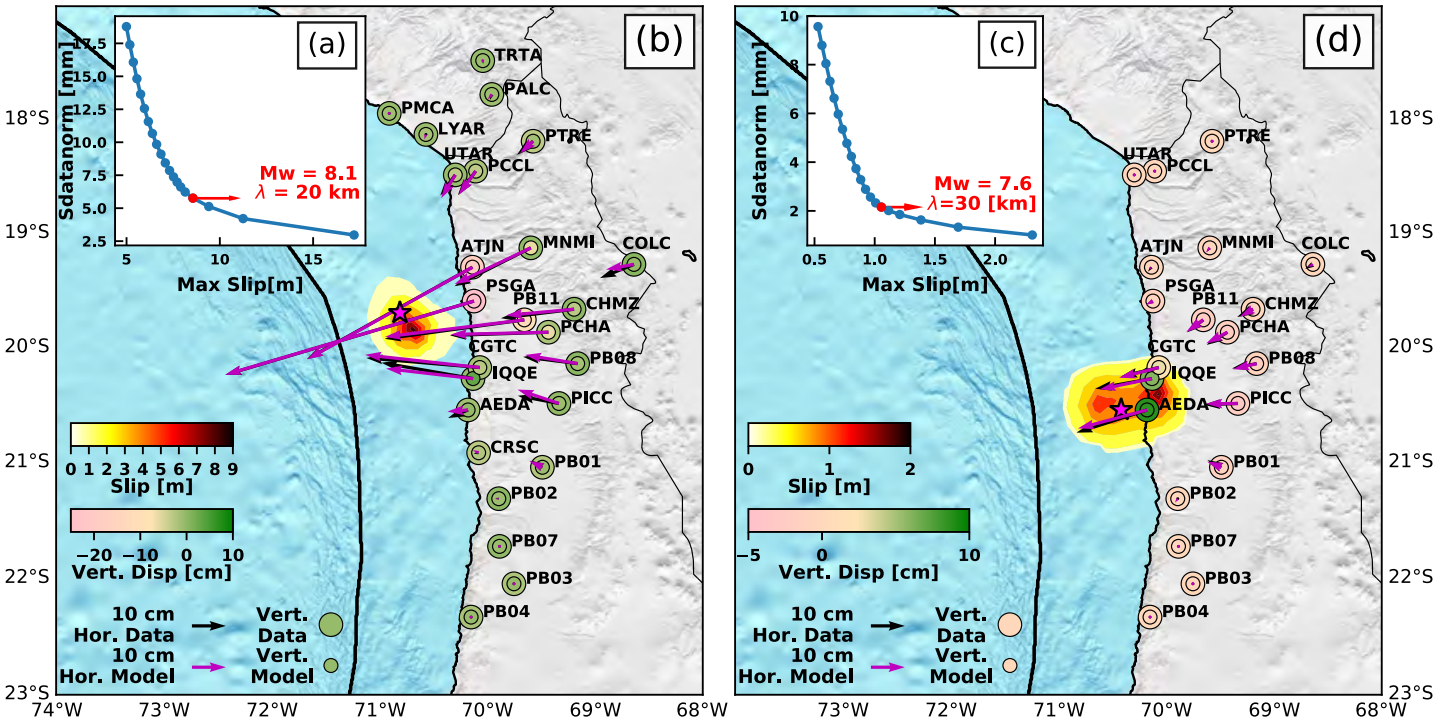

Figure 8.2: Static inversion results obtained using HRGPS for the mainshock and the aftershock. (a), (c) Normalized misfit as a function of the maximum slip, showing the correlation length of the preferred slip model for mainshock ((a), $\lambda = 20$ km) and aftershock ((c), $\lambda = 30$ km). Slip model and comparison between data and model (horizontal in arrows and vertical in circles) for the mainshock (b) and aftershock (d). Pink stars symbolize the epicenter of the events reported by the CSN catalog.

the static solution obtained from inversion of geodetic data will be used as the prior model in the kinematic inversion. The synthetic displacement waveform in the frequency domain is computed following the sparse parameterization proposed by *Cotton and Campillo* [1995] as:

$$V_i(w) = \sum_{k=1}^{n} G_{ski}(w)\ [slip_{sk}\ \ \exp(-iwt_k) S_k(R_k, w)] + \sum_{k=1}^{n} G_{dki}(w)\ [slip_{dk}\ \ \exp(-iwt_k) S_k(R_k, w)] \tag{8.8}$$

where the Green's function (i.e. the displacement for a unit constant slip on the k-th subfault for the frequency w) is denoted by the symbol G_{ski} for the strike component and by G_{dki} for the dip. The slip is parametrized depending on the component as well: slip along strike by $slip_{sk}$ and slip along dip by $slip_{dk}$. The rupture time is indicated by t_k, while the source time function (STF) is given by the following analytical expression $S_k(t) = 0.5(1 + tanh(t + R_k/2.0)^2))$, depending on the rise time R_k. Therefore, four parameters have to be reconstructed for each sub-fault. Each subfault is represented by an array of point sources, separated by distances of less than one sixth of the shortest wavelength to be considered locally. For these point sources, Green's functions are computed and then, the sum of all point sources response delayed in time to include the travel-time

difference, due to the rupture front propagation across each subfault [*Cotton and Campillo*, 1995]. The Green's functions are calculated using the same strategy as for the static inversion with the program AXITRA [*Coutant*, 1989], but keeping all the frequency range. We do not consider variable rupture velocity inside each subfault which is allowed to slip once. The velocity model is the same as the one used during the static inversion for both events.

The four parameters, namely strike slip, dip slip, rise time and rupture time in each subfault, are inverted using the non-linear least-squares formulation proposed by *Tarantola and Valette* [1982]. A non-linear operator f relates the model parameters m to the data vector d through the general expression $d = f(m)$. The model solution is obtained through an repetitive procedure based on a linearized approximation where the next model m_{l+1} is obtained from the current model m_l following the iterative algorithm:

$$m_{l+1} = m_l + b(A_l^t C_d^{-1} A_l + C_m^{-1})^{-1} \ (A_l^t C_d^{-1}(d - f(m_l)) + C_m^{-1}(m_0 - m_l)), \tag{8.9}$$

which minimizes the least-squares data misfit. At each frequency, the initial model m_0 will be used also as a prior model. For the lowest frequency, the static solution will be considered as the initial/prior model and the final solution at this frequency will be used as the initial/prior model for the next frequency. The Jacobian matrix A_l are obtained by taking the closed-form derivative of the Equation 8.8 with respect to the related parameter. The damping factor b between 0 and 1 prevents any divergence. The data covariance C_d has a diagonal matrix filled with ones, reflecting the good quality of data in the region, while the model covariance requires more attention as we see in the multigrid approach we associate with the frequency sweeping.

Based on a multigrid approach, the inversion starts with a Large Subfault Size (LSS) discretization sweeping over frequencies, obtaining a final solution [*Bunks et al.*, 1995]. The final solution is interpolated in a Small Subfault Size (SSS) discretization, repeating again the inversion scheme with another set of frequency windows still sweeping from low to high frequencies. By combining this dynamic frequency sampling and a recursive spatial sampling, we are able to improve the data fit and to increase the model resolution with still stable results. For the LSS sampling , we have adopted the same subfault geometry employed during the static inversion (168 subfaults). The SSS sampling is obtained by dividing each subfault in four subsequent subfaults, so that the total fault encompasses 672 subfaults (24 along strike with 8.75 km and 28 along dip with 6.25 km) for both events.

The inversion procedure is performed by using a progressively broadened frequency range for both events for fixed spatial sampling. The LSS model is initiated with a frequency range of 0.01 - 0.02 Hz using the static solution as the initial/prior model. The obtained solution is then used as the new initial/prior model for the new frequency range of 0.01 - 0.03 Hz. We repeat this procedure until the frequency range of 0.01 - 0.25 Hz is reached (24 models in total). The last LSS model is then interpolated and used as the initial/prior model for the SSS sampling, considering the first frequency range of 0.01 - 0.02 Hz. The same iterative procedure is repeated for the small-subfaults

configuration until the frequency range of 0.01 - 0.3 Hz is reached (29 models in total).

For both events, the model covariance matrix C_m is defined as a diagonal matrix, leaving the interaction between spatial points under the supervision of the multigrid strategy. The variances σ_{strike} and σ_{dip} are defined following the Equation 8.5 with the same strategy employed during the static inversion. The σ_{rup_time} is defined with the same idea as in Equation 8.5, but increasing the values from the epicenter of the earthquakes, because the rupture time may be better estimated near the epicenter, but not far from it. We have started by allowing a considerable variability through σ_{dip} (main slip direction) and σ_{rup_time}, but a lower one in the strike slip component (Table 8.B.3). When the seismic moment reported for the earthquakes is reached, we keep the same proportion mentioned to define σ in terms of variability, but reducing the values where the parameters are allowed to move, in order to hold the seismic moment (Table 8.B.3). There is no physical reason to constrain the rise time, so we have assigned the same σ_{rise_time} value to all the subfaults in both models and events (LSS and SSS, Tables S3).

In order to avoid spurious jumps in the model parameters (slip along dip and strike, rise time), we introduce a correlation length of 17.5 km in LSS model and 8.75 km in SSS model, for both events. It allows to connect the adjacent subfaults providing a smooth rupture process. To evaluate the fit to the data, we compute the variance reduction proposed by *Cohee and Beroza* [1994]. The sensitivity is also analyzed (Equation 8.7) for the mainshock (Figure 8.B.15) and the aftershock (Figure 8.B.16).

8.5 Results

8.5.1 Static Inversion

The mainshock has broken an asperity localized between 15 - 40 km depth with a maximum slip of ∼9 m. It is located south of the epicenter reported by CSN (∼40 km). The seismic moment obtained is 1.52 x 10^{21} Nm, equivalent to M_w 8.1. The aftershock is composed of two asperities localized on each side of the epicenter, with a maximum slip of ∼1.2 m. The shallower asperity (close to the trench) is confined between 15 - 30 km depth, and the deeper one between 40 - 50 km depth. The seismic moment obtained from the inversion is 3.68 x 10^{20} Nm, associated with an earthquake magnitude M_w 7.6. Comparing those slip models to the resolution analysis (resolution matrix and sensitivity) it appears that the data can better resolve the slip close to the coast than close to the trench (Figures 8.B.7 for the mainshock and 8.B.8 for the aftershock). The poor resolution obtained at the trench vicinity is typical for subduction zones lacking offshore instrumentation, due to the lack of data close to the trench. The results are good enough to be used as our *apriori* model in the kinematic inversion, especially because the spatial distribution is well resolved where the slip is located.

8.5.2 Kinematic Inversion

Mainshock

Some differences can be appreciated between the resulting kinematic and static slip distributions. The final slip obtained during the kinematic inversion shows a very concentrated asperity south of the epicenter (∼43 km) with a maximum slip of ∼9 m and confined between 15 - 35 km depth. Conversely to the static solution, less slip is seen north of the epicenter and the emergence of a second deep asperity is observed between 40 and 55 km depths (Figure 8.3 a) with a maximum slip of 5 m.

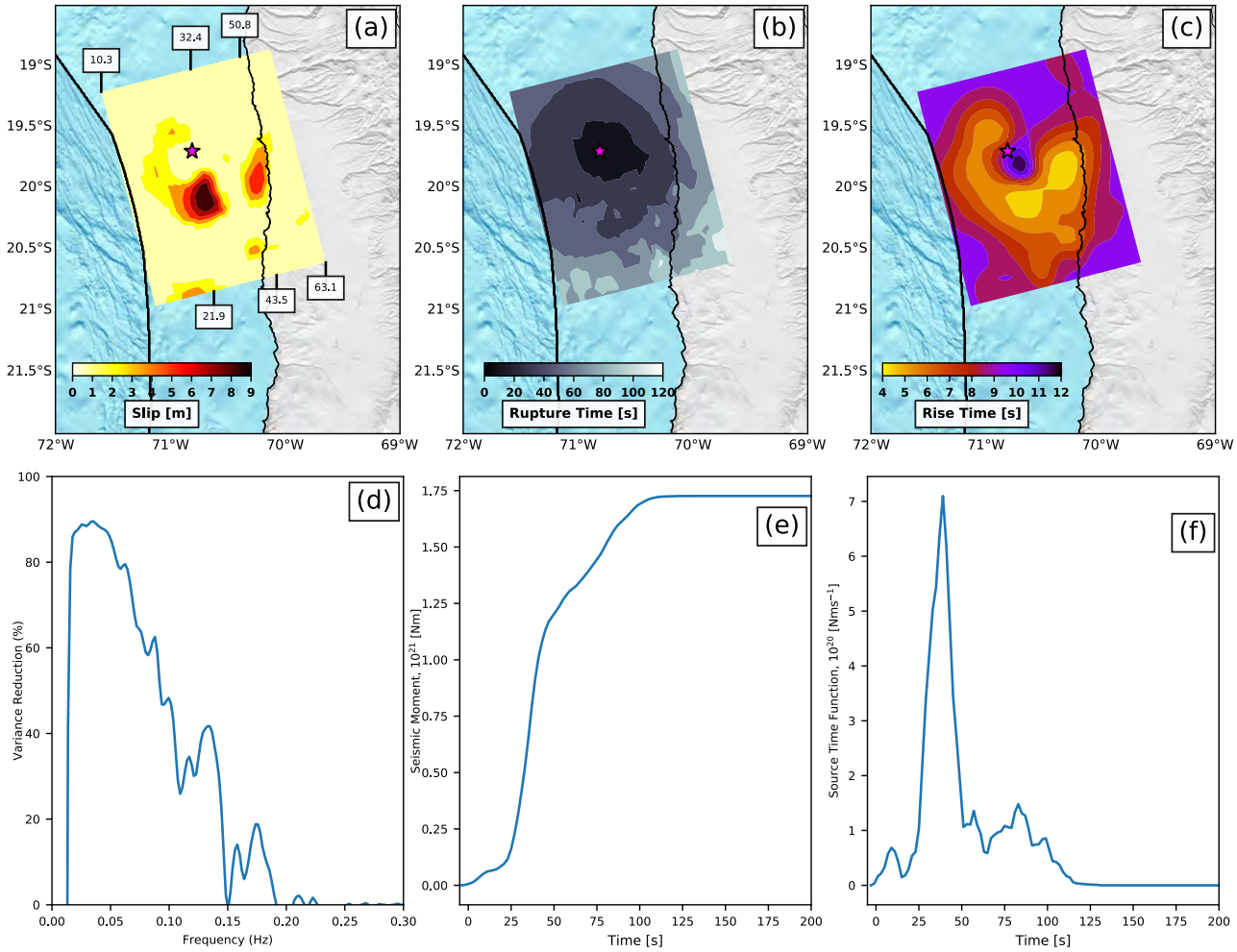

Figure 8.3: Mainshock kinematic inversion results. Preferred slip model (a), rupture time (b) and rise time (c). Plane depths are indicated inside white boxes in (a). The pink star indicates the epicenter location reported by CSN catalog. (d) Mean variance reduction computed for each frequency between data of all the stations and synthetics. (e) Cumulative seismic moment and (f) and STF.

The rupture is characterized by a very slow moment-rate during the first 25 s, leading to an abrupt acceleration in the moment liberation at 30 s (Figure 8.3 e and f). After that, the moment-rate decreases to reach the final rupture time at 125 s (Figure 8.3 e and f). The total seismic moment obtained is 1.73 x 10^{21} Nm (Figure 8.3 e), equivalent to a magnitude M_w 8.1. The difference between

data and synthetics corresponds to a mean variance reduction of 82.37%, fitting better the lower frequencies 0.01 - 0.15 Hz (Figure 8.3 d). At higher frequencies, a limited mean variance reduction up to 0.2 Hz is obtained. This is also visible in the data fit, where the low frequencies are better fitted (Figure 8.4 a, see Supplementary Information for not normalized and frequency domain fit, Figures 8.B.11 and 8.B.13), while the high frequencies are not well solved. Some complexity in the rupture time (Figure 8.3 b) and rise time (Figure 8.3 c) are required to the south of the rupture to fit the signal of southern stations. This complexity is also reflected in the STF after the 75 s (Figure 8.3 f). To the north, the rupture propagates at a much more constant rate than to the south (Figure 8.3 b). This variation in complexity might be associated with changes in the lithology that are not reflected in the velocity model.

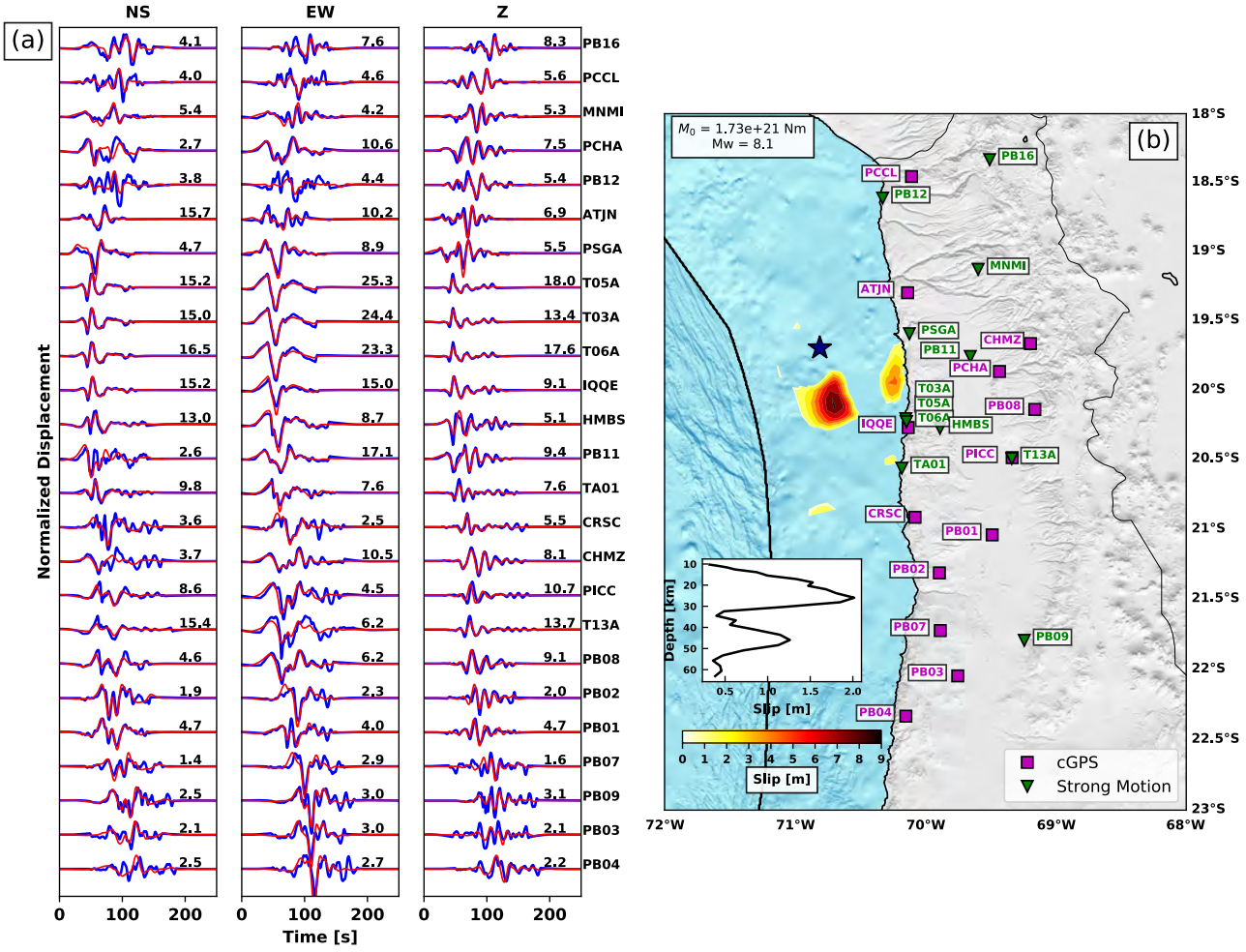

Figure 8.4: (a) Mainshock normalized Strong Motion - HRGPS (blue) and synthetic seismograms (red). For each station and component, the maximum data displacement is shown in [cm]. (b) Final preferred slip model and stations map used during the kinematic inversion. Green triangles symbolize strong motion location and magenta squares HRGPS. Star indicates the epicenter of the event by CSN catalog. Also, at the bottom left is shown the slip averaged along strike as a function of depth.

Aftershock

The slip distribution of the largest aftershock is characterized by two asperities located on both sides of the epicenter (Figure 8.5 a). The shallow asperity is confined between 15 - 30 km depths with a maximum slip of 1.5 m, while the deeper one is located between 30 - 50 km depths with a maximum slip of ∼3 m (Figure 8.5 a, see Supplementary Information for not normalized and frequency domain fit, Figures 8.B.12 and 8.B.14). The calculated seismic moment is 3.88 x 10^{20} Nm, equivalent to a magnitude M_w 7.7 (Figure 8.5 e and f). The result obtained during the kinematic inversion is similar to the static one, but provides further details in the asperities location and the slip distribution.

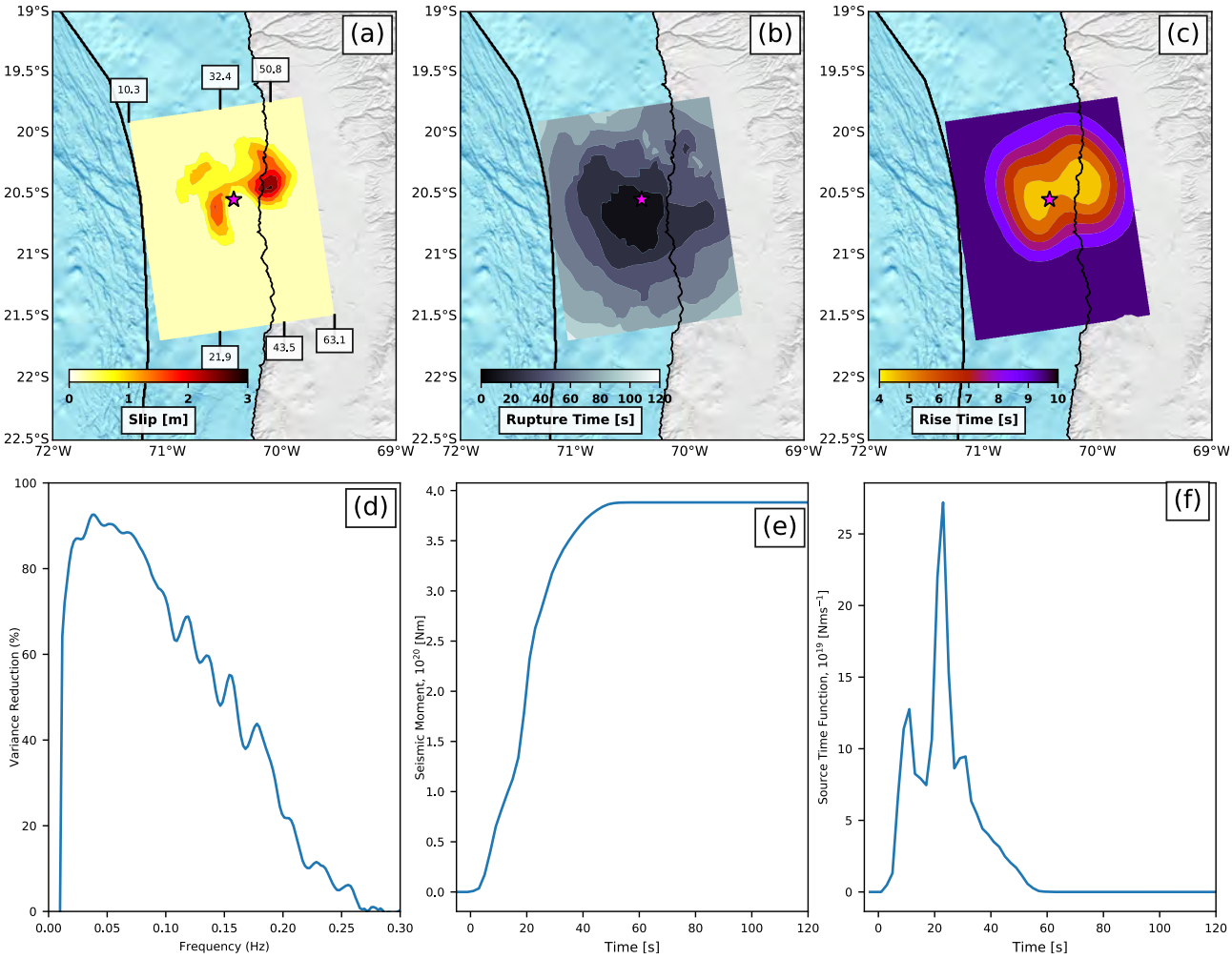

Figure 8.5: Same captionas as in Figure 8.3, but for the aftershock case.

The rupture has begun with an acceleration during the first 18 s (Figure 8.5 e), breaking the asperity close to the trench. Then, the second deeper asperity has slipped during 40 s (Figure 8.5 e). The STF is more simple than the mainshock (Figure 8.5 f), and lasts 60 s. The fit to the data corresponds to a mean variance reduction of 85.74%, solving the frequency range of 0.01 - 0.3 Hz (Figure 8.5 d).

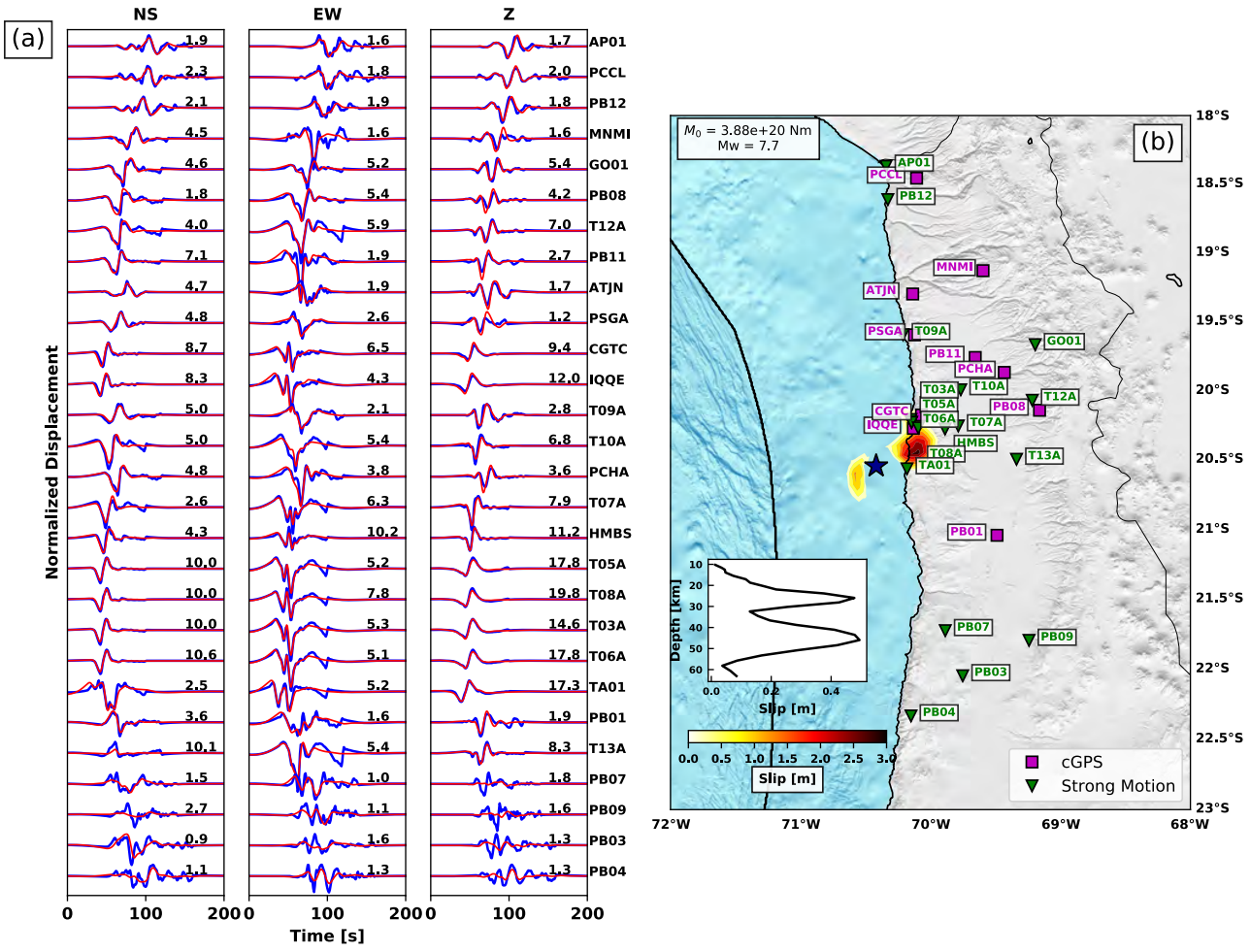

Figure 8.6: Same caption as in Figure 8.4, but for the aftershock case.

Comparison between LSS and SSS models

LSS and SSS models have been compared in order to explore the differences and advantage of SSS model for the mainshock (Figure 8.B.9) and the aftershock (Figure 8.B.10). For both earthquakes, the slip resolution is improved. Rupture time (Figures 8.B.9 and 8.B.10 c, d) and rise time (Figures 8.B.9 and 8.B.10 e, f) show the same variation than the slip, but do not change the general pictures of their behaviors. One important change between LSS and SSS models is the increase in the frequency range resolution. For the mainshock (Figure 8.B.9 g), the resolution is improved by about 40% in the frequency range of 0.1 - 0.15 Hz. At higher frequencies, the resolution still slightly increases (∼15%), but not significantly. For the aftershock (Figure 8.B.10, g) the SSS models improves significantly the mean variance reduction in the frequency range 0.1 - 0.25 Hz. The seismic moment obtained with both models is of the same order (Figures 8.B.9 and 8.B.10 h, i). The STF show some differences between LSS and SSS models (Figures 8.B.9 and 8.B.10 i): the STF is slightly more smoothed in the SSS models due to the change in the subfault size, avoiding any large change of the parameters between the adjacent subfaults. The resolution of the kinematic models (Figures 8.B.15 for the mainshock and 8.B.16 for the aftershock) is similar between LSS and SSS models.

The number of parameters inverted during the inversion increases from 672 in the LSS model

to 2688 parameters in the SSS model. For both earthquakes the resolution close to the trench is quite low because the stations are located inland. The increase of the number of parameters seems to reduce the local resolution on each subfault, but the spatial pattern of the resolution is kept (well resolved close to the epicenter, and poorly resolved by the trench, Figures 8.B.15 and 8.B.16).

8.6 Discussion

8.6.1 Along Strike Segmentation of the Seismogenic Zone

Our results confirm that 2014 M_w 8.1 Iquique earthquake together with its largest aftershock ruptured a limited portion of the seismic gap (Figure 8.1). Moreover, the obtained slip distributions show that both earthquakes ruptured into two distinct asperities, quite concentrated spatially (Figure 8.7).

Following *Aki* [1979], it is therefore likely that the earthquake stopped because it encountered a geometric or inhomogeneous barrier. It has been proposed that large earthquakes rupture areas that are strongly coupled, while aseismic slip as seen in poorly coupled zones has been proposed to act as a barrier for seismic ruptures. This is supported by the occurrence of an 8-month slow slip event surrounding the mainshock rupture area as derived from GPS time-series [*Socquet et al.*, 2017] (Figure 8.8 d). Our coseismic slip distribution compared to the interseismic slip distribution obtained by *Métois et al.* [2016] tends to confirm this finding, at least for the mainshock (Figure 8.8 c). The mainshock was initiated in an area at the transition between low and high coupling, prone to high stresses, possibly even further loaded by the 8-month slow slip that preceded the rupture. The earthquake has then propagated southward and ruptured a highly locked patch, and eventually stopped at the southern termination of this highly coupled patch (Figure 8.8 c). The mainshock has therefore contributed to release the slip deficit accumulated in this locked asperity during the interseismic period.

On the contrary, the largest aftershock has broken areas that were poorly coupled in the interseismic period (Figure 8.8 c). In order to understand this apparent contradiction, we have calculated the stress change produced by the mainshock on the subduction plane (Figure 8.7 a). The aftershock is located in areas with positive Coulomb Stress change (Figure 8.7 a), and negative normal change (Figure 8.7 c) that accounts for unclamping. This therefore suggests that the largest aftershock has been triggered by the mainshock.

To further understand the parameters that control the location of such a seismic asperity and high coupling patch, we compared our findings with the bathymetry and the free-air gravity anomaly (Figure 8.8 a and b). Geological features affecting the subducting slab or the overriding plate (such as fracture zones, ridges, changes in the slab geometry, peninsulas, fault systems and marine basins) have been shown to correlate with low coupling zones and the arrest of seismic rupture [e.g., *Armijo and Thiele*, 1990; *Song and Simons*, 2003; *Wells et al.*, 2003; *Audin et al.*, 2008; *Perfettini et al.*,

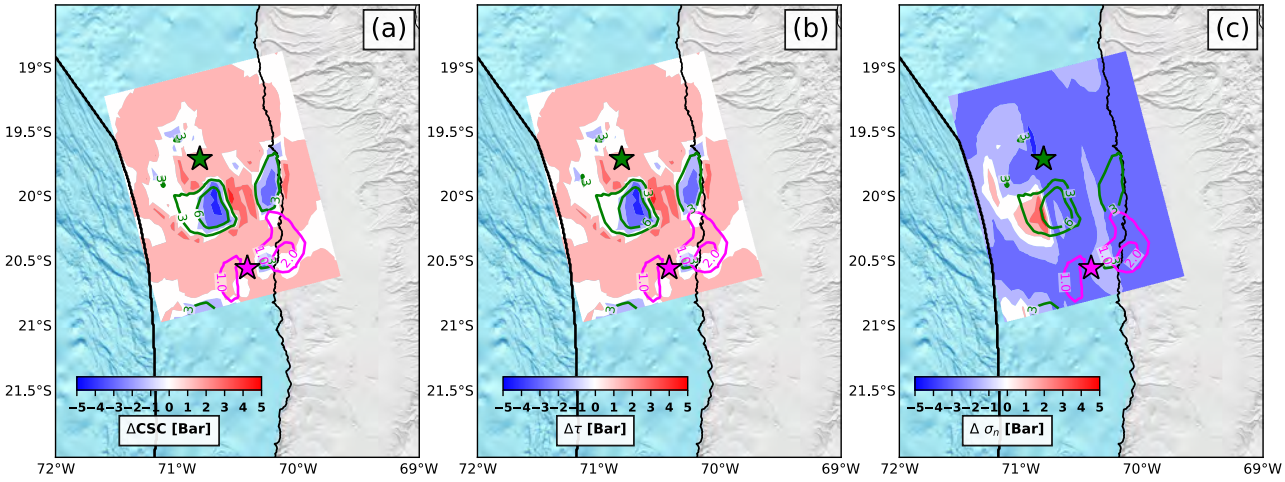

Figure 8.7: Coulomb stress change (a), shear stress change (b) and normal stress change (c) on the fault plane calculated using the mainshock preferred slip model. Green (pink) star and contours denote the epicenter of the mainshock (aftershock) reported by CSN catalog and the slip produced by the event.

2010; *Béjar-Pizarro et al.*, 2010; *Contreras-Reyes and Carrizo*, 2011; *Contreras-Reyes et al.*, 2012; *Maksymowicz et al.*, 2015], and can be interpreted as a structural complexity that acts as a geometrical barrier for the seismic rupture [*Aki*, 1979; *King*, 1986]. Using seismic velocity profiles and gravity data, *Wells et al.* [2003] evidenced a spatial correlation between forearc basins and the peak of slip of several great earthquakes, suggesting that the basin is an indicator of a long-term seismic moment release. *Song and Simons* [2003] have proposed another way to analyse the gravity data through the definition of the Trench Parallel Gravity Anomaly (TPGA), where areas of negatives values correlate with the coseismic slip in subdution zones.

The asperity with highest slip value of 2014 Iquique mainshock is centered in the Iquique basin [*Armijo et al.*, 2015], inferred from high resolution bathymetry (Figure 8.8 a) and free-air gravity anomaly (Figure 8.8 b). This is in agreement with the results shown and discussed by *Meng et al.* [2015], who demonstrated that the main asperity is located in an area with negative value of TPGA. The southern limit of the main rupture is characterized by an important change in the gravity extracted from free-air anomaly gravity (Figure 8.8 b) and density gravity models [*Maksymowicz et al.*, 2016], probably associated with a change in the lithology, fracturing and fluid content inside the continental wedge. This is supported by velocity models [*Patzwahl et al.*, 1999; *Comte et al.*, 2016] and density gravity models [*Maksymowicz et al.*, 2016], that evidence a strong change in the size of the deformation front in the area, leaving the southern part more tectonically erosive than the northern part. This strong gravity change is associated with a geological change that could explain the complexity observed in the southern part of the rupture and the heterogeneities in the tail of the STF (Figure 8.3 b and f).

The north limit of the aftershock also seems related to the gravity changes discussed above. This sharp change marks an E-W line that separates both earthquakes. The southern limit of the aftershock is not associated with any clear change in the gravity, but might be related to geological features of the overriding plates responsible to stop the rupture. *Audin et al.* [2008] have pointed

out the relationship between the Chololo coastal fault system and the southern end of Arequipa coseismic rupture in Peru (M_w 8.4, 2001, Figure 8.1). The tectonic map of *González et al.* [2003] indicates that the region where the aftershock stops at 21^{o}S is characterized by an increased complexity in the faults system. South of 21^{o}S almost all the fault are parallel to the trench and the coastal scarp (mainly normal faults), but north to this limit, the area of the Salar Grande is affected by a series of E-W thrust faults combined with conjugated strike-slip faults [*González et al.*, 2003]. This tectonic difference might be related to the southern termination of the aftershock rupture.

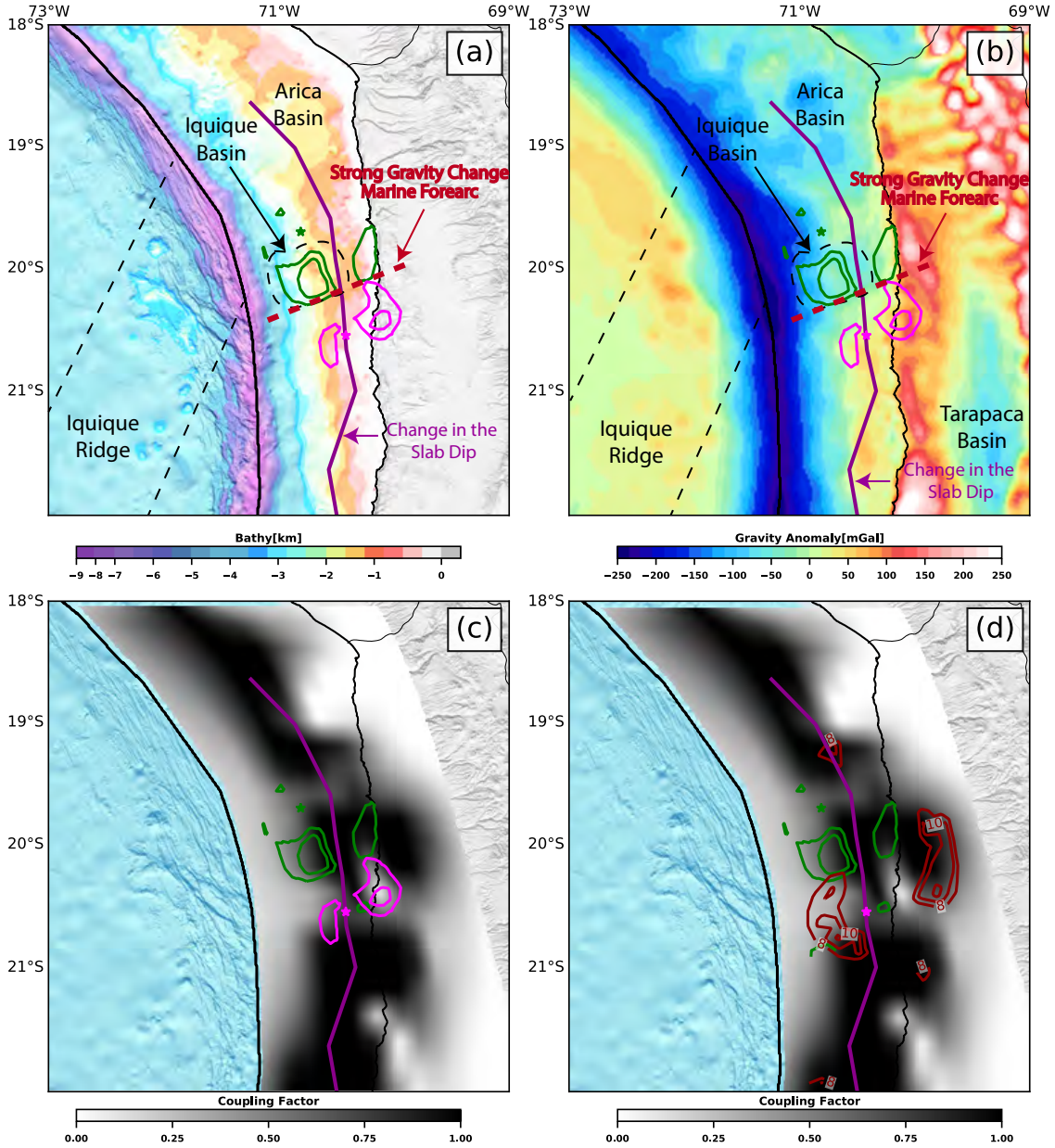

Figure 8.8: (a) High-resolution topography [*Contreras-Reyes et al.*, 2012] , (b) free air gravity anomaly [*Sandwell et al.*, 2014] and (c) and (d) coupling distribution [*Métois et al.*, 2016] on the study area. Mainshock (green) and aftershock (pink) slip contour of 2.0 m and 0.5 m are plotted. Violet line parallel to the trench represents the abrupt change on dip proposed by [*Contreras-Reyes et al.*, 2012] interpolated to the north, extracted from gravity models. (d) Coupling map with the mainshock contours (green) and the 8-month SSE (red) shown by [*Socquet et al.*, 2017] contoured in mm.

8.6.2 Along Dip Segmentation of the Seismogenic Zone

Both the mainshock and the large aftershock show an interesting bimodal pattern along dip (Figure 8.4 b and Figure 8.6 b). In both cases, the shallow patch of slip extends from 15 km and 30 km depths, while the deep patch of slip is confined between 35 and 50 km depths. The upper limit at 15 km depth corresponds to the deformation front extracted from gravity [*Maksymowicz et al.*, 2016] and seismic velocity models [*Patzwahl et al.*, 1999; *Comte et al.*, 2016]. The downdip limit at ∼50 km depth is in agreement with other seismological [*Comte and Suárez*, 1995] and geodetic [*Béjar-Pizarro et al.*, 2010; *Chlieh et al.*, 2011; *Béjar-Pizarro et al.*, 2013; *Métois et al.*, 2016] definitions of the lower extent of the seismogenic zone in North Chile subduction.

The most intriguing aspect of the observed along dip segmentation is the separation between shallow and deep asperities. Indeed both earthquakes present almost no slip at 30 - 35 km depths. *Armijo and Thiele* [1990] proposed that the coastal scarp could be a west-dipping normal fault reaching the subduction zone at depth. A change in the slab dip has been inferred from wide-angle seismic refraction and reflection data, complemented with relocated aftershock seismicity in the Tocopilla area (∼22^{o}S) [*Contreras-Reyes et al.*, 2012] (M_w 7.7, 2007, Figure 8.1). Based on a correlation with the coastal scarp and following the idea proposed by *Armijo and Thiele* [1990], the authors suggest that this change in dip from 10^o to 22^o affects a wide portion of the slab. *Maksymowicz et al.* [2016] have modeled the gravimetry in the region observing the same change in dip proposed by *Contreras-Reyes et al.* [2012] in the Tocopilla area. Employing those results, we have inferred the location towards the north of this change in the dip (purple line in Figure 8.8 a and b), observing that in the area affected by Iquique earthquake, this feature seems to delimit a separation between the deep and shallow asperities. This change in slab geometry may therefore act as a barrier for the rupture by slowing its velocity and reducing the amount of slip in between the shallow and deep asperities. Such an along dip segmentation had already been observed in the area during the 2007 Tocopilla earthquake that ruptured the deeper part of the seismogenic interface [*Béjar-Pizarro et al.*, 2010].

This along-dip segmentation is also associated with a change in the frequency content of the seismic rupture. The deeper asperities both rupture into a pulse of slip that is much shorter than the slippage of the shallower asperities (as shown from the rise time and the rupture speed, Figure 8.3 b and c and Figure 8.5 b and c). *Meng et al.* [2015] and *Lay et al.* [2014] have shown a compatible observation: back projected high frequency energy is radiated in the deeper portion of the rupture, close the to deep asperity. Although the structural complexity might be invoked, numerical simulations also provide the simple explanation that the base of the coupled area is a zone of high prestress that tends to keep partial ruptures confined, producing pulse-like ruptures that propagate along strike [*Michel et al.*, 2017]. Such observations are compatible with the along-dip segmentation of the megathrust described in North Chile from the analysis of the frequency content of moderate magnitude earthquakes [*Piña-Valdés et al.*, In Press]. Also, *Lay* [2015] characterizes the segmentation of the subduction zone through four domains (A, B, C and D), based on the radiated energy generated by the earthquakes, using teleseismic data. Domain A corresponds to depths less than 15 km, experiencing either aseismic deformation or large coseismic displacement in tsunami earthquakes. Domain B is located between 15 - 35 km, observing the nucleation of megathrust

earthquakes that generate large slip and high amount of low-frequency radiation. Domain C is localized between 35 - 60 km depths, where a large amount of high-frequency radiation is emitted and asperities much smaller than region B are seen. Finally, the Domain D is placed deeper than 60 km and is where slow slip events, low-frequency events, and seismic tremor have been reported, and it is not reported in all subductions zones. Following the model proposed by *Lay* [2015], our results show that the shallow asperities for the mainshock such as the aftershock, are located at depths between 15 - 35, suggesting they would break the Domain B. Also, for both events, the deeper asperities are emplaced at depths between 35 - 60 km, suggesting they would break the Domain C, depicting the heterogeneity of the seismogenic zone.

8.6.3 Differences Between our Results and Previous Works

Our results are very consistent with those presented by *Duputel et al.* [2015] for the mainshock as well for the aftershock, although we use a different methodology. The main difference between their work and ours, is the number of stations used in near field for the kinematic inversion. We have employed 25 HRGPS and strong motion while they have used 19 HRGPS and strong motion (plus all the other data set). We have found a rupture with 125 s of duration, they have used just 80 s. This longer rupture allows us to observe the second deep asperity and the complexity of the rupture process to the south. We have found a similar static patch as *Duputel et al.* [2015] for the aftershock, but our results are more clear because we have included more data. Comparing our mainshock results with those of *Liu et al.* [2015], we obtain the same shallow asperity, but their slip is closer to the trench and further north with respect to the epicenter. The difference in the obtained slip can be attributed to the simpler geometry used by *Liu et al.* [2015] that does not follow a realistic slab geometry. We conclude that the parametrization of the fault plane is a first order characteristic required to perform kinematics inversions. For both events we have used more near field data than *Liu et al.* [2015], allowing to get a better resolution and the apparition of the second deep asperity. The use of HRGPS therefore seems to improve the resolution of the rupture process, filling the data gap in areas where strong motion instruments are not installed.

When authors have used teleseismic data to invert the rupture process [*Lay et al.*, 2014; *Hayes et al.*, 2014], the differences are due to the lack of resolution of those datasets to solve details that the near field data can solve. Also, our models present more details in terms of the rupture process than the static inversions [e.g., *Socquet et al.*, 2017] because modelling the waveforms provides details occurring during the rupture that a static change cannot see. The results obtained by *Meng et al.* [2015] seem to move all the asperities landward, using repetitive earthquakes and backprojection. As they do not have any *apriori* information of where the asperities provided by the static inversion or teleseismic data are located, we suspect that their results are affected by a shift in the asperity localization, providing a general picture about the slip, but incrementing the resolution in terms of the frequency content generation through back projection technique.

Table 8.1: Mainshock moment estimation and data fit using different parameterizations.

N^o of Subfaults	Starting Velocity of Initial Rupture Front km/s	Moment x10^{21} Nm	Mean Variance Reduction (%)
168	1.2	1.92	76.65
168	1.3	1.74	78.53
168	1.4	1.71	79.73
168	1.5	1.62	79.15
168	1.6	1.57	79.20
168	1.7	1.52	77.71
672	1.4	1.73	82.37

Table 8.2: Aftershock moment estimation and data fit using different parameterizations.

N^o of Subfaults	Starting Velocity of Initial Rupture Front km/s	Moment x10^{20} Nm	Mean Variance Reduction (%)
168	2.4	4.23	81.56
168	2.5	4.28	81.75
168	2.6	4.04	83.26
168	2.7	4.30	82.15
168	2.8	4.32	81.96
672	2.6	3.88	85.74

8.7 Conclusions

The kinematic rupture process of Iquique earthquake M_w 8.1 and its biggest aftershock M_w 7.7 provides interesting insights about the segmentation of the seismogenic zone. Both ruptures are confined within 15 - 50 km depths, with a low slip zone that separates shallow and deep asperities, which may be related to a change of dip in the subducting slab (or bending of it). We show that the segmentation along strike depends on several factors. The mainshock is centered on a forearc basin associated with an important gravity change in the area of $\sim$20.5^{o}S, limiting the rupture to the south. The aftershock rupture might have stopped in the vicinity of a fault system dissecting the overriding plate. Several aseismic processes may affect the rupture extension, including the long precursory slow slip surrounding the mainshock area, and the spatial distribution of interseismic coupling before the earthquake. The mainshock contributed to fill the slip deficit in the area, but changed the stresses in the region and likely triggered the biggest aftershock that ruptured a poorly coupled zone. An along-dip segmentation is also observed, notably in the frequency content of the earthquakes, in agreement with previous works in the area [*Meng et al.*, 2015; *Piña-Valdés et al.*, In Press]. These results are very important to the seismic hazard studies, where the segmentation is a primordial element of the models.

8.8 Acknowledgements

The authors thank the International Plate Boundary Observatory Chile (IPOC, www.ipoc-network.org), Laboratoire International Associé "Montessus de Ballore" (www.lia-mb.net), Cen-

tral Andean Tectonic Observatory Geodetic Array (CAnTO, http://www.tectonics .caltech.edu/resources/continuous_gps.html), Instituto Geofísico del Perú (www.igp.gob.pe) and Centro Sismológico Nacional de Chile (CSN, www.csn.uchile.cl) for making the raw GPS and strong motion data available. Jorge Jara acknowledges a Ph.D. scholarship granted by Chilean National Science Cooperation (CONICYT) through "Becas Chile" Program. Hugo Sanchez-Reyes thanks the Centre National de la Recherche Scientifique (CNRS) for a Ph.D. scholarship. The authors would like to thank E. Contreras-Reyes, M. Radiguet, M. Causse, L. Audin, J. Piña-Valdes and M. Bouchon for all the constructive discussions about this work.

Appendix

8.A GPS processing

8.A.1 Processing of co-seismic Highrate cGPS data

We have processed 25 HRGPS for the mainshock (Mw 8.1 2014/04/01, Figure 8.B.1) and 20 High-rate continuous (HRGPS) for the aftershock (Mw 7.7 2014/04/03, Figure 8.B.1) using TRACK software [*Herring et al.*, 2016]. This program uses the IGS orbits, LC combination and the tropospheric delay to obtain the relative position between each station in the network and one reference station. Because the kinematic processing of HRGPS is very sensitive to the atmosphere delay used, we fixed the zenithal tropospheric delay to the values obtained every two hours from daily processing of 186 continuous GPS stations performed in the Andes in the frame of other studies [e.g. *Socquet et al.*, 2017; *Jara et al.*, 2017]. UCNF was chosen as our reference for the kinematic processing, because of its location ∼150 km far from the epicenters of both events that allows a sufficient time delay before the arrival of the surface waves (Figure 8.B.1). UCNF station position has been estimated one hour before and after of both earthquakes.

To remove the errors coming from the orbits or multipath effect, a sidereal filtering is estimated [*Larson et al.*, 2003; *Zhong et al.*, 2010]. The filter is estimated using 2 days before or one day after the mainshock, and 2 days before the aftershock (depending on the data availability). The sidereal delay is taken into account at the moment to calculate the kinematic processing for the previous and after days of each earthquake. This value is considered as 246 s [*Larson et al.*, 2007]. For each component (North, East, Up), the signal obtained at the time of the earthquakes in the days preceding or following it is stacked, and then removed from the co-seismic signal (Figure 8.B.2).

After removing the sidereal filtering from the original signal, a spatial filtering or common mode has been calculated. It allows to remove any effect produced by the earthquake, notably the effect of the arrival of surface waves, at the reference site[*Wdowinski et al.*, 1997]. We have stacked the stations close to the reference site (PB06, PB05, PB04, PB07, PB02 and PB03 that are located within a distance range of 100 km of the reference station, Figure 8.B.1), and removed this signal from the entire network (e.g Figure 8.B.3), thus removing the effect of the surface waves passing through the reference site.

8.A.2 Static coseismic offset

The static co-seismic offsets have been estimated for each component in all the network. The most simple Trajectory Model proposed by *Bevis and Brown* [2014] is considered:

$$x(t) = x_R + v(t - t_R) + bH(t - t_R) \tag{8.10}$$

where x_R is the position at a given reference time t_R, v the velocity and H is the Heaviside function associated with the coseismic offset b. Assuming that the station should be stable before and after the earthquake, we have taken 500 s since one minute before the earthquake occurrence (to avoid any precursor effect) and 500 s ∼8 minutes after the event, avoiding the pass of the surface waves (e.g. Figure 8.B.4). Table 8.B.1 shows the positions estimated for each station, the coseismic offsets inverted from the data, with their respective errors for both the Mw 8.1 2014/04/01 mainshock and the Mw 7.7 2014/04/03 aftershock.

8.B Appendix Figures and Tables

Table 8.B.1: GPS Position from the daily processing and mainshock - aftershock static displacements for North (N), East (E) and Vertical (V) with their respectives errors in cm from kinematic processing.

Station Name	Position		Mainshock						Aftershock					
	Lon(^{o})	Lat (^{o})	N	eN	E	eE	Z	eZ	N	eN	E	eE	Z	eZ
TRTA	-70.041	-17.482	-0.960	0.080	0.130	0.060	-0.310	0.090	-	-	-	-	-	-
PALC	-69.957	-17.781	-1.610	0.090	-0.550	0.160	-0.750	0.270	-	-	-	-	-	-
PMCA	-70.909	-17.949	-0.220	0.080	-0.590	0.100	-0.280	0.220	-	-	-	-	-	-
LYAR	-70.569	-18.134	-0.850	0.080	-0.390	0.060	-0.560	0.100	-	-	-	-	-	-
PTRE	-69.574	-18.194	-3.990	0.120	-4.710	0.060	-2.880	0.150	0.070	0.130	-0.010	0.060	0.030	0.090
PCCL	-70.107	-18.458	-7.040	0.280	-5.260	0.050	-1.610	0.220	-0.140	0.160	-0.370	0.040	-0.140	0.080
UTAR	-70.296	-18.491	-6.080	0.150	-4.420	0.070	-0.460	0.130	0.070	0.480	-0.200	0.090	-0.250	0.140
MNMI	-69.596	-19.131	-11.320	0.070	-22.490	0.090	0.060	0.140	-1.210	0.280	-0.940	0.090	-0.460	0.200
ATJN	-70.137	-19.301	-27.110	0.080	-48.840	0.090	-17.480	0.120	-1.300	0.090	-1.010	0.070	-0.140	0.130
PSGA	-70.123	-19.597	-21.760	0.100	-73.300	0.120	-26.620	0.530	-0.940	0.230	-1.790	0.090	-1.050	0.190
COLC	-68.639	-19.276	-4.030	0.610	-10.010	0.080	0.710	0.180	-1.360	0.350	-2.260	0.080	-0.110	0.130
IQQE	-70.132	-20.274	4.690	0.100	-27.020	0.190	-0.520	0.240	-2.980	0.260	-16.710	0.110	6.170	0.190
CHMZ	-69.194	-19.669	-2.650	0.150	-21.580	0.060	0.320	0.120	-2.300	0.130	-4.680	0.060	-0.160	0.130
PB11	-69.656	-19.761	-5.600	0.060	-41.140	0.090	-9.770	0.180	-3.680	0.390	-4.790	0.080	-1.780	0.160
PCHA	-69.432	-19.869	-0.940	0.040	-29.040	0.060	-1.720	0.100	-3.750	0.580	-6.100	0.080	-1.460	0.180
PB08	-69.161	-20.143	2.000	0.090	-16.100	0.080	0.510	0.140	-1.420	0.080	-7.240	0.090	-0.900	0.250
CGTC	-70.069	-20.177	2.830	0.100	-33.480	0.060	-1.580	0.110	-2.670	0.670	-11.150	0.070	2.340	0.190
PICC	-69.335	-20.490	2.290	0.190	-12.130	0.070	0.130	0.300	-0.380	0.080	-10.040	0.080	-1.780	0.130
AEDA	-70.178	-20.546	-2.370	0.260	-5.880	0.110	-0.970	0.150	-6.700	0.490	-20.810	0.100	8.800	0.150
CRSC	-70.080	-20.918	-0.260	0.150	-1.470	0.090	-2.720	0.130	-	-	-	-	-	-
PB01	-69.488	-21.044	1.950	0.140	-3.530	0.080	-2.230	0.110	2.130	0.100	-4.100	0.080	-1.350	0.170
PB02	-69.893	-21.315	0.170	0.060	-0.980	0.050	0.380	0.080	-0.100	0.960	-0.720	0.050	-0.160	0.140
PB07	-69.886	-21.727	0.240	0.050	0.060	0.050	0.050	0.070	-0.040	0.090	-0.240	0.040	0.020	0.090
PB03	-69.752	-22.049	-0.110	0.050	-0.250	0.050	-1.930	0.100	-0.040	0.060	0.000	0.050	-0.050	0.110
PB04	-70.150	-22.335	-0.420	0.090	0.110	0.050	-1.620	0.090	-0.020	0.040	0.060	0.040	0.100	0.100

Table 8.B.2: Velocity Model from *Peyrat et al.* [2010].

Depth km	V_P km/s	V_s km/s	Density g/cm^3
0	5.30	3.10	2.5
4	5.30	3.10	2.5
10	6.00	3.45	2.7
15	6.90	3.95	2.8
40	7.60	4.40	3.3
60	8.45	4.80	3.4

Table 8.B.3: Standard deviations (σ) of model parameters (strike and dip slip, rise time and rupture time), used to define the variances in C_m. Model 1 refers to the model with high variability in the main text, while Model 2 with less variability.

	σ_{strike} m	σ_{dip} m	σ_{rt} s	σ_{time} s
Model 1 Mainshock	0.04 - 0.3	0.3 - 3	2	0.001-30
Model 2 Mainshock	0.003 - 0.02	0.1 - 1	1	0.001-4
Model 1 Aftershock	0.03 - 0.35	0.07 - 1.32	2	0.001-27
Model 2 Aftershock	0.007 - 0.06	0.06 - 0.5	1	0.001-4

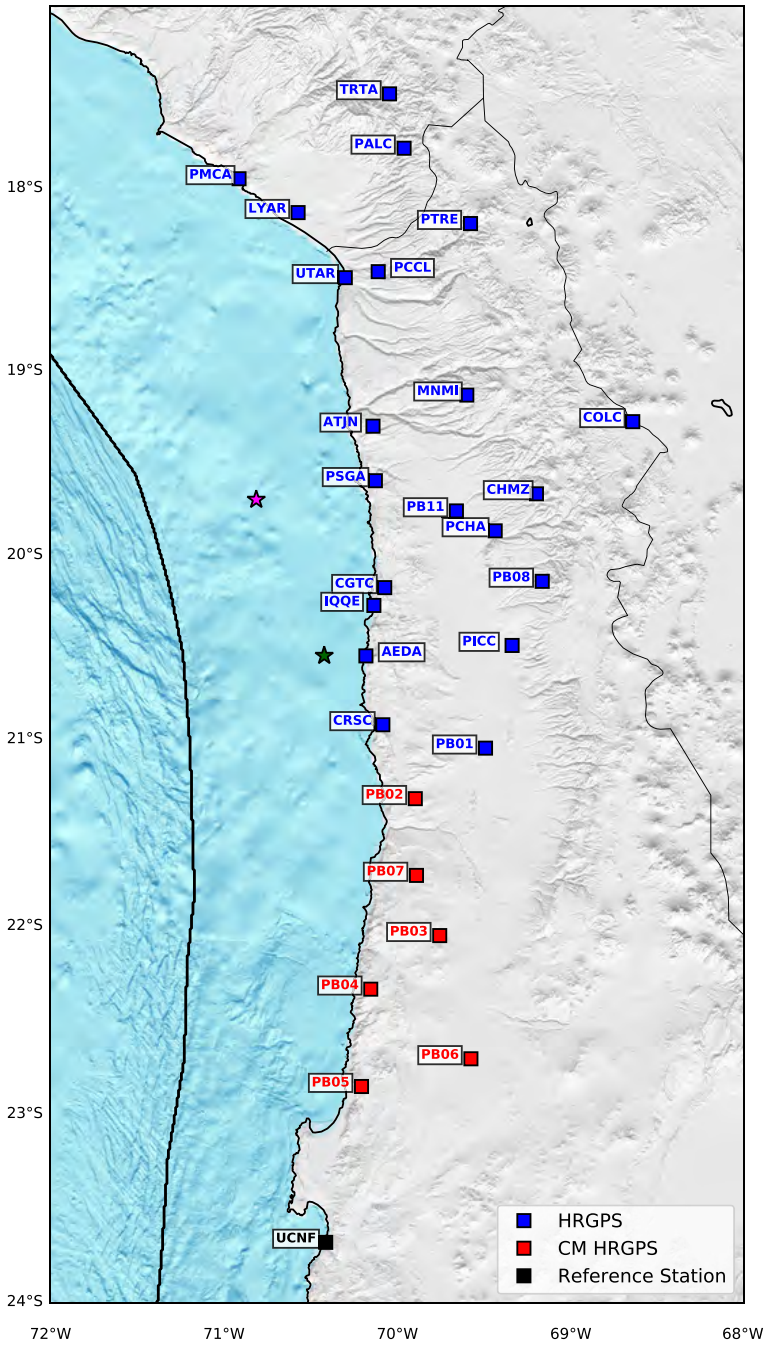

Figure 8.B.1: Map of HRGPS used during this study (blue squares), stations employed to calculate the common mode (red squares) and reference site (black square). Pink (green) star simbolizes the epicenter of the mainshock (aftershock) reported by the CSN catalog.

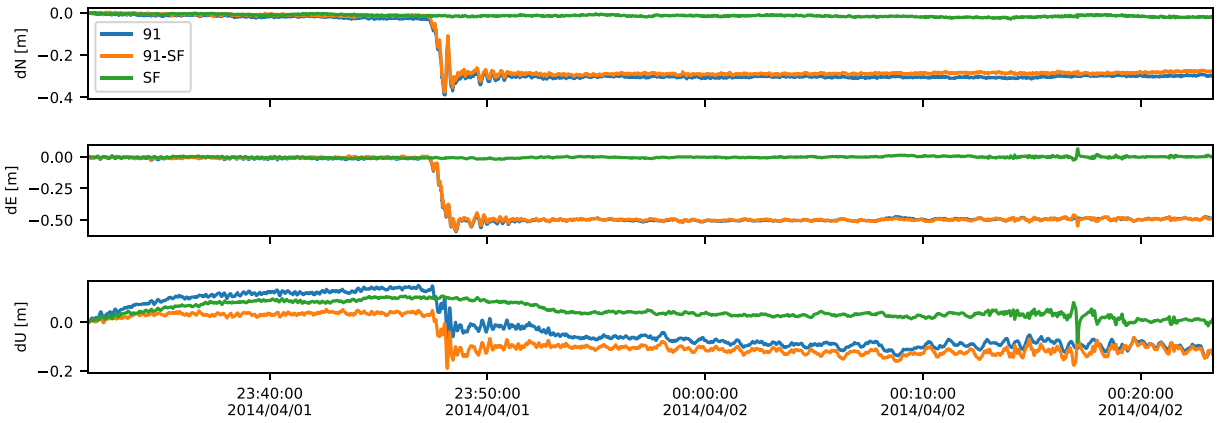

Figure 8.B.2: North, east and vertical sidereal filtering (green), original GPS signal for ATJN station (blue) and corrected GPS signal by the sidereal filtering (orange).

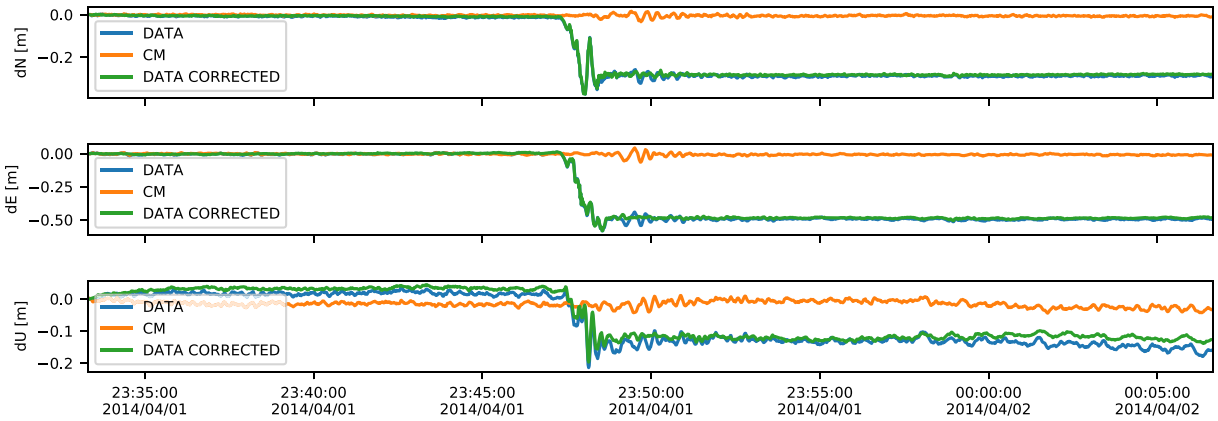

Figure 8.B.3: Common mode signal (orange), GPS signal corrected from Figure 8.B.2 (ATJN station, blue) and GPS corrected by Common Mode (green).

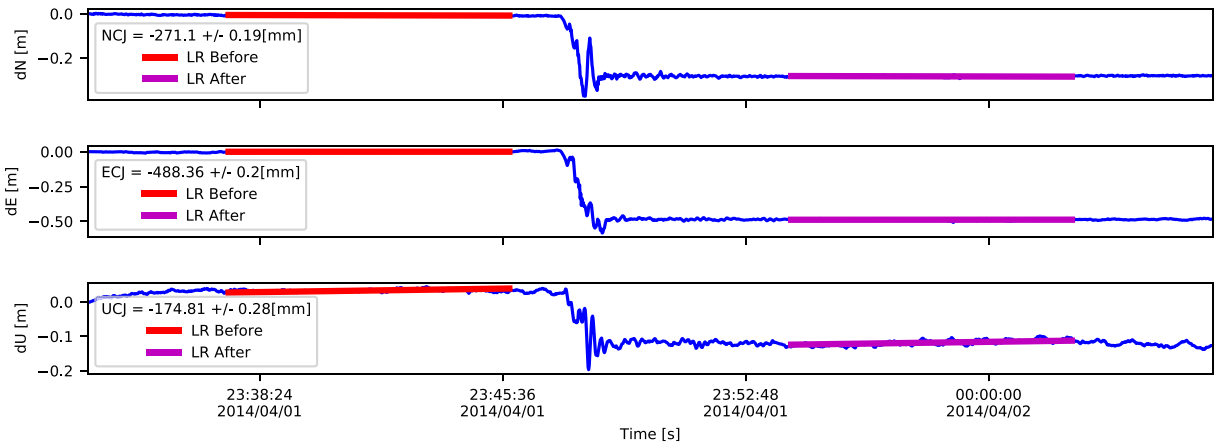

Figure 8.B.4: ATJN station GPS signal (blue) and inverted linear regressions before (red) and after (magenta) for the mainshock. Boxes show the static offset caculated during the inversion procedure in mm.

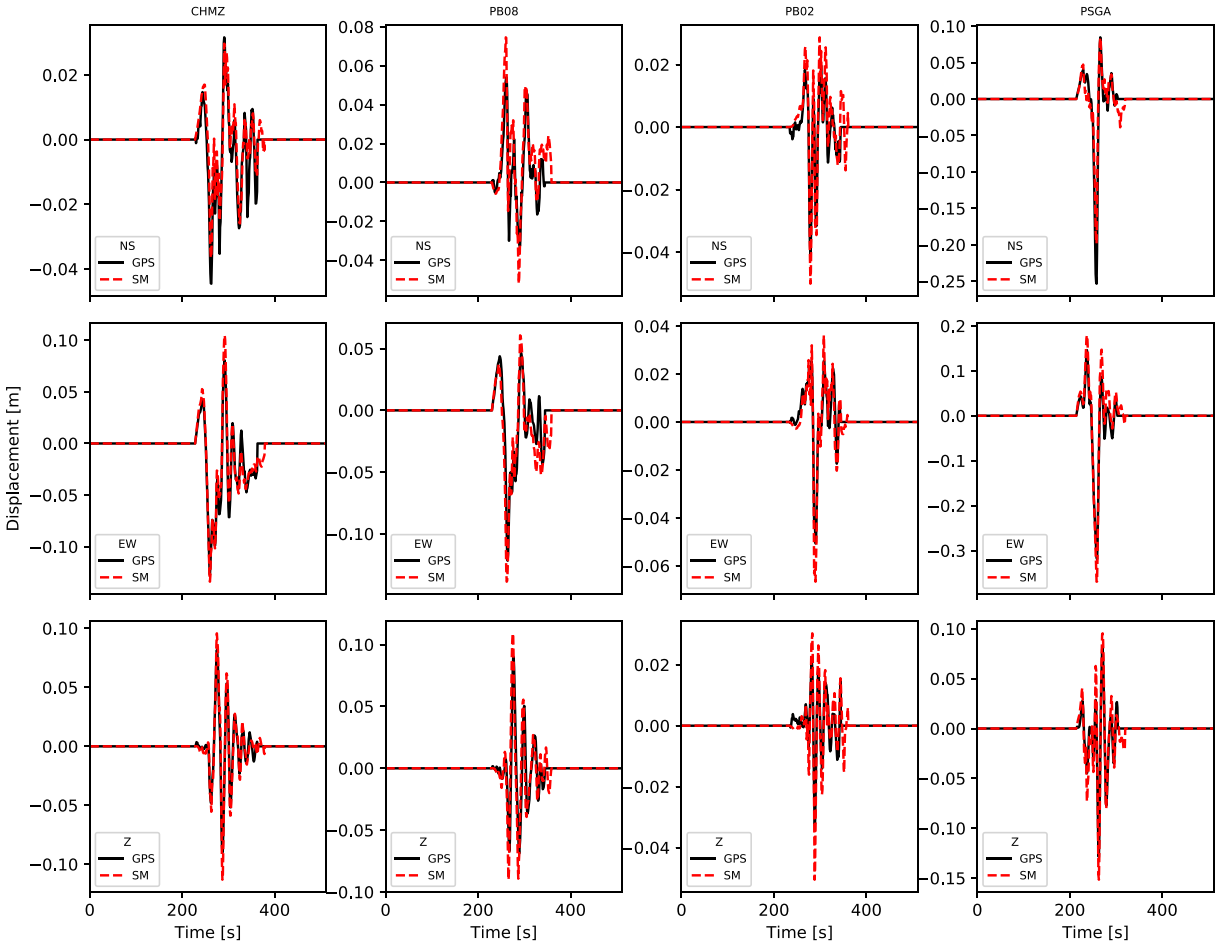

Figure 8.B.5: North, east and vertical compared displacements for HRGPS (continuous black line) and Strong Motion (dashed red line), filtered for 0.01 - 0.5 Hz.

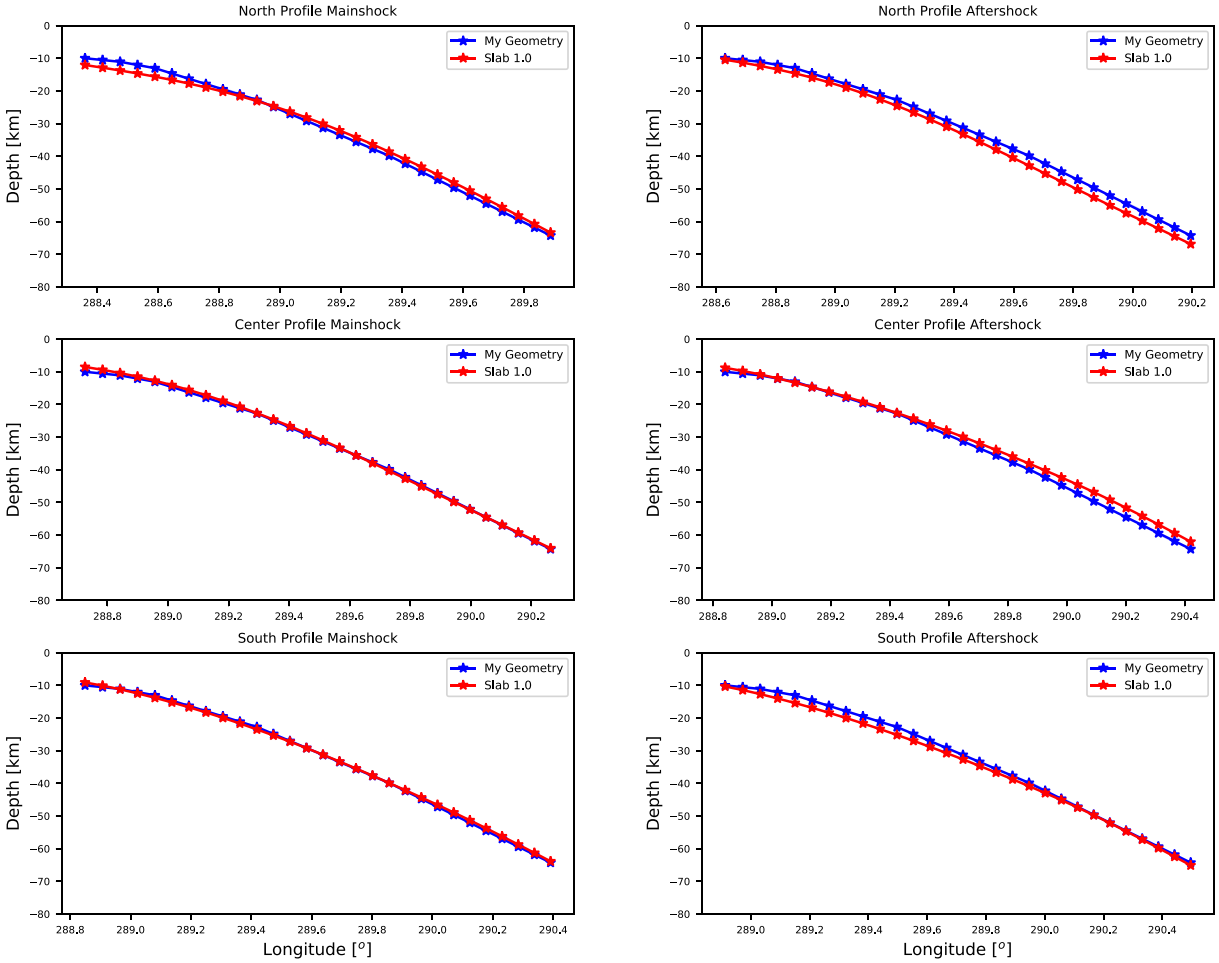

Figure 8.B.6: Comparison between geometries used in the static and kinematic inversions with Slab 1.0 [*Hayes et al.*, 2012]. On the left, north, east and vertical profiles at depth for the mainshock and on the right for the aftershock. The profiles were made at the north, center and south of the fault plane.

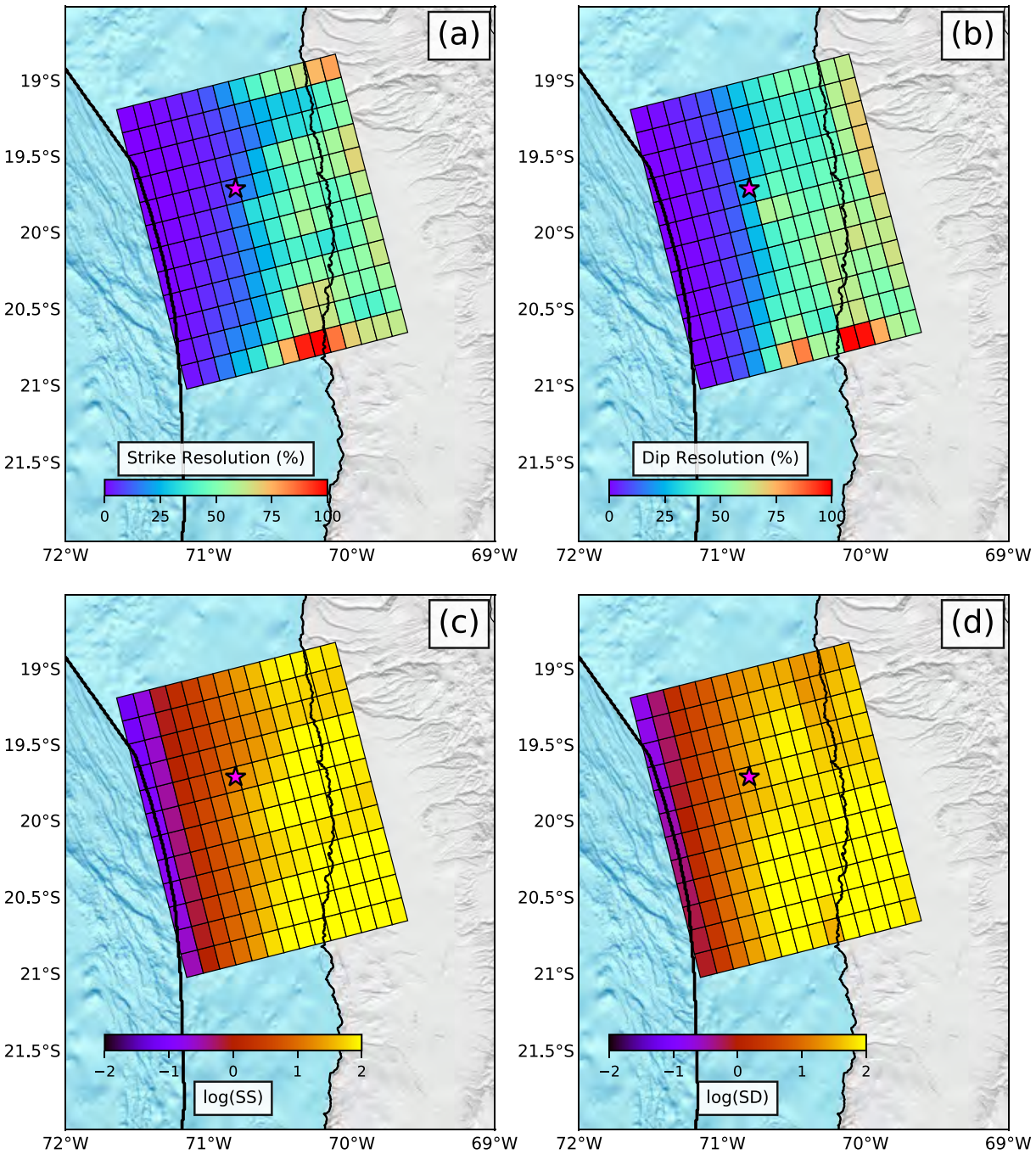

Figure 8.B.7: Mainshock Static Inversion Resolution Analysis. (a) and (b) show diagonal of the resolution matrix on strike and dip component. (c) and (d) present the sensitivity performed on strike and dip.

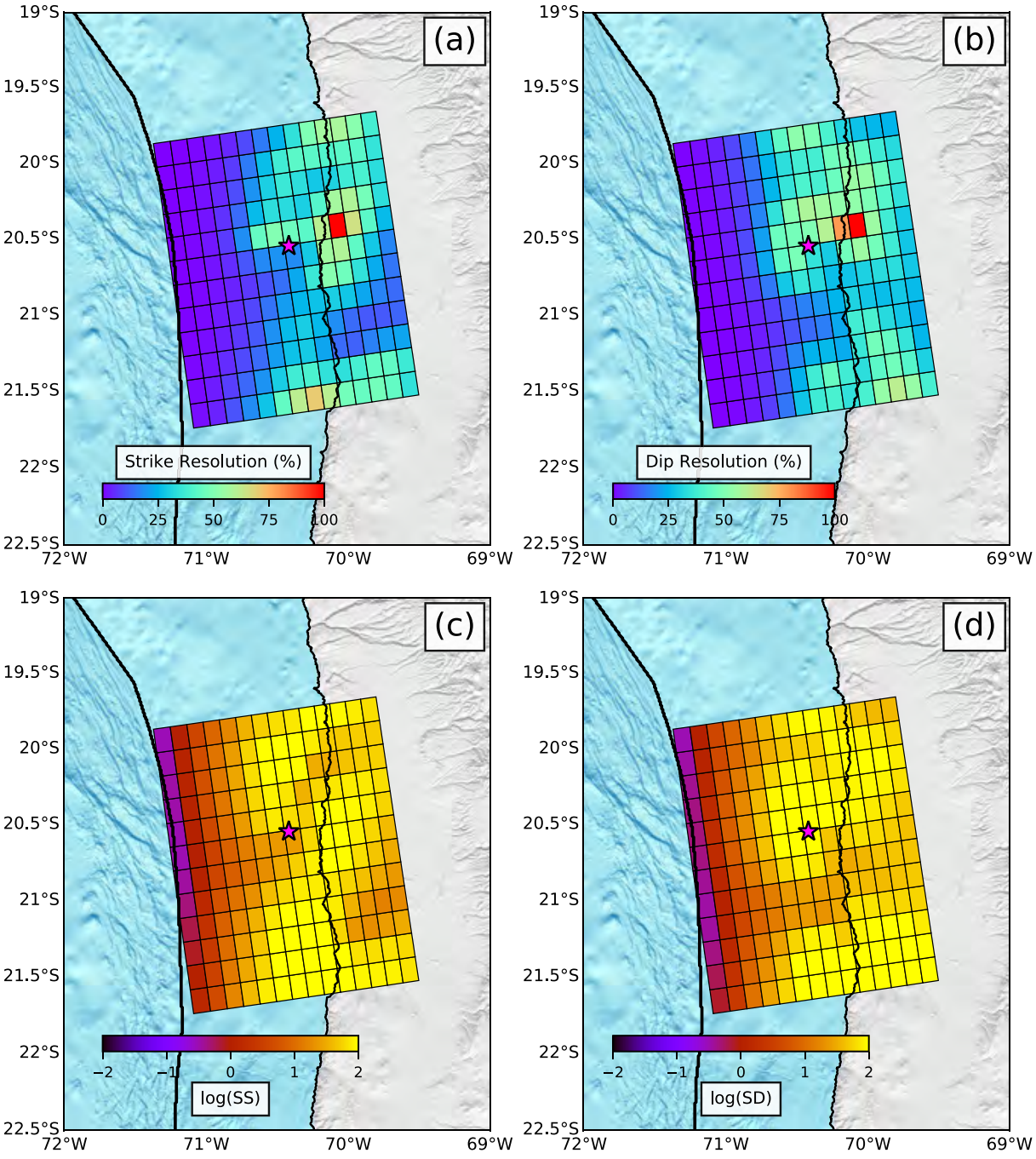

Figure 8.B.8: Same caption as in Figure 8.B.7 but for the aftershock.

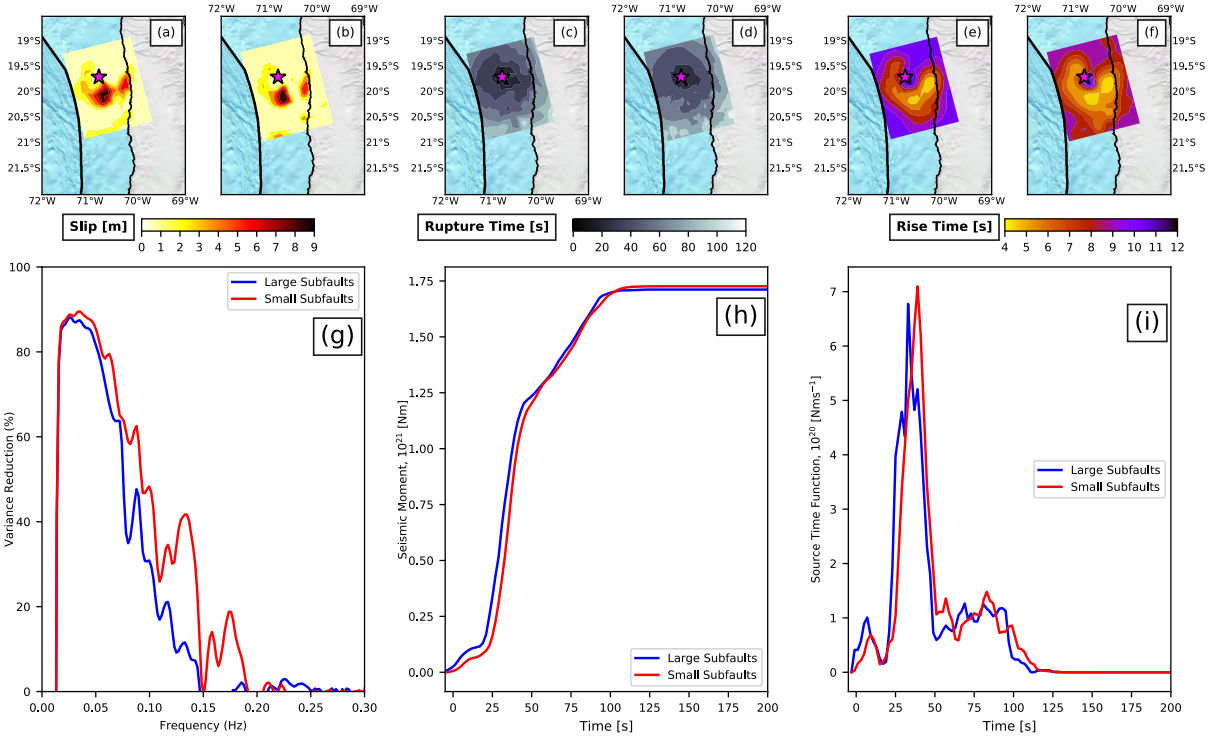

Figure 8.B.9: Comparison between mainshock kinematic results (slip, rupture time and rise time) obtained using large subfaults (a), (c) and (e) and a small discretization (b), (d) and (f). (g), (h) and (i) show the comparison between the mean variance reductions, cumulative seismic moments and source time functions for large (blue) and small (red) subfault.

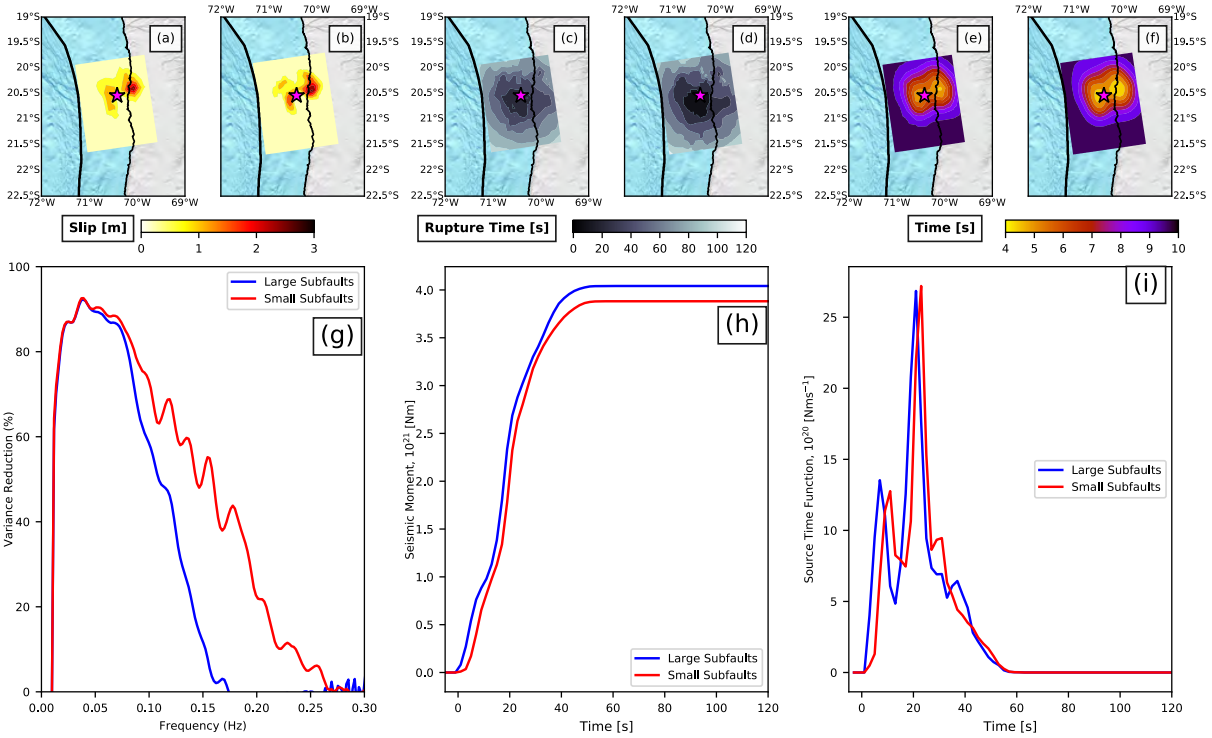

Figure 8.B.10: Same caption as in Figure 8.B.9 but for the aftershock.

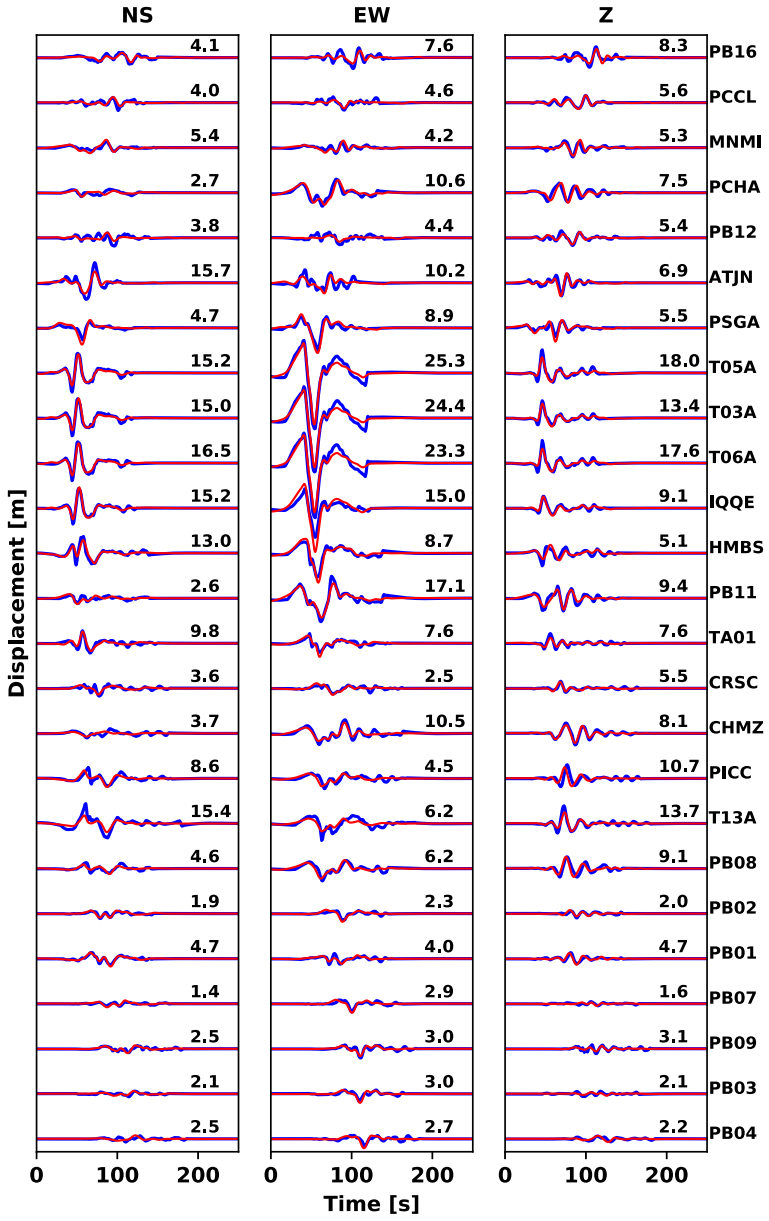

Figure 8.B.11: Mainshock Strong Motion - HRGPS (blue) and synthetics seismograms (red). For each station and component, the maximum data displacement is shown in cm.

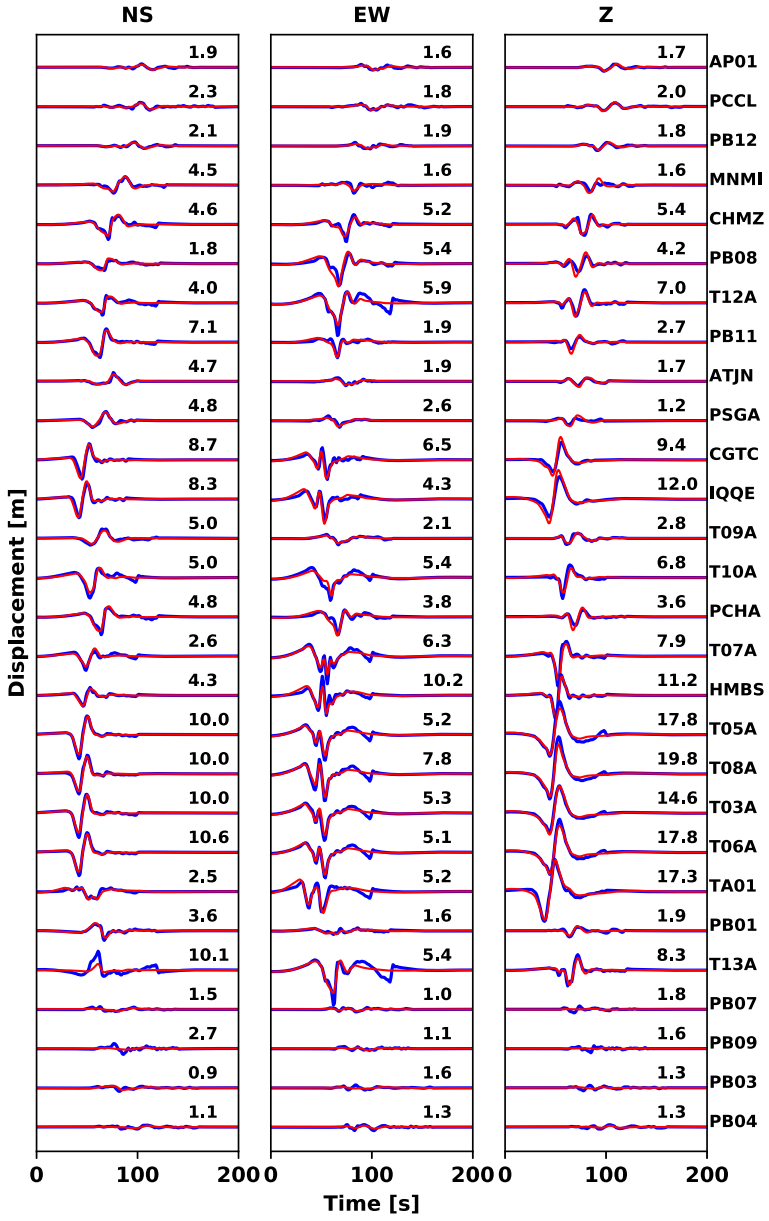

Figure 8.B.12: Same caption as in Figure 8.B.11 but for the aftershock.

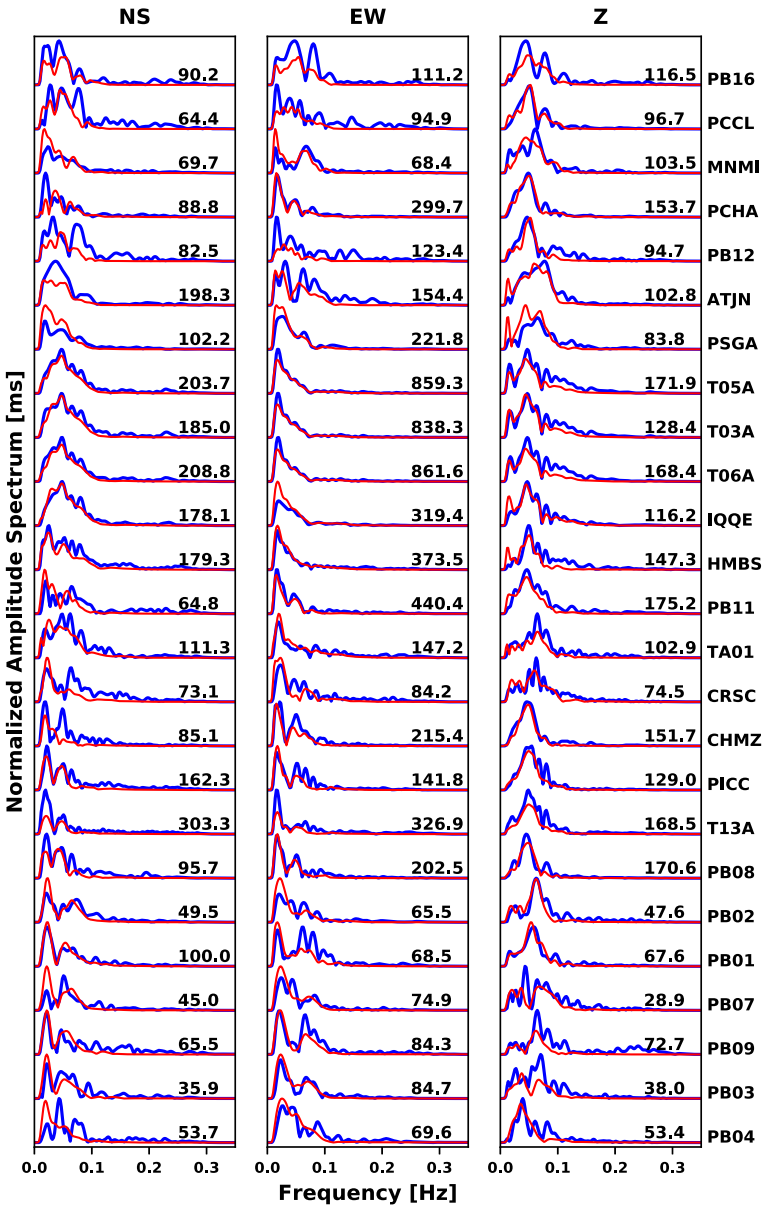

Figure 8.B.13: Mainshock normalized Strong Motion and - HRGPS and synthetics in frequency. For each station and component, the maximum data amplitude spectrum is shown in ms.

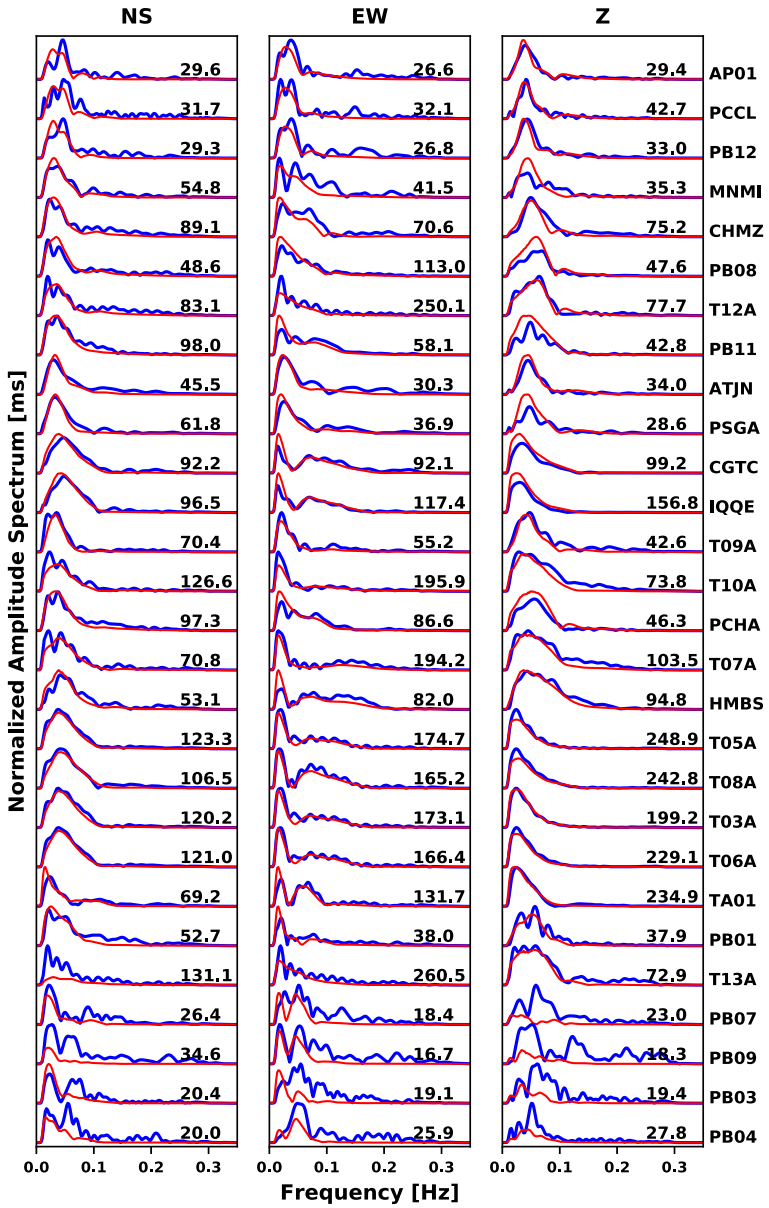

Figure 8.B.14: Same caption as in Figure 8.B.13 but for the aftershock.

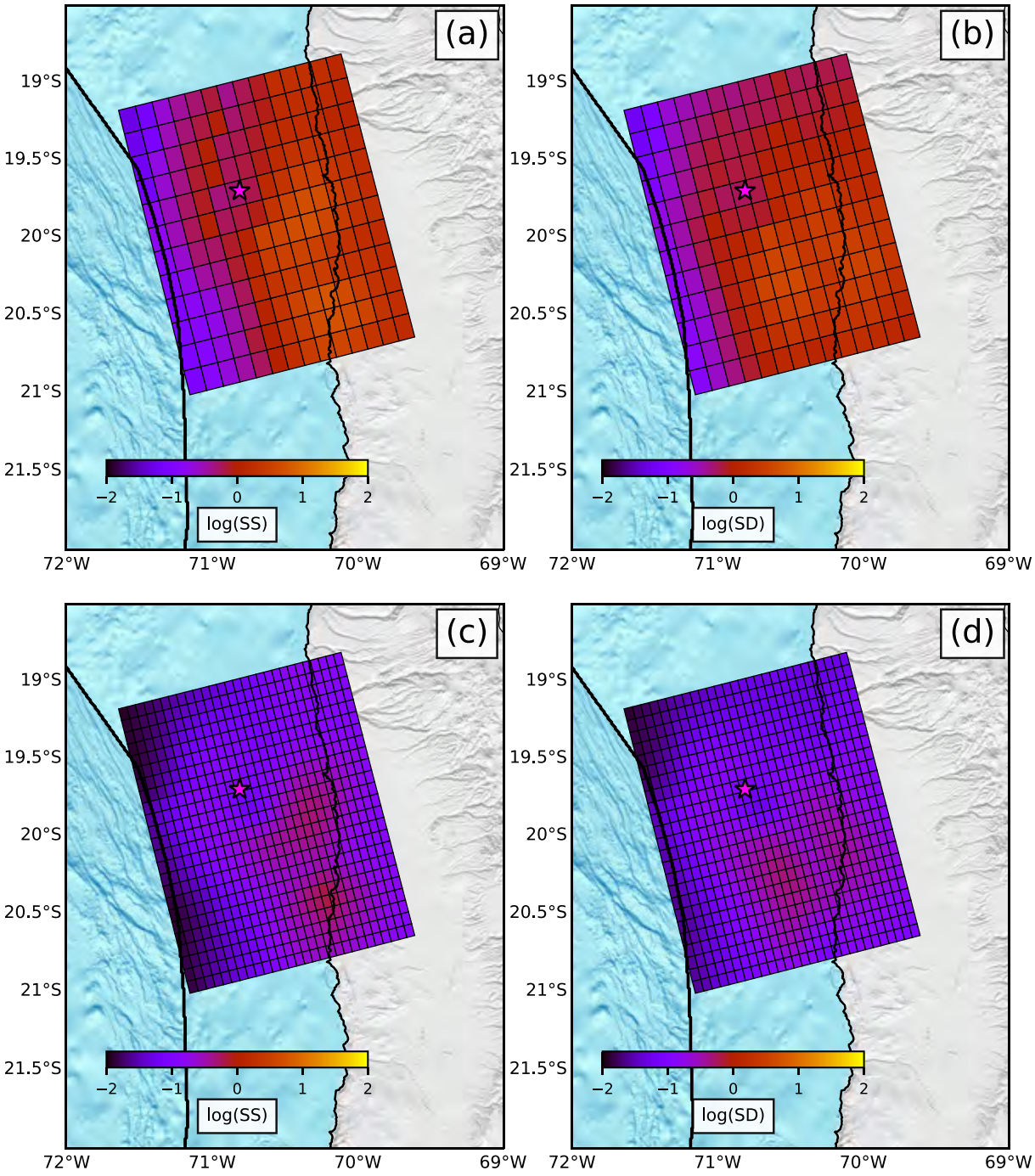

Figure 8.B.15: Mainshock kinematic sensitive for large ((a) strike and (b) dip) and small ((c) strike and (d)) subfaults.

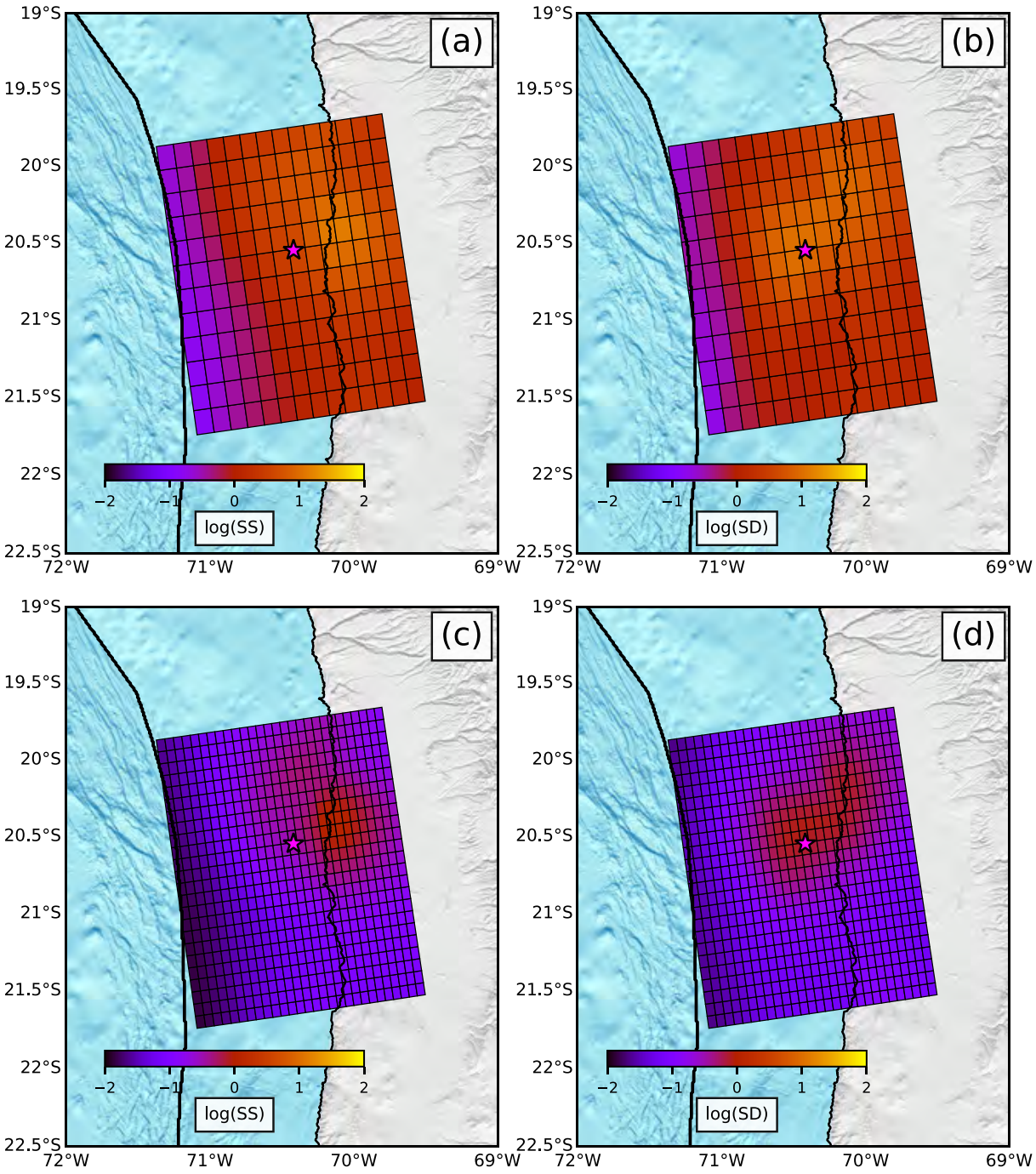

Figure 8.B.16: Same caption as in Figure 8.B.15 but for the aftershock.

Chapter 9

General Conclusions

During the four years of this thesis work, my research was focused on a better comprehension of the relationship between the geodetic and seismological data. The need to integrate these data sets becomes of great importance to understand the seismic versus aseismic behavior of a fault and their relationships. My interest in this point becomes primordial in subduction zones, because of the great earthquakes that are generated in these regions affecting the lives of millions of people worldwide. The study area analyzed is the subduction zone of South Peru - North Chile, because of the amount and good quality data available on both earthquakes and interseismic phase. In addition, my Chilean nationality generates a particular personal interest in the seismic behavior of this region. Understanding the physical processes that generate the earthquakes should provide information that could be used to mitigate their effects on the population.

A brief summary of the main results obtained in the Chapters 5, 6, 7 and 8 is presented, indicating as well, the potential future work in perspective to continue the research subject.

In Chapter 5, we show evidence for the interactions between shallow and intermediate depth seismicity. The Taparaca slab-pull earthquake in 2005 initiates an increment of the shallow seismicity associated with the decoupling of the subduction interface, eventually leading to the Iquique earthquake in 2014 (Figure 9.1). The 16 interactions between shallow and intermediate depth seismicity after Tarapaca earthquake occurrence, suggest that the subduction interface decoupling is associated with aseismic deformation due to the slab plunge. An interesting future work would be investigating how the aseismic deformation produced by the slab plunge is propagated to shallow depths through a mechanical model. Because the magnitudes of the events are quite low ($4 < M_w < 5.5$), it is difficult to invoke changes in the Coulomb stress, suggesting that other interaction mechanisms need to be explored. The large completeness magnitude of the catalog may be a problem, leading to a loss of informations for earthquakes of small magnitudes. One approach that could be valuable to apply in the future on the seismological data is the matched-filter technique. It allows detecting more events from continuous records, revealing phenomena like migration of seismicity and repeating earthquakes, that might be an indicator of the seismic and aseismic interaction during the shallow - deep synchronizations.

In Chapter 6, the preliminary results on the sSSEs detection in South Peru and Chile are pre-

sented. 41 events are found with magnitudes between 6.1 - 6.9 and durations ranging between 3 - 93 days, located mostly in the deeper part of the seismogenic zone (Figure 9.1). Comparing the results with the interseismic coupling indicates that 68% of these events are in zones with low or intermediate coupling values. The temporal evolution of the detected sSSEs show an intense activity in the region affected by Tocopilla earthquake after its occurrence, that may be an indicator of a long-postseismic phase associated with mantle viscoelastic relaxation. Close to the region affected by Iquique earthquake, the increment of sSSEs activity towards the date of the earthquake may be associated with the long preparation phase of the earthquake. A better characterization of the sSSEs is needed, notably on the recurrence time of SSEs in some areas and on repetitive events. It would be interesting in the future to compare the results obtained in this chapter with seismological studies on repeating earthquakes [e.g., *Kato and Nakagawa*, 2014; *Meng et al.*, 2015; *Kato et al.*, 2016], since no tremor nor low-frequency earthquakes have been detected so far in the area.

In Chapter 7, the observations confirm that a long-term slow slip event of the subduction interface led to the nucleation of Iquique earthquake in 2014 (Figure 9.1). The results show the capability of the geodetic data in studying the preparation phase of the earthquakes, if one looks at them carefully, revealing the strong interaction between seismic and aseismic slip at this stage of the seismic cycle. An interesting perspective work would be studying the spatial and temporal evolution of the SSE employing a quasistatic approach [e.g., *Radiguet et al.*, 2011]. Potentially, it would provide a better constrain in the location and source information as well.

In Chapter 8, the kinematic rupture process of Iquique earthquake and its biggest aftershock is explored. The results reveal a complex segmentation of the seismogenic zone in the area affected by the earthquakes both along strike and along dip (Figure 9.1). This segmentation seems to be controlled by changes in the gravimetry and tectonic structures in the forearc, and a change in the slab geometry along dip. The results show the advantage to perform inversions in the frequency domain, having a continuum between the static and kinematic solutions in terms of frequency, that helped identifying an along depth change in frequency content. Also, the fact to provide a better preconditioning to the inversions helps a lot to find the final solution. We find that the geometry is of first-order importance for the kinematics of the rupture exploration. Advancing in models including more realistic geometry design seems to be a step to consider. In the future progresses should be made towards the implementation of a Bayesian inversion in the frequency domain as well as in dynamic inversions, in order to explore more physical parameters.

The results presented in this thesis allow for a general conclusion that in the study area, the interseismic period is not quiescent, revealing the complexity of the tectonic loading/release processes, including the presence of small aseismic slip burst that had not been observed before (Figure 9.1). Those results are made possible by going beyond the first order in the data exploration. The GPS noise seems to contain masked information [*Métois et al.*, 2014; *Frank*, 2016; *Rousset et al.*, 2017] that requires innovative methods to be investigated and exploited.

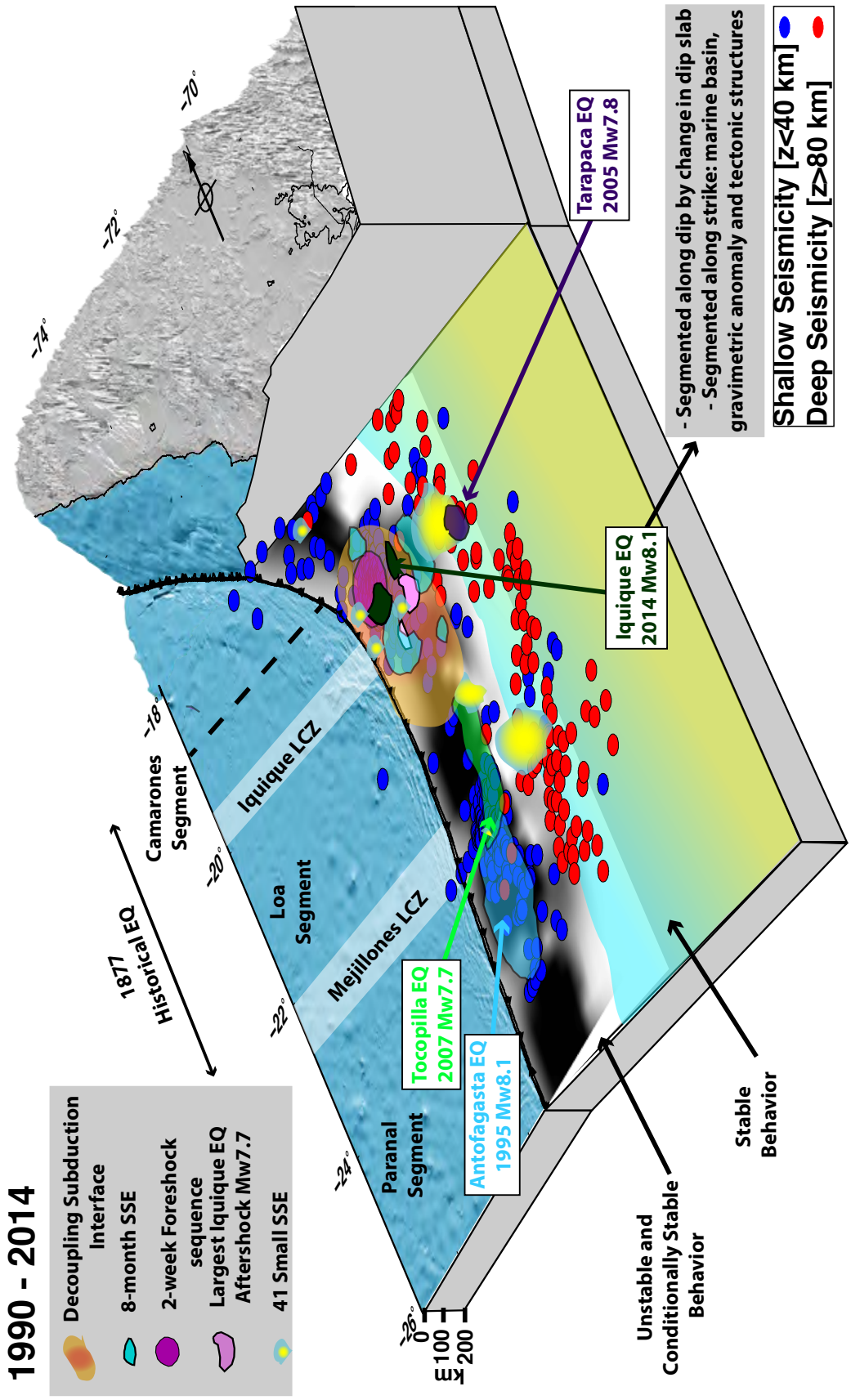

Figure 9.1: 3D schematic overview of main results obtained during this Ph.D. Shallow (deep) seismicity are color coded in blue (red) and scaled by magnitude in the period 1990 - 2014. Antofagasta, Tocopilla, Tarapaca and Iquique rupture areas are plotted. The main slip behaviors in the area struck by Iquique earthquake are plotted since 2005. Areas affected by sSSE's are in yellow. Coupling map from *Métois et al.* [2016].

The interaction between seismic and aseismic slip seems to play an important role in the preparation phase of earthquakes, as well as in the loading processes. This work shows one of the first evidence of a long preparation phase of earthquakes due to aseismic processes loading the mainshock area until the triggering of the main earthquake, supporting some models proposed [*Ellsworth et al.*, 1995; *Dodge et al.*, 1996] and laboratory experiments [*Dieterich*, 1992; *Ohnaka*, 2003; *McLaskey and Lockner*, 2014; *Scuderi et al.*, 2016].

Another interesting point observed during the course of this thesis is the role of the slab in the generation of slip on the subduction interface, whatever it is seismic or aseismic [*Durand et al.*, 2014; *Bouchon et al.*, 2016; *Lay et al.*, 2017]. The plunge of the slab seems to trigger a spread deformation that helps decoupling the interface generating aseismic deformation on it and favors slow slip that leads the preparation phase of megathrust earthquakes. The observations need to be further explored to find a mechanical model that explains this behavior.

Using a kinematic approach, the coupling maps provide some insights into the locking degree on faults but not about the mechanical properties of the subduction interface. A manner to move on, is the genesis of asperity models based on realistic physical parameters and geodetic data [*Bürgmann et al.*, 2005; *Hetland and Simons*, 2010; *Kanda et al.*, 2013; *Johnson et al.*, 2016]. Part of this work has been started in collaboration with M. Simons during the course of this thesis, but it is not finalized yet. I will continue working on this problem during my postdoc, in order to compare the interseismic maps with models based on rate-and-state friction law. Also, these models provide an insight into how the seismic and aseismic slip are interacting on the subduction interface, providing a complementary approach to continue the work based on the scientific questions raised in this thesis.

Bibliography

Abercrombie, R. E., M. Antolik, K. Felzer, and G. Ekström (2001), The 1994 Java tsunami earthquake: Slip over a subducting seamount, *Journal of Geophysical Research: Solid Earth*, *106*(B4), 6595–6607, doi:10.1029/2000JB900403.

Abrahamson, N., N. Gregor, and K. Addo (2016), BC Hydro ground motion prediction equations for subduction earthquakes, *Earthquake Spectra*, *32*(1), 23–44, doi:10.1193/051712eqs188mr.

Abrahamson, N. A., and R. Youngs (1992), A stable algorithm for regression analyses using the random effects model, *Bulletin of the Seismological Society of America*, *82*(1), 505–510.

Agnew, D. C. (1992), The time-domain behavior of power-law noises, *Geophysical research letters*, *19*(4), 333–336, doi:10.1029/91gl02832.

Aki, K. (1979), Characterization of barriers on an earthquake fault, *Journal of Geophysical Research: Solid Earth*, *84*(B11), 6140–6148, doi:10.1029/JB084iB11p06140.

Al Atik, L., N. Abrahamson, J. J. Bommer, F. Scherbaum, F. Cotton, and N. Kuehn (2010), The variability of ground-motion prediction models and its components, *Seismological Research Letters*, *81*(5), 794–801, doi:10.1785/gssrl.81.5.794.

Allmendinger, R. W., and G. González (2010), Neogene to Quaternary tectonics of the coastal Cordillera, northern Chile, *Tectonophysics*, *495*(1), 93–110, doi:10.1016/j.tecto.2009.04.019.

Allmendinger, R. W., V. A. Ramos, T. E. Jordan, M. Palma, and B. L. Isacks (1983), Paleogeography and Andean structural geometry, northwest Argentina, *Tectonics*, *2*(1), 1–16, doi:10.1029/TC002i001p00001.

Allmendinger, R. W., T. E. Jordan, S. M. Kay, and B. L. Isacks (1997), The evolution of the Altiplano-Puna plateau of the Central Andes, *Annual review of earth and planetary sciences*, *25*(1), 139–174, doi:10.1146/annurev.earth.25.1.139.

Altamimi, Z., P. Sillard, and C. Boucher (2002), ITRF2000: A new release of the International Terrestrial Reference Frame for earth science applications, *Journal of Geophysical Research: Solid Earth*, *107*(B10), doi:10.1029/2001JB000561.

Altamimi, Z., X. Collilieux, and L. Métivier (2011), ITRF2008: an improved solution of the international terrestrial reference frame, *Journal of Geodesy*, *85*(8), 457–473, doi:10.1007/s00190-011-0444-4.

Altamimi, Z., P. Rebischung, L. Métivier, and X. Collilieux (2016), ITRF2014: A new release of the International Terrestrial Reference Frame modeling nonlinear station motions, *Journal of Geophysical Research: Solid Earth*, *121*(8), 6109–6131, doi:10.1002/2016jb013098.

Ammon, C. J., C. Ji, H.-K. Thio, D. Robinson, S. Ni, V. Hjorleifsdottir, H. Kanamori, T. Lay, S. Das, D. Helmberger, et al. (2005), Rupture process of the 2004 Sumatra-Andaman earthquake, *Science*, *308*(5725), 1133–1139, doi:10.1126/science.1112260.

Ammon, C. J., H. Kanamori, T. Lay, and A. A. Velasco (2006), The 17 July 2006 Java tsunami earthquake, *Geophysical Research Letters*, *33*(24), doi:10.1029/2006gl028005.

Ammon, C. J., T. Lay, and D. W. Simpson (2010), Great earthquakes and global seismic networks, *Seismological Research Letters*, *81*(6), 965–971, doi:10.1785/gssrl.81.6.965.

Angermann, D., J. Klotz, and C. Reigber (1999), Space-geodetic estimation of the Nazca-South America Euler vector, *Earth and Planetary Science Letters*, *171*(3), 329–334, doi:10.1016/S0012-821X(99)00173-9.

Armijo, R., and R. Thiele (1990), Active faulting in northern Chile: ramp stacking and lateral decoupling along a subduction plate boundary?, *Earth and Planetary Science Letters*, *98*(1), 40–61, doi:10.1016/0012-821X(90)90087-E.

Armijo, R., R. Rauld, R. Thiele, G. Vargas, J. Campos, R. Lacassin, and E. Kausel (2010), The West Andean thrust, the San Ramon fault, and the seismic hazard for Santiago, Chile, *Tectonics*, *29*(2), doi:10.1029/2008TC002427.

Armijo, R., R. Lacassin, A. Coudurier-Curveur, and D. Carrizo (2015), Coupled tectonic evolution of Andean orogeny and global climate, *Earth-Science Reviews*, *143*, 1–35, doi:10.1016/j.earscirev.2015.01.005.

Asano, K., and T. Iwata (2012), Source model for strong ground motion generation in the frequency range 0.1–10 Hz during the 2011 Tohoku earthquake, *Earth, planets and space*, *64*(12), 1111–1123, doi:10.5047/eps.2012.05.003.

Asano, Y., T. Saito, Y. Ito, K. Shiomi, H. Hirose, T. Matsumoto, S. Aoi, S. Hori, and S. Sekiguchi (2011), Spatial distribution and focal mechanisms of aftershocks of the 2011 off the Pacific coast of Tohoku Earthquake, *Earth, planets and space*, *63*(7), 29, doi:10.5047/eps.2011.06.016.

Astiz, L., and H. Kanamori (1986), Interplate coupling and temporal variation of mechanisms of intermediate-depth earthquakes in Chile, *Bulletin of the Seismological Society of America*, *76*(6), 1614–1622.

Astiz, L., T. Lay, and H. Kanamori (1988), Large intermediate-depth earthquakes and the subduction process, *Physics of the Earth and Planetary Interiors*, *53*(1), 80–166, doi:10.1016/0031-9201(88)90138-0.

Audin, L., P. Lacan, H. Tavera, and F. Bondoux (2008), Upper plate deformation and seismic barrier in front of Nazca subduction zone: The Chololo Fault System and active tectonics along the Coastal Cordillera, southern Peru, *Tectonophysics*, *459*(1), 174–185, doi:10.1016/j.tecto.2007.11.070.

Avouac, J.-P. (2015), From geodetic imaging of seismic and aseismic fault slip to dynamic modeling of the seismic cycle, *Annual Review of Earth and Planetary Sciences*, *43*, 233–271, doi:10.1146/annurev-earth-060614-105302.

Baby, P., P. Rochat, G. Mascle, and G. Hérail (1997), Neogene shortening contribution to crustal thickening in the back arc of the Central Andes, *Geology*, *25*(10), 883–886, doi:10.1130/0091-7613(1997)025<0883:NSCTCT>2.3.CO;2.

Bartlow, N. M., S. Miyazaki, A. M. Bradley, and P. Segall (2011), Space-time correlation of slip and tremor during the 2009 Cascadia slow slip event, *Geophysical Research Letters*, *38*(18), doi:10.1029/2011GL048714.

Beck, M. E. (1998), On the mechanism of crustal block rotations in the central Andes, *Tectonophysics*, *299*(1), 75–92, doi:10.1029/2001JB000282.

Beck, S. L., and L. J. Ruff (1989), Great earthquakes and subduction along the Peru trench, *Physics of the Earth and Planetary Interiors*, *57*(3-4), 199–224, doi:10.1016/0031-9201(89)90112-X.

Bedford, J., M. Moreno, B. Schurr, M. Bartsch, and O. Oncken (2015), Investigating the final seismic swarm before the Iquique-Pisagua 2014 Mw 8.1 by comparison of continuous GPS and seismic foreshock data, *Geophysical Research Letters*, *42*(10), 3820–3828, doi:10.1002/2015GL063953, 2015GL063953.

Béjar-Pizarro, M., D. Carrizo, A. Socquet, R. Armijo, S. Barrientos, F. Bondoux, S. Bonvalot, J. Campos, D. Comte, J. De Chabalier, et al. (2010), Asperities and barriers on the seismogenic zone in North Chile: state-of-the-art after the 2007 Mw 7.7 Tocopilla earthquake inferred by GPS and InSAR data, *Geophysical Journal International*, *183*(1), 390–406, doi:10.1111/j.1365-246X.2010.04748.x.

Béjar-Pizarro, M., A. Socquet, R. Armijo, D. Carrizo, J. Genrich, and M. Simons (2013), Andean structural control on interseismic coupling in the North Chile subduction zone, *Nature Geoscience*, *6*(6), 462–467, doi:doi:10.1038/ngeo1802.

Beroza, G. C., and S. Ide (2011), Slow earthquakes and nonvolcanic tremor, *Annual review of Earth and planetary sciences*, *39*, 271–296.

Bevis, M., and A. Brown (2014), Trajectory models and reference frames for crustal motion geodesy, *Journal of Geodesy*, *88*(3), 283–311, doi:10.1007/s00190-013-0685-5.

Bevis, M., S. Businger, T. A. Herring, C. Rocken, R. A. Anthes, and R. H. Ware (1992), GPS meteorology: Remote sensing of atmospheric water vapor using the Global Positioning System, *Journal of Geophysical Research: Atmospheres*, *97*(D14), 15,787–15,801, doi:10.1029/92JD01517.

Bevis, M., S. Businger, S. Chiswell, T. A. Herring, R. A. Anthes, C. Rocken, and R. H. Ware (1994), GPS meteorology: Mapping zenith wet delays onto precipitable water, *Journal of Applied Meteorology*, *33*(3), 379–386, doi:10.1175/1520-0450(1994)033<0379:GMMZWD>2.0.CO;2.

Bevis, M., E. Kendrick, R. Smalley, B. Brooks, R. Allmendinger, and B. Isacks (2001), On the strength of interplate coupling and the rate of back arc convergence in the central Andes: An analysis of the interseismic velocity field, *Geochemistry, Geophysics, Geosystems*, *2*(11), doi:10.1029/2001GC000198.

Bie, L., I. Ryder, and M. Metois (2017), Deep postseismic viscoelastic relaxation excited by an intraslab normal fault earthquake in the Chile subduction zone, *Tectonophysics*, doi:10.1016/j.tecto.2017.07.012.

Biggs, J., D. P. Robinson, and T. H. Dixon (2009), The 2007 Pisco, Peru, earthquake (M8. 0): seismology and geodesy, *Geophysical Journal International*, *176*(3), 657–669, doi:10.1111/j.1365-246X.2008.03990.x.

Bilek, S. L. (2010), Invited review paper: Seismicity along the South American subduction zone: Review of large earthquakes, tsunamis, and subduction zone complexity, *Tectonophysics*, *495*(1), 2–14, doi:10.1016/j.tecto.2009.02.037.

Bilek, S. L., and T. Lay (2002), Tsunami earthquakes possibly widespread manifestations of frictional conditional stability, *Geophysical Research Letters*, *29*(14), doi:10.1029/2002gl015215.

Bilek, S. L., S. Y. Schwartz, and H. R. DeShon (2003), Control of seafloor roughness on earthquake rupture behavior, *Geology*, *31*(5), 455–458, doi:10.1130/0091-7613(2003)031<0455:COSROE>2.0.CO;2.

Bilek, S. L., C. P. Conrad, and C. Lithgow-Bertelloni (2005), Slab pull, slab weakening, and their relation to deep intra-slab seismicity, *Geophysical research letters*, *32*(14), doi:10.1029/2005GL022922.

Bindi, D., S. Parolai, E. Görgün, H. Grosser, C. Milkereit, M. Bohnhoff, and E. Durukal (2007), ML scale in Northwestern Turkey from 1999 Izmit aftershocks: updates, *Bulletin of the Seismological Society of America*, *97*(1B), 331–338, doi:10.1785/0120060071.

Bird, P. (2003), An updated digital model of plate boundaries, *Geochemistry, Geophysics, Geosystems*, *4*(3), doi:10.1029/2001GC000252.

Bird, P., and C. Kreemer (2015), Revised tectonic forecast of global shallow seismicity based on version 2.1 of the Global Strain Rate Map, *Bulletin of the Seismological Society of America*, *105*(1), 152–166.

Blanpied, M., D. Lockner, and J. Byerlee (1991), Fault stability inferred from granite sliding experiments at hydrothermal conditions, *Geophysical Research Letters*, *18*(4), 609–612, doi:10.1029/91GL00469.

Blanpied, M. L., D. A. Lockner, and J. D. Byerlee (1995), Frictional slip of granite at hydrothermal conditions, *Journal of Geophysical Research: Solid Earth*, *100*(B7), 13,045–13,064, doi:10.1029/95JB00862.

Blewitt, G. (2007), GPS and Space-Based Geodetic Methods-3.11.

Bock, Y., and D. Melgar (2016), Physical applications of GPS geodesy: a review, *Reports on Progress in Physics*, *79*(10), 106,801, doi:10.1088/0034-4885/79/10/106801.

Boehm, J., B. Werl, and H. Schuh (2006), Troposphere mapping functions for GPS and very long baseline interferometry from European Centre for Medium-Range Weather Forecasts operational analysis data, *Journal of Geophysical Research: Solid Earth*, *111*(B2), doi:10.1029/2005jb003629.

Boore, D. M., A. A. Sisi, and S. Akkar (2012), Using pad-stripped acausally filtered strong-motion data, *Bulletin of the seismological society of america*, *102*(2), 751–760, doi:10.1785/0120110222.

Bouchon, M. (1981), A simple method to calculate Green's functions for elastic layered media, *Bulletin of the Seismological Society of America*, *71*(4), 959–971.

Bouchon, M., H. Karabulut, M. Aktar, S. Özalaybey, J. Schmittbuhl, and M.-P. Bouin (2011), Extended nucleation of the 1999 Mw 7.6 Izmit earthquake, *Science*, *331*(6019), 877–880, doi:10.1126/science.1197341.

Bouchon, M., V. Durand, D. Marsan, H. Karabulut, and J. Schmittbuhl (2013), The long precursory phase of most large interplate earthquakes, *Nature Geoscience*, *6*(4), 299–302, doi:doi:10.1038/ngeo1770.

Bouchon, M., D. Marsan, V. Durand, M. Campillo, H. Perfettini, R. Madariaga, and B. Gardonio (2016), Potential slab deformation and plunge prior to the Tohoku, Iquique and Maule earthquakes, *Nature Geoscience*, *9*(5), 380–383, doi:10.1038/ngeo2701.

Bowman, D. D., and G. C. King (2001), Accelerating seismicity and stress accumulation before large earthquakes, *Geophysical Research Letters*, *28*(21), 4039–4042, doi:10.1029/2001GL013022.

Brace, W., and J. Byerlee (1966), Stick-slip as a mechanism for earthquakes, *Science*, *153*(3739), 990–992, doi:10.1126/science.153.3739.990.

Brace, W., and J. Byerlee (1970), California earthquakes: why only shallow focus?, *Science*, *168*(3939), 1573–1575, doi:10.1126/science.168.3939.1573.

Brooks, B. A., M. Bevis, K. Whipple, J. R. Arrowsmith, J. Foster, T. Zapata, E. Kendrick, E. Minaya, A. Echalar, M. Blanco, et al. (2011), Orogenic-wedge deformation and potential for great earthquakes in the central Andean backarc, *Nature Geoscience*, *4*(6), 380–383, doi:10.1038/ngeo1143.

Bunks, C., F. M. Saleck, S. Zaleski, and G. Chavent (1995), Multiscale seismic waveform inversion, *Geophysics*, *60*(5), 1457–1473, doi:10.1190/1.1443880.

Bürgmann, R., M. Kogan, V. Levin, C. Scholz, R. King, and G. Steblov (2001), Rapid aseismic moment release following the 5 December, 1997 Kronotsky, Kamchatka, earthquake, *Geophysical Research Letters*, *28*(7), 1331–1334, doi:10.1029/2000GL012350.

Bürgmann, R., M. G. Kogan, G. M. Steblov, G. Hilley, V. E. Levin, and E. Apel (2005), Interseismic coupling and asperity distribution along the Kamchatka subduction zone, *Journal of Geophysical Research: Solid Earth*, *110*(B7), doi:10.1029/2005JB003648.

Byrne, D. E., D. M. Davis, and L. R. Sykes (1988), Loci and maximum size of thrust earthquakes and the mechanics of the shallow region of subduction zones, *Tectonics*, *7*(4), 833–857, doi:10.1029/TC007i004p00833.

Byrne, T., and D. Fisher (1990), Evidence for a weak and overpressured decollement beneath sediment-dominated accretionary prisms, *Journal of Geophysical Research: Solid Earth*, *95*(B6), 9081–9097, doi:10.1029/JB095iB06p09081.

Carena, S. (2011), Subducting-plate topography and nucleation of great and giant earthquakes along the South American trench, *Seismological Research Letters*, *82*(5), 629–637, doi:10.1785/gssrl.82.5.629.

Carlo, D. L., T. Lay, C. J. Ammon, and J. Zhang (1999), Rupture process of the 1995 Antofagasta subduction earthquake (M w= 8.1), in *Seismogenic and Tsunamigenic Processes in Shallow Subduction Zones*, pp. 677–708, Springer, doi:10.1007/978-3-0348-8679-6_13.

Cesca, S., F. Grigoli, S. Heimann, T. Dahm, M. Kriegerowski, M. Sobiesiak, C. Tassara, and M. Olcay (2016), The Mw 8.1 2014 Iquique, Chile, seismic sequence: a tale of foreshocks and aftershocks, *Geophysical Journal International*, *204*(3), 1766–1780, doi:10.1093/gji/ggv544.

Charrier, R., A. N. Chávez, S. Elgueta, G. Hérail, J. J. Flynn, D. A. Croft, A. R. Wyss, R. Riquelme, and M. García (2005), Rapid tectonic and paleogeographic evolution associated with the development of the Chucal anticline and the Chucal-Lauca Basin in the Altiplano of Arica, northern Chile, *Journal of South American Earth Sciences*, *19*(1), 35–54, doi:10.1016/j.jsames.2004.06.008.

Chiou, B., R. Darragh, N. Gregor, and W. Silva (2008), NGA project strong-motion database, *Earthquake Spectra*, *24*(1), 23–44, doi:10.1193/1.2894831.

Chlieh, M., J. De Chabalier, J. Ruegg, R. Armijo, R. Dmowska, J. Campos, and K. Feigl (2004), Crustal deformation and fault slip during the seismic cycle in the North Chile subduction zone, from GPS and InSAR observations, *Geophysical Journal International*, *158*(2), 695–711, doi:10.1111/j.1365-246X.2004.02326.x.

Chlieh, M., J.-P. Avouac, V. Hjorleifsdottir, T.-R. A. Song, C. Ji, K. Sieh, A. Sladen, H. Hebert, L. Prawirodirdjo, Y. Bock, et al. (2007), Coseismic slip and afterslip of the great Mw 9.15 Sumatra–Andaman earthquake of 2004, *Bulletin of the Seismological Society of America*, *97*(1A), S152–S173, doi:10.1785/0120050631.

Chlieh, M., J.-P. Avouac, K. Sieh, D. H. Natawidjaja, and J. Galetzka (2008), Heterogeneous coupling of the Sumatran megathrust constrained by geodetic and paleogeodetic measurements, *Journal of Geophysical Research: Solid Earth*, *113*(B5), doi:10.1029/2007jb004981.

Chlieh, M., H. Perfettini, H. Tavera, J.-P. Avouac, D. Remy, J.-M. Nocquet, F. Rolandone, F. Bondoux, G. Gabalda, and S. Bonvalot (2011), Interseismic coupling and seismic potential along the Central Andes subduction zone, *Journal of Geophysical Research: Solid Earth*, *116*(B12), doi:10.1029/2010JB008166.

Cifuentes, I. L., and P. G. Silver (1989), Low-frequency source characteristics of the great 1960 Chilean earthquake, *Journal of Geophysical Research: Solid Earth*, *94*(B1), 643–663, doi:10.1029/jb094ib01p00643.

Cohee, B. P., and G. C. Beroza (1994), Slip distribution of the 1992 Landers earthquake and its implications for earthquake source mechanics, *Bulletin of the Seismological Society of America*, *84*(3), 692–712.

Collot, J.-Y., B. Marcaillou, F. Sage, F. Michaud, W. Agudelo, P. Charvis, D. Graindorge, M.-A. Gutscher, and G. Spence (2004), Are rupture zone limits of great subduction earthquakes controlled by upper plate structures? Evidence from multichannel seismic reflection data acquired across the northern Ecuador–southwest Colombia margin, *Journal of Geophysical Research: Solid Earth*, *109*(B11), doi:10.1029/2004JB003060.

Comte, D., and M. Pardo (1991), Reappraisal of great historical earthquakes in the northern Chile and southern Peru seismic gaps, *Natural hazards*, *4*(1), 23–44, doi:10.1007/BF00126557.

Comte, D., and G. Suárez (1995), Stress distribution and geometry of the subducting Nazca plate in northern Chile using teleseismically recorded earthquakes, *Geophysical Journal International*, *122*(2), 419–440, doi:10.1111/j.1365-246X.1995.tb07005.x.

Comte, D., D. Carrizo, S. Roecker, F. Ortega-Culaciati, and S. Peyrat (2016), Three-dimensional elastic wave speeds in the northern Chile subduction zone: variations in hydration in the supraslab mantle, *Geophysical Supplements to the Monthly Notices of the Royal Astronomical Society*, *207*(2), 1080–1105, doi:10.1093/gji/ggw318.

Conrad, C. P., and C. Lithgow-Bertelloni (2002), How mantle slabs drive plate tectonics, *Science*, *298*(5591), 207–209, doi:10.1126/science.1074161.

Conrad, C. P., S. Bilek, and C. Lithgow-Bertelloni (2004), Great earthquakes and slab pull: interaction between seismic coupling and plate–slab coupling, *Earth and Planetary Science Letters*, *218*(1), 109–122, doi:10.1016/S0012-821X(03)00643-5.

Contreras-Reyes, E., and D. Carrizo (2011), Control of high oceanic features and subduction channel on earthquake ruptures along the Chile–Peru subduction zone, *Physics of the Earth and Planetary Interiors*, *186*(1), 49–58, doi:10.1016/j.pepi.2011.03.002.

Contreras-Reyes, E., J. Jara, I. Grevemeyer, S. Ruiz, and D. Carrizo (2012), Abrupt change in the dip of the subducting plate beneath north Chile, *Nature Geoscience*, *5*(5), 342–345, doi:10.1038/ngeo1447.

Cotton, F., and M. Campillo (1995), Frequency domain inversion of strong motions: application to the 1992 Landers earthquake, *Journal of Geophysical Research: Solid Earth*, *100*(B3), 3961–3975, doi:10.1029/94jb02121.

Coutant, O. (1989), Program of numerical simulation AXITRA, *Res. Rep. LGIT (in French), Universite Joseph Fourier, Grenoble*.

Cummins, P. R., T. Baba, S. Kodaira, and Y. Kaneda (2002), The 1946 Nankai earthquake and segmentation of the Nankai Trough, *Physics of the Earth and Planetary Interiors*, *132*(1), 75–87, doi:10.1016/s0031-9201(02)00045-6.

Daniel, G., D. Marsan, and M. Bouchon (2008), Earthquake triggering in southern Iceland following the June 2000 Ms 6.6 doublet, *Journal of Geophysical Research: Solid Earth*, *113*(B5), doi:10.1029/2007jb005107.

Das, S., and K. Aki (1977), Fault plane with barriers: a versatile earthquake model, *Journal of Geophysical Research*, *82*(36), 5658–5670, doi:10.1029/jb082i036p05658.

Delbridge, B. G., S. Kita, N. Uchida, C. W. Johnson, T. Matsuzawa, and R. Bürgmann (2017), Temporal variation of intermediate-depth earthquakes around the time of the M 9.0 Tohoku-oki earthquake, *Geophysical Research Letters*, doi:10.1002/2017GL072876.

Delouis, B., and D. Legrand (2007), Mw 7.8 Tarapaca intermediate depth earthquake of 13 June 2005 (northern Chile): Fault plane identification and slip distribution by waveform inversion, *Geophysical Research Letters*, *34*(1), doi:10.1029/2006GL028193.

Delouis, B., A. Cisternas, L. Dorbath, L. Rivera, and E. Kausel (1996), The Andean subduction zone between 22 and 25 S (northern Chile): precise geometry and state of stress, *Tectonophysics*, *259*(1), 81–100, doi:10.1016/0040-1951(95)00065-8.

Delouis, B., T. Monfret, L. Dorbath, M. Pardo, L. Rivera, D. Comte, H. Haessler, J. Caminade, L. Ponce, E. Kausel, et al. (1997), The Mw= 8.0 Antofagasta (northern Chile) earthquake of 30 July 1995: A precursor to the end of the large 1877 gap, *Bulletin of the Seismological Society of America*, *87*(2), 427–445.

Delouis, B., M. Pardo, D. Legrand, and T. Monfret (2009), The Mw 7.7 Tocopilla earthquake of 14 November 2007 at the southern edge of the northern Chile seismic gap: Rupture in the deep part of the coupled plate interface, *Bulletin of the Seismological Society of America*, *99*(1), 87–94, doi:10.1785/0120080192.

Delouis, B., J.-M. Nocquet, and M. Vallée (2010), Slip distribution of the February 27, 2010 Mw= 8.8 Maule earthquake, central Chile, from static and high-rate GPS, InSAR, and broadband teleseismic data, *Geophysical Research Letters*, *37*(17), doi:10.1029/2010gl043899.

DeMets, C., R. G. Gordon, D. Argus, and S. Stein (1990), Current plate motions, *Geophysical Journal International*, *101*(2), 425–478, doi:10.1007/978-94-009-2949-4_119.

DeMets, C., R. G. Gordon, D. F. Argus, and S. Stein (1994), Effect of recent revisions to the geomagnetic reversal time scale on estimates of current plate motions, *Geophysical research letters*, *21*(20), 2191–2194, doi:10.1029/94gl02118.

Dessa, J.-X., F. Klingelhoefer, D. Graindorge, C. André, H. Permana, M.-A. Gutscher, A. Chauhan, S. Singh, S.-O. S. Team, et al. (2009), Megathrust earthquakes can nucleate in the forearc mantle: Evidence from the 2004 Sumatra event, *Geology*, *37*(7), 659–662, doi:10.1130/g25653a.1.

Dieterich, J. H. (1972), Time-dependent friction in rocks, *Journal of Geophysical Research*, *77*(20), 3690–3697, doi:10.1029/jb077i020p03690.

Dieterich, J. H. (1979), Modeling of rock friction: 1. Experimental results and constitutive equations, *Journal of Geophysical Research: Solid Earth*, *84*(B5), 2161–2168, doi:10.1029/jb084ib05p02161.

Dieterich, J. H. (1992), Earthquake nucleation on faults with rate-and state-dependent strength, *Tectonophysics*, *211*(1-4), 115–134, doi:10.1016/0040-1951(92)90055-b.

Ding, K., J. T. Freymueller, Q. Wang, and R. Zou (2015), Coseismic and early postseismic deformation of the 5 January 2013 Mw 7.5 Craig earthquake from static and kinematic GPS solutions, *Bulletin of the Seismological Society of America*, *105*(2B), 1153–1164, doi:10.1785/0120140172.

Dmowska, R., J. R. Rice, L. C. Lovison, and D. Josell (1988), Stress transfer and seismic phenomena in coupled subduction zones during the earthquake cycle, *Journal of Geophysical Research*, *93*, 7869–7884, doi:10.1029/JB093iB07p07869.

Dodge, D. A., G. C. Beroza, and W. Ellsworth (1996), Detailed observations of California foreshock sequences: Implications for the earthquake initiation process, *Journal of Geophysical Research: Solid Earth*, *101*(B10), 22,371–22,392, doi:10.1029/96JB02269.

Dorbath, L., A. Cisternas, and C. Dorbath (1990), Assessment of the size of large and great historical earthquakes in Peru, *Bulletin of the Seismological Society of America*, *80*(3), 551–576.

Douglas, A., J. Beavan, L. Wallace, and J. Townend (2005), Slow slip on the northern Hikurangi subduction interface, New Zealand, *Geophysical Research Letters*, *32*(16), doi:10.1029/2005GL023607.

Dragert, H., K. Wang, and T. S. James (2001), A silent slip event on the deeper Cascadia subduction interface, *Science*, *292*(5521), 1525–1528, doi:10.1126/science.1060152.

Dragert, H., K. Wang, and G. Rogers (2004), Geodetic and seismic signatures of episodic tremor and slip in the northern Cascadia subduction zone, *Earth, planets and space*, *56*(12), 1143–1150, doi:10.1186/bf03353333.

Drouet, S., G. Montalva, M. Dimaté, L. Castillo, G. Fernandez, C. Morales, N. Bastías, M. Pirchiner, J. Singaucho, and G. Weatherill (2016), Building a ground-motion logic tree for South America within the GEM-SARA project framework, in *16th World Conference on Earthquake Engineering, 16WCEE 2017*.

Duputel, Z., J. Jiang, R. Jolivet, M. Simons, L. Rivera, J.-P. Ampuero, B. Riel, S. Owen, A. Moore, S. Samsonov, et al. (2015), The Iquique earthquake sequence of April 2014: Bayesian modeling accounting for prediction uncertainty, *Geophysical Research Letters*, *42*(19), 7949–7957, doi:10.1002/2015GL065402.

Durand, V., M. Bouchon, M. A. Floyd, N. Theodulidis, D. Marsan, H. Karabulut, and J. Schmittbuhl (2014), Observation of the spread of slow deformation in Greece following the breakup of the slab, *Geophysical Research Letters*, *41*(20), 7129–7134, doi:10.1002/2014GL061408.

Ellsworth, W., G. Beroza, et al. (1995), Seismic evidence for an earthquake nucleation phase, *SCIENCE-NEW YORK THEN WASHINGTON-*, pp. 851–851, doi:10.1126/science.268.5212.851.

Elst, N. J., and B. E. Shaw (2015), Larger aftershocks happen farther away: Nonseparability of magnitude and spatial distributions of aftershocks, *Geophysical Research Letters*, *42*(14), 5771–5778, doi:10.1002/2015gl064734.

Fitch, T. J. (1972), Plate convergence, transcurrent faults, and internal deformation adjacent to southeast Asia and the western Pacific, *Journal of Geophysical Research*, *77*(23), 4432–4460, doi:10.1029/jb077i023p04432.

Frank, W. B. (2016), Slow slip hidden in the noise: The intermittence of tectonic release, *Geophysical Research Letters*, *43*(19), doi:10.1002/2016gl069537.

Frohlich, C. (2006), *Deep earthquakes*, Cambridge university press.

Fuenzalida, A., B. Schurr, M. Lancieri, M. Sobiesiak, and R. Madariaga (2013), High-resolution relocation and mechanism of aftershocks of the 2007 Tocopilla (Chile) earthquake, *Geophysical Journal International*, *194*(2), 1216–1228, doi:10.1093/gji/ggt163.

Gardonio, B. (2017), Seismic and Aseismic slip: The Japanese Subduction Alzone, Ph.D. thesis, Université Grenoble Alpes.

Garzione, C. N., P. Molnar, J. C. Libarkin, and B. J. MacFadden (2006), Rapid late Miocene rise of the Bolivian Altiplano: Evidence for removal of mantle lithosphere, *Earth and Planetary Science Letters*, *241*(3), 543–556, doi:10.1016/j.epsl.2005.11.026.

González, G., J. Cembrano, D. Carrizo, A. Macci, and H. Schneider (2003), The link between forearc tectonics and Pliocene–Quaternary deformation of the Coastal Cordillera, northern Chile, *Journal of South American Earth Sciences*, *16*(5), 321–342, doi:10.1016/s0895-9811(03)00100-7.

Gordon, R. G., and D. M. Jurdy (1986), Cenozoic global plate motions, *Journal of Geophysical Research: Solid Earth*, *91*(B12), 12,389–12,406, doi:10.1029/jb091ib12p12389.

Gripp, A. E., and R. G. Gordon (2002), Young tracks of hotspots and current plate velocities, *Geophysical Journal International*, *150*(2), 321–361, doi:10.1046/j.1365-246x.2002.01627.x.

Gutscher, M.-A. (2001), An Andean model of interplate coupling and strain partitioning applied to the flat subduction zone of SW Japan (Nankai Trough), *Tectonophysics*, *333*(1), 95–109, doi:10.1016/s0040-1951(00)00269-9.

Gutscher, M.-A., W. Spakman, H. Bijwaard, and E. R. Engdahl (2000), Geodynamics of flat subduction: Seismicity and tomographic constraints from the Andean margin, *Tectonics*, *19*(5), 814–833, doi:10.1029/1999tc001152.

Hacker, B. R., S. M. Peacock, G. A. Abers, and S. D. Holloway (2003), Subduction factory 2. Are intermediate-depth earthquakes in subducting slabs linked to metamorphic dehydration reactions?, *Journal of Geophysical Research: Solid Earth*, *108*(B1), doi:10.1029/2001JB001129.

Hansen, P. C. (1992), Analysis of discrete ill-posed problems by means of the L-curve, *SIAM review*, *34*(4), 561–580, doi:10.1137/1034115.

Hartzell, S. H., and T. H. Heaton (1983), Inversion of strong ground motion and teleseismic waveform data for the fault rupture history of the 1979 Imperial Valley, California, earthquake, *Bulletin of the Seismological Society of America*, *73*(6A), 1553–1583.

Hasegawa, A., and K. Yoshida (2015), Preceding seismic activity and slow slip events in the source area of the 2011 Mw 9.0 Tohoku-Oki earthquake: a review, *Geoscience Letters*, *2*(1), 6, doi:10.1186/s40562-015-0025-0.

Hatch, R. (1991), Instantaneous ambiguity resolution, in *Kinematic systems in geodesy, surveying, and remote sensing*, pp. 299–308, Springer, doi:10.1007/978-1-4612-3102-8_27.

Hayes, G. P., D. J. Wald, and R. L. Johnson (2012), Slab1. 0: A three-dimensional model of global subduction zone geometries, *Journal of Geophysical Research: Solid Earth*, *117*(B1), doi:10.1029/2011JB008524.

Hayes, G. P., M. W. Herman, W. D. Barnhart, K. P. Furlong, S. Riquelme, H. M. Benz, E. Bergman, S. Barrientos, P. S. Earle, and S. Samsonov (2014), Continuing megathrust earthquake potential in Chile after the 2014 Iquique earthquake, *Nature*, *512*(7514), 295–298, doi:10.1038/nature13677.

Heki, K., S. Miyazaki, and H. Tsuji (1997), Silent fault slip following an interplate thrust earthquake at the Japan Trench, *Nature*, doi:10.1038/386595a0.

Hernandez, B., F. Cotton, and M. Campillo (1999), Contribution of radar interferometry to a two-step inversion of the kinematic process of the 1992 Landers earthquake, *Journal of Geophysical Research: Solid Earth*, *104*(B6), 13,083–13,099, doi:10.1029/1999jb900078.

Herring, T., R. W. King, M. A. Floyd, and S. C. McClusky (2016), *GAMIT, Reference Manual*, Departament of Earth, Atmospheric, and Planetary Sciences, Massachusetts Institute of Technology.

Hetland, E., and M. Simons (2010), Post-seismic and interseismic fault creep II: transient creep and interseismic stress shadows on megathrusts, *Geophysical Journal International*, *181*(1), 99–112, doi:10.1111/j.1365-246x.2009.04482.x.

Hetland, E., M. Simons, and E. Dunham (2010), Post-seismic and interseismic fault creep I: model description, *Geophysical Journal International*, *181*(1), 81–98, doi:10.1111/j.1365-246x.2010.04522.x.

Hirose, H., K. Hirahara, F. Kimata, N. Fujii, and S. Miyazaki (1999), A slow thrust slip event following the two 1996 Hyuganada earthquakes beneath the Bungo Channel, southwest Japan, *Geophysical Research Letters*, *26*(21), 3237–3240.

Hoffmann-Rothe, A., N. Kukowski, G. Dresen, H. Echtler, O. Oncken, J. Klotz, E. Scheuber, and A. Kellner (2006), Oblique convergence along the Chilean margin: partitioning, margin-parallel faulting and force interaction at the plate interface, in *The Andes*, pp. 125–146, Springer.

House, L., and K. Jacob (1983), Earthquakes, plate subduction, and stress reversals in the eastern Aleutian arc, *Journal of Geophysical Research: Solid Earth*, *88*(B11), 9347–9373, doi:10.1029/jb088ib11p09347.

Hsu, Y.-J., M. Simons, J.-P. Avouac, J. Galetzka, K. Sieh, M. Chlieh, D. Natawidjaja, L. Prawirodirdjo, and Y. Bock (2006), Frictional afterslip following the 2005 Nias-Simeulue earthquake, Sumatra, *Science*, *312*(5782), 1921–1926, doi:10.1126/science.1126960.

Huene, R., and D. W. Scholl (1991), Observations at convergent margins concerning sediment subduction, subduction erosion, and the growth of continental crust, *Reviews of Geophysics*, *29*(3), 279–316, doi:10.1029/91rg00969.

Hyndman, R., and K. Wang (1993), Thermal constraints on the zone of major thrust earthquake failure: The Cascadia subduction zone, *Journal of Geophysical Research: Solid Earth*, *98*(B2), 2039–2060, doi:10.1029/92jb02279.

Hyndman, R., and K. Wang (1995), The rupture zone of Cascadia great earthquakes from current deformation and the thermal regime, *Journal of Geophysical Research: Solid Earth*, *100*(B11), 22,133–22,154, doi:10.1029/95jb01970.

Hyndman, R., M. Yamano, and D. Oleskevich (1997), The seismogenic zone of subduction thrust faults, *Island Arc*, *6*(3), 244–260, doi:10.1111/j.1440-1738.1997.tb00175.x.

Ide, S., D. R. Shelly, and G. C. Beroza (2007a), Mechanism of deep low frequency earthquakes: Further evidence that deep non-volcanic tremor is generated by shear slip on the plate interface, *Geophysical Research Letters*, *34*(3), doi:10.1029/2006gl028890.

Ide, S., G. C. Beroza, D. R. Shelly, and T. Uchide (2007b), A scaling law for slow earthquakes, *Nature*, *447*(7140), 76–79, doi:10.1038/nature05780.

Igarashi, T., T. Matsuzawa, and A. Hasegawa (2003), Repeating earthquakes and interplate aseismic slip in the northeastern Japan subduction zone, *Journal of Geophysical Research: Solid Earth*, *108*(B5), doi:10.1029/2002jb001920.

Ihmlé, P. F. (1998), On the interpretation of subevents in teleseismic waveforms: the 1994 Bolivia deep earthquake revisited, *Journal of Geophysical Research: Solid Earth*, *103*(B8), 17,919–17,932, doi:10.1029/98jb00603.

International Seismological Centre (2014), *On-line Bulletin*, Internatl. Seismol. Cent., Thatcham, United Kingdom, http://www.isc.ac.uk.

International Seismological Centre (2017), *On-line Bulletin*, Internatl. Seismol. Cent., Thatcham, United Kingdom, http://www.isc.ac.uk.

Isacks, B. L. (1988), Uplift of the central Andean plateau and bending of the Bolivian orocline, *Journal of Geophysical Research: Solid Earth*, *93*(B4), 3211–3231, doi:10.1029/jb093ib04p03211.

Ishii, M., P. M. Shearer, H. Houston, and J. E. Vidale (2005), Extent, duration and speed of the 2004 Sumatra–Andaman earthquake imaged by the Hi-Net array, *Nature*, *435*(7044), 933–936, doi:10.1038/nature03675.

Ito, A., G. Fujie, S. Miura, S. Kodaira, Y. Kaneda, and R. Hino (2005), Bending of the subducting oceanic plate and its implication for rupture propagation of large interplate earthquakes off Miyagi, Japan, in the Japan Trench subduction zone, *Geophysical research letters*, *32*(5), doi:10.1029/2004gl022307.

Ito, K. (1990), Regional variations of the cutoff depth of seismicity in the crust and their relation to heat flow and large inland-earthquakes., *Journal of Physics of the Earth*, *38*(3), 223–250, doi:10.4294/jpe1952.38.223.

James, D. E. (1971), Andean crustal and upper mantle structure, *Journal of Geophysical Research*, *76*(14), 3246–3271, doi:10.1029/JB076i014p03246.

Jara, J., A. Socquet, D. Marsan, and M. Bouchon (2017), Long-Term Interactions Between Intermediate Depth and Shallow Seismicity in North Chile Subduction Zone, *Geophysical Research Letters*, *44*(18), 9283–9292, doi:10.1002/2017GL075029, 2017GL075029.

Johnson, K. M., A. Mavrommatis, and P. Segall (2016), Small interseismic asperities and widespread aseismic creep on the northern Japan subduction interface, *Geophysical Research Letters*, *43*(1), 135–143, doi:10.1002/2015gl066707.

Jolivet, R., C. Lasserre, M.-P. Doin, G. Peltzer, J.-P. Avouac, J. Sun, and R. Dailu (2013), Spatio-temporal evolution of aseismic slip along the Haiyuan fault, China: Implications for fault frictional properties, *Earth and Planetary Science Letters*, *377-378*(Supplement C), 23 – 33, doi:https://doi.org/10.1016/j.epsl.2013.07.020.

Jolivet, R., T. Candela, C. Lasserre, F. Renard, Y. Klinger, and M.-P. Doin (2015), The Burst-Like Behavior of Aseismic Slip on a Rough Fault: The Creeping Section of the Haiyuan Fault, China, *Bulletin of the Seismological Society of America*, *105*(1), 480–488.

Jónsson, S., H. Zebker, P. Segall, and F. Amelung (2002), Fault slip distribution of the 1999 Mw 7.1 Hector Mine, California, earthquake, estimated from satellite radar and GPS measurements, *Bulletin of the Seismological Society of America*, *92*(4), 1377–1389, doi:10.1785/0120000922.

Jonsson, S., P. Segall, R. Pedersen, and G. Björnsson (2003), Post-earthquake ground movements correlated to pore-pressure transients, *Nature*, *424*(6945), 179–183, doi:10.1038/nature01776.

Kanamori, H. (1986), Rupture process of subduction-zone earthquakes, *Annual Review of Earth and Planetary Sciences*, *14*(1), 293–322, doi:10.1146/annurev.earth.14.1.293.

Kanamori, H. (2006), Seismological aspects of the December 2004 great Sumatra-Andaman earthquake, *Earthquake Spectra*, *22*(S3), 1–12, doi:10.1193/1.2201969.

Kanamori, H., and E. E. Brodsky (2004), The physics of earthquakes, *Reports on Progress in Physics*, *67*(8), 1429, doi:10.1088/0034-4885/67/8/r03.

Kanamori, H., and J. J. Cipar (1974), Focal process of the great Chilean earthquake May 22, 1960, *Physics of the Earth and Planetary Interiors*, *9*(2), 128–136, doi:10.1016/0031-9201(74)90029-6.

Kanamori, H., and M. Kikuchi (1993), The 1992 Nicaragua earthquake: a slow tsunami earthquake associated with subducted sediments, *Nature*, *361*(6414), 714, doi:10.1038/361714a0.

Kanda, R. V., E. A. Hetland, and M. Simons (2013), An asperity model for fault creep and interseismic deformation in northeastern Japan, *Geophysical Journal International*, *192*(1), 38–57, doi:10.1093/gji/ggs028.

Kaneko, Y., J.-P. Avouac, and N. Lapusta (2010), Towards inferring earthquake patterns from geodetic observations of interseismic coupling, *Nature Geoscience*, *3*(5), 363–369, doi:10.1038/ngeo843.

Kato, A., and S. Nakagawa (2014), Multiple slow-slip events during a foreshock sequence of the 2014 Iquique, Chile Mw 8.1 earthquake, *Geophysical Research Letters*, *41*(15), 5420–5427, doi:10.1002/2014gl061138.

Kato, A., K. Obara, T. Igarashi, H. Tsuruoka, S. Nakagawa, and N. Hirata (2012), Propagation of slow slip leading up to the 2011 Mw 9.0 Tohoku-Oki earthquake, *Science*, *335*(6069), 705–708, doi:10.1126/science.1215141.

Kato, A., J. Fukuda, T. Kumazawa, and S. Nakagawa (2016), Accelerated nucleation of the 2014 Iquique, Chile Mw 8.2 Earthquake, *Scientific reports*, *6*, doi:10.1038/srep24792.

Kausel, E. (1986), Los terremotos de agosto de 1868 y mayo de 1877 que afectaron el sur del Perú y norte de Chile, *Boletín de la Academia Chilena de Ciencias*, *3*(1), 8–13.

Kausel, E., and J. Campos (1992), The Ms= 8 tensional earthquake of 9 December 1950 of northern Chile and its relation to the seismic potential of the region, *Physics of the Earth and Planetary Interiors*, *72*(3-4), 220–235, doi:10.1016/0031-9201(92)90203-8.

Kelleher, J., and W. McCann (1976), Buoyant zones, great earthquakes, and unstable boundaries of subduction, *Journal of Geophysical Research*, *81*(26), 4885–4896, doi:10.1029/jb081i026p04885.

Kelleher, J., and W. McCann (1977), Bathymetric highs and the development of convergent plate boundaries, *Island Arcs, Deep Sea Trenches and Back-Arc Basins*, pp. 115–122, doi:10.1029/me001p0115.

Kelleher, J., L. Sykes, and J. Oliver (1973), Possible criteria for predicting earthquake locations and their application to major plate boundaries of the Pacific and the Caribbean, *Journal of Geophysical Research*, *78*(14), 2547–2585, doi:10.1029/jb078i014p02547.

Kelleher, J. A. (1972), Rupture zones of large South American earthquakes and some predictions, *Journal of Geophysical Research*, *77*(11), 2087–2103, doi:10.1029/jb077i011p02087.

Kendrick, E., M. Bevis, R. Smalley, and B. Brooks (2001), An integrated crustal velocity field for the central Andes, *Geochemistry, Geophysics, Geosystems*, *2*(11), doi:10.1029/2001gc000191.

Kendrick, E., M. Bevis, R. Smalley, B. Brooks, R. B. Vargas, E. Lauria, and L. P. S. Fortes (2003), The Nazca–South America Euler vector and its rate of change, *Journal of South American Earth Sciences*, *16*(2), 125–131, doi:10.1016/s0895-9811(03)00028-2.

Kendrick, E., B. A. Brooks, M. Bevis, R. Smalley, E. Lauria, M. Araujo, and H. Parra (2006), Active orogeny of the South-Central Andes studied with GPS geodesy, *Revista de la Asociación Geológica Argentina*, *61*(4), 555–566.

Khazaradze, G., and J. Klotz (2003), Short-and long-term effects of GPS measured crustal deformation rates along the south central Andes, *Journal of Geophysical Research: Solid Earth*, *108*(B6), doi:10.1029/2002jb001879.

Khazaradze, G., K. Wang, J. Klotz, Y. Hu, and J. He (2002), Prolonged post-seismic deformation of the 1960 great Chile earthquake and implications for mantle rheology, *Geophysical Research Letters*, *29*(22), doi:10.1029/2002gl015986.

Kikuchi, M., and H. Kanamori (1994), The mechanism of the deep Bolivia earthquake of June 9, 1994, *Geophysical Research Letters*, *21*(22), 2341–2344.

King, G. (1986), Speculations on the geometry of the initiation and termination processes of earthquake rupture and its relation to morphology and geological structure, *Pure and Applied Geophysics*, *124*(3), 567–585, doi:10.1007/bf00877216.

Klein, E., L. Fleitout, C. Vigny, and J. Garaud (2016), Afterslip and viscoelastic relaxation model inferred from the large-scale post-seismic deformation following the 2010 Mw 8.8 Maule earthquake (Chile), *Geophysical Journal International*, *205*(3), 1455–1472, doi:10.1093/gji/ggw086.

Klein, E., C. Vigny, L. Fleitout, R. Grandin, R. Jolivet, E. Rivera, and M. Métois (2017), A comprehensive analysis of the Illapel 2015 Mw8.3 earthquake from {GPS} and InSAR data, *Earth and Planetary Science Letters*, pp. –, doi:https://doi.org/10.1016/j.epsl.2017.04.010.

Kley, J. (1996), Transition from basement-involved to thin-skinned thrusting in the Cordillera Oriental of southern Bolivia, *Tectonics*, *15*(4), 763–775, doi:10.1029/95tc03868.

Kley, J., and C. R. Monaldi (1998), Tectonic shortening and crustal thickness in the Central Andes: How good is the correlation?, *Geology*, *26*(8), 723–726, doi:10.1130/0091-7613(1998)026<0723:tsacti>2.3.co;2.

Klotz, J., D. Angermann, G. Michel, R. Porth, C. Reigber, J. Reinking, J. Viramonte, R. Perdomo, V. Rios, S. Barrientos, et al. (1999), GPS-derived deformation of the Central Andes including the 1995 Antofagasta M w= 8.0 earthquake, in *Seismogenic and Tsunamigenic Processes in Shallow Subduction Zones*, pp. 709–730, Springer, doi:10.1007/978-3-0348-8679-6_14.

Klotz, J., G. Khazaradze, D. Angermann, C. Reigber, R. Perdomo, and O. Cifuentes (2001), Earthquake cycle dominates contemporary crustal deformation in Central and Southern Andes, *Earth and Planetary Science Letters*, *193*(3), 437–446, doi:10.1016/s0012-821x(01)00532-5.

Kodaira, S., E. Kurashimo, J.-O. Park, N. Takahashi, A. Nakanishi, S. Miura, T. Iwasaki, N. Hirata, K. Ito, and Y. Kaneda (2002), Structural factors controlling the rupture process of a megathrust earthquake at the Nankai trough seismogenic zone, *Geophysical Journal International*, *149*(3), 815–835, doi:10.1046/j.1365-246x.2002.01691.x.

Kodaira, S., T. Hori, A. Ito, S. Miura, G. Fujie, J.-O. Park, T. Baba, H. Sakaguchi, and Y. Kaneda (2006), A cause of rupture segmentation and synchronization in the Nankai trough revealed by seismic imaging and numerical simulation, *Journal of Geophysical Research: Solid Earth*, *111*(B9), doi:10.1029/2005jb004030.

Konca, A. O., J.-P. Avouac, A. Sladen, A. J. Meltzner, K. Sieh, P. Fang, Z. Li, J. Galetzka, J. Genrich, M. Chlieh, et al. (2008), Partial rupture of a locked patch of the Sumatra megathrust during the 2007 earthquake sequence, *Nature*, *456*(7222), 631–635, doi:10.1038/nature07572.

Kopp, H. (2013), Invited review paper: The control of subduction zone structural complexity and geometry on margin segmentation and seismicity, *Tectonophysics*, *589*, 1–16, doi:10.1016/j.tecto.2012.12.037.

Larson, K. M., J. T. Freymueller, and S. Philipsen (1997), Global plate velocities from the Global Positioning System, *Journal of Geophysical Research*, *102*(B5), 9961–9981, doi:doi:10.1029/97JB00514.

Larson, K. M., P. Bodin, and J. Gomberg (2003), Using 1-Hz GPS data to measure deformations caused by the Denali fault earthquake, *Science*, *300*(5624), 1421–1424, doi:10.1126/science.1084531.

Larson, K. M., A. R. Lowry, V. Kostoglodov, W. Hutton, O. Sánchez, K. Hudnut, and G. Suárez (2004), Crustal deformation measurements in Guerrero, Mexico, *Journal of Geophysical Research: Solid Earth*, *109*(B4), doi:10.1029/2003jb002843.

Larson, K. M., A. Bilich, and P. Axelrad (2007), Improving the precision of high-rate GPS, *Journal of Geophysical Research: Solid Earth*, *112*(B5), doi:10.1029/2006jb004367.

Lay, T. (2015), The surge of great earthquakes from 2004 to 2014, *Earth and Planetary Science Letters*, *409*, 133–146, doi:10.1016/j.epsl.2014.10.047.

Lay, T., and H. Kanamori (1981), An asperity model of large earthquake sequences, *Earthquake Prediction*, pp. 579–592, doi:10.1029/me004p0579.

Lay, T., and S. Y. Schwartz (2004), Comment on "Coupling semantics and science in earthquake research", *EOS, Transactions American Geophysical Union*, *85*(36), 339–340, doi:10.1029/2004eo360003.

Lay, T., L. Astiz, H. Kanamori, and D. H. Christensen (1989), Temporal variation of large intraplate earthquakes in coupled subduction zones, *Physics of the Earth and Planetary Interiors*, *54*(3-4), 258–312, doi:10.1016/0031-9201(89)90247-1.

Lay, T., C. J. Ammon, H. Kanamori, Y. Yamazaki, K. F. Cheung, and A. R. Hutko (2011), The 25 October 2010 Mentawai tsunami earthquake (Mw 7.8) and the tsunami hazard presented by shallow megathrust ruptures, *Geophysical Research Letters*, *38*(6), doi:10.1029/2010gl046552.

Lay, T., H. Kanamori, C. J. Ammon, K. D. Koper, A. R. Hutko, L. Ye, H. Yue, and T. M. Rushing (2012), Depth-varying rupture properties of subduction zone megathrust faults, *Journal of Geophysical Research: Solid Earth*, *117*(B4), doi:10.1029/2011jb009133.

Lay, T., H. Yue, E. E. Brodsky, and C. An (2014), The 1 April 2014 Iquique, Chile, Mw 8.1 earthquake rupture sequence, *Geophysical Research Letters*, *41*(11), 3818–3825, doi:10.1002/2014GL060238.

Lay, T., L. Ye, C. J. Ammon, and H. Kanamori (2017), Intraslab rupture triggering megathrust rupture coseismically in the 17 December 2016 Solomon Islands Mw 7.9 earthquake, *Geophysical Research Letters*, *44*(3), 1286–1292, doi:10.1002/2017GL072539.

Lemoine, A., R. Madariaga, and J. Campos (2001), Evidence for earthquake interaction in Central Chile: the July 1997–September 1998 sequence, *Geophysical Research Letters*, *28*(14), 2743–2746, doi:10.1029/2000gl012314.

Lemoine, A., R. Madariaga, and J. Campos (2002), Slab-pull and slab-push earthquakes in the Mexican, Chilean and Peruvian subduction zones, *Physics of the Earth and Planetary Interiors*, *132*(1), 157–175, doi:10.1016/s0031-9201(02)00050-x.

Li, S., M. Moreno, J. Bedford, M. Rosenau, and O. Oncken (2015), Revisiting viscoelastic effects on interseismic deformation and locking degree: A case study of the Peru-North Chile subduction zone, *Journal of Geophysical Research: Solid Earth*, *120*(6), 4522–4538, doi:10.1002/2015jb011903.

Lin, Y.-n. N., A. Sladen, F. Ortega-Culaciati, M. Simons, J.-P. Avouac, E. J. Fielding, B. A. Brooks, M. Bevis, J. Genrich, A. Rietbrock, et al. (2013), Coseismic and postseismic slip associated with the 2010 Maule Earthquake, Chile: Characterizing the Arauco Peninsula barrier effect, *Journal of Geophysical Research: Solid Earth*, *118*(6), 3142–3159, doi:10.1002/jgrb.50207.

Linde, A. T., K. Suyehiro, S. Miura, I. S. Sacks, and A. Takagi (1988), Episodic aseismic earthquake precursors, *Nature*, *334*(6182), 513–515, doi:10.1038/334513a0.

Linde, A. T., M. T. Gladwin, M. J. Johnston, R. L. Gwyther, and R. G. Bilham (1996), A slow earthquake sequence on the San Andreas fault, *Nature*, *383*(6595), 65, doi:10.1038/383065a0.

Liu, C., Y. Zheng, R. Wang, and X. Xiong (2015), Kinematic rupture process of the 2014 Chile Mw 8.1 earthquake constrained by strong-motion, GPS static offsets and teleseismic data, *Geophysical Journal International*, *202*(2), 1137–1145, doi:10.1093/gji/ggv214.

Liu, Y., and J. R. Rice (2007), Spontaneous and triggered aseismic deformation transients in a subduction fault model, *Journal of Geophysical Research: Solid Earth*, *112*(B9), doi:10.1029/2007jb004930.

Lorito, S., A. Piatanesi, V. Cannelli, F. Romano, and D. Melini (2010), Kinematics and source zone properties of the 2004 Sumatra-Andaman earthquake and tsunami: Nonlinear joint inversion of tide gauge, satellite altimetry, and GPS data, *Journal of Geophysical Research: Solid Earth*, *115*(B2), doi:10.1029/2008jb005974.

Lorito, S., F. Romano, S. Atzori, X. Tong, A. Avallone, J. McCloskey, M. Cocco, E. Boschi, and A. Piatanesi (2011), Limited overlap between the seismic gap and coseismic slip of the great 2010 Chile earthquake, *Nature Geoscience*, *4*(3), 173–177, doi:10.1038/ngeo1073.

Loveless, J. P., and B. J. Meade (2011), Spatial correlation of interseismic coupling and coseismic rupture extent of the 2011 MW= 9.0 Tohoku-oki earthquake, *Geophysical Research Letters*, *38*(17), doi:10.1029/2011gl048561.

Lowry, A. R., K. M. Larson, V. Kostoglodov, and R. Bilham (2001), Transient fault slip in Guerrero, southern Mexico, *Geophysical Research Letters*, *28*(19), 3753–3756, doi:10.1029/2001gl013238.

Madariaga, R. (1998), Sismicidad de Chile., *Física de la Tierra*, (10), 221.

Maksymowicz, A., A. M. Tréhu, E. Contreras-Reyes, and S. Ruiz (2015), Density-depth model of the continental wedge at the maximum slip segment of the Maule Mw8. 8 megathrust earthquake, *Earth and Planetary Science Letters*, *409*, 265–277, doi:10.1016/j.epsl.2014.11.005.

Maksymowicz, A., J. Ruiz, and E. Contreras-Reyes (2016), Heterogeneous density-structure of the northern Chile marine fore-arc and its relation to the rupture of the 2014 Mw8. 2 Iquique earthquake, in *EGU General Assembly Conference Abstracts*, vol. 18, p. 9878.

Maksymowicz, A., C. Chadwell, J. Ruiz, A. Tréhu, E. Contreras-Reyes, W. Weinrebe, J. Díaz-Naveas, J. Gibson, P. Lonsdale, and M. Tryon (2017), Coseismic seafloor deformation in the trench region during the Mw8. 8 Maule megathrust earthquake, *Scientific Reports*, *7*, doi:10.1038/srep45918.

Malgrange, M., and R. Madariaga (1983), Complex distribution of large thrust and normal fault earthquakes in the Chilean subduction zone, *Geophysical Journal International*, *73*(2), 489–505, doi:10.1111/j.1365-246x.1983.tb03326.x.

Mandelbrot, B. B., and R. Pignoni (1983), *The fractal geometry of nature*, vol. 173, WH freeman New York.

Marquez-Azua, B., and C. DeMets (2009), Deformation of Mexico from continuous GPS from 1993 to 2008, *Geochemistry, Geophysics, Geosystems*, *10*(2), doi:10.1029/2008gc002278.

Marsan, D., T. Reverso, A. Helmstetter, and B. Enescu (2013), Slow slip and aseismic deformation episodes associated with the subducting Pacific plate offshore Japan, revealed by changes in seismicity, *Journal of Geophysical Research: Solid Earth*, *118*(9), 4900–4909, doi:10.1002/jgrb.50323.

Marsan, D., M. Bouchon, B. Gardonio, H. Perfettini, A. Socquet, and B. Enescu (2017), Change in seismicity along the Japan trench, 1990–2011, and its relationship with seismic coupling, *Journal of Geophysical Research: Solid Earth*, pp. n/a–n/a, doi:10.1002/2016JB013715, 2016JB013715.

Mavrommatis, A. P., P. Segall, and K. M. Johnson (2014), A decadal-scale deformation transient prior to the 2011 Mw 9.0 Tohoku-oki earthquake, *Geophysical Research Letters*, *41*(13), 4486–4494, doi:10.1002/2014gl060139.

Mazzotti, S., X. Le Pichon, P. Henry, and S.-I. Miyazaki (2000), Full interseismic locking of the Nankai and Japan-west Kurile subduction zones: An analysis of uniform elastic strain accumulation in Japan constrained by permanent GPS, *Journal of Geophysical Research: Solid Earth*, *105*(B6), 13,159–13,177, doi:10.1029/2000jb900060.

McCaffrey, R. (1992), Oblique plate convergence, slip vectors, and forearc deformation, *Journal of Geophysical Research: Solid Earth*, *97*(B6), 8905–8915, doi:10.1029/92jb00483.

McCaffrey, R. (2007), The next great earthquake, *Science*, *315*(5819), 1675.

McCaffrey, R. (2014), Interseismic locking on the Hikurangi subduction zone: Uncertainties from slow-slip events, *Journal of Geophysical Research: Solid Earth*, *119*(10), 7874–7888, doi:10.1002/2014jb010945.

McCaffrey, R., and J. Nabelek (1998), Role of oblique convergence in the active deformation of the Himalayas and southern Tibet plateau, *Geology*, *26*(8), 691–694, doi:10.1130/0091-7613(1998)026<0691:roocit>2.3.co;2.

McCaffrey, R., L. M. Wallace, and J. Beavan (2008), Slow slip and frictional transition at low temperature at the Hikurangi subduction zone, *Nature Geoscience*, *1*(5), 316–320, doi:10.1038/ngeo178.

McCann, W., S. Nishenko, L. Sykes, and J. Krause (1979), Seismic gaps and plate tectonics: seismic potential for major boundaries, in *Earthquake Prediction and Seismicity Patterns*, pp. 1082–1147, Springer, doi:10.1007/bf00876211.

McLaskey, G. C., and D. A. Lockner (2014), Preslip and cascade processes initiating laboratory stick slip, *Journal of Geophysical Research: Solid Earth*, *119*(8), 6323–6336, doi:10.1002/2014jb011220.

Melbourne, T. I., and F. H. Webb (2002), Precursory transient slip during the 2001 Mw= 8.4 Peru earthquake sequence from continuous GPS, *Geophysical Research Letters*, *29*(21), doi:10.1029/2002gl015533.

Melbourne, W. G. (1985), The case for ranging in GPS-based geodetic systems, in *Proceedings of the first international symposium on precise positioning with the Global Positioning System*, vol. 1519.

Melgar, D., W. Fan, S. Riquelme, J. Geng, C. Liang, M. Fuentes, G. Vargas, R. M. Allen, P. M. Shearer, and E. J. Fielding (2016), Slip segmentation and slow rupture to the trench during the 2015, Mw8. 3 Illapel, Chile earthquake, *Geophysical Research Letters*, *43*(3), 961–966, doi:10.1002/2015gl067369.

Melnick, D., B. Bookhagen, M. R. Strecker, and H. P. Echtler (2009), Segmentation of megathrust rupture zones from fore-arc deformation patterns over hundreds to millions of years, Arauco peninsula, Chile, *Journal of Geophysical Research: Solid Earth*, *114*(B1), doi:10.1029/2008jb005788.

Melnick, D., M. Moreno, J. Quinteros, J. C. Baez, Z. Deng, S. Li, and O. Oncken (2017), The super-interseismic phase of the megathrust earthquake cycle in Chile, *Geophysical Research Letters*, *44*(2), 784–791, doi:10.1002/2016gl071845.

Meng, L., H. Huang, R. Bürgmann, J. P. Ampuero, and A. Strader (2015), Dual megathrust slip behaviors of the 2014 Iquique earthquake sequence, *Earth and Planetary Science Letters*, *411*, 177–187, doi:10.1016/j.epsl.2014.11.041.

Metois, M. (2012), Quantification du couplageau long de la subduction Chilienne, Ph.D. thesis, Université Paris Diderot, Sorbonne Paris Cité, Ecole doctorale des Sciences de la Terre, Laboratoire de géologie, École Normale Supérieure.

Métois, M., A. Socquet, and C. Vigny (2012), Interseismic coupling, segmentation and mechanical behavior of the central Chile subduction zone, *Journal of Geophysical Research: Solid Earth*, *117*(B3), doi:10.1029/2011jb008736.

Métois, M., A. Socquet, C. Vigny, D. Carrizo, S. Peyrat, A. Delorme, E. Maureira, M.-C. Valderas-Bermejo, and I. Ortega (2013), Revisiting the North Chile seismic gap segmentation using GPS-derived interseismic coupling, *Geophysical Journal International*, *194*(3), 1283–1294, doi:10.1093/gji/ggt183.

Métois, M., C. Vigny, and A. Socquet (2014), Slow-slip events hiding in low-coupled areas of the Chilean subduction zone?, in *EGU General Assembly Conference Abstracts*, vol. 16.

Métois, M., C. Vigny, and A. Socquet (2016), Interseismic Coupling, Megathrust Earthquakes and Seismic Swarms Along the Chilean Subduction Zone (38°–18° S), *Pure and Applied Geophysics*, *173*(5), 1431–1449, doi:10.1007/s00024-016-1280-5.

Michel, S., J.-P. Avouac, N. Lapusta, and J. Jiang (2017), Pulse-like partial ruptures and high-frequency radiation at creeping-locked transition during megathrust earthquakes, *Geophysical Research Letters*, *44*(16), 8345–8351, doi:10.1002/2017GL074725, 2017GL074725.

Minster, J., T. Jordan, P. Molnar, and E. Haines (1974), Numerical modelling of instantaneous plate tectonics, *Geophysical Journal International*, *36*(3), 541–576, doi:10.1111/j.1365-246x.1974.tb00613.x.

Miyazaki, S., J. J. McGuire, and P. Segall (2003), A transient subduction zone slip episode in southwest Japan observed by the nationwide GPS array, *Journal of Geophysical Research: Solid Earth*, *108*(B2), doi:10.1029/2001jb000456.

Molnar, P., and W.-P. Chen (1983), Focal depths and fault plane solutions of earthquakes under the Tibetan plateau, *Journal of Geophysical Research: Solid Earth*, *88*(B2), 1180–1196, doi:10.1029/jb088ib02p01180.

Moore, J. C., and D. Saffer (2001), Updip limit of the seismogenic zone beneath the accretionary prism of southwest Japan: An effect of diagenetic to low-grade metamorphic processes and increasing effective stress, *Geology*, *29*(2), 183–186, doi:10.1130/0091-7613(2001)029<0183:ulotsz>2.0.co;2.

Moreno, M., M. Rosenau, and O. Oncken (2010), 2010 Maule earthquake slip correlates with pre-seismic locking of Andean subduction zone, *Nature*, *467*(7312), 198–202, doi:10.1038/nature09349.

Moreno, M., D. Melnick, M. Rosenau, J. Baez, J. Klotz, O. Oncken, A. Tassara, J. Chen, K. Bataille, M. Bevis, et al. (2012), Toward understanding tectonic control on the M w 8.8 2010 Maule Chile earthquake, *Earth and Planetary Science Letters*, *321*, 152–165, doi:10.1016/j.epsl.2012.01.006.

Mortimer, C. (2010), Drainage evolution in the Atacama Desert of northernmost Chile, *Andean Geology*, (11), doi: 10.5027/andgeoV7n3-a01.

Moscoso, E., I. Grevemeyer, E. Contreras-Reyes, E. R. Flueh, Y. Dzierma, W. Rabbel, and M. Thorwart (2011), Revealing the deep structure and rupture plane of the 2010 Maule, Chile earthquake (Mw= 8.8) using wide angle seismic data, *Earth and Planetary Science Letters*, *307*(1), 147–155, doi:10.1016/j.epsl.2011.04.025.

Nigam, N. C., and P. C. Jennings (1969), Calculation of response spectra from strong-motion earthquake records, *Bulletin of the Seismological Society of America*, *59*(2), 909–922.

Nishenko, S., and W. McCann (1981), Seismic potential for the world's major plate boundaries: 1981, *Earthquake Prediction*, pp. 20–28, doi:10.1029/me004p0020.

Nishenko, S. P. (1985), Seismic potential for large and great interplate earthquakes along the Chilean and southern Peruvian margins of South America: a quantitative reappraisal, *Journal of Geophysical Research: Solid Earth*, *90*(B5), 3589–3615, doi:10.1029/jb090ib05p03589.

Nishenko, S. P. (1991), Circum-Pacific seismic potential: 1989–1999, *Pure and applied geophysics*, *135*(2), 169–259, doi:10.1007/978-3-0348-5639-3_2.

Nocquet, J.-M. (2017), PYACS: un outils pour l'analyse des données géodésiques, in *Colloque G2 2017, Geodesy - Rheology*.

Nocquet, J.-M., J. Villegas-Lanza, M. Chlieh, P. Mothes, F. Rolandone, P. Jarrin, D. Cisneros, A. Alvarado, L. Audin, F. Bondoux, et al. (2014), Motion of continental slivers and creeping subduction in the northern Andes, *Nature Geoscience*, *7*(4), 287–291, doi:10.1038/ngeo2099.

Nocquet, J.-M., P. Jarrin, M. Vallée, P. Mothes, R. Grandin, F. Rolandone, B. Delouis, H. Yepes, Y. Font, D. Fuentes, et al. (2016), Supercycle at the Ecuadorian subduction zone revealed after the 2016 Pedernales earthquake, *Nature Geoscience*, doi:10.1038/ngeo2864.

Norabuena, E., L. Leffler-Griffin, A. Mao, T. Dixon, S. Stein, I. S. Sacks, L. Ocola, and M. Ellis (1998), Space geodetic observations of Nazca-South America convergence across the central Andes, *Science*, *279*(5349), 358–362, doi:10.1126/science.279.5349.358.

Obara, K. (2002), Nonvolcanic deep tremor associated with subduction in southwest Japan, *Science*, *296*(5573), 1679–1681, doi:10.1126/science.1070378.

Obara, K., and A. Kato (2016), Connecting slow earthquakes to huge earthquakes, *Science*, *353*(6296), 253–257, doi:10.1126/science.aaf1512.

Ogata, Y. (1988), Statistical models for earthquake occurrences and residual analysis for point processes, *Journal of the American Statistical association*, *83*(401), 9–27, doi:10.1080/01621459.1988.10478560.

Ogata, Y., and K. Katsura (1993), Analysis of temporal and spatial heterogeneity of magnitude frequency distribution inferred from earthquake catalogues, *Geophysical Journal International*, *113*(3), 727–738, doi:10.1111/j.1365-246x.1993.tb04663.x.

Ohnaka, M. (2003), A constitutive scaling law and a unified comprehension for frictional slip failure, shear fracture of intact rock, and earthquake rupture, *Journal of Geophysical Research: Solid Earth*, *108*(B2), doi:10.1029/2000jb000123.

Okada, Y. (1985), Surface deformation due to shear and tensile faults in a half-space, *Bulletin of the Seismological Society of America*, *75*(4), 1135–1154, doi:10.1016/0148-9062(86)90674-1.

Oleskevich, D., R. Hyndman, and K. Wang (1999), The updip and downdip limits to great subduction earthquakes: Thermal and structural models of Cascadia, south Alaska, SW Japan, and Chile, *Journal of Geophysical Research: Solid Earth*, *104*(B7), 14,965–14,991, doi:10.1029/1999jb900060.

Ortlieb, L., C. Zazo, J. Goy, C. Hillaire-Marcel, B. Ghaleb, and L. Cournoyer (1996), Coastal deformation and sea-level changes in the northern Chile subduction area (23 S) during the last 330 ky, *Quaternary Science Reviews*, *15*(8-9), 819–831, doi:10.1016/s0277-3791(96)00066-2.

Ozawa, S., M. Murakami, and T. Tada (2001), Time-dependent inversion study of the slow thrust event in the Nankai trough subduction zone, southwestern Japan, *Journal of Geophysical Research: Solid Earth*, *106*(B1), 787–802.

Ozawa, S., T. Nishimura, H. Suito, T. Kobayashi, M. Tobita, and T. Imakiire (2011), Coseismic and postseismic slip of the 2011 magnitude-9 Tohoku-Oki earthquake, *Nature*, *475*(7356), 373–376, doi:10.1038/nature10227.

Ozawa, S., T. Nishimura, H. Munekane, H. Suito, T. Kobayashi, M. Tobita, and T. Imakiire (2012), Preceding, coseismic, and postseismic slips of the 2011 Tohoku earthquake, Japan, *Journal of Geophysical Research: Solid Earth*, *117*(B7), doi:10.1029/2011jb009120.

Pacheco, J. F., L. R. Sykes, and C. H. Scholz (1993), Nature of seismic coupling along simple plate boundaries of the subduction type, *Journal of Geophysical Research: Solid Earth*, *98*(B8), 14,133–14,159, doi:10.1029/93jb00349.

Pagani, M., D. Monelli, G. Weatherill, L. Danciu, H. Crowley, V. Silva, P. Henshaw, L. Butler, M. Nastasi, L. Panzeri, et al. (2014), OpenQuake engine: an open hazard (and risk) software for the global earthquake model, *Seismological Research Letters*, *85*(3), 692–702, doi:10.1785/0220130087.

Pardo, M., D. Comte, and T. Monfret (2002), Seismotectonic and stress distribution in the central Chile subduction zone, *Journal of South American Earth Sciences*, *15*(1), 11–22, doi:10.1016/s0895-9811(02)00003-2.

Pardo-Casas, F., and P. Molnar (1987), Relative motion of the Nazca (Farallon) and South American plates since Late Cretaceous time, *Tectonics*, *6*(3), 233–248, doi:10.1029/tc006i003p00233.

Patzwahl, R., J. Mechie, A. Schulze, and P. Giese (1999), Two-dimensional velocity models of the Nazca plate subduction zone between 19.5 S and 25 S from wide-angle seismic measurements during the CINCA95 project, *Journal of Geophysical Research: Solid Earth*, *104*(B4), 7293–7317, doi:10.1029/1999jb900008.

Peacock, S. M., and R. D. Hyndman (1999), Hydrous minerals in the mantle wedge and the maximum depth of subduction thrust earthquakes, *Geophysical Research Letters*, *26*(16), 2517–2520, doi:10.1029/1999gl900558.

Peltzer, G., P. Rosen, F. Rogez, and K. Hudnut (1998), Poroelastic rebound along the Landers 1992 earthquake surface rupture, *Journal of Geophysical Research*, *103*(B12), 30,131–30,145, doi:10.1029/98jb02302.

Peng, Z., and J. Gomberg (2010), An integrated perspective of the continuum between earthquakes and slow-slip phenomena, *Nature Geoscience*, *3*(9), 599–607.

Perfettini, H., J.-P. Avouac, and J.-C. Ruegg (2005), Geodetic displacements and aftershocks following the 2001 Mw= 8.4 Peru earthquake: Implications for the mechanics of the earthquake cycle along subduction zones, *Journal of Geophysical Research: Solid Earth*, *110*(B9), doi:10.1029/2004jb003522.

Perfettini, H., J.-P. Avouac, H. Tavera, A. Kositsky, J.-M. Nocquet, F. Bondoux, M. Chlieh, A. Sladen, L. Audin, D. L. Farber, et al. (2010), Seismic and aseismic slip on the Central Peru megathrust, *Nature*, *465*(7294), 78–81, doi:10.1038/nature09062.

Peyrat, S., and P. Favreau (2010), Kinematic and spontaneous rupture models of the 2005 Tarapacá intermediate depth earthquake, *Geophysical Journal International*, *181*(1), 369–381, doi:10.1111/j.1365-246X.2009.04493.x.

Peyrat, S., J. Campos, J.-B. De Chabalier, A. Perez, S. Bonvalot, M.-P. Bouin, D. Legrand, A. Nercessian, O. Charade, G. Patau, et al. (2006), Tarapacá intermediate-depth earthquake (Mw 7.7, 2005, northern Chile): A slab-pull event with horizontal fault plane constrained from seismologic and geodetic observations, *Geophysical research letters*, *33*(22), doi:10.1029/2006gl027710.

Peyrat, S., R. Madariaga, E. Buforn, J. Campos, G. Asch, and J. Vilotte (2010), Kinematic rupture process of the 2007 Tocopilla earthquake and its main aftershocks from teleseismic and strong-motion data, *Geophysical Journal International*, *182*(3), 1411–1430, doi:10.1111/j.1365-246x.2010.04685.x.

Pilger, R. H. (1984), Cenozoic plate kinematics, subduction and magmatism: South American Andes, *Journal of the Geological Society*, *141*(5), 793–802, doi:10.1144/gsjgs.141.5.0793.

Piña-Valdés, J., A. Socquet, F. Cotton, and S. Specht (In Press), Spatio-temporal variations of ground motion in northern Chile2 before and after the 2014 MW 8.1 Iquique megathrust event, *Bulletin of the Seismological Society of America*.

Prawirodirdjo, L., Y. Bocl, R. McCaffrey, J. Genrich, E. Calais, C. Stevens, S. Puntodewo, C. Subarya, J. Rais, P. Zwick, et al. (1997), Geodetic observations of interseismic strain segmentation at the Sumatra subduction zone, *Geophysical research letters*, *24*(21), 2601–2604, doi:10.1029/97gl52691.

Pritchard, M., and M. Simons (2006), An aseismic slip pulse in northern Chile and along-strike variations in seismogenic behavior, *Journal of Geophysical Research: Solid Earth*, *111*(B8), doi:10.1029/2006jb004258.

Pritchard, M., M. Simons, P. Rosen, S. Hensley, and F. Webb (2002), Co-seismic slip from the 1995 July 30 Mw= 8.1 Antofagasta, Chile, earthquake as constrained by InSAR and GPS observations, *Geophysical Journal International*, *150*(2), 362–376, doi:10.1046/j.1365-246x.2002.01661.x.

Pritchard, M., E. Norabuena, C. Ji, R. Boroschek, D. Comte, M. Simons, T. H. Dixon, and P. Rosen (2007), Geodetic, teleseismic, and strong motion constraints on slip from recent southern Peru subduction zone earthquakes, *Journal of Geophysical Research: Solid Earth*, *112*(B3), doi:10.1029/2006jb004294.

Radiguet, M., F. Cotton, I. Manighetti, M. Campillo, and J. Douglas (2009), Dependency of near-field ground motions on the structural maturity of the ruptured faults, *Bulletin of the Seismological Society of America*, *99*(4), 2572–2581, doi:10.1785/0120080340.

Radiguet, M., F. Cotton, M. Vergnolle, M. Campillo, B. Valette, V. Kostoglodov, and N. Cotte (2011), Spatial and temporal evolution of a long term slow slip event: the 2006 Guerrero Slow Slip Event, *Geophysical Journal International*, *184*(2), 816–828, doi:10.1111/j.1365-246x.2010.04866.x.

Radiguet, M., F. Cotton, M. Vergnolle, M. Campillo, A. Walpersdorf, N. Cotte, and V. Kostoglodov (2012), Slow slip events and strain accumulation in the Guerrero gap, Mexico, *Journal of Geophysical Research: Solid Earth*, *117*(B4), doi:10.1029/2011JB008801.

Radiguet, M., H. Perfettini, N. Cotte, A. Gualandi, B. Valette, V. Kostoglodov, T. Lhomme, A. Walpersdorf, E. C. Cano, and M. Campillo (2016), Triggering of the 2014 Mw7. 3 Papanoa earthquake by a slow slip event in Guerrero, Mexico, *Nature Geoscience*, *9*(11), 829–833, doi:10.1038/ngeo2817.

Ranero, C., and R. Von Huene (2000), Subduction erosion along the Middle America convergent margin, *Nature*, *404*(6779), 748–752, doi:10.1038/35008046.

Reid, H. (1910), The Mechanism of the Earthquake. The California Earthquake of April 18, 1906: Rep. of the State Investigation Commiss. Vol. 2. P. 1.

Reinen, L. A., T. E. Tullis, and J. D. Weeks (1992), Two-mechanism model for frictional sliding of serpentinite, *Geophysical Research Letters*, *19*(15), 1535–1538, doi:10.1029/92gl01388.

Remy, D., H. Perfettini, N. Cotte, J.-P. Avouac, M. Chlieh, F. Bondoux, A. Sladen, H. Tavera, and A. Socquet (2016), Postseismic relocking of the subduction megathrust following the 2007 Pisco, Peru, earthquake, *Journal of Geophysical Research: Solid Earth*, *121*(5), 3978–3995, doi:10.1002/2015jb012417.

Reverso, T., D. Marsan, and A. Helmstetter (2015), Detection and characterization of transient forcing episodes affecting earthquake activity in the Aleutian Arc system, *Earth and Planetary Science Letters*, *412*, 25–34, doi:10.1016/j.epsl.2014.12.012.

Reverso, T., D. Marsan, A. Helmstetter, and B. Enescu (2016), Background seismicity in Boso Peninsula, Japan: Long-term acceleration, and relationship with slow slip events, *Geophysical Research Letters*, doi:10.1002/2016gl068524.

Rice, J. R. (1983), Constitutive relations for fault slip and earthquake instabilities, *Pure and applied geophysics*, *121*(3), 443–475, doi:10.1007/978-3-0348-6608-8_7.

Rivera, E. (2015), Procesamiento y anásis de motogramas de terremotos de subducción chilenos, Master's thesis, Departamento de Geofísica, Facultad de Ciencias Físicas y Matemáticas, Universidad de Chile.

Rogers, G., and H. Dragert (2003), Episodic tremor and slip on the Cascadia subduction zone: The chatter of silent slip, *Science*, *300*(5627), 1942–1943, doi:10.1126/science.1084783.

Rothacher, M., G. Beutler, W. Gurtner, T. Schildknecht, and U. Wild (1990), *BERNESE GPS Software Version 3.2. Printing Office*, University of Berne: Switzerland.

Rousset, B., C. Lasserre, N. Cubas, S. Graham, M. Radiguet, C. DeMets, A. Socquet, M. Campillo, V. Kostoglodov, E. Cabral-Cano, et al. (2015), Lateral variations of interplate coupling along the mexican subduction interface: Relationships with long-term morphology and fault zone mechanical properties, *Pure and Applied Geophysics*, pp. 1–20, doi:10.1007/978-3-319-51529-8_14.

Rousset, B., R. Jolivet, M. Simons, C. Lasserre, B. Riel, P. Milillo, Z. Çakir, and F. Renard (2016), An aseismic slip transient on the North Anatolian Fault, *Geophysical Research Letters*, *43*(7), 3254–3262, doi:10.1002/2016GL068250, 2016GL068250.

Rousset, B., M. Campillo, C. Lasserre, W. B. Frank, N. Cotte, A. Walpersdorf, A. Socquet, and V. Kostoglodov (2017), A geodetic matched-filter search for slow slip with application to the Mexico subduction zone, *Journal of Geophysical Research: Solid Earth*, pp. n/a–n/a, doi:10.1002/2017JB014448, 2017JB014448.

Ruegg, J. (1994), Deformación de la corteza terrestre y terremotos: aplicación al estudio del ciclo sísmico en el norte de Chile., *Física de la Tierra*, (6), 201.

Ruegg, J., J. Campos, R. Armijo, S. Barrientos, P. Briole, R. Thiele, M. Arancibia, J. Canuta, T. Duquesnoy, M. Chang, et al. (1996), The Mw= 8.1 Antofagasta (North Chile) earthquake of July 30, 1995: first results from teleseismic and geodetic data, *Geophysical Research Letters*, *23*(9), 917–920, doi:10.1029/96gl01026.

Ruegg, J., M. Olcay, and D. Lazo (2001), Co-, post-and pre (?)-seismic displacements associated with the Mw 8.4 Southern Peru earthquake of 23 June 2001 from continuous GPS measurements, *Seismological Research Letters*, *72*(6), 673–678, doi:10.1785/gssrl.72.6.673.

Ruegg, J., A. Rudloff, C. Vigny, R. Madariaga, J. De Chabalier, J. Campos, E. Kausel, S. Barrientos, and D. Dimitrov (2009), Interseismic strain accumulation measured by GPS in the seismic gap between Constitución and Concepción in Chile, *Physics of the Earth and Planetary Interiors*, *175*(1), 78–85, doi:10.1016/j.pepi.2008.02.015.

Ruina, A. (1983), Slip instability and state variable friction laws, *Journal of Geophysical Research: Solid Earth*, *88*(B12), 10,359–10,370, doi:10.1029/jb088ib12p10359.

Ruiz, S., E. Kausel, J. Campos, G. Saragoni, and R. Madariaga (2011), Identification of high frequency pulses from earthquake asperities along Chilean subduction zone using strong motion, *Pure and Applied Geophysics*, *168*(1-2), 125–139, doi:10.1007/s00024-010-0117-x.

Ruiz, S., R. Madariaga, M. Astroza, G. R. Saragoni, M. Lancieri, C. Vigny, and J. Campos (2012), Short-period rupture process of the 2010 Mw 8.8 Maule earthquake in Chile, *Earthquake Spectra*, *28*(S1), S1–S18, doi:10.1193/1.4000039.

Ruiz, S., M. Metois, A. Fuenzalida, J. Ruiz, F. Leyton, R. Grandin, C. Vigny, R. Madariaga, and J. Campos (2014), Intense foreshocks and a slow slip event preceded the 2014 Iquique Mw 8.1 earthquake, *Science*, *345*(6201), 1165–1169, doi:10.1126/science.1256074.

Ruiz, S., E. Klein, F. del Campo, E. Rivera, P. Poli, M. Metois, V. Christophe, J. C. Baez, G. Vargas, F. Leyton, et al. (2016), The Seismic Sequence of the 16 September 2015 Mw 8.3 Illapel, Chile, Earthquake, *Seismological Research Letters*, doi:10.1785/0220150281.

Ruiz, S., F. Aden-Antoniow, J. Baez, C. Otarola, B. Potin, F. Campo, P. Poli, C. Flores, C. Satriano, F. Leyton, et al. (2017a), Nucleation phase and dynamic inversion of the Mw 6.9 Valparaíso 2017 earthquake in Central Chile, *Geophysical Research Letters*, *44*(20).

Ruiz, S., H. Tavera, P. Poli, C. Herrera, C. Flores, E. Rivera, and R. Madariaga (2017b), The deep Peru 2015 doublet earthquakes, *Earth and Planetary Science Letters*, *478*, 102–109, doi:10.1016/j.epsl.2017.08.036.

Sandwell, D. T., R. D. Müller, W. H. Smith, E. Garcia, and R. Francis (2014), New global marine gravity model from CryoSat-2 and Jason-1 reveals buried tectonic structure, *Science*, *346*(6205), 65–67, doi:10.1126/science.1258213.

Sato, T., S. Hiratsuka, and J. Mori (2013), Precursory Seismic Activity Surrounding the High-Slip Patches of the 2011 Mw 9.0 Tohoku-Oki Earthquake, *Bulletin of the Seismological Society of America*, doi:10.1785/0120130042.

Savage, J. C., and G. Plafker (1991), Tide gage measurements of uplift along the south coast of Alaska, *Journal of Geophysical Research: Solid Earth*, *96*(B3), 4325–4335, doi:10.1029/90jb02540.

Scheuber, E., and K.-J. Reutter (1992), Magmatic arc tectonics in the Central Andes between 21 and 25 S, *Tectonophysics*, *205*(1-3), 127–140, doi:10.1016/0040-1951(92)90422-3.

Scholz, C., and J. Campos (1995), On the mechanism of seismic decoupling and back arc spreading at subduction zones, *Journal of Geophysical Research*, *100*, 22–103, doi:10.1029/95jb01869.

Scholz, C., and J. Engelder (1976), The role of asperity indentation and ploughing in rock friction—I: Asperity creep and stick-slip, in *International Journal of Rock Mechanics and Mining Sciences & Geomechanics Abstracts*, vol. 13, pp. 149–154, Elsevier.

Scholz, C. H. (1998), Earthquakes and friction laws, *Nature*, *391*(6662), 37–42, doi:10.1038/34097.

Scholz, C. H., and J. Campos (2012), The seismic coupling of subduction zones revisited, *Journal of Geophysical Research: Solid Earth*, *117*(B5), doi:10.1029/2011jb009003.

Schurr, B., G. Asch, M. Rosenau, R. Wang, O. Oncken, S. Barrientos, P. Salazar, and J.-P. Vilotte (2012), The 2007 M7. 7 Tocopilla northern Chile earthquake sequence: Implications for along-strike and downdip rupture segmentation and megathrust frictional behavior, *Journal of Geophysical Research: Solid Earth*, *117*(B5), doi:10.1029/2011jb009030.

Schurr, B., G. Asch, S. Hainzl, J. Bedford, A. Hoechner, M. Palo, R. Wang, M. Moreno, M. Bartsch, Y. Zhang, et al. (2014), Gradual unlocking of plate boundary controlled initiation of the 2014 Iquique earthquake, *Nature*, *512*(7514), 299–302, doi:10.1038/nature13681.

Schwartz, S. Y., and J. M. Rokosky (2007), Slow slip events and seismic tremor at circum-Pacific subduction zones, *Reviews of Geophysics*, *45*(3), doi:10.1029/2006rg000208.

Scuderi, M., C. Marone, E. Tinti, G. Di Stefano, and C. Collettini (2016), Precursory changes in seismic velocity for the spectrum of earthquake failure modes, *Nature geoscience*, *9*(9), 695–700, doi:10.1038/ngeo2775.

Seno, T. (2005), Variation of downdip limit of the seismogenic zone near the Japanese islands: Implications for the serpentinization mechanism of the forearc mantle wedge, *Earth and Planetary Science Letters*, *231*(3), 249–262, doi:10.1016/j.epsl.2004.12.027.

Shapiro, N. M., M. Campillo, L. Stehly, and M. H. Ritzwoller (2005), High-resolution surface-wave tomography from ambient seismic noise, *Science*, *307*(5715), 1615–1618, doi:10.1126/science.1108339.

Shelly, D. R., G. C. Beroza, S. Ide, and S. Nakamula (2006), Low-frequency earthquakes in Shikoku, Japan, and their relationship to episodic tremor and slip, *Nature*, *442*(7099), 188–191, doi:10.1038/nature04931.

Silgado Ferro, E. (1978), Historia de los sismos más notables ocurridos en el Perú (1513-1974).

Silver, P. G., S. L. Beck, T. C. Wallace, C. Meade, et al. (1995), Rupture characteristics of the deep Bolivian earthquake of 9 June 1994 and the mechanism of deep-focus earthquakes, *Science*, *268*(5207), 69, doi:10.1126/science.268.5207.69.

Simoes, M., J. P. Avouac, R. Cattin, and P. Henry (2004), The Sumatra subduction zone: A case for a locked fault zone extending into the mantle, *Journal of Geophysical Research: Solid Earth*, *109*(B10), doi:10.1029/2003jb002958.

Simons, M., S. E. Minson, A. Sladen, F. Ortega, J. Jiang, S. E. Owen, L. Meng, J.-P. Ampuero, S. Wei, R. Chu, et al. (2011), The 2011 magnitude 9.0 Tohoku-Oki earthquake: Mosaicking the megathrust from seconds to centuries, *Science*, *332*(6036), 1421–1425, doi:10.1126/science.1206731.

Sladen, A., H. Tavera, M. Simons, J. Avouac, A. Konca, H. Perfettini, L. Audin, E. Fielding, F. Ortega, and R. Cavagnoud (2010), Source model of the 2007 Mw 8.0 Pisco, Peru earthquake: Implications for seismogenic behavior of subduction megathrusts, *Journal of Geophysical Research: Solid Earth*, *115*(B2), doi:10.1029/2009jb006429.

Smith, W. D. (1981), The b-value as an earthquake precursor, *Nature*, *289*, 136–139, doi:10.1038/289136a0.

Socquet, A., J. Piña Valdes, J. Jara, F. Cotton, A. Walpersdorf, N. Cotte, S. Specht, F. Ortega-Culaciati, D. Carrizo, and E. Norabuena (2017), An 8-month slow slip event triggers progressive nucleation of the 2014 Chile megathrust, *Geophysical Research Letters*, *44*(9), 4046–4053, doi:10.1002/2017gl073023.

Song, T.-R. A., and M. Simons (2003), Large trench-parallel gravity variations predict seismogenic behavior in subduction zones, *Science*, *301*(5633), 630–633, doi:10.1126/science.1085557.

Spence, W. (1987), Slab pull and the seismotectonics of subducting lithosphere, *Reviews of Geophysics*, *25*(1), 55–69, doi:10.1029/RG025i001p00055.

Stewart, J. P., J. Douglas, M. Javanbarg, Y. Bozorgnia, N. A. Abrahamson, D. M. Boore, K. W. Campbell, E. Delavaud, M. Erdik, and P. J. Stafford (2015), Selection of ground motion prediction equations for the Global Earthquake Model, *Earthquake Spectra*, *31*(1), 19–45, doi:10.1193/013013eqs017m.

Strasser, F., M. Arango, and J. Bommer (2010), Scaling of the source dimensions of interface and intraslab subduction-zone earthquakes with moment magnitude, *Seismological Research Letters*, *81*(6), 941–950, doi:10.1785/gssrl.81.6.941.

Suzuki, W., S. Aoi, H. Sekiguchi, and T. Kunugi (2011), Rupture process of the 2011 Tohoku-Oki mega-thrust earthquake (M9. 0) inverted from strong-motion data, *Geophysical Research Letters*, *38*(7), doi:10.1029/2011gl049136.

Tarantola, A. (2005), *Inverse problem theory and methods for model parameter estimation*, SIAM, doi:10.1137/1.9780898717921.

Tarantola, A., and B. Valette (1982), Generalized nonlinear inverse problems solved using the least squares criterion, *Reviews of Geophysics*, *20*(2), 219–232, doi:10.1029/rg020i002p00219.

Tavera, H., and I. Bernal (2008), The pisco (peru) earthquake of 15 august 2007, *Seismological Research Letters*, *79*(4), 510–515, doi:10.1785/gssrl.79.4.510.

Tavera, H., and E. Buforn (1998), Sismicidad y sismotectónica de Perú, *Física de la Tierra*, *10*, 187–219.

Tavera, H., E. Buforn, I. Bernal, Y. Antayhua, and L. Vilacapoma (2002), The Arequipa (Peru) earthquake of June 23, 2001, *Journal of Seismology*, *6*(2), 279–283, doi:10.1023/A:1015698621075.

Tichelaar, B. W., and L. J. Ruff (1991), Seismic coupling along the Chilean subduction zone, *Journal of Geophysical Research: Solid Earth*, *96*(B7), 11,997–12,022, doi:10.1029/91jb00200.

Tichelaar, B. W., and L. J. Ruff (1993), Depth of seismic coupling along subduction zones, *Journal of Geophysical Research: Solid Earth*, *98*(B2), 2017–2037, doi:10.1029/92jb02045.

Tilmann, F., Y. Zhang, M. Moreno, J. Saul, F. Eckelmann, M. Palo, Z. Deng, A. Babeyko, K. Chen, J. Baez, et al. (2016), The 2015 Illapel earthquake, central Chile: A type case for a characteristic earthquake?, *Geophysical Research Letters*, *43*(2), 574–583, doi:10.1002/2015gl066963.

Tompkins, M., and N. Christensen (2001), Ultrasonic P-and S-wave attenuation in oceanic basalt, *Geophysical Journal International*, *145*(1), 172–186, doi:10.1046/j.0956-540x.2001.01354.x.

Trenkamp, R., J. N. Kellogg, J. T. Freymueller, and H. P. Mora (2002), Wide plate margin deformation, southern Central America and northwestern South America, CASA GPS observations, *Journal of South American Earth Sciences*, *15*(2), 157–171, doi:10.1016/s0895-9811(02)00018-4.

Tse, S. T., and J. R. Rice (1986), Crustal earthquake instability in relation to the depth variation of frictional slip properties, *Journal of Geophysical Research*, *91*(9), 452–9, doi:10.1029/jb091ib09p09452.

Uchida, N., T. Matsuzawa, A. Hasegawa, and T. Igarashi (2003), Interplate quasi-static slip off Sanriku, NE Japan, estimated from repeating earthquakes, *Geophysical Research Letters*, *30*(15), doi:10.1029/2003gl017452.

Utsu, T., and A. Seki (1955), A relation between the area of aftershock region and the energy of main shock, *J. Seism. Soc. Japan*, *7*, 233–240, doi:10.4294/zisin1948.7.4233.

Vaca, S., M. Vallée, J.-M. Nocquet, J. Battaglia, and M. Régnier (2017), Recurrent slow slip events as a barrier to the northward rupture propagation of the 2016 Pedernales earthquake (Central Ecuador), *Tectonophysics*, doi:10.1016/j.tecto.2017.12.012.

Vallee, M., J.-M. Nocquet, J. Battaglia, Y. Font, M. Segovia, M. Regnier, P. Mothes, P. Jarrin, D. Cisneros, S. Vaca, et al. (2013), Intense interface seismicity triggered by a shallow slow slip event in the Central Ecuador subduction zone, *Journal of Geophysical Research: Solid Earth*, *118*(6), 2965–2981, doi:10.1002/jgrb.50216.

Vergnolle, M., A. Walpersdorf, V. Kostoglodov, P. Tregoning, J. Santiago, N. Cotte, and S. Franco (2010), Slow slip events in Mexico revised from the processing of 11 year GPS observations, *Journal of Geophysical Research: Solid Earth*, *115*(B8), doi:10.1029/2009jb006852.

Victor, P., M. Sobiesiak, J. Glodny, S. Nielsen, and O. Oncken (2011), Long-term persistence of subduction earthquake segment boundaries: evidence from Mejillones Peninsula, northern Chile, *Journal of Geophysical Research: Solid Earth*, *116*(B2), doi:10.1029/2010jb007771.

Vigny, C., W. Simons, S. Abu, R. Bamphenyu, C. Satirapod, N. Choosakul, C. Subarya, A. Socquet, K. Omar, H. Abidin, et al. (2005), Insight into the 2004 Sumatra–Andaman earthquake from GPS measurements in southeast Asia, *Nature*, *436*(7048), 201–206, doi:10.1038/nature03937.

Vigny, C., A. Rudloff, J.-C. Ruegg, R. Madariaga, J. Campos, and M. Alvarez (2009), Upper plate deformation measured by GPS in the Coquimbo Gap, Chile, *Physics of the Earth and Planetary Interiors*, *175*(1), 86–95, doi:10.1016/j.pepi.2008.02.013.

Vigny, C., A. Socquet, S. Peyrat, J.-C. Ruegg, M. Métois, R. Madariaga, S. Morvan, M. Lancieri, R. Lacassin, J. Campos, et al. (2011), The 2010 Mw 8.8 Maule megathrust earthquake of Central Chile, monitored by GPS, *Science*, *332*(6036), 1417–1421, doi:10.1126/science.1204132.

Villegas-Lanza, J., M. Chlieh, O. Cavalié, H. Tavera, P. Baby, J. Chire-Chira, and J.-M. Nocquet (2016a), Active tectonics of Peru: Heterogeneous interseismic coupling along the Nazca megathrust, rigid motion of the Peruvian Sliver, and Subandean shortening accommodation, *Journal of Geophysical Research: Solid Earth*, *121*(10), 7371–7394, doi:10.1002/2016jb013080.

Villegas-Lanza, J., J.-M. Nocquet, F. Rolandone, M. Vallée, H. Tavera, F. Bondoux, T. Tran, X. Martin, and M. Chlieh (2016b), A mixed seismic-aseismic stress release episode in the Andean subduction zone, *Nature Geoscience*, *9*(2), 150–154.

von Huene, R., and I. A. Pecher (1999), Vertical tectonics and the origins of BSRs along the Peru margin, *Earth and Planetary Science Letters*, *166*(1), 47–55, doi:10.1016/s0012-821x(98)00274-x.

Vrolijk, P. (1990), On the mechanical role of smectite in subduction zones, *Geology*, *18*(8), 703–707, doi:10.1130/0091-7613(1990)018<0703:otmros>2.3.co;2.

Wallace, L. M., and J. Beavan (2006), A large slow slip event on the central Hikurangi subduction interface beneath the Manawatu region, North Island, New Zealand, *Geophysical Research Letters*, *33*(11), doi:10.1029/2006gl026009.

Wallace, L. M., and J. Beavan (2010), Diverse slow slip behavior at the Hikurangi subduction margin, New Zealand, *Journal of Geophysical Research: Solid Earth*, *115*(B12), doi:10.1029/2010jb007717.

Walter, J. I., S. Y. Schwartz, J. M. Protti, and V. Gonzalez (2011), Persistent tremor within the northern Costa Rica seismogenic zone, *Geophysical Research Letters*, *38*(1), doi:10.1029/2010gl045586.

Wang, K. (2007), Elastic and viscoelastic models of crustal deformation in subduction earthquake cycles, *The Seismogenic Zone of Subduction Thrust Faults*, pp. 540–575, doi:10.7312/dixo13866-017.

Wang, K., and T. Dixon (2004), "Coupling" semantics and science in earthquake research, *EOS, Transactions American Geophysical Union*, *85*(18), 180–180, doi:10.1029/2004eo180005.

Wang, K., R. D. Hyndman, and M. Yamano (1995), Thermal regime of the Southwest Japan subduction zone: effects of age history of the subducting plate, *Tectonophysics*, *248*(1), 53–69, doi:10.1016/0040-1951(95)00028-l.

Wang, K., R. Wells, S. Mazzotti, R. D. Hyndman, and T. Sagiya (2003a), A revised dislocation model of interseismic deformation of the Cascadia subduction zone, *Journal of Geophysical Research: Solid Earth*, *108*(B1), doi:10.1029/2001jb001227.

Wang, K., Y. Hu, M. Bevis, E. Kendrick, R. Smalley, R. B. Vargas, and E. Lauría (2007), Crustal motion in the zone of the 1960 Chile earthquake: Detangling earthquake-cycle deformation and forearc-sliver translation, *Geochemistry, Geophysics, Geosystems*, *8*(10), doi:10.1029/2007gc001721.

Wang, R., F. L. Martin, and F. Roth (2003b), Computation of deformation induced by earthquakes in a multi-layered elastic crust—FORTRAN programs EDGRN/EDCMP, *Computers and Geosciences*, *29*(2), 195–207, doi:10.1016/S0098-3004(02)00111-5.

Wdowinski, S., Y. Bock, J. Zhang, P. Fang, and J. Genrich (1997), Southern California permanent GPS geodetic array: Spatial filtering of daily positions for estimating coseismic and postseismic displacements induced by the 1992 Landers earthquake, *Journal of Geophysical Research: Solid Earth*, *102*(B8), 18,057–18,070, doi:10.1029/97jb01378.

Webb, F., and J. Zumberge (1993), *An introduction to GIPSY-OASIS II.*, JPL Publication D-11088. Pasadena, CA: JetPropulsion Laboratory.

Weiss, J. R., B. A. Brooks, J. H. Foster, M. Bevis, A. Echalar, D. Caccamise, J. Heck, E. Kendrick, K. Ahlgren, D. Raleigh, et al. (2016), Isolating active orogenic wedge deformation in the southern Subandes of Bolivia, *Journal of Geophysical Research: Solid Earth*, *121*(8), 6192–6218, doi:10.1002/2016jb013145.

Wellington, P., R. Brossier, O. Hamitou, P. Trinh, and J. Virieux (2017), Efficient anisotropic dip filtering via inverse correlation functions, *Geophysics*, *82*(4), A31–A35, doi:10.1190/geo2016-0552.1.

Wells, R. E., R. J. Blakely, Y. Sugiyama, D. W. Scholl, and P. A. Dinterman (2003), Basin-centered asperities in great subduction zone earthquakes: A link between slip, subsidence, and subduction erosion?, *Journal of Geophysical Research: Solid Earth*, *108*(B10), doi:10.1029/2002jb002072.

Wesnousky, S. G. (2006), Predicting the endpoints of earthquake ruptures, *Nature*, *444*(7117), 358–360, doi:10.1038/nature05275.

Williams, S. D., Y. Bock, P. Fang, P. Jamason, R. M. Nikolaidis, L. Prawirodirdjo, M. Miller, and D. J. Johnson (2004), Error analysis of continuous GPS position time series, *Journal of Geophysical Research: Solid Earth*, *109*(B3).

Wong, I. G., and D. S. Chapman (1990), Deep intraplate earthquakes in the western United States and their relationship to lithospheric temperatures, *Bulletin of the Seismological Society of America*, *80*(3), 589–599.

Wübbena, G. (1985), Software developments for geodetic positioning with GPS using TI-4100 code and carrier measurements, in *Proceedings of the first international symposium on precise positioning with the global positioning system*, vol. 19, sl]:[sn].

Yagi, Y., R. Okuwaki, B. Enescu, S. Hirano, Y. Yamagami, S. Endo, and T. Komoro (2014), Rupture process of the 2014 Iquique Chile earthquake in relation with the foreshock activity, *Geophysical Research Letters*, *41*(12), 4201–4206, doi:10.1002/2014gl060274.

Yao, H., P. Gerstoft, P. M. Shearer, and C. Mecklenbräuker (2011), Compressive sensing of the Tohoku-Oki Mw 9.0 earthquake: Frequency-dependent rupture modes, *Geophysical Research Letters*, *38*(20), doi:10.1029/2011gl049223.

Yokota, Y., and K. Koketsu (2015), A very long-term transient event preceding the 2011 Tohoku earthquake, *Nature communications*, *6*, doi:10.1038/ncomms6934.

Yoshioka, S., K. Wang, and S. Mazzotti (2005), Interseismic locking of the plate interface in the northern Cascadia subduction zone, inferred from inversion of GPS data, *Earth and Planetary Science Letters*, *231*(3), 239–247, doi:10.1016/j.epsl.2004.12.018.

Youngs, R., N. Abrahamson, F. Makdisi, and K. Sadigh (1995), Magnitude-dependent variance of peak ground acceleration, *Bulletin of the Seismological Society of America*, *85*(4), 1161–1176.

Zhong, P., X. Ding, L. Yuan, Y. Xu, K. Kwok, and Y. Chen (2010), Sidereal filtering based on single differences for mitigating GPS multipath effects on short baselines, *Journal of Geodesy*, *84*(2), 145–158, doi:10.1007/s00190-009-0352-z.

Zumberge, J., M. Heflin, D. Jefferson, M. Watkins, and F. H. Webb (1997), Precise point positioning for the efficient and robust analysis of GPS data from large networks, *Journal of Geophysical Research: Solid Earth*, *102*(B3), 5005–5017, doi:10.1029/96jb03860.

Appendix A

Supporting Information for Chapter 4: “Processing and Analysis of GPS Data"

In this appendix can be find all the supporting information of the Chapter 4.

A.1 GPS Parameters Estimated

A.1.1 Annual and Semi-Annual Parameters

Station	N C1xcos A	E C1xcos A	V C1xcos A	N C2xsin A	E C2xsin A	V C2xsin A
AEDA	-0.43+/-0.03	-0.69+/-0.04	1.32+/-0.10	1.92+/-0.03	1.08+/-0.04	-0.59+/-0.11
AREQ	0.68+/-0.03	-0.24+/-0.04	0.40+/-0.08	1.22+/-0.04	1.91+/-0.04	-3.51+/-0.09
ATIC	-1.40+/-0.03	-1.90+/-0.04	2.45+/-0.08	0.99+/-0.03	-0.44+/-0.04	-0.20+/-0.08
ATJN	-1.12+/-0.03	-1.64+/-0.03	2.64+/-0.06	1.24+/-0.03	0.41+/-0.03	-0.64+/-0.06
CBAA	-1.09+/-0.03	-1.56+/-0.03	2.20+/-0.06	1.27+/-0.03	0.04+/-0.03	-0.34+/-0.05
CDLC	-1.18+/-0.03	-1.74+/-0.03	1.70+/-0.07	1.18+/-0.03	0.14+/-0.03	-0.45+/-0.06
CGTC	-1.46+/-0.03	-0.92+/-0.03	2.34+/-0.06	-0.55+/-0.03	-1.55+/-0.03	1.75+/-0.06
CHMZ	-0.83+/-0.03	0.31+/-0.03	-0.17+/-0.06	-1.39+/-0.03	-1.61+/-0.03	3.37+/-0.06
CHRA	1.44+/-0.03	0.56+/-0.03	-1.92+/-0.11	0.83+/-0.03	2.43+/-0.03	-3.46+/-0.10
CJNT	-0.95+/-0.03	-1.52+/-0.03	2.66+/-0.07	1.33+/-0.03	0.30+/-0.03	0.18+/-0.06
CLLA	-1.12+/-0.03	-0.35+/-0.03	0.71+/-0.06	-1.20+/-0.03	-1.62+/-0.03	1.55+/-0.06
COLC	-0.78+/-0.03	-1.86+/-0.04	2.23+/-0.10	0.91+/-0.03	0.60+/-0.04	0.67+/-0.10
COLL	-0.26+/-0.04	1.08+/-0.04	-2.43+/-0.08	-1.75+/-0.07	-1.66+/-0.08	-4.16+/-0.15
CRSC	-0.77+/-0.03	-1.42+/-0.03	2.20+/-0.06	1.42+/-0.03	0.63+/-0.03	-0.95+/-0.06
CTLR	-0.62+/-0.03	0.23+/-0.03	0.05+/-0.08	-1.21+/-0.03	-1.54+/-0.03	1.33+/-0.07
DANC	0.83+/-0.03	2.09+/-0.03	-3.33+/-0.06	-1.68+/-0.03	-1.08+/-0.03	3.85+/-0.06
ENAP	-1.41+/-0.03	-0.89+/-0.04	0.29+/-0.09	0.28+/-0.03	-0.81+/-0.04	1.47+/-0.09
FBAQ	-1.78+/-0.04	-1.38+/-0.04	1.54+/-0.09	1.15+/-0.04	-0.31+/-0.05	0.30+/-0.10
GLRV	0.91+/-0.03	3.11+/-0.03	-2.79+/-0.06	-1.50+/-0.03	0.42+/-0.03	2.39+/-0.07
GUAD	-1.47+/-0.03	-0.96+/-0.04	1.32+/-0.09	-0.01+/-0.03	-1.17+/-0.04	1.87+/-0.09
HMBS	1.35+/-0.03	1.52+/-0.04	-4.06+/-0.11	0.04+/-0.03	0.92+/-0.04	0.31+/-0.12
HUAN	-1.05+/-0.03	1.61+/-0.04	0.01+/-0.09	-2.12+/-0.04	-3.09+/-0.04	5.79+/-0.10
IQQE	-0.42+/-0.03	0.40+/-0.03	-0.74+/-0.08	-1.26+/-0.03	-1.58+/-0.03	1.62+/-0.08
JRGN	-1.04+/-0.03	-1.26+/-0.03	1.27+/-0.07	1.46+/-0.03	0.65+/-0.03	-0.67+/-0.07
LAGN	5.36+/-0.89	23.83+/-0.87	38.66+/-2.39	1.08+/-0.24	2.04+/-0.23	12.22+/-0.64
LAGU	-1.42+/-0.03	-1.11+/-0.04	0.10+/-0.10	0.11+/-0.03	-1.34+/-0.04	-0.31+/-0.10
LOMI	-1.69+/-0.06	-2.01+/-0.05	1.34+/-0.09	1.97+/-0.06	1.42+/-0.04	-2.23+/-0.07
LYAR	-1.14+/-0.03	-1.68+/-0.03	2.78+/-0.08	1.25+/-0.03	0.17+/-0.03	-0.06+/-0.07
MCLA	-0.82+/-0.03	-1.33+/-0.03	1.87+/-0.06	1.19+/-0.03	0.33+/-0.03	-0.39+/-0.06
MICA	1.14+/-0.02	0.71+/-0.03	-0.45+/-0.05	1.10+/-0.03	1.56+/-0.03	-2.49+/-0.06
MNMI	1.54+/-0.03	1.61+/-0.03	-1.54+/-0.07	-0.66+/-0.03	0.24+/-0.03	-0.41+/-0.07
NZCA	-1.35+/-0.03	-2.72+/-0.04	2.55+/-0.09	1.20+/-0.03	-0.44+/-0.04	-0.07+/-0.09
PALC	0.92+/-0.03	2.13+/-0.03	-1.47+/-0.07	-1.88+/-0.03	-0.61+/-0.03	5.08+/-0.07
PB01	-0.61+/-0.03	-1.38+/-0.03	1.58+/-0.07	1.55+/-0.03	0.91+/-0.03	-0.71+/-0.07
PB02	-0.34+/-0.03	-1.47+/-0.03	0.57+/-0.07	1.77+/-0.03	1.04+/-0.03	-1.13+/-0.07
PB03	-0.36+/-0.03	-1.31+/-0.04	1.47+/-0.08	1.90+/-0.03	0.84+/-0.04	0.01+/-0.08
PB04	-0.53+/-0.03	-1.14+/-0.03	1.42+/-0.07	1.52+/-0.03	0.89+/-0.03	-0.01+/-0.06
PB05	-0.50+/-0.03	-1.54+/-0.04	1.39+/-0.08	1.57+/-0.03	0.86+/-0.04	0.25+/-0.07
PB06	-1.45+/-0.03	-1.25+/-0.03	1.44+/-0.07	0.63+/-0.03	-0.27+/-0.03	0.36+/-0.07
PB07	-0.99+/-0.03	-1.59+/-0.04	1.22+/-0.08	1.58+/-0.03	0.32+/-0.03	-1.12+/-0.07
PB08	-1.32+/-0.03	-1.73+/-0.04	2.56+/-0.08	1.22+/-0.03	-0.19+/-0.03	-1.14+/-0.07
PB11	2.03+/-0.09	4.47+/-0.13	-4.35+/-0.23	-0.87+/-0.10	2.53+/-0.14	-1.85+/-0.25
PCCL	-1.47+/-0.03	-1.77+/-0.03	2.92+/-0.07	1.32+/-0.03	-0.09+/-0.03	-0.19+/-0.07
PCHA	-0.46+/-0.03	0.53+/-0.03	-0.02+/-0.08	-1.68+/-0.03	-1.40+/-0.03	2.80+/-0.08
PICC	0.98+/-0.03	-0.21+/-0.04	0.77+/-0.07	1.10+/-0.04	1.52+/-0.04	-1.85+/-0.08
PMCA	0.69+/-0.02	1.79+/-0.03	-1.06+/-0.06	-1.71+/-0.03	-1.01+/-0.04	2.63+/-0.09
PMEJ	-0.06+/-0.03	-1.03+/-0.04	0.49+/-0.09	1.53+/-0.03	1.00+/-0.04	0.09+/-0.08
PSGA	1.41+/-0.03	1.41+/-0.03	-1.73+/-0.08	-0.15+/-0.03	0.19+/-0.03	-1.16+/-0.08
PTCL	-0.28+/-0.04	-1.78+/-0.04	3.71+/-0.14	2.01+/-0.04	1.75+/-0.04	-1.66+/-0.15
PTIN	0.30+/-0.03	1.61+/-0.03	-1.25+/-0.08	-1.46+/-0.03	-1.33+/-0.03	3.36+/-0.08
PTRE	-1.31+/-0.03	-1.80+/-0.03	3.69+/-0.06	1.41+/-0.03	0.29+/-0.03	-1.66+/-0.06
QUCA	0.55+/-0.03	1.89+/-0.03	-3.73+/-0.08	-2.11+/-0.05	-0.94+/-0.05	5.87+/-0.15
QUIL	-0.11+/-0.03	-0.39+/-0.04	3.02+/-0.08	2.14+/-0.04	0.90+/-0.04	0.13+/-0.09
RADO	-0.04+/-0.03	-1.20+/-0.03	1.41+/-0.07	1.57+/-0.03	1.14+/-0.03	-1.83+/-0.06
SJUA	1.43+/-0.03	0.46+/-0.04	-1.04+/-0.08	1.10+/-0.03	2.45+/-0.04	-1.31+/-0.08
SLRZ	-0.63+/-0.03	-2.68+/-0.04	3.37+/-0.08	0.01+/-0.03	-0.37+/-0.04	-1.05+/-0.09
SRGD	-0.62+/-0.03	-1.46+/-0.03	1.96+/-0.08	1.34+/-0.03	0.68+/-0.03	-0.99+/-0.07
TORA	0.62+/-0.03	2.57+/-0.03	-3.52+/-0.08	-2.25+/-0.04	-0.99+/-0.04	1.96+/-0.11
TQPL	-1.79+/-0.03	-1.58+/-0.03	4.23+/-0.07	0.16+/-0.03	-0.98+/-0.04	1.30+/-0.08
TRTA	2.29+/-0.04	2.39+/-0.04	-4.07+/-0.09	-1.05+/-0.04	0.22+/-0.04	1.86+/-0.08
UAPE	0.85+/-0.04	0.13+/-0.04	1.29+/-0.10	0.90+/-0.04	1.61+/-0.04	-1.80+/-0.10
UCNF	0.95+/-0.03	0.65+/-0.03	0.53+/-0.07	1.11+/-0.03	1.13+/-0.03	-0.94+/-0.08
URCU	0.43+/-0.04	-1.36+/-0.05	0.59+/-0.10	1.66+/-0.07	1.56+/-0.09	1.42+/-0.16
UTAR	0.15+/-0.03	-1.31+/-0.04	1.69+/-0.09	1.81+/-0.03	1.33+/-0.04	-2.01+/-0.09
VLZL	-1.41+/-0.03	-1.36+/-0.03	1.81+/-0.06	0.38+/-0.03	-0.53+/-0.03	1.01+/-0.06

Table A.1: North, East and Vertical Annual amplitude coefficients inverted with equation 4.2. Coefficients are in mm.

Station	N C3xcos SA	E C3xcos SA	V C3xcos SA	N C4xsin SA	E C4xsin SA	V C4xsin SA
AEDA	0.32+/-0.03	0.05+/-0.03	0.84+/-0.09	0.08+/-0.03	-0.41+/-0.04	-0.22+/-0.09
AREQ	0.32+/-0.03	-0.28+/-0.04	0.03+/-0.08	-0.16+/-0.03	0.02+/-0.04	-0.57+/-0.08
ATIC	0.22+/-0.03	-0.26+/-0.03	-0.94+/-0.07	-0.05+/-0.03	0.06+/-0.03	0.41+/-0.07
ATJN	0.02+/-0.03	0.19+/-0.03	0.46+/-0.06	0.23+/-0.03	-0.32+/-0.03	-0.01+/-0.06
CBAA	0.20+/-0.03	0.09+/-0.03	-0.17+/-0.05	0.04+/-0.03	-0.47+/-0.03	-0.26+/-0.05
CDLC	0.16+/-0.03	0.05+/-0.03	-0.19+/-0.06	-0.08+/-0.03	-0.37+/-0.03	-0.43+/-0.06
CGTC	0.02+/-0.03	0.11+/-0.03	-0.43+/-0.06	-0.01+/-0.03	-0.06+/-0.03	-0.76+/-0.06
CHMZ	-0.09+/-0.03	-0.27+/-0.03	-0.73+/-0.06	-0.12+/-0.03	0.23+/-0.03	-0.05+/-0.06
CHRA	-0.27+/-0.03	0.42+/-0.03	1.69+/-0.10	0.02+/-0.03	0.03+/-0.03	0.76+/-0.10
CJNT	0.09+/-0.03	0.24+/-0.03	1.07+/-0.06	0.10+/-0.03	-0.46+/-0.03	0.00+/-0.06
CLLA	-0.20+/-0.02	-0.05+/-0.03	0.26+/-0.06	-0.04+/-0.02	0.25+/-0.03	0.19+/-0.06
COLC	-0.02+/-0.03	0.08+/-0.03	0.37+/-0.09	0.01+/-0.03	-0.59+/-0.03	0.17+/-0.09
COLL	1.31+/-0.04	0.43+/-0.04	1.04+/-0.09	0.83+/-0.04	-0.85+/-0.04	-1.02+/-0.08
CRSC	0.12+/-0.03	-0.01+/-0.03	0.21+/-0.05	0.17+/-0.03	-0.34+/-0.03	-0.33+/-0.06
CTLR	-0.09+/-0.03	-0.27+/-0.03	-0.47+/-0.07	-0.10+/-0.03	0.37+/-0.03	0.57+/-0.07
DANC	0.03+/-0.03	-0.47+/-0.03	0.78+/-0.06	-0.43+/-0.03	-0.30+/-0.03	1.19+/-0.06
ENAP	-0.35+/-0.03	0.89+/-0.04	1.60+/-0.08	-0.05+/-0.03	-0.18+/-0.04	0.95+/-0.08
FBAQ	0.47+/-0.03	-0.05+/-0.03	0.68+/-0.07	0.32+/-0.03	-0.04+/-0.03	-0.35+/-0.07
GLRV	0.08+/-0.03	-0.18+/-0.03	-0.51+/-0.06	-0.17+/-0.03	-0.41+/-0.03	0.64+/-0.06
GUAD	-0.04+/-0.03	0.19+/-0.03	-0.70+/-0.09	0.22+/-0.03	0.43+/-0.03	-0.33+/-0.09
HMBS	-0.39+/-0.03	0.52+/-0.03	2.74+/-0.11	0.62+/-0.03	-0.33+/-0.03	0.30+/-0.10
HUAN	0.16+/-0.03	1.38+/-0.03	2.16+/-0.08	-0.04+/-0.03	0.84+/-0.03	1.67+/-0.08
IQQE	0.09+/-0.03	-0.05+/-0.03	0.33+/-0.08	-0.14+/-0.03	0.09+/-0.03	-0.04+/-0.07
JRGN	0.13+/-0.03	0.14+/-0.03	-0.05+/-0.07	0.05+/-0.03	-0.39+/-0.03	-0.24+/-0.06
LAGN	1.08+/-0.11	2.89+/-0.10	4.00+/-0.29	-1.68+/-0.18	-5.57+/-0.18	-8.68+/-0.50
LAGU	-0.24+/-0.03	0.35+/-0.04	1.02+/-0.10	0.22+/-0.03	0.29+/-0.04	-0.15+/-0.10
LOMI	-0.73+/-0.05	-0.07+/-0.04	2.14+/-0.07	-0.91+/-0.06	-0.54+/-0.04	1.04+/-0.07
LYAR	0.01+/-0.03	0.16+/-0.03	-0.37+/-0.07	0.12+/-0.03	-0.26+/-0.03	-0.09+/-0.07
MCLA	0.15+/-0.03	0.12+/-0.03	0.03+/-0.06	0.17+/-0.03	-0.39+/-0.03	-0.10+/-0.06
MICA	-0.45+/-0.03	-0.19+/-0.03	0.12+/-0.05	-0.08+/-0.02	0.38+/-0.03	0.83+/-0.05
MNMI	-0.10+/-0.03	0.02+/-0.03	-0.37+/-0.06	0.09+/-0.03	-0.06+/-0.03	-0.11+/-0.06
NZCA	0.27+/-0.03	-0.10+/-0.04	-1.20+/-0.09	-0.25+/-0.03	-0.24+/-0.04	0.47+/-0.08
PALC	-0.24+/-0.03	-0.14+/-0.03	0.30+/-0.07	-0.43+/-0.03	-0.22+/-0.03	1.18+/-0.07
PB01	0.07+/-0.03	-0.30+/-0.03	-0.18+/-0.07	0.12+/-0.03	-0.35+/-0.03	-0.43+/-0.07
PB02	0.08+/-0.03	-0.21+/-0.03	-0.18+/-0.06	0.00+/-0.03	-0.47+/-0.03	-0.34+/-0.07
PB03	-0.07+/-0.03	-0.14+/-0.03	-0.04+/-0.07	-0.07+/-0.03	-0.24+/-0.03	-0.34+/-0.07
PB04	0.05+/-0.03	-0.16+/-0.03	-0.18+/-0.06	-0.05+/-0.03	-0.35+/-0.03	0.04+/-0.06
PB05	0.06+/-0.03	-0.24+/-0.03	-0.37+/-0.07	0.08+/-0.03	-0.38+/-0.03	-0.21+/-0.07
PB06	-0.01+/-0.03	0.07+/-0.03	-0.24+/-0.07	-0.04+/-0.03	-0.28+/-0.03	0.02+/-0.07
PB07	-0.15+/-0.03	0.11+/-0.03	0.18+/-0.07	-0.15+/-0.03	0.04+/-0.03	0.69+/-0.07
PB08	-0.20+/-0.03	-0.07+/-0.03	0.48+/-0.07	0.00+/-0.03	0.07+/-0.03	0.66+/-0.07
PB11	0.07+/-0.05	1.09+/-0.07	0.44+/-0.12	0.40+/-0.05	-1.05+/-0.07	0.63+/-0.12
PCCL	-0.08+/-0.03	0.27+/-0.03	0.38+/-0.07	0.18+/-0.03	-0.32+/-0.03	-0.01+/-0.06
PCHA	0.12+/-0.03	-0.36+/-0.03	-0.37+/-0.08	-0.04+/-0.03	0.12+/-0.03	-0.35+/-0.08
PICC	0.01+/-0.03	-0.08+/-0.04	0.66+/-0.07	-0.26+/-0.03	0.18+/-0.04	0.05+/-0.07
PMCA	-0.19+/-0.03	-0.13+/-0.03	-0.11+/-0.07	-0.12+/-0.03	0.14+/-0.03	1.60+/-0.07
PMEJ	0.27+/-0.03	-0.23+/-0.03	-0.25+/-0.08	0.07+/-0.03	-0.26+/-0.03	-0.09+/-0.08
PSGA	-0.06+/-0.03	0.43+/-0.03	0.34+/-0.08	0.21+/-0.03	-0.04+/-0.03	0.21+/-0.07
PTCL	0.15+/-0.03	-0.80+/-0.04	-1.14+/-0.13	0.15+/-0.03	-0.17+/-0.04	-0.56+/-0.13
PTIN	0.23+/-0.03	-0.16+/-0.03	-0.21+/-0.07	-0.68+/-0.03	0.12+/-0.03	0.97+/-0.07
PTRE	-0.07+/-0.03	0.23+/-0.03	0.60+/-0.06	0.24+/-0.03	-0.37+/-0.03	0.49+/-0.06
QUCA	0.25+/-0.03	-0.24+/-0.03	-1.36+/-0.09	-0.74+/-0.03	-0.16+/-0.03	1.44+/-0.10
QUIL	1.12+/-0.03	-0.33+/-0.03	-0.29+/-0.08	0.65+/-0.03	-0.39+/-0.04	-1.21+/-0.08
RADO	0.11+/-0.03	-0.18+/-0.03	0.35+/-0.06	-0.12+/-0.03	-0.30+/-0.03	-0.01+/-0.06
SJUA	0.18+/-0.03	0.14+/-0.03	0.24+/-0.07	0.28+/-0.03	-0.31+/-0.03	-0.94+/-0.07
SLRZ	0.55+/-0.03	-0.07+/-0.03	-0.25+/-0.08	-0.07+/-0.03	-0.18+/-0.03	0.03+/-0.08
SRGD	0.19+/-0.03	-0.09+/-0.03	0.00+/-0.07	0.03+/-0.03	-0.44+/-0.03	-0.07+/-0.07
TORA	-0.11+/-0.03	0.12+/-0.03	-0.68+/-0.08	-0.40+/-0.03	0.03+/-0.03	-1.12+/-0.08
TQPL	0.13+/-0.03	0.33+/-0.03	-1.47+/-0.06	0.08+/-0.03	0.32+/-0.03	0.07+/-0.06
TRTA	0.37+/-0.03	0.62+/-0.03	-0.14+/-0.07	-0.39+/-0.03	-0.23+/-0.03	0.83+/-0.07
UAPE	0.03+/-0.03	-0.28+/-0.04	0.48+/-0.10	-0.28+/-0.03	0.30+/-0.04	-0.36+/-0.10
UCNF	-0.10+/-0.03	0.03+/-0.03	0.43+/-0.07	-0.29+/-0.03	0.27+/-0.03	0.15+/-0.07
URCU	0.48+/-0.03	-0.94+/-0.04	-1.99+/-0.07	-0.51+/-0.03	-0.19+/-0.04	-0.67+/-0.08
UTAR	0.05+/-0.03	-0.20+/-0.04	0.90+/-0.09	-0.14+/-0.03	-0.46+/-0.04	0.21+/-0.09
VLZL	-0.10+/-0.03	0.47+/-0.03	0.37+/-0.06	0.05+/-0.03	-0.04+/-0.03	0.08+/-0.06

Table A.2: North, East and Vertical Semi-Annual amplitude coefficients inverted with equation 4.2. Coefficients are in mm.

A.1.2 Coseismic and Postseismic Offsets for Earthquakes $M_w \geq 7.5$

Station	North	East	Vertical	PS North	PS East	PS Vertical
AREQ	-288.09+/-1.15	-418.92+/-1.32	-25.7+/-2.76	-65.71+/-1.61	-130.22+/-1.85	57.15+/-3.88

Table A.3: Coseismic (North, East and Vertical) and Postseismic (PS) values obtained inverted the Equation 4.2 for Arequipa Earthquake (M_w 8.4, 2001/06/23). Values and errors are in mm.

Station	North	East	Vertical	PS North	PS East	PS Vertical
AREQ	-31.46+/-0.63	-34.02+/-0.73	-1.77+/-1.52	-14.41+/-0.79	-0.42+/-0.91	-12+/-1.90
UAPE	-1.38+/-0.67	0.13+/-0.76	-0.35+/-1.88	-8.9+/-1.06	-3.77+/-1.21	-16.06+/-2.97

Table A.4: Coseismic (North, East and Vertical) and Postseismic (PS) values obtained inverted the Equation 4.2 for the biggest aftershock of Arequipa Earthquake (M_w 7.6, 2001/07/07). Values and errors are in mm.

Station	North	East	Vertical	PS North	Ps East	Ps Vertical
AEDA	-22.04+/-0.22	-41.88+/-0.28	29.4+/-0.73	-3.93+/-0.24	-3.38+/-0.3	3.27+/-0.78
AREQ	-0.33+/-0.19	-0.95+/-0.22	-1.52+/-0.46	-0.54+/-0.26	-4.06+/-0.3	-0.78+/-0.62
COLL	0.84+/-0.07	-3.29+/-0.08	6.02+/-0.15	1.19+/-0.11	24.18+/-0.12	3.59+/-0.23
FBAQ	3.55+/-0.12	-15.14+/-0.12	4.73+/-0.26	-5.65+/-0.31	-10.72+/-0.32	-1.95+/-0.68
IQQE	-13.14+/-0.27	-48.91+/-0.28	40.11+/-0.67	1.06+/-0.58	-12.19+/-0.62	3.96+/-1.47
PICC	34.42+/-0.18	-8.03+/-0.2	-55.43+/-0.4	-3.78+/-0.28	-9.7+/-0.31	-0.07+/-0.62
PMEJ	-1.8+/-0.13	-1.35+/-0.17	2.54+/-0.4	-0.36+/-0.21	-4.24+/-0.26	-3.14+/-0.61
QUIL	-0.16+/-0.24	0.88+/-0.27	0.19+/-0.6	0.65+/-0.18	-1.02+/-0.21	0.49+/-0.45
UAPE	-13.88+/-0.42	-48.96+/-0.48	38.08+/-1.18	-2.95+/-0.26	-6.28+/-0.29	-6.05+/-0.72
UCNF	1.05+/-0.21	-1.52+/-0.25	-2.03+/-0.55	-2.22+/-0.4	-4.42+/-0.48	-1.63+/-1.07
UTAR	1.82+/-0.25	-4.31+/-0.29	5.24+/-0.69	0.45+/-0.25	-2.73+/-0.29	-2.29+/-0.69

Table A.5: Coseismic (North, East and Vertical) and Postseismic (PS) values obtained inverted the Equation 4.2 for Tarapaca Earthquake (M_w 7.7, 2005/06/13). Values and errors are in mm.

Station	North	East	Vertical	PS North	PS East	PS Vertical
AEDA	1.99+/-0.22	1.3+/-0.27	-3.56+/-0.71	-0.08+/-0.49	1.41+/-0.61	7.4+/-1.61
AREQ	2.13+/-0.34	-1.61+/-0.39	0.16+/-0.83	1.4+/-0.74	-5.41+/-0.85	6.13+/-1.78
ATJN	2+/-0.23	-0.93+/-0.25	-1.97+/-0.52	-1.4+/-0.52	3.36+/-0.56	8.3+/-1.17
CHMZ	1.91+/-0.24	-0.96+/-0.26	-0.66+/-0.53	-1.97+/-0.42	3.32+/-0.46	9.98+/-0.93
CRSC	0.58+/-0.24	-0.64+/-0.27	-1.49+/-0.5	-0.26+/-0.55	4.03+/-0.61	8.18+/-1.16
CTLR	0.77+/-0.26	-0.88+/-0.27	2.27+/-0.67	-0.57+/-0.49	4.86+/-0.51	1.18+/-1.24
ENAP	-0.44+/-0.31	3.17+/-0.39	-4.89+/-0.88	0.71+/-0.09	1.64+/-0.12	-0.17+/-0.26
GUAD	-2.13+/-0.84	-1.35+/-1.02	2.35+/-2.56	-1.98+/-0.86	0.07+/-1.04	5.37+/-2.62
HMBS	1.18+/-0.19	-0.42+/-0.22	-7.94+/-0.68	0.74+/-0.46	5.35+/-0.55	10.27+/-1.70
JRGN	1.41+/-0.26	-2.6+/-0.29	-1.03+/-0.59	-1.65+/-0.61	5.18+/-0.67	9.2+/-1.36
LAGU	-2.43+/-0.97	-0.51+/-1.18	-2.61+/-3	-1.63+/-1	-6.87+/-1.22	-7.32+/-3.08
MCLA	0.37+/-0.23	-0.98+/-0.27	-3.1+/-0.51	0.07+/-0.54	5.38+/-0.62	10.02+/-1.18
MNMI	1.13+/-0.46	-0.01+/-0.51	-4.23+/-1.09	4.26+/-5.03	-2.51+/-5.55	57.22+/-11.79
PCCL	1.76+/-0.22	-1.1+/-0.24	-1.78+/-0.54	0.17+/-0.49	2.87+/-0.55	7.3+/-1.23
PCHA	-7.26+/-1.15	-8.51+/-1.16	-6.08+/-2.89	-4.15+/-0.79	-157.44+/-0.79	-15.04+/-1.99
PICC	2.95+/-0.38	-0.43+/-0.42	2.57+/-0.84	-2.82+/-0.89	3.23+/-0.99	2.81+/-1.96
PMEJ	1.45+/-0.28	-4.34+/-0.34	-3.3+/-0.82	0.38+/-0.62	10.9+/-0.77	7.42+/-1.84
PSGA	2.83+/-0.23	1.46+/-0.27	0.95+/-0.64	-4.6+/-0.48	-0.42+/-0.57	-5.62+/-1.37
PTRE	2.1+/-0.22	-2.42+/-0.23	-0.38+/-0.49	-1.6+/-0.51	4.77+/-0.53	5.24+/-1.12
QUIL	3.16+/-0.09	-3.04+/-0.1	3.88+/-0.23	-1.19+/-0.19	-6.69+/-0.22	-16.24+/-0.47
SRGD	1.15+/-0.24	0.84+/-0.27	-1.31+/-0.64	-1.02+/-0.52	0.71+/-0.59	6.65+/-1.39
UAPE	0.93+/-0.38	1.74+/-0.43	1.16+/-1.06	0.1+/-0.83	-1.21+/-0.95	4.48+/-2.33
UTAR	0.03+/-0.29	-2.01+/-0.34	-3.2+/-0.8	2.41+/-0.66	3.77+/-0.76	4.41+/-1.79
VLZL	1.05+/-0.23	-1.48+/-0.26	-3.08+/-0.51	-0.97+/-0.51	4.01+/-0.58	7.03+/-1.14

Table A.6: Coseismic (North, East and Vertical) and Postseismic (PS) values obtained inverted the Equation 4.2 for Pisco Earthquake (M_w 8.0, 2007/08/15). Values and errors are in mm.

Station	North	East	Vertical	PS North	PS East	PS Vertical
AEDA	0.14+/-0.88	-2.58+/-1.1	-11.61+/-2.88	-0.41+/-0.32	0.17+/-0.4	8.13+/-1.05
AREQ	0.04+/-0.34	-0.15+/-0.39	-2.79+/-0.81	-0.22+/-0.44	0.6+/-0.5	-0.7+/-1.05
ATJN	-0.21+/-0.23	-1.68+/-0.25	-0.57+/-0.52	0.92+/-0.36	-2.06+/-0.39	-0.12+/-0.80
CBAA	0.36+/-0.89	-9.39+/-0.96	3.27+/-1.86	-2.56+/-0.14	-14.77+/-0.15	5.9+/-0.29
CDLC	-16.45+/-0.93	-11.58+/-1.03	-1.41+/-2.13	-6.61+/-0.14	-9.55+/-0.16	-2.83+/-0.33
CHMZ	-0.48+/-0.18	-2.51+/-0.2	-1.43+/-0.41	-0.48+/-0.27	-1.4+/-0.3	-0.54+/-0.61
CJNT	1.74+/-0.96	-7.33+/-1.04	4.79+/-2.23	2.56+/-0.15	-9.45+/-0.16	3.66+/-0.34
COLC	-0.69+/-0.41	0.59+/-0.46	3.36+/-1.24	0.01+/-0.24	-4.75+/-0.27	-4.78+/-0.73
CRSC	-1.64+/-1.02	-3+/-1.14	-3.05+/-2.16	-0.6+/-0.4	-3.13+/-0.45	0.81+/-0.86
CTLR	7.5+/-0.2	-15.48+/-0.21	84.16+/-0.52	-2.67+/-0.31	-5.25+/-0.32	-4.7+/-0.79
JRGN	-43.22+/-1.15	-19.29+/-1.26	87.71+/-2.57	-8.97+/-0.4	-20.41+/-0.44	16.33+/-0.90
LYAR	1.89+/-0.26	0.13+/-0.28	-2.27+/-0.67	-1.25+/-0.13	-1.59+/-0.14	3.51+/-0.34
MCLA	-19.23+/-1.03	-12.79+/-1.18	93+/-2.25	-6.8+/-0.36	-13.78+/-0.41	0.22+/-0.78
PCCL	-0.17+/-0.22	-1.51+/-0.24	-2.3+/-0.54	1.11+/-0.34	-0.57+/-0.37	1.24+/-0.84
PCHA	2.15+/-0.23	-2.03+/-0.24	0.97+/-0.59	0.7+/-0.54	5.74+/-0.54	-5.86+/-1.35
PMEJ	-40.93+/-1.16	-26.52+/-1.44	139.99+/-3.43	-4.93+/-0.45	-23.73+/-0.56	25.93+/-1.33
PSGA	2.39+/-0.22	0.04+/-0.26	4.56+/-0.63	0.14+/-0.32	-2.34+/-0.38	-0.42+/-0.90
PTRE	1.59+/-0.22	-1.89+/-0.23	-3.61+/-0.49	-1.16+/-0.29	-1.61+/-0.3	2.71+/-0.63
QUIL	3.38+/-0.16	-1.15+/-0.19	-1.49+/-0.41	-0.97+/-0.36	2.14+/-0.41	-4.25+/-0.90
SRGD	-0.4+/-0.97	-18.42+/-1.09	3.09+/-2.57	-1.91+/-0.34	-17.23+/-0.38	-8.1+/-0.90
UAPE	-0.82+/-1.7	-2.12+/-1.94	-4.21+/-4.78	0.01+/-0.58	-1.92+/-0.66	4.4+/-1.63
UTAR	-0.14+/-0.32	-1.63+/-0.37	-1.1+/-0.88	0.67+/-0.44	-1.09+/-0.51	-1.06+/-1.20
VLZL	-11.23+/-0.94	-8.57+/-1.06	5.85+/-2.08	-1.59+/-0.33	-16.07+/-0.38	-4.75+/-0.74

Table A.7: Coseismic (North, East and Vertical) and Postseismic (PS) values obtained inverted the Equation 4.2 for Tocopilla Earthquake (M_w 7.7, 2007/11/14). Values and errors are in mm.

Station	North	East	Vertical	PS North	PS East	PS Vertical
AEDA	-6.74+/-0.17	-47.76+/-0.22	-5.58+/-0.57	0.57+/-0.92	0.48+/-1.15	-2+/-3.01
AREQ	1.15+/-0.3	0.06+/-0.34	-0.69+/-0.71	-1.53+/-1.15	0.8+/-1.32	4.26+/-2.76
ATIC	1.93+/-0.21	0.05+/-0.24	-3.73+/-0.53	-1.21+/-0.51	0.15+/-0.58	4.06+/-1.28
ATJN	-18.33+/-0.2	-57.42+/-0.22	-20.13+/-0.45	0.44+/-1.11	-1.53+/-1.19	-2.74+/-2.46
CBAA	-0.49+/-0.72	1.53+/-0.78	2.99+/-1.51	-0.99+/-0.61	-0.55+/-0.66	2.27+/-1.28
CGTC	-12.03+/-0.15	-66.51+/-0.16	-20.81+/-0.32	-0.01+/-0.78	-0.39+/-0.86	3.36+/-1.72
CHMZ	-9.5+/-0.33	-52.37+/-0.36	1.82+/-0.73	0.84+/-0.84	-0.96+/-0.92	0.84+/-1.87
CJNT	-0.72+/-0.28	2.17+/-0.3	-0.71+/-0.65	0.26+/-0.68	-0.51+/-0.74	5.04+/-1.58
COLC	-9.54+/-0.18	-35.68+/-0.2	1.49+/-0.53	0.64+/-0.94	-2.69+/-1.05	-0.4+/-2.84
CRSC	-4.51+/-0.23	-21.52+/-0.26	-3.24+/-0.49	0.26+/-1.06	-2.31+/-1.18	2.41+/-2.24
DANC	-0.58+/-0.05	-0.42+/-0.05	-0.2+/-0.11	0.14+/-0.58	-0.04+/-0.62	6.27+/-1.32
IQQE	-9.42+/-0.22	-66.07+/-0.23	-15.3+/-0.56	0.02+/-1.22	-0.29+/-1.3	2.57+/-3.09
JRGN	-1.38+/-0.21	1.48+/-0.23	-6.98+/-0.47	-1.49+/-0.8	3.29+/-0.88	3.11+/-1.80
LYAR	-7.08+/-0.17	-8.69+/-0.18	-7.39+/-0.43	1.02+/-0.9	-2.12+/-0.98	2.93+/-2.31
MCLA	-2.86+/-0.19	1.95+/-0.21	-2.49+/-0.41	-2.04+/-1.01	0.16+/-1.17	1.78+/-2.22
MNMI	-21.11+/-0.18	-58.95+/-0.2	-4.99+/-0.41	-3.04+/-0.95	-2.81+/-1.04	2.04+/-2.22
NZCA	1.91+/-0.18	0.86+/-0.25	-0.3+/-0.57	0.28+/-0.46	0.42+/-0.62	3.52+/-1.42
PALC	-19.56+/-8.4	-27.45+/-9.18	-2.96+/-21	0.96+/-0.59	-1.28+/-0.65	2.15+/-1.48
PB01	3.98+/-0.17	-21.97+/-0.18	-5.22+/-0.44	1.03+/-0.89	-1.37+/-0.93	5.51+/-2.28
PB02	-2.26+/-0.15	-6.46+/-0.17	-3.85+/-0.36	0.04+/-0.79	-0.02+/-0.89	2.14+/-1.91
PB03	-2.09+/-0.14	1.11+/-0.16	-0.96+/-0.34	0.63+/-0.73	-0.11+/-0.84	4.97+/-1.75
PB04	-3.31+/-0.17	2.07+/-0.2	-1.07+/-0.4	-0.32+/-0.92	-0.26+/-1.1	3.28+/-2.22
PB05	-2.82+/-0.15	3.2+/-0.19	-0.85+/-0.38	-1.99+/-0.8	-0.05+/-0.99	7.77+/-2.00
PB06	-1.53+/-0.15	-0.29+/-0.18	-3.17+/-0.4	-1.58+/-0.66	1.84+/-0.76	4.01+/-1.70
PB07	-2.71+/-0.16	-1.17+/-0.18	-3.72+/-0.41	0.85+/-0.7	-0.44+/-0.8	-0.57+/-1.82
PB08	-3.71+/-0.14	-51.88+/-0.16	-4.37+/-0.33	0.54+/-0.7	-1.33+/-0.76	1.45+/-1.63
PB11	-16.99+/-0.18	-65.87+/-0.27	-6.04+/-0.48	-0.01+/-0.33	-1.58+/-0.49	0.2+/-0.85
PCCL	-21.3+/-0.19	-28.72+/-0.21	-9.85+/-0.46	0.06+/-1.03	-0.73+/-1.15	0.39+/-2.58
PCHA	1.53+/-0.39	-1.73+/-0.39	1.89+/-0.98	-3.49+/-0.25	-2.98+/-0.25	-0.46+/-0.62
PICC	-0.12+/-0.25	-47.47+/-0.27	-5.93+/-0.54	0.21+/-1.36	-1.96+/-1.5	4.64+/-2.98
PMCA	-7.26+/-4.31	-23.88+/-4.67	-8.65+/-11.5	-2.46+/-0.45	2.06+/-0.48	9.59+/-1.19
PMEJ	-2.28+/-0.21	1.77+/-0.26	-0.66+/-0.62	-0.95+/-0.81	2.52+/-1.01	5.04+/-2.40
PSGA	-18.21+/-0.18	-53.17+/-0.21	-20.65+/-0.5	0.77+/-0.97	-0.81+/-1.15	1.23+/-2.73
PTCL	3.34+/-0.21	-1.21+/-0.23	-1.07+/-0.81	-1.02+/-1.01	-0.53+/-1.13	7.94+/-3.91
PTRE	-21.78+/-0.22	-17.98+/-0.23	0.6+/-0.47	0.31+/-1.1	-1.66+/-1.15	-1.73+/-2.41
RADO	1.18+/-0.17	-0.22+/-0.2	-0.2+/-0.41	-0.15+/-0.89	-1.66+/-1.03	1.78+/-2.17
SJUA	-0.29+/-0.14	1.18+/-0.17	-0.82+/-0.36	-0.44+/-0.5	-0.66+/-0.61	3.74+/-1.28
SRGD	-1.81+/-0.18	2.06+/-0.2	-2.27+/-0.47	-1.25+/-0.95	0.72+/-1.07	4.52+/-2.53
TORA	-0.11+/-0.05	-0.11+/-0.05	-0.03+/-0.14	0.58+/-0.52	-1.65+/-0.61	-2.38+/-1.55
TQPL	-1.3+/-0.15	0.55+/-0.16	-3.09+/-0.35	0.54+/-0.74	-2.05+/-0.8	0.88+/-1.79
TRTA	-7.15+/-0.19	-0.37+/-0.17	-11.37+/-0.4	-0.55+/-0.96	-1.61+/-0.89	9.68+/-2.07
UAPE	-9.43+/-0.32	-66.73+/-0.36	-10.88+/-0.89	-0.66+/-1.77	-0.12+/-2.02	-9.78+/-4.98
UCNF	-2+/-0.17	1.37+/-0.2	-3.13+/-0.44	-1.77+/-0.62	0.91+/-0.74	4.51+/-1.66
UTAR	-24+/-0.23	-27.75+/-0.27	-8.42+/-0.64	0.2+/-1.32	-2.13+/-1.51	-0.51+/-3.59
VLZL	-2.31+/-0.18	1.36+/-0.2	-3.29+/-0.4	-2.26+/-0.66	1.02+/-0.74	4.06+/-1.46

Table A.8: Coseismic (North, East and Vertical) and Postseismic (PS) values obtained inverted the Equation 4.2 for Iquique Earthquake (M_w 8.1, 2014/04/01). Values and errors are in mm.

A.1.3 Coseismic Offsets Earthquakes of $M_w < 7.5$

Station	North	East	Vertical
AREQ	-10.67+/-1.24	-14.15+/-1.42	0.82+/-2.98
UAPE	-3.09+/-1.09	2.17+/-1.25	-3.93+/-3.08

Table A.9: Coseismic parameters earthquake M_w 6.7 in 2001/06/26. Values and errors are in mm.

Station	North	East	Vertical
UAPE	3.03+/-0.63	3.32+/-0.72	0.82+/-2.98

Table A.10: Coseismic parameters earthquake M_w 6.4 in 2001/07/24. Values and errors are in mm.

Station	North	East	Vertical
AEDA	0.13+/-0.90	-0.02+/-1.13	-3.93+/-3.08
CDLC	-37.00+/-0.91	-107.78+/-1.01	2.92+/-1.78
CJNT	2.21+/-0.97	-13.86+/-1.06	5.61+/-2.95
CRSC	0.25+/-1.04	-0.68+/-1.16	-70.17+/-2.10
JRGN	-109.19+/-1.16	-151.42+/-1.28	-4.34+/-2.26
MCLA	-52.22+/-1.04	-91.67+/-1.20	-3.09+/-2.20
PMEJ	-84.47+/-1.18	-218.49+/-1.47	144.20+/-2.61
QUIL	-38.11+/-0.65	-58.13+/-0.74	172.75+/-2.28
SRGD	4.17+/-0.98	-119.08+/-1.10	191.02+/-3.50
UAPE	1.26+/-1.73	1.57+/-1.98	-29.00+/-1.62
VLZL	-19.54+/-0.95	-96.91+/-1.08	-44.76+/-2.60

Table A.11: Coseismic parameters earthquake M_w 6.3 in 2007/11/15. Values and errors are in mm.

Station	North	East	Vertical
CBAA	1.05+/-0.22	3.45+/-0.23	-2.06+/-4.87
CDLC	2.50+/-0.22	1.66+/-0.25	-34.13+/-2.11
CJNT	-1.16+/-0.23	2.60+/-0.25	-2.71+/-0.45
CRSC	0.26+/-0.27	0.63+/-0.30	-0.91+/-0.52
CTLR	0.37+/-0.24	0.72+/-0.25	-1.61+/-0.54
JRGN	5.40+/-0.31	-6.13+/-0.34	0.07+/-0.58
MCLA	-0.16+/-0.27	-1.78+/-0.31	3.43+/-0.60
PB01	1.68+/-0.26	0.88+/-0.28	-11.31+/-0.69
PB02	0.66+/-0.23	0.77+/-0.26	-1.02+/-0.60
PB03	1.45+/-0.22	2.39+/-0.26	-4.91+/-0.67
PB04	1.69+/-0.26	-0.10+/-0.32	-2.41+/-0.56
PB05	1.46+/-0.24	-0.44+/-0.29	0.82+/-0.54
PMEJ	-1.30+/-0.36	-4.93+/-0.45	-5.24+/-0.64
QUIL	-0.16+/-0.24	0.88+/-0.27	-1.83+/-0.59
RADO	1.85+/-0.37	7.12+/-0.42	-26.07+/-1.07
SRGD	0.74+/-0.26	4.91+/-0.29	0.19+/-0.60
URCU	0.16+/-0.13	-0.61+/-0.15	2.41+/-0.89
VLZL	-3.58+/-0.25	5.37+/-0.29	3.22+/-0.68

Table A.12: Coseismic parameters earthquake M_w 6.8 in 2007/11/15. Values and errors are in mm.

Station	North	East	Vertical
AEDA	-4.38+/-0.21	0.82+/-0.26	-2.22+/-0.29
ATJN	-1.48+/-0.22	-0.45+/-0.23	10.60+/-0.56
CHMZ	-1.92+/-0.17	-1.30+/-0.18	0.38+/-0.68
COLC	-1.50+/-0.25	-0.22+/-0.27	-0.52+/-0.48
CRSC	-1.85+/-0.21	0.00+/-0.23	-0.76+/-0.37
MICA	-2.28+/-0.47	0.42+/-0.49	2.03+/-0.74
PB01	-0.05+/-0.19	-0.27+/-0.20	-1.45+/-0.44
PB02	-0.61+/-0.17	0.06+/-0.19	-4.11+/-0.96
PCCL	-1.62+/-0.20	-0.43+/-0.23	-3.16+/-0.48
PCHA	-4.18+/-0.22	-3.68+/-0.22	-3.39+/-0.40
PSGA	-0.95+/-0.21	0.69+/-0.25	-1.96+/-0.50
QUIL	0.65+/-0.18	-1.02+/-0.21	3.65+/-0.56
UAPE	-1.58+/-0.34	0.66+/-0.39	1.93+/-0.59
URCU	0.12+/-0.13	-2.01+/-0.16	0.49+/-0.45
UTAR	-2.16+/-0.28	-0.73+/-0.33	2.00+/-0.95

Table A.13: Coseismic parameters earthquake M_w 6.3 in 2008/02/04. Values and errors are in mm.

Station	North	East	Vertical
ATJN	-4.96+/-0.13	-10.82+/-0.14	-3.36+/-0.30
CGTC	0.04+/-0.12	-2.49+/-0.13	2.82+/-0.77
CHMZ	-0.61+/-0.10	-1.83+/-0.11	-3.04+/-0.28
CLLA	-0.56+/-0.10	-0.92+/-0.11	-1.93+/-0.27
COLC	5.28+/-0.11	-1.61+/-0.13	-0.48+/-0.22
CRSC	-1.17+/-0.12	-0.60+/-0.13	0.64+/-0.23
HMBS	-0.20+/-0.09	-2.02+/-0.11	-14.98+/-0.34
IQQE	-1.36+/-0.15	-0.87+/-0.16	-1.39+/-0.25
LYAR	-1.27+/-0.11	-1.30+/-0.12	7.13+/-0.33
MNMI	-2.32+/-0.13	-3.70+/-0.14	-1.49+/-0.37
PB01	-0.11+/-0.09	0.06+/-0.09	-1.69+/-0.27
PB08	-0.56+/-0.21	-1.82+/-0.22	-2.98+/-0.31
PCCL	-2.15+/-0.12	-1.29+/-0.14	1.44+/-0.22
PSGA	-0.85+/-0.11	-9.10+/-0.13	1.99+/-0.48
PTCL	-0.65+/-0.13	-2.22+/-0.15	-2.11+/-0.30
PTRE	-2.65+/-0.12	-0.68+/-0.13	-3.63+/-0.32
TQPL	0.06+/-0.13	-1.40+/-0.14	14.06+/-0.51
TRTA	-1.57+/-0.13	-0.11+/-0.12	1.29+/-0.27
UAPE	-1.42+/-0.85	-1.25+/-0.97	-1.89+/-0.30

Table A.14: Coseismic parameters earthquake M_w 6.5 in 2009/11/13. Values and errors are in mm.

Station	North	East	Vertical
AREQ	0.65+/-0.15	-1.21+/-0.17	0.65+/-0.27
ATJN	0.66+/-0.13	-1.15+/-0.13	1.44+/-2.38
CBAA	-1.01+/-0.39	-1.35+/-0.42	-0.08+/-0.35
CDLC	-1.08+/-0.40	-1.45+/-0.45	0.20+/-0.28
CGTC	0.94+/-0.09	0.37+/-0.10	-1.02+/-0.81
CHMZ	0.76+/-0.10	0.52+/-0.11	-3.56+/-0.93
CJNT	0.45+/-0.43	-1.85+/-0.47	1.39+/-0.20
CLLA	-0.24+/-0.36	-0.39+/-0.40	1.15+/-0.21
COLC	1.08+/-0.11	-0.91+/-0.13	0.27+/-1.01
CRSC	1.58+/-0.12	0.67+/-0.13	3.97+/-0.82
CTLR	-1.48+/-0.39	0.08+/-0.40	2.71+/-0.34
ENAP	0.71+/-0.09	1.64+/-0.12	1.38+/-0.24
HMBS	1.51+/-0.12	0.43+/-0.14	-2.33+/-0.99
IQQE	0.49+/-0.14	1.82+/-0.15	-0.17+/-0.26
JRGN	0.50+/-0.16	-1.25+/-0.17	0.66+/-0.42
LAGU	-1.78+/-0.10	2.88+/-0.12	0.35+/-0.36
LYAR	0.81+/-0.11	0.31+/-0.11	1.92+/-0.35
MCLA	1.40+/-0.08	-0.61+/-0.10	-19.74+/-0.32
MICA	-0.19+/-0.30	-0.24+/-0.31	2.95+/-0.27
MNMI	0.63+/-0.12	-0.15+/-0.13	0.82+/-0.18
PB04	0.38+/-0.52	1.06+/-0.62	-1.27+/-0.61
PB06	0.66+/-0.12	0.17+/-0.14	-0.32+/-0.28
PB07	1.60+/-0.13	-0.42+/-0.15	-2.00+/-1.25
PCCL	1.10+/-0.12	-1.24+/-0.13	3.24+/-0.31
PICC	1.39+/-0.17	1.07+/-0.19	-2.57+/-0.33
PMEJ	1.25+/-0.11	0.74+/-0.14	1.62+/-0.29
PSGA	0.52+/-0.11	0.41+/-0.14	1.08+/-0.38
PTRE	-0.04+/-0.12	0.04+/-0.13	-5.03+/-0.33
RADO	-0.62+/-0.39	-1.35+/-0.45	2.84+/-0.32
SLRZ	1.08+/-0.08	0.72+/-0.10	2.46+/-0.27
SRGD	-0.27+/-0.48	-1.39+/-0.54	-1.77+/-0.95
TQPL	-0.42+/-0.10	-0.43+/-0.10	-0.49+/-0.22
TRTA	-1.70+/-0.13	-2.81+/-0.12	0.63+/-1.28
UAPE	1.37+/-0.20	0.13+/-0.22	3.31+/-0.23
UCNF	1.61+/-0.09	1.28+/-0.11	0.13+/-0.28
UTAR	1.50+/-0.16	-1.67+/-0.18	0.54+/-0.55
VLZL	1.85+/-0.19	1.14+/-0.21	-2.58+/-0.25

Table A.15: Coseismic parameters Maule earthquake M_w 8.8 in 2010/02/27. Values and errors are in mm.

Station	North	East	Vertical
CBAA	1.99+/-0.39	0.48+/-0.43	3.98+/-0.43
CDLC	1.43+/-0.41	-0.19+/-0.46	-0.71+/-0.42
CJNT	1.59+/-0.44	-0.08+/-0.48	-0.06+/-0.82
CLLA	0.77+/-0.36	0.23+/-0.39	1.82+/-0.95
CTLR	2.53+/-0.39	0.14+/-0.41	-1.17+/-1.02
MICA	1.20+/-0.31	0.74+/-0.32	-2.49+/-0.81
PB04	0.82+/-0.52	-0.81+/-0.62	-0.85+/-0.99
RADO	0.93+/-0.39	0.89+/-0.45	3.38+/-0.63
SRGD	1.47+/-0.49	0.30+/-0.55	1.98+/-1.25

Table A.16: Coseismic parameters earthquake M_w 6.3 in 2010/03/24. Values and errors are in mm.

Station	North	East	Vertical
GUAD	0.36+/-0.09	0.52+/-0.11	1.99+/-0.95

Table A.17: Coseismic parameters earthquake M_w 6.1 in 2010/05/23. Values and errors are in mm.

Station	North	East	Vertical
CBAA	0.70+/-0.09	0.26+/-0.10	-1.04+/-1.29
CDLC	-0.10+/-0.16	-0.20+/-0.18	4.15+/-0.28
CJNT	0.85+/-0.12	0.51+/-0.13	-0.46+/-0.20
MICA	1.35+/-0.08	1.28+/-0.09	3.10+/-0.37
PB06	0.66+/-0.10	-0.98+/-0.12	0.67+/-0.28
SRGD	0.33+/-0.10	-0.16+/-0.12	-1.08+/-0.17

Table A.18: Coseismic parameters earthquake M_w 6.3 in 2010/07/12. Values and errors are in mm.

Station	North	East	Vertical
ATJN	1.32+/-0.17	-0.57+/-0.18	0.02+/-0.26
LYAR	-0.30+/-0.11	-0.46+/-0.12	0.55+/-0.27
MNMI	-0.48+/-0.10	-1.03+/-0.11	-1.67+/-0.37
PCCL	0.09+/-0.10	0.17+/-0.11	-0.16+/-0.27
PTRE	0.23+/-0.09	0.11+/-0.09	-0.90+/-0.23
TRTA	0.31+/-0.12	-2.31+/-0.11	-1.77+/-0.24

Table A.19: Coseismic parameters earthquake M_w 6.3 in 2011/03/06. Values and errors are in mm.

Station	North	East	Vertical
CBAA	0.21+/-0.08	-0.55+/-0.09	-2.03+/-0.20
CDLC	-0.26+/-0.10	-1.29+/-0.11	0.38+/-0.26
CLLA	0.18+/-0.08	-1.08+/-0.09	0.27+/-0.17
MICA	1.13+/-0.07	-0.35+/-0.07	-0.39+/-0.22
PB01	0.12+/-0.09	-1.01+/-0.10	0.79+/-0.18
PB07	-0.45+/-0.10	-0.93+/-0.12	-1.32+/-0.13
RADO	-0.16+/-0.09	-0.60+/-0.10	0.78+/-0.24

Table A.20: Coseismic parameters earthquake M_w 6.4 in 2011/06/20. Values and errors are in mm.

Station	North	East	Vertical
ATIC	-0.56+/-0.09	-0.57+/-0.10	1.30+/-0.27
CHRA	-0.43+/-0.08	-1.42+/-0.09	2.98+/-0.21
GLRV	-1.42+/-0.09	-2.61+/-0.10	-2.25+/-0.23
GUAD	-11.07+/-0.11	-8.29+/-0.13	0.49+/-0.29
HUAN	-1.77+/-0.10	-2.50+/-0.12	-0.75+/-0.21
NZCA	-0.31+/-0.10	-8.45+/-0.13	-4.64+/-0.33
PTIN	-0.55+/-0.08	-1.00+/-0.08	-1.97+/-0.28
SJUA	-0.03+/-0.09	-2.14+/-0.11	-2.49+/-0.30

Table A.21: Coseismic parameters earthquake M_w 6.9 in 2011/10/28. Values and errors are in mm.

Station	North	East	Vertical
GLRV	1.30+/-0.08	-2.65+/-0.09	2.73+/-0.20
GUAD	1.91+/-0.11	-4.05+/-0.13	-1.99+/-0.24
LAGU	3.30+/-0.18	-5.75+/-0.22	0.22+/-0.19
LOMI	-3.43+/-0.18	-2.42+/-0.13	0.76+/-0.34

Table A.22: Coseismic parameters earthquake M_w 6.4 in 2012/01/30. Values and errors are in mm.

Station	North	East	Vertical
ATJN	0.55+/-0.09	0.13+/-0.10	-3.25+/-0.57
COLC	-0.64+/-0.11	-0.34+/-0.12	2.93+/-0.25
DANC	0.45+/-0.08	-1.06+/-0.09	0.97+/-0.21
LYAR	0.24+/-0.10	-0.71+/-0.11	5.13+/-0.33
MNMI	-0.44+/-0.11	-0.23+/-0.12	0.69+/-0.19
PALC	0.80+/-0.08	-1.14+/-0.09	0.08+/-0.27
PCCL	0.90+/-0.11	0.57+/-0.12	1.28+/-0.25
PSGA	-0.72+/-0.10	0.83+/-0.11	-1.54+/-0.21
PTCL	-0.64+/-0.12	-1.55+/-0.13	1.06+/-0.26
TQPL	-0.15+/-0.10	-0.13+/-0.11	-0.72+/-0.27
TRTA	2.07+/-0.13	1.51+/-0.12	-5.22+/-0.47
UTAR	0.16+/-0.12	1.23+/-0.14	1.77+/-0.24

Table A.23: Coseismic parameters earthquake M_w 6.2 in 2012/05/14. Values and errors are in mm.

Station	North	East	Vertical
AREQ	0.66+/-0.18	-0.15+/-0.20	1.43+/-0.28
ATIC	0.13+/-0.09	-0.42+/-0.11	-1.68+/-0.33
CHRA	-0.26+/-0.08	-0.26+/-0.09	2.80+/-0.43
QUCA	2.70+/-0.14	0.50+/-0.14	0.63+/-0.24

Table A.24: Coseismic parameters earthquake M_w 6.1 in 2012/06/07. Values and errors are in mm.

Station	North	East	Vertical
AREQ	0.55+/-0.16	-0.75+/-0.18	0.44+/-0.30
ATIC	-1.87+/-0.10	-0.30+/-0.11	-10.58+/-0.40
CHRA	-1.58+/-0.10	0.72+/-0.10	-0.77+/-0.38
DANC	0.30+/-0.09	1.01+/-0.09	-2.55+/-0.25
GLRV	-6.84+/-0.15	-1.89+/-0.16	-0.34+/-0.35
GUAD	-0.23+/-0.10	-0.39+/-0.12	-1.27+/-0.20
LAGU	0.58+/-0.11	-0.42+/-0.14	-3.08+/-0.34
LOMI	8.42+/-0.15	1.74+/-0.11	-0.27+/-0.30
LYAR	0.04+/-0.10	0.05+/-0.10	-2.22+/-0.35
NZCA	-2.54+/-0.08	-0.56+/-0.11	-3.61+/-0.20
PALC	1.04+/-0.09	-0.69+/-0.09	-1.41+/-0.25
PCCL	0.88+/-0.10	1.08+/-0.12	-1.47+/-0.26
PTCL	0.49+/-0.17	0.24+/-0.19	-1.41+/-0.21
SJUA	6.47+/-0.09	-5.16+/-0.11	-1.56+/-0.26
TQPL	0.29+/-0.08	0.45+/-0.09	-7.57+/-0.66
TRTA	-0.95+/-0.11	1.00+/-0.10	3.02+/-0.23
UTAR	0.62+/-0.13	0.31+/-0.15	-1.06+/-0.19
RADO	1.83+/-0.10	-1.06+/-0.12	-1.24+/-0.24
PTIN	-6.04+/-0.10	-7.26+/-0.11	-5.04+/-0.35

Table A.25: Coseismic parameters Acari earthquake M_w 7.1 in 2013/09/25. Values and errors are in mm.

Station	North	East	Vertical
AEDA	-0.72+/-0.26	-0.65+/-0.32	24.06+/-0.24
ATJN	0.33+/-0.30	0.76+/-0.32	-0.99+/-0.27
CGTC	-0.91+/-0.21	0.61+/-0.23	-0.52+/-0.83
CHMZ	-0.16+/-0.23	0.55+/-0.25	-4.00+/-0.67
CRSC	0.54+/-0.29	0.13+/-0.32	-2.98+/-0.47
IQQE	0.17+/-0.33	0.03+/-0.35	-1.74+/-0.51
LYAR	-0.11+/-0.25	1.85+/-0.27	-2.47+/-0.61
MNMI	-1.64+/-0.24	0.22+/-0.27	-3.30+/-0.84
PB01	0.02+/-0.25	1.02+/-0.27	-0.87+/-0.64
PB02	-0.10+/-0.22	0.63+/-0.25	0.67+/-0.57
PB08	-0.61+/-0.19	1.09+/-0.21	-2.25+/-0.65
PB11	-2.37+/-0.14	-0.98+/-0.20	-0.81+/-0.53
PCCL	-0.53+/-0.29	1.54+/-0.32	0.77+/-0.45
PCHA	0.72+/-0.32	2.60+/-0.32	2.11+/-0.35
PICC	0.06+/-0.37	2.09+/-0.41	-2.91+/-0.72
PSGA	0.06+/-0.26	0.22+/-0.31	0.87+/-0.80
UAPE	-0.68+/-0.48	-0.74+/-0.55	-1.88+/-0.81
UTAR	-0.88+/-0.37	2.72+/-0.42	0.34+/-0.74

Table A.26: Coseismic parameters earthquake M_w 6.3 in 2014/03/03. Values and errors are in mm.

Station	North	East	Vertical
GUAD	-2.13+/-0.84	-1.35+/-1.02	-5.65+/-1.34
LAGU	-2.43+/-0.97	-0.51+/-1.18	-3.84+/-0.99
LOMI	0.00+/-1.08	1.53+/-0.76	2.35+/-2.56
NZCA	-3.14+/-0.16	1.08+/-0.22	-2.61+/-3.00
SJUA	-2.21+/-0.18	0.78+/-0.22	4.38+/-1.44

Table A.27: Coseismic parameters earthquake M_w 6.2 in 2014/03/14. Values and errors are in mm.

Station	North	East	Vertical
GUAD	-1.98+/-0.86	0.07+/-1.04	2.71+/-0.50
LAGU	-1.63+/-1.00	-6.87+/-1.22	2.58+/-0.47
LOMI	0.26+/-1.11	0.04+/-0.78	5.37+/-2.62

Table A.28: Coseismic parameters earthquake M_w 6.0 in 2014/03/15. Values and errors are in mm.

Station	North	East	Vertical
AEDA	-0.93+/-0.90	1.68+/-1.12	-7.32+/-3.08
ATJN	-1.60+/-1.09	0.62+/-1.17	-1.96+/-1.48
CDLC	-1.59+/-0.29	0.97+/-0.32	-3.00+/-2.95
CGTC	-1.22+/-0.77	2.29+/-0.85	-2.48+/-2.42
CHMZ	-1.24+/-0.83	1.73+/-0.90	0.38+/-0.67
COLC	-2.97+/-0.24	-0.19+/-0.27	-6.76+/-1.69
CRSC	-1.24+/-1.04	1.81+/-1.17	-1.03+/-1.84
DANC	-2.70+/-0.16	0.14+/-0.17	2.52+/-0.73
IQQE	-1.63+/-1.20	2.76+/-1.28	-0.15+/-2.21
LYAR	-2.74+/-0.40	-0.39+/-0.43	4.78+/-0.36
PALC	-3.38+/-0.16	0.99+/-0.17	-4.90+/-3.05
PB01	-2.26+/-0.32	-0.88+/-0.34	4.80+/-1.03
PB02	0.04+/-0.80	0.90+/-0.89	4.04+/-0.40
PB03	-2.39+/-0.19	1.31+/-0.22	5.48+/-0.83
PB04	-1.80+/-0.23	1.41+/-0.28	-1.93+/-1.92
PB07	-2.55+/-0.18	1.69+/-0.21	0.77+/-0.45
PB08	-0.93+/-0.69	1.50+/-0.75	1.90+/-0.56
PB11	-1.69+/-0.32	0.11+/-0.48	2.94+/-0.47
PCCL	-2.36+/-0.48	-0.10+/-0.54	0.92+/-1.60
PCHA	-1.23+/-1.16	1.18+/-1.17	2.86+/-0.84
PICC	-1.46+/-1.34	1.04+/-1.48	4.50+/-1.21
PSGA	-1.02+/-0.95	2.38+/-1.13	-3.22+/-2.92
PTCL	-3.55+/-0.27	2.19+/-0.30	-3.43+/-2.93
PTRE	-2.30+/-0.40	1.72+/-0.42	-0.16+/-2.69
RADO	-2.62+/-0.23	1.01+/-0.27	3.42+/-1.04
TORA	-2.97+/-0.14	2.77+/-0.16	2.24+/-0.88
TQPL	-2.37+/-0.19	1.64+/-0.21	3.14+/-0.56
TRTA	-4.92+/-0.25	1.23+/-0.24	1.52+/-0.42
UAPE	-1.34+/-1.74	2.54+/-1.99	5.59+/-0.47
UTAR	-1.21+/-1.30	-0.34+/-1.49	4.55+/-0.55

Table A.29: Coseismic parameters earthquake M_w 6.6 in 2014/03/16. Values and errors are in mm.

Station	North	East	Vertical
AEDA	0.91+/-0.95	-3.11+/-1.19	-5.08+/-4.90
ATJN	-3.58+/-1.15	-4.52+/-1.24	-2.68+/-3.53
CGTC	0.41+/-0.81	-5.79+/-0.89	4.38+/-3.11
CHMZ	-1.60+/-0.86	-2.65+/-0.94	5.45+/-2.56
CRSC	0.89+/-1.10	-1.64+/-1.23	9.85+/-1.79
IQQE	1.10+/-1.27	-6.81+/-1.35	5.10+/-1.92
PB02	-1.98+/-0.79	-1.42+/-0.89	4.19+/-2.33
PB08	-1.37+/-0.72	-1.13+/-0.78	9.00+/-3.21
PB11	-1.02+/-0.34	-3.66+/-0.51	4.87+/-1.91
PCHA	-1.20+/-1.23	-2.54+/-1.23	3.15+/-1.67
PICC	0.06+/-1.39	-2.32+/-1.54	4.79+/-0.88
PSGA	-4.24+/-1.00	-6.05+/-1.19	8.95+/-3.08
UAPE	0.75+/-1.84	-5.63+/-2.10	6.45+/-3.05
UTAR	-1.62+/-1.37	0.65+/-1.57	3.28+/-2.84

Table A.30: Coseismic parameters earthquake M_w 6.1 in 2014/03/17. Values and errors are in mm.

Station	North	East	Vertical
AEDA	-1.23+/-0.95	-4.16+/-1.19	12.14+/-5.17
ATJN	-2.80+/-1.15	-5.23+/-1.24	8.16+/-3.73
CGTC	-1.90+/-0.81	-6.22+/-0.89	-3.77+/-3.11
CRSC	-2.36+/-1.10	-5.35+/-1.23	-3.03+/-2.56
IQQE	-1.80+/-1.27	-4.92+/-1.35	-3.52+/-1.79
PB11	-2.78+/-0.34	-6.29+/-0.51	-2.89+/-2.33
PCCL	-2.30+/-1.06	-5.51+/-1.18	-2.98+/-3.21
PCHA	-2.59+/-1.23	-5.22+/-1.23	-4.50+/-0.88
PSGA	-2.29+/-1.00	-6.63+/-1.19	-4.04+/-2.64
UAPE	-1.86+/-1.84	-7.07+/-2.10	-2.87+/-3.08
UTAR	-2.15+/-1.37	-6.92+/-1.57	-1.26+/-2.84

Table A.31: Coseismic parameters earthquake M_w 6.0 in 2014/03/22. Values and errors are in mm.

Station	North	East	Vertical
AEDA	1.57+/-0.92	2.83+/-1.15	1.30+/-5.17
ATJN	-0.92+/-1.11	-0.14+/-1.19	-3.89+/-3.73
CGTC	1.65+/-0.78	2.31+/-0.86	7.43+/-3.01
CHMZ	-0.54+/-0.42	-1.69+/-0.46	5.00+/-2.46
CRSC	1.48+/-1.06	4.27+/-1.18	4.99+/-1.72
IQQE	1.60+/-1.22	2.48+/-1.30	0.38+/-0.94
LYAR	-0.70+/-0.43	-0.46+/-0.47	5.48+/-2.24
PB08	-0.36+/-0.35	-1.11+/-0.38	2.45+/-3.09
PB11	1.19+/-0.33	1.69+/-0.49	0.08+/-1.10
PCCL	0.63+/-1.03	3.66+/-1.15	0.80+/-0.81
PCHA	0.97+/-1.18	2.55+/-1.18	5.82+/-0.85
PICC	-0.66+/-0.68	-1.14+/-0.75	5.82+/-2.58
PSGA	-0.60+/-0.97	-1.61+/-1.15	6.90+/-2.97
PTRE	-1.23+/-0.53	-0.90+/-0.55	0.79+/-1.49
UAPE	2.37+/-1.77	4.46+/-2.02	1.11+/-2.73
UTAR	1.10+/-1.32	4.63+/-1.51	1.67+/-1.15

Table A.32: Coseismic parameters earthquake M_w 6.2 in 2014/03/23. Values and errors are in mm.

Station	North	East	Vertical
AEDA	-10.78+/-1.23	-72.46+/-1.53	1.40+/-4.98
ATJN	-282.16+/-1.49	-540.47+/-1.60	3.83+/-3.59
CGTC	68.26+/-1.05	-409.04+/-1.16	-15.69+/-4.02
CHMZ	-15.33+/-0.56	-116.08+/-0.62	-158.32+/-3.30
COLC	-13.30+/-0.65	-54.06+/-0.72	-6.82+/-1.26
CRSC	-2.03+/-0.71	-8.11+/-0.79	-0.23+/-1.95
DANC	-10.09+/-0.79	-5.28+/-0.85	-9.38+/-1.50
LYAR	-19.99+/-1.21	-13.81+/-1.31	-9.38+/-1.50
MCLA	-0.86+/-1.43	1.43+/-1.65	0.03+/-1.81
MNMI	-61.06+/-0.65	-125.81+/-0.72	-3.49+/-3.14
PALC	-28.25+/-0.99	-17.25+/-1.08	-10.46+/-1.52
PB05	-1.84+/-1.13	0.93+/-1.40	-8.44+/-2.40
PB06	-1.24+/-0.93	0.03+/-1.08	-5.07+/-3.05
PB07	-1.79+/-0.96	-3.65+/-1.09	-9.05+/-2.82
PB11	-60.20+/-0.44	-461.92+/-0.65	-0.96+/-2.40
PCCL	-37.22+/-0.69	-33.80+/-0.77	-87.45+/-1.14
PCHA	-4.15+/-0.79	-157.44+/-0.79	-4.62+/-1.73
PICC	20.43+/-0.91	-62.43+/-1.01	-15.04+/-1.99
PMCA	-2.69+/-0.69	-1.66+/-0.75	-7.98+/-2.00
PSGA	-231.52+/-1.30	-810.67+/-1.54	-7.98+/-2.00
PTCL	3.57+/-1.38	-0.61+/-1.55	-12.31+/-1.84
PTRE	-26.88+/-0.74	-24.50+/-0.77	-6.08+/-5.36
RADO	3.94+/-1.22	-3.66+/-1.41	-0.33+/-1.62
SRGD	-0.96+/-1.35	-0.99+/-1.52	-0.33+/-1.62
TORA	-1.62+/-0.71	-1.53+/-0.83	-0.96+/-2.97
TQPL	-5.72+/-1.02	-1.13+/-1.10	-2.00+/-3.58
TRTA	-17.39+/-1.32	-9.32+/-1.22	-0.27+/-2.12
UTAR	-35.25+/-0.89	-28.16+/-1.02	-4.03+/-2.85

Table A.33: Coseismic parameters earthquake M_w 6.7 in 2014/04/02. Values and errors are in mm.

Station	North	East	Vertical
AEDA	-68.88+/-1.23	-243.14+/-1.53	-13.17+/-2.41
AREQ	3.11+/-1.20	-1.07+/-1.38	-13.17+/-2.41
ATIC	-1.35+/-0.54	2.30+/-0.62	97.55+/-4.02
ATJN	-5.48+/-1.49	-13.26+/-1.60	-2.37+/-2.89
CBAA	3.84+/-0.74	-4.36+/-0.80	1.72+/-1.36
CGTC	-30.33+/-1.05	-139.43+/-1.16	-4.17+/-3.30
CHMZ	-28.96+/-0.84	-52.87+/-0.92	-1.54+/-1.54
CJNT	2.58+/-0.71	-4.94+/-0.77	7.37+/-2.31
COLC	-11.89+/-0.94	-19.88+/-1.05	-4.86+/-1.87
CRSC	-16.75+/-1.42	-67.12+/-1.59	-1.44+/-1.65
DANC	1.65+/-0.79	-1.25+/-0.85	-2.54+/-2.83
IQQE	7.94+/-1.64	-477.44+/-1.74	-3.82+/-3.01
JRGN	-0.96+/-0.84	-1.22+/-0.93	-3.87+/-1.81
LYAR	-0.68+/-0.88	-1.38+/-0.95	13.24+/-4.15
MCLA	-0.56+/-1.04	-1.53+/-1.20	2.40+/-1.89
MNMI	-15.85+/-0.94	-20.88+/-1.04	6.12+/-2.25
NZCA	0.07+/-0.47	-0.91+/-0.63	2.53+/-2.27
PALC	0.51+/-1.12	0.00+/-1.22	-3.54+/-2.21
PB01	19.92+/-1.22	-48.17+/-1.28	-2.88+/-1.45
PB02	2.41+/-1.09	-15.82+/-1.21	-2.05+/-2.79
PB03	0.77+/-0.72	-4.75+/-0.84	0.64+/-3.13
PB04	-0.92+/-0.91	-1.70+/-1.09	-5.69+/-2.61
PB05	0.13+/-0.82	-2.05+/-1.02	-1.79+/-1.74
PB06	0.56+/-0.68	-0.97+/-0.79	-2.56+/-2.21
PB07	1.41+/-0.96	-1.89+/-1.09	1.02+/-2.04
PB08	3.32+/-0.94	-256.17+/-1.02	0.63+/-1.75
PB11	-38.91+/-0.44	-59.15+/-0.65	-1.07+/-2.49
PCCL	-5.25+/-1.01	-4.08+/-1.12	-21.95+/-2.18
PCHA	-35.66+/-1.58	-72.14+/-1.59	-16.27+/-1.14
PICC	0.32+/-1.82	-103.48+/-2.01	-6.68+/-2.51
PMCA	2.57+/-0.74	-0.86+/-0.81	-21.47+/-3.98
PMEJ	-1.36+/-0.85	-1.40+/-1.06	-23.11+/-3.99
PSGA	-11.98+/-1.30	-27.52+/-1.54	-0.22+/-1.99
PTCL	2.14+/-1.01	-0.84+/-1.13	-5.50+/-2.52
PTRE	-3.07+/-1.08	-3.83+/-1.12	-3.96+/-3.66
RADO	4.21+/-0.89	-8.29+/-1.03	-8.67+/-3.90
SJUA	1.06+/-0.49	1.25+/-0.61	-0.35+/-2.36
SRGD	1.17+/-0.98	-1.68+/-1.10	-2.02+/-2.17
TQPL	1.78+/-0.74	-2.54+/-0.80	-3.17+/-1.28
TRTA	-0.85+/-0.96	-3.08+/-0.89	1.00+/-2.59
UAPE	15.95+/-2.37	-514.78+/-2.71	-0.14+/-1.78
UCNF	-0.11+/-0.65	0.09+/-0.77	-2.23+/-2.07
UTAR	-6.08+/-1.28	-7.43+/-1.47	110.75+/-6.68
VLZL	-0.59+/-0.69	-1.06+/-0.78	0.13+/-1.74

Table A.34: Coseismic parameters earthquake M_w 7.6 in 2014/04/03. Values and errors are in mm.

Station	North	East	Vertical
AEDA	-7.37+/-0.89	-23.83+/-1.11	11.07+/-3.49
ATJN	-3.92+/-1.08	-12.03+/-1.16	-1.09+/-1.53
CGTC	-7.08+/-0.76	-15.87+/-0.84	4.20+/-2.91
CRSC	-0.43+/-1.04	-12.42+/-1.16	-2.98+/-2.39
IQQE	-8.00+/-1.18	-20.82+/-1.26	-5.99+/-1.67
PB01	0.95+/-0.89	-6.84+/-0.93	3.42+/-2.20
PB02	0.44+/-0.79	-4.09+/-0.88	-7.17+/-3.01
PB07	-2.00+/-0.70	-3.34+/-0.81	-13.65+/-2.27
PB08	-2.36+/-0.68	-5.88+/-0.74	-1.84+/-1.89
PB11	-7.51+/-0.33	-8.98+/-0.48	-1.51+/-1.84
PCHA	-7.26+/-1.15	-8.51+/-1.16	-1.48+/-1.59
PICC	-1.88+/-1.32	-9.00+/-1.46	-1.90+/-0.84
PSGA	-3.70+/-0.94	-9.43+/-1.11	-6.08+/-2.89
UAPE	-6.43+/-1.72	-16.25+/-1.96	-4.71+/-2.89

Table A.35: Coseismic parameters earthquake M_w 6.0 in 2014/04/04. Values and errors are in mm.

Station	North	East	Vertical
ATIC	-1.30+/-0.14	1.29+/-0.17	-8.46+/-2.65
NZCA	-1.91+/-0.13	0.09+/-0.17	-15.25+/-4.83

Table A.36: Coseismic parameters earthquake M_w 6.2 in 2014/08/24. Values and errors are in mm.

A.2 North, East and Vertical Displacements of Network Stations

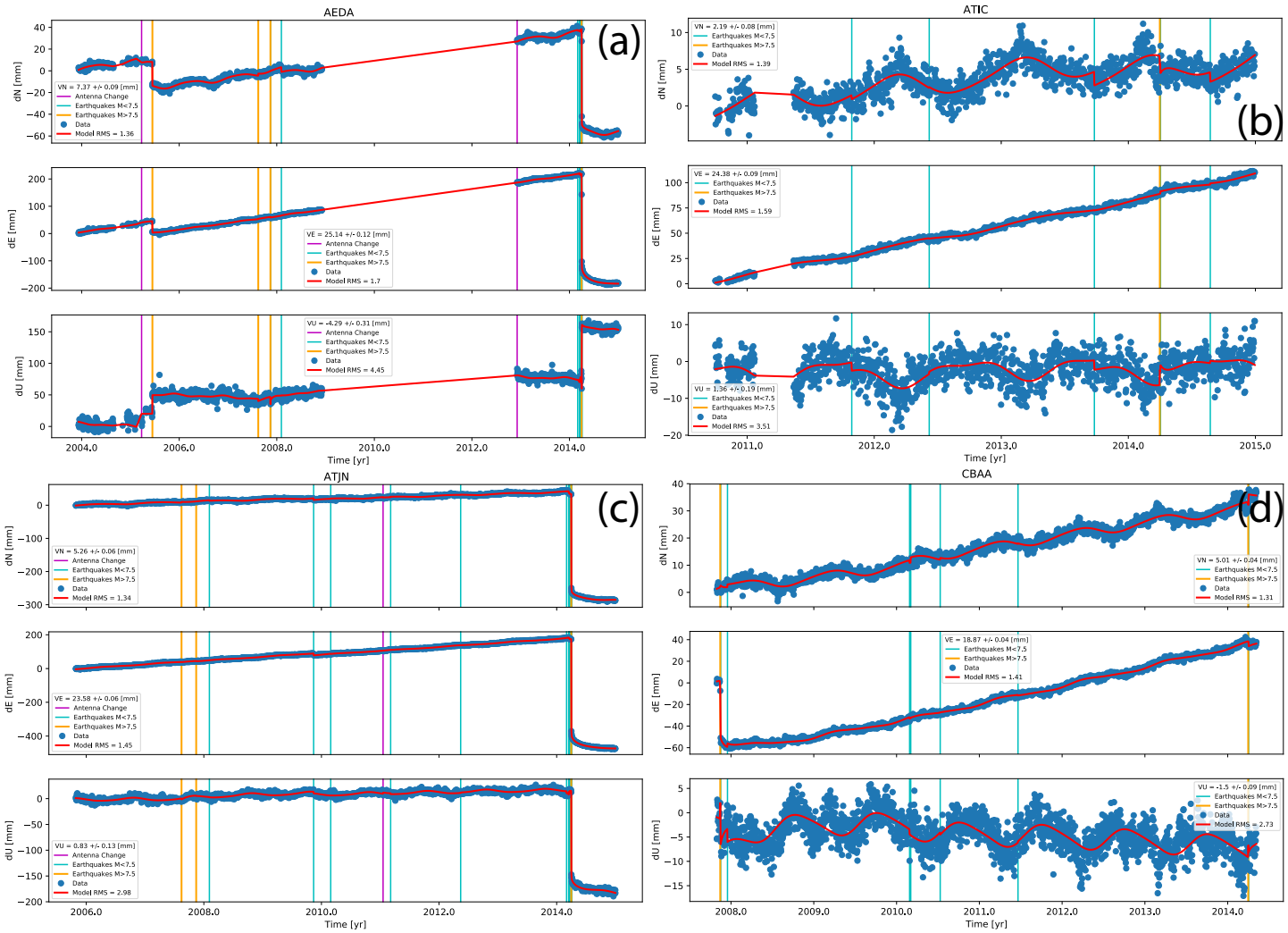

Figure A.1: Daily Displacement Time Series and its best-fit trajectory model (red curves) for (a) AEDA, (b) ATIC, (c) ATJN and (d) CBAA stations. The box shows the velocity obtained for each component with its respective error associated. Purple vertical lines indcate the antenna changes, yellow vertical lines are earthquake with $M \geq 7.5$ (for which post-seismic signal is modeled), while cyan vertical lines represent the earthquakes $6.0 \leq M < 7.5$. Model RMS is annotated on the information boxes.

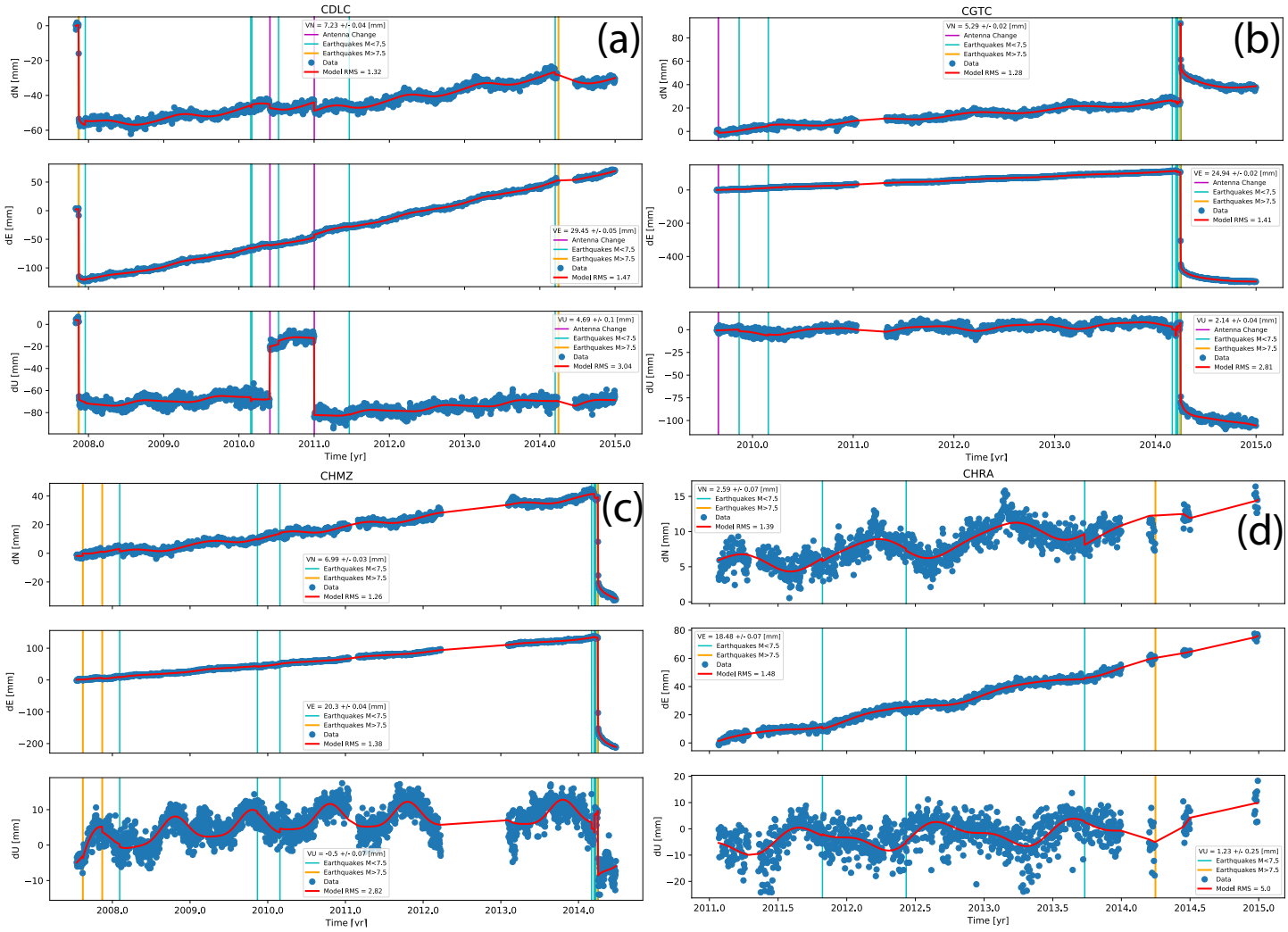

Figure A.2: Same caption as in Figure A.1, but for (a) CDLC, (b) CGTC, (c) CHMZ and (d) CHRA stations.

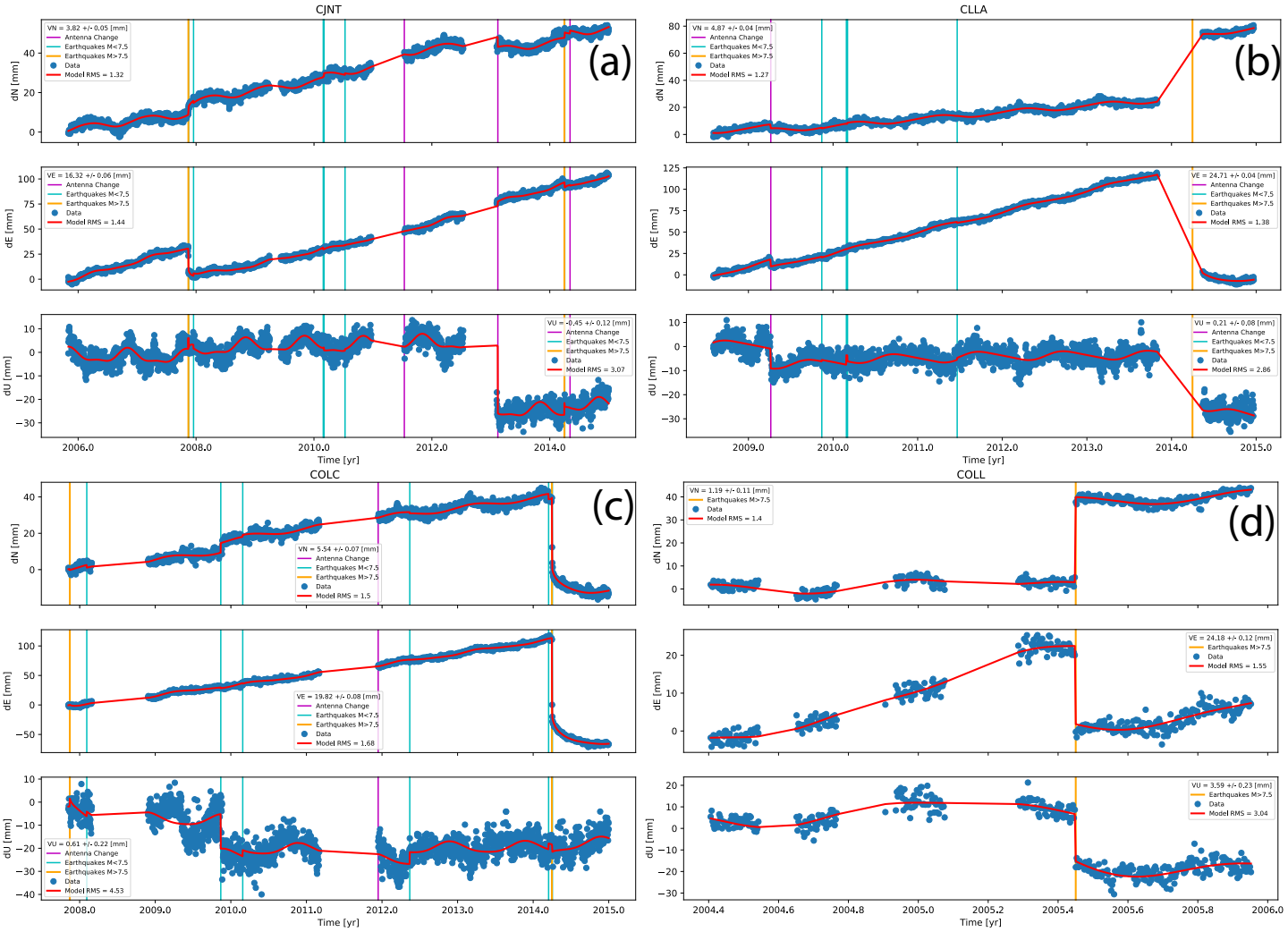

Figure A.3: Same caption as in Figure A.1, but for (a) CJNT, (b) CLLA, (c) COLC and (d) COLL stations.

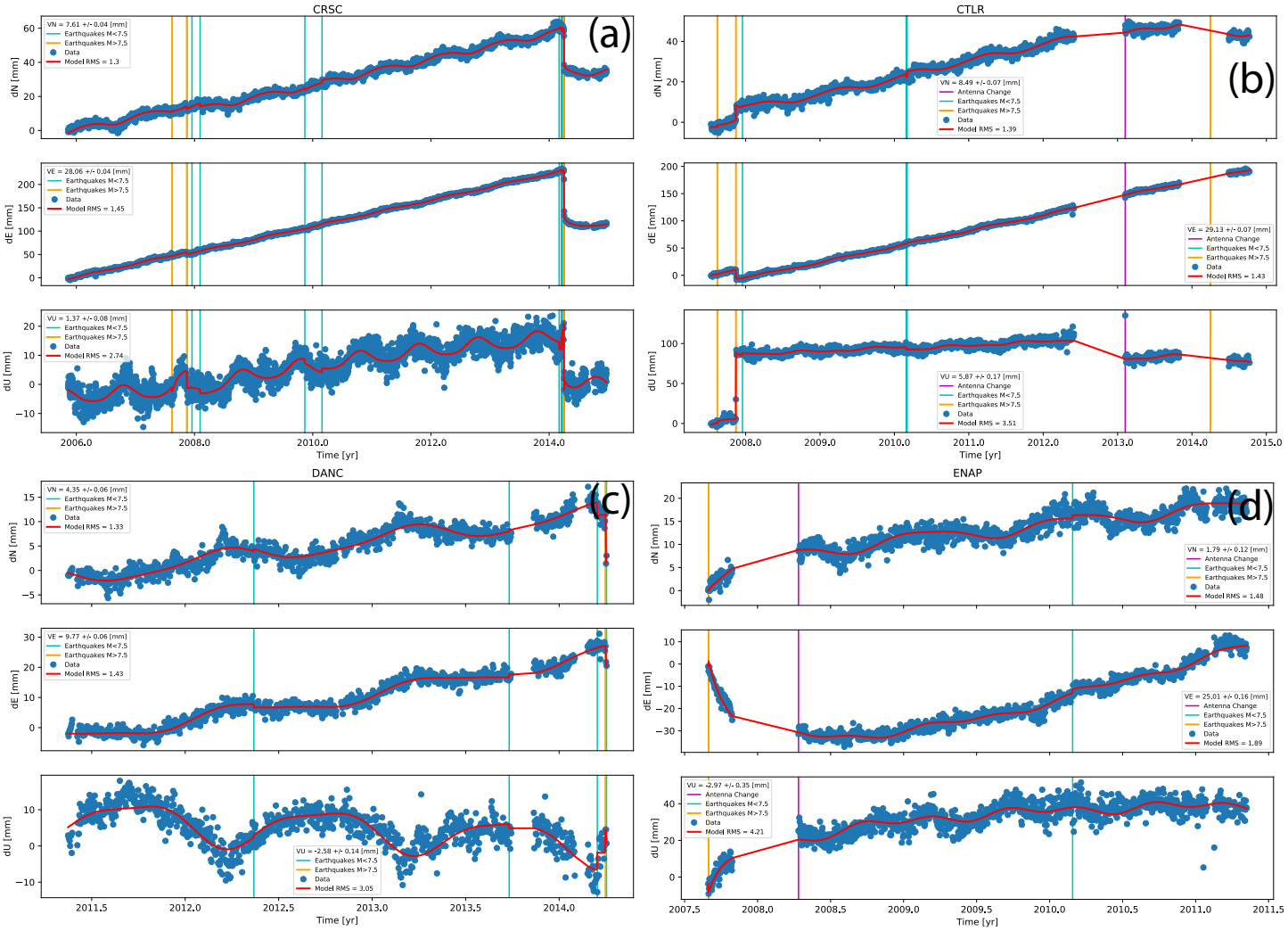

Figure A.4: Same caption as in Figure A.1, but for (a) CRSC, (b) CTLR, (c) DANC and (d) ENAP stations.

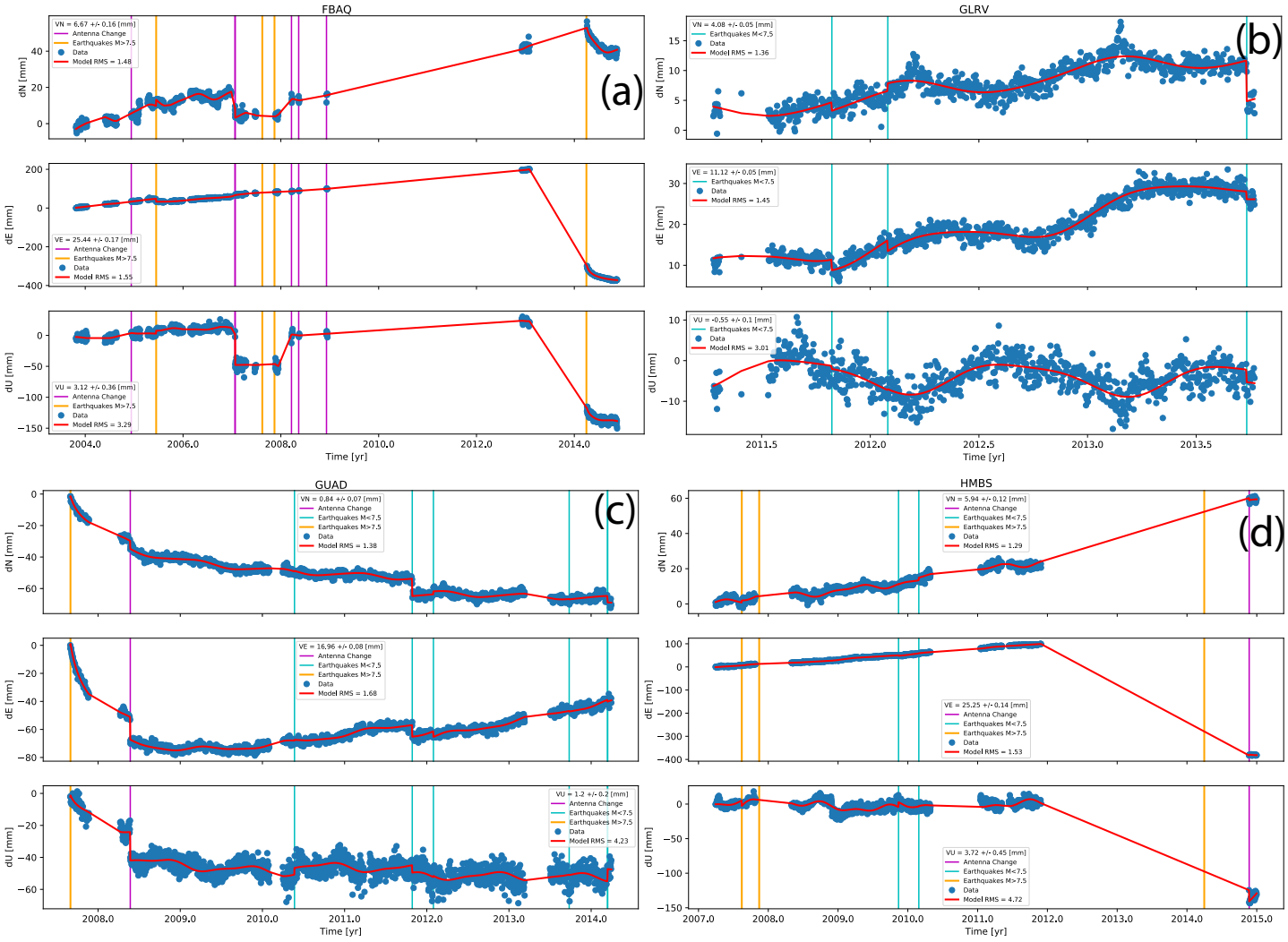

Figure A.5: Same caption as in Figure A.1, but for (a) FBAQ, (b) GLRV, (c) GUAD and (d) HMBS stations.

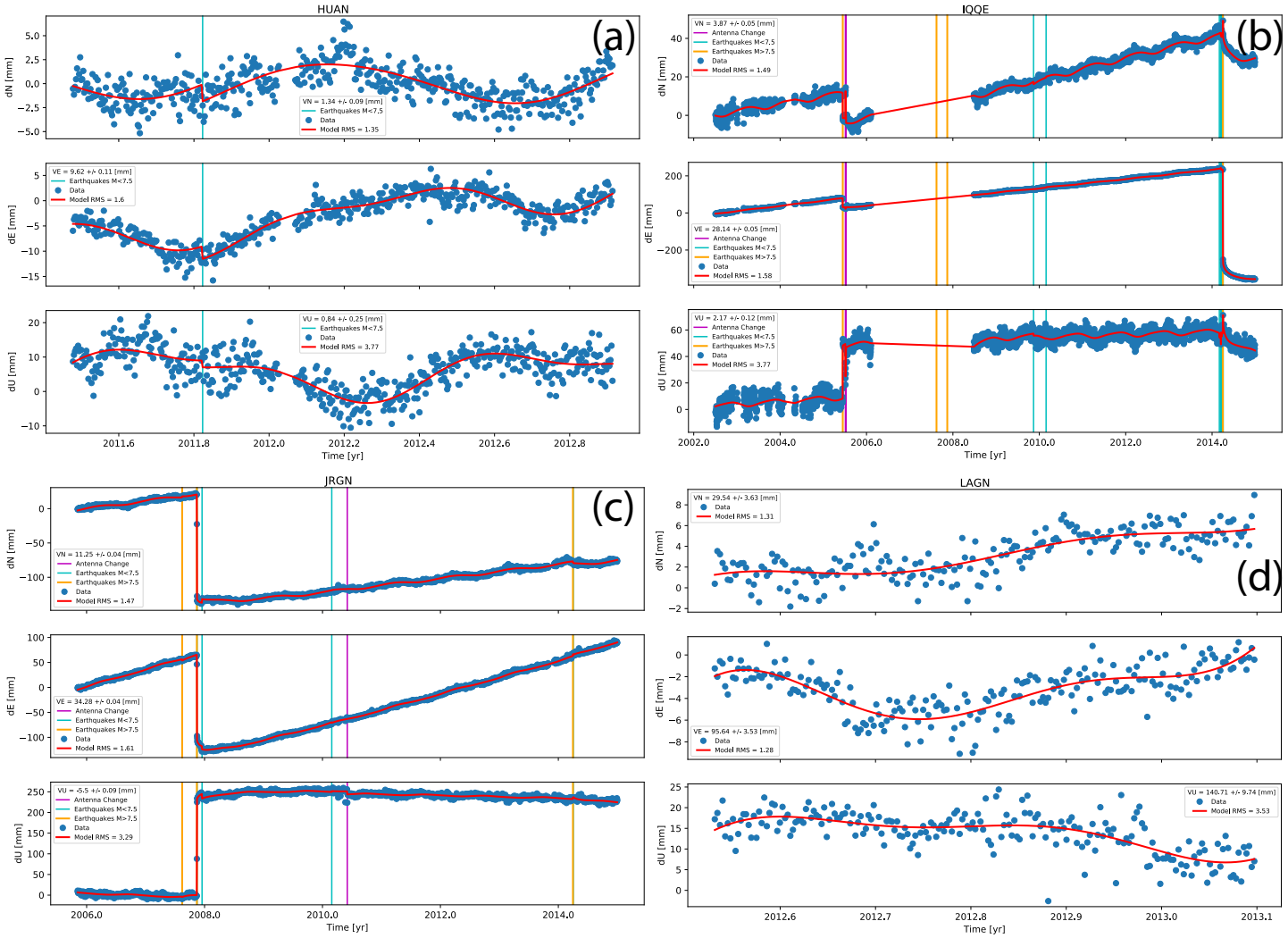

Figure A.6: Same caption as in Figure A.1, but for (a) HUAN, (b) IQQE, (c) JRGN and (d) LAGN stations.

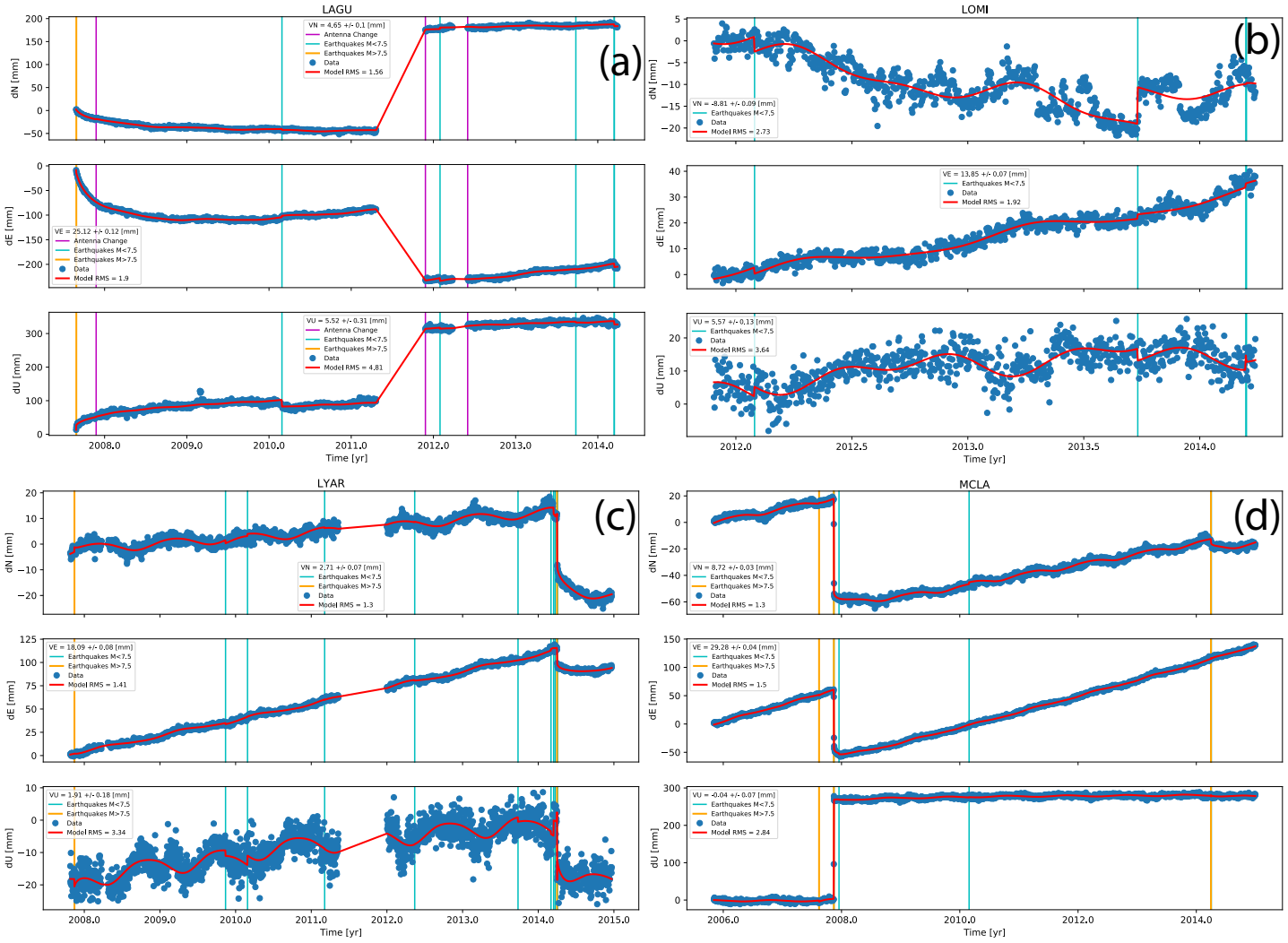

Figure A.7: Same caption as in Figure A.1, but for (a) LAGU, (b) LOMI, (c) LYAR and (d) MCLA stations.

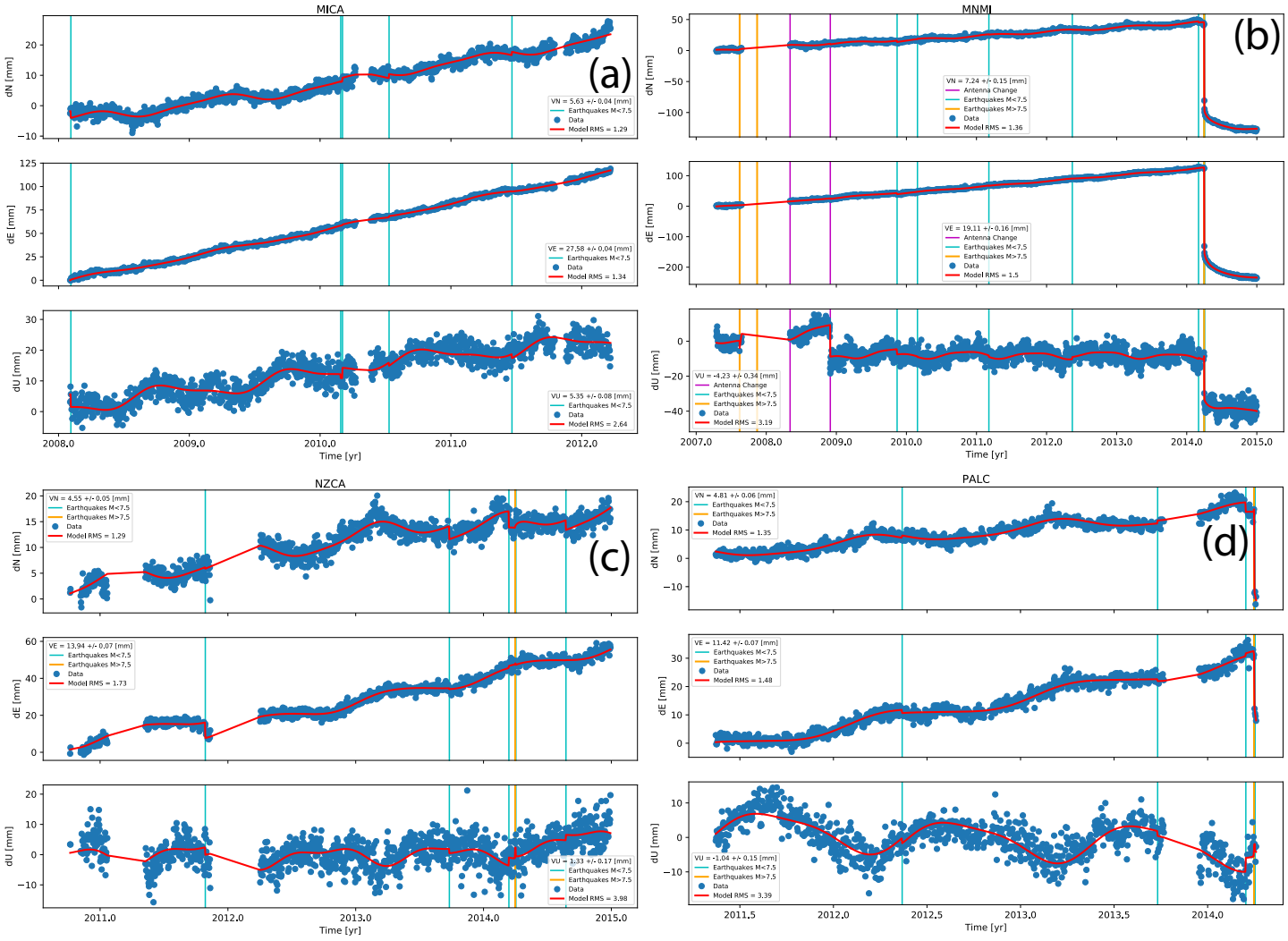

Figure A.8: Same caption as in Figure A.1, but for (a) MICA, (b) MNMI, (c) NZCA and (d) PALC stations.

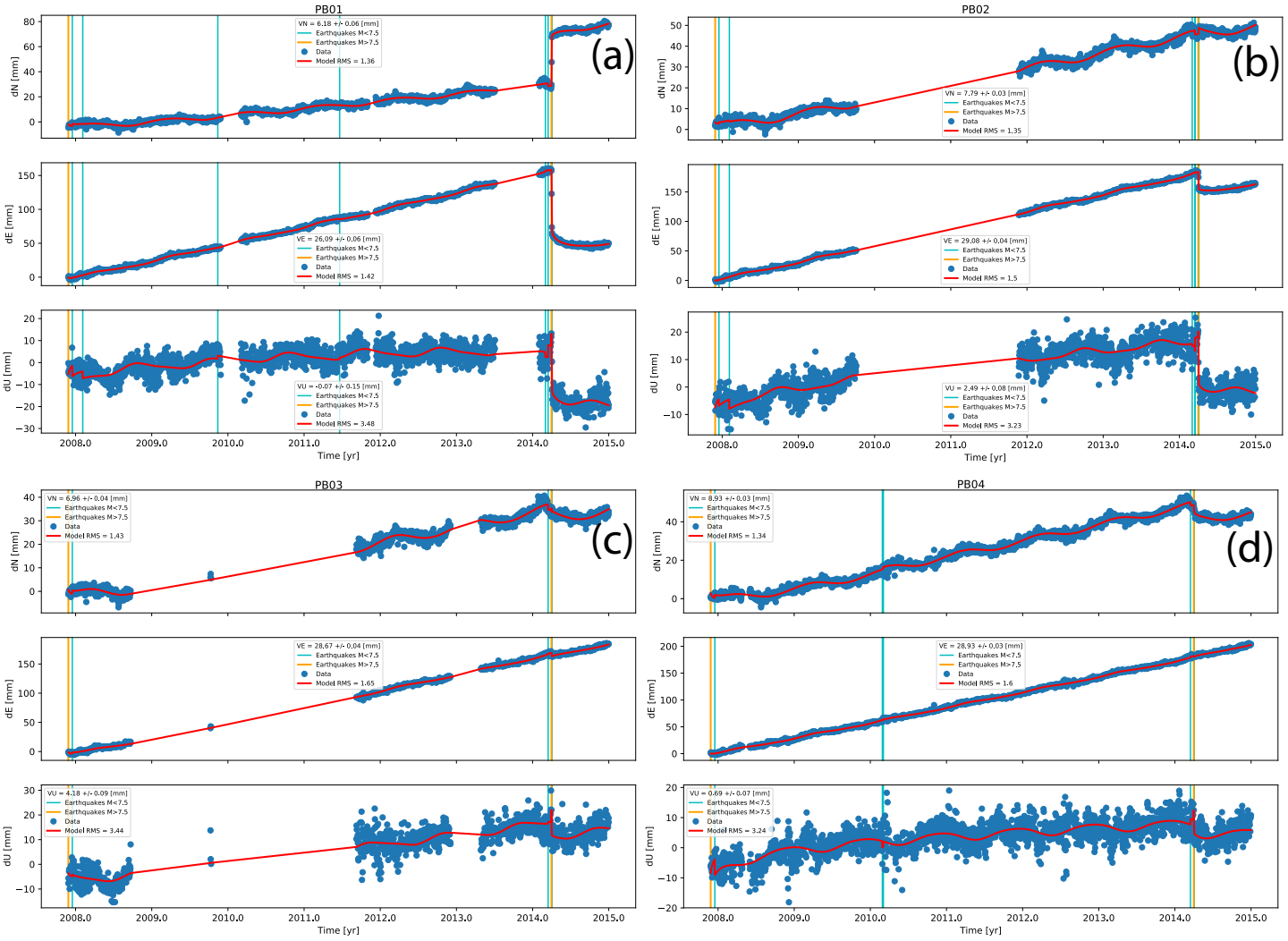

Figure A.9: Same caption as in Figure A.1, but for (a) PB01, (b) PB02, (c) PB03 and (d) PB04 stations.

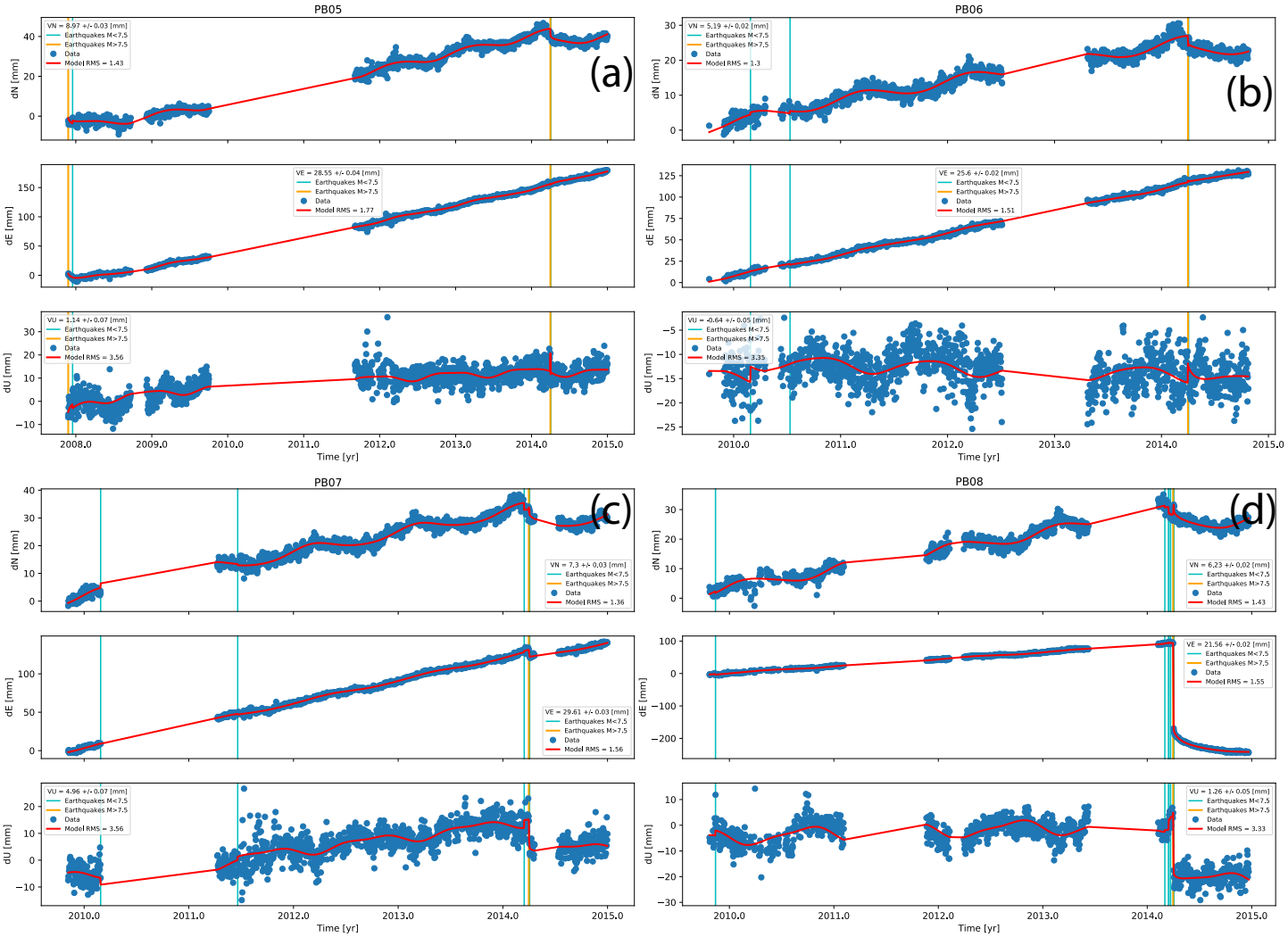

Figure A.10: Same caption as in Figure A.1, but for (a) PB05, (b) PB06, (c) PB07 and (d) PB08 stations.

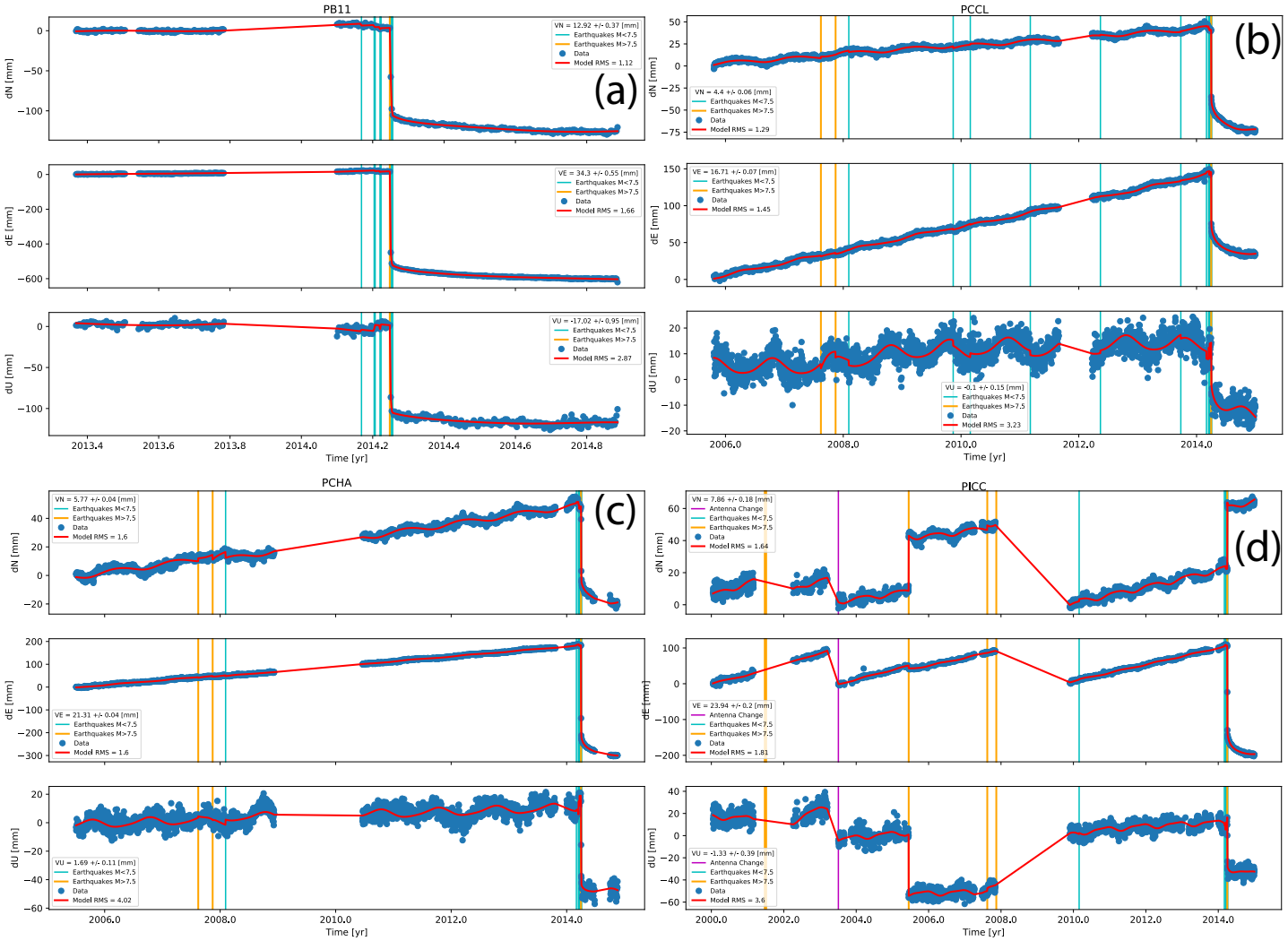

Figure A.11: Same caption as in Figure A.1, but for (a) PB11, (b) PCCL, (c) PCHA and (d) PICC stations.

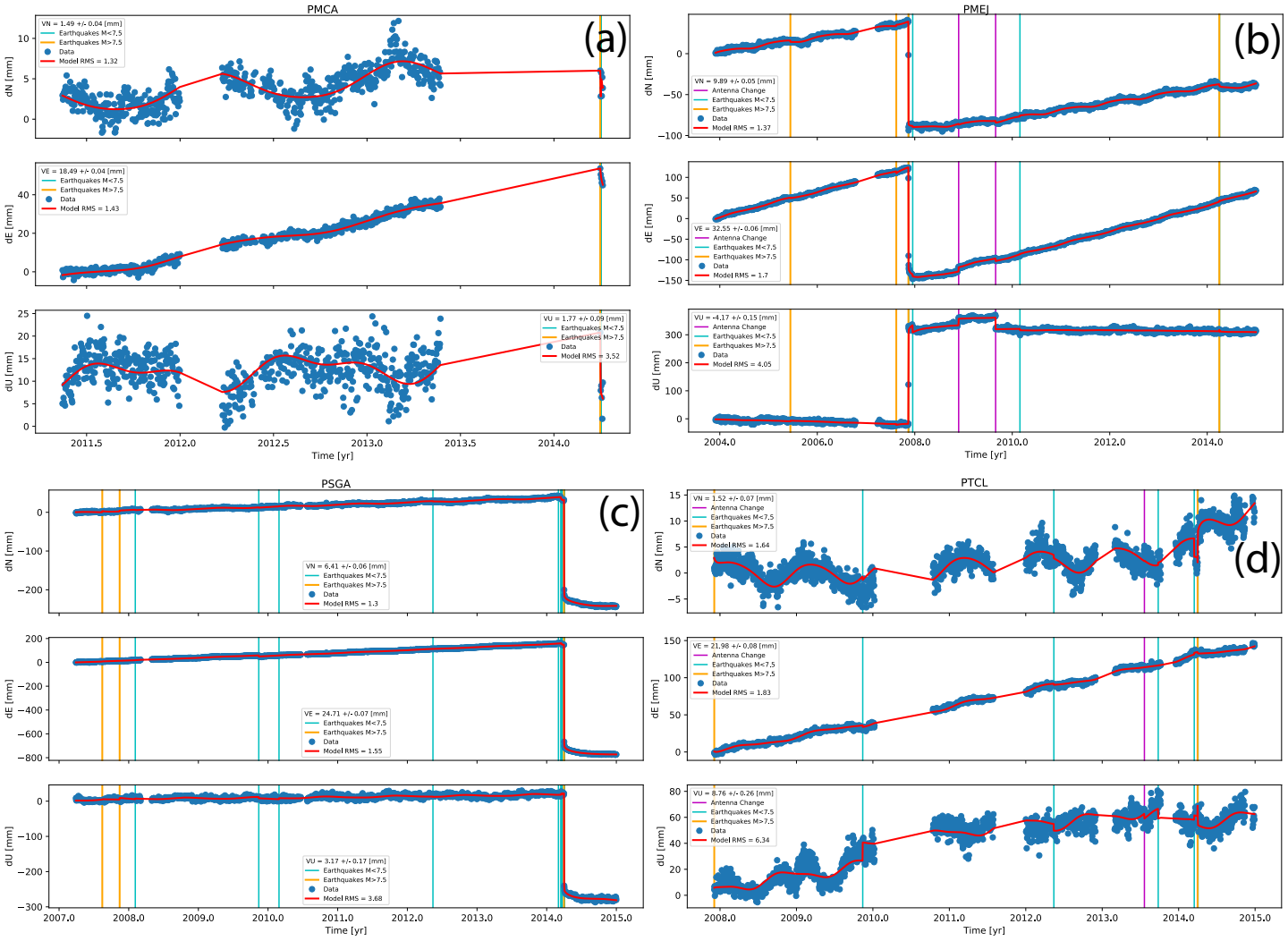

Figure A.12: Same caption as in Figure A.1, but for (a) PMCA, (b) PMEJ, (c) PSGA and (d) PTCL stations.

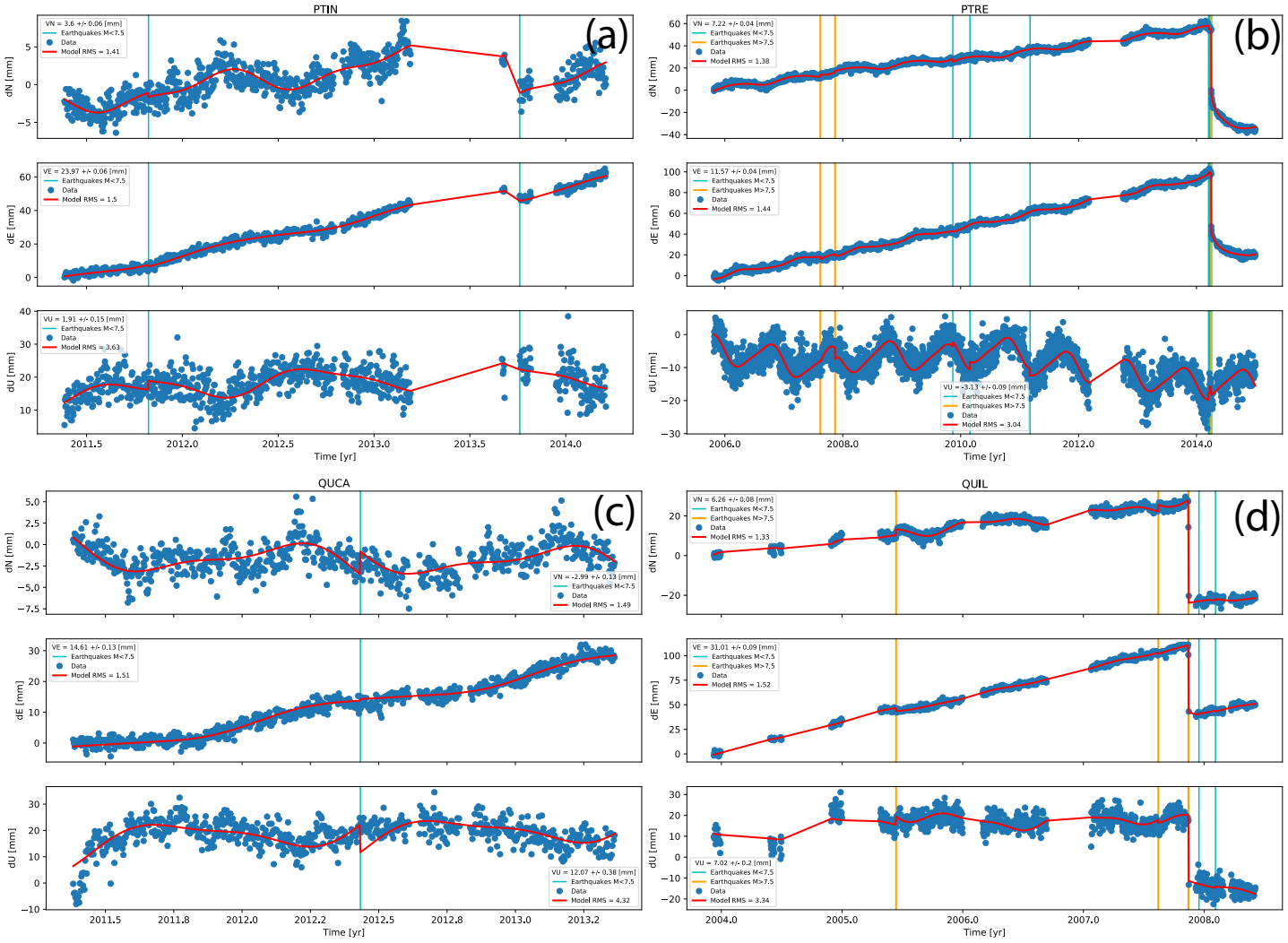

Figure A.13: Same caption as in Figure A.1, but for (a) PTIN, (b) PTRE, (c) QUCA and (d) QUIL stations.

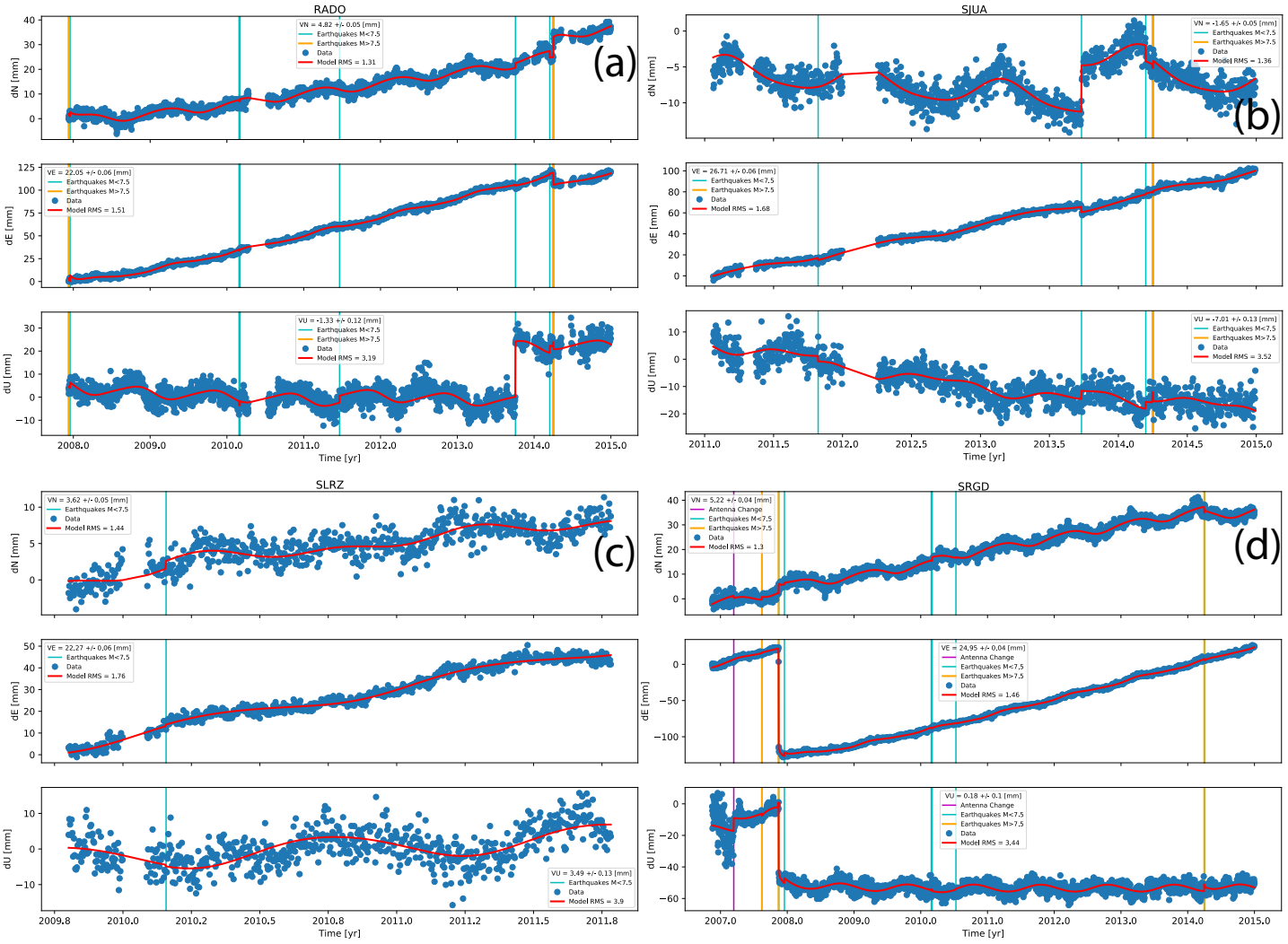

Figure A.14: Same caption as in Figure A.1, but for (a) RADO, (b) SJUA, (c) SLRZ and (d) SRGD stations.

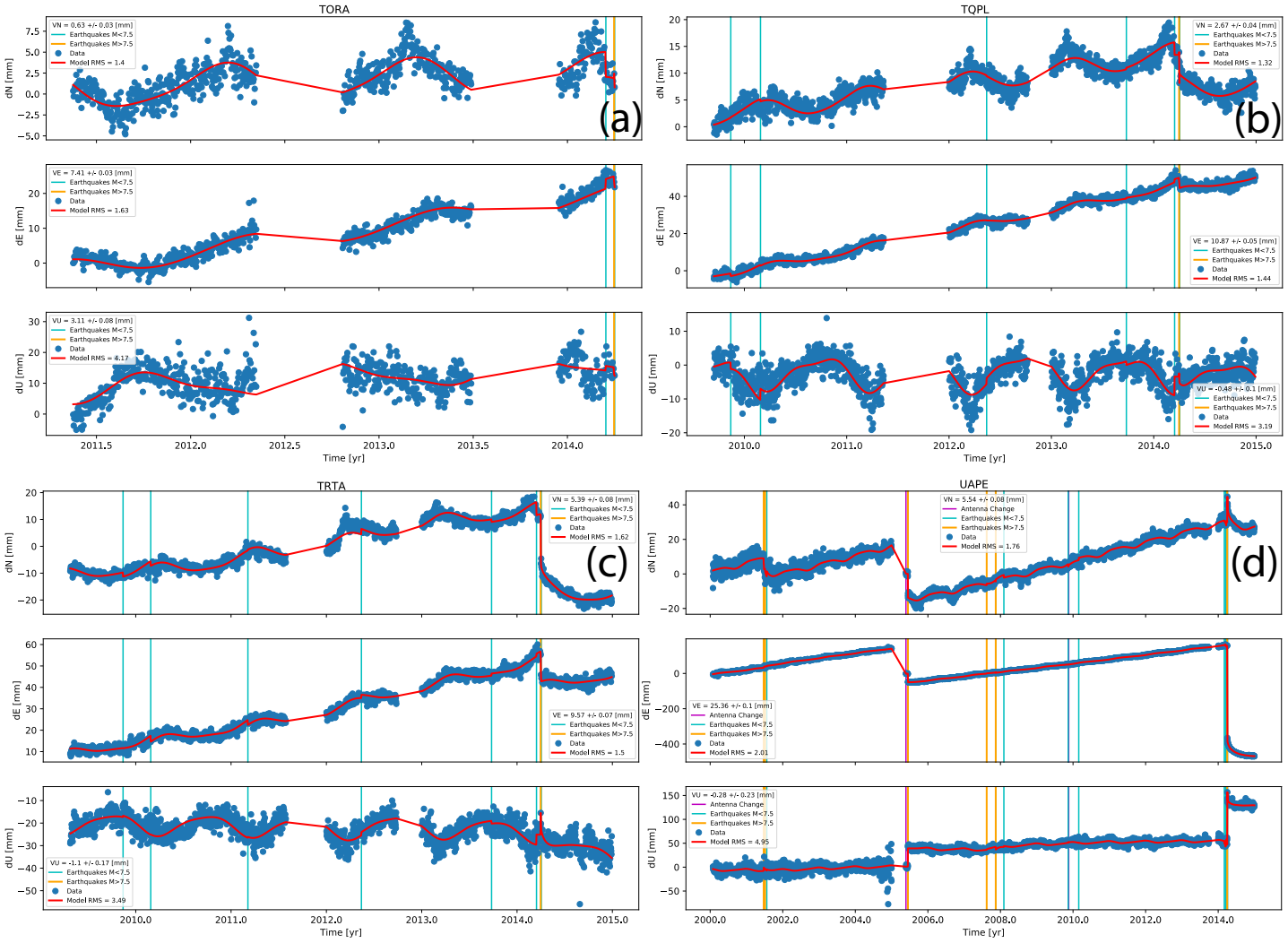

Figure A.15: Same caption as in Figure A.1, but for (a) TORA, (b) TQPL, (c) TRTA and (d) UAPE stations.

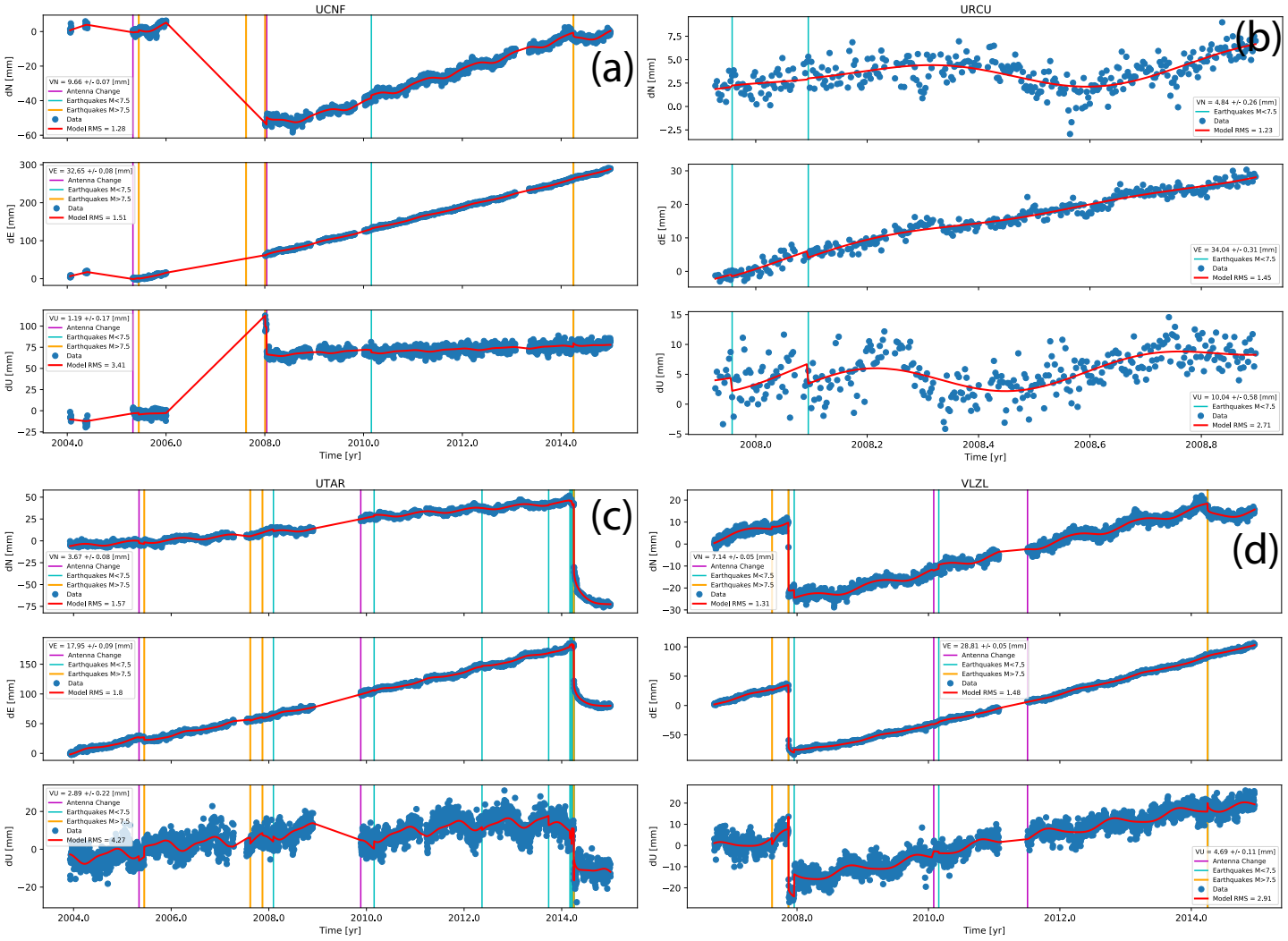

Figure A.16: Same caption as in Figure A.1, but for (a) UCNF, (b) URCU, (c) UTAR and (d) VLZL stations.